ELECTROCHEMICAL WATER DESALINATION FOR ION SEPARATION TOWARD ION-SELECTIVITY AND SUSTAINABLE MATERIALS

Dissertation
zur Erlangung des Grades
der Doktorin der Naturwissenschaften
der Naturwissenschaftlich-Technischen Fakultät
der Universität des Saarlandes

von

Panyu Ren

Saarbrücken
February 2025

Tag des Kolloquiums: 26.05.2025

Dekan:	Prof. Dr.-Ing. Dirk Bähre
Berichterstatter:	Prof. Dr. Volker Presser
	Priv.-Doz. Dr.-Ing. Guido Falk
Akad. Mitglied:	Dr. Christoph Zollitsch
Vorsitz:	Prof. Dr.-Ing. Markus Gallei

Abstract

The challenges of freshwater shortages and energy depletion in the 21st century are intensifying due to the unprecedented growth in the global population and the fast advancement in modern industry. Electrochemical water treatment technologies have developed promising solutions for tackling global water scarcity and contamination challenges. Capacitive deionization (CDI) was considered economically feasible for various scenarios, particularly in achieving efficient ion separation and selectivity. Carbon materials have been the most widely and deeply studied in electrochemical desalination for decades. Most research has emphasized the design of small, highly porous, or chemically modified carbon materials. This dissertation explores the correlation between electrode materials properties and ion separation/selectivity performance. The main focus is on investigating static CDI electrodes and flowable electrodes. Based on electrode properties such as particle size, pore structure, components, and viscosity (especially for flowable electrodes), the mechanisms of electrochemical ion separation during charge transfer and ion electrosorption processes were revealed. This thesis also explores redox flow batteries for continuous and effective recovery of lithium ions from seawater and the removal of contaminants from wastewater. Furthermore, this work also considers the feasibility of repurposing electrodes for sustainable end-of-life management.

Zusammenfassung

Die Herausforderungen der Wasser- und Energieknappheit im 21. Jahrhundert verschärfen sich durch das rapide Bevölkerungswachstum und den schnellen Fortschritt der modernen Industrie. Elektrochemische Wasseraufbereitungstechnologien bieten vielversprechende Lösungen gegen globale Wasserknappheit und Kontaminationsprobleme. Kapazitive Deionisation (CDI) gilt als wirtschaftlich machbar für verschiedene Anwendungsbereiche, insbesondere für effiziente Ionentrennung und hohe Selektivität. Kohlenstoffmaterialien wurden dabei am intensivsten untersucht, wobei der Fokus meist auf kleinen, hochporösen oder chemisch modifizierten Strukturen lag. Diese Dissertation untersucht die Korrelation zwischen den Eigenschaften von Elektrodenmaterialien und der Leistung bei der Ionentrennung/-selektivität. Der Schwerpunkt liegt auf der Untersuchung statischer CDI-Elektroden und fließfähiger Elektroden. Basierend auf Eigenschaften der Elektroden wie Partikelgröße, Porenstruktur, Komponenten und Viskosität (insbesondere bei fließfähigen Elektroden) wurden die elektrochemischen Mechanismen der Ionenadsorption und der Ladungsübertragungsprozesse offenlegt. Darüber hinaus werden Redox-Fluss-Batterien untersucht, die eine effizientere und kontinuierlichere Gewinnung von Lithiumionen aus Meerwasser sowie die Entfernung von Kontaminationen aus Abwasser ermöglichen. Zudem wird die Möglichkeit der Wiederverwendung von Elektroden im Hinblick auf ein nachhaltiges End-of-Life-Management geprüft.

Acknowledgments

I sincerely express my deep appreciation to everyone who contributed to completing my doctoral dissertation. The guidance, encouragement, and support I received have allowed me to complete this dissertation and facilitated my growth as a researcher.

I would like first to express my gratitude to my supervisor, Prof. Dr. Volker Presser, for deeply inspiring my interest in the research area of electrochemical water treatment. His expertise was instrumental in developing the research framework and methodology, and his valuable feedback motivated me to refine my thinking and enhance the quality of my work. His guidance was invaluable at every stage of my research process, especially when encountering bottlenecks in my study. He was extremely patient in teaching me how to write a compelling research article that was clear for readers to understand and engaging enough to hold their interest. Thanks to my supervisor's help and support, I have achieved remarkable results in completing my doctoral degree.

I would also like to thank Dr. Guido Falk from Saarland University. His support and guidance during my doctoral studies and his role as the second reviewer for my doctoral thesis were invaluable.

Working in the energy materials group (EMG) at Leibniz Institute for New Materials (INM) makes me grow a lot during my Ph.D. period. I want to thank Dr. Samantha Husmann, Dr. Yuan Zhang, Dr. Wang Lei, Dr. Stefanie Arnold, Bin Wang, Dr. Mohammad Torkamanzadeh, Jean Gustavo Ruthes, Dr. Delvina Tarimo, Dr. Gracita Tomboc, Dr. Meenu Meenu Dr. Mingren Liu, Dejia Liu, Liying Xue, Thi Thao Le, Cansu Kök, Peter Burger, Saïd Mondahchouo, Amir Haghipour, Chiraz Layouni, and Zeyu Fu for all the excellent support and warm encouragement either in life or research. Many thanks to Robert Drumm for his superb technical support, Andrea Jung for her measurement support, and all the members of the INM workshop for their valuable contributions. In addition, collaborating with Dr. Choonsoo Kim outside of INM was a remarkable experience. His kind and robust support significantly contributed to the success of the publications.

Finally, I want to thank my parents and my fiancé, Yizhang Tang, for their wise counsel and unwavering support. No matter the happy moments or the difficult times, they have always been there for me. Thank you very much for everything.

Contents

1. Motivation

Ongoing economic development, rapidly rising population, climate change, environmental pollution, and land development are worsening the depletion of freshwater resources.[1] By 2025, the Food and Agriculture Organization (FAO) predicts that 1.8 billion people will encounter absolute water scarcity, while $^2/_3$ of the world's population is anticipated to experience water stress.[2] Most of our planet's water is not potable; nearly 76 % of the Earth is covered by water, 96.5 % is seawater, and only 3.5 % is freshwater.[3] Water scarcity has emerged as an urgent issue affecting a growing number of countries. Particularly impacted regions include Central Asia, South Asia, and North Africa, where the situation is considered extremely critical. Even nations with a well-developed infrastructure, such as the United States of America, experience unprecedented drops in water levels.[4] As the world's population expands and living standards improve, the global demand for clean water is growing rapidly, and natural freshwater supplies are proving insufficient to meet the rising need for safe drinking water. Therefore, desalination addresses a technology to combat the anticipated water shortages in the years ahead.[1, 5]

Driven by electricity produced from renewable energy, electrochemical technologies have emerged as a sustainable and efficient desalination strategy. Many current electrochemical water desalination technologies have achieved significant advancements but still demonstrate some drawbacks and limitations. Thus, it is crucial to develop more energy-efficient and high-performance desalination technologies. This dissertation focuses on studying static and flowable electrodes for electrochemical water desalination, emphasizing exploring ion and charge transport mechanisms during the electrochemical process. The properties of various carbon materials, such as pore structure and surface functional groups, substantially impact the ion separation performance, highlighting the importance of understanding the mechanisms behind these effects in more detail. Considering the importance of sustainability in electrochemical technologies, electrode repurposing facilitates resource consolidation and recycling, aligning with the principles of sustainable development.

2. Theoretical Background

2.1. Water desalination

Desalination is necessary for procuring fresh water, which is defined as the technical process of converting saline sources, such as brackish water or seawater, into potable water. Beyond producing potable water, desalination is also essential for regulating salt levels in industrial process water, supporting pharmaceutical and chemical manufacturing, and enabling water supply for agriculture. This technology has a wide range of applications across multiple sectors, making it integral to meeting diverse water demands.[6] For decades, remarkable advances have been made in developing water desalination technologies. Currently, available desalination technologies can be divided into three primary categories: thermally-driven desalination, pressure-driven membrane desalination, and electro-driven desalination (**Figure 1**),[7] including multi-stage flash evaporation (MSF),[8] multi-effect distillation (MED),[9] and reverse osmosis (RO),[10, 11] electrodialysis (ED),[12, 13] CDI,[14, 15] and flow electrode capacitive deionization (FCDI),[16, 17] which led to substantial advancements in the economic viability and technical efficiency of desalination processes.

Thermally-driven desalination via MSF has been widely implemented as a primary desalination method due to the fact that 34 % of total freshwater production is generated through this method.[18] However, the MSF water recovery rate is relatively low, and the process requires harsh operating conditions, including high temperatures and pressures.[19] Over time, inefficiencies can arise due to fouling on process equipment, where mineral and salt deposits accumulate, reducing the system's effectiveness.[20] This fouling not only diminishes heat transfer efficiency but also increases energy consumption and maintenance needs, leading to operational inefficiencies after prolonged use.[21]

RO is an efficient and practically applicable water purification technology that removes dissolved salts by utilizing pressure to force water through a semi-permeable membrane.[22] This process enables water to flow through while blocking contaminants, making RO ideal for desalination and producing high-quality drinking water.[23] Although membrane-based technologies such as RO are effective methods for purifying water, from which the majority of freshwater is obtained, there are also some limitations, including high energy consumption, expensive membrane costs, and limited applicability that need to be near coastal areas.[24]

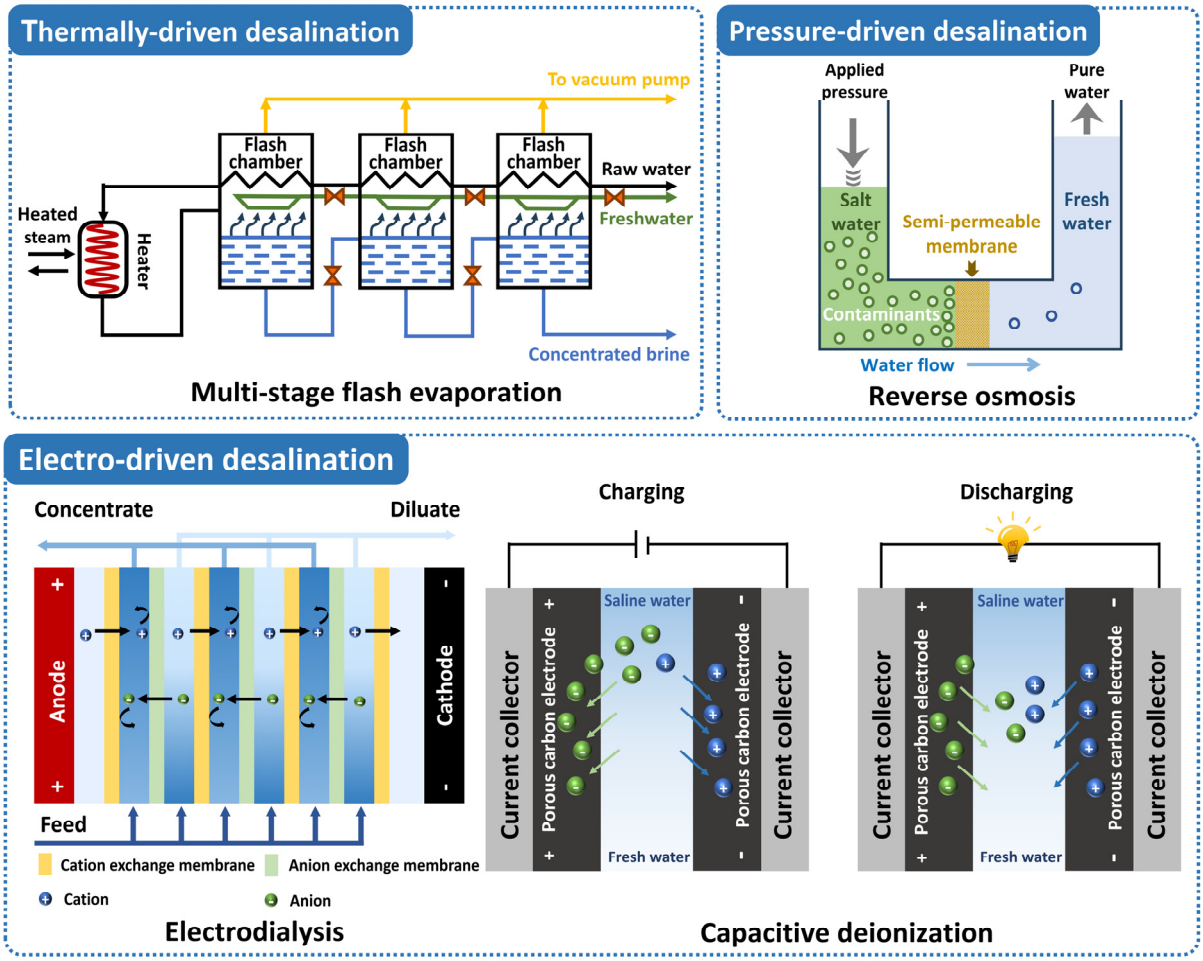

Figure 1 Schematic diagrams illustrate the main water desalination technologies, categorized into three types: (A) thermally-driven desalination, this figure adapted from [8]; (B) pressure-driven membrane desalination, this figure adapted from [25]; and (C) electro-driven desalination, this figure adapted from [12, 26].

Like RO, ED is another desalination method that relies on membranes. Both methods use membranes to separate ions from the influent. However, electro-driven desalination does not require high pressures or temperatures, making ED technology account for about 6 % of global brackish water desalination capacity.[27] ED relies on an electric field and employs ion exchange membranes (IEMs) to remove ions through them, which renders it particularly energy-efficient for desalinating brackish groundwater.[28, 29] In contrast to the high energy consumption of ED in electrically driven desalination technology, CDI utilizes porous electrodes to remove ions from aqueous solutions through electrosorption at a low applied potential.[30] This approach provides a more energy-efficient desalination process and has the potential to achieve better energy efficiency and ion selectivity compared to ED.[31]

2.2. Capacitive deionization

CDI operates on the principle of removing charged species from aqueous solutions through electrosorption.[26, 32] Typically, when a small electrical potential (below 1.2 V) is applied to a pair of static porous carbon electrodes, charged species in the solution are captured within the electrode, producing freshwater. Once the electrodes reach saturation, polarity reversal or short-circuiting is used to release the captured ions back into the solution, generating a concentrated brine stream. These reversible electrochemical processes are promising for energy-efficient water treatment.[33] The subject of CDI has been fundamentally studied, focusing on theoretical modeling, [34, 35] mechanisms,[36, 37] the design of electrode materials,[38, 39] and cell architectures.[34, 40] These investigations aim to enhance the desalination capacity, ion selectivity, and energy efficiency of CDI systems.

2.2.1. Mechanisms of capacitive deionization

Many theories and models have been proposed to explain the mechanism of ion electrosorption in porous carbon electrodes, one of the most notable being the electrical double layer (EDL) theory structure described by the Gouy-Chapman-Stern (GCS) theory (**Figure 2A**).[41] According to this theory, a bilayer consists of a diffuse layer containing distributed ions within electrolyte-filled pores and a dielectric layer that separates the diffuse layer from the carbon substrate.[39, 41-44] The modified Donnan Model theory suggests that electrosorption is influenced by factors such as pore size, the specific surface area of the material, and the concentration of the salt solution.[45] For microporous carbon materials with average pore diameters below 2 nm, there is a significant overlap of the EDL at the pore walls as the pore diameter is smaller than the Debye length. This model introduces the so-called Stern layer, the region where ions are closest to the charged surface, incorporating an additional chemical attraction force for ions to move from the macropores into the micropores (**Figure 2B**).[32]

In practice, typical CDI electrodes often experience significant overlap of EDL due to pore size limitation, especially in microporous structures, resulting in charge efficiencies below 100 %.[46] Consequently, the pore size and ion size strongly influence the distribution of ions on the microporous surface of the electrode, as well as the repulsive effect of the EDL within the pore, impacting the adsorption capacity of the electrode material.[47] Generally, micropores (<2 nm) increase specific surface area, thus enhancing CDI desalination capacity,

while mesopores (2-50 nm) facilitate ion transport, thereby improving desalination rates.[48] Electrodes adsorption capacity can be improved by tuning the pore structure and specific surface area of the electrode materials.[49] Hierarchical porous structures, which facilitate the formation of ion transport channels, further enable ion adsorption.[50] Studies focusing on specific ion adsorption aim to determine optimal pore structures that align with hydrated radii, providing a valuable approach to enhance CDI performance.

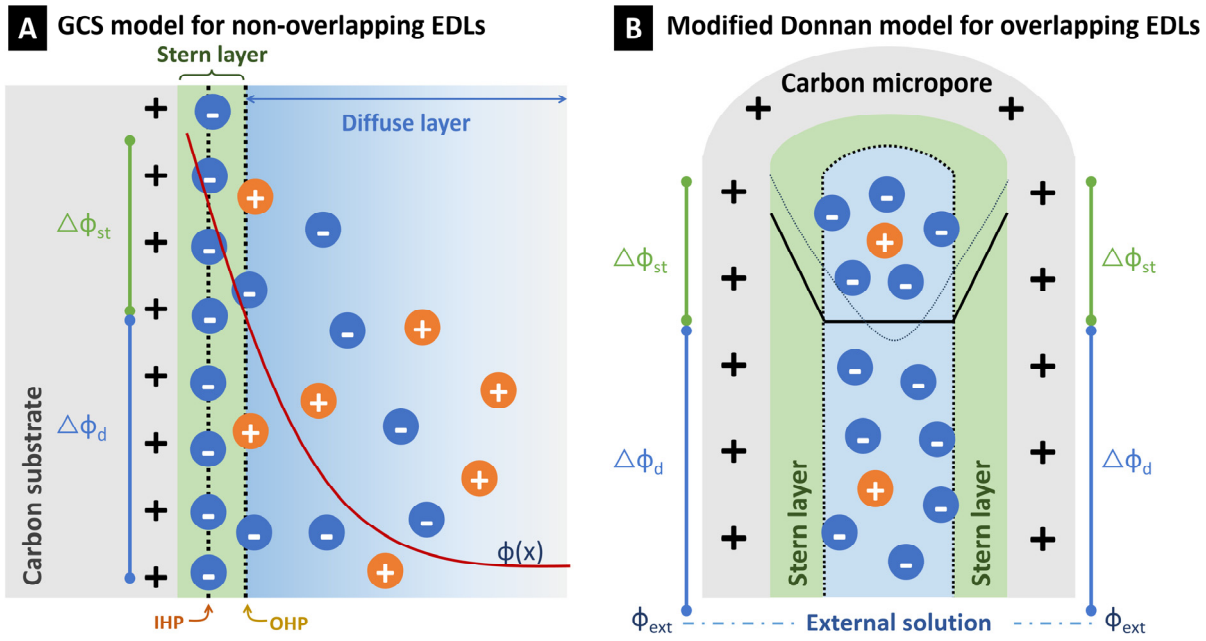

Figure 2 The models of charge and ion storage in porous CDI electrodes. a) Structure of the EDL based on the GCS theory,[32] b) modified Donnan Model. Figure adapted from [26].

The ion concentration of feedwater also influences both the ion electrosorption capacity and charge efficiency of CDI carbon electrodes. Studies indicate that symmetric CDI systems based on porous carbon materials can achieve stable desalination with feedwater concentrations in the range of 5-20 mM.[51] Typically, open porous networks require adding IEMs or designing a charge transfer process to achieve ion permselectivity. Without permselectivity, the charge in the carbon porous network is balanced through the simultaneous release of co-ions and immobilization of counterions. At feedwater concentrations exceeding approximately 100-200 mM, the release of co-ions can lower the system's charge efficiency to below 100 %, potentially affecting the desalination process.[33] When the feedwater concentration is low, its low conductivity leads to high resistance during the desalination process, resulting in reduced specific adsorption capacity of the electrode. Conversely, when the feedwater

concentration is high, and the system is under an open-circuit or low-voltage state, the porous CDI electrode could adsorb both anions and cations into the pores due to its non-selective properties (**Figure 3Ai**). In continuous charging, ions need to undergo two key processes: co-ion repulsion (**Figure 3Aii**) and ion exchange (**Figure 3Aiii**) before reaching the counterion uptake stage (**Figure 3Aiv**), as governed by the charge compensation mechanism.[52] The corresponding ion concentration in the solution decreases steadily only when the desalination cell voltage is raised above a specific threshold (**Figure 3B**). Therefore, in the practical charging process, the effective charge used for counterion adsorption is only a part of the total input charge, which causes the charge efficiency to be less than 100 %. Based on the above theoretical analysis, simply increasing the discharge voltage from 0 V to 0.3 V can reduce the charge input required for co-ion repulsion in the initial stage and then improve the charge efficiency during the desalination process.[53]

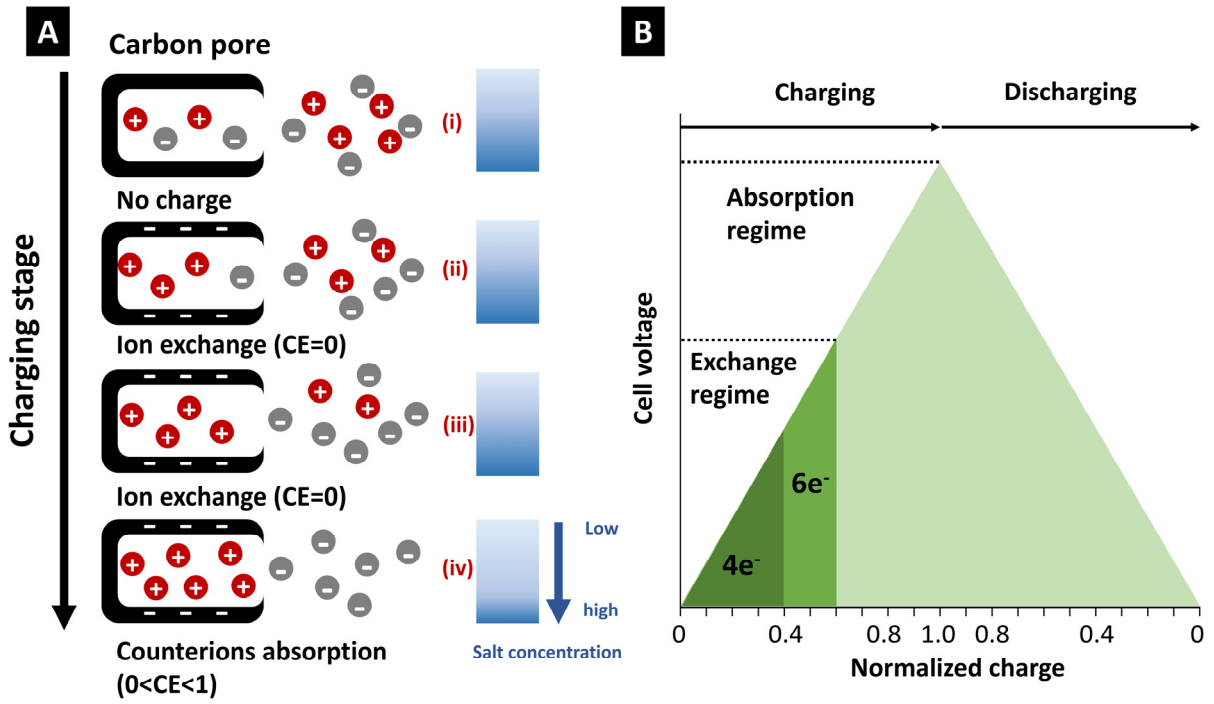

Figure 3 Ion exchange process and corresponding brine concentration change in nanopore during electrode charging. (a) From ion exchange to counterion adsorption process, (b) corresponding voltage and input charge. Figure adapted from [33].

2.2.2. Mechanisms of Faradaic ion separation

The ion separation mechanism based on EDLc has been discussed above. In addition, the deionization mechanism involving Faradaic reactions pertains to ions captured during the charge transfer process. These can be categorized into the following main types: insertion reaction, surface redox, conversion reaction, and charge compensation with redox electrolyte.[54]

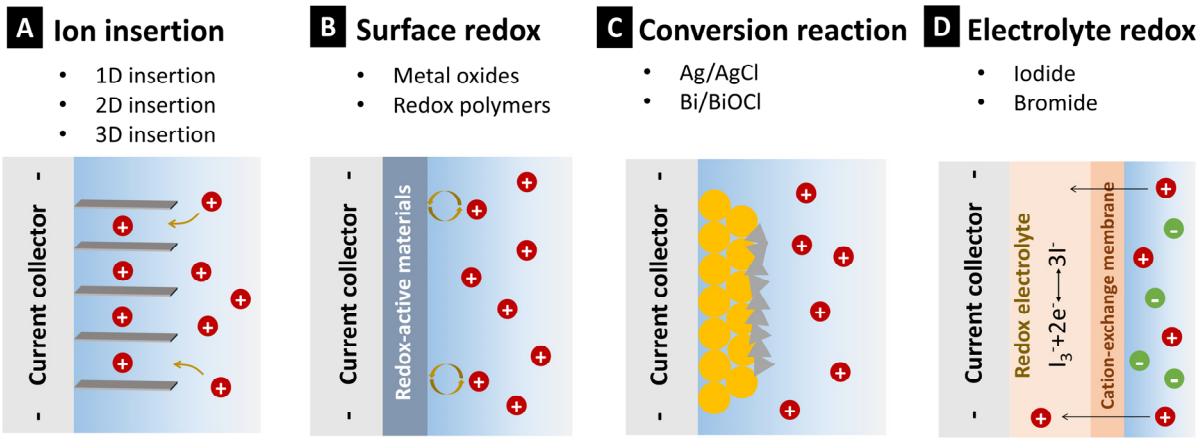

Figure 4 Faradaic ion removal mechanisms: A) ion insertion, B) surface redox, C) Faradaic conversion reaction, and D) charge compensation with redox electrolyte. Figure adapted from [54].

Ion capture by ion insertion or intercalation) relates the insertion of cations or anions into specific or non-specific interstitial sites of the electrode materials (**Figure 4A**). The insertion mechanism varies based on the structure of the host materials. One-dimensional (1D) insertion materials, such as tunnel-structured manganese oxides, provide channels for ion storage and transport.[55] Two-dimensional (2D), including transition metal dichalcogenides (TMDs) and MXenes, accommodate ions within their interlayer spaces.[56] Three-dimensional (3D) materials, such as lithium iron phosphate[57] or Prussian blue and its analogs[58], feature an open framework or cage-like structure that enables ion insertion from all directions and offers large spacings for ion accommodation, facilitating efficient transport and storage.[59] Due to the limitations of the electrosorption mechanism, CDI is primarily effective for low-concentration solutions. Replacing the porous carbon with MoS_2/carbon nanotube (CNT) binder-free electrodes provides good cycling stability and moderate desalination capacity in various molar concentrations.[51]

In surface redox reactions (**Figure 4B**), the charged species migrate from the bulk water to the electrode surface, where they transfer or receive electrons from the electrode. Metal oxides like MnO_2 and RuO_2 exhibit rectangular cyclic voltammograms (CV) shapes without the kinetic limiting effect.[60, 61] In contrast, redox polymers like poly(vinyl ferrocene) display battery-like CV profiles with reversible redox peaks.[62]

Typical conversion electrode materials for electrochemical ion separation are Ag/AgCl and Bi/BiOCl. For example, Cl^- in solution reacts with Ag to form AgCl during oxidation, and Cl^- is released from AgCl into feed water during reduction (**Figure 4C**). These materials show a high desalination capacity, but their enhanced charge storage capacity is usually achieved through processes with limited reversibility, and the performance may degrade over time.

Redox-active ions dissolved in an electrolyte, such as iodide, bromide, or $[Fe(CN)_6]^{3-}$, can change oxidation state by accepting or donating electrons at solid/liquid interfaces.[63, 64] For example, when applying the potential, triiodide (I_3^-) is reduced to iodide ions (I^-). To maintain charge balance in the redox electrolyte, two cations are drawn into the electrolyte, and cations migrate through the cation exchange membrane (CEM) to maintain charge neutrality in the electrolyte. Conversely, during the reverse process (oxidation of I^- back to I_3^-), the cations are expelled into the feed water (**Figure 4D**).[65] Redox-active electrolytes can offer a high charge-storage capacity due to reactions that often involve the transfer of multiple electrons.[66, 67]

2.2.3. Cell architectures and operational mode of capacitive deionization

Typical CDI cell architectures are mainly categorized into flow-by CDI, flow-through CDI, membrane CDI (MCDI), hybrid CDI (HCDI), FCDI, and battery desalination (**Figure 5**). A conventional flow-by cell comprises two current collectors that facilitate electron transfer, a pair of porous carbon electrodes responsible for capacitive (non-Faradaic) ion adsorption, and a spacer channel allowing feed water to flow through the system.[26, 68] When feed water flows directly through the electrodes, instead of between them, and parallel to the direction of the applied electric field, the cell is known as a flow-through CDI.[69, 70] It is reported that flow-by CDI demonstrated higher SAC and better charge efficiency than flow-through CDI. However, flow-through CDI demonstrated a higher average salt adsorption rate (ASAR), particularly for shorter half-cycle times.[69]

As CDI advanced, IEMs were introduced into the system. These membranes are positioned between the electrodes and the water channel to prevent co-ion expulsion, creating MCDI

cells. In this configuration, co-ions are expelled from the pores during the charging process. However, they cannot pass through the IEMs, remaining in the macropores inside of the particles. Since the macropores maintain electrical neutrality, they act as additional storage space for counterions, enhancing ion removal performance.[71-73] Lee et al. compared the desalination performance of CDI with that of MCDI and found that the salt removal rate of the MCDI was 19 % higher than that of conventional CDI.[71] The maximum salt removal rate and energy consumption were about 92 % and 1.96 Wh L^{-1} at a flow rate of 40 mL min^{-1} and an operating voltage of 1.2 V.[71] When MCDI employs the reverse discharge mode to regenerate the electrodes, up to 83 % of the energy used for charging the electrodes during desalination can be recovered, contributing to low-energy desalination.[74] Almost no H_2O_2 was generated in MCDI due to the IEMs preventing oxygen penetration, and the pH change of the treated water in the MCDI system is less than in CDI, remaining mainly within the near-neutral pH range.[75]

In 2012, the desalination battery cell was first proposed and demonstrated by Pasta et al.[76] In the latter work, the cell consists of two battery electrodes: cation adsorption/desorption and anion adsorption/desorption. IEMs could be placed in front of both electrodes.[76] This cell removes ions through the mechanism of the Faradaic process (i.e., reversible redox reactions). Na^+ is chemically intercalated in the body of the M_nO_2 electrode to form $Na_2Mn_5O_{10}$ (positive electrode). At the same time, Cl^- is captured from the feed water and transferred onto the Ag electrode (negative electrode) to form AgCl. To date, the development of new Cl^- or Na^+ capturing/intercalation electrode materials represents the key research direction for desalination batteries.[76]

Instead of the structure of the symmetric carbon materials electrode in CDI, an HCDI cell is formed by incorporating non-capacitive electrodes into the system, which offer a charge storage capacity exceeding that of conventional electric double-layer capacitance (EDLc) materials. The HCDI was first identified in 2014, and it consists of a porous carbon positive electrode, a $Na_4Mn_9O_{18}$ negative electrode, and an anion exchange membrane (AEM) placed in front of the carbon electrode. The SAC was more than double that of the conventional CDI, reaching 31 mg g^{-1}. This type of cell configuration enhances desalination performance, particularly at high molarity levels where most activated carbons are ineffective.[15, 77, 78] Torkamanzadeh et al. studied the desalination performance of $Ti_3C_2T_x$-MXene/activated-

carbon HCDI, achieving high charge efficiency of up to 85 % and stable desalination performance over 100 cycles.[79]

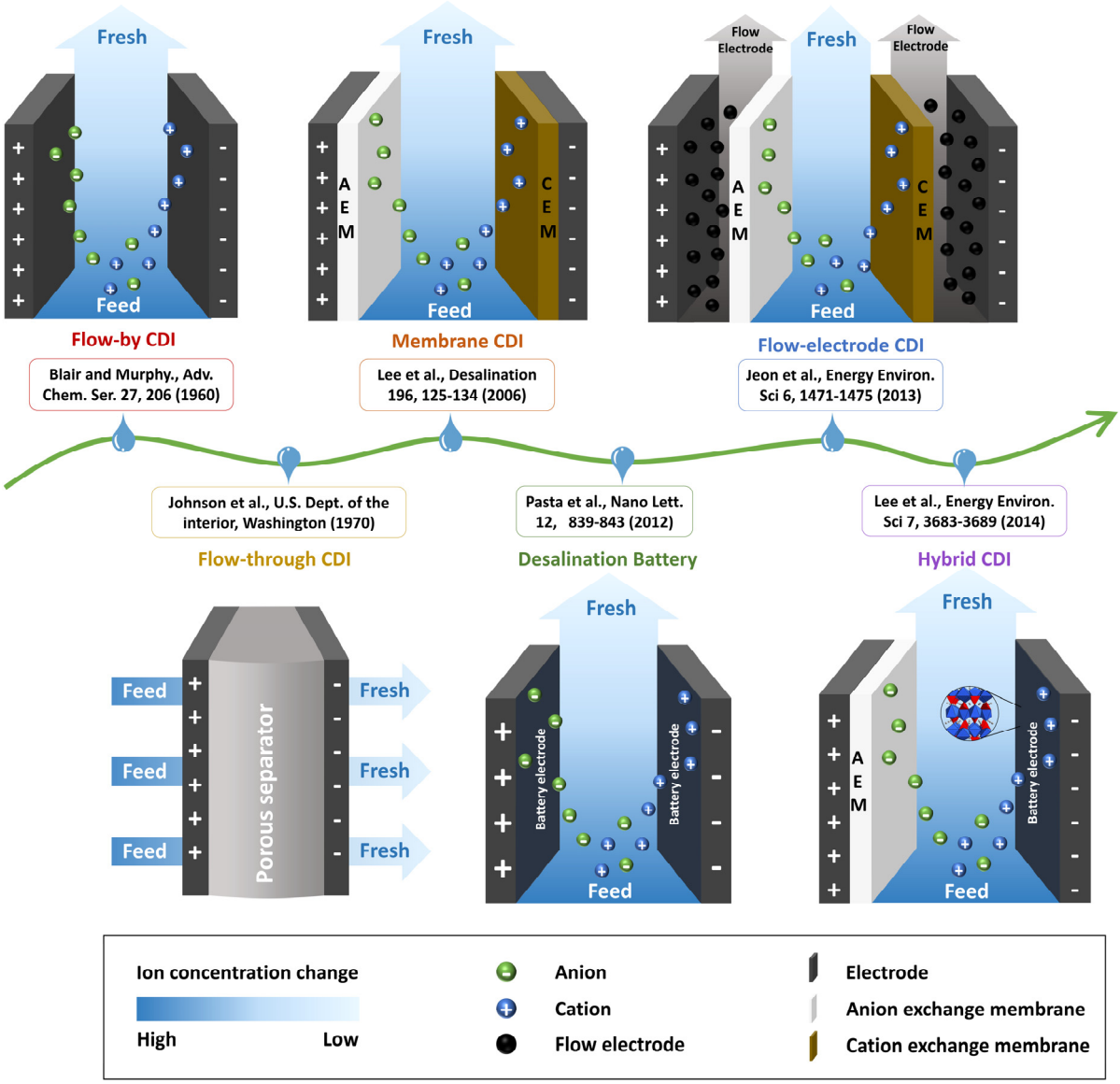

Figure 5 Typical cell configurations of various CDI. Figure adapted from [15, 76, 80-83].

Since the introduction of CDI, the cell configuration has evolved through more than half a century of innovation and development, leading to continuous advancements in desalination performance and system stability. In the type of flow-by CDI, flow-through CDI, MCDI, or HCDI, the key factor limiting desalination efficiency and practicality remains the electrode, which, in all these devices, operates as a static electrode.[84] The static electrode's mode of operation, which is not continuous, limits its suitability for high-concentration brines. In contrast, FCDI offers a constant mode of operation that addresses this limitation. Moreover, during the

desalination period, both the adsorption and desorption processes need to be conducted alternately or intermittently inside the cell, which could reduce the desalination efficiency.[85] The FCDI concept utilizes a flowing carbon slurry as the electrode rather than a static electrode positioned between the IEMs and the current collector, allowing for continuous ion separation.[86-88]

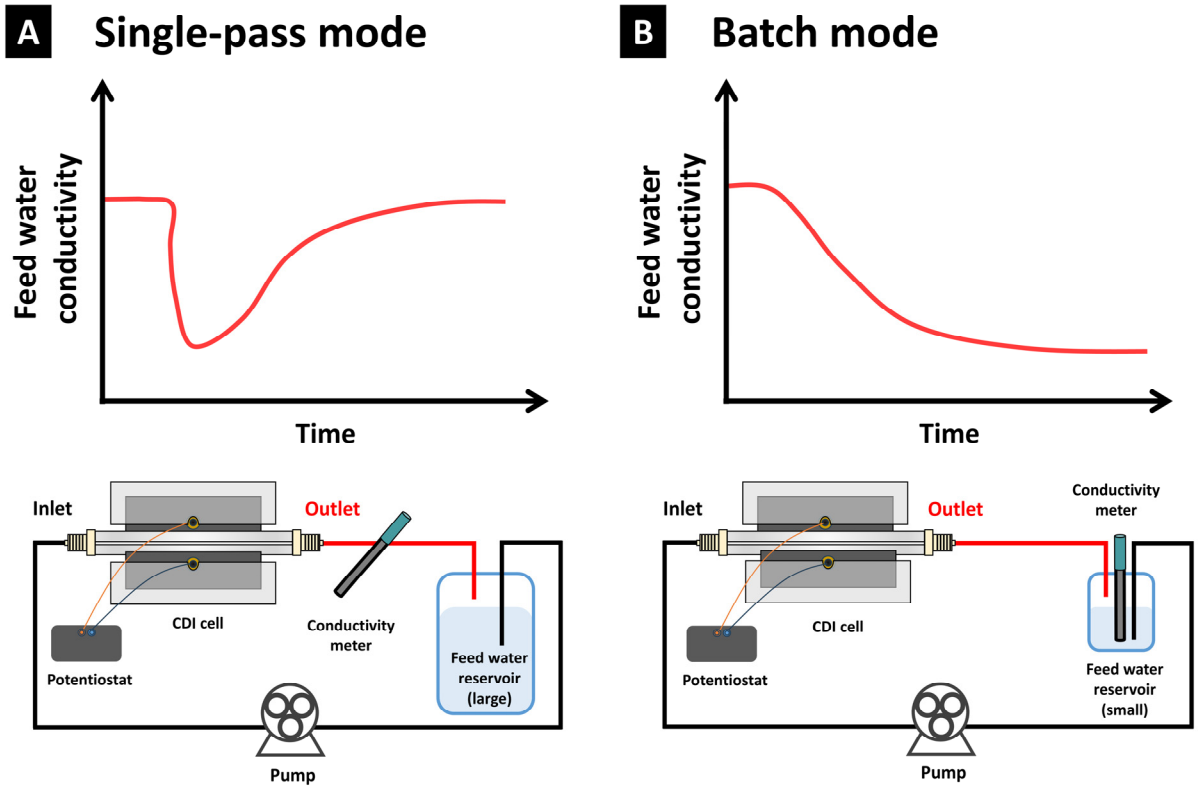

Figure 6 Schematic diagram of CDI experiments and the corresponding conductivity curves during the charging process. (A) Single-pass mode: water conductivity is monitored at the outlet of the cell, with the effluent recycled or discarded into a large feed water reservoir; (B) Batch mode: the water conductivity is measured in the small feed water reservoir, with the effluent recycled. Figure inspired by [89].

For the layout of the CDI setup used for laboratory operations, two methods are applied according to the actual location of the conductivity meter.[32] In the single-pass mode, the conductivity meter is placed at the output of the cell. During the charging stage, ions move to the electrodes under the force of the electric field, leading to a rapid decrease in conductivity. Since the outflow can be discarded or recycled into the feed water reservoir, the reservoir is sufficiently large (generally 10 L), and its total conductivity does not change. Once the

electrodes reach their adsorption limit, the outflow salinity increases again, approaching the conductivity of the feed water.[90] In the batch mode, the volume of feed water is less than in the single-pass mode, and the conductivity meter is located in the feed water container to measure the change in salinity accurately.[91] During the adsorption step, the measured conductivity gradually decreases without reaching a minimum value, eventually stabilizing at a final low level.[92] Single-pass mode is closer to the real CDI applications, with the feed water only passing through the cell once, while the batch mode is simpler to operate and analyze than single-pass mode.[93]

2.2.4. Electrode materials and preparation for capacitive deionization

The performance of CDI is primarily determined by the properties of the electrode materials. Ideally, these materials should have the following qualities: high conductivity and ion mobility;[94, 95] large specific surface area for ion adsorption;[96, 97] suitable hydrophilicity to ensure full utilization of the porous structure of the electrode;[97, 98] sufficient electrochemical stability under varying pH and voltage conditions for operational durability.[35, 99]

Blair and Murphy discovered in 1960 that ion removal (called demineralization) could be achieved using a porous carbon-based material as the sodium removal electrode and an Ag/AgCl electrode for chloride removal.[80] Carbon materials are more suitable for CDI electrodes and are considered ideal and promising electrode materials. Metal oxides and conductive polymers based on pseudocapacitance undergo electrochemical reactions that affect their cycling efficiency and lifespan, as the by-products of these reactions could contaminate the feed water.[100]

The pore structure, which includes the distribution of pore size, total pore volume, and specific surface area, also plays a crucial role in determining the performance of carbon materials.[101, 102] The charge storage capacity of porous carbon electrodes relies on several factors: the ion transport properties, conductivity, and the physicochemical interactions between the electrolyte and the carbon material. Different pore sizes have distinct functions.[103] Macropores (>50 nm) primarily store the electrolyte and can facilitate ion transport over larger volumes, while mesopores assist in ion transport by serving as effective channels for ion diffusion. Macropores and mesopores together facilitate the rapid diffusion of electrolyte ions. Micropores, with their high electrostatic adsorption capacity, lead to high specific surface

area and provide abundant ion adsorption sites. Different pore structures contribute synergistically to electrochemical performance by balancing storage, transport, and diffusion properties.[104] Activated carbon is a widely available commercial material attributed to its high specific surface area and versatility.[84] Its unique properties make it an ideal choice for various industries, particularly for energy storage and water treatment.[105]

Activated carbon can be derived from various natural and synthetic raw materials, including biomass sources such as nutshells, wood, coal, and starch, as well as synthetic precursors like resins and other organic materials.[106] Adjusting the surface chemistry of activated carbon, for instance, by doping with heteroatoms or grafting functional groups, provides a viable and attractive approach to enhance CDI performance.[107, 108] Zou et al. compared activated carbon, KOH-activated carbon, and TiO_2/activated carbon composites.[109] Their work indicated that KOH treatment enhanced the hydrophilicity of the activated carbon and improved the surface wettability. Doping carbon with heteroatoms such as nitrogen, phosphorus, or sulfur can greatly improve its conductivity and surface wettability.[110] Employing nitrogen-doped mesostructured carbon nanocrystals for CDI, Xu et al. achieved an impressive salt adsorption capacity (SAC) of 21 mg g^{-1}.[111] Aslan et al. demonstrated that mixing CO_2-treated hydrophobic carbon with as-received hydrophilic carbon for CDI electrodes without membranes enhances charge storage ability.[112]

Activated carbon exhibits a broad pore size distribution. Due to its well-balanced pore size distribution, it serves as a suitable electrode material for CDI compared to other nanoporous carbons.[113] Optimizing the pore structure of activated carbon can enhance the CDI performance. The established knowledge in the field of supercapacitors supports the understanding that micropores enhance electrode capacitance (charge storage) compared to mesopores.[114] When predicting the CDI performance, the combined volume of micropores and mesopores needs to be considered. However, the differential SAC is higher for micropores.[39] The importance of the subnanopores (micropores with pore sizes smaller than 1 nm) has been established in EDLc electrodes.[115] Though mesopores facilitate ion transport, some carbons with micropores, like activated carbon and carbide-derived carbon, demonstrated better performance in CDI.[116, 117]

Porous electrodes that integrate a large volume of micropores with networks of mesopores and macropores can achieve higher deionization efficiency, optimizing the capacity and transport properties.[118] Hierarchical porous carbons have been developed to combine the

advantages of different pore scales into the structure. Using an eco-friendly dual organic salt activation strategy, 3D hierarchical porous carbon was synthesized by Shi et al. It exhibited a well-balanced hierarchical porous structure, encompassing micro-, meso-, and macropores with a substantial pore volume of 1.02 $cm^3 g^{-1}$. It achieved a high SAC of 25 mg g^{-1} in approximately 17 mM NaCl solution at 1.2 V.[119] Miao et al. reported that biochar derived from the sunflower plate demonstrated the best desalination performance (9 mg g^{-1}) and charge efficiency (77 %) due to its porous structure, enhanced surface charge, good surface wettability, and larger specific capacitance.[120] The hierarchical porous structure facilitates accelerated ion transport and adsorption. Wang et al. introduced a "pore-on-pore" strategy by using $KHCO_3$ activation of natural cattle bone to produce micro-meso hierarchical porous carbon. This material achieved a high specific surface area of 2147 $m^2 g^{-1}$ and exhibited a SAC of 31 mg g^{-1} in approximately 26 mM NaCl solution under 1.2 V compared to traditional activated carbon, highlighting the effectiveness of tailored porosity design.[121]

Traditional CDI electrodes are typically made by casting a slurry.[122] The active material is combined with conductive agents (e.g., carbon black (CB)) using polymer binders (e.g., polytetrafluoroethylene (PTFE) or polyvinylidene (PVDF)), then cast the slurry onto a conductive substrate uniformly.[123] Since some polymer binders, including PTFE, are generally inactive and hydrophobic, they could deplete the conductivity of the electrode.[124] Binder-free electrodes have attracted increasing attention due to the simple electrode fabrication process and low costs.[125] In this case, active materials are directly encapsulated into the conductive matrix, which can enhance the effective charge transfer while preventing active mass shedding.[126]

2.2.5. Capacitive deionization performance metrics

Various terminologies were introduced during the development of CDI to evaluate its performance. Initially, researchers primarily reported the reduction trend of the salt concentration in feed water under the constant voltage mode.[127] Many operational parameters, including the feed water flow rate and composition, could influence the salt removal properties.[128, 129]

The CDI performance metrics mainly include SAC, ASAR, Kim-Yoon plot, charge efficiency, energy consumption, and cycle stability. SAC is the essential metric for evaluating the performance of the CDI cell. It is common to represent the mass of salt removed per mass of the electrode material, resulting in a unit of $mg_{salt}\ g_{electrode}^{-1}$ (gravimetric adsorption capacity). It is also possible to report the volumetric salt removal capacity. The maximum SAC, also called equilibrium salt adsorption capacity, is determined once equilibrium salt adsorption is achieved. In this case, the constant voltage or current and the continuous feed water flow rate are maintained until the charging process is finished to ensure the recorded effluent conductivity remains constant. The methods for calculating the salt removal are different for the single-pass mode and batch mode. The mass of the removed salt in the single-pass mode is equal to the time integral of the concentration change, multiplied by the flow rate and the molecular mass of the removed salt species. For the batch mode, it is calculated by multiplying the decrease in salt concentration with the feed water volume.[32] Then, the SAC can be obtained by dividing the mass of salt removed from the feed water by a representative mass or volume of the electrode. Here, the representative electrode mass needs to be clarified. The components in the static electrode include the active material, binder, and conductive additives (CAs), not only the mass of the active component. The electrode´s mass loading of the inactive components typically ranges from 5 to 10 %.[130] Therefore, clarification is needed as to whether the SAC value is based on the total mass of the electrode (including CAs and binder) or the mass of the active electrode components.

ASAR is the division of the SAC over the corresponding charging time in the unit of $mg\ g^{-1}\ min^{-1}$, which is a measure of the salt removal rate. There are many factors that could affect the ASAR. For instance, cell architectures such as the flow-through capacitive desalination cell can achieve a higher ASAR than a flow-by structure in two systems using the same electrodes.[14] This is because the flow-through configuration minimizes the width of the gap between electrodes, reducing the resistance of a cell and thereby shortening the charging time of the

cell. The choice of the charging time could also affect the ASAR; under constant voltage mode, a shorter charging time typically results in a higher ASAR in the MCDI system.[131] Electrodes with subnanometer pores exhibit high SAC but may face kinetic limitations due to their small pore size, potentially restricting ion adsorption dynamics and limiting the ASAR.[39] An optimal level of electrode compression during preparation is essential to obtain a larger ASAR, as it balances minimizing the resistance with retaining the pore structure for efficient ion transport.[26]

The Kim-Yoon plot, also referred to as the CDI Ragone plot, illustrates the trade-off between SAC and the corresponding ASAR, a tool for evaluating CDI kinetics.[132] This plot draws inspiration from Ragone charts, which represent the relationship between power (energy delivery rate) and energy stored in energy storage devices.[133]

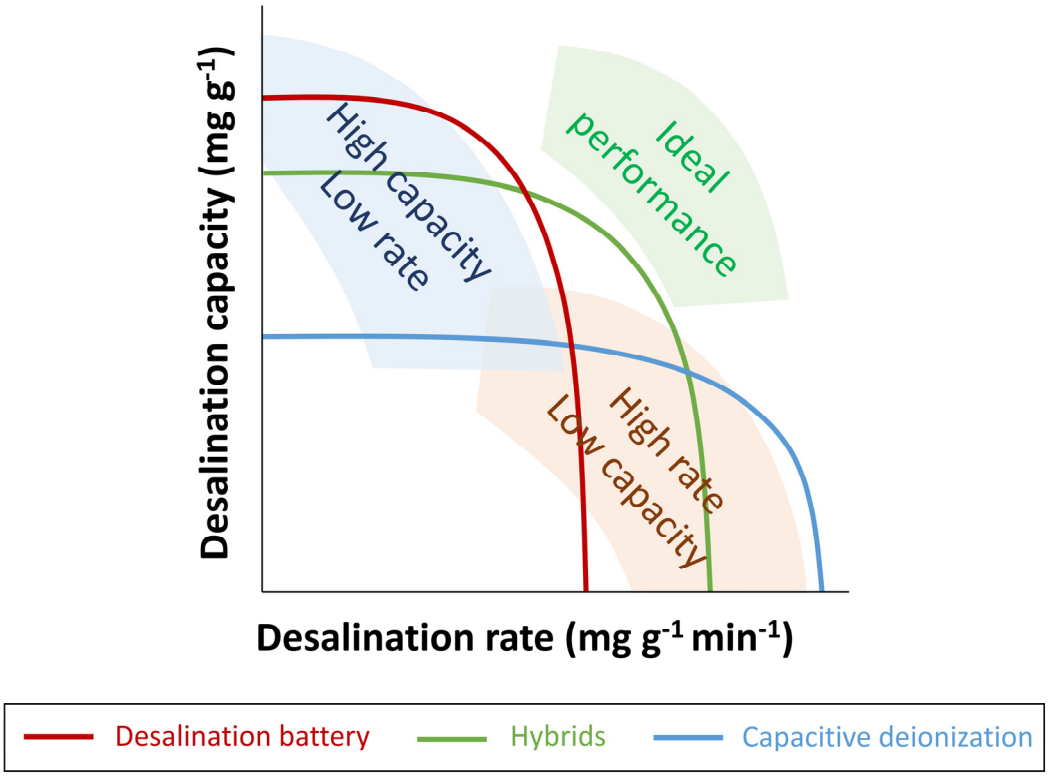

Figure 7 A conceptual diagram of a Kim-Yoon plot. The position of the curves indicates the desalination performance in different cases: a low rate and high capacity (blue) and a low capacity and high rate (orange). The curve location of an ideal CDI system is expected to be toward the upper right region of the plot (green), indicating improved performance in both capacity and rate. Figure adapted from [132]

The Kim-Yoon plot facilitates the identification of optimal cell operational conditions, specifically when the ASAR and the SAC approach their upper limits (**Figure 7**). Kim-Yoon plot serves as a framework for understanding the dynamics of ion transport and adsorption, which is essential for improving the performance of desalination systems.

Charge efficiency is expressed mathematically by dividing the moles of salt adsorbed by the moles of charge. The total charge accumulated in an electrode pair during operation can be converted into moles by dividing it by the Faraday constant (26801 mAh mol^{-1}).[45] This parameter calculation is different in the batch mode and the single-pass mode, providing insights into the effectiveness of ion adsorption relative to the input charge.[134] A higher value of charge efficiency is associated with lower energy consumption in a CDI system. Charge efficiency indicates how effectively the invested charge contributes to ion electrosorption. When the ion concentration is high, a larger proportion of the input charge contributes to desalination, minimizing energy losses associated with side reactions or inefficiencies, thereby reducing the overall energy demand of the process. In the system with IEMs, charge efficiency can approach unity because the membranes only allow the counterions to pass through and prevent co-ions from entering the electrode.[53]

The stability (cycling performance) of CDI can be evaluated as the ratio of SAC at the n-th cycle to the maximum SAC (usually the first cycle). A complete CDI cycle involves ion adsorption by the electrode until the equilibrium is reached, followed by ion desorption achieved by applying either reverse voltage or a short circuit.[135] The degradation affecting the stability of CDI systems depends on the electrode materials. In general, oxidative carbon corrosion (by reaction with water) occurs at the anode during the charging phase, especially when operating at high voltages (**Figure 8**).[136] The oxidation process damages the carbon structure, reducing its electrical conductivity and adsorption capacity over repeated cycles. For Faradaic electrodes, stability is often compromised due to volume expansion and dissolution in water.[137, 138] To address the stability issues in CDI, employing IEMs in activated carbon electrodes enhances stability compared to traditional CDI systems.[139]

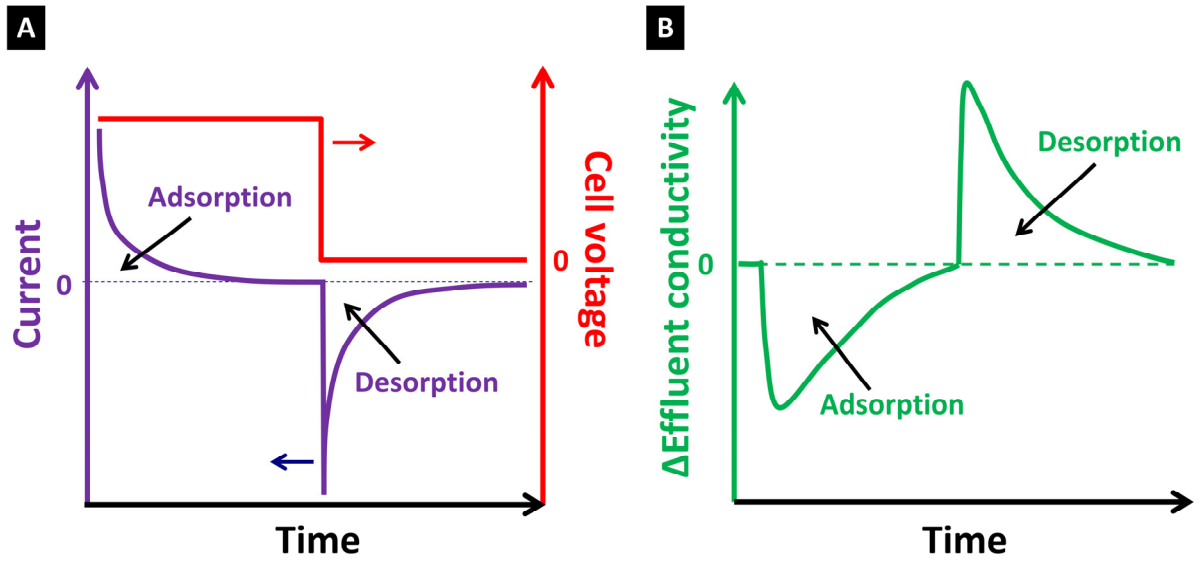

Figure 8 CDI cycle curve in single pass method under constant voltage (CV) mode, the effluent salt concentration and current signals are analyzed. Figure adapted from [32]

2.2.6. Applications of capacitive deionization

The CDI applications have continuously expanded, showing their potential in various fields. These applications can be categorized as follows: brackish water desalination,[65, 140, 141] water softening,[142-144] heavy metal removal,[145-147] phosphorous/nitrate recovery,[148-151] and lithium recovery.[57, 152] (**Figure 9**)

The development of advanced electrode materials is essential for improving the desalination performance of the CDI process. However, the real challenge lies in bridging the gap between high-performance laboratory-scale materials and their practical application in commercial systems. Major companies, such as EST Water & Technologies Co., Ltd. (China), Siontech (South Korea), and Voltea (Netherlands), currently rely on conventional activated carbon electrodes in their CDI modules. This choice highlights the trade-off between material performance and economic viability.[153] Despite advanced materials' potential, their adoption capacity in real-scale operations is hindered by challenges such as high production costs, complex synthesis methods, and limited scalability.[154]

As mentioned in section 2.2.3, there are two main modes of CDI operation: single-pass mode and batch mode.[32] In the single-pass mode, feed water flows through the CDI cell only once without recycling. In contrast, batch mode involves recycling the feed water through the CDI cell several times. In practical industrial applications, the single-pass mode is implemented due to its ability to ensure a continuous water supply and handle a sufficiently high treatment

volume. Additionally, there has been an increase in the number of industries using batch mode for specific applications.[36] Brine recirculation facilitates the treatment of highly concentrated CDI brines in the zero-liquid discharge (ZLD) process. It consists of recirculating the brine stream from a previous desorption cycle as the brine stream for a subsequent desorption cycle.[155] This approach ensures higher brine concentrations, which are crucial for achieving ZLD goals, minimizing environmental impacts, and improving cost-effectiveness. However, brine recirculation may lead to increased system fouling, as the foulant could accumulate over time in the recirculated brine. A thorough evaluation of the long-term impacts of brine recirculation on fouling and overall system performance is necessary for effective implementation.

High concentrations of Ca^{2+} and Mg^{2+} cause water hardness, which challenges industrial applications due to scaling in boilers and heat exchangers.[156] Chemical precipitation, ion exchange, RO, and ED can address this problem, but these methods require large chemical and energy inputs.[142] Innovative CDI electrodes have been designed for water softening. Calcium alginate (Ca-alginate) coated electrodes have demonstrated a 44 % increase in Ca^{2+} removal compared to conventional CDI electrodes.[157] This improvement is attributed to the enhanced charge efficiency of the system, which increased from 55 % in traditional CDI to 85 % in the Ca-alginate-CDI configuration. It is reported that the electrodes´ strong electrostatic attraction towards multivalent ions improves CDI effectiveness for softening applications.[142] Increasing the flow rate and applied voltage also improves water softening.[158] The efficiency of Ca^{2+} removal in CDI systems is influenced not only by the coating materials but also by the type of carbon substrates used. For instance, a carbon cloth coated with SiO_2 achieved only 16 % removal efficiency, and SiO_2-coated carbon foam and nanofoam demonstrated higher efficiencies (ranging from approximately 89 % to 98 %).[159]

Heavy metals, broadly used to describe metals with high density or atomic weight, are harmful to human health and toxic and carcinogenic after prolonged exposure.[160] Current approaches, including adsorption, chemical precipitation, and membrane separation, can remove heavy metal ions from wastewater.[161] CDI emerging as an feasible and cost-effective approach,[146, 162] which can remove the individual metals such as chromium (Cr^{3+}),[163] lead (Pb^{2+}),[164, 165] copper (Cu^{2+}),[166, 167], cadmium (Cd^{2+}),[168] iron (Fe^{2+}),[169] arsenic (As^{3+}),[170] and nickel (Ni^{2+}).[171] from aqueous solutions through electrosorption processes. Huang et al. found that the presence of Pb^{2+} and Cr^{3+} inhibited the

removal of Cd^{2+}, primarily due to Cr^{3+} having a higher charge and Pb^{2+} having a smaller hydrated radius ($Pb^{2+} < Cd^{2+} < Cr^{3+}$).[146] Carbon aerogels can remove 97.5 % of the Cd^{2+} from a 1.8 mM solution at 1.2 V and a pH value of around 6.[172] Modified carbon aerogels with metal oxides show an enhanced Cu^{2+} removal capacity of 57 mg g^{-1} at 1.2 V.[173] The molybdenum dioxide/carbon electrode demonstrates a high selective capacitive removal efficiency for Pb^{2+} from a multi-component system.[174] Metal-oxide composite electrodes like reduced graphene oxide/TiO_2 nanotubes (rGO/TNT) can achieve a SAC of 253 mg g^{-1} from a 1.3 mM Cu^{2+} solution at 1.2 V.[175]

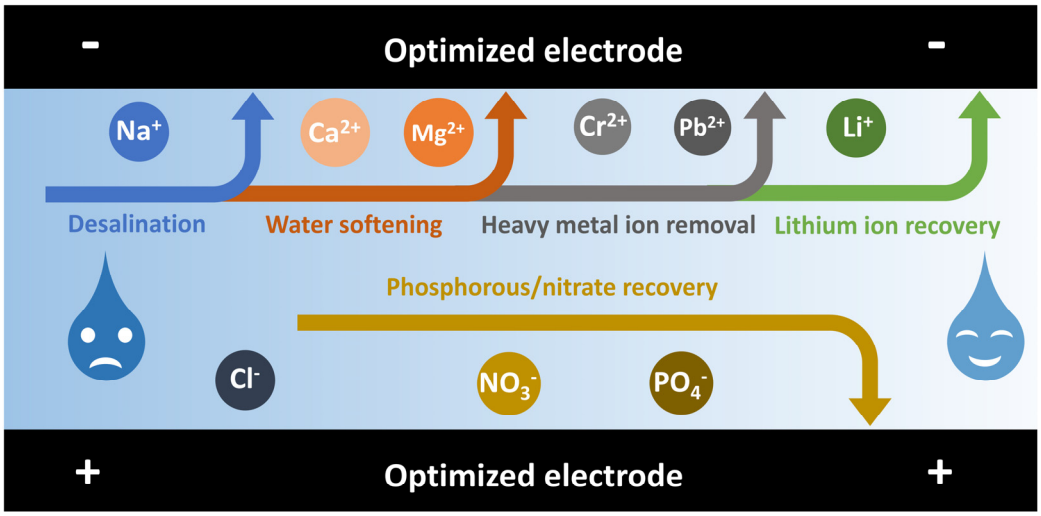

Figure 9 Applications of CDI. Cations (Na^+, Ca^{2+}, Mg^{2+}, Li^+, and heavy metal ions) are electrosorbed onto negatively charged electrodes, and anions (Cl^-, PO_4^{3-}, and NO_3^-) are captured on positively charged electrodes. Figure adapted from [153].

Nitrogen and phosphorus are essential nutrients for food production, yet a substantial amount is lost in wastewater, contributing to eutrophication.[176] Hence, it is necessary not only to remove them from the wastewater but also to recycle them.[148] A novel nitrate-selective composite carbon electrode (NSCCE) exhibited high adsorption of nitrate ions of 19 mM m^{-2} (2 to 3 times better than the capacity in the MCDI system to remove nitrate ions).[177] Bian et al. reported that the FCDI system achieved removal efficiencies of 70-99 % for salinity, 49-91 % for PO_4^{3-}-P, 89-99 % for NH_4^+-N, and 83-99 % for NO_3^--N with slurry loadings of 5-15 mass %, which demonstrates that FCDI can efficiently remove nitrogen and phosphate from wastewater while simultaneously recovering them as concentrated products.[149]

Lithium is a vital element for energy storage devices.[178]. Due to its small ionic radius and high electrochemical activity, lithium-ion batteries have emerged as the most popular electrochemical energy storage devices.[179] Underground brine, salt lake brine, and seawater contain large amounts of lithium resources, making lithium recovery from water a recent research hotspot.[180] To enhance the selective recovery of Li^+, the MCDI process was further modified by incorporating a monovalent selective CEM designed explicitly for Li^+, called monovalent selective membrane CDI (MSMCDI).[181] The result shows a higher removal rate of 38 % for Li^+ and a lower energy consumption of 0.002 kWh mol^{-1}, enhancing the feasibility of Lithium recovery using MSMCDI. HCDI is introduced to enhance the recovery of specific ions and the deionization efficiency. Lee et al. reported a modified MCDI system that employs a lithium manganese oxide (LMO) electrode for Li^+ capture and an activated carbon electrode for anion capture. This λ-LMO/activated carbon HCDI cell was evaluated for its ability to selectively recover lithium from an aqueous solution containing Li^+, Na^+, K^+, Ca^{2+}, and Mg^{2+} with a specific recovery of 0.4 μmol(Li^+) $g_{adsorbent}^{-1}$.[182] The intercalating electrodes mainly influence lithium recovery in HCDI. The higher recovery ratio reported reached 800 mg(Li^+) g^{-1} of the electrode when a geothermal brine solution containing 2.3 mM Li^+ with a flow rate of 67 mL min^{-1} at 2 V. FCDI eliminates the need for a rinsing process by utilizing the suspended electrode, which enables continuous adsorption and desorption of target ions. Ha et al. investigated the continuous extraction of Li^+ using activated carbon slurry in two operational modes. The study shows that the batch mode has a higher salt removal efficiency of 91.7 %.[183]

2.3. From static electrodes to flowable electrodes

Flowable electrodes, or semi-solid flow electrodes, refer to the slurry or suspension composed of activated solid conductive particles dispersed in the electrolyte.[184] Typically, the flowable electrodes are prepared by mixing porous carbon particles with either an aqueous or organic electrolyte.[185] Compared to the traditional static electrodes, the flowable electrodes have a higher energy density, faster charge storage capability, and longer cycle life.[186] As a mixed conductor of electrons and ions, the flowable electrodes enable charge transfer through electronic and ionic transport mechanisms.[187] During operation, the slurry is circulated in a closed loop driven by a peristaltic pump, with its viscosity and flow rate adjustable to suit specific requirements.

FCDI was developed based on flowable electrodes. It improves upon conventional capacitive CDI by overcoming key challenges, such as limited ion adsorption capacity and the difficulty of maintaining continuous ion removal over time.[16] The main innovation of FCDI lies in utilizing flowable electrodes, which is the suspension of conductive particles like activated carbon. These electrodes continuously circulate through the system, enabling ongoing ion removal from water without the need to regenerate the electrodes through the discharge process, as is the case with conventional CDI.[188] By continuously replenishing the electroactive region with uncharged materials, flowable electrodes facilitate ongoing ion removal. The continuous operation property of FCDI benefits the scalability and further industrial applications of electrochemical desalination. This setup allows for higher desalination efficiency and ensures consistency in continuous effluent quality.[128] In the FCDI system, IEMs play a crucial role by allowing the selective passage of specific ions (anions or cations) while blocking water molecules. Coupling IEMs with flowable electrodes enhances the system's efficiency in separating ions from water, providing greater flexibility and operational efficiency.[189] In addition, a novel, low-cost, and scalable FCDI system with porous separators (e.g., polymeric or non-woven glass fibers) is reported for ion separation through flowable carbon suspensions without ion IEMs.[190] Research in FCDI primarily focuses on the operational mechanism, the design of cell configuration and slurry channels, various operational modes, and applications, such as desalination and resource recovery.[191]

2.3.1. Mechanisms of flow electrode capacitive deionization

Over the past decade, FCDI has made significant advancements in the research of flowable electrode development,[192-194] charge transport theory, and operational mechanisms.[195, 196] flowable electrodes were first introduced by Kastening et al. to achieve ion electrosorption and charge transport in 1985.[197] Until 2012, energy storage technologies primarily focused on supercapacitors and flow batteries separately. That year, an electrochemical flow capacitor (EFC) was proposed, combining the advantages of both systems. Presser et al. demonstrated the rapid charging and discharging of energy storage with a carbon-electrolyte suspension as the flowable electrode.[198] In 2013, a flowing carbon suspension of 5 mass% as an electrode was introduced in CDI, effectively desalinated high-salinity brine water (32.1 g L^{-1} NaCl), achieving an impressive salt removal efficiency of 95 %.[83, 199, 200] The key factors influencing flowable electrodes include the properties,[193, 201] mass loading,[202, 203] and flowability of active materials.[195, 204] Collectively, these factors determine the electron and ion transport properties of the electrode, thus achieving a higher mass loading, which is ideal for enhanced ion removal.[205] Additionally, improved charge transport can be facilitated through the formation of interconnected percolation networks. Although increasing the mass loading of active materials can improve ion removal, it increases the risk of clogging in the FCDI system.[196] The suspension with spherical carbon particles reduces the viscosity of flowable electrodes to address the challenges associated with flowability at high-mass loadings.[185] In contrast, fine-grained activated carbon poses challenges (with the average particle size range of 5-20 nm) when exceeding about 20 mass%.[206] Using slurries with higher mass loading will not necessarily improve charge transport due to the particle agglomeration and increasing viscosity. Different characteristics, such as viscosity, conductivity, particle dispersion, and slurry stability, will change as FCDI experiments occur.[207]

FCDI operates similarly to other electro-driven deionization processes (e.g., CDI and MCDI) and is mainly based on the EDL.[75] In the FCDI system, typically, two flowable electrode channels uptake and store ions, thereby removing them from the feed water through electrosorption. The charged ions can also be released back into the feed water through short circuit and polarity reversal, similar to the classic CDI process.[208, 209] Based on the ion separation mechanism, flowable electrodes can be generally categorized into carbon-based materials (rely on EDL) and charge-transfer materials (rely on Faradaic reactions).[210, 211]

2.3.2. Cell designs and operational modes of flow electrode capacitive deionization

A lab-scale FCDI system comprises current collectors, flowable electrode channels, separators, and a water channel.[212] The feedwater flows through the water channel between the two separators. The flowable electrode channels are placed between the separators and the graphite current collectors. Flowable electrode channels can also be created by carving the current collectors with serpentine channels.[213, 214] The flowable electrodes are typically recirculated inside and outside the FCDI cell using a peristaltic pump (**Figure 10**).

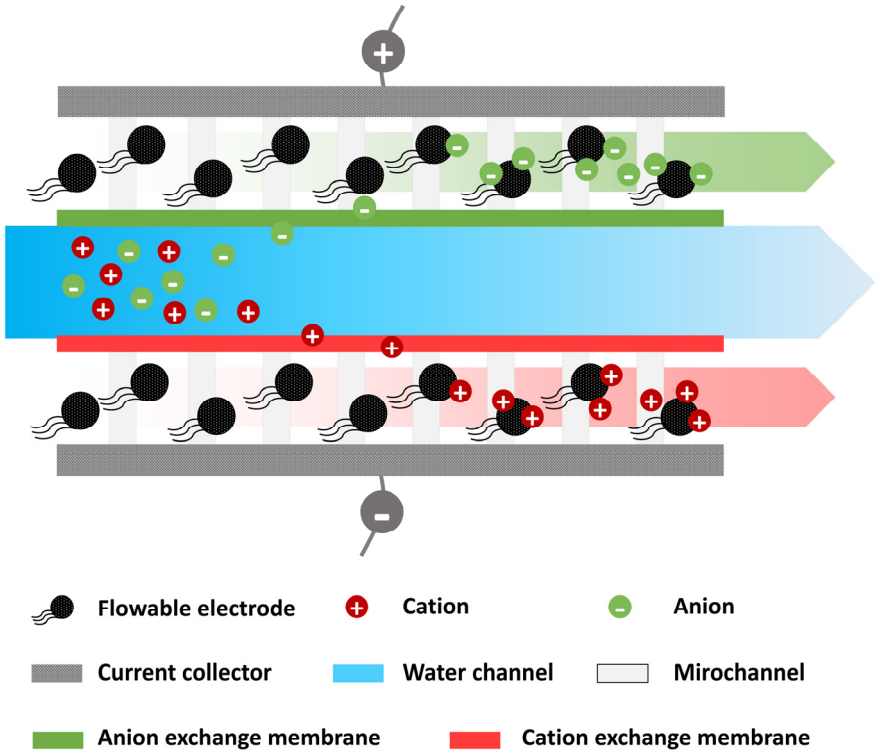

Figure 10 Principle diagram of the FCDI system. Figure inspired by [196].

Flowable electrodes generally consist of three components: active materials, electrolytes, and CAs.[196] The solid mass loading (mass %) of flowable electrodes can be designated as:

$$\text{Solid mass loading (mass \%)} = \frac{\text{active materials+conductive additives}}{\text{active materials+conductive additives+electrolyte}} \quad (1)$$

Active materials

Active materials are essential for electron transport and ion adsorption during the FCDI process, which can be classified into carbon-based materials (which store target ions in the

structure mainly through EDL) and charge-transfer materials (rely on Faradaic reactions).[33, 215]

Many advances have been achieved in developing advanced carbon-based materials for flowable electrodes, which exhibit enhanced ion adsorption capabilities, superior conductivity, and improved overall system durability. The electrochemical and rheological properties of the flowable electrodes are crucial to improve energy efficiency. Oxidation methods have proven effective in enhancing energy storage properties in supercapacitors by improving wettability and enabling better ion access to the surface.[216] Hatzell et al.[206] investigated the function of surface groups on the rheological and electrochemical properties of flowable electrodes in the FCDI processes by oxidation of granular activated carbon particles. They achieved higher mass loading of the flowable electrodes without increasing the pumping energy consumption. Suspension stability indicates reduced aggregation and a more uniform (monodisperse) distribution of the active material.[217] The characteristics of the slurry change as FCDI experiments progress. A better understanding of the trade-offs between factors such as the surface chemistry and mass loading of the active material, suspension stability, viscosity, and the deionization/regeneration performance of suspension-type flowable electrodes is critical for optimizing their design and achieving enhanced operational efficiency. Achieving the optimal balance among these factors is essential to optimize the overall efficiency and performance of FCDI systems.[184, 206] It has also been studied that sulfonating CNT-derived flowable electrodes can form an effective conductive network, reducing particle aggregation and enhancing charge transport between the current collector and the flowable electrode particles.[218] Other methods like nitrogen doping, CO_2 activation, and coating (such as transition metal oxides, electron mediators, and polymers) of the active materials can improve the dispersibility and stability of flowable electrodes.[219, 220]

Charge-transfer materials are emerging active materials of flowable electrodes due to their good ion storage capacity and selectivity.[221, 222] Chang et al. were the first to propose using CuHCF as the cathode in the FCDI cell, paired with activated carbon as the anode. Compared to conventional activated carbon-activated carbon paired electrodes, the novel FCDI system with a CuHCF-activated carbon pair demonstrates enhanced performance, achieving an ASRR of 0.12 mg cm^{-2} min^{-1} versus 0.11 mg cm^{-2} min^{-1} and a charge efficiency of approximately 91 % compared to 84 % in a 170 mM NaCl solution at 2.8 V.[221]

Conductive additives

Generally, the mass loading of flowable electrodes is between 5 and 20 mass % to balance conductivity and viscosity.[212] High mass loading of active materials can enhance the flowable electrodes´ conductivity but intensify the flow channel clogging frequency.[223] Therefore, selecting suitable CAs and electrolytes is crucial to further enhance the conductivity and dispersibility of flowable electrodes.[224]

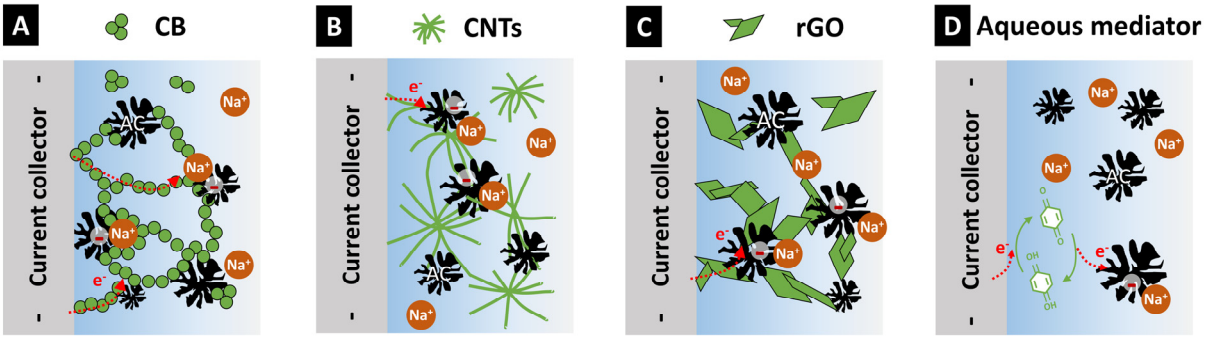

Figure 11 Schematic illustration of the role of conductive additives (CAs) in FCDI systems. (A) carbon black (CB); (B) carbon nanotubes (CNTs); (C) reduced graphene oxide (rGO); and (D) aqueous electron mediators (hydroquinone (H_2Q) is used as an example). Figure inspired by [212, 225]

CAs can be divided into two types: solid substances, including CNTs, carbon black (CB), graphene, or rGO, and aqueous electron mediators, including hydroquinone (H_2Q), *p*-phenylenediamine (PPD), and *m*-phenylenediamine (MPD).[212] CB is a popular additive in both flowable electrodes and static electrodes due to its high conductivity. When using low-conductivity materials such as activated carbon, CAs can support the establishment of a conductive network that enhances the overall conductivity of the flowable electrodes.[226] Adding 1.5 mass % CB (average diameter of 40 µm) to flowable electrodes has been shown to improve the salt removal rate and charge efficiency of FCDI. This improvement is attributed to more efficient electron transport between activated carbon particles and current collectors and increased collisions at higher loadings (**Figure 11A**).[227] It has been shown that adding a small amount of CNTs (e.g., 0.25 mass %) can double the ASRR because CNTs can serve as an electron percolation pathway between the activated carbon particles (**Figure 11B**).[228] rGO sheets can also act as effective CAs, enhancing connectivity and facilitating faster electron transport within the charge percolation network of flowable electrodes (**Figure 11C**).[87] For

these solid CAs, it is vital to carefully control the amount of additives for high conductivity while avoiding particle aggregation and cell clogging.[229] Aqueous electron mediators facilitate rapid and reversible redox reactions at the electrode/electrolyte and current collector/electrolyte interfaces. This process accelerates electron transport between the active materials and the current collectors. Ma et al. presented the addition of H_2Q into flowable electrodes since it can act as an electron shuttle at the electrode-electrolyte interface due to the redox conversion between H_2Q and benzoquinone (Q) (**Figure 11D**).[230]

Electrolytes

Almost 80 mass% of flowable electrodes contain supporting electrolytes such as NaCl or Na_2SO_4. Yang et al. pointed out that a higher concentration of NaCl in the flowable electrodes can promote the fast transport of charge between carbon particles.[231] However, the elevated electrolyte concentration could also result in more severe particle aggregation.[232] Keeping the feed water at the same concentration can reduce cell resistance and improve the FCDI ion separation efficiency, especially in the recovery solution.[233]

Current collectors

Current collectors not only facilitate electron transport and charge distribution among electrode particles but also support the separators.[234] Based on the FCDI mechanism, the contact resistance between the current collector and the flowable electrode particles impacts the overall charge transfer transport.[235] Dennison et al. investigated the relationship between flow electrode composition and cell design.[217] Their findings revealed that the cell resistance (up to 40 %) is attributed to fixed resistances in the current collectors and the interfacial resistance between the current collector and the flowable electrodes. Graphite-based plates commonly act as current collectors due to their good conductivity and chemical stability in salt solutions.[236] Although thick graphite plates have robust mechanical strength, machining the coiled flow channels also causes higher costs.[237] Xu et al. utilized membrane-current collectors in FCDI, which combine one pair of IEMs with a titanium mesh. Such 3D current collectors, based on metal meshes or foams, provide a higher surface area for interaction between the current collector and flowable electrodes.[238] Zhang et al. reported a 3D titanium mesh current collector that increases the charge transport area by strategically stacking titanium meshes.[239] This intensifies the contact between the flowable electrodes and the current collector, improving ion separation in high-salinity water. Additionally, the lower surface roughness is also suitable for the mobility of flowable electrodes. Traditional

current collectors coated with polyaniline can reduce surface roughness and minimize resistance at the interface between the flowable electrodes and the current collector.[240] Additional carbon felts in the FCDI system can achieve a 63 % increase in ASRR.[241] Linnartz et al. developed the membrane-electrode assembly (MEA) in which the membrane and the current collector are integrated into a single component, with carbon fiber fabric as functional reinforcement.[242] Köller et al. compared different structures suitable for use as current collectors in FCDI. The results show better ion transport in the expanded graphite bipolar plate (BP) current collectors, which are also cheaper to fabricate than graphite plates and simpler to apply than MEA.[236].

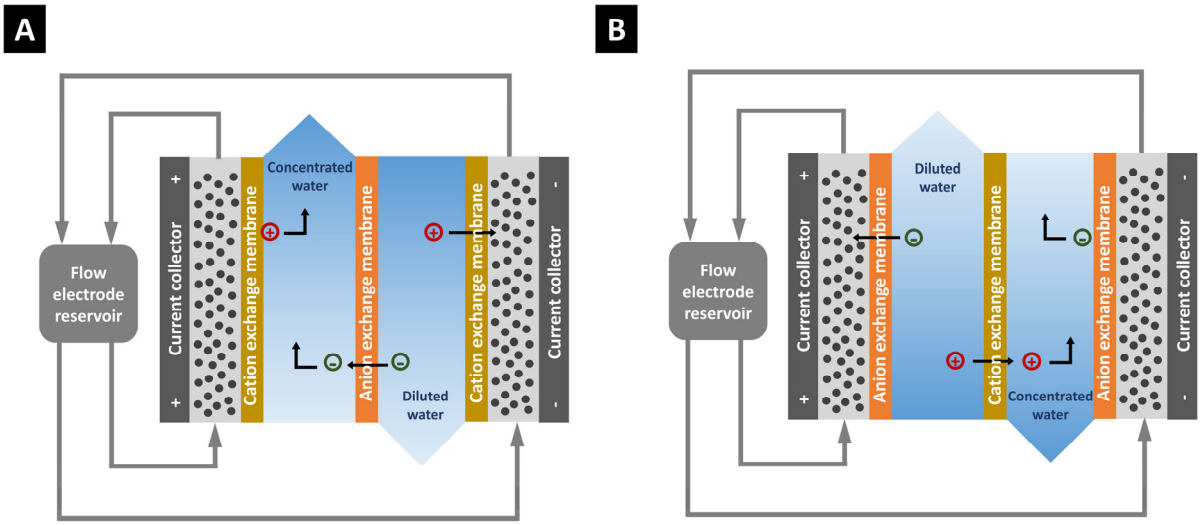

Figure 12 Illustration of the ion migration during desalination processes in (A) CAC-FCDI and (B) ACA-FCDI with IEMs. Figure adapted from [243].

Separators

The separator is another key component of an FCDI cell. It functions as a physical barrier between the flowable electrode channel and the water channel and as a mass transport pathway, facilitating the ion transport between these two channels.[244] IEMs are commonly used separators in the FCDI system. Two basic types of IEMs are AEM and CEM. The AEM contains positively charged functional groups (e.g., NH_3^+, NRH_2^+, NR_2H^+, and NR_3^+), while the CEM incorporates negatively charged groups (e.g., SO_3^-, COO^-, PO_3^{2-}, and PO_3H^-) within their polymeric backbone.[245] These charged groups permit the IEMs to pass counterions (ions with opposite charges) while repelling co-ions (ions with the same charges). The advantages

of introducing IEMs to FCDI cells are mainly because of their low resistance, good mechanical strength, and antifouling capability.[246]

Generally, an FCDI cell contains a pair of IEMs, and ion concentration polarization phenomena arise during ion transport through the IEMs, leading to the ion concentration gradient existing on both sides of the IEMs.[247] Han et al. reported that ion concentration polarization desalination was developed only with CEM to improve salt removal and energy efficiency. [248] Zhang et al. introduced two types of dual-channel FCDI systems featuring three IEMs arranged in sequence, enabling the simultaneous production of concentrated and fresh water.[243] The cell configuration with two CEMs and one AEM positioned in the middle is termed CAC-FCDI (**Figure 12A**), while the arrangement with two AEMs and one CEM is known as ACA-FCDI (**Figure 12B**). The diffusion coefficient of Cl^- is higher than that of Na^+, leading to a thicker ion enrichment/depletion layer throughout the CEM.[249] This phenomenon may vary with other ion pairs. Compared to the ACA-FCDI cell, the asymmetric diffusion of cations and anions enhances the performance of the CAC-FCDI mode, leading to a higher salt removal efficiency of 90 %.[243]

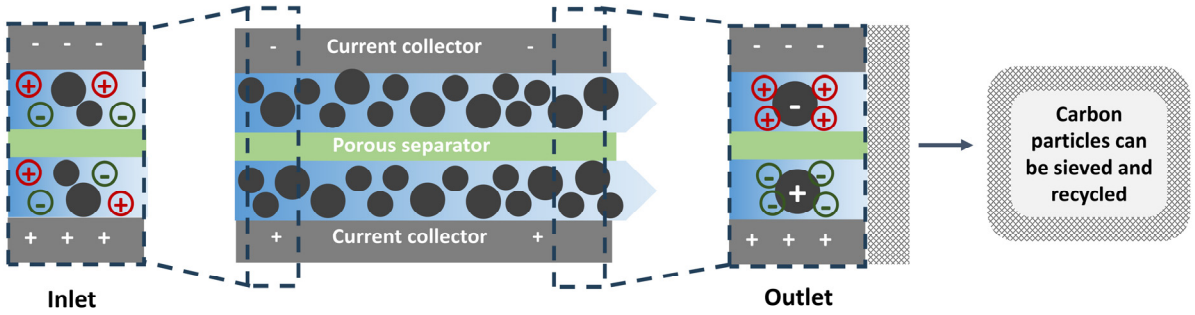

Figure 13 Schematic diagram of ion transport during desalination processes in a porous separator FCDI cell (without IEMs). Figure adapted from and [190].

Hatzell et al. developed the IEMs-free FCDI system with a porous separator in 2014 for treating brackish and seawater.[190] The flowable electrodes for this experiment were made of a mixture of activated carbon, CB, and feed water. At the same time, a filtering device was added at the outlet to sieve the carbon particles in the filtration solution and determine the amount of residual Cl^- in the solution by titration with $AgNO_3$ solution to determine the amount of adsorption of the carbon particles. This sieving process also enables the reuse of carbon particles. This device has the advantages of lower cost and controllable outlet

concentration (**Figure 13**) and achieved a specific capacity of 92 F g^{-1} and an adsorption rate of 68 % in static mode.

FCDI cells can be classified into single-channel, dual-channel, and multi-channel FCDI based on the number of water outlet channels.[208] The single-channel FCDI utilizes a pair of IEMs between the corresponding anode and cathode flowable electrode channels and the feed water channel (**Figure 14A**). The flowable electrodes are charged by either receiving electrons from the current collector or donating electrons to the current collector in the flowable electrode channel. The charged ions in the feed water cause cations to migrate toward the cathode chamber under the action of an electric field, eventually crossing the CEM. Similarly, anions enter the anode chamber through the AEM. The migrating anions and cations are eventually adsorbed onto the surface of the porous flowable electrodes, resulting in a gradual decrease in ion concentration in the feed water.[250] The single-channel cell is easy to operate. However, it has limitations in regenerating in the flowable electrode channel, making it unsuitable for large-volume seawater desalination applications. **Figure 14B** shows desalination and concentration cells with diluted and concentrated water, respectively.[221]

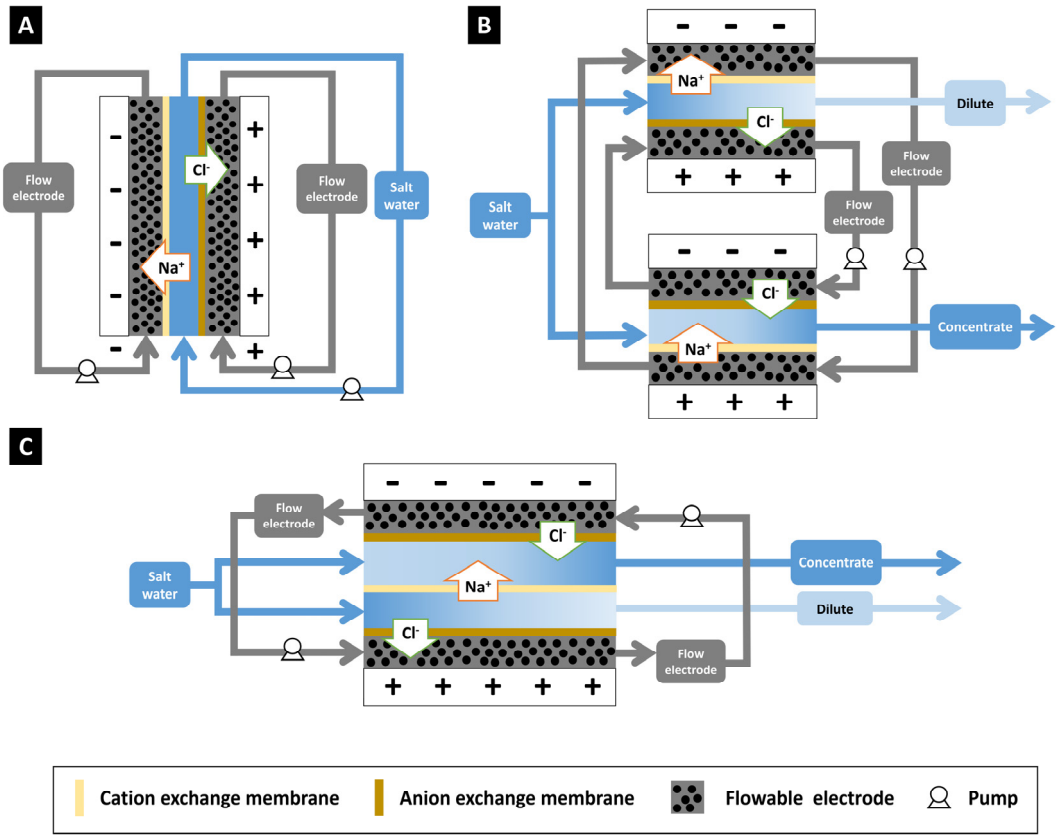

Figure 14 Schematic representation of various FCDI configurations: (A) single-channel FCDI cell, (B) dual-channel FCDI cell, (C) dual-channel with two FCDI cells. Figure inspired by [251].

In the dual-channel FCDI cell, influent water flows in the system through two channels, with the two streams separated by IEMs for dilution and ion concentration (**Figure 14C**). In this configuration, ions adsorb onto the surface of the flowable electrodes in one channel and circulate with the water flow to the opposite side of the flowable electrode channel, where it receives a reverse charge, leading to the desorption of the adsorbed ion into the concentration channel.[252] This design enables simultaneous desalination and ion concentration processes. The advantage of this structure is that it can produce dual-channel outlet water, allowing desalinated and concentrated water to flow out simultaneously.[253]

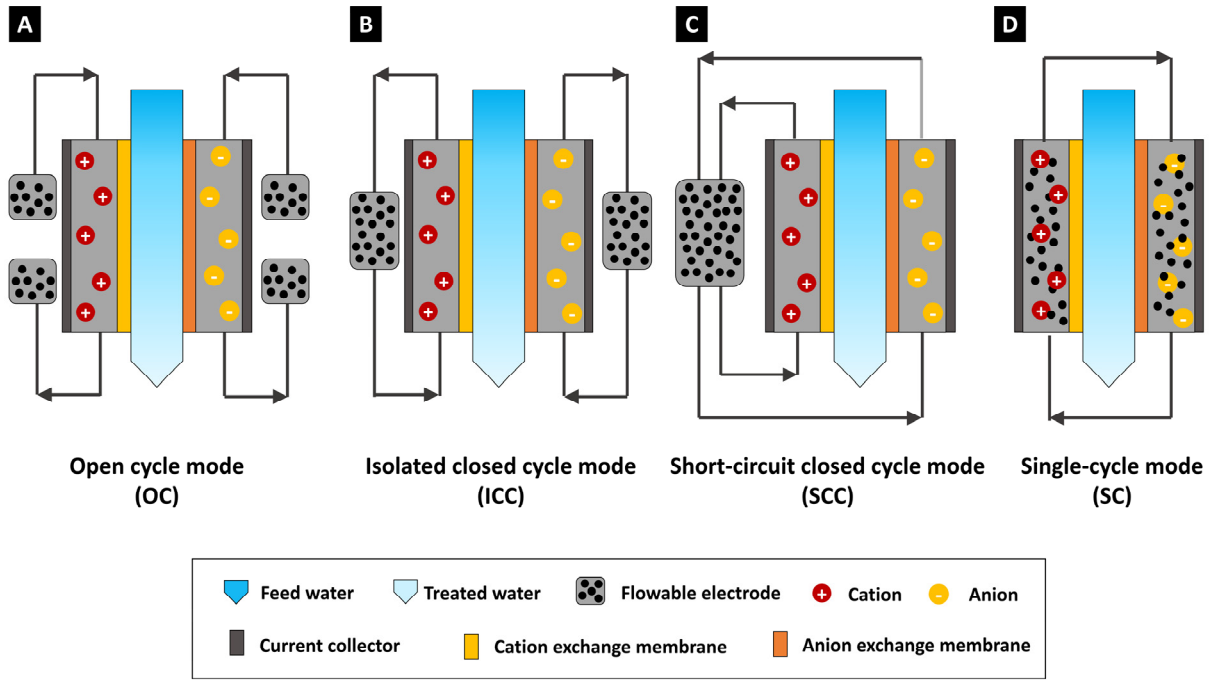

Figure 15 Schematic of different operation modes of FCDI: (A) Open cycle (OC) mode, (B) isolated closed-cycle (ICC) mode, (C) short-circuited closed cycle (SCC) mode, (D) single cycle (SC) mode. Figure adapted from [254].

The initial FCDI operation mode is the open cycle (OC) (**Figure 14A**), which allows for an unlimited amount of flowable electrodes supplied to the FCDI cell.[128] The OC mode is impractical in industrial applications due to the great demand for flowable electrodes. Consequently, the closed-cycle (CC) mode is introduced as a more efficient operation for FCDI. Variants of the CC mode include the isolated closed cycle (ICC; **Figure 15B**), short-circuit closed cycle (SCC; **Figure 15C**), and single cycle (SC) mode (**Figure 15D**).[255] In the ICC mode, the reservoirs of the flowable electrodes in the cathode and anode channels are separate. In contrast, the SCC mode allows the flowable electrodes in the cathode and anode to flow into

one reservoir, where charge neutralization and ion desorption occur. The ICC and SCC modes demonstrate lower FCDI energy consumption than the OC mode.[224] SC mode utilizes a single slurry flow loop, enabling adsorption and desorption at the same time.[256] During the SC process, flowable electrodes from one charged channel directly flow into the reversely charged one for regeneration and further adsorption. It is reported that the ASAR for the flowable electrodes in SC mode is higher (1 μmol cm^{-2} min^{-1}) than that of the SCC mode, with the energy consumption decreased by 50 %.[257] The key factors influencing desalination performance vary with the mode of operation, highlighting the importance of selecting the appropriate mode based on the specific salt separation application.

2.3.3. Flow electrode capacitive deionization performance metrics

Some CDI metrics can be directly used in the FCDI systems, such as ASAR, charge efficiency, and energy consumption. Others need to be modified only for the FCDI performance evaluation, such as SAC, which might not be suitable for the FCDI system.[258] This is because the mechanism of FCDI is the combination of capacitive and electrodialytic effects.

ASRR in FCDI refers to the amount of salt removal by a unit flowable electrode area per unit of time with the unit of mg cm^{-2} min^{-1}. It serves as an effective metric for evaluating FCDI performance.

Water recovery refers to the volumetric fraction of the feed water that is recovered as deionized water.[250] During the ideal FCDI process, ions are supposed to be transported through IEMs unidirectionally (from the dilute channel to the concentrate channel) and completely rejecting water molecules. However, a little bit of water could still be driven through the IEMs, diluting the brine solution or flowable electrodes, which affects the water recovery.[244]

2.3.4. Applications of flow electrode capacitive deionization

The applications of FCDI reach the following areas: water desalination, heavy metal removal, resource recovery, and Lithium extraction (**Figure 16**).

Figure 16 Applications of FCDI. Water desalination, heavy metal ions, Li^+ recovery, and resource recovery.

Like CDI, most studies of FCDI applications focus on water desalination.[259] A major benefit of FCDI over static electrode CDI is its ability to continuously desalinate higher salinity feed water, enabled by the greater SAC of the flowable electrodes.[260] A key direction of FCDI research is improving the freshwater production capacity.

Studies focus on modifying FCDI to meet the requirements of actual applications. Although scaling up the desalination capacity in FCDI systems can be achieved by enlarging the reservoir, mass production of freshwater remains challenging due to the limited influent flow rate of the FCDI unit cells. Hatzell et al. used an influent flow rate of 5 mL min^{-1}.[206] The flow rate of influent used by Zhang et al. was 4.5 mL min^{-1}.[261] Jeon et al. used 3 mL min^{-1}.[208] Yang et al. designed an FCDI stack comprising five unit cells to address the capacity limitation due to inlet flow rate restriction. The results show that the FCDI stack achieved higher desalination efficiency than a single FCDI system, validating that the FCDI stack design can scale up desalination production.[262]

A highly compact and scalable 3D FCDI desalination system using honeycomb-shaped porous lattice scaffolds was developed by Cho et al.[263] This porous structure served as a separator and support without using the IEMs and current collectors, enabling the system to be scaled up in 3D and thereby enhancing the SAC.[263] Inspired by ED, Ma et al. introduced a membrane-stacked FCDI cell.[264] Köller et al. presented a methodology for scaling FCDI from lab-scale to pilot-scale systems by increasing membrane cross-section and utilizing a cell stacking approach. This resulted in a module demonstrating an ASRR of 1.1 µmol cm^{-2} min^{-1}.[265] As the resistance of the repeating cell pairs increases, the current across the cell decreases. Different stacking concepts in FCDI should also be considered. The higher ohmic iR drop in the upper stacked system with four cell pairs results in lower currents between the current collectors. This issue can be mitigated by incorporating a second stacking unit instead (**Figure 17**).[265] These achievements promote the scalability and commercialization of FCDI.

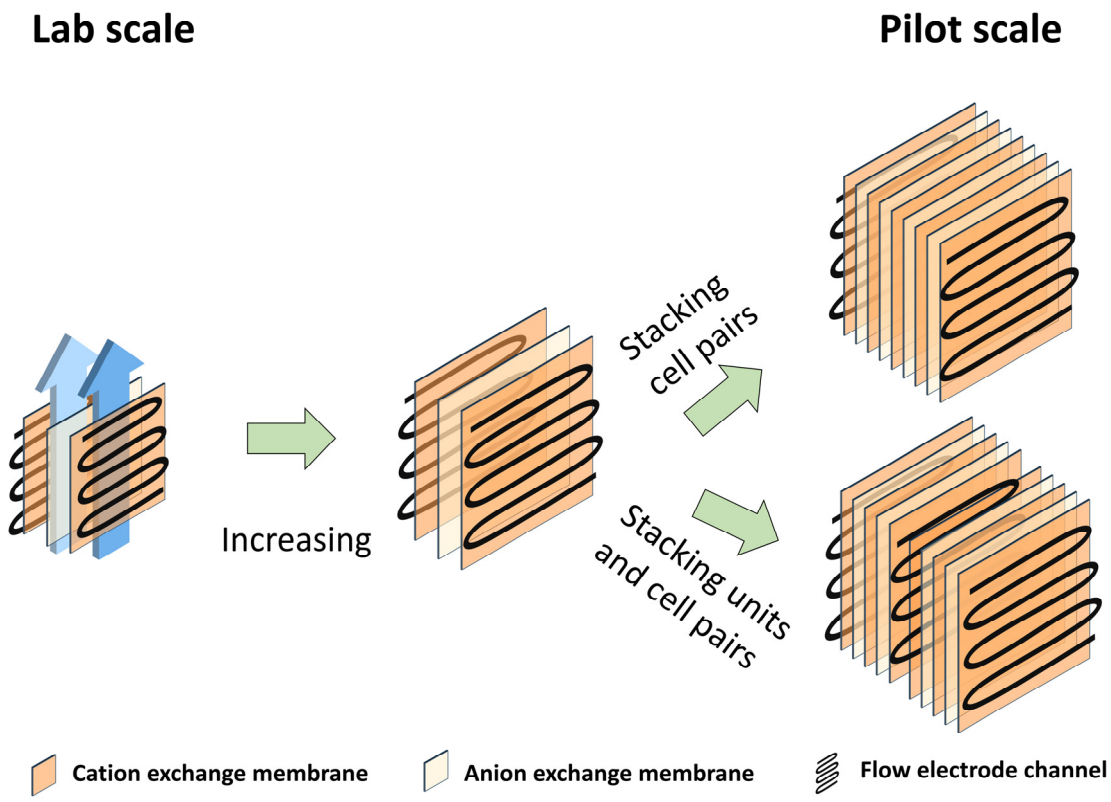

Figure 17 Schematic Illustration of FCDI scale-up from lab scale to pilot scale. Pilot scale systems can be reached by stacking the cell pairs. Figure inspired by [265].

The accumulation of nitrogen and phosphate in water bodies can lead to eutrophication.[266] Therefore, the question of how to constantly and efficiently remove and recover nutritional components has been a popular study area.[267] Song et al. utilized an SCC mode FCDI system to desalinate wastewater with varying nitrate concentrations.[268] The system maintained a water recovery rate of 91.4 % by periodically replacing the electrolyte while achieving continuous desalination. Fang et al. studied the effects of activated carbon and electrolyte concentration on ammonium removal and recovery in FCDI systems.[247] The results indicated that activated carbon concentration had a negligible impact on ammonium removal. When the electrolyte concentration is too high, the flow electrode should be refreshed rapidly to prevent concentration polarization and ion back-diffusion. Yu et al. conducted FCDI dephosphorization experiments using a novel carbon aerogel to form flowable electrodes. Due to its good conductivity and dispersion properties, carbon aerogel achieved a faster dephosphorization rate (1.2 μg cm^{-2} min^{-1}) and lower energy consumption (1.7 kWh kg^{-1} -P) than activated carbon.[269] Using potassium titanate in an SC mode FCDI system, flowable electrodes achieved a selectivity factor of 31 towards NH_4^+ over Na^+, even through the initial NH_4^+ concentration was only $^1/_3$ of the competing Na^+. In contrast, traditional CDI cells with static electrodes show a lower NH_4^+/Na^+ selectivity factor of less than 10 when treating similar wastewater.[270]

Many methods for removing heavy metal pollutants require extensive pretreatment steps and chemical additives.[271] Some adsorbents also suffer from instability in solution.[16] Gong et al. demonstrated that FCDI could achieve a Cd^{2+} removal efficiency of 54 % under optimal conditions, with the functional groups on the activated carbon particle surface remaining unchanged after Cd^{2+} adsorption.[272] Dong et al. reported the continuous and selective removal of Cr(VI) from brackish water using FCDI, with a preference for Cr(VI) over Cl^-.[223] Lim et al. improved FCDI performance (approximately 1.8 times) by utilizing composite flowable electrodes made from biochar and activated carbon, which achieved good adsorption of lead ions.[273] Ma et al. used FCDI to remediate radioactive wastewater, achieving a final uranium concentration lower than 10 μg L^{-1} with low energy consumption (0.1 kWh m^{-3}).[274]

Traditional lithium extraction from ores is labor-intensive and energy-consuming, and the availability of these resources is declining.[275] Consequently, recovering lithium from brine and saltwater has become crucial.[276] Ha et al. applied FCDI to extract lithium ions from brine

solutions, achieving a high desalination efficiency of 91.7 % and a rapid ASRR of 215.1 µmol m^{-2} s^{-1} with an initial LiCl concentration of 100 mg L^{-1}.[183] Saif et al. presented a promising novel process, Lithium Membrane FCDI, that effectively recovers lithium from synthetic geothermal brine with a high Na^+ concentration, achieving 99.9 % Na^+ rejection and good lithium selectivity. The Li-MFCDI demonstrates stable performance (over a 7-day test period) and energy consumption of 16.7 ± 1.6 kWh kg^{-1} for Li^+ recovered.[277] The primary challenge in extracting lithium from seawater is the high cost associated with the process, mainly due to the low concentration of lithium in seawater and the large amount of competing ions. Some research on FCDI for lithium extraction has primarily focused on pure lithium chloride solutions, but real seawater contains other competing cations like Na^+. Thus, enhancing the selective Li^+ adsorption is a key challenge for using FCDI in seawater lithium extraction.[16]

2.3.5. Redox flow desalination

Redox-mediated electrodialysis, also known as redox flow desalination (RFD) or redox flow battery desalination, is a promising electrochemical deionization method that employs IEMs.[278] The redox electrolyte capacitive deionization system based on carbon electrodes utilizes the oxidation reaction at the zinc electrode ($Zn \rightarrow Zn^{2+}$) to enhance the storage capacity of Cl^-. At the same time, the reduction reaction ($[Fe(CN)_6]^{3-} \rightarrow [Fe(CN)_6]^{4-}$) to increase Na^+ storage capacity. The standard potential difference between the electrodes facilitates the adsorption of cations and anions, improving the overall storage capacity.[279] After a period of operation, this system (ICC mode) requires a discharge step to regenerate the electrodes and concentrate salt ions.[280] Continuous redox reactions can occur when the electrolyte constantly circulates between the positive and negative channels (SC mode). Kim et al. reported that a novel multi-channel redox CDI system improves desalination performance by integrating the redox couple of ferricyanide/ferrocyanide with activated carbon electrodes. [64] The system achieves a SAC of 68 mg g^{-1} and a charge efficiency of 90 % while enabling continuous desalination without a discharging step (**Figure 18**).

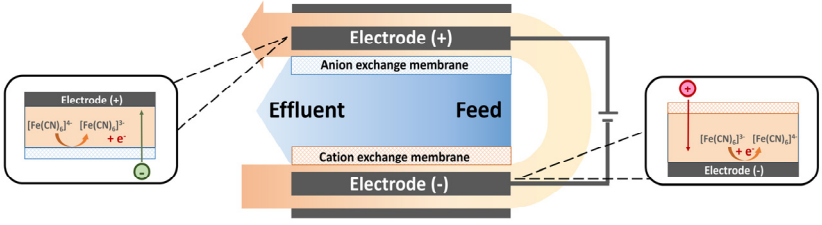

Figure 18 Schematic of the multi-channel redox CDI with $[Fe(CN)_6]^{3-}/[Fe(CN)_6]^{4-}$ redox couple electrolyte. Figure inspired by [64].

Generally, IEMs are always incorporated into the RFD system to ensure that active electrolyte ions do not leak from the electrode channel. For instance, anion electrolytes such as I^-/I^{3-} [87] and $[Fe(CN)_6]^{3-}/[Fe(CN)_6]^{4-}$ [281] are separated from the feed water channel by using CEM. Electrolytes containing cations like V^{3+}/V^{2+} using the AEM.[279] An additional water channel with IEMs (opposite charge to the flowable electrode channel) can be added beside the feed water channel, forming a continuous desalination and concentration RFD system. The RFD of circulating the ferrocyanide/ferricyanide electrolyte between the cathode and anode (SC mode) can achieve simultaneous dilution and concentration. At the cathode, $[Fe(CN)_6]^{3-}$ in the electrolyte is reduced to $[Fe(CN)_6]^{4-}$, and cations pass through the CEM and are captured in the water desalination channel. At the anode, $[Fe(CN)_6]^{4-}$ is oxidized to $[Fe(CN)_6]^{3-}$, releasing cations through the CEM into the water concentration channel. Meanwhile, anions from the desalination channel migrate to the concentration channel through the AEM and are retained (**Figure 19**).[282] The desalination capacity of the redox flow CDI system primarily arises from charge compensation during redox reactions of the electrolytes.

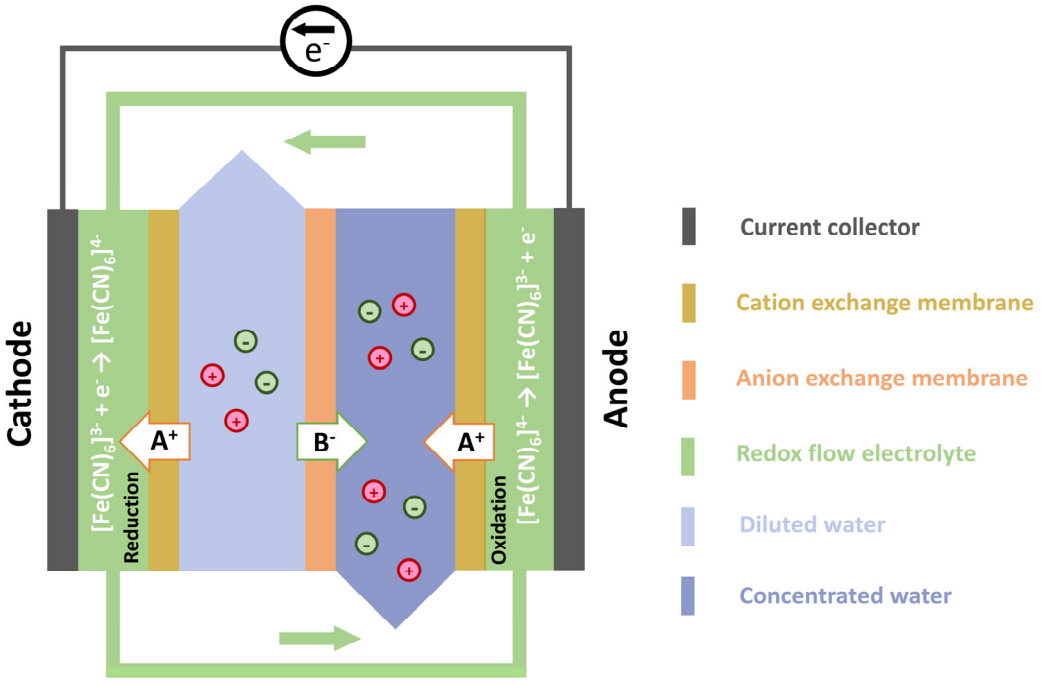

Figure 19 Schematic of the continuous desalination cell with ($[Fe(CN)_6]^{3-}/[Fe(CN)_6]^{4-}$ redox couple as electrolyte. Figure inspired by [283].

2.4. Selective ion separation in capacitive deionization

Selective ion separation, one of the pivotal technologies at the water-energy nexus, is crucial for water purification and resource recovery.[284] Increasing attention has been focused on utilizing CDI for selective ion removal and recovery.[150, 285-287] Various methods have been proposed to enhance or introduce the selectivity of CDI. These include using electrode materials with different pore sizes and compositions, adding functional groups, incorporating commercial IEMs or functionalized IEMs, or optimizing operational parameters.[288]

The selectivity towards the target ion in CDI is influenced by its mobility rate in bulk solution, which is usually faster than the competing ions due to the differences in ionic properties (ion charge and ion size) and low target ion concentration.[147]

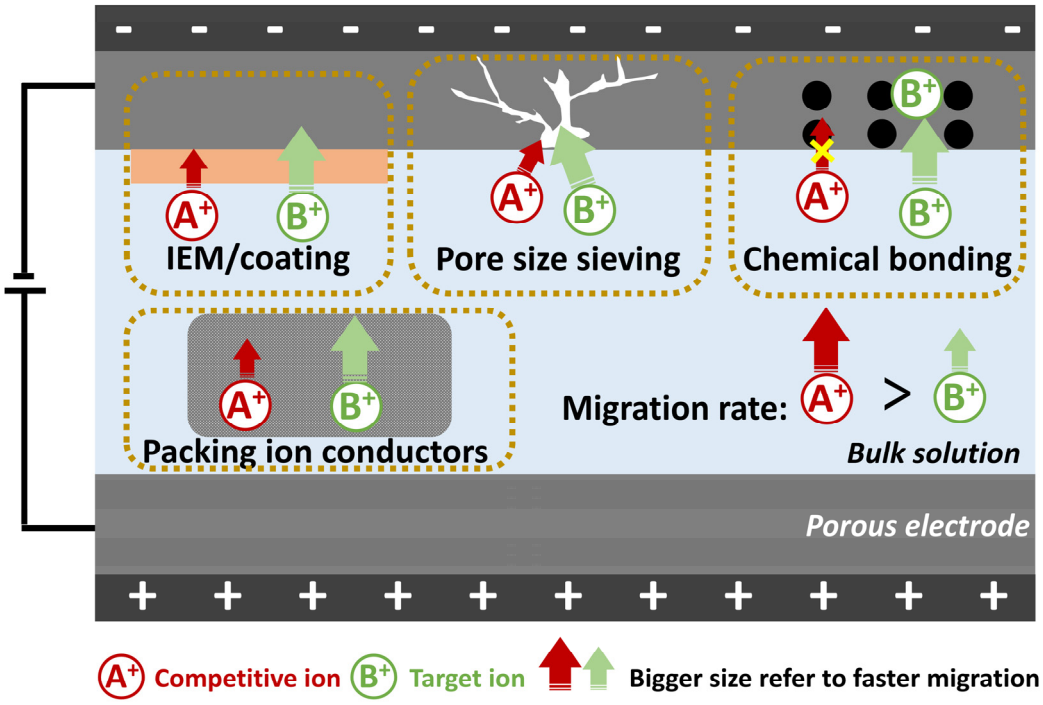

Figure 20 Selective ion removal in CDI. Figure inspired by [289].

Selective ion removal can be achieved at different processes along the CDI pathway, including the electrolyte, electrode, and the electrolyte/electrode interface. (**Figure 20**). In the electrolyte, the mobility rate of the target ion can be adjusted by introducing ion conductors. Ion exchange resins have been reported to enhance the mobility of Ca^{2+} and Mg^{2+} over Na^{+}.[290] When treating low-salinity water, packing granular activated carbon in the MCDI's feed water flow channel enhanced its desalination rate by ~20--150 % compared to the regular MCDI.[291]

At the interface of the electrode, membranes or coatings are added to enable selective ion separation. For instance, monovalent IEMs or nanofiltration membranes can block large, multi-valent ions, improving the selectivity for monovalent ions.[292] Selective ion exchange coatings can enhance the capture of divalent ions like Ca^{2+} over monovalent ions like Na^{+}.[293] Electrode materials with special physicochemical characteristics offer promising routes to improve CDI selectivity. Adjusting the pore size distribution in porous carbon electrodes can influence ion adsorption via pore sieving.[294] Functional groups introduced onto carbon material surfaces can also improve selectivity through chemical bonding or ion exchange mechanisms. Emerging Faradaic materials, such as metal oxides, metal-organic frameworks, and MXene, have been explored for the potential to achieve selective ion removal through chemical reactions.[295]

Carbon materials

Porous carbon is used in CDI for selective ion removal due to the high specific surface area.[84] Zhang et al. demonstrated that subnanometer carbon pores can discriminate ions based on size. The divalent cations are blocked in pores smaller than 0.6 nm. Due to its size ratio, K^{+} exhibits better selectivity over Na^{+}.[296] Later, they observed that the electrolyte confinement in carbon nanopores affects ion electrosorption in CDI, with subnanometer pores requiring ions to overcome a dehydration energy barrier before entering. The results show high electrochemical selectivity for Cs^{+} and K^{+} over other ions (Na^{+}, Li^{+}, Mg^{2+}, and Ca^{2+}), suggesting a potential for selective heavy metal removal by adjusting pore and ion sizes.[297] Eliad et al. concluded that monovalent ions are preferred over divalent ions, revealing the relationship between ion selectivity and hydrated radius.[298] Li et al. investigated the selective order in mixed monovalent ion solutions. The results showed that ions with smaller hydrated radii exhibit higher electrosorption capacity.[299] Surface modification can introduce functional groups onto the carbon electrode, which improves selective ion separation through chemical reactions with target ions.[300] Ethylenediamine triacetic acid (ETDA) was applied to functionalize graphene, enabling the selective removal of heavy metal ions.[301] An oxidized activated carbon cloth electrode achieved a selectivity improvement for K^{+} over Li^{+} from 1 to 1.8.[302]

Faradaic materials

Faradaic electrode materials exhibit enhanced selectivity for target ions due to ion intercalation and surface reactions, which store ions by Faradaic reaction rather than electrosorption.[303] Sodium manganese oxides show over 13 times higher selectivity of Na^+ over K^+ and 6-8 times for Ca^{2+} and Mg^{2+}, driven by redox interactions with sodium ions.[295]. Redox-active molybdenum dioxide/carbon electrodes as the cathode of an asymmetric CDI achieve a high selective capacitive removal efficiency (>99 %) of Pb^{2+} in a mixed solution containing lead and sodium ions.[174] Prussian blue analogs (PBAs), such as CuHCF, enable selective adsorption of NH_4^+.[174] NiHCF exhibits higher selectivity for monovalent ions than divalent ions.[304] Studies reported selective adsorption of NO_3^- by quaternary ammonium salt-modified activated carbon in an inverted CDI system.[305] The selective phosphate recovery can be achieved using magnetic Fe_3O_4/activated carbon in FCDI systems.[261] Wang et al. exhibited a high selective Pb^{2+} uptake capacity of 37.4 mg g^{-1} using the industrially exhausted granular ferric hydroxide as the electrode material.[306] Carbon-coated $Li_3V_2(PO_4)_3$ is developed as a cathode electrode using an HCDI system for selective Li^+ extract from salt lake brine. A reversible transition of the V valence state during electrosorption/desorption based on the Faradaic redox reaction was confirmed in this study. The results show lithium selectivity coefficients of 445 and 351 at high Mg^{2+}/Li^+ ratios of 1:5 and high Na^+/Li^+ ratios of 1:15, respectively.[307]

Selective ion separation through IEMs

Selective ion separation can also be achieved using IEMs. A Ca^{2+}-selective coating on the carbon electrode with IEMs was developed by Kim et al. They accomplished a Ca^{2+} over Na^+ selectivity of 3.5-5.4 with the Na^+:Ca^{2+} concentration ratio from 10:1 to 1:1 over 60 cycles.[293] By modifying CEM with a polyelectrolyte multilayer membrane, the electrode achieved a Na^+/Mg^{2+} selectivity ratio of 2.8.[308] Nativ et al. explored the selective separation of monovalent and divalent ions (Na^+/Mg^{2+} and Cl^-/SO_4^{2-}) combined with a CEM and nanofiltration membrane using an FCDI system. The nanofiltration membrane showed permselectivity for Na^+ over Mg^{2+} of 0.7-1, while it demonstrated better selectivity for Cl^- over SO_4^{2-} (1.3-7), highlighting the potential of the nanofiltration-FCDI system for selective anions separation.[309] Wang et al. utilized the Li-ion-selective ceramic membranes in the redox flow battery, achieving a superior Li^+/Mg^{2+} selectivity factor of about 500.000:1.[310]

Operational parameters

Selective ion separation can also be modified by adjusting operational parameters such as applied potential, current density, holding time, feed composition, influent pH, and flow rate.[289] MCDI can achieve selective SO_4^{2-} adsorption over Cl^- when using low current density and flow rate.[311] At low flow rates, higher voltages (less than 1.2 V). facilitate selective adsorption of Cl^- in the mixed solution containing Cl^-, PO_4^{3-}, and SO_4^{2-}.[311] Zhao et al. reported a time-dependent selectivity, with Na^+ being adsorbed 5 times higher than Ca^{2+} at the beginning stage of the desalination cycle. They also investigated the influence of applied potential on the SACs of various cations and found that the selectivities towards K^+ over Na^+ and Na^+ over Ca^{2+} align with the increase of applied potential.[312] Shi et al. achieved a Li^+/Mg^{2+} selectivity of 3 using an MCDI system with a selective CEM, finding that the flow rate also influences the selectivity.[181]

2.5. Second-life applications

The increasing global energy demand and escalating environmental damage propel the search for sustainable energy and storage technologies.[313] Carbon-based materials are among the most versatile materials in modern renewable energy applications, including generation and storage and environmental science for purification and remediation.[314] The aim of sustainable development requires the conservation, rational use, and enhancement of natural resources.[315] Hence, the entire life cycle of used resources should be considered, from the sourcing of precursors ("cradle") to environmentally friendly manufacturing processes and sustainable end-of-life management ("grave").[316]

Researchers are increasingly interested in innovative strategies for reusing used and end-of-life resources, such as recycling spent lithium-ion batteries.[317, 318] Pyrometallurgy and hydrometallurgy methods are commonly used to recover precious metals.[319] The metal is recovered by treatment of the spent batteries at high temperatures in pyrometallurgy, while solvents must be used in the hydrometallurgy process.[320] Recycling waste offers economic benefits by recovering valuable materials and conserving raw resources, contributing to sustainable development.[321] Unlike batteries, supercapacitors do not contain valuable elements such as lithium, cobalt, or nickel, while their recycling still needs to be considered.[322] Jiang et al. described a recycling approach for end-of-life supercapacitors based on shredding and mild thermal treatment.[323] Dong et al. reported a simple steam

physical activation method to regenerate high-class activated carbon from spent supercapacitors. The activation-recycled activated carbon enhances the mesopore ratios, improving rate performance and cycling stability to a level comparable to fresh activated carbon.[324] Wu et al. recycled carbon materials from spent commercial supercapacitors and then applied the materials as low-cost adsorbents for high-efficiency removal of Ag(I) and Cr(VI) ions from aqueous solutions.[325] These innovative recycling strategies demonstrate the potential to repurpose spent supercapacitor materials into valuable secondary applications and align with the principles of circular economy and sustainability.[326]

3. Approach and overview

My work is motivated by electrochemical water desalination for ion separation toward ion-selectivity and sustainable materials. The publications within my thesis work are separated into three segments (**Figure 21**).

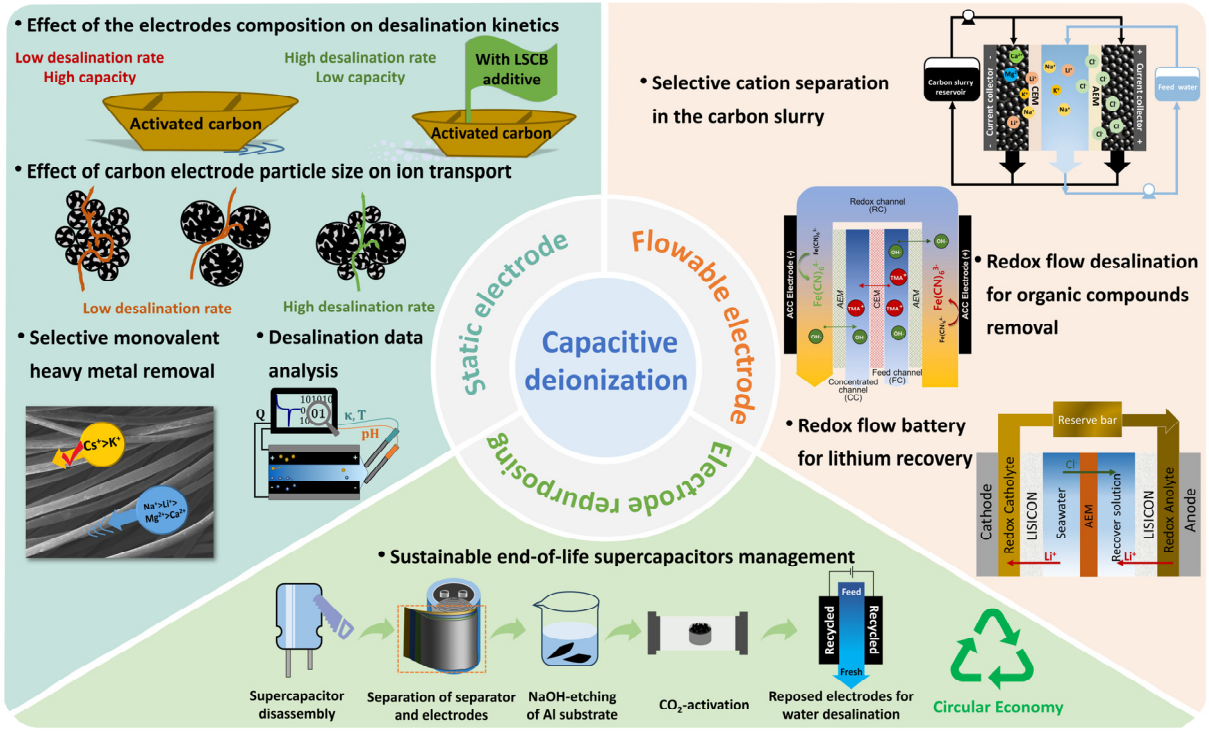

Figure 21 Overview of the three main segments of this dissertation. Peer-reviewed publications are cited in all chapters.

In the first segment, we focus on static electrode exploration. In **Chapter 4.1**, We investigated and summarized efficient data generation and analysis practices for electrochemical water desalination. Our study focuses on setting up the experimental setup, processing the data, and calculating the relevant metrics commonly used in CDI studies (such as salt removal capacity, charge efficiency, and energy consumption). We provided guidance on ensuring accurate and reliable data generation and analysis in CDI.

In **Chapter 4.2**, we studied the effect of activated carbon particle size and gave guides for electrode design. By separating the activated carbon into large and small particle size distributions and evaluating their desalination capabilities, we found that larger particles will cause a longer intraparticle ion diffusion pathway, leading to a lower desalination rate. Additionally, smaller particle size distribution will cause higher packing density and tortuosity

for interparticle ions transportation, leading to a lower desalination rate. Mixing larger particles with smaller particles can weaken these two limiting factors, and a higher desalination rate can be obtained.

Building on this, in **Chapter 4.3**, we studied the suitable choice of CAs. We selected various commercial and lab-synthesized carbon additives with diverse physicochemical properties to investigate their impact on electrochemical water desalination. By testing seven electrode types with different mixing recipes, we systematically evaluated the performance of salt uptake capacity, desalination rate, and stability over 100 cycles. Our study demonstrates that high desalination rates can be achieved by combining high surface area activated carbon with small, low surface area carbon additives, thereby reducing the overall diffusion path length. However, to maximize desalination capacity, it is essential to combine large, high surface area activated carbon particles with small, highly porous carbon additive particles to prevent a reduction in the overall surface area of the electrode.

In **Chapter 4.4**, we studied the ion selectivity performance based on activated carbon cloth with a narrower pore size distribution. A transition of "ion sieving-ion dehydration-ion insertion" for monovalent cations was observed during the electrochemical process. The results show ion selectivity for Cs^+ and K^+ over Na^+, Li^+, Mg^{2+}, and Ca^{2+}. This phenomenon is related to the difference in the hydrated ion size and the lower dehydration energy for heavier cations.

In the second segment, we utilized the flowable electrodes for electrochemical ion separation. In **Chapter 4.5**, we systematically evaluated the selective ion separation of activated carbon with varying physicochemical properties in multi-ion salt solutions, investigating the relationship between pore characteristics and ion selectivity. We comprehensively studied and optimized key parameters for the FCDI system, including mass loading of electrode slurry, CAs, applied voltage, slurry flow rate, and feedwater flow rate, to enhance selective ion separation. Results demonstrated nearly 100% removal of all ions within 32 h at optimized operating parameters, achieving a charge efficiency exceeding 70 %. A universal ion separation sequence ($Ca^{2+} > Mg^{2+} > K^+ > Na^+ > Li^+$) in FCDI was observed, which is related to the valence and hydration sizes of these cations. Ion selectivity can be effectively tuned by adjusting critical systematic parameters, facilitating the controlled separation of specific ions from multi-ion environments.

In **Chapter 4.6**, We developed a lithium-extraction redox flow battery to continuously recover lithium from seawater. This system consists of four channels: one for the recovery solution, one for feed water, and two for flowable redox electrolytes ($[Fe(CN)_6]^{3-}$/$[Fe(CN)_6]^{4-}$). The ceramic lithium superionic conductor membrane separates the recovery solution and feed-water channels from the redox-electrolyte channels. The green redox electrolyte is oxidized and reduced at the anode and cathode, creating an electrostatic force that draws lithium ions from seawater into the recovery solution. At the same time, chloride ions migrate through the AEM to maintain charge balance. The results show a high selectivity towards Li^+, with a Li^+ purity of 93.5 % in the extracts, associated with a high selectivity factor (Li^+/Mg^{2+}) of ca. 500000:1 at low cell voltage (0.6 V).

Using the same redox electrolytes for further study, in **Chapter 4.7**, we evaluated the potential of RFD for the valorization of tetramethylammonium hydroxide (TMAH) from wastewater. The cell configuration uses the two water channel modes (one for dilution and another for concentration) and SC mode. We achieved a reversible redox reaction that allowed for the continuous removal of TMAH from the wastewater stream while simultaneously recovering it as tetramethylammonium cations. The TMAH removal rate was approximately 4.3 mM $g^{-1}h^{-1}$, with a 40 % recovery ratio. Our system demonstrated potential for TMAH valorization under various operational conditions, achieving a 60 % reduction in capital costs compared to conventional desalination processes.

In the third segment, we discussed the potential for repurposing electrodes. In **Chapter 4.8**, we investigate the repurposing of carbon electrodes from supercapacitors for water desalination. We applied various electrode modifications, including direct reuse, NaOH-etching, CO_2-activation, and reformulation into new electrodes. These modified electrodes were then tested for electrochemical desalination of low-salinity NaCl solutions. Highlighting circular economy principles, our work demonstrates the potential to transform end-of-life supercapacitors into functional components for desalination systems, offering an innovative and valuable approach to resource reuse in electrochemical applications.

4. Results and discussion

This thesis includes the following peer-reviewed research papers as subchapters of the results and discussion section.

4.1 Best practice for electrochemical water desalination data generation and analysis

4.2 Particle size distribution influence on capacitive deionization: Insights for electrode preparation

4.3 Conductive carbon additives: Friend or foe of capacitive deionization with activated carbon?

4.4 Selectivity toward heavier monovalent cations of carbon ultramicropores used for capacitive deionization

4.5 Cation selectivity during flow electrode capacitive deionization

4.6 Redox flow battery for continuous and energy-effective lithium recovery from aqueous solution

4.7 Redox flow desalination for tetramethylammonium hydroxide removal and recovery from semiconductor wastewater

4.8 Life after death: Re-purposing end-of-life supercapacitors for electrochemical water desalination

4.1. Best practice for electrochemical water desalination data generation and analysis

Mohammad Torkamanzadeh,[1,2] Cansu Kök,[1,2] Peter Rolf Burger,[1,2] Panyu Ren,[1,2] Yuan Zhang,[1,3] Juhan Lee,[1,4] Choonsoo Kim,[5] and Volker Presser[1,2,6]

[1] *INM - Leibniz Institute for New Materials, Campus D2 2, 66123, Saarbrücken, Germany*

[2] *Department of Materials Science & Engineering, Saarland University, Campus D2 2, 66123, Saarbrücken, Germany*

[3] *Department of Materials Science and Engineering and A.J. Drexel Nanotechnology Institute, Drexel University, Philadelphia, Pennsylvania 19104, USA*

[4] *Heraeus Battery Technology GmbH, Reinhard-Heraeus-Ring 23, 63801 Kleinostheim, Germany*

[5] *Department of Environmental Engineering with Institute of Energy/Environment Convergence Technologies and Department of Future Convergence Engineering, Kongju National University, 1223-24, Cheonan-daero, Cheonan-si 31080, Republic of Korea*

[6] *saarene, Saarland Center for Energy Materials and Sustainability, Campus C4 2, 66123 Saarbrücken, Germany*

Citation:

M. Torkamanzadeh, C. Kök, P. Burger, P. Ren, Y. Zhang, J. Lee, C. Kim, and V. Presser, Best practice for electrochemical water desalination data generation and analysis, Cell Reports Physical Science 4(11) (2023) 101661.

Own contribution:

Writing - Review & Editing.

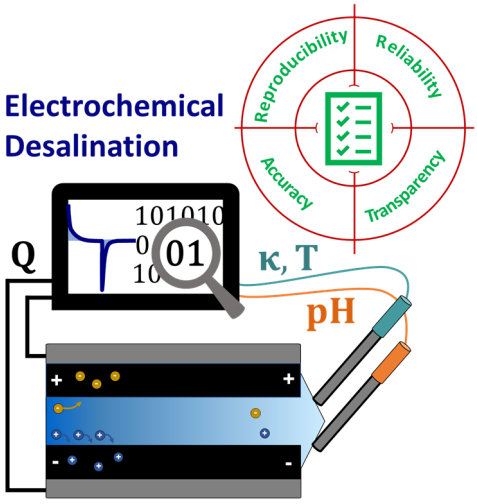

Cell Reports
Physical Science

CellPress
OPEN ACCESS

Article

Best practice for electrochemical water desalination data generation and analysis

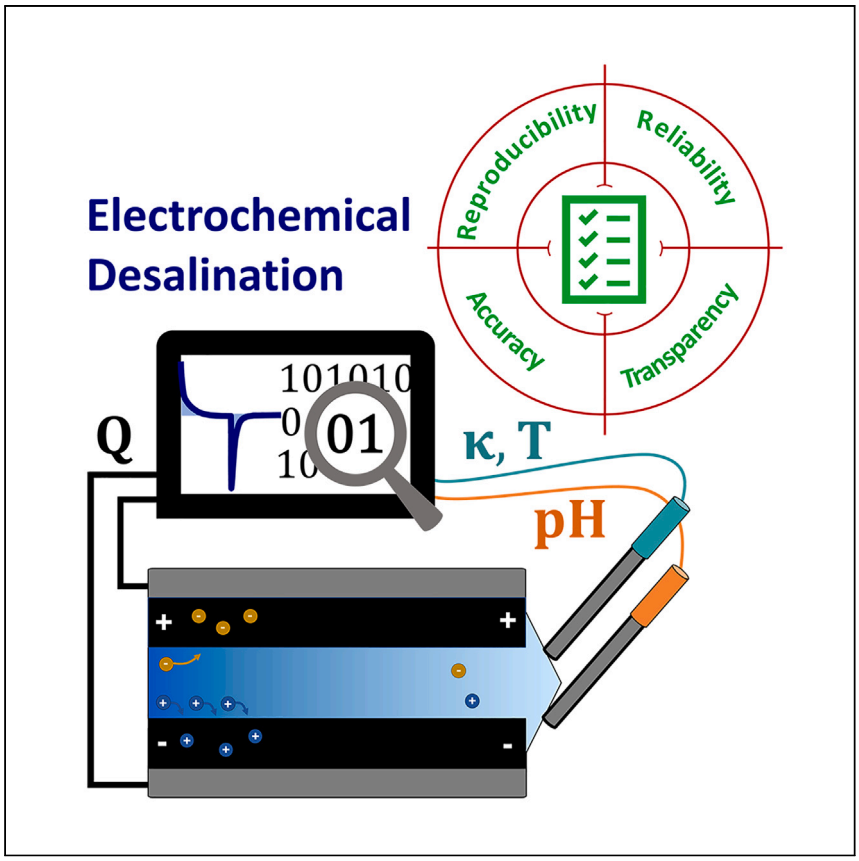

Electrochemical desalination shows promise for ion-selective, energy-efficient water desalination. Torkamanzadeh et al. provide a step-by-step guide on acquiring, processing, and calculating raw desalination data, emphasizing informative and reliable figures of merit.

Mohammad Torkamanzadeh, Cansu Kök, Peter Rolf Burger, ..., Juhan Lee, Choonsoo Kim, Volker Presser

volker.presser@leibniz-inm.de

Highlights

Detailed guide for acquiring and processing desalination data

Thorough demonstration for calculating critical desalination metrics

Insight on avoiding inaccuracies from leakage current and probe aging

Checklist and spreadsheet tools for enhanced test planning and accuracy

Torkamanzadeh et al., Cell Reports Physical Science 4, 101661
November 15, 2023
https://doi.org/10.1016/j.xcrp.2023.101661

Cell Reports
Physical Science

CellPress
OPEN ACCESS

Article

Best practice for electrochemical water desalination data generation and analysis

Mohammad Torkamanzadeh,[1,2] Cansu Kök,[1,2] Peter Rolf Burger,[1,2] Panyu Ren,[1,2] Yuan Zhang,[1,3] Juhan Lee,[1,4] Choonsoo Kim,[5] and Volker Presser[1,2,6,7,*]

SUMMARY

Electrochemical desalination shows promise for ion-selective, energy-efficient water desalination. This work reviews performance metrics commonly used for electrochemical desalination. We provide a step-by-step guide on acquiring, processing, and calculating raw desalination data, emphasizing informative and reliable figures of merit. A typical experiment uses calibrated conductivity probes to relate measured conductivity to concentration. Using a standard electrochemical desalination cell with activated carbon electrodes, we demonstrate the calculation of desalination capacity, charge efficiency, energy consumption, and ion selectivity metrics. We address potential pitfalls in performance metric calculations, including leakage current (charge) considerations and aging of conductivity probes, which can lead to inaccurate results. The relationships between pH, temperature, and conductivity are explored, highlighting their influence on final concentrations. Finally, we provide a checklist for calculating performance metrics and planning electrochemical desalination tests to ensure accuracy and reliability. Additionally, we offer simplified spreadsheet tools to aid data processing, system design, estimations, and upscaling.

INTRODUCTION

Electrochemical water desalination is a promising technology that removes the salt ions from aqueous saline media by applying electrical potential as the driving force. Electrodialysis and capacitive deionization are two powerful electrochemical desalination techniques that have the potential toward ion-selective,[1,2] low-energy-consuming,[3] high water recovery,[4] and economical[5] water remediation. In filtration processes such as reverse osmosis, by contrast, pressure serves as the driving force for ion migration; in thermal processes such as distillation processes, heat is the driving force that draws the water molecules out of a saline stream. In contrast, the fundamentally different driving force in electrothermal water desalination is the electrical field that draws the salt molecules out of a saline stream. As such, what makes electrochemical water desalination particularly interesting, among other factors, is that its energy consumption strongly depends on the initial salt concentration of the feed water, unlike other conventional thermal- or pressure-driven processes.[6,7] Comprehensive techno-economic analysis indicates that for a threshold between 3,000 and 30,000 ppm NaCl concentration levels in feedwater, a crossover point occurs for electrochemical water desalination and reverse osmosis. That is, electrochemical water desalination technologies below the mentioned threshold have become increasingly more economically attractive than reverse osmosis.[7]

[1]INM - Leibniz Institute for New Materials, D2 2, 66123 Saarbrücken, Germany

[2]Department of Materials Science & Engineering, Saarland University, Campus D2 2, 66123 Saarbrücken, Germany

[3]Department of Materials Science and Engineering and A.J. Drexel Nanotechnology Institute, Drexel University, Philadelphia, PA 19104, USA

[4]Heraeus Battery Technology GmbH, Reinhard-Heraeus-Ring 23, 63801 Kleinostheim, Germany

[5]Department of Environmental Engineering with Institute of Energy/Environment Convergence Technologies and Department of Future Convergence Engineering, Kongju National University, 1223-24 Cheonan-daero, Cheonan-si 31080, Republic of Korea

[6]Saarene, Saarland Center for Energy Materials and Sustainability, Campus C4 2, 66123 Saarbrücken, Germany

[7]Lead contact

*Correspondence: volker.presser@leibniz-inm.de

https://doi.org/10.1016/j.xcrp.2023.101661

The energy and cost efficiency,[8] along with many other attractive unique capabilities, such as partially recovering the invested energy[9] or selective separation of ions,[2,10,11] have made electrochemical desalination the subject of numerous studies during the past two decades.[12–15] The key to making those studies reliable, comparable, and reproducible are clear guidelines on how electrochemical desalination data are acquired, processed, and reported. Yet such best-practice studies are limited in the literature, which could limit the rapid advancement of electrochemical desalination technology.

In a typical electrochemical desalination cell, a voltage is applied to a pair of electrodes, and an aqueous saline medium, commonly NaCl, is the electrolyte that continuously flows in and out of the cell. As such, an electrochemical desalination cell could be considered a supercapacitor/battery, only different in that the electrolyte flows through an electrochemical desalination cell. In contrast, it is stagnant in regular supercapacitors/batteries. The standard and probably simplest form of an electrochemical desalination cell is where the water stream passes between and tangentially to the two electrodes, known as the flow-by configuration (Figure S1). Upon polarization of carbon electrodes by applying a charging or discharging voltage, the system's response is commonly recorded in the form of the following key variables: (1) the amount of electric charge stored in the electrodes and (2) the change in the conductivity of the outflowing water. Depending on the available infrastructure, one might record additional variables, such as pH and temperature of outflowing water.

In the present study, we first deal with the conversion of the measured conductivity and pH data into actual salt concentration. We then establish the design of a typical electrochemical water desalination setup consisting of an electrochemical desalination cell with a pair of symmetric activated carbon electrodes in its core and conductivity and pH probes placed downstream of the cell. We show how the obtained conductivity and pH data can be related to the concentration and how the latter concentration obtained is further processed into commonly reported desalination performance metrics in the literature,[16] namely, desalination capacity, charge efficiency, and energy consumption. With the aid of an online elemental monitoring apparatus, we also investigate electrochemical desalination with a mixed-salt electrolyte and show how the preferential removal of specific ions could be quantified and reported in terms of selectivity metrics.

We then systematically investigate the effects of temperature and the aging of the conductivity probe over a 6-month period and how that influences the final reported desalination performance metrics. Finally, we recommend to the community of electrochemical water desalination researchers when and how to best calibrate the conductivity probes to avoid skewing the results. We also provide several simplified and easy-to-use spreadsheets that readily enable the synchronization between pH and concentration data, calculation of concentrations, conversion of standard concentration units (mg L^{-1}, ppm, mmol L^{-1}) into one another, calculation of the electrode mass needed to achieve a desired water quality, and much more.

RESULTS AND DISCUSSION

Description of a typical desalination setup and experiment

Figure 1A schematically shows a typical electrochemical desalination setup. An electrolyte tank (in our case, typically 10 L) provides a practically constant concentration of saline water fed into the cell. However, the size of the tank needs to be adjusted for

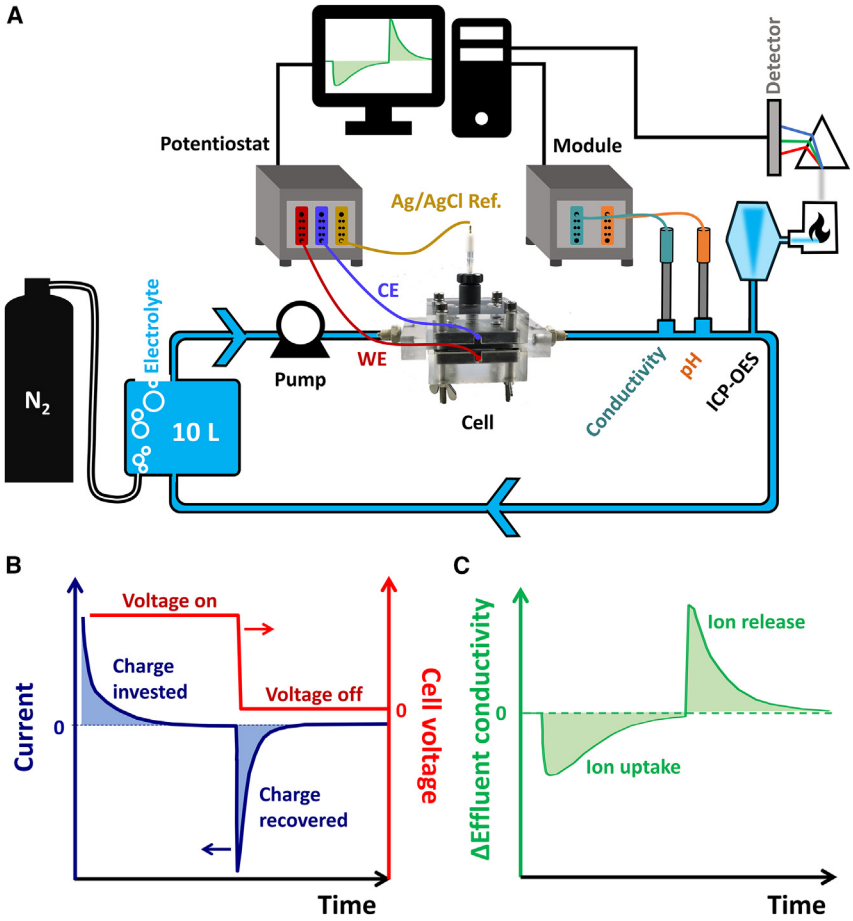

Figure 1. Electrochemical desalination setup and real-time response of the cell

(A) Schematic representation of a typical electrochemical desalination setup; WE, working electrode; CE, counter electrode.

(B) The applied cell voltage profile and the current response of the cell.

(C) The corresponding conductivity profile during one full electrochemical desalination cycle.

the size of the desalination cell, and one must also consider the possible water evaporation over time during long-term operation. Such a setup is known as a single-pass mode of operation, in contrast to the batch mode.[12] A peristaltic pump continuously circulates the electrolyte from the tank to the cell through the conductivity and pH chambers and directs the electrolyte back to the tank. A nitrogen gas tube is inserted into the tank to constantly bubble the electrolyte with a small nitrogen gas flow to remove the air, and particularly the dissolved oxygen, from the water. The latter measure was taken to minimize carbon oxidation and performance degradation, since the dissolved oxygen in the electrolyte can take part in parasitic oxygen reduction reaction and peroxide formation during charge and discharge.[17,18]

As outlined before, two key datasets are commonly recorded in an electrochemical desalination experiment: (1) electrochemical data provided by the electrochemical workstation, which can include current-time (*I*-*t*), cell voltage-time (*V*-*t*), electrode potential-time (*E*-*t*), or energy-time (*U*-*t*) data, among others, and (2) the cell's effluent electrolyte properties provided by the probes installed at the downstream side of the cell, which can include conductivity-time, pH-time, or temperature-time data, among others.

Figure 1B shows the cell voltage applied during charge and discharge, together with the current response of the cell. As will be shown later, the electric charge stored in the carbon electrodes can be calculated by integrating the area under the *I*-*t* curve presented here. In a single-pass mode of operation, the concentration-time profile of the outflowing water from the cell resembles the scheme shown in Figure 1C. In the latter mode of operation, there is a quasi-infinite abundance of salt ions present in the circulating electrolyte, which is more than sufficient for the electrodes to take up. As a result, after applying a cell voltage for a while, the electrodes saturate with an overabundance of the present salt ions and reach their maximum (equilibrium) capacities, and the salt concentration of the water flowing out of the cell will finally reach the level of the water that flew into the cell. Likewise, the stored salt ions in the electrodes are ejected back to the circulating electrolyte (brine solution) upon applying the discharge voltage.

The conductivity change is translated into concentration change (see the section "calibration of conductivity probes"), and the integrated area under the concentration-time curve measures the capacity of the electrodes to remove salt ions, a merit called desalination capacity (DC). The electrode's capacity to remove salt ions can then be compared with its capacity to store electric charge in the same cycle. A measure that reports the fraction of the former to the latter is called charge efficiency (CE). CE is not to be confused with Coulombic efficiency, which states the fraction of electric charge obtained during discharging to that while charging an electrochemical cell, a standard metric reported in battery research.

Finally, the energy consumed during the charging of the electrodes could be reported as normalized to the number of ions removed. Assuming no other losses, the net consumed energy in one complete cycle could be envisioned as the sum of the enthalpies of demixing the saline feed water into the desalinated solution produced during charging and the brine solution produced during discharging.[19] The consumed energy for demixing can be harvested again upon mixing the two latter solutions (the capmix process), giving rise to the concept of blue energy or osmotic power.[20]

Calibration of conductivity probes

To calculate standard desalination performance metrics, such as desalination capacity, one has to convert the obtained conductivity-time data (Figure 1C) into concentration-time data. As a first step, the conductivity probes should be calibrated (or standardized) using several NaCl stock solutions with known concentrations. Figure 2A shows a conductivity probe calibrated with 17 stock solutions of NaCl in pure water, ranging from 1 mmol L^{-1} to 1,000 mmol L^{-1}. For accuracy, the conductivity probes are best calibrated with stock solutions with concentrations around the target electrolyte desired to be tested in an electrochemical desalination experiment. In this study, since the target electrolyte for the subsequent electrochemical desalination tests is 20 mmol L^{-1} NaCl, the calibration curve is constructed for the concentration regime of 1–50 mmol L^{-1} (Figure 2B), resulting in a good coefficient of determination (R^2) of 0.999 between conductivity and concentration values. Similarly, if an electrolyte simulating seawater-level concentrations of NaCl (~600 mmol L^{-1}) is to be used, a calibration curve between 500 and 1,000 mmol L^{-1} can be constructed (Figure 2C) and used.

Using the concentration-conductivity equation in Figure 2B, the conductivity data obtained in an electrochemical desalination experiment (Figure 3A) could be converted into concentration data (Figure 3B), enabling further calculations on the desalination capacity and CE.

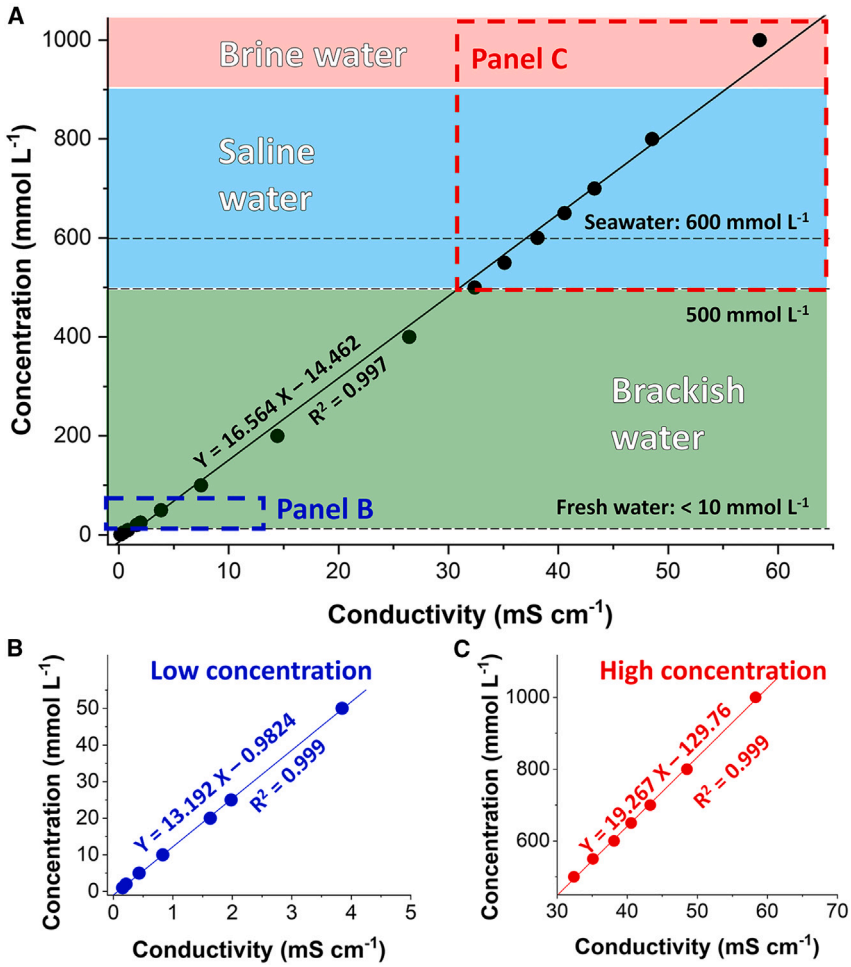

Figure 2. Construction of the calibration curves relating the conductivity to the concentration

Calibration curves were constructed to convert the measured conductivity into concentration in (A) the entire 1–1,000 mmol L^{-1} range, (B) a low-concentration regime of 1–50 mmol L^{-1}, and (C) a high-concentration regime of 500–1,000 mmol L^{-1}.

Desalination capacity

Figure 3A shows the conductivity variations of a standard single-pass electrochemical desalination experiment during several cycles. In this study, we have used a symmetric cell composed of two activated carbon electrodes, charged and discharged at 1.2 V and 0.3 V, respectively. The experimental procedures section details the experimental and operational conditions used in the latter test. Figure 3B shows the typical concentration variations upon cycling of an electrochemical desalination cell. As illustrated in Figure 1A, the electrolyte solution is constantly bubbled by nitrogen gas to remove the dissolved oxygen, accelerating the electrolyte's evaporation over time. As a result, the concentration slightly increases and, hence, the feed concentration of ~22 mmol L^{-1} is reached in Figure 3B instead of the initially made 20 mmol L^{-1}. To alleviate electrolyte evaporation, one might pre-wet the dry nitrogen flow by passing it through a gas-washing water bottle.

For the sake of simplicity, the x axis (time) in Figure 3B could be converted to cycle number by dividing the time by the cycle duration (a peak-to-peak separation), which is 7,220 s in the present case, as illustrated in Figure S2. Based on the

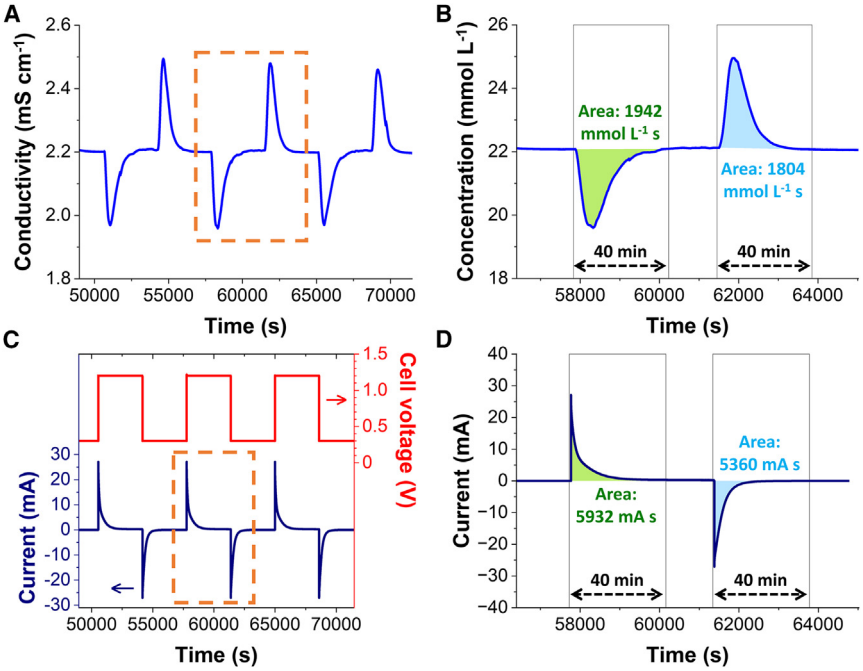

Figure 3. Integration of the area under the curves of concentration-time and current-time profiles

(A and B) Processing steps for converting the (A) raw conductivity-time data into (B) concentration-time data and the integration of the area under the curve for charging and discharging half-cycles.

(C) The applied cell voltage during charge and discharge and the current response.

(D) The integration of the area under the current-time curve for charging and discharging half-cycles.

decrease/increase in concentration curve versus time (Figure 3B), induced by charging/discharging of the cell by the electrochemical workstation, the DC (mg_{salt} $g_{electrode}^{-1}$) is then calculated following Equation 1:

$$DC = \frac{\nu M_{NaCl}}{m_{total}} \int C\, dt, \qquad \text{(Equation 1)}$$

where ν is the flow rate (L s^{-1}), M_{NaCl} is the molar mass of NaCl (58.44 g mol^{-1}), m_{total} is the total mass of both electrodes combined (g), and t is the time (s) during which a concentration change (mmol L^{-1}) occurs.

However, one commonly deals with more practical units at laboratory-scale electrochemical desalination, namely, mL min^{-1} for flow rate (v) and mg for electrode mass (m_{total}). Also, the collective term $\int C\, dt$, with the unit mmol L^{-1} s, is obtained by integrating the area under each half-cycle in concentration-time curves. In this case, Equation 1 must be divided by 60 as a conversion factor to give Equation 2:

$$DC\left(\frac{\text{mg NaCl}}{g_{electrode}}\right) = \frac{\nu\left(\frac{\text{mL}}{\text{min}}\right) \times 58.44\left(\frac{\text{g NaCl}}{\text{mol NaCl}}\right)}{60\, m_{total}(\text{mg})} \int C\, dt\left(\frac{\text{mmol s}}{\text{L}}\right), \qquad \text{(Equation 2)}$$

which further simplifies into Equation 3:

$$DC\left(\frac{\text{mg NaCl}}{g_{electrode}}\right) = \frac{0.974\, \nu\left(\frac{\text{mL}}{\text{min}}\right)}{m_{total}(\text{mg})} \int C\, dt\left(\frac{\text{mmol s}}{\text{L}}\right), \qquad \text{(Equation 3)}$$

Substituting in Equation 3 1.6 mL min^{-1} for the flow rate, 270.6 mg for the total mass of both electrodes (137.1 mg + 133.5 mg), and 1,873 mmol L^{-1} s as the average of

integrated areas under the two charging and discharging half-cycles in concentration-time curves $\left(\frac{1,942+1,804}{2}\right)$, will result in DC = 10.8 mg NaCl removal capacity per gram of electrode, or 10.8 mg g^{-1} in short.

In some cases, mainly where selectivity toward certain cations or anions is involved,[11] total NaCl salt removal capacity (DC) may be less relevant than specific removal capacities toward certain ions. If those ions are sodium and chloride,[21] the DC can be broken down to sodium removal capacity and chloride removal capacity following Equations 4 and 5, respectively.

Na^+ removal capacity:

$$\left(\frac{\text{mg Na}^+}{g_{\text{electrode}}}\right) = \text{DC}\left(\frac{\text{mg NaCl}}{g_{\text{electrode}}}\right) \times \frac{\text{mol NaCl}}{58.44\ \text{mg NaCl}} \times \frac{1\ \text{mol Na}^+}{1\ \text{mol NaCl}} \times \frac{22.99\ \text{mg Na}^+}{1\ \text{mol Na}^+} = 0.39\ \text{DC}, \quad \text{(Equation 4)}$$

Cl^- removal capacity:

$$\left(\frac{\text{mg Na}^+}{g_{\text{electrode}}}\right) = \text{DC}\left(\frac{\text{mg NaCl}}{g_{\text{electrode}}}\right) \times \frac{\text{mol NaCl}}{58.44\ \text{mg NaCl}} \times \frac{1\ \text{mol Cl}^-}{1\ \text{mol NaCl}} \times \frac{35.45\ \text{mg Cl}^-}{1\ \text{mol Cl}^-} = 0.61\ \text{DC}, \quad \text{(Equation 5)}$$

For the example above, Na^+ and Cl^- removal capacities would then be 4.2 mg g^{-1} and 6.6 mg g^{-1}, respectively. Adjustments must be made if a different salt system is investigated, such as KCl or $NaSO_4$.

Charge efficiency

After DC, another key metric of an electrochemical desalination system, not always reported in the literature, is the CE. CE is a unitless value between zero and unity (commonly given in percent) that gauges the portion of the invested electric charge that contributes to removing salt ions from the saline stream. The closer the CE to unity (or to 100%), the less the system suffers from parasitic losses. The latter parasitic losses stem from co-ion expulsion phenomena and electrode-electrolyte faradic side reactions.[22] As a result, side processes that do not contribute to the electrochemical desalination bottom line, that is, maximum net salt removal, will decrease the CE value. For a review of different sources of parasitic losses, readers are referred to other studies.[12,23,24]

The CE (%) can be formulated as Equation 6:

$$\text{CE}\ (\%) = \frac{\text{DC}}{\frac{M_{\text{NaCl}}}{\frac{Q}{F}}} \times 100\%, \quad \text{(Equation 6)}$$

where F is the Faraday constant and Q is the average of total charge stored in the two electrodes normalized to the total mass of both electrodes combined. In Equation 6, the nominator expresses the population of salt ions taken up by the electrode, and the denominator expresses the population of invested electric charge. A critical point that needs to be stressed here is that the charge substituted in the CE formula should be obtained from the same cycle and the duration from which the DC was obtained. As such, the charge capacity/capacitance of the electrodes obtained via any other techniques performed prior to desalination experiments, such as cyclic voltammetry or charge/discharge, will be irrelevant to use here.

For practical reasons, the term Q in Equation 6 can be defined as $Q = \frac{q}{m_{total}}$, where q is obtained by integrating the area under each half-cycle in current-time curves or readily obtained by the electrochemical workstation software (EC-Lab in this work). More discussion on the significance of employing either of the latter methods for calculating charge will follow later in this article (see the section "leakage current subtraction"). One might find the following units convenient to use at the laboratory-scale tests: 96,485 C mol^{-1} for the Faraday constant (F), mg for electrodes mass (m_{total}), mA s for charge (Q), and 58.44 g mol^{-1} for the molar mass of NaCl (M_{NaCl}). In that case, Equation 6 must be divided by 1,000 as a conversion factor to turn into Equation 7:

$$CE\ (\%) = \frac{DC\left(\frac{mg\ NaCl}{g_{electrode}}\right) \times 96,485\left(\frac{C}{mol}\right) \times m_{total}(mg)}{1,000 \times q\ (mA\ s) \times 58.44\left(\frac{g\ NaCl}{mol\ NaCl}\right)} \times 100, \qquad \text{(Equation 7)}$$

which simplifies into Equation 8:

$$CE\ (\%) = \frac{165.10\ DC\left(\frac{mg\ NaCl}{g_{electrode}}\right) \times m_{total}(mg)}{q\ (mA\ s)}, \qquad \text{(Equation 8)}$$

Substituting in Equation 8 10.8 mg g^{-1} for DC, 270.6 mg for the total mass of both electrodes (137.1 mg + 133.5 mg), and 5,646 mA s as the average of integrated areas under the two charging and discharging half-cycles in I-t curves $\left(\frac{5,932+5,360}{2}\right)$ will result in CE = 85%.

In an ideal case, the DC or CE obtained in the charging half-cycle (desalination) should be equal to that in the discharging half-cycle (regeneration). Because of non-idealities and parasitic losses, such as leakage current (which will be dealt with later in this work), non-equal, but often close, values of DC or CE are obtained for the two half-cycles. In such a case, one might choose to average the two values, as done above. Without averaging, the DC and CE for the charging half-cycle would be 11.2 mg g^{-1} and 84%, respectively, and the DC and CE for the discharging half-cycle would be 10.4 mg g^{-1} and 87%, respectively.

As seen, the values calculated herein differ well below 10% between charging and discharging half-cycles. If those two values differ largely, that is, >10%, one might need to check whether the baseline selection for integration of the area under the curves was precise. A simple method to get better baselines is to prolong the holding times for charging and discharging half-cycles (for relevant considerations, see also the section "leakage current subtraction"), which allows the concentration of the cell's effluent water to reach equilibrium. Moreover, one might also entertain the possible presence of detrimental faradic processes present significantly more in one half-cycle and absent in the other half-cycle. The latter phenomenon is often the case during the charging half-cycle, mainly when the cell is not carefully mass-balanced, and the electric potentials developed in one or both electrodes exceed their stability windows.

Energy consumption

The energy consumed to accomplish the desalination is a key metric for comparing an electrochemical desalination system to other adjacent technologies. Also, within the realm of electrochemical desalination, the energy consumption analysis provides vital insight when comparing different system components, such as electrode materials, cell configurations, or electrolyte concentrations, as to which combination yields the most energy-efficient results. Such energy consumption analysis, for

instance, can reveal that while carbon electrodes show an increased energy consumption going toward higher electrolyte concentrations, faradic materials such as 2D transition metal sulfides or MXenes show a rather constant energy consumption across wide concentration ranges.[16,21,25]

Two approaches could be taken for energy consumption analysis: macroscopic and microscopic. The macroscopic approach involves the Wh energy required for producing x liters of freshwater, commonly reported in the unit Wh L^{-1}. The salt content of freshwater is variously defined as less than 500 ppm[26] (<9 mmol L^{-1} NaCl) or less than 1,000 ppm[27] (<17 mmol L^{-1} NaCl). The macroscopic approach is more common in reverse osmosis technology, although its application for electrochemical desalination systems must be cautiously employed. In the case of reverse osmosis filtration, more than 99% of the salt content in the feedwater is removed from the product water.[28] In contrast, in electrochemical desalination at the laboratory scale, only a few percent of the salt content is removed in each charging half-cycle in a single-pass mode of operation.[29] As such, calculating energy consumption for complete salt removal via an electrochemical desalination system might require extrapolation calculations which assume that the system consumes the same energy rate all the way down to a very-low-salt-content electrolyte. However, the latter assumption could be erroneous, as electrolytes of lower concentrations would show a higher solution resistance, resulting in more energy consumed as the concentration decreases.

The microscopic approach, however, eliminates the need for extrapolations or unreliable assumptions. The latter approach involves the energy consumed to remove one salt formula unit in a single electrochemical desalination cycle, which will also be dealt with herein. As outlined before, the energy consumed during the charging (U_{charge}) of the electrodes are often considered the basis for energy calculations, even though part of that energy could be potentially recovered during the discharging of the electrodes.[9,30] Equation 9 can then be formulated to calculate the energy invested to remove a single salt molecule from the saline stream.

$$\text{Energy consumption per ion} = \frac{\frac{U_{charge}}{m_{total}}}{\frac{DC}{M_{NaCl}}}, \qquad \text{(Equation 9)}$$

where the nominator in Equation 9 provides the consumed energy normalized to the mass of both electrodes combined (Wh g^{-1}), and the denominator gives the moles of salt ions removed normalized to the mass of both electrodes combined (mmol g^{-1}).

The practical energy unit that one commonly deals with at laboratory-scale electrochemical desalination tests is Wh for energy consumed, while the desirable energy unit to report the energy values in molecular-scale systems is the product of the Boltzmann constant and temperature (k_BT). Given that For T = 298 K, 1 Wh is equal to 8.75 × 10^{23} k_BT, the substitution of the Avogadro number yields Equation 10:

$$\text{Energy consumption per ion}\left(\frac{k_BT}{\text{ion}}\right) = \frac{\frac{U_{charge}\ (\text{Wh})}{m_{total}\ (\text{mg})}}{\frac{DC\left(\frac{\text{mg}}{\text{g}}\right)}{M_{NaCl}\left(\frac{\text{g}}{\text{mol}}\right)}} = \frac{\frac{U_{charge}\ (\text{Wh})}{m_{total}\ (\text{mg})} \times \frac{1{,}000\ \text{mg}}{1\ \text{g}} \times \frac{8.75 \times 10^{23}\ k_BT}{1\ \text{Wh}}}{\frac{DC\left(\frac{\text{mg}}{\text{g}}\right)}{58.44\left(\frac{\text{g}}{\text{mol}}\right) \times \frac{1{,}000\ \text{mg}}{1\ \text{g}} \times \frac{1\ \text{mol}}{6.02214076 \times 10^{23}}}}, \qquad \text{(Equation 10)}$$

which, upon further simplification, yields Equation 11:

$$\text{Energy consumption per ion}\left(\frac{k_BT}{\text{ion}}\right) = \frac{8.49\times10^{7}\ U_{\text{charge}}\ (\text{Wh})}{m_{\text{total}}\ (\text{mg})\times \text{DC}\left(\frac{\text{mg}}{\text{g}}\right)}, \qquad \text{(Equation 11)}$$

Referring to the electrochemical workstation software, the U_{charge} for the cycle studied above (Figure 3B) is 2.08×10^{-3} Wh. Substituting the latter value in Equation 11, along with 10.8 mg g^{-1} for DC and 270.6 mg for the total mass of both electrodes, will result in 60.4 k_BT per single salt molecule (NaCl) removed.

Ion selectivity

There has been an ever-growing interest in the electrochemical desalination research toward selective separation and recovery of ions from aqueous media, either to remove toxic/undesired species from water streams or to capture valuable elements.[2,31] Table 1 lists several works that have reported the selective electrochemical removal of certain ionic species from aqueous media in the presence of other competing ions in a cyclic manner. Lithium, nickel, cobalt, and manganese, for instance, are among the value-added elements that can be recovered from the leaching solution of spent lithium-ion batteries,[32–34] contributing toward a circular economy. The target ionic species in Table 1 are highlighted in a periodic system of elements with their significance and critical applications, as illustrated in Figure 4. As can be seen, the electrochemical desalination world is no longer limited to mere sodium chloride removal. Still, it has expanded in scope for selective removal of cations or anions of various types.

To calculate the performance metrics of an electrochemical desalination system, one has to determine the change in the concentrations of ionic species flowing out of the cell. However, when there is more than one salt species involved, the concentration cannot be related to the conductivity of the effluent water stream, as the measured conductivity is a product of the contribution of multiple ionic species (Figure 5A). Developing methods to quantify the individual ion concentration in a mixed-salt electrolyte is crucial in studying the system's selectivity. Inductively coupled plasma optical emission spectroscopy (ICP-OES), for instance, is a powerful and accurate tool that can individually quantify many ionic species simultaneously.

Techniques such as ICP-OES,[71] inductively coupled plasma mass spectrometry,[72] or ion chromatography[37,45,73] are methods to monitor individual ionic species. Alternatives include the EDTA titration of mixtures of Ca^{2+} and Mg^{2+} ions,[74] or the colorimetric method for determining Pb^{2+} ions in the presence of alkali metal and alkaline earth metal ions.[75] The latter process required the treatment of lead ions with sulfide ions to convert the colorless lead ions into adsorptive lead sulfide, followed by UV-visible-near-infrared (UV-vis-NIR) spectrophotometry.

Ion-selective electrodes have been used when dual-salt electrolytes are involved. An example of the latter is surfactant-functionalized activated carbon electrodes developed to demonstrate a high affinity for NO_3^- compared to Cl^- ions.[73] Combined use of ion-selective electrodes and conductivity/pH measurements have also been shown for mixtures of Na^+ and Ca^{2+} ions[53,76] using the extended Onsager-Fuoss model.[77] The latter theoretical foundation helps to predict the complex conductivity changes that occur with concentration changes. This theoretical guidance provides calibration methods that consider the impact of ionic association on conductivity assessments, ensuring that accuracy and precision are maintained over a wide range of concentrations.[78]

Table 1. Overview of electrochemical desalination research on selective recovery of ions from aqueous media

Target element	Competing ions	Electrode material	References
Li^+	Na^+, K^+, Mg^{2+}	$LiFePO_4$	Trócoli et al.,[35,36] Pasta et al.[35,36]
Li^+	Na^+, K^+, Mg^{2+}, Ca^{2+}	λ-MnO_2	Lee et al.,[37–39] Trócoli et al.,[37–39] Kim et al.[37–39]
Li^+	Na^+, K^+, Mg^{2+}	flow electrodes of ($Fe[CN]_6^{4-}$/$Fe[CN]_6^{3-}$) redox pair + LISICON membrane	Wang et al.[8]
Li^+	Co^{2+}	activated carbon fiber + MXene-based ion-sieving membrane	Jiang et al.[40]
Na^+	Mg^{2+}, Ca^{2+}	nickel hexacyanoferrate (NiHCF Prussian blue analog)	Singh et al.[41]
Cs^+	Na^+, Sr^{2+}	copper hexacyanoferrate (CuHCF Prussian blue analog)	Lee et al.[42]
NH_4^+	Na^+, K^+, Mg^{2+}, Ca^{2+}	nickel hexacyanoferrate (NiHCF Prussian blue analog)	Tsai et al.[43]
ClO_4^-	Cl^-	activated carbon cloth	Xing et al.[44]
PO_4^{3-}	Cl^-, NO_3^-, SO_4^{2-}	layered double hydroxide-reduced graphene oxide composite	Hong et al.[45]
NO_3^-	Cl^-, SO_4^{2-}	hierarchical carbon aerogel monoliths	Hawks et al.[46]
SO_4^{2-}	Cl^-	amine functionalized activated carbon	Zuo et al.[47]
Cl^-	SO_4^{2-}	Bi	Chang et al.[48]
Br^-	Cl^-	activated carbon + ion-exchange membranes	Li et al.[49]
I^-	Cl^-	flow electrodes of activated carbon	Liu et al.[50]
F^-	SO_4^{2-}	activated carbon + monovalent anion selective membrane	Pan et al.[51]
F^-	Cl^-, NO_3^-	graphene oxide-hydroxyapatite composite	Park et al.[52]
Ca^{2+}	Na^+	H_2SO_4-treated activated carbon cloths	Uwayid et al.[53]
Sr^{2+}	Na^+	aryl diazonium salt-modified porous carbon	Xiang et al.[54]
Cu^{2+}	Na^+	flow electrodes of activated carbon	Zhang et al.[55]
Fe^{3+}	Na^+, Mg^{2+}, Ca^{2+}	graphene nanoflakes	Li et al.[56]
Ni^{2+}	–	conductive graphite adhesive-activated ion-exchange resin composite	Wang et al.[57]
Co^{2+}	Li^+, Ni^{2+}	electrodialysis with polymeric ion-exchange membranes	Siekierka and Yalcinkaya[58]
Mn^{2+}	–	flow electrodes of dilute H_2SO_4 with polymeric ion-exchange membranes	Soysüren et al.[59]
Zn^{2+}	–	activated carbon cloth	Tang et al.[60]
Pb^{2+}	Mg^{2+}, Ca^{2+}	thiol-functionalized graphene oxide-activated carbon composite	Huang et al.[61]
Pb^{2+}	Co^{2+}, Ni^{2+}	FeOOH	Wang et al.[62]
Cd^{2+}	–	flow electrodes of δ-MnO_2	Peng et al.[63]
V^{5+} (as VO^{3-})	SO_4^{2-}, PO_4^{3-}, SiO_3^{2-}	resin-activated carbon composite	Bao et al.[64]
Cr^{6+} (as $Cr_2O_7^{2-}$)	Cl^-, ClO_4^-	poly(vinyl)ferrocene-carbon nanotubes composite	Su et al.[65]
As^{5+} (as AsO_4^{3-})	Cl^-	poly(vinyl)ferrocene-carbon nanotubes composite	Su et al.[65]
Sc^{3+}	Na^+, K^+, Mg^{2+}, Ca^{2+}, Zn^{2+}, Al^{3+}, Fe^{3+}	electrodialysis with polymeric ion-exchange membranes	Li et al.[66]
Sm^{3+}	Ag^+, Cd^{2+}, Co^{2+}, Mn^{2+}, Al^{3+}, Cr^{3+}, Fe^{3+}, Cu^{2+}, Pb^{2+}, Hg^{2+}, Ni^{2+}, Zn^{2+}, NH_4^+, Na^+, K^+, Mg^{2+}, Ca^{2+}	$B_{12}S$ nanoflakes	Xiang et al.[67]
La^{3+}	Na^+, Ca^{2+}	P-doped carbon	Xiong et al.[68]
La^{3+}, ND^{3+}, Ce^{3+}	–	sodium diphenylamine sulfonate-modified activated carbon	Wang et al.[69]
U^{6+} (as UO_2^{2+})	seawater (majorly Na^+, K^+, Mg^{2+}, Ca^{2+})	BP nanosheets	Chen and Tong[70]

The selection of measurement techniques should align with experimental goals to ensure accurate and relevant results in electrochemical desalination investigations. In this work, we have used online ICP-OES monitoring to showcase a selectivity measurement and its relevant considerations and relationships. As outlined previously,

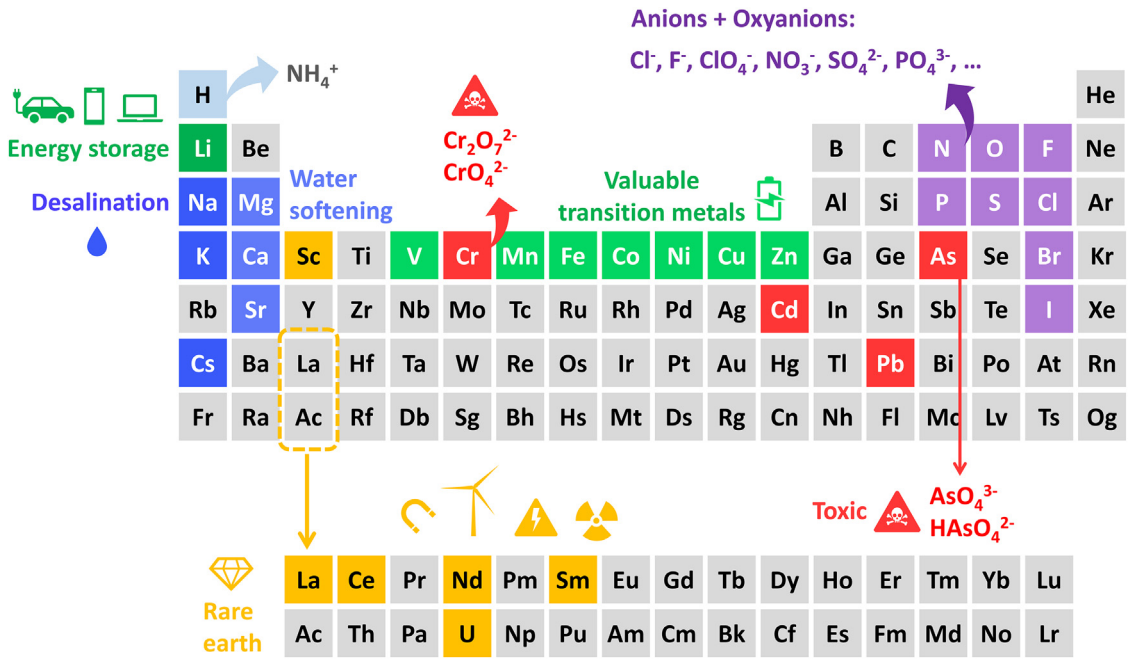

Figure 4. All elements targeted so far for electrochemical recovery from water

Periodic table showing elements targeted in electrochemical desalination (capacitive deionization, battery desalination) for selective recovery from aqueous media in a cyclic manner.

an electrochemical desalination cell with symmetric carbon electrodes was charged and discharged. The electrolyte in this case consisted of $CaCl_2$, KCl, and NaCl, each with 10 mmol L^{-1}, instead of the previously examined single-salt NaCl electrolyte.

To enhance the signal-to-noise ratio, one can increase the electrode mass and, if possible, a lower flow rate. The latter measures increase the amplitude of concentration change in each cycle, thereby maximizing the signal-to-noise ratio. A side-by-side comparison of raw ICP-OES data for two cells with carbon electrodes of significantly different masses is included in Figure S3. A noisy raw ICP-OES dataset will translate into less accurate concentration profiles (Figure S4), rendering further integrations and calculations inaccurate.

Further processing of raw ICP-OES data will result in Figures 5B–5D, individually showing the concentration-change profiles of calcium, potassium, and sodium ions. The process to convert raw ICP-OES data into the concentration of ions includes the calibration of the ICP-OES instrument with a set of samples with known concentrations (Figure S5) in the same manner shown previously to convert conductivity data into the concentration of a single-salt electrolyte (Figure 2).

The procedure to calculate the DC will be similar to what has been carried out to calculate the DC of a single-salt system (Figure 3B). For instance, to calculate the desalination capacity of the system for calcium ions (DC_{Ca}^{2+}) using Equation 1, one has to substitute the molar mass of calcium ions (40.08 g mol^{-1}) instead of the previously used molar mass of NaCl. Also, since the Ca^{2+} ions are attracted to the negative electrodes, the m_{total} in Equation 1 has to be replaced by the mass of only the negative electrode. Substitution of the latter values, the average of integrated areas under the two charging and discharging half-cycles in concentration-time curves, and the flow rate gives DC_{Ca}^{2+} = 7.4 mg g^{-1}. Similarly, the desalination

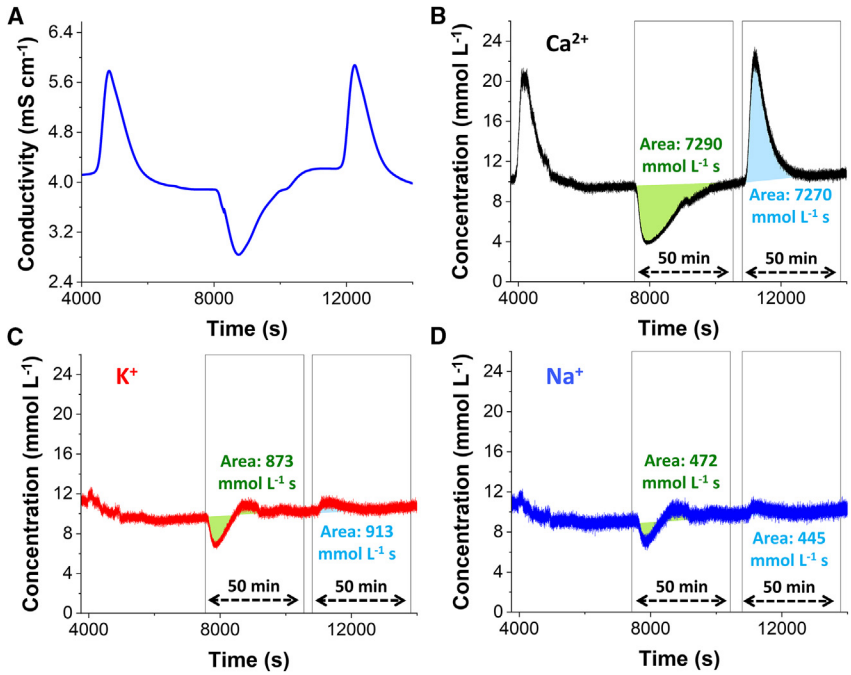

Figure 5. Online elemental monitoring of the effluent of an electrochemical cell

(A) Conductivity variations as a result of cycling a carbon/carbon electrochemical cell containing 506 mg of carbon cloth as negative electrode and 501 mg of carbon cloth as positive electrode in a mixed aqueous electrolyte containing $CaCl_2$, KCl, and NaCl, and the corresponding change in the concentration of (B) calcium, (C) potassium, and (D) sodium ions measured online by ICP-OES.

capacity for potassium ions (DC_{K^+}) and desalination capacity for sodium ions (DC_{Na^+}) can be calculated by substitution of the respective molar masses and integration areas to result in DC_{K^+} = 0.9 mg g^{-1} and DC_{Na^+} = 0.3 mg g^{-1}.

Figures 5C and 5D show that for K^+ and Na^+ ions, after an initial dip in concentration induced by charging the electrochemical cell, a slight increase occurs in concentration. This is unlike the case for Ca^{2+} ions in Figure 5B, where the concentration profile is dipped and gradually reaches its past level to the feed concentration. This effect has been observed before in the electrochemical desalination of multicomponent electrolytes via activated carbon electrodes, where the monovalent ions are preferentially adsorbed initially but are gradually replaced by divalent ions.[79] The latter intricate information on such time-dependent ion dynamics is provided exclusively by online monitoring with ICP-OES, as offline manual sampling techniques can hardly reveal such behaviors.[80] For the calculation of DC_{K^+} and DC_{Na^+} in Figures 5C and 5D, during the charging half-cycle the integrated areas above and under the concentration profiles were subtracted from each other to result in a net removal capacity during the charging half-cycle.

The merit of a system for the preferential removal of a particular element against another elements could be formulated as Equation 12[76]:

$$\beta_{A/B} = \left(\frac{DC_A}{DC_B}\right)\left(\frac{C_{B,feed}}{C_{A,feed}}\right), \qquad \text{(Equation 12)}$$

where $\beta_{A/B}$ is a unitless separation factor for element A with respect to element B, DC_A (mg g^{-1}) is the desalination capacity of A ions, DC_B (mg g^{-1}) is the desalination capacity of B ions, and $C_{A,feed}$ (mg L^{-1}) and $C_{B,feed}$ (mg L^{-1}) are the concentration of A

and B ions, respectively, at the beginning of the process (that is, their concentrations in feedwater). One must note the use of consistent units in Equation 12 for concentrations and desalination capacities, which were, in this case, mg L^{-1} and mg g^{-1}, respectively. Alternatively, one could use mmol L^{-1} for concentrations, which then mandates the use of mmol g^{-1} for desalination capacities.

According to the latter definition, a system that removes both A and B ions indiscriminately, that is, non-selective, will have a separation factor of $\beta_{A/B} = 1$. Any value of $\beta_{A/B}$ greater than unity indicates a favorable removal capacity toward A compared to B. In the example above, to calculate the separation factor for Ca^{2+} ions with respect to Na^{+} ions ($\beta_{Ca^{2+}/Na^{+}}$), the following values have to be substituted in Equation 12: $DC_{Ca}{}^{2+} = 7.4$ mg g^{-1}, $DC_{Na}{}^{+} = 0.3$ mg g^{-1}, $C_{Ca}{}^{2+}{}_{,feed} = 400$ mg L^{-1}, and $C_{Na}{}^{+}{}_{,feed} = 230$ mg L^{-1}, which results in $\beta_{Ca^{2+}/Na^{+}} = 14$. Alternatively, one could use the following units to reach the same result: $DC_{Ca}{}^{2+} = 0.185$ mmol g^{-1}, $DC_{Na}{}^{+} = 0.013$ mmol g^{-1}, $C_{Ca}{}^{2+}{}_{,feed} = 10$ mmol L^{-1}, and $C_{Na}{}^{+}{}_{,feed} = 10$ mmol L^{-1}.

In a similar fashion, the separation factor for Ca^{2+} ions with respect to K^{+} ions ($\beta_{Ca^{2+}/K^{+}}$) will be calculated as 8. This means that the water flowing out of the cell during charging will be calcium deficient, which is relevant for water-softening applications. Similarly, the water flowing out of the cell during discharging will be calcium-rich while being sodium- and potassium-deficient. The volume of the latter flow, the calcium-rich brine, could be minimized by shortening the discharge time for more efficient water softening.

In certain studies, the above process is carried out in a batch mode. In the latter case, the feedwater is introduced into a usually larger cell (also called an electrochemical reactor[81]). After applying the charging voltage and selective uptake of the desired ions from the solution into the electrodes, the solution is exchanged with a fresh solution of lower volume (and of higher purity than feedwater). The discharging is then accomplished in the latter solution, and the ions previously immobilized in the electrodes are released, yielding an enriched solution of the desired ions called the recovery solution. The recovery solution is again exchanged with a fresh feedwater batch, regenerating the cell for a new cycle.

The batch-mode process, though interrupted, eliminates the need for online monitoring of elements, since one only needs to manually collect samples for elemental analysis at certain stages of the process, which are the feedwater and the recovery solutions.[38] In such a case, the separation factor expression can be reformulated as Equation 13:

$$\beta_{A/B} = \left(\frac{C_{A,feed} - C_{A,final}}{C_{B,feed} - C_{B,final}}\right)\left(\frac{C_{B,feed}}{C_{A,feed}}\right), \quad \text{(Equation 13)}$$

where $C_{A,feed}$ and $C_{A,final}$ refer to the concentrations of A ions in the feedwater and the recovery solutions, respectively; and $C_{B,feed}$ and $C_{B,final}$ refer to the concentrations of B ions in the feedwater and the recovery solutions, respectively.[41]

Parameters affecting accuracy and meaningfulness of desalination performance metrics

Leakage current is one of the leading parasitic losses in the operation of electrochemical desalination cells, leading to energy loss.[82] We consider here the charging mechanism of a capacitor as an analogy to that of an electrochemical desalination cell. When a capacitor is being charged by applying a voltage to its terminals, once the electrodes are fully charged the current passing through the terminals

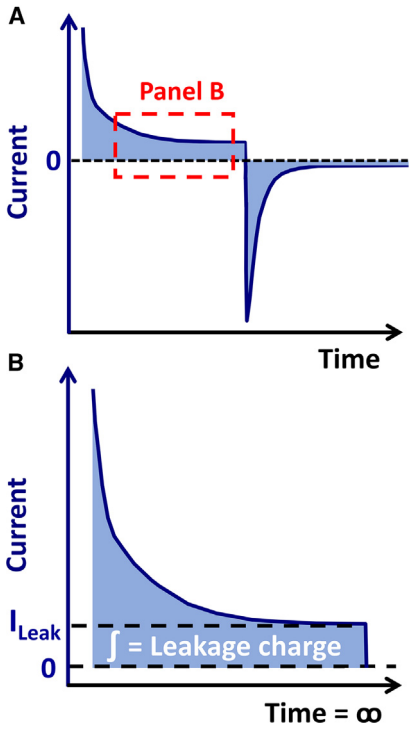

Figure 6. Leakage current during cycling of an electrochemical desalination cell

Schematic illustrations of (A) current response of an electrochemical desalination cell during charging and discharging half-cycles and the concomitant leakage current, and (B) calculation of leakage charge.

decays to zero. In an electrochemical desalination cell, the latter indicates that the electrodes are fully charged, that the maximum population of salt ions is drawn into the electrode, and that the electrode capacity is fully realized. The rate at which the current decays depends on the time constant (τ) of the capacitor known from classic resistor-capacitor circuits. The latter states that the "natural" current response of a capacitor follows an exponential function of time ($I \propto e^{\frac{-t}{\tau}}$). For instance, the current falls to 37% of its initial value once a period equal to one time constant (1τ) has elapsed since the start of the application of potential bias to its terminals.[83] Likewise, the current should fall to less than 1% of its initial value after a lapse of a period equal to the five times the constant (5τ).

In practice, however, the *I*-*t* curve of an electrochemical desalination cell typically approaches a non-zero value, known as the leakage current, as schematically shown in Figure 6. In this case, an electrochemical desalination cell can be modeled as an ideal capacitor (or other charge sources such as a battery) paralleled to a leakage resistance element.[84] When a voltage is applied to the cell, a relatively small (leakage) current constantly passes through the cell in the background. One approach to calculating the leakage resistance is to perform impedance spectroscopy measurements. Another approach, which takes less effort, is to prolong the voltage holding time so that the current contribution from the capacitor decays to zero. As a result, the remaining current could be approximated as the leakage current, as shown in Figure 6B.

The origin of the leakage current (I_{Leak}) is partly due to the slightly conductive saline electrolyte (in contrast to an insulating dielectric in a capacitor), where the sodium and chloride ions constantly carry (leak) a small fraction of electronic charge across the separator from electrode/current collector on one side to those on the other side upon the polarization of the cell. Another possible origin of the leakage current

could be water splitting, mainly when a cell voltage near 1.2 V is applied and held. More information on other possible sources of leakage current may be found elsewhere.[85,86] As illustrated in Figure 6A, the leakage current is larger during charging than in discharging, since the leakage current is mainly a voltage-dependent phenomenon.[23] As outlined above, one has to prolong the voltage holding time long enough to obtain the leakage current. Integration of the marked rectangular area under the *I*-*t* curve (Figure 6B) then gives the charge leaked between the electrodes/current collectors via the electrolyte, also known as the leakage charge (q_{Leak}).

The leakage charge mentioned above should then be subtracted from the charge stored in the electrodes (obtained by the displacement current passing through the external circuit). Leakage charge considerations do not affect DC values. However, failure to consider the leakage charge in the calculations will result in inaccurate CE values, which follow further.

Zooming in on the *I*-*t* profiles shown before (Figure 3D) reveals that the leakage current during the discharging half-cycle is insignificant and very close to zero. However, as expected, the leakage current is indeed significant during the charging half-cycle (Figure S6A), and its contribution to the overall charge invested by the power supply needs to be considered. Figure S6B shows how the leakage current is quantified and how the leakage charge can subsequently be obtained by multiplication of the latter to the duration of the cycle in the study, as indicated by the shaded area. Although the I_{Leak} of 0.241 mA may seem small, over time it yields a significant charge of q_{Leak} = 579 mA s relative to the total charge of 5,932 mA s. Subtraction of the latter by the former gives a net charge of 5,353 mA s for the charging half-cycle, which is very close to that for the discharging half-cycle in Figure 3D (5,360 mA s). Averaging the latter two values (5,357 mA s) and substituting them in the CE formula gives a CE of 90%, a 5% increase from previously calculated without consideration of leakage charge.

To shed further light on the complications that might arise from failure to consider leakage charge subtraction, we base the DC and CE calculations this time on a different cycle duration, 60 min instead of 40 min. A glance at concentration-time profiles in Figures 3A and 3B reveals that the electrodes seemingly saturate after 40 min voltage holding time and reach their equilibrium. Calculations based on a 60-min time window for each half-cycle (Figure S7) yield an average CE of 83% and a DC of 10.8 mg g^{-1}. Leakage charge corrections, however, will result in the same CE of 90%, previously obtained for a 40-min half-cycle duration. As can be seen, leakage current considerations ensure accurate CE calculations regardless of the duration of the voltage holding step. Otherwise, the more extended voltage holding times will result in lower and lower calculated CE values.

The example above highlights the significance of leakage current considerations, although care must be taken to report it in the proper context. Leakage current is a highly system-dependent value, which depends on cell configuration, electrolyte concentration, and presence or absence of ion-exchange membranes, among others. As such, subtraction of leakage charge would help obtain more precise CE values, which in turn more accurately captures the mechanisms involved, such as the presence of co-ion-expulsion phenomenon or other faradic side reactions (decreasing the CE) or the absence of such phenomena (increasing the CE). Although leakage current considerations are educational within a research context, in a commercial setting where performance benchmarking of an electrochemical cell is being discussed or advertised, one must avoid subtracting the leakage charge.

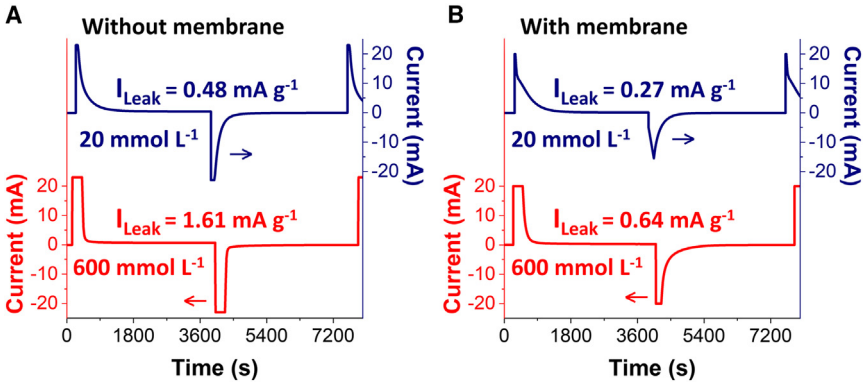

Figure 7. Effect of electrolyte concentration and cell configuration on the magnitude of leakage current

Current-time profile for one full cycle of electrochemical desalination cells in electrolytes made of 20 mmol L^{-1} and 600 mmol L^{-1} NaCl solutions (A) without any ion-exchange membranes and (B) with anion- and cation-exchange membranes.

Reporting leakage charge-subtracted performance metrics in the latter case might lead to mischaracterization of the actual efficiency of the system.

To investigate the system dependency of leakage current, we have also examined the effect of electrolyte concentration and the presence of ion-exchange membranes in electrochemical desalination cells. Figure 7A shows the specific leakage current magnitude (that is, leakage current normalized to the mass of both carbon electrodes) of a single cell when cycled between 0.3 V and 1.2 V in 20 mmol L^{-1} and 600 mmol L^{-1} aqueous NaCl solutions. Swapping the electrolyte tank from a lower concentration to a higher concentration significantly increases the leakage current during the charging half-cycle. The latter observation is in line with the hypothesis outlined previously, which stated that one source of leakage current could be arising from the conductivity of the saline electrolyte. In 600 mmol L^{-1} aqueous NaCl electrolyte, there will be more leakage of electronic charge from one electrode across the spacer channel to the other electrode.

In a fresh cell (Figure 7B), we introduced polymeric anion- and cation-exchange membranes before positive and negative carbon electrodes. It is seen again that the leakage current magnitudes scale with the concentration level. However, introducing such membranes has resulted in lower magnitudes of specific leakage currents than the membrane-less cell. Even though a barrier such as a membrane could constitute an extra resistive element in the cell, the membranes, which are electrically insulating, probably hinder the passage of electronic charges, resulting in a net diminishing effect on leakage current magnitude. In all cases, the leakage current magnitude during the discharging half-cycle has been shown to be negligible.

Next, we investigate the aging of conductivity probes and test whether it significantly changes the reported desalination metrics. Figure 8A shows two concentration-conductivity calibration curves performed on the same conductivity probe with an interval of 6 months. As understood by the slope change of the latter two curves, the sensitivity of the conductivity probes decreases over time, meaning that lower conductivity values are obtained for the same concentration as the probe ages. This slope change can affect the amplitude of concentration change when applied to an electrochemical desalination dataset. To test this, the linear equations of the fitted calibration curves are applied to the conductivity data shown in

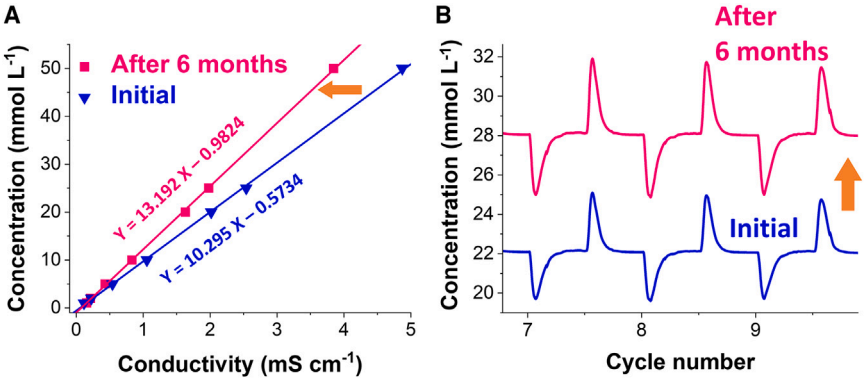

Figure 8. Effect of aging of the conductivity probes

(A) Calibration curves of the same conductivity probe, performed two times with a 6-month interval in between.

(B) The obtained concentration profiles of an electrochemical cell obtained from the latter two calibration equations.

Figure 2A to construct the concentration data presented in Figure 8B. As observed, two concentration profiles are obtained, which, although they follow the same trend, differ mainly in terms of both baseline concentration values (22 mmol L^{-1} vs. 28 mmol L^{-1}) and the amplitude of concentration change.

Performing the same calculations explained previously (Figure 3), DC and CE values of 13.8 mg g^{-1} and 115% (after leakage charge subtraction) are obtained, respectively. The latter values vary primarily with the desalination metrics previously calculated, that is, an overestimation of DC by 3.0 mg g^{-1} and CE by 25%. This pinpoints the importance of regular calibration of the conductivity probes before desalination experiments to avoid such inaccuracies. Assuming a monotonous loss of sensitivity for the conductivity probes tested herein within a 6-month interval, the inaccuracy could be approximated as 0.5 mg g^{-1} per month for DC and around 4% per month for CE. As such, a calibration frequency of at least once per month is recommended to ensure the conductivity probes are fresh enough for reliable calculations.

More calibration curves for low and high-concentration regimes for two different conductivity probes with a 6-month interval may be found in Figure S8. Either of the two approaches may lead to inaccurate calculations: treating the old conductivity data with the equations obtained from a newly calibrated conductivity probe or treating the newly generated conductivity data with the equations obtained from an old formerly calibrated conductivity probe.

Relationships between pH, temperature, and conductivity

By definition, the conductivity of a solution κ (S m^{-1}) measures its ability to conduct electricity. The said conductivity of the solution arises from the sum of conductivity contributions of all individual ions present in the solution. As such, one needs to consider the conductivity contributions of pure water and dissolved salt.

The molar conductivity Λ_m (S m^2 mol^{-1}) of an electrolyte solution can be defined[87] as its measured conductivity κ (S m^{-1}) divided by its molar concentration C (mol m^{-3}) following Equation 14:

$$\Lambda_m = \frac{\kappa}{C}, \qquad \text{(Equation 14)}$$

In the case of an electrolyte with infinitely dilute concentrations of ions, Kohlrausch's law of independent ionic migration[88] can be applied to break down the molar conductivity into its contributions coming from each ion, as expressed in Equation 15:

$$\Lambda_m^\circ = \sum_i \nu_i \lambda_i, \quad \text{(Equation 15)}$$

where Λ_m° is the molar conductivity at infinite dilution, also known as limiting molar conductivity. λ_i is the limiting molar ionic conductivity of ion i, and ν_i is the number of ions i in the formula unit of the electrolyte.

What causes ions to conduct an electric current is their ability to move in a solution, that is, their mobility. As such, the molar ionic conductivity of an ion (λ_i) is a direct function of its electrical mobility (μ_q) following Equation 16:

$$\lambda_i = F z_i \mu_{q_i}, \quad \text{(Equation 16)}$$

where F is the Faraday constant, and z_i is the ionic charge (unitless) for the ion i. Replacing Equation 16 in Equation 15 gives us Equation 17:

$$\Lambda_m^\circ = F \sum_i \nu_i z_i \mu_{q_i}, \quad \text{(Equation 17)}$$

For a simple A:B electrolyte with monovalent ions, Equation 17 for this electrolyte can be written for A^+ and B^- ions as Equation 18:

$$\Lambda_m = F\left(\mu_{q_{A^+}} + \mu_{q_{B^-}}\right), \quad \text{(Equation 18)}$$

From the Einstein relation (the kinetic theory), we know that the mobility of a particle can be related to its diffusion coefficient via Equation 19:

$$D = \mu k_B T, \quad \text{(Equation 19)}$$

where D is the diffusion coefficient, μ is the mobility defined as the ratio of the particle's drift velocity to an applied force, k_B is the Boltzmann constant, and T is the absolute temperature. In the particular case of a particle with electrical charge q, the electrical mobility term μ_q can be related to the generalized mobility μ in Einstein's relation as Equation 20:

$$\mu = \frac{\mu_q}{q}, \quad \text{(Equation 20)}$$

where μ_q is defined as the ratio of the particle's drift velocity per unit electric field.

Combining Equation 19 and Equation 20 gives the Einstein-Smoluchowski equation for the diffusion of charged particles,[89] also known as the electrical mobility equation, as expressed in Equation 21:

$$D = \frac{\mu_q k_B T}{q}, \quad \text{(Equation 21)}$$

Solving Equation 21 for μ_q gives Equation 22:

$$\mu_q = \frac{Dq}{k_B T}, \quad \text{(Equation 22)}$$

The Nernst-Einstein[90] equation can then be written for the AB electrolyte by substitution of Equation 22 in Equation 18 to result in Equation 23:

$$\Lambda_m = F\left(\frac{D_{A^+} q_{A^+}}{k_B T} + \frac{D_{B^-} q_{B^-}}{k_B T}\right), \quad \text{(Equation 23)}$$

Given that A^+ and B^- ions are monovalent ions, q_{A^+} and q_{B^-} will be equal to one elementary charge. Equation 23, thus, upon further simplifications and substitution of eN_A for F, becomes Equation 24:

$$\Lambda_m = \frac{Fe}{k_B T}(D_{A^+} + D_{B^-}) = \frac{e^2 N_A}{k_B T}(D_{A^+} + D_{B^-}), \quad \text{(Equation 24)}$$

Replacing Equation 14 in Equation 24 gives Equation 25:

$$\kappa = \frac{e^2 N_A}{k_B T}(C_{A^+} D_{A^+} + C_{B^-} D_{B^-}), \quad \text{(Equation 25)}$$

where C_{A^+} and C_{B^-} are molar concentrations of A^+ and B^- ions, respectively.

In the case of hypothetically pure water with absolutely no contaminants, the weak self-ionization of water molecules into protons and hydroxide ions can be formulated as Equation 26:

$$H_2O \rightleftharpoons H^+ + OH^-$$

$$K_w = [H^+][OH^-] = 10^{-14} \text{ at } 25°C \quad \text{(Equation 26)}$$

where K_w is the equilibrium constant for the self-ionization of water. Given that H^+ and OH^- ions will be responsible for the electrical conductivity of the electrolyte (water), Equation 25 can be written for them as in the form of Equation 27:

$$\kappa = \frac{e^2 N_A}{k_B T}\left([H^+]D_{H^+} + [OH^-]D_{OH^-}\right), \quad \text{(Equation 27)}$$

where $[H^+]$ and $[OH^-]$ in Equation 27 can be related to the pH as Equation 28:

$$[H^+] = 10^{-pH}, \text{and } [OH^-] = \frac{10^{-14}}{[H^+]} = \frac{10^{-14}}{10^{-pH}} = 10^{pH-14}, \quad \text{(Equation 28)}$$

Substitution of the relationships in Equation 28 in Equation 27 then gives Equation 29:

$$\kappa = \frac{e^2 N_A}{k_B T}\left(10^{-pH} D_{H^+} + 10^{pH-14} D_{OH^-}\right), \quad \text{(Equation 29)}$$

Equation 29 then provides the relationship between the conductivity, temperature, and water pH.

As expressed by Equation 29, temperature and pH are the only variables influencing the conductivity of ideally pure water. Assuming a constant temperature of 25°C (298 K), the conductivity can then be plotted as a function of pH after substituting all physicochemical constants, as illustrated by Figure S9A. The V-shaped curve shows a weak pH dependency of water conductivity around near-neutral pH regimes. Approaching either of the acidic or basic extreme ends of the pH spectrum results in infinitely large conductivities (Figure S9). At pH 7, a theoretical conductivity of 0.0549 μS cm^{-1} is obtained for ideally pure water free of contaminants, which is very close to the experimentally measured conductivity of ultrapure deionized water reported elsewhere (<0.0555 μS cm^{-1}).[91]

The derivation of all the above expressions was based on the assumption that the H^+ and OH^- ions are in dilute concentrations. Therefore, far deviations from the near-neutral regimes to either side of the pH range will negate the latter assumption for one of the ionic species and renders the calculations inaccurate. As such, a zoomed-in view of the near-neutral pH regimes (Figures S9B and S9C) would better

satisfy the starting assumptions regarding the dilute concentrations of both H^+ and OH^- ions. As observed, within the pH range of 5–9, the conductivity is negligibly affected by the pH of the water, with a conductivity change of <0.005 mS cm^{-1} in that pH window. Hence, while working within the pH window of 5–9, one could safely disregard the contribution of pH and be sure that the measured conductivity arises only from the presence of salt ions.

In contrast to pH, temperature variation has a much more complex effect on conductivity. Temperature variations change the self-ionization (K_w) of water, as expressed in Equation 26, and shifts the pH values as a result. Consequently, the expression pH + pOH = 14 will no longer hold. Temperature also affects the diffusion coefficients of H^+ and OH^- ions in water, further making it less straightforward to plot a theoretical dependence of conductivity on temperature using Equation 25. As such, we measure the temperature dependency of conductivity experimentally in a wide temperature range of 15°C–55°C, as shown in Figure 9.

As expected, a steady increase in conductivity is observed upon increasing the temperature. Elevated temperatures increase the K_w in Equation 26, resulting in more populations of protons and hydroxide ions and thereby increasing the conductivity. The two different conductivity probes show very similar slopes in conductivity-temperature graphs. Going from 15°C to 55°C, we see that the gain in conductivity in the case of a low-concentration NaCl electrolyte (10 mmol L^{-1}) is 10%–11%, whereas it is 6%–7% in the case of the high-concentration NaCl electrolyte (600 mmol L^{-1}). The slightly higher conductivity gain in the case of low-concentration electrolyte indicates the conductivity contribution coming from the water as a result of temperature change, which becomes only significant when dealing with low-concentration electrodes ($\leq$10 mM NaCl) and upon huge temperature variations such as 40°C. In the case of higher concentrations and slight temperature variations, it can be concluded that the temperature will not significantly influence conductivity and, hence, the concentration obtained.

In summary, the present work has illustrated in a step-by-step manner how a simple electrochemical desalination system is built and operated at the laboratory scale. At the heart of an electrochemical desalination setup, a cell houses a pair of electrodes that cyclically accomplish desalination when being charged and discharged. A conductivity meter monitors the conductivity change downstream of the cell. Once the conductivity meter is freshly calibrated with an array of stock solutions with known concentrations, it can reliably convert the measured conductivity of the cell's effluent water into the salt concentration, from which desalination capacity can be calculated. From the desalination capacity, the CE (and energy consumption) can also be calculated knowing the electronic charge data provided by the electrochemical workstation that applied voltage to the cell. The equations to calculate the said desalination metrics are also presented, which could be minimally modified for systems other than NaCl, such as LiCl.

We have emphasized that the conductivity meter has to be calibrated correctly and on time and have showcased how basing the calculations on 6-month-old calibration data could result in a significant deviation from actual performance metrics, specifically, 25%–30% relative error in final DC and CE values reported. We have additionally shown the significance of leakage current, how it is calculated, and how it could affect the CE values. We finally illustrated the relatively minimal effects of pH and temperature on the measured conductivities. The checklists provided in Notes S1 and S2 are developed to help the researchers have a quick overview of what is

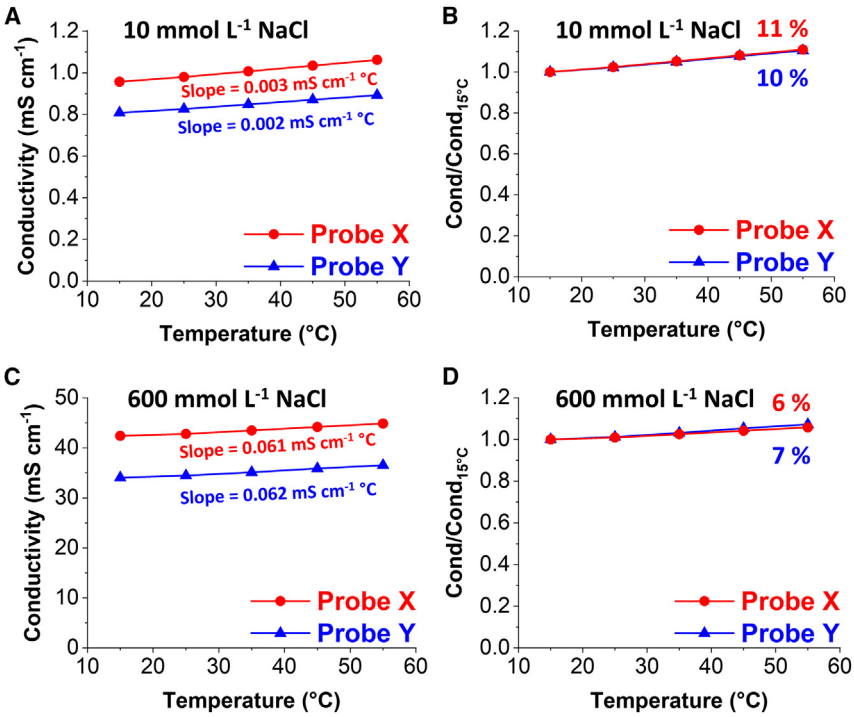

Figure 9. Wide variation of temperature and its effect on conductivity

Experimental temperature dependency of the conductivity of two conductivity probes from 15°C to 55°C in (A) low NaCl concentration electrolyte and (B) its normalized gain in conductivity, and (C) high NaCl concentration electrolyte and (D) its normalized gain in conductivity.

needed when designing electrochemical desalination setups and what and how to report once the raw data are generated from such a setup.

EXPERIMENTAL PROCEDURES

Resource availability

Lead contact

Requests for further information, resources, or materials should be directed to and will be fulfilled by the lead contact, Volker Presser (volker.presser@leibniz-inm.de), upon reasonable request.

Materials availability

This study did not generate new unique materials.

Data and code availability

The data generated in this study are included in the manuscript and supplemental information and will be made available from the lead contact upon reasonable request.

Conductivity and pH measurements

Aqueous stock solutions of sodium chloride with concentrations of 1–1,000 mmol L^{-1} were prepared by first making 0.5 L of 1 mol L^{-1} NaCl (VWR Chemicals) parent solution, followed by dilution with deionized water (Milli-Q, Merck Millipore) to the target concentration values. The solutions were kept in plastic centrifuge vials in a climatized chamber (BINDER) at constant temperatures of 25°C overnight to reach the equilibrium temperature before measuring.

The ionic conductivity of each solution was measured by the conductivity probe (Metrohm, 5-ring conductivity measuring cell with integrated Pt1000 temperature sensor) connected to a module (Metrohm, 856 conductivity module), which communicates the data to a desktop computer. Likewise, the pH was measured by a glassy pH probe (Metrohm, 3 mol L^{-1} KCl electrolyte, with an integrated Pt1000 temperature sensor) connected to a module (Metrohm, 867 pH module) that communicates the pH data to the computer. Both conductivity and pH online data are shown in real time on the computer (Tiamo, Metrohm).

For temperature-dependent investigations of conductivity and pH, the aqueous stock solutions were kept in a climatized chamber (BINDER) at constant temperatures of 15°C, 25°C, 35°C, 45°C, and 55°C (each case: $\pm$1°C). At each temperature, the solutions were left in the climatized chamber overnight to equilibrate with the target temperature before the measurements were made.

Electrode preparation

To prepare free-standing carbon electrodes, we followed the procedure outlined in our previous works.[16,92] Typically, the electrodes were made by adding enough ethanol to activated carbon (type YP-80F, Kuraray) in an agate mortar until it became entirely wet while manually stirring the mixture with a pestle. Once a homogeneous mixture was reached, polytetrafluoroethylene binder (60 mass % dispersion in water, from Sigma-Aldrich) was added to serve as a polymeric binder, using a carbon/binder mass ratio of 9:1. Stirring was continued under the fume hood until ethanol partially evaporated from the mixture to result in a carbon paste, which was further cold-rolled in a rolling machine (MTI HR01, MTI). The free-standing carbon films with a wet thickness of 600 μm were then dried in a vacuum oven (Memmert) at 50°C overnight.

Electrochemical desalination tests

A pair of round pieces of the free-standing carbon electrodes were cut in 30-mm circular diameter and used as positive and negative electrodes for the electrochemical desalination cell. The carbon electrodes were sandwiched in a custom-made cell,[93] separated by a few round-shaped glass fiber filters (GF/A, Whatman) and nylon mesh pieces to allow the water stream to flow between the electrodes (flow-by configuration). To monitor the potential development in each electrode individually upon charge and discharge, a spectator Ag/AgCl reference electrode (3 M NaCl, BASi) was mounted on the cell near the electrodes. When needed, polymeric ion-exchange membranes with a diameter of 50 mm were cut and soaked into 20 mmol L^{-1} NaCl electrolyte overnight. Anion-exchange membrane (Fumasep FAA-3-20, Fuma-tech) was placed in between the positive electrode and the flow channel, and the cation-exchange membrane (Fumasep FKE-20, Fuma-tech) was placed in between the negative electrode and the flow channel.

Ten liters of 20 mmol L^{-1} aqueous NaCl solution was stored in a tank as the electrolyte, where it is constantly bubbled with a small nitrogen flow to minimize carbon electrode oxidation due to the presence of dissolved oxygen in the electrolyte. The electrolyte was pumped from the tank via a peristaltic pump (Masterflex) at flow rate of ~2 mL min^{-1} into the cell. To ensure that accurate flow-rate values were obtained, the flow was collected manually using a 10-mL graduated cylinder for 5 min after each day of desalination measurements. The water stream flowing out of the cell went further into the chamber containing the conductivity probe, followed by the pH probe chamber, and finally cycled back into the tank to complete the loop (called a single-pass mode of operation). The entire setup was kept in a

climatized chamber at 25°C ± 1°C to eliminate possible effects from day/night fluctuations in temperature.

Electrochemical testing was then carried out using an electrochemical workstation (Bio-Logic, potentiostat/galvanostat, type VSP300), programmed to repeatedly charge and discharge the cell at the rate of 0.1 A g^{-1} concerning the total mass of both carbon electrodes combined.

For selectivity measurements, a 1-L aqueous electrolyte of KCl (Sigma-Aldrich), NaCl (Roth), and $CaCl_2$ (Sigma-Aldrich), each at 10 mmol L^{-1} concentration, was prepared. The electrolyte was constantly bubbled with nitrogen and pumped via a peristaltic pump (Masterflex Reglo ICC Digital Pump with independent channel control, 3-channel, 8-roller) into an electrochemical cell with symmetric carbon/carbon cloth electrodes (Kynol ACC-5092-20). The water stream flowing out of the cell first went into the chamber containing the conductivity probe and then proceeded to the ICP-OES instrument (ICP-OES, ARCOS FHX22, SPECTRO Analytical Instruments) before finally being discarded. The concentration of each ionic species was determined individually by intensity-concentration equations obtained by calibration of known samples beforehand (Table S1 and Figure S5).

SUPPLEMENTAL INFORMATION

Supplemental information can be found online at https://doi.org/10.1016/j.xcrp.2023.101661.

ACKNOWLEDGMENTS

The INM authors acknowledge funding by the German Research Foundation (DFG, Deutsche Forschungsgemeinschaft) of the MXene-CDI project (PR-1173/11). Y.Z. acknowledges the financial support of the Alexander von Humboldt Foundation. C. Kim acknowledges the support of the Basic Science Research Program through the National Research Foundation of Korea (NRF) funded by the Ministry of Education (NRF-2021R1I1A3040360).

AUTHOR CONTRIBUTIONS

M.T.: investigation, conceptualization, data curation, visualization, supervision, writing – original draft, writing – review & editing. C. Kök: investigation, data curation, writing – review & editing. P.R.B.: investigation, data curation, writing – review & editing. P.R.: writing – review & editing. Y.Z.: supervision, validation, writing – review & editing. J.L.: conceptualization, supervision, validation, writing – review & editing. C. Kim: supervision, validation, writing – original draft, writing – review & editing. V.P.: conceptualization, supervision, validation, resources, visualization, writing – original draft, writing – review & editing, project administration, funding acquisition.

DECLARATION OF INTERESTS

The authors declare no competing interests.

Received: June 27, 2023
Revised: August 29, 2023
Accepted: October 5, 2023
Published: October 30, 2023

REFERENCES

1. Shocron, A.N., Roth, R.S., Guyes, E.N., Epsztein, R., and Suss, M.E. (2022). Comparison of ion selectivity in electrodialysis and capacitive deionization. Environ. Sci. Technol. Lett. *9*, 889–899. https://doi.org/10.1021/acs.estlett.2c00551.

2. Gamaethiralalage, J.G., Singh, K., Sahin, S., Yoon, J., Elimelech, M., Suss, M.E., Liang, P., Biesheuvel, P.M., Zornitta, R.L., and de Smet, L.C.P.M. (2021). Recent advances in ion selectivity with capacitive deionization. Energy Environ. Sci. *14*, 1095–1120. https://doi.org/10.1039/D0EE03145C.

3. Deng, D., Dydek, E.V., Han, J.H., Schlumpberger, S., Mani, A., Zaltzman, B., and Bazant, M.Z. (2013). Overlimiting current and shock electrodialysis in porous media. Langmuir *29*, 16167–16177. https://doi.org/10.1021/la4040547.

4. Tian, H., Alkhadra, M.A., Conforti, K.M., and Bazant, M.Z. (2021). Continuous and selective removal of lead from drinking water by shock electrodialysis. ACS ES. T. Water *1*, 2269–2274. https://doi.org/10.1021/acsestwater.1c00234.

5. Alkhadra, M.A., Gao, T., Conforti, K.M., Tian, H., and Bazant, M.Z. (2020). Small-scale desalination of seawater by shock electrodialysis. Desalination *476*, 114219. https://doi.org/10.1016/j.desal.2019.114219.

6. Sharan, P., Yoon, T.J., Jaffe, S.M., Ju, T., Currier, R.P., and Findikoglu, A.T. (2021). Can capacitive deionization outperform reverse osmosis for brackish water desalination? Cleaner Engineering and Technology *3*, 100102. https://doi.org/10.1016/j.clet.2021.100102.

7. Metzger, M., Besli, M.M., Kuppan, S., Hellstrom, S., Kim, S., Sebti, E., Subban, C.V., and Christensen, J. (2020). Techno-economic analysis of capacitive and intercalative water deionization. Energy Environ. Sci. *13*, 1544–1560. https://doi.org/10.1039/D0EE00725K.

8. Wang, L., Arnold, S., Ren, P., Wang, Q., Jin, J., Wen, Z., and Presser, V. (2022). Redox flow battery for continuous and energy-effective lithium recovery from aqueous solution. ACS Energy Lett. *7*, 3539–3544. https://doi.org/10.1021/acsenergylett.2c01746.

9. Kang, J., Zhang, P., Gao, Z., Zhang, J., Yan, Z., Wang, H., and Chen, R. (2016). Direct energy recovery system for membrane capacitive deionization. Desalination *130*, 144–151. https://doi.org/10.1016/j.desal.2016.07.025.

10. Zhang, Y., Ren, P., Wang, L., Pameté, E., Husmann, S., and Presser, V. (2022). Selectivity toward heavier monovalent cations of carbon ultramicropores used for capacitive deionization. Desalination *542*, 116053. https://doi.org/10.1016/j.desal.2022.116053.

11. Wang, L., Torkamanzadeh, M., Majed, A., Zhang, Y., Wang, Q., Breitung, B., Feng, G., Naguib, M., and Presser, V. (2022). Time-dependent cation selectivity of titanium carbide MXene in aqueous solution. Advanced Sustainable Systems *6*, 2100383. https://doi.org/10.1002/adsu.202100383.

12. Porada, S., Zhao, R., van der Wal, A., Presser, V., and Biesheuvel, P.M. (2013). Review on the science and technology of water desalination by capacitive deionization. Prog. Mater. Sci. *58*, 1388–1442. https://doi.org/10.1016/j.pmatsci.2013.03.005.

13. Suss, M.E., Porada, S., Sun, X., Biesheuvel, P.M., Yoon, J., and Presser, V. (2015). Water desalination via capacitive deionization: what is it and what can we expect from it? Energy Environ. Sci. *8*, 2296–2319. https://doi.org/10.1039/C5EE00519A.

14. Srimuk, P., Su, X., Yoon, J., Aurbach, D., and Presser, V. (2020). Charge-transfer materials for electrochemical water desalination, ion separation and the recovery of elements. Nat. Rev. Mater. *5*, 517–538. https://doi.org/10.1038/s41578-020-0193-1.

15. Wang, L., Zhang, Y., Moh, K., and Presser, V. (2021). From capacitive deionization to desalination batteries and desalination fuel cells. Curr. Opin. Electrochem. *29*, 100758. https://doi.org/10.1016/j.coelec.2021.100758.

16. Torkamanzadeh, M., Wang, L., Zhang, Y., Budak, Ö., Srimuk, P., and Presser, V. (2020). MXene/activated-carbon hybrid capacitive deionization for permselective ion removal at low and high salinity. ACS Appl. Mater. Interfaces *12*, 26013–26025. https://doi.org/10.1021/acsami.0c05975.

17. Srimuk, P., Zeiger, M., Jäckel, N., Tolosa, A., Krüner, B., Fleischmann, S., Grobelsek, I., Aslan, M., Shvartsev, B., Suss, M.E., and Presser, V. (2017). Enhanced performance stability of carbon/titania hybrid electrodes during capacitive deionization of oxygen saturated saline water. Electrochim. Acta *224*, 314–328. https://doi.org/10.1016/j.electacta.2016.12.060.

18. Srimuk, P., Ries, L., Zeiger, M., Fleischmann, S., Jäckel, N., Tolosa, A., Krüner, B., Aslan, M., and Presser, V. (2016). High performance stability of titania decorated carbon for desalination with capacitive deionization in oxygenated water. RSC Adv. *6*, 106081–106089. https://doi.org/10.1039/C6RA22800C.

19. Wang, L., Violet, C., DuChanois, R.M., and Elimelech, M. (2020). Derivation of the theoretical minimum energy of separation of desalination processes. J. Chem. Educ. *97*, 4361–4369. https://doi.org/10.1021/acs.jchemed.0c01194.

20. Porada, S., Weingarth, D., Hamelers, H.V.M., Bryjak, M., Presser, V., and Biesheuvel, P.M. (2014). Carbon flow electrodes for continuous operation of capacitive deionization and capacitive mixing energy generation. J. Mater. Chem. A Mater. *2*, 9313–9321. https://doi.org/10.1039/C4TA01783H.

21. Srimuk, P., Halim, J., Lee, J., Tao, Q., Rosen, J., and Presser, V. (2018). Two-dimensional molybdenum carbide (MXene) with divacancy ordering for brackish and seawater desalination via cation and anion intercalation. ACS Sustain. Chem. Eng. *6*, 3739–3747. https://doi.org/10.1021/acssuschemeng.7b04095.

22. Biesheuvel, P., and Van der Wal, A. (2010). Membrane capacitive deionization. J. Membr. Sci. *346*, 256–262.

23. Hemmatifar, A., Palko, J.W., Stadermann, M., and Santiago, J.G. (2016). Energy breakdown in capacitive deionization. Water Res. *104*, 303–311. https://doi.org/10.1016/j.watres.2016.08.020.

24. Zhang, C., He, D., Ma, J., Tang, W., and Waite, T.D. (2018). Faradaic reactions in capacitive deionization (CDI) - problems and possibilities: A review. Water Res. *128*, 314–330. https://doi.org/10.1016/j.watres.2017.10.024.

25. Srimuk, P., Lee, J., Tolosa, A., Kim, C., Aslan, M., and Presser, V. (2017). Titanium disulfide: a promising low-dimensional electrode material for sodium ion intercalation for seawater desalination. Chem. Mater. *29*, 9964–9973. https://doi.org/10.1021/acs.chemmater.7b03363.

26. Harb, C., Pan, J., DeVilbiss, S., Badgley, B., Marr, L.C., Schmale, D.G., III, and Foroutan, H. (2021). Increasing freshwater salinity impacts aerosolized bacteria. Environ. Sci. Technol. *55*, 5731–5741. https://doi.org/10.1021/acs.est.0c08558.

27. United States Geological Survey (2018). Saline Water and Salinity. https://www.usgs.gov/special-topics/water-science-school/science/saline-water-and-salinity.

28. Bartels, C., Franks, R., Rybar, S., Schierach, M., and Wilf, M. (2005). The effect of feed ionic strength on salt passage through reverse osmosis membranes. Desalination *184*, 185–195. https://doi.org/10.1016/j.desal.2005.04.032.

29. Zhang, Y., Ren, P., Liu, Y., and Presser, V. (2022). Particle size distribution influence on capacitive deionization: Insights for electrode preparation. Desalination *525*, 115503. https://doi.org/10.1016/j.desal.2021.115503.

30. Długołęcki, P., and van der Wal, A. (2013). Energy recovery in membrane capacitive deionization. Environ. Sci. Technol. *47*, 4904–4910. https://doi.org/10.1021/es3053202.

31. Alkhadra, M.A., Su, X., Suss, M.E., Tian, H., Guyes, E.N., Shocron, A.N., Conforti, K.M., de Souza, J.P., Kim, N., Tedesco, M., et al. (2022). Electrochemical methods for water purification, ion separations, and energy conversion. Chem. Rev. *122*, 13547–13635. https://doi.org/10.1021/acs.chemrev.1c00396.

32. Vieceli, N., Vonderstein, C., Swiontekc, T., Stopić, S., Dertmann, C., Sojka, R., Reinhardt, N., Ekberg, C., Friedrich, B., and Petranikova, M. (2023). Recycling of Li-ion batteries from industrial processing: upscaled hydrometallurgical treatment and recovery of high purity manganese by solvent extraction. Solvent Extr. Ion Exch. *41*, 205–220. https://doi.org/10.1080/07366299.2023.2165405.

33. Mo, D., Yu, G., Zeng, Z., Ni, S., Zhang, S., and Sun, X. (2023). Separation of lithium and transition metals in leaching solution of used lithium ion battery with Sec-octylphenoxyacetic acid. ChemistrySelect *8*, e202301036. https://doi.org/10.1002/slct.202301036.

34. Asadi Dalini, E., Karimi, G., and Zandevakili, S. (2021). Treatment of valuable metals from leaching solution of spent lithium-ion batteries.

Miner. Eng. *173*, 107226. https://doi.org/10.1016/j.mineng.2021.107226.

35. Trócoli, R., Battistel, A., and Mantia, F.L. (2014). Selectivity of a lithium-recovery process based on $LiFePO_4$. Chemistry *20*, 9888–9891. https://doi.org/10.1002/chem.201403535.

36. Pasta, M., Battistel, A., and La Mantia, F. (2012). Batteries for lithium recovery from brines. Energy Environ. Sci. *5*, 9487–9491. https://doi.org/10.1039/C2EE22977C.

37. Lee, J., Yu, S.H., Kim, C., Sung, Y.E., and Yoon, J. (2013). Highly selective lithium recovery from brine using a lambda-MnO_2-Ag battery. Phys. Chem. Chem. Phys. *15*, 7690–7695. https://doi.org/10.1039/c3cp50919b.

38. Trócoli, R., Erinmwingbovo, C., and La Mantia, F. (2017). Optimized lithium recovery from brines by using an electrochemical ion-pumping process based on λ-MnO_2 and nickel hexacyanoferrate. Chemelectrochem *4*, 143–149. https://doi.org/10.1002/celc.201600509.

39. Kim, S., Lee, J., Kang, J.S., Jo, K., Kim, S., Sung, Y.E., and Yoon, J. (2015). Lithium recovery from brine using a lambda-MnO_2/activated carbon hybrid supercapacitor system. Chemosphere *125*, 50–56. https://doi.org/10.1016/j.chemosphere.2015.01.024.

40. Jiang, L., Zhu, L., Chen, L., Ding, Y., Zhang, W., and Brice, S. (2022). Coupling hybrid membrane capacitive deionization (HMCDI) with electric-enhanced direct contact membrane distillation (EE-DCMD) for lithium/cobalt separation and concentration. Separ. Purif. Technol. *302*, 122082. https://doi.org/10.1016/j.seppur.2022.122082.

41. Singh, K., Qian, Z., Biesheuvel, P., Zuilhof, H., Porada, S., and de Smet, L.C. (2020). Nickel hexacyanoferrate electrodes for high mono/divalent ion-selectivity in capacitive deionization. Desalination *481*, 114346. https://doi.org/10.1016/j.desal.2020.114346.

42. Lee, S.-H., Choi, M., Moon, J.-K., Kim, S.-W., Lee, S., Ryu, I., Choi, J., and Kim, S. (2022). Electrosorption removal of cesium ions with a copper hexacyanoferrate electrode in a capacitive deionization (CDI) system. Colloids Surf. A Physicochem. Eng. Asp. *647*, 129175. https://doi.org/10.1016/j.colsurfa.2022.129175.

43. Tsai, S.-W., Cuong, D.V., and Hou, C.-H. (2022). Selective capture of ammonium ions from municipal wastewater treatment plant effluent with a nickel hexacyanoferrate electrode. Water Res. *221*, 118786. https://doi.org/10.1016/j.watres.2022.118786.

44. Xing, W., Liang, J., Tang, W., Zeng, G., Wang, X., Li, X., Jiang, L., Luo, Y., Li, X., Tang, N., and Huang, M. (2019). Perchlorate removal from brackish water by capacitive deionization: Experimental and theoretical investigations. Chem. Eng. J. *361*, 209–218. https://doi.org/10.1016/j.cej.2018.12.074.

45. Hong, S.P., Yoon, H., Lee, J., Kim, C., Kim, S., Lee, J., Lee, C., and Yoon, J. (2020). Selective phosphate removal using layered double hydroxide/reduced graphene oxide (LDH/rGO) composite electrode in capacitive deionization. J. Colloid Interface Sci. *564*, 1–7. https://doi.org/10.1016/j.jcis.2019.12.068.

46. Hawks, S.A., Cerón, M.R., Oyarzun, D.I., Pham, T.A., Zhan, C., Loeb, C.K., Mew, D., Deinhart, A., Wood, B.C., Santiago, J.G., et al. (2019). Using ultramicroporous carbon for the selective removal of nitrate with capacitive deionization. Environ. Sci. Technol. *53*, 10863–10870. https://doi.org/10.1021/acs.est.9b01374.

47. Zuo, K., Kim, J., Jain, A., Wang, T., Verduzco, R., Long, M., and Li, Q. (2018). Novel composite electrodes for selective removal of sulfate by the capacitive deionization process. Environ. Sci. Technol. *52*, 9486–9494. https://doi.org/10.1021/acs.est.8b01868.

48. Chang, J., Li, Y., Duan, F., Su, C., Li, Y., and Cao, H. (2020). Selective removal of chloride ions by bismuth electrode in capacitive deionization. Separ. Purif. Technol. *240*, 116600. https://doi.org/10.1016/j.seppur.2020.116600.

49. Li, Y., Wu, J., Yong, T., Fei, Y., and Qi, J. (2021). Investigation of bromide removal and bromate minimization of membrane capacitive deionization for drinking water treatment. Chemosphere *280*, 130857. https://doi.org/10.1016/j.chemosphere.2021.130857.

50. Liu, Q., Xie, B., and Xiao, D. (2022). High efficient and continuous recovery of iodine in saline wastewater by flow-electrode capacitive deionization. Separ. Purif. Technol. *296*, 121419. https://doi.org/10.1016/j.seppur.2022.121419.

51. Pan, J., Zheng, Y., Ding, J., Gao, C., Van der Bruggen, B., and Shen, J. (2018). Fluoride removal from water by membrane capacitive deionization with a monovalent anion selective membrane. Ind. Eng. Chem. Res. *57*, 7048–7053. https://doi.org/10.1021/acs.iecr.8b00929.

52. Park, G., Hong, S.P., Lee, C., Lee, J., and Yoon, J. (2021). Selective fluoride removal in capacitive deionization by reduced graphene oxide/hydroxyapatite composite electrode. J. Colloid Interface Sci. *581*, 396–402. https://doi.org/10.1016/j.jcis.2020.07.108.

53. Uwayid, R., Guyes, E.N., Shocron, A.N., Gilron, J., Elimelech, M., and Suss, M.E. (2022). Perfect divalent cation selectivity with capacitive deionization. Water Res. *210*, 117959. https://doi.org/10.1016/j.watres.2021.117959.

54. Xiang, S., Mao, H., Geng, W., Xu, Y., and Zhou, H. (2022). Selective removal of Sr(II) from saliferous radioactive wastewater by capacitive deionization. J. Hazard Mater. *431*, 128591. https://doi.org/10.1016/j.jhazmat.2022.128591.

55. Zhang, X., Yang, F., Ma, J., and Liang, P. (2020). Effective removal and selective capture of copper from salty solution in flow electrode capacitive deionization. Environ. Sci, Water Res. Technol. *6*, 341–350. https://doi.org/10.1039/C9EW00467J.

56. Li, H., Zou, J., Yao, Z., Yu, J., Wang, H., and Xu, J. (2010). Using graphene nano-flakes as electrodes to remove ferric ions by capacitive deionization. J. Neuroimmunol. *219*, 8–16. https://doi.org/10.1016/j.seppur.2010.07.003.

57. Wang, C., Li, T., Yu, G., and Deng, S. (2021). Removal of low concentrations of nickel ions in electroplating wastewater using capacitive deionization technology. Chemosphere *284*, 131341. https://doi.org/10.1016/j.chemosphere.2021.131341.

58. Siekierka, A., and Yalcinkaya, F. (2022). Selective cobalt-exchange membranes for electrodialysis dedicated for cobalt recovery from lithium, cobalt and nickel solutions. Separ. Purif. Technol. *299*, 121695. https://doi.org/10.1016/j.seppur.2022.121695.

59. Soysüren, G., Yetgin, A.G., Arar, Ö., and Arda, M. (2022). Removal of manganese (II) from aqueous solution by ionic liquid impregnated polymeric sorbent and electrodeionization (EDI) techniques. Process Saf. Environ. Protect. *158*, 189–198. https://doi.org/10.1016/j.psep.2021.11.053.

60. Tang, W., Wang, X., Zeng, G., Liang, J., Li, X., Xing, W., He, D., Tang, L., and Liu, Z. (2019). Electro-assisted adsorption of Zn(II) on activated carbon cloth in batch-flow mode: experimental and theoretical investigations. Environ. Sci. Technol. *53*, 2670–2678. https://doi.org/10.1021/acs.est.8b05909.

61. Huang, X., Guo, X., Dong, Q., Liu, L., Tallon, R., and Chen, J. (2019). Zero-wastewater capacitive deionization: selective removal of heavy metal ions in tap water assisted by phosphate ions. Environ. Sci.: Nano *6*, 3225–3231. https://doi.org/10.1039/C9EN00730J.

62. Wang, L., Deligniere, L., Husmann, S., Leiner, R., Bahr, C., Zhang, S., Dun, C., Montemore, M.M., Gallei, M., Urban, J.J., et al. (2023). Selective Pb^{2+} removal and electrochemical regeneration of fresh and recycled FeOOH. Nano Res. *16*, 9352–9363. https://doi.org/10.1007/s12274-023-5569-2.

63. Peng, Q., Liu, L., Luo, Y., Zhang, Y., Tan, W., Liu, F., Suib, S.L., and Qiu, G. (2016). Cadmium removal from aqueous solution by a deionization supercapacitor with a birnessite electrode. ACS Appl. Mater. Interfaces *8*, 34405–34413. https://doi.org/10.1021/acsami.6b12224.

64. Bao, S., Duan, J., and Zhang, Y. (2018). Recovery of V(V) from complex vanadium solution using capacitive deionization (CDI) with resin/carbon composite electrode. Chemosphere *208*, 14–20. https://doi.org/10.1016/j.chemosphere.2018.05.149.

65. Su, X., Kushima, A., Halliday, C., Zhou, J., Li, J., and Hatton, T.A. (2018). Electrochemically-mediated selective capture of heavy metal chromium and arsenic oxyanions from water. Nat. Commun. *9*, 4701. https://doi.org/10.1038/s41467-018-07159-0.

66. Li, C., Ramasamy, D.L., Sillanpää, M., and Repo, E. (2021). Separation and concentration of rare earth elements from wastewater using electrodialysis technology. Separ. Purif. Technol. *254*, 117442. https://doi.org/10.1016/j.seppur.2020.117442.

67. Xiang, H.D., Liu, P., Deng, M., and Tong, D.G. (2021). Separation of rare-earth ions from mine wastewater using $B_{12}S$ nanoflakes as a capacitive deionization electrode material. J. Nanosci. Nanotechnol. *21*, 5459–5476. https://doi.org/10.1166/jnn.2021.19466.

68. Xiong, Y., Yang, X., Liu, Y., Chen, X., Wang, G., Lu, B., Lin, G., and Huang, B. (2022). Fabrication of phosphorus doping porous carbon derived from bagasse for highly-efficient removal of

La^{3+} ions via capacitive deionization. Electrochim. Acta *404*, 139735. https://doi.org/10.1016/j.electacta.2021.139735.

69. Wang, L., Gao, Y., Chai, Y., and Sun, X. (2022). Recovery of rare earth by electro-sorption with sodium diphenylamine sulfonate modified activated carbon electrode. Separ. Purif. Technol. *292*, 121005. https://doi.org/10.1016/j.seppur.2022.121005.

70. Chen, L., and Tong, D.G. (2020). Amorphous boron phosphide nanosheets: A highly efficient capacitive deionization electrode for uranium separation from seawater with superior selectivity. Separ. Purif. Technol. *250*, 117175. https://doi.org/10.1016/j.seppur.2020.117175.

71. Zhang, Y., Peng, J., Feng, G., and Presser, V. (2021). Hydration shell energy barrier differences of sub-nanometer carbon pores enable ion sieving and selective ion removal. Chem. Eng. J. *419*, 129438. https://doi.org/10.1016/j.cej.2021.129438.

72. Hemmatifar, A., Oyarzun, D.I., Palko, J.W., Hawks, S.A., Stadermann, M., and Santiago, J.G. (2017). Equilibria model for pH variations and ion adsorption in capacitive deionization electrodes. Water Res. *122*, 387–397. https://doi.org/10.1016/j.watres.2017.05.036.

73. Oyarzun, D.I., Hemmatifar, A., Palko, J.W., Stadermann, M., and Santiago, J.G. (2018). Ion selectivity in capacitive deionization with functionalized electrode: Theory and experimental validation. Water Res. X *1*, 100008. https://doi.org/10.1016/j.wroa.2018.100008.

74. Liu, Y., Ma, W., Cheng, Z., Xu, J., Wang, R., and Gang, X. (2013). Preparing CNTs/Ca-Selective zeolite composite electrode to remove calcium ions by capacitive deionization. Desalination *326*, 109–114. https://doi.org/10.1016/j.desal.2013.07.022.

75. Yan, J., and Indra, E.M. (2012). Colorimetric Method for Determining Pb2+ Ions in Water Enhanced with Non-Precious-Metal Nanoparticles. Anal. Chem. *84*, 6122–6127. https://doi.org/10.1021/ac301018y.

76. Guyes, E.N., Shocron, A.N., Chen, Y., Diesendruck, C.E., and Suss, M.E. (2021). Long-lasting, monovalent-selective capacitive deionization electrodes. npj Clean Water *4*, 1–11. https://doi.org/10.1038/s41545-021-00109-2.

77. Bahga, S.S., Bercovici, M., and Santiago, J.G. (2010). Ionic strength effects on electrophoretic focusing and separations. Electrophoresis *31*, 910–919. https://doi.org/10.1002/elps.200900560.

78. Kay, R.L. (1960). An application of the fuoss-onsager conductance theory to the alkali halides in several solvents. J. Am. Chem. Soc. *82*, 2099–2105.

79. Zhao, R., van Soestbergen, M., Rijnaarts, H.H.M., van der Wal, A., Bazant, M.Z., and Biesheuvel, P.M. (2012). Time-dependent ion selectivity in capacitive charging of porous electrodes. J. Colloid Interface Sci. *384*, 38–44. https://doi.org/10.1016/j.jcis.2012.06.022.

80. Dykstra, J.E., Dijkstra, J., van der Wal, A., Hamelers, H.V.M., and Porada, S. (2016). On-line method to study dynamics of ion adsorption from mixtures of salts in capacitive deionization. Desalination *390*, 47–52. https://doi.org/10.1016/j.desal.2016.04.001.

81. Santos, C., and La Mantia, F. (2022). Recent advances in reactor design and control for lithium recovery by means of electrochemical ion pumping. Curr. Opin. Electrochem. *35*, 101089. https://doi.org/10.1016/j.coelec.2022.101089.

82. Qu, Y., Campbell, P.G., Gu, L., Knipe, J.M., Dzenitis, E., Santiago, J.G., and Stadermann, M. (2016). Energy consumption analysis of constant voltage and constant current operations in capacitive deionization. Desalination *400*, 18–24. https://doi.org/10.1016/j.desal.2016.09.014.

83. Halliday, D., Resnick, R., and Walker, J. (2013). Fundamentals of Physics (John Wiley & Sons).

84. Rafik, F., Gualous, H., Gallay, R., Crausaz, A., and Berthon, A. (2007). Frequency, thermal and voltage supercapacitor characterization and modeling. J. Power Sources *165*, 928–934. https://doi.org/10.1016/j.jpowsour.2006.12.021.

85. Haque, M., Li, Q., Smith, A.D., Kuzmenko, V., Rudquist, P., Lundgren, P., and Enoksson, P. (2020). Self-discharge and leakage current mitigation of neutral aqueous-based supercapacitor by means of liquid crystal additive. J. Power Sources *453*, 227897. https://doi.org/10.1016/j.jpowsour.2020.227897.

86. Kötz, R., Sauter, J.-C., Ruch, P., Dietrich, P., Büchi, F., Magne, P., and Varenne, P. (2007). Voltage balancing: Long-term experience with the 250 V supercapacitor module of the hybrid fuel cell vehicle HY-LIGHT. J. Power Sources *174*, 264–271. https://doi.org/10.1016/j.jpowsour.2007.08.078.

87. Atkins, P., Atkins, P.W., and de Paula, J. (2014). Atkins' Physical Chemistry (Oxford University Press).

88. Castellan, G.W. (1983). Physical Chemistry (Wesley Publishing Company).

89. Dill, K., and Bromberg, S. (2010). Molecular Driving Forces: Statistical Thermodynamics in Biology, Chemistry, Physics, and Nanoscience (Garland Science).

90. Dalal, M. (2018). A Textbook of Physical Chemistry (Dalal Institute).

91. Light, T.S., Kingman, B., and Bevilacqua, A.C. (1995). The conductivity of low concentrations of CO_2 dissolved in ultrapure water from 0-100°C. In 209th American Chemical Society National Meeting.

92. Aslan, M., Zeiger, M., Jäckel, N., Grobelsek, I., Weingarth, D., and Presser, V. (2016). Improved capacitive deionization performance of mixed hydrophobic/hydrophilic activated carbon electrodes. J. Phys. Condens. Matter *28*, 114003. https://doi.org/10.1088/0953-8984/28/11/114003.

93. Bi, S., Zhang, Y., Cervini, L., Mo, T., Griffin, J.M., Presser, V., and Feng, G. (2020). Permselective ion electrosorption of subnanometer pores at high molar strength enables capacitive deionization of saline water. Sustain. Energy Fuels *4*, 1285–1295. https://doi.org/10.1039/C9SE00996E.

Cell Reports Physical Science, Volume *4*

Supplemental information

Best practice for electrochemical water desalination data generation and analysis

Mohammad Torkamanzadeh, Cansu Kök, Peter Rolf Burger, Panyu Ren, Yuan Zhang, Juhan Lee, Choonsoo Kim, and Volker Presser

Supplemental Figures

Figure S1.

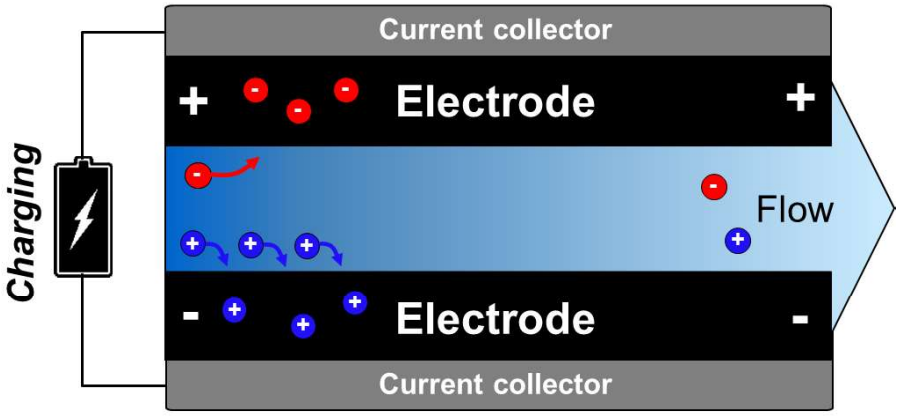

Figure S1. A simple electrochemical desalination cell. Schematic representation of an electrochemical desalination cell with flow-by configuration, where the water stream passes in between the two electrodes.

Figure S2.

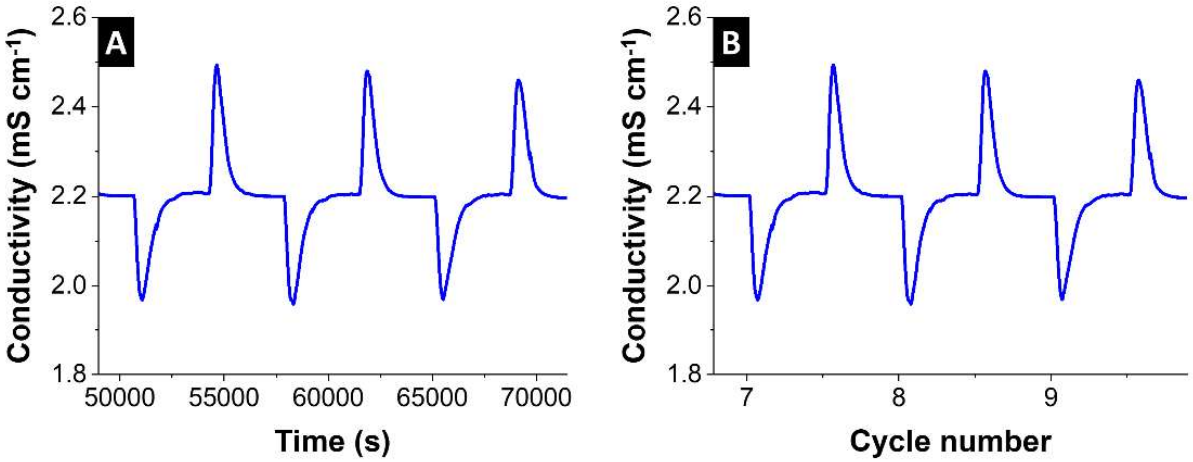

Figure S2. Changing the time into cycle number. Conversion of conductivity vs. time data (A) into conductivity vs. cycle number (B).

Figure S3.

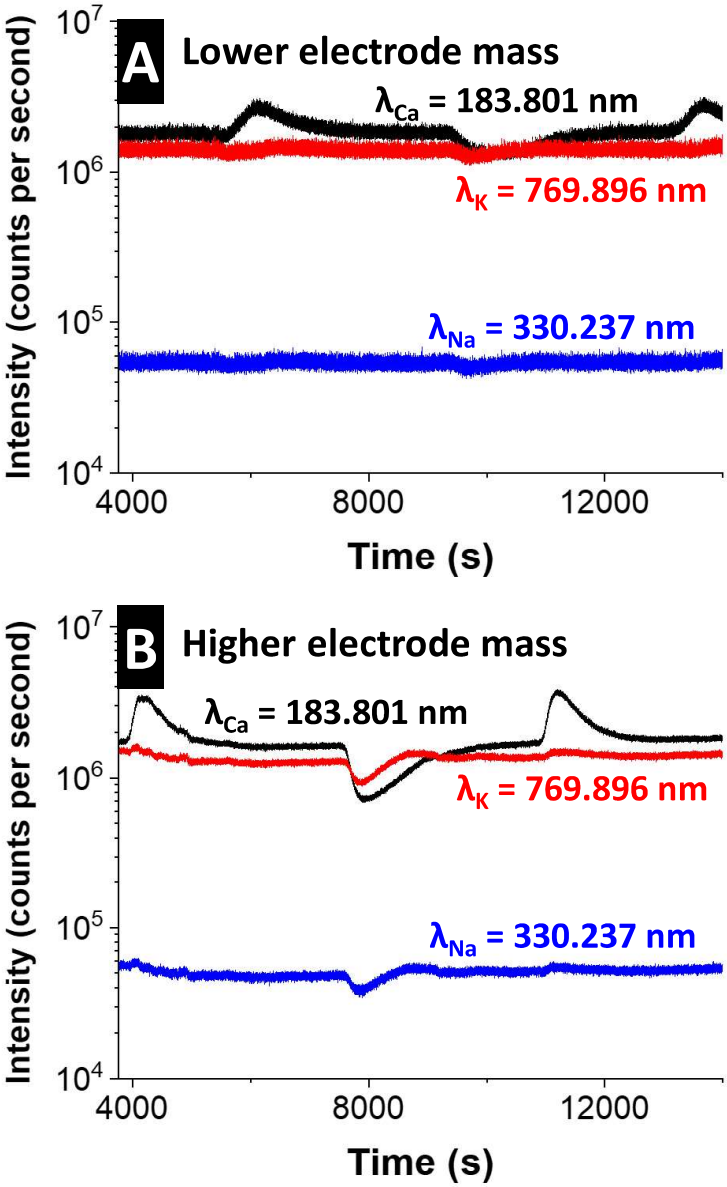

Figure S3. Raw online elemental monitoring data. Variation of the intensities individually recorded from calcium, potassium, and sodium ions using online ICP-OES monitoring of effluent water stream of a carbon/carbon electrochemical cell showing (A) rather noisy data with a cell containing 294 mg carbon cloth as negative electrode and 293 mg carbon cloth as positive electrode, and (B) less noisy data with a cell containing 506 mg carbon cloth as negative electrode and 501 mg carbon cloth as positive electrode.

Figure S4.

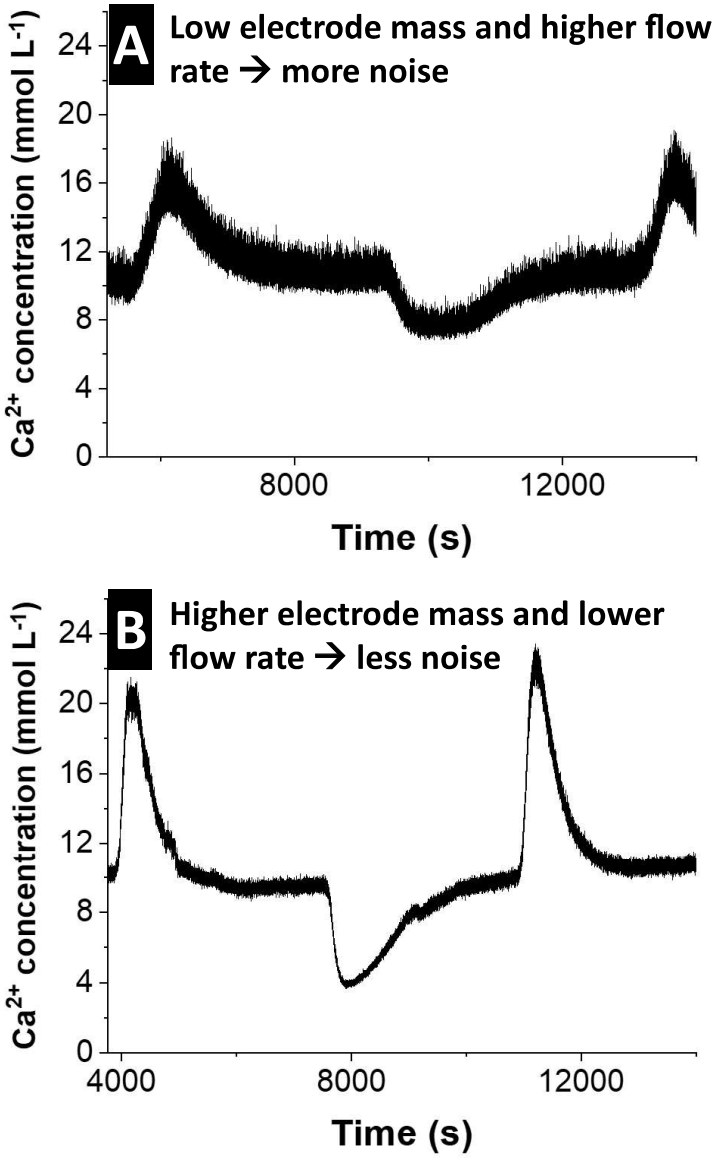

Figure S4. Improving the signal to noise ratio. Calcium concentration change derived from raw ICP-OES intensity data (**Figure S7**) using concentration-intensity equations obtained from calibration curves (**Figure S6**): (A) a rather noisy concentration profile with a cell containing 294 mg carbon cloth as negative electrode and 293 mg carbon cloth as positive electrode and (B) less noisy concentration profile with a cell containing 506 mg carbon cloth as negative electrode and 501 mg carbon cloth as positive electrode.

Figure S5.

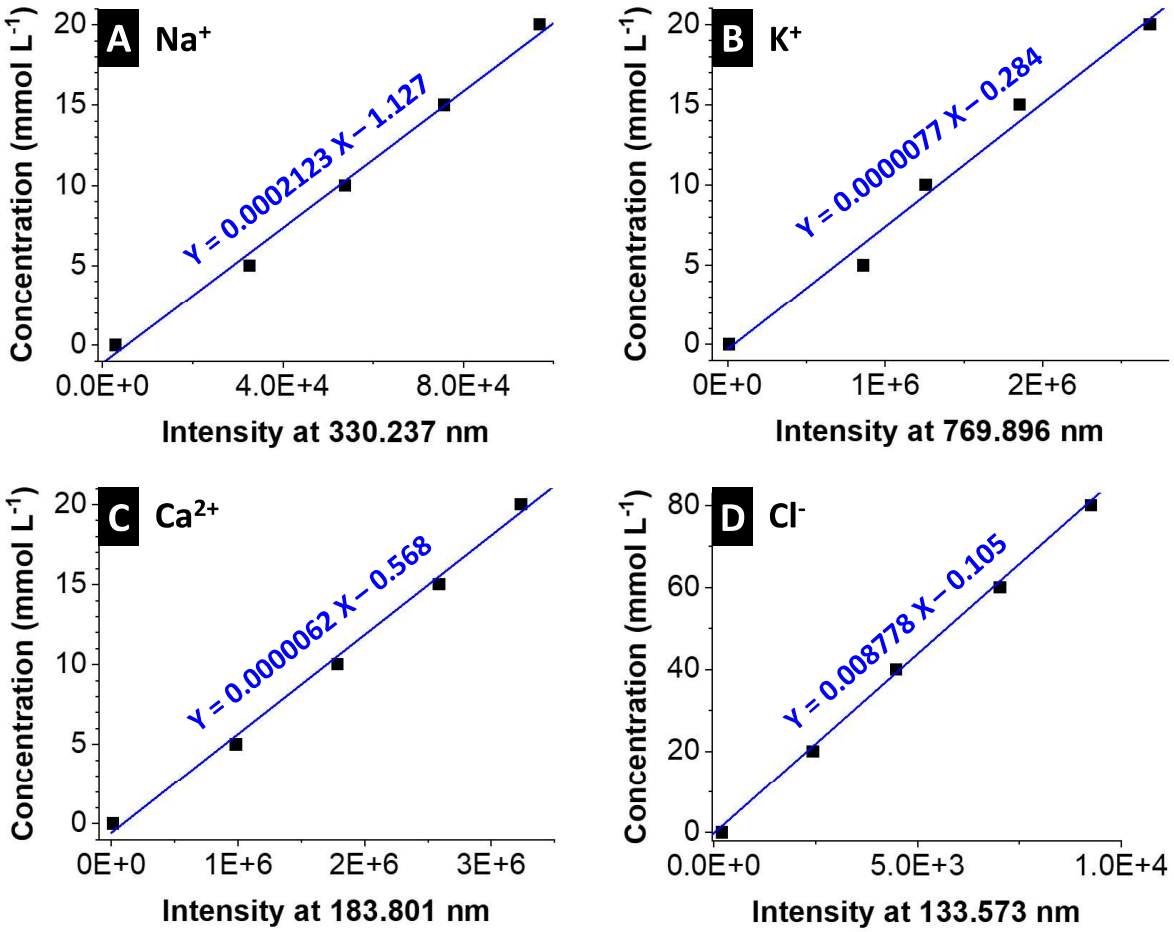

Figure S5. Construction of the calibration curves relating the ICP-OES intensity to the concentration. Concentration-intensity curves constructed using the solutions listed in **Table S1** to calibrate the ICP-OES instrument so that the measured optical emission intensity of each element can be individually converted into its concentration for (A) sodium, (B) potassium, (C) calcium, and (D) chloride ions.

Figure S6.

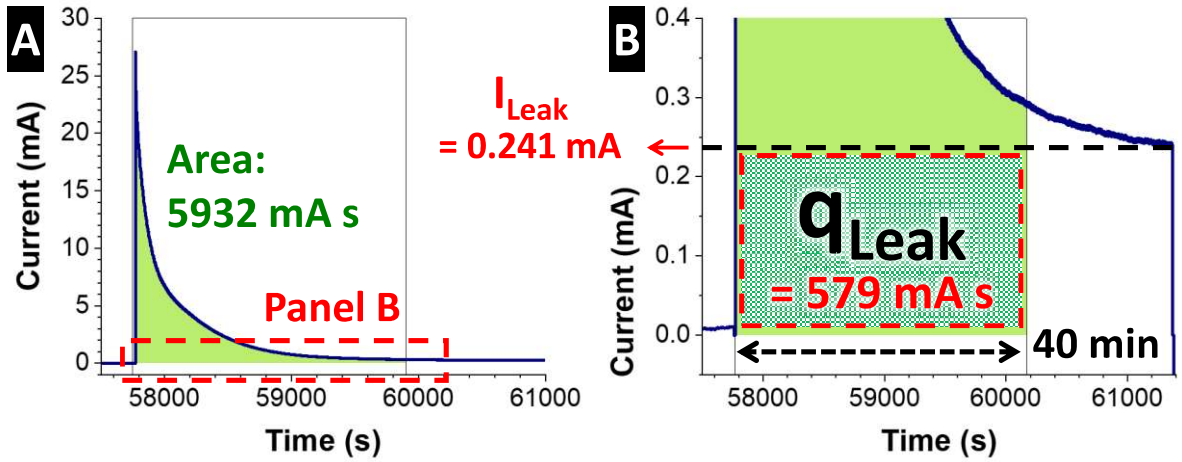

Figure S6. Calculation of the leakage current of the electrochemical desalination cell in this study. (A) Current-time profile for the charging half-cycle of an electrochemical desalination cell and (B) the zoomed view of the current-time curve showing the leakage current and leakage charge.

Figure S7.

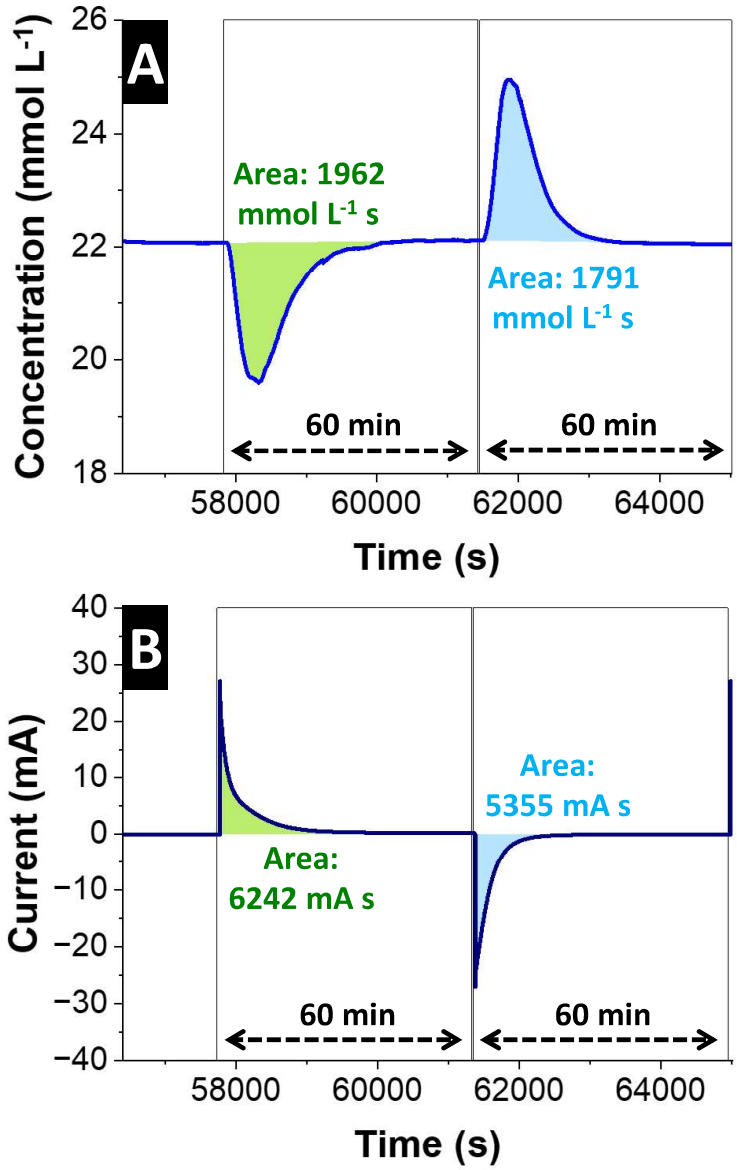

Figure S7. Integration of the area under the curves of concentration-time and current-time profiles. Integration of area under curve for charging and discharging half-cycles with 60 min duration each: (A) Concentration-time data and (B) current-time data.

Figure S8.

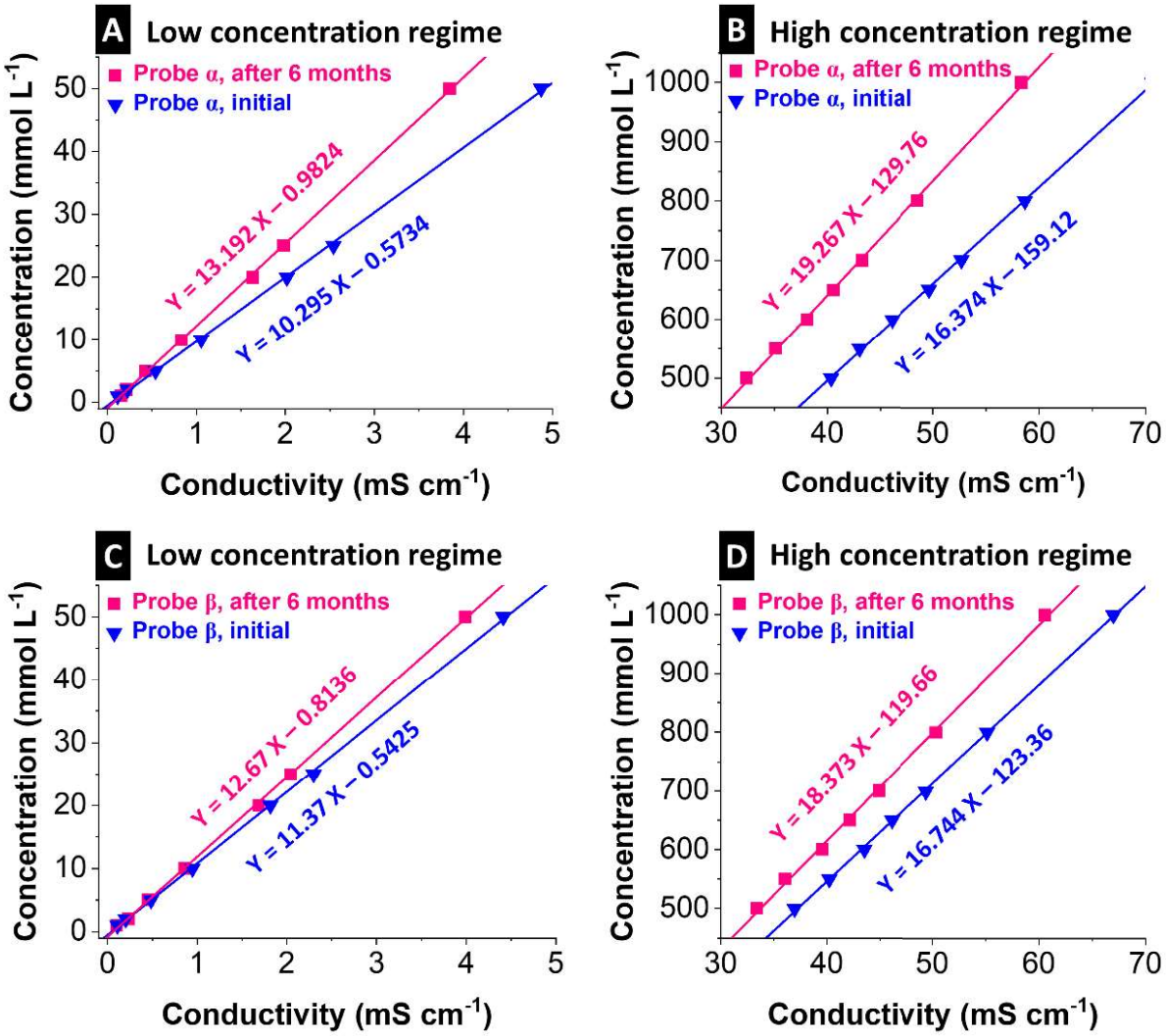

Figure S8. Effect of aging of the conductivity probes. Calibration curves of conductivity probe α, performed two times with 6 months interval in between for (A) low concentration and (B) high concentration regimes; calibration curves of conductivity probe β, performed two times with 6 months interval in between for (C) low concentration and (D) high concentration regimes.

Figure S9.

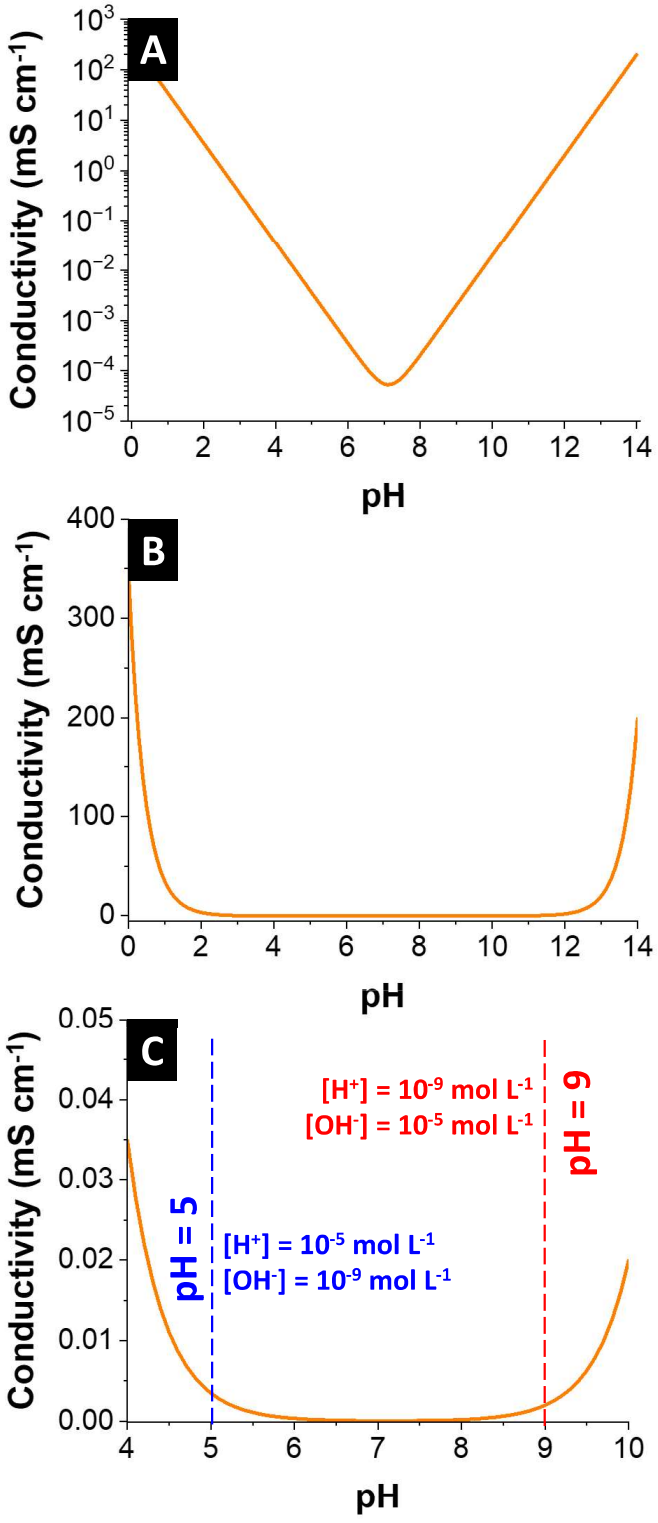

Figure S9. How pH can theoretically affect the conductivity. Theoretical dependence of the conductivity of ideally pure water on its pH is shown via (A) wide conductivity-pH scale, showing a conductivity of 0.055 µS cm^{-1} at pH = 7; (B) narrower, and (C) narrower conductivity-pH scales showing a pH range where conductivity contribution of water is minimal.

Supplemental Table

Table S1. Composition and concentrations of the solutions used to calibrate ICP-OES instrument prior to ion selectivity measurements.

Sample number	NaCl concentration (mmol L^{-1})	KCl concentration (mmol L^{-1})	$CaCl_2$ concentration (mmol L^{-1})
1 (blank)	0	0	0
2	5	5	5
3	10	10	10
4	15	15	15
5	20	20	20

Supplemental Notes

Note S1. The following is a checklist of what to report as the results of an electrochemical desalination experiment.

- Electrolyte parameters:
  - electrolyte concentration (mM, mg/L, or ppm)
  - electrolyte flow rate (mL/min)
  - de-aerated with an inert gas? (e.g., Ar or N_2)
- Cell parameters:
  - cell configuration (e.g., flow-by, flow-through, or flow-electrode)
  - for each electrode: type, mass, thickness
  - types of membranes used, if any.
  - electrodes configuration (2-electrode system or 3-electrode system, half-cell or full-cell, with or without reference electrode)
- Other operational parameters:
  - single-pass or batch-mode
  - conductivity probe calibration status: when was it last calibrated? what was the concentration range used for calibration? how was the goodness-of-fit (R^2 value)?
  - pH probe calibration status: when was it last calibrated?
  - pH variation: pH-time or pH-cycle curves, showing pH variation upon charge and discharge
- Electrochemical parameters:
  - specific current applied for charging and discharging (e.g., in A/g). it is important to specify here which mass was considered: the mass of both electrodes combined, the average mass of both electrodes, or the mass of a single electrode?
  - charging and discharging voltage, and voltage holding time in each step
  - number of cycles tested
- Performance metrics:
  - concentration-time or concentration-cycle curves
  - electrode potential-time (or cycle), cell voltage-time (or cycle), and current-time (or cycle) curves
  - average desalination capacity for each cycle, as well as the DC for charging half-cycle and for discharging half-cycle
  - the time duration considered for integration of C-t curve
  - charge efficiency, with and without leakage current subtraction
  - is the time duration considered for integration of I-t curve the same as that in C-t curve?
  - energy consumption (kT/ion removed)

Note S2. The following is a checklist of necessary items/considerations for an electrochemical desalination experiment.

- Hardware and infrastructure:
  - peristaltic pump: does the flow rate set on the pump match the real flow rate passing through its tubes? One can measure the flow rate manually by using a graduated cylinder and a simple chronometer.
  - conductivity probe: freshly calibrated with stock solutions
  - pH probe
  - temperature-controlled environment
  - inert gas source to bubble the electrolyte, as well as a gas washing bottle to minimize electrolyte evaporation
  - galvanostat/potentiostat that is capable of exporting outputs such as: electric charge stored in the electrodes during charging and the charge retrieved during discharging; energy consumed during charge; potential and current vs. time
- Software and other considerations:
  - reproducibility ensuring: does the software used for integration of area under concentration-time or current-time curves generate the same results when handled at a different time, or by a different user?
  - are the conductivity and pH probes close enough to the cell effluent to capture the characteristics of the outflowing water without long delays from the electrochemical results obtained by the galvanostat/potentiostat?

4.2. Particle size distribution influence on capacitive deionization: Insights for electrode preparation

Yuan Zhang,[1,2] Panyu Ren,[1,2] Yang Liu,[1,2] and Volker Presser[1,2,3]

[1] *INM - Leibniz Institute for New Materials, Campus D2 2, 66123, Saarbrücken, Germany*

[2] *Department of Materials Science & Engineering, Saarland University, Campus D2 2, 66123, Saarbrücken, Germany*

[3] *saarene - Saarland Center for Energy Materials and Sustainability, Campus C4 2, 66123 Saarbrücken, Germany*

Citation:

Y. Zhang, P. Ren, Y. Liu, and V. Presser, Particle size distribution influence on capacitive deionization: Insights for electrode preparation, Desalination 525 (2022) 115503.

Own contribution:

Investigation, Visualization, Review & Editing, Investigation.

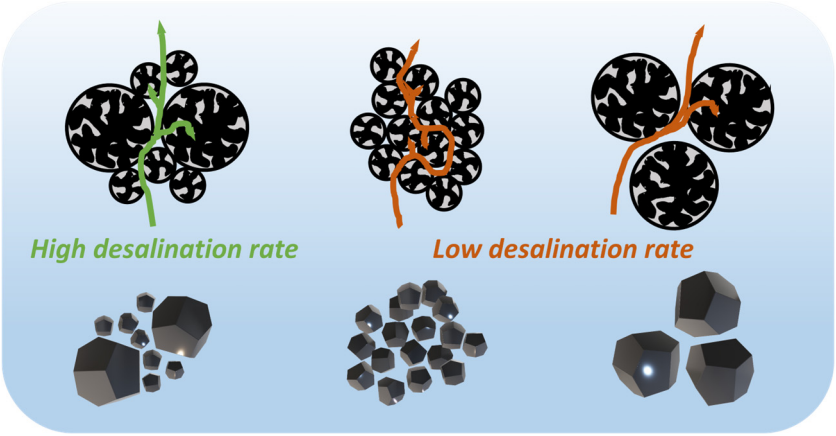

Desalination 525 (2022) 115503

Contents lists available at ScienceDirect

Desalination

journal homepage: www.elsevier.com/locate/desal

Particle size distribution influence on capacitive deionization: Insights for electrode preparation

Yuan Zhang [a,b], Panyu Ren [a,b], Yang Liu [a,b], Volker Presser [a,b,c,*]

[a] INM - Leibniz Institute for New Materials, Campus D2 2, 66123 Saarbrücken, Germany
[b] Saarland University, Campus D2 2, 66123 Saarbrücken, Germany
[c] Saarene - Saarland Center for Energy Materials and Sustainability, Campus C4 2, 66123 Saarbrücken, Germany

HIGHLIGHTS

- Activated carbon powders consist of particles of different size which can be separated via physical methods.
- Different particle sizes of activated carbon electrodes will provide different performance for capacitive deionization.
- A mixture of larger and smaller particles was found to be most beneficial for electrochemical desalination.

GRAPHICAL ABSTRACT

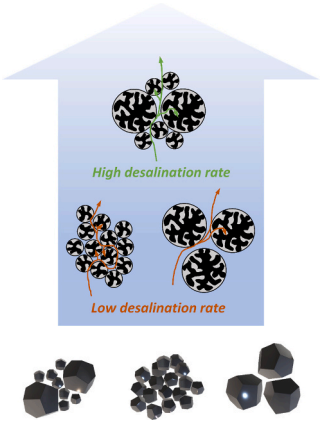

ARTICLE INFO

Keywords:
Microporous carbon
Particle size
Ion transport
Water desalination

ABSTRACT

As freshwater shortage has become a global issue, water desalination technique is of great importance to meet the increasing demand for freshwater resources of human beings. Capacitive deionization (CDI) has attracted significant attention in the current desalination technology portfolio. This is because of the use of low-cost electrode materials and the promise of high energy efficiency when including the energy recovery process. CDI, which has its advantage for applying low ionic strength by using various materials, has been explored to improve the system's performance. However, very few have addressed the importance of proper parameter designs, especially the electrodes. In our work, the same activated carbon of different average particle sizes has been studied by applying different desalination parameters (flow rate, holding time, salt concentrations). Our data show that larger particles limit intraparticle ion transportation because of the increased diffusion path length. We also see that a higher packing density, often favored by smaller particles or distribution of particle sizes, is detrimental to interparticle ion transportation. Our work addressed the importance of proper electrode and desalination parameter design for higher desalination performances.

* Corresponding author at: Saarland University, Campus D2 2, 66123 Saarbrücken, Germany.
E-mail address: volker.presser@leibniz-inm.de (V. Presser).

https://doi.org/10.1016/j.desal.2021.115503
Received 17 September 2021; Received in revised form 6 December 2021; Accepted 13 December 2021
Available online 29 December 2021

1. Introduction

Freshwater scarcity has been increasingly perceived as a global issue [1]. With the large water consumption compared with freshwater availability, the river flows have decreased, with the lake water and groundwater levels declining. Around two-thirds of the global population live under severe water scarcity at least one month of the year [2]. With almost 98% of the water in the world being seawater or brackish water, the increasing demand for freshwater had aroused great attention in the water desalination area [3]. Conventional desalination technologies, including thermal distillation [4–6], electrodialysis [7,8], and reverse osmosis [9–11], are effective, but more energy-efficient technologies are in high demand to reach the goal of sustainable water remediation [12]. Electrochemical water desalination technologies are attracting increasing attention in the water treatment field. Due to the higher reversibility of the capacitive electrode materials, this technology can recover most of the energy consumed for desalination by releasing the charge to a saline medium [13]. Capacitive deionization (CDI), which applies capacitive materials with highly porous pore structures and high surface areas as electrodes, is beneficial from energy efficiency and long-term stability point of view [14–16]. The use of ion-exchange membranes (membrane capacitive deionization) and/or chemically functionalized carbon electrodes (inverted capacitive deionization) allows to increase the desalination performance [17,18].

In 1960, Blair and Murphy first introduced an electrochemical desalination setup that applies carbon and Ag/AgCl to store/release Na^+ and Cl^- separately [19]. Later in 1967, Murphy and Caudle applied a symmetric carbon-carbon electrode pair to study the first CDI setup [20]. Later on, the first theoretical study of the CDI has addressed the importance of the surface area of the carbon materials in 1971 [21]. Thus, in recent decades, more CDI works are applying carbon materials with high specific surface areas such as carbon xerogels [22], carbon nanotubes [23], graphene [24], activated carbon [25], carbide-derived carbons [26,27], and salt-templated carbon materials [3]. Microporous carbons, which have an average pore size smaller than 2 nm, are of greater interest due to higher specific surface area compared to mesoporous carbons (2–50 nm) and carbon macropores (>50 nm) [28]. For pores smaller than 2 nm, due to the strong overlapping of the electrical double layer, the classical Gouy-Chapman-Stern model is no longer suitable to describe the ion distribution within a charged pore [29,30]. Instead, a Donnan model is developed by Basser et al. to describe ion distributions in micropores where electrostatic repulsion should be considered at low ionic strength [27]. Later, Biesheuvel et al. considered the charge transfer processes, extended the theory, and modified the Donnan theory significantly [31].

While past works attributed a dominant role for water desalination performance with CDI to the specific surface area and pore volume of carbon materials, in recent years, the ionic strength and pore size distribution are important factors. The former strongly influences the ion number repelled from a charged electrode during the desalination process, and the latter influences the number of ion pairs initially existed at the uncharged state [32]. When a potential is applied to the carbon electrodes, the counter-ions (ions with opposite charge) will be electroadsorbed in the pore of the electrodes, and meantime, the co-ions (ions with the same charge as the electrode) will be repelled and released from the pores. In high ionic strength, this co-ion and counter-ion exchange would reach a 1:1 ratio [33]. When the pore size decreases to below 1 nm, where the ion solvation shell being distorted, there is not only anomalous capacitance increase [34] but also increased ion permselectivity in the carbon pores, which is caused by ionophobicity at the uncharged state and thus much less co-ion release during the cycling process [34].

From a carbon material point of view, choosing carbon materials with small pore size distribution and high surface area can improve the desalination performance. For subnanometer size pores, the ion transport kinetics will also be limited [35]. Thus, it is not practical to have large carbon materials with single pore size distribution because ion transportation from the bulk electrolyte to the pores (interparticle ion transportation in carbon materials) [36] is also an essential factor in the desalination process which has not been well explored yet. Porada et al. showed that there is a strong correlation between electrode packing density and desalination rate [3]. By varying the particle size distributions, a clear change of desalination performance can be obtained. Recently, Shen et al. applied MXene of different sizes and showed that smaller particles improve the electrochemical and desalination performance [34]. In their work, the mixture of small and large particles exhibited the best performance (169 F/g and 72 $mg_{NaCl}/g_{electrode}$) [34]. Yet, a more systematic study based on ion transportation mechanisms under different particle size distributions is needed to find out the limiting factor to change the desalination performance.

Therefore, when designing a CDI electrode, texture (interparticle space) and ion transport pathlength (intraparticle pore volume) must be considered. Yet, any activated carbon powder always contains particles of different sizes – so what is the best particle size for capacitive deionization? In our work, the activated carbon material is separated by different particle size distributions by applying different desalination parameters (ion concentration, potential holding time, feedwater flow rate), a deeper understanding of particle size influence on ion transport and desalination performance are explored. To that end, we choose commercially available activated carbon as a model material to show that the right electrode design must critically consider particle size aspects to enable an optimized desalination performance.

2. Experimental description

2.1. Materials preparation

Commercially available activated carbon YP-80F from Kuraray was used in this study. The particles with different size distributions were separated by the centrifugation method. 20 g of YP-80F was added to 750 g of ethanol and was mixed by magnetic stirring for 1 h to form a uniform dispersion solution at the first step. Then the mixture is centrifuged at different speeds and periods to separate the particles depending on their sizes. To obtain large particles, the mixture was centrifuged at a rate of 500 rpm for 1 min, and the obtained sediment material is labeled as AC-L; for the smaller particles, the mixture was centrifuged at a speed of 1000 rpm for 1 min, and the obtained supernatant material is labeled as AC-S. The original material without particle separation is labeled as AC-M. Later on, the obtained sediment and supernatant material was collected and dried in the oven at 80 °C under a vacuum condition to obtain dry carbon powders for electrode preparations.

For electrode preparation, the carbon powder samples were first mixed with ethanol to form a uniform slurry in a mortar, then a water dispersion with polytetrafluoroethylene (PTFE; 60 mass%) from Sigma Aldrich was added and mixed with the carbon slurry with a carbon: binder mass ratio of 9:1. The mixing process is accomplished by stirring in the mortar to prevent destroying the carbon particles. Then the obtained carbon paste was rolled and pressed by an electric hot rolling press (MTI HR01, MTI Corporation) to have electrodes with a homogeneous thickness of 600 μm. Afterward, the electrodes were placed in the oven and heated at 120 °C for 24 h under a vacuum condition. The electrode densities of different materials are listed in Table 1. Two different electrode compactions were studied for the initial material AC-M: densified AC-M-d with a heavier mass loading and AC-M with lower packing density (Table 1). Both AC-M and AC-M-d electrodes have the same electrode area and thickness.

2.2. Materials characterization

2.2.1. Laser diffraction

The particle size distribution of the carbon samples was

Table 1
Electrode packing densities.

Material	Electrode density (g/cm^3)
AC-M	0.11
AC-L	0.25
AC-S	0.14
AC-M-d	0.34

characterized by laser diffraction technology. The carbon samples were flushed with deionized water and fed to the Mastersizer 2000. Once the obscuration degree of the particle suspension reaches a suitable range (8–14%), each sample was measured three times, and an average particle size distribution result was obtained at a size range of 0.02–2000 μm.

2.2.2. Nitrogen gas sorption analysis

Nitrogen gas sorption analysis (GSA) was conducted to analyze the pore size distribution of the materials. An Autosorb IQ system was applied with a liquid nitrogen-controlled temperature of −196 °C for the analysis process. At first, the samples were degassed at +200 °C for 1 h and then heated to 300 °C for up to 20 h to remove the humidity and solvent residue. Then, the samples were analyzed via nitrogen gas sorption at −196 °C. A slit-shaped pore configuration was assumed, and a quenched solid density functional theory was applied to analyze the pore size distribution of the microporous carbon materials [37,38]. The average pore size d_{50} was calculated by using the pore size of half of the maximum cumulative pore volume. The BET surface area (named after Brunauer Emmett Teller) was determined within the linear pressure range [39,40].

2.2.3. Scanning electron microscope

A Zeiss Germini SEM 500 is applied at 1 kV with a working distance of 2–4 mm to observe the particle morphology and compare the particle size of the obtained carbon materials. The samples were sticked on copper tape without any sputtering coating on top.

2.2.4. CHNS-O elemental analysis

To compare the chemical information and possible functional groups of the samples, the CHNS-O measurement was conducted. The amount of H, C, and N was quantified using a Vario MICRO Cube (Elementar Analysensysteme GmbH) and heating up to +1150 °C at the combustion tube and +850 °C at the reduction tube. The O content was quantified with an OXY cube elemental analyzer (Elementar Analysensysteme GmbH) at a pyrolysis temperature of +1450 °C.

2.3. Desalination experiments

In this work, a symmetric cell type was chosen to test the desalination materials at different conditions. In alignment with previous work [41], the free-standing carbon electrodes were cut into a 30 mm diameter round disk with a thickness of 600 μm. Between the two electrodes, a fixed 3 mm distance is separated by the middle feedwater channel. There is a 3 mm thick, 30 mm diameter flow chamber filled with six glass fiber separators (Millipore) and four pieces of polyethylene terephthalate in the feedwater channel. The feedwater is pumped at a flow rate of 1 mL/min, 2.5 mL/min, or 5 mL/min to flow between the electrodes. The feedwater is cycled back to a 10 L reservoir to minimize the concentration fluctuation between the desalination cycles. In this work, to study the ionic strength influence on desalination performance, NaCl (Sigma Aldrich) was dissolved in MiliQ water to prepare 5 mM and 20 mM of NaCl solution.

At the outlet of the CDI cell, the feedwater conductivity and pH change were recorded by pH (Metrohm 867 pH Module) and conductivity (Metrohm 856 conductivity) sensors. A Bio-Logic VSP-300 system was used to observe the electrochemical performance of the system. For each galvanostatic charging and discharging step, a specific current of 0.1 A/g was set between 0 and + 1.0 V cell voltages, after reaching the set voltage, a potential holding time of 20 min, 30 min, and 60 min was applied. The cycling number for 20 min, 30 min, and 60 min holding times are 6, 5, and 4, separately. To avoid the effect of first-cycle conditioning, the calculation of the performance metrics is carried out only starting with the second cycle for each condition.

The desalination capacity was determined by Eq. (1):

$$DC = \left(v\frac{M_{salt}}{M_{tot}}\right)\int (c_t - c_0)dt \tag{1}$$

where M_{salt} is the molar mass of the salt, M_{tot} is the total mass of the two electrodes, v is the flow rate, c_0 and c_t are the initial outlet salt concentration and concentrate of the feedwater at time t, respectively.

The charge efficiency was calculated according to the following Eq. (2):

$$CE(\%) = \frac{F \times DC_{mol}}{M_{salt} \times Q} \times 100\% \tag{2}$$

where F is the Faraday constant (26,801 mAh/mol), DC_{mol} is the desalination capacity obtained from Eq. (1), and Q is the total charge (normalized to the total electrode mass, mAh/g) stored/released during the cycling process.

3. Results and discussion

3.1. Materials

The morphologies, particle size distributions, and pore size distributions are shown in Fig. 1. In Fig. 1A-C, the scanning electron micrographs show AC-M, AC-L, and AC-S are composed of particles of different sizes. Among them, AC-M is a mixture of particles with different sizes, AC-L and AC-S are the larger and smaller particles obtained from the sediment and supernatant of the centrifuging process, separately. In Fig. 1D, the laser scattering data shows the different particle size distribution of the three samples. AC-S shows the smallest particle size with an average particle size of 1.8 μm (d_{50}). Since AC-M is a mixture of particle sizes without particle separation treatment, it shows a broader particle size distribution compare to AC-L, and the average particle size (d_{50}) of AC-L (6.2 μm) is slightly larger compared to AC-M (5.4 μm).

Fig. 1E shows the pore size distribution of the materials. Comparing the three materials, AC-L and AC-S show similar pore size distributions, while AC-M shows slightly higher cumulative pore volume, especially at the pore size below 2 nm. The gas sorption data are given in Table 2. Despite that the centrifuging treatment of the carbon samples seemingly slightly reduces the micropore volume to around 10–13%, the difference of particle size distributions has little influence on the pore size distributions of the materials, in this case, the pore size influence of the desalination performances can be excluded.

Table 3 shows the CHNO-S chemical analysis results. The carbon content of all samples is above 93%, with some oxygen content of less than 8%, the nitrogen and hydrogen contents are all below 2%. According to the chemical analysis data, there is no significant chemical composition difference among the three samples.

3.2. Concentration profiles

The concentration profiles of activated carbons with different particle size distributions are plotted in Fig. 2. We show the concentration profiles at different flow rates during galvanostatic cycling (3 cycles). Three materials of different particle size distributions were compared at different salt concentrations and feedwater flow rates. In each cycle, one negative and one positive peak of concentration change can be observed. As the flow rate increases, the concentration change amplitudes will

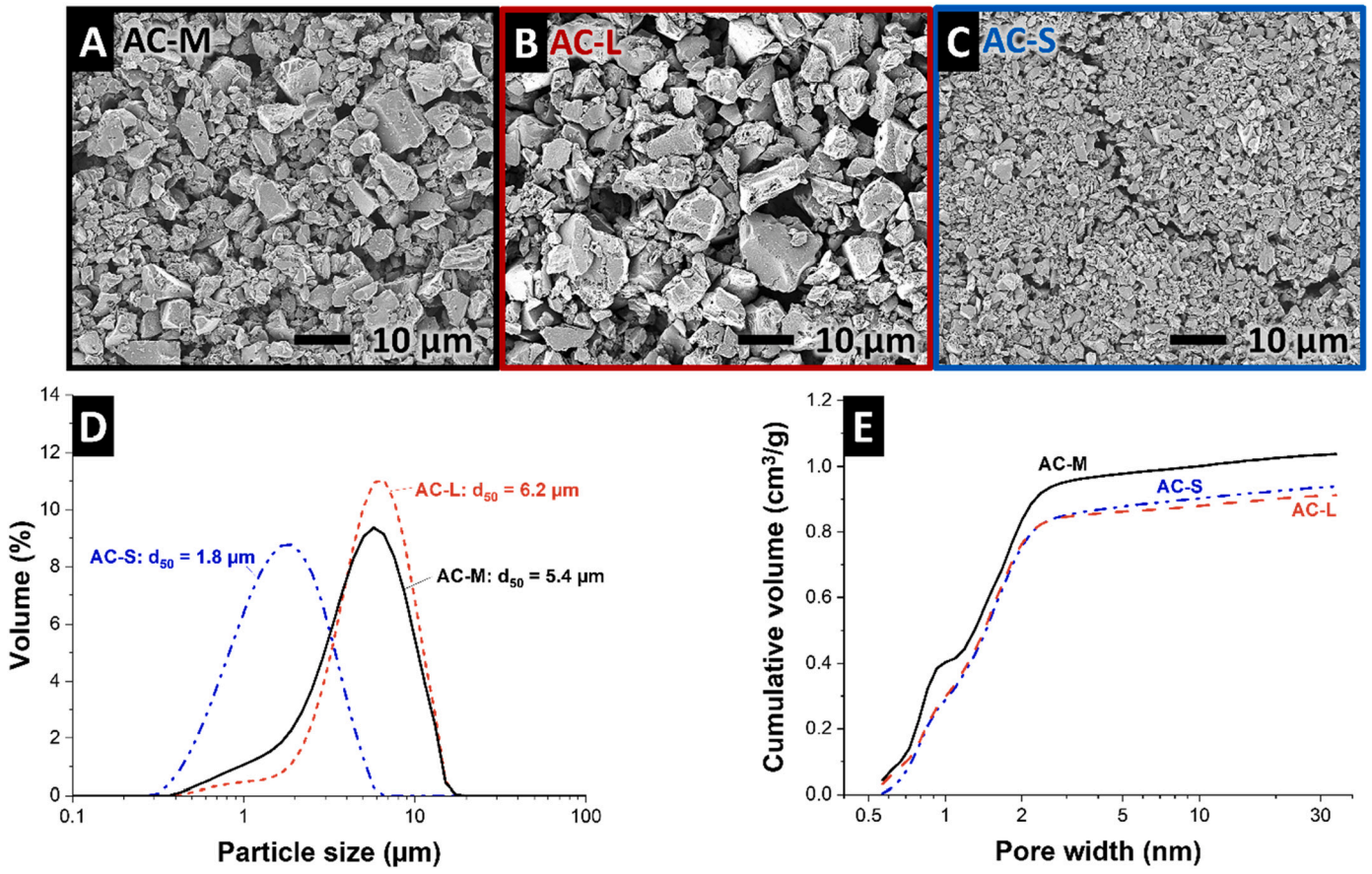

Fig. 1. Material characterization of AC-M, AC-L, and AC-S. A, B, C) SEM images of the three samples at the same scale; D) laser diffraction result of three samples showing the different particle size distributions. d_{50} is the average particle size of the material; E) Cumulative pore size distribution of the three samples, obtained from QSDFT analysis of nitrogen gas sorption data.

Table 2
Gas sorption analysis with nitrogen at −196 °C for the electrode materials using the quenched solid density functional theory (QSDFT) and the Brunauer-Emmett-Teller theory (BET). The average pore size refers to the volume-normalized value d_{50}. The micropore volume percentage pertains to the volume fraction of micropores regarding the total pore volume.

Material	d_{50} (nm)	Specific surface area (m^2/g)	Micropore volume (cm^3/g)	Total pore volume (cm^3/g)
AC-M	1.34	1741	0.84 (80.0%)	1.04
AC-L	1.34	1489	0.76 (83.5%)	0.91
AC-S	1.39	1449	0.76 (80.8%)	0.94

Table 3
CHNO elemental chemical analysis of the electrode materials.

Material	Carbon (mass %)	Hydrogen (mass %)	Nitrogen (mass %)	Oxygen (mass %)
AC-M	94.58	0.564	0.57	2.488
AC-L	94.95	0.718	0.48	3.105
AC-S	93.22	0.609	1.13	7.321

decrease accordingly for all carbon materials.

Compared to the material with a larger average particle size (AC-L), the amplitude of the measured concentration changes of AC-M are consistently higher at different flow rates and different concentrations (Fig. 2A, D, G). The adsorption and desorption peaks are also more narrow, and the concentration profile reaches an equilibrium value faster than AC-L. As the flow rate increases from 1 mL/min to 2.5 mL/min for AC-M, both adsorption and desorption peaks get narrower. As the flow rate increases to 5 mL/min, the adsorption peaks in 5 mM NaCl get wider, and the concentration stabilization time for AC-M becomes longer. For AC-M, when the flow rate of feedwater exceeds 2.5 mL/min, the interparticle ions were easily transported away before they were able to be adsorbed inside of the carbon pores. Thus, the intraparticle ion diffusion will become a more dominating limiting factor, the increase of the flow rate will lead to a non-effective ion uptake process. This phenomenon is more evident in the electrolyte with low ionic strength (5 mM) since, in lower electrolyte concentrations, the interparticle ion number is lower. This seemingly limits the ion transport from the bulk electrolyte to the particles.

As shown in Fig. 2B, E, H, the material with a larger average particle size (AC-L) shows an intense ion diffusion-limited effect in 5 mM and 20 mM NaCl solutions. In 5 mM NaCl solution, although by increasing the flow rate, the desorption peaks became narrower, in all different flow rates, the concentration profiles for adsorption processes require longer time to stabilize. Due to the larger average particle size, the intraparticle ion diffusion has a longer pathway than smaller particles. Thus, it becomes the limiting factor of ion uptake rate.

For AC-S (Fig. 2C, F, I), the average particle size of the activated carbon is smaller compared to AC-M and AC-L. In direct comparison with AC-L, we see AC-S providing much more narrow concentration change profiles. AC-S and AC-M, however, show a comparable pattern at all concentrations and all flow rates (Fig. 2). However, AC-S requires more time until an equilibrium concentration is reached; this makes the width of the adsorption/desorption peaks at the base broader in the case of AC-S in comparison with AC-M (and AC-L). This phenomenon is due to the smaller particles being closely packed. Thus, there is a more

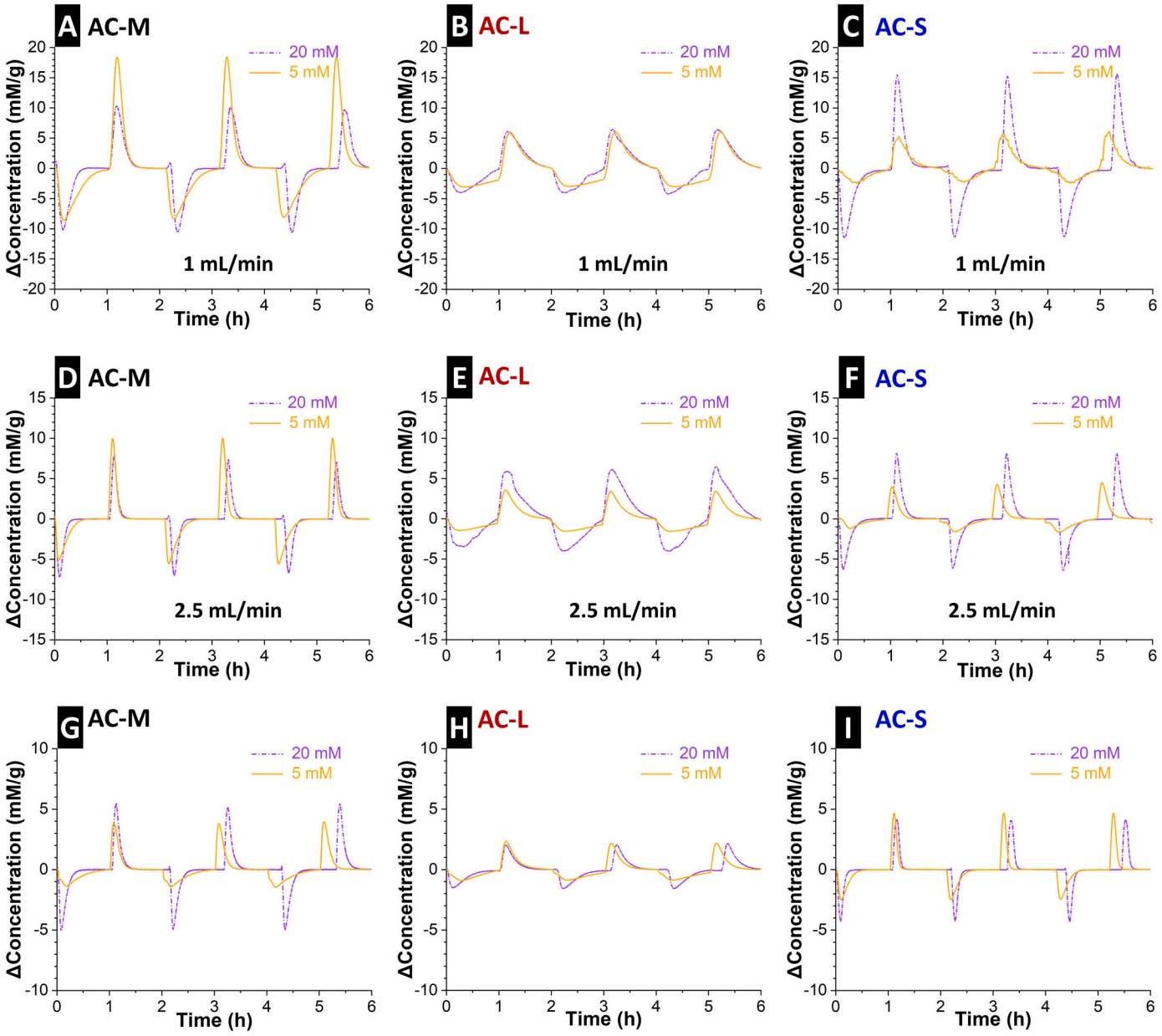

Fig. 2. Concentration profiles of different samples in 5 mM and 20 mM NaCl NaCl solutions under different flow rates. A-C) 1 L/min; D-F) 2.5 mL/min; G-I) 5 mL/min. Under all working conditions, the holding time is 60 min.

tortuous interparticle electrolyte pathway than that of AC-M, which slows down ion transport. As the flow rate increases from 1 mL/min to 5 mL/min, the adsorption and desorption peaks are sharper, indicating faster interparticle ion transport. When 20 mM NaCl is applied as the electrolyte, the concentration is reaching maximum adsorption more quickly (baseline). Sharp adsorption and desorption peaks are also observed due to the increased ionic strength that improves the interparticle ion transport.

3.3. Desalination capacity comparison

The desalination performance for AC-M, AC-L, AC-S in different salt concentrations, with varying times of holding and flow rates, are summarized and compared in Fig. 3. The individual desalination performance for each configuration is summarized in *Supporting Information*, Fig. S1. Among the materials studied by us, AC-M shows the highest desalination performance, and the extension of holding time and the electrolyte flow rate has only slightly increased the desalination performance (Fig. 3A-B). In addition, in 5 mM salt concentration, the use of AC-S and AC-L increases the desalination capacity and charge efficiency as the holding time increases. This behavior indicates that the desalination processes did not reach an equilibrium during shorter holding times due to slower ion transport kinetics. As the flow rate increases, the desalination performance for both AC-S and AC-L increases, showing that the accelerated electrolyte flow can improve the rate-limiting desalination performances of the two materials.

As seen in Fig. 3C-D, similarly, AC-M shows a slight reduction in desalination performance in 20 mM NaCl, yet it shows a much higher desalination performance compared to AC-L. The desalination performance for AC-S has vastly improved when using 20 mM NaCl solution instead of 5 mM. Its desalination capacity has increased from 5 to 8 mg/g to nearly 11 mg/g at the holding time of 60 min, and the charge efficiency has increased from 54–70% to 79–86%. The same trend is observed when 20 min and 30 min holding time were applied. This

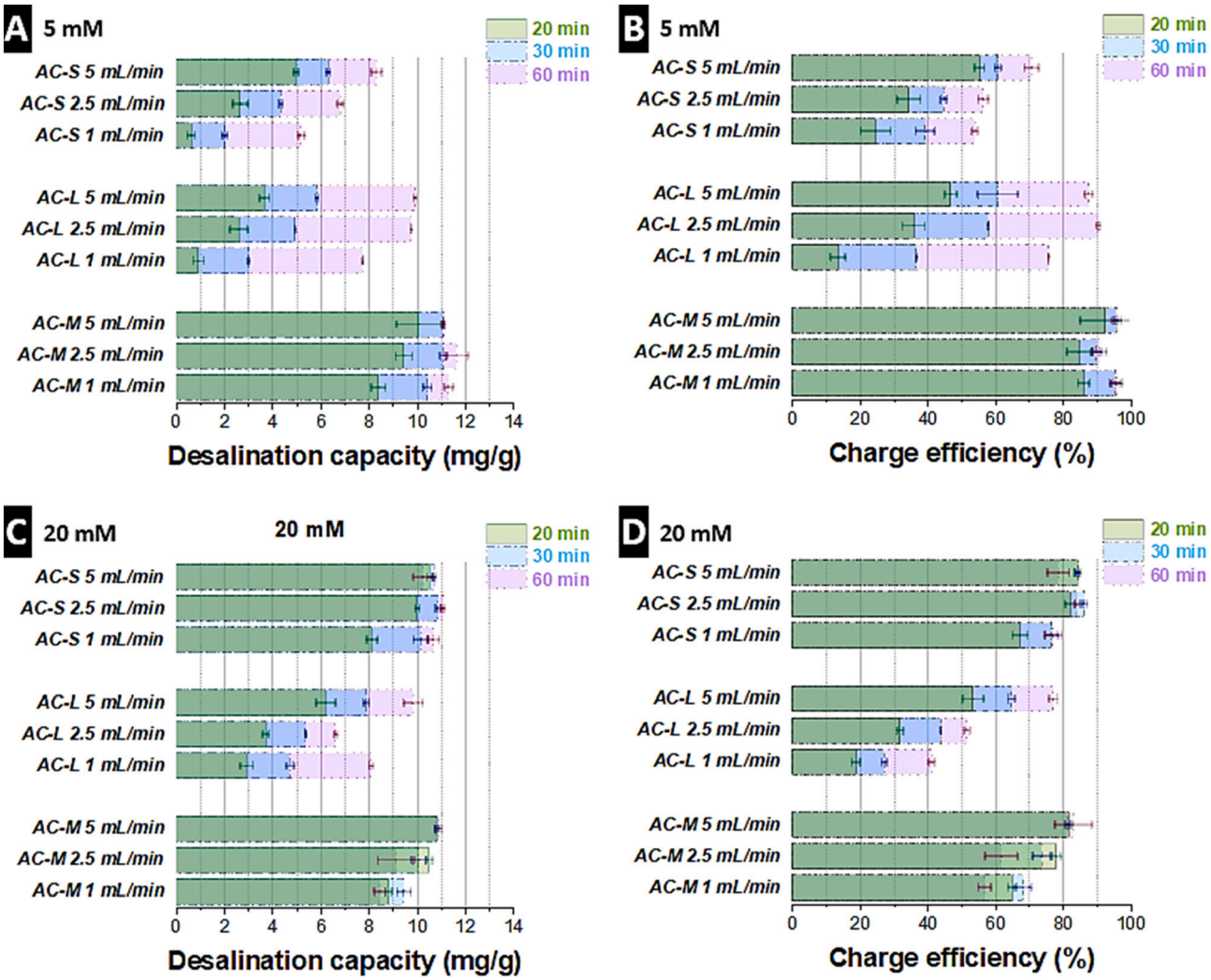

Fig. 3. Summary of desalination capacity and charge efficiency of activated carbon of different average particle sizes AC-M, AC-L, and AC-S in different concentrations. A-B) 5 mM; C-D) 20 mM. The effect of different holding times and flow rates has been compared.

observation agrees with improved interparticle ion transport. For AC-L in 20 mM NaCl, although by increasing the feedwater flow rate, a higher desalination performance is obtained, the desalination performance is lower than that in 5 mM, even a longer holding time was applied. Due to the larger average particle size, the ion diffusion in the particles is slower so that increasing the ionic strength or the flow rate of the feedwater is not effective to improve the desalination performance. Moreover, the increase of the ionic strength would lead to more co-ion and counter-ion exchange during the cycling process and cause a decrease in charge efficiency [42].

Apart from the particle size of the materials, the packing density of the electrode should also be considered. Merrill et al. applied graphene macro-assembly electrodes in supercapacitors and showed that high electrode density leads to a slower charging/discharging process [43]. Jelle et al. have investigated the electrode density influence on Li-ion battery performance [37]. They show that for electrodes with lower packing density, a higher performance is observed at high rates [37]. In our study, the desalination performance of AC-M-d with a much higher packing density is shown in *Supporting Information*, Fig. S2, a higher electrode density provides less space for the electrolyte and more tortuous for ion transport in electrolytes [34]. Thus, the slower ion transport kinetics result in a lower desalination capacity and a lower desalination rate.

3.4. Kim-Yoon plot and kinetic discussions

Fig. 4A, B, C shows the Kim-Yoon plot of the three materials in different concentrations and flow rates. For a better comparison of the desalination rate, the desalination capacity is normalized by the highest desalination capacity. The Kim Yoon plot of desalination capacity vs. desalination rate is shown in *Supporting Information*, Fig. S3. By increasing the flow rate of the feedwater, the desalination rate for all materials increases at different molarities. Among all materials, AC-L (Fig. 4B) shows the slowest desalination rates at all flow rates, the absence of plateau shows the desalination process was not reaching equilibrium. For AC-M (Fig. 4A), the desalination rate is much higher, the increase of flow rate and ionic strength improve the desalination rates. As seen from the data plotted in Fig. 4C, AC-S shows a much higher desalination rate in 20 mM NaCl solution (0.007, 0.010, 0.014 mg/g/s) than in 5 mM NaCl solution (0.001, 0.003, 0.005 mg/g/s) at the flow rates of 1, 2.5, and 5 mL/min.

These results show that two kinetic limitations can decrease the desalination rate, as illustrated in Fig. 5, one of them is intraparticle ion diffusion, another limitation is interparticle ion transportation. When the particle size is bigger, the ion diffusion length inside of the particle is longer, when the particle size is smaller, the interparticle ion transport length will become longer, which can also lead to higher electrode packing density. For the former case, it can be improved by decreasing

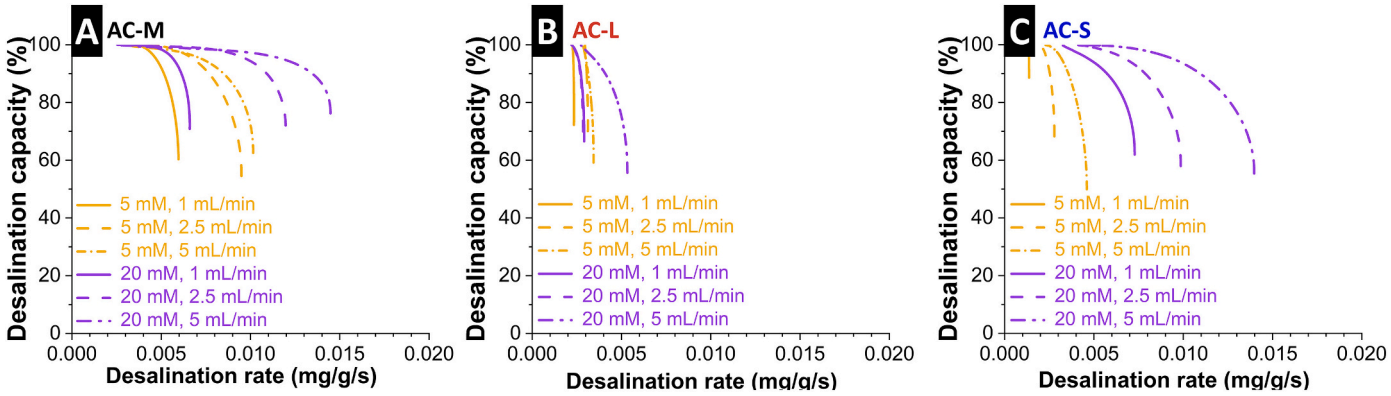

Fig. 4. Normalized Kim-Yoon plot of different average particle sizes under different ionic strengths and flow rates. A) AC-M; B) AC-L; C) AC-S. The desalination capacity is normalized to each maximum value for better comparison.

the average particle size. For the latter case, it can be improved by improving the mass transport (increasing the flow rate or the concentration) of the feed water. When mixing the larger particle with the smaller particles, the two limiting factors can be weakened at the same time. The involvement of the smaller particles can help to improve the intraparticle ion diffusion, and the existence of the larger particles can help to shorten the interparticle ion transport pathway.

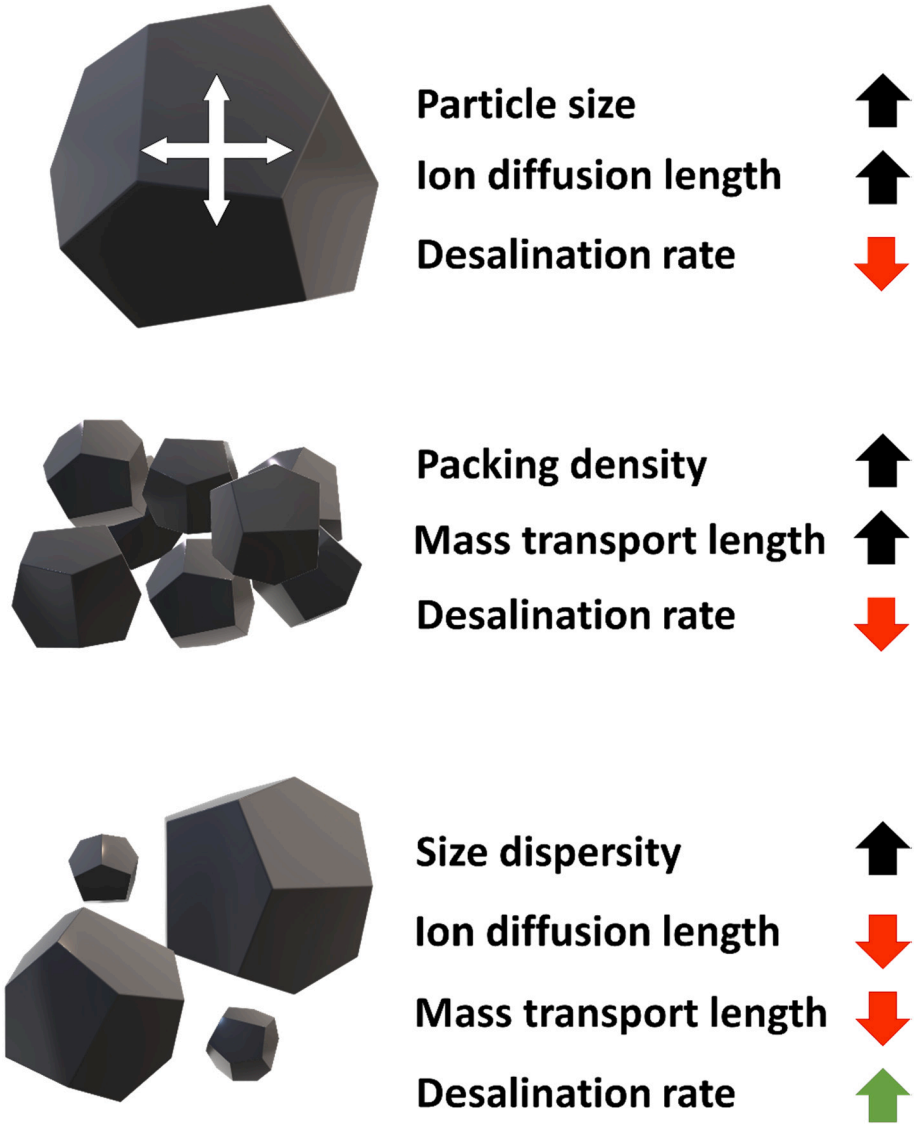

Fig. 5. Schematic illustration of particle influence on desalination rate.

4. Conclusions

In this work, the microporous activated carbon of different particle size distributions has been studied. Two factors that influence desalination performance have been studied by applying different desalination parameters, like different ionic strengths (5 mM and 20 mM NaCl solution) and different feedwater flow rates and holding times. One of them is the intraparticle ion diffusion length that is caused by different particle sizes. Another factor is the diffusion length of the ion transport pathway that relates to smaller average particles with higher packing densities. Specifically, in lower feedwater concentrations and electrodes with larger particle sizes, intraparticle and interparticle ion diffusion can limit the desalination capacity.

In comparison, intraparticle ion diffusion is the main limiting factor in higher feedwater concentrations. By mixing larger and smaller particles to form a broad particle size distribution (d_{50} of 5.4 μm), increasing the feedwater flow rate (5 mL/min) and meanwhile using electrodes with a lower packing density (0.11 g/cm^3), the two limiting factors can be balanced. Thus higher desalination performances can be obtained. Our results show the importance of average particle size and packing density for making the electrodes and have optimized electrode preparation for capacitive deionization applications.

Declaration of competing interest

The authors declare the following financial interests/personal relationships which may be considered as potential competing interests: Volker Presser reports financial support was provided by RAG-Stiftung.

Acknowledgments

The authors thank Eduard Arzt (INM) for his continuing support. The authors thank Andrea Jung, Maike Ulbricht, and Aron Schorr (all at INM) for their support with CHNS-O measurements, scanning electron microscopy, and laser diffraction characterizations. Y.Z. and V.P. acknowledge support for the MERLIN project from the RAG-Stiftung; the RAG-Stiftung generates long-term momentum for the transformation of the regions along the Ruhr and Saar Rivers and in Ibbenbüren.

CRediT author statement

Y.Z.: Data Curation, Writing - Original Draft, Supervision, Visualization, Investigation.

P.R.:Validation, Review & Editing, Investigation.

Y.L.: Data Curation, Review & Editing, Investigation.

V.P.: Conceptualization, Data Curation, Writing - Review & Editing, Visualization, Funding acquisition, Project administration, Supervision

Appendix A. Supplementary data

Supplementary data to this article can be found online at https://doi.org/10.1016/j.desal.2021.115503.

References

[1] M.A. Shannon, P.W. Bohn, M. Elimelech, J.G. Georgiadis, B.J. Mariñas, A. M. Mayes, Science and technology for water purification in the coming decades, Nature 452 (2008) 301–310.
[2] T. Humplik, J. Lee, S.C. O'Hern, B.A. Fellman, M.A. Baig, S.F. Hassan, M.A. Atieh, F. Rahman, T. Laoui, R. Karnik, E.N. Wang, Nanostructured materials for water desalination, Nanotechnology 22 (2011), 292001.
[3] S. Porada, L. Borchardt, M. Oschatz, M. Bryjak, J.S. Atchison, K.J. Keesman, S. Kaskel, P.M. Biesheuvel, V. Presser, Direct prediction of the desalination performance of porous carbon electrodes for capacitive deionization, Energy Environ. Sci. 6 (2013) 3700–3712.
[4] M.M. Mekonnen, A.Y. Hoekstra, Four billion people facing severe water scarcity, Sci. Adv. 2 (2016), e1500323.
[5] J.E. Miller, Review of Water Resources and Desalination Technologies, in, United States, 2003.
[6] Z. Wang, T. Horseman, A.P. Straub, N.Y. Yip, D. Li, M. Elimelech, S. Lin, Pathways and challenges for efficient solar-thermal desalination, Science Advances 5 (2019), eaax0763.
[7] A.D. Khawaji, I.K. Kutubkhanah, J.-M. Wie, Advances in seawater desalination technologies, Desalination 221 (2008) 47–69.
[8] A.M. El-Nashar, Cogeneration for power and desalination - state of the art review, Desalination 134 (2001) 7–28.
[9] S. Al-Amshawee, M.Y.B.M. Yunus, A.A.M. Azoddein, D.G. Hassell, I.H. Dakhil, H. A. Hasan, Electrodialysis desalination for water and wastewater: a review, Chem. Eng. J. 380 (2020), 122231.
[10] L.F. Greenlee, D.F. Lawler, B.D. Freeman, B. Marrot, P. Moulin, Reverse osmosis desalination: water sources, technology, and today's challenges, Water Res. 43 (2009) 2317–2348.
[11] Y. Ayyash, H. Imai, T. Yamada, T. Fukuda, Y. Yanaga, T. Taniyama, Performance of reverse osmosis membrane in Jeddah Phase I plant, Desalination 96 (1994) 215–224.
[12] B. Durham, A. Walton, Membrane pretreatment of reverse osmosis: long-term experience on difficult waters, Desalination 122 (1999) 157–170.
[13] S.H. Ebrahim, M.M. Abdel-Jawad, M. Safar, Conventional pretreatment system for the Doha reverse osmosis plant: technical and economic assessment, Desalination 102 (1995) 179–187.
[14] S. Lin, Energy efficiency of desalination: fundamental insights from intuitive interpretation, Environ. Sci. Technol. 54 (2020) 76–84.
[15] F. Chen, Y. Huang, L. Guo, L. Sun, Y. Wang, H.Y. Yang, Dual-ions electrochemical deionization: a desalination generator, Energy Environ. Sci. 10 (2017) 2081–2089.
[16] L. Wang, Y. Zhang, K. Moh, V. Presser, From capacitive deionization to desalination batteries and desalination fuel cells, Curr. Opin. Electrochem. 29 (2021), 100758.
[17] J. Landon, X. Gao, A. Omosebi, K. Liu, Progress and outlook for capacitive deionization technology, Curr. Opin. Chem. Eng. 25 (2019) 1–8.
[18] P.M. Biesheuvel, A. van der Wal, Membrane capacitive deionization, J. Membr. Sci. 346 (2010) 256–262.
[19] M.A. Anderson, A.L. Cudero, J. Palma, Capacitive deionization as an electrochemical means of saving energy and delivering clean water. Comparison to present desalination practices: will it compete? Electrochim. Acta 55 (2010) 3845–3856.
[20] S. Porada, R. Zhao, A. van der Wal, V. Presser, P.M. Biesheuvel, Review on the science and technology of water desalination by capacitive deionization, Prog. Mater. Sci. 58 (2013) 1388–1442.
[21] J.W. Blair, G.W. Murphy, Electrochemical demineralization of water with porous electrodes of large surface area, in: Saline water conversion, American Chemical Society, 1960, pp. 206–223.
[22] J. Landon, X. Gao, B. Kulengowski, J.K. Neathery, K. Liu, Impact of pore size characteristics on the electrosorption capacity of carbon xerogel electrodes for capacitive deionization, J. Electrochem. Soc. 159 (2012) A1861–A1866.
[23] G.W. Murphy, D.D. Caudle, Mathematical theory of electrochemical demineralization in flowing systems, Electrochim. Acta 12 (1967) 1655–1664.
[24] A.M. Johnson, J. Newman, Desalting by means of porous carbon electrodes, J. Electrochem. Soc. 118 (1971) 510.
[25] L. Wang, M. Wang, Z.-H. Huang, T. Cui, X. Gui, F. Kang, K. Wang, D. Wu, Capacitive deionization of NaCl solutions using carbon nanotube sponge electrodes, J. Mater. Chem. 21 (2011) 18295.
[26] W. Shi, H. Li, X. Cao, Z.Y. Leong, J. Zhang, T. Chen, H. Zhang, H.Y. Yang, Ultrahigh performance of novel capacitive deionization electrodes based on a three-dimensional graphene architecture with nanopores, Sci. Rep. 6 (2016) 18966.
[27] S. Porada, L. Weinstein, R. Dash, A. van der Wal, M. Bryjak, Y. Gogotsi, P. M. Biesheuvel, Water desalination using capacitive deionization with microporous carbon electrodes, ACS Appl. Mater. Interfaces 4 (2012) 1194–1199.
[28] P. Ratajczak, M.E. Suss, F. Kaasik, F. Béguin, Carbon electrodes for capacitive technologies, Energy Storage Mater. 16 (2019) 126–145.
[29] A. Levy, J.P. de Souza, M.Z. Bazant, Breakdown of electroneutrality in nanopores, J. Colloid Interface Sci. 579 (2020) 162–176.
[30] E. Partheniades, Forces between clay particles and the process of flocculation, in: E. Partheniades (Ed.), Cohesive Sediments in Open Channels, Butterworth-Heinemann, Boston, 2009, pp. 47–88.
[31] S. Porada, F. Schipper, M. Aslan, M. Antonietti, V. Presser, T.-P. Fellinger, Capacitive deionization using biomass-based microporous salt-templated heteroatom-doped carbons, ChemSusChem 8 (2015) 1867–1874.
[32] P.J. Basser, A.J. Grodzinsky, The donnan model derived from microstructure, Biophys. Chem. 46 (1993) 57–68.
[33] P.M. Biesheuvel, Y. Fu, M.Z. Bazant, Diffuse charge and Faradaic reactions in porous electrodes, Phys. Rev. E 83 (2011), 061507.
[34] S. Bi, Y. Zhang, L. Cervini, T. Mo, J.M. Griffin, V. Presser, G. Feng, Permselective ion electrosorption of subnanometer pores at high molar strength enables capacitive deionization of saline water, Sustain.Energy Fuel 4 (2020) 1285–1295.
[35] J. Chmiola, G. Yushin, Y. Gogotsi, C. Portet, P. Simon, P.L. Taberna, Anomalous increase in carbon capacitance at pore sizes less than 1 nanometer, Science 313 (2006) 1760–1763.
[36] K. Breitsprecher, M. Janssen, P. Srimuk, B.L. Mehdi, V. Presser, C. Holm, S. Kondrat, How to speed up ion transport in nanopores, Nat. Commun. 11 (2020) 6085.
[37] Y. Zhang, P. Srimuk, S. Husmann, M. Chen, G. Feng, V. Presser, Effect of pore size on the ion electrosorption and hydrogen/deuterium electrosorption using sodium chloride in H2O and D2O, J. Electrochem. Soc. 166 (2019) A4158–A4167.

[38] X. Shen, Y. Xiong, R. Hai, F. Yu, J. Ma, All-MXene-based integrated membrane electrode constructed using Ti3C2Tx as an intercalating agent for high-performance desalination, Environ. Sci. Technol. 54 (2020) 4554–4563.
[39] C. Prehal, S. Grätz, B. Krüner, M. Thommes, L. Borchardt, V. Presser, O. Paris, Comparing pore structure models of nanoporous carbons obtained from small angle X-ray scattering and gas adsorption, Carbon 152 (2019) 416–423.
[40] S. Choudhury, B. Krüner, P. Massuti-Ballester, A. Tolosa, C. Prehal, I. Grobelsek, O. Paris, L. Borchardt, V. Presser, Microporous novolac-derived carbon beads/sulfur hybrid cathode for lithium-sulfur batteries, J. Power Sources 357 (2017) 198–208.
[41] M. Thommes, K. Kaneko, A.V. Neimark, J.P. Olivier, F. Rodriguez-Reinoso, J. Rouquerol, K.S.W. Sing, Physisorption of gases, with special reference to the evaluation of surface area and pore size distribution, Pure Appl. Chem. 87 (2015) 1051–1069.
[42] S. Brunauer, P.H. Emmett, E. Teller, Adsorption of gases in multimolecular layers, J. Am. Chem. Soc. 60 (1938) 309–319.
[43] M.D. Merrill, E. Montalvo, P.G. Campbell, Y.M. Wang, M. Stadermann, T. F. Baumann, J. Biener, M.A. Worsley, Optimizing supercapacitor electrode density: achieving the energy of organic electrolytes with the power of aqueous electrolytes, RSC Adv. 4 (2014) 42942–42946.

Supporting Information

Particle size distribution influence on capacitive deionization: insights for electrode preparation

Yuan Zhang,[1,2] Panyu Ren,[1,2] Yang Liu,[1,2] and Volker Presser[1,2,3*]

INM - Leibniz Institute for New Materials, Campus D2 2, 66123 Saarbrücken, Germany

Saarland University, Campus D2 2, 66123 Saarbrücken, Germany

Saarene - Saarland Center for Energy Materials and Sustainability, Campus C4 2, 66123 Saarbrücken, Germany

* Corresponding author's eMail: volker.presser@leibniz-inm.de

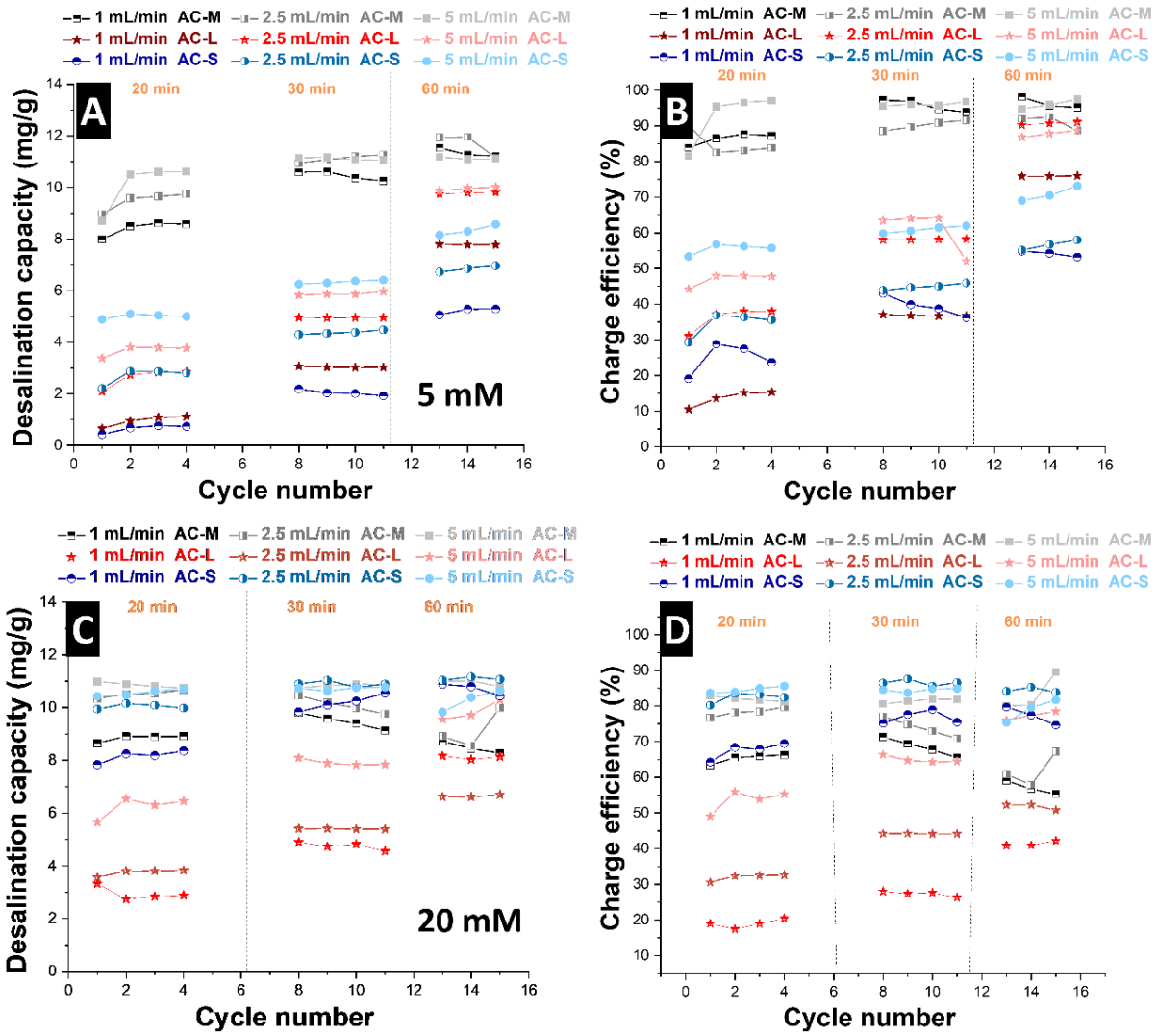

Figure S1: Desalination capacity and charge efficiency of activated carbon of different average particle sizes AC-M, AC-L, and AC-S in different concentrations. A-B) 5 mM; C-D) 20 mM. The performance under different holding times and flow rates have been compared.

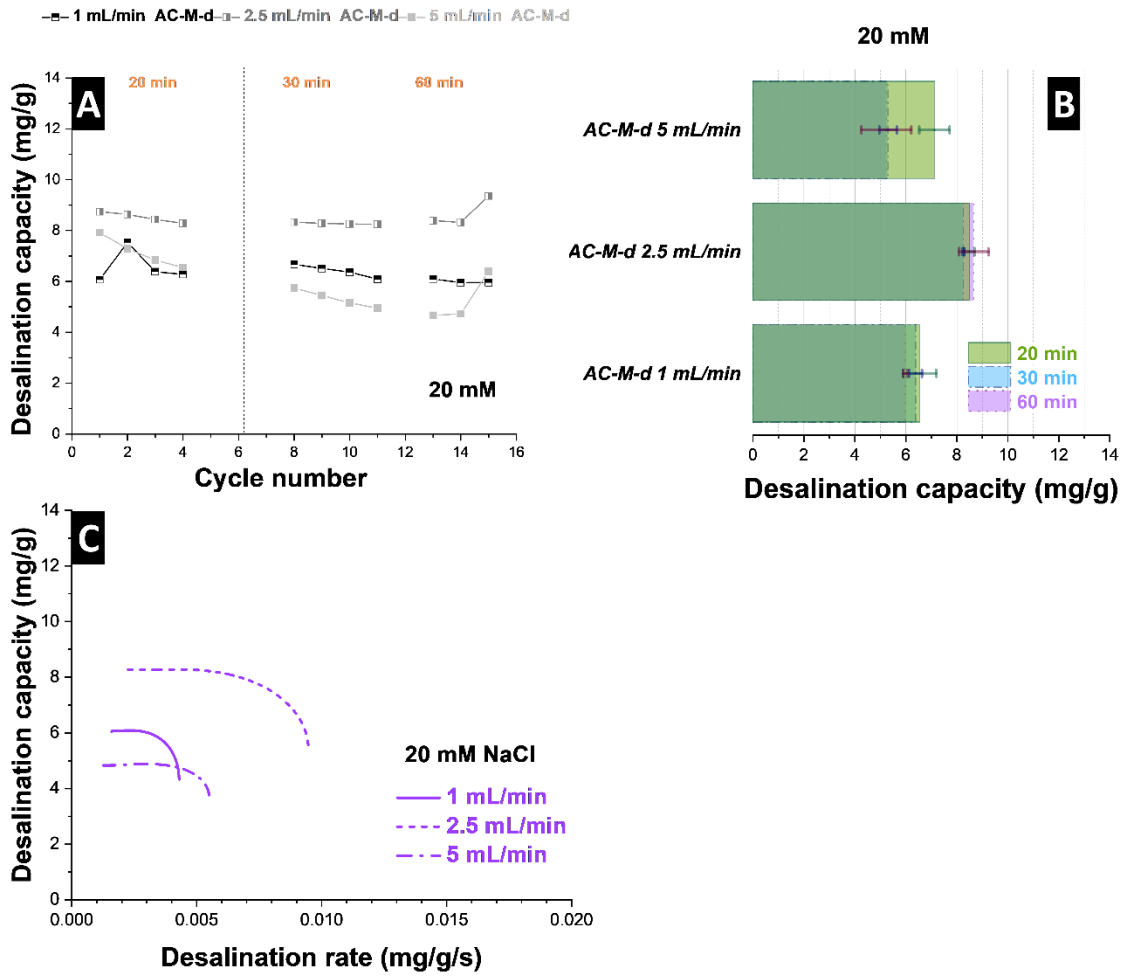

Figure S2: The desalination capacity of AC-M-d material with higher electrode packing density under 20 mM NaCl molar strength. Different holding times and flow rates have been applied for comparison. A) Desalination performance over the 15 cycles; B) Desalination capacity at different holding times; C) Kim-Yoon plot at different flow rates.

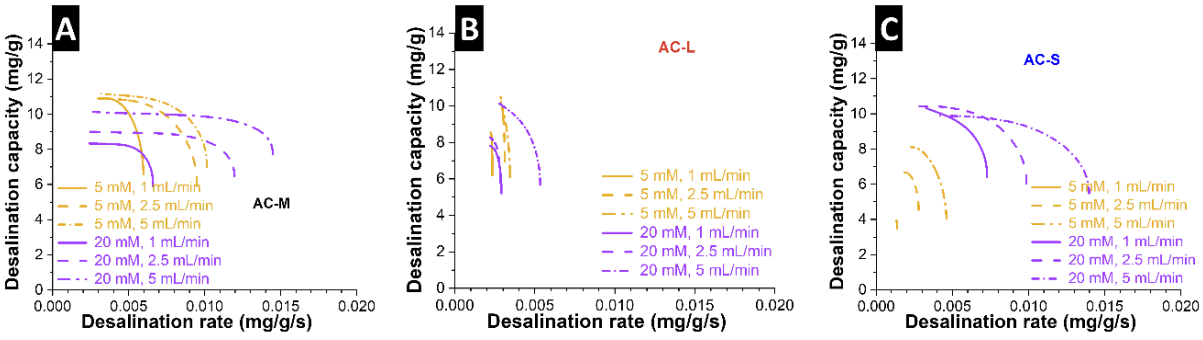

Figure S3: Conventional Kim-Yoon plot of materials of different average particle sizes under different ionic strengths and flow rates. A) AC-M; B) AC-L; C) AC-S.

4.3. Conductive carbon additives: Friend or foe of capacitive deionization with activated carbon?

Panyu Ren,[1,2] Mohammad Torkamanzadeh,[1,2] Xiao Zhang,[1,2] Marek Twardoch,[1] Choonsoo Kim,[4] and Volker Presser[1,2,3]

[1] *INM - Leibniz Institute for New Materials, Campus D2 2, 66123, Saarbrücken, Germany*

[2] *Department of Materials Science & Engineering, Saarland University, Campus D2 2, 66123, Saarbrücken, Germany*

[3] *saarene - Saarland Center for Energy Materials and Sustainability, Campus C4 2, 66123 Saarbrücken, Germany*

[4] *Department of Environmental Engineering with Institute of Energy/Environment Convergence Technologies and Department of Future Convergence Engineering, Kongju National University, 1223-24, Cheonan-daero, Cheonan-si 31080, Republic of Korea*

Citation:

P. Ren, M. Torkamanzadeh, X. Zhang, M. Twardoch, C. Kim, and V. Presser, Conductive carbon additives: Friend or foe of capacitive deionization with activated carbon? Carbon 213 (2023) 118191.

Own contribution:

Investigation, Data curation, Visualization, Writing - original draft, Writing - review & editing.

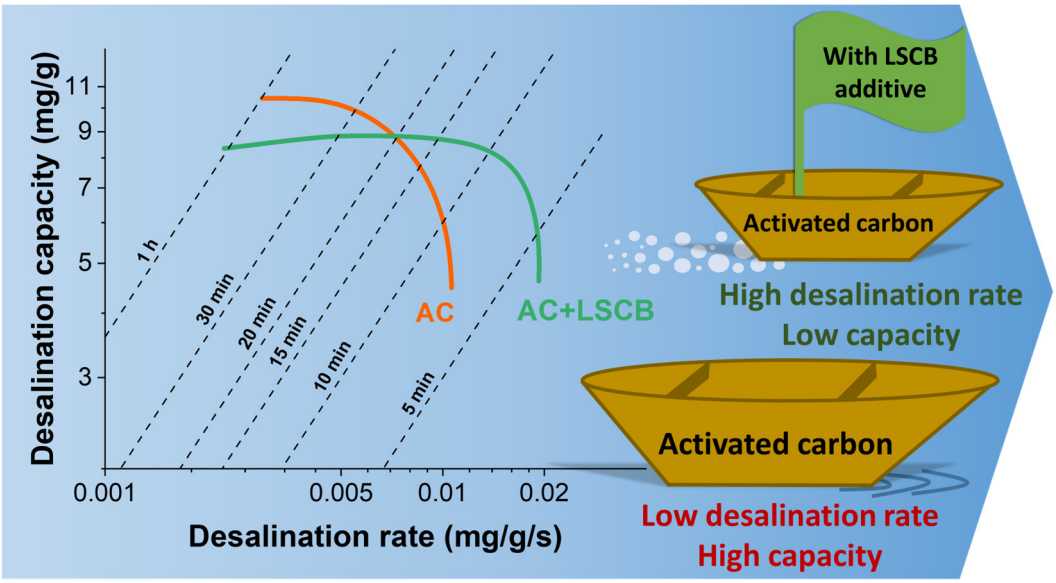

Carbon 213 (2023) 118191

Contents lists available at ScienceDirect

Carbon

journal homepage: www.elsevier.com/locate/carbon

Conductive carbon additives: Friend or foe of capacitive deionization with activated carbon?

Panyu Ren [a,b], Mohammad Torkamanzadeh [a,b], Xiao Zhang [a,b], Marek Twardoch [a], Choonsoo Kim [d], Volker Presser [a,b,c,*]

[a] INM – Leibniz Institute for New Materials, Campus D2 2, 66123, Saarbrücken, Germany
[b] Department of Materials Science & Engineering, Saarland University, Campus D2 2, 66123, Saarbrücken, Germany
[c] Saarene – Saarland Center for Energy Materials and Sustainability, Campus C4 2, 66123, Saarbrücken, Germany
[d] Department of Environmental Engineering with Institute of Energy/Environment Convergence Technologies and Department of Future Convergence Engineering, Kongju National University, 1223-24, Cheonan-daero, Cheonan-si, 31080, Republic of Korea

ARTICLE INFO

Keywords:
Carbon additive
Desalination rate
Ion transport
Size distribution
Capacitive deionization

ABSTRACT

Capacitive deionization with activated carbon (AC) electrodes has been widely applied for removing charged ions from aqueous solutions. Such carbon electrodes commonly contain a minor polymer binder and a minor carbon additive content. The choice of carbon additives is rarely investigated in depth regarding the performance enhancement/deterioration they might bring. In this work, we explored the influence of various carbon types, namely, onion-like carbon, carbon black, and micro-mesoporous carbons, on the desalination capacity and rate. Based on the cycling performance of 100 cycles, we draw relationships between the physicochemical properties of different carbon types and their results on electrochemical desalination performance. The results indicate that the direct use of the activated carbon electrode without additives leads to a higher desalination capacity of approximately 10 mg/g in early cycles, though at the cost of a lower desalination rate of 6 μg/g/s. The larger AC particles limit the intraparticle ion transportation due to the increased diffusion path length. The highest desalination rate (20 μg/g/s) is enabled by the incorporation of small and less porous additives, as it shortens the ion diffusion path length due to the increased size dispersion, hence improving the overall ion transport and desalination rates.

1. Introduction

The growing global shortage and uneven distribution of freshwater have emerged as a critical challenge for technological, economic, and social development in the 21st century [1]. Given the overuse of freshwater resources beyond their renewability and the depletion of groundwater [2], developing economic and sustainable water treatment technologies has become a global concern and priority. Over time, a wide variety of desalination methods has emerged, including the widespread use of distillation [3,4], electrodialysis [5,6], and reverse osmosis [7,8]. However, the development of these methods is limited by their high cost and high energy consumption. Capacitive deionization (CDI), as a cost-effective technology, eco-friendly and energy-efficient, has steadily gained growing attention during the past decades, particularly in desalination of water streams of low to moderate salt contents [9,10].

Blair and Murphy first introduced the CDI concept in 1960 [11], where a porous carbon electrode was paired with an Ag/AgCl electrode for, as it was called at the time, demineralization of aqueous NaCl solutions. Following this pioneering work, CDI with symmetric carbon-carbon electrodes has become the subject of electrochemical desalination studies for the following decades [12], serving as the first-generation electrode material for CDI [13,14]. To this date, carbon materials stand out as one of the cheapest, safest, most abundant, and most stable choices as CDI electrodes. The question of which carbon type to utilize is paramount, as its physicochemical characteristics dictate the bottom-line desalination performance. Routinely, carbon species with high surface areas are chosen. The larger micropore surface area, the higher population of electrolyte salt ions can be accommodated in the electrical double layers (EDLs) of carbon micropores, goes the rationale. As such, carbon aerogels [15,16], activated carbons (ACs) [17,18], activated carbon fibers [19–21], carbon nanotubes [22,23], graphene

* Corresponding author. INM – Leibniz Institute for New Materials, Campus D2 2, 66123, Saarbrücken, Germany.
E-mail address: volker.presser@leibniz-inm.de (V. Presser).

https://doi.org/10.1016/j.carbon.2023.118191
Received 15 March 2023; Received in revised form 9 May 2023; Accepted 5 June 2023
Available online 6 June 2023

[24–27], and carbide-derived carbons [28,29] have been extensively examined as CDI electrodes. Notably, porous activated carbon has been widely applied commercially due to its low costs, high internal specific surface area, and pore volume.

The main parameters for evaluating water desalination performance with CDI are the desalination capacity (DC) and the salt adsorption rate [30] of the electrodes. It is well-established from previous studies that a combination of carbon electrode properties, such as specific surface area, pore structure, and electrical conductivity, collectively affect the desalination performance [31–33]. To improve the DC of carbon materials, choosing carbon materials with narrow pore size distributions and high surface areas can increase the population of ions that can be stored inside the pores of the carbon electrode [34]. However, ion transport from the bulk electrolyte to the carbon micropores, such as interparticle ion transport in carbon materials, is also a critical limitation on the desalination performance [35]. For example, sub-micrometer sized MXene synthesized from molten salt as a CDI electrode material based on the ion intercalation mechanism performs exceedingly well due to its sub-micrometer particle size and larger interlayer space, which can effectively expand the interlayer space, shorten diffusion path lengths, and reduce diffusion barriers [36]. Similarly, it has been shown that a mixture of small and large particles exhibited the best performance when MXenes of different sizes were used [37].

Recently, Zhang et al. studied a number of activated carbons of different average particle sizes, and the results indicated that larger particles limit intraparticle ion transportation due to the increased diffusion path lengths [34]. To explore the right carbon additive for optimized Na-ion batteries, Pfeifer et al. [38] investigated the effects of adding an array of carbon species to Sb/C electrodes. The results have shown that carbon onions were most homogenously distributed within the Sb matrix and resulted in a high-rate performance. Although those are systematic studies that explore the influence of carbons in battery [38,39] or supercapacitor [40,41] electrodes, reports on such studies on CDI electrodes are scarce [42].

It is reported that porous electrodes combining a large micropore volume (the volume of pores <2 nm) yield a high DC, whereas a network of mesopores (2–50 nm) helps ion transport [33]. Carbon black, as a common additive, is generally used as a conductivity enhancer to improve the desalination performance since it can act as a conductive bridge between the current collector and activated carbon, or within activated carbon particles [43]. Yet, how to choose the suitable carbon additive in composite film electrodes (i.e., activated carbon plus conductive additive plus polymer binder) and the mechanistic investigation thereof remain poorly understood.

The objectives of this work, therefore, are to evaluate the desalination performance of the electrodes made of activated carbon with various carbon additive types. In addition, the influence of the composition of the electrodes on the salt removal kinetics from water is studied. We report here the ion transportation mechanism for the effect of particle size distribution and size dispersion on intraparticle ion transport. We provide a qualitative guide to aid in choosing the electrode with a suitable carbon additive for the desired target desalination performance.

2. Experimental description

2.1. Electrode materials and preparation

Commercially available activated carbon (AC), type YP-80F (Kuraray Chemicals Co.), was combined with five different commercial conductive additives. Low surface area carbon black super C45 and super C65 were provided by Imerys Graphite & Carbon, Switzerland, and referred to by LSCB1 and LSCB2 (here, LSCB refers to low specific surface area carbon black), respectively. Medium surface area carbon additive, Porocarb (PC), was purchased from Heraeus. This carbon has shown promising applications as a material for adding to Lithium-ion battery electrodes [44] and redox flow battery research [45]. This is because of its ability to increase kinetics and enhance rate handling capabilities. Carbon onions (called herein OLC, which stands for onion-like carbon), were synthesized by heat treatment of detonation nanodiamond powder (NaBond) in a graphite heated furnace (LHTG from Carbolite Gero) at 1700 °C under Argon flow of 300 L/h for 2 h. High surface area carbon black BP2000 (HSCB, abbreviation for high specific surface area carbon black) was purchased from Cabot. The latter carbon type is a widely-employed additive in battery research, often to improve the conductivity of the active electrode material such as transition metal oxides [46,47].

For electrode preparation, a homogeneous distribution of AC and additive components was first obtained by mixing the materials with ethanol in mortar, then polytetrafluoroethylene (PTFE, 60 mass% solution in water from Sigma-Aldrich) was added as a binder and mixed with the carbon slurry with an AC: carbon additive: binder mass ratio of 8:1:1. The mixture was continually stirred and manually ground to evaporate the ethanol until the slurry reached a paste-like consistency. The resulting carbon paste was cold-rolled and pressed by the rolling machine (MTI HR01, MTI Corp.) to prepare electrodes with a uniform thickness of 600 μm. Afterwards, the free-standing electrodes were placed in the oven and heated at 120 °C overnight under vacuum. In addition, as control group, an AC electrode with no carbon additive was made following the same procedure, only different in AC:binder mass ratio being 9:1. Similarly, the HSCB electrode was also prepared with the 9:1 mass ratio of BP2000:binder. The composition of each electrode in mass percentages is listed in Table 1.

2.2. Material characterization

2.2.1. Structural characterization

Scanning electron microscopy (SEM) analysis was carried out with a Zeiss Gemini SEM 500 at 1 kV with a working distance of 2–4 mm to observe the particle morphology of the studied carbon powders and electrodes. The samples were mounted on Aluminum stubs with copper tape and measured without conductive coatings.

Raman spectroscopy was carried out with a Renishaw inVia Raman system using a Nd-YAG laser with $\lambda = 532$ nm and an excitation power of 0.5 mW at the sample's surface, using an objective lens with a numeric aperture of 0.75 within 110–2000 cm^{-1}. Before measurements, calibration was freshly performed using a silicon wafer, where the peak position was adjusted to 520.50 ± 0.02 cm^{-1}. The sample material was put on a glass slide and measured without further modification.

X-ray diffraction (XRD) analysis was conducted with a D8 Advance diffractometer (Bruker AXS) with a copper source (Cu Kα, 40 kV, 40

Table 1
The composition of each electrode in mass percentages. "n.a." stands for "not available", that is, the electrode does not contain this material.

Electrode	AC	PTFE	PC	OLC	LSCB1	LSCB2	HSCB
80% AC + 10% PTFE + 10% PC	80%	10%	10%	n.a.	n.a.	n.a.	n.a.
80% AC + 10% PTFE + 10% OLC	80%	10%	n.a.	10%	n.a.	n.a.	n.a.
80% AC + 10% PTFE + 10% LSCB1	80%	10%	n.a.	n.a.	10%	n.a.	n.a.
80% AC + 10% PTFE + 10% LSCB2	80%	10%	n.a.	n.a.	n.a.	10%	n.a.
80% AC + 10% PTFE + 10% HSCB	80%	10%	n.a.	n.a.	n.a.	n.a.	10%
90% AC + 10% PTFE	90%	10%	n.a.	n.a.	n.a.	n.a.	n.a.
90% HSCB + 10% PTFE	n.a.	10%	n.a.	n.a.	n.a.	n.a.	90%

mA). The signal was collected using a 1D Lynxeye detector at 0.02 2θ step with 1 s per step. X-ray beam was calibrated using National Institute of Standards and Technology (NIST) 1976a corundum as a standard material. The samples were used with no preparation. The powders were flattened with glass. In case of electrode samples, the free-standing electrodes were placed on the sample holder.

2.2.2. Porosity analysis

Nitrogen gas sorption analysis (GSA) was conducted to analyze the pore characteristics of the studied carbon powders and electrodes. These measurements were conducted with an Autosorb iQ system (Quantachrome; now Anton-Paar) at the temperature of liquid nitrogen (−196 °C) after outgassing at 150 °C for 10 h for electrode samples (to avoid damaging the polymer binder PTFE) and at 300 °C for 24 h for powder samples. The specific surface area (SSA) was calculated by the ASiQwin-software using the Brunauer-Emmett-Teller (BET) equation [48]. In addition, we also quantified the SSA and pore size distribution via quenched-solid density functional theory (QSDFT) [49].

2.2.3. CHNS–O elemental analysis

CHNS–O measurements were carried out to study the elemental composition and possible functional groups of the precursors, poristine, and post mortem electrodes. The Carbon, Hydrogen, and Nitrogen contents were measured using a Vario MICRO Cube (Elementar Analysensysteme GmbH), where the samples first heated to 1150 °C in the combustion tube and to 850 °C in the reduction tube. To measure the Oxygen content, an OXY Cube Elemental Analyzer (Elementar Analysensysteme GmbH) was used at a pyrolysis temperature of 1450 °C.

2.2.4. Sheet resistance analysis

A custom-built four-point probe with gold contacts (tip diameter: 1.5 mm, tip distance: 3.0 mm) was used to calculate sheet resistances of the fabricated electrodes. The spring-loaded probes were connected to a Multimeter (Keithley, Model DMM6500). The four-point resistance measure function with offset compensation settings were used to measure sheet resistance of the electrodes. The latter value was then multiplied by the thickness of the electrode to obtain specific resistivity (Ω cm). Every electrode was laterally large enough to eliminate the need for any shape correction factors. The measurements were repeated for at least three repetitions in three different spots to calculate a mean value.

2.2.5. Particle size distribution analysis

The suspension's particle size distribution (hydrodynamic diameter) was estimated using dynamic light scattering (DLS). The measurements were performed with the Malvern Mastersizer 2000 device with the Hydro 2000S add-on. Before the measurement, 30 mg of carbon particles was placed in 30 g ethanol solvent and stirred on a magnetic stirrer for 2 h. Then, the sample was sonicated in the ultrasound bath for 30 min. Directly after the sonication, the sample was gradually added by a pipette to the DLS device reservoir containing around 150 mL of deionized water until the laser obscuration reached a level of 7%. The refractive index of the dispersant (water) and for carbon materials were set at 1.33 and 2.42, respectively. During the DLS measurement, the diluted suspension was constantly stirred at 2000 rpm and sonicated at 50% output power. The light scattering from the particles passing through the light beam was detected from forward, side, and backscattering detectors.

2.3. Basic electrochemical characterization

A custom-built polyether ether ketone (PEEK) cell was used for half-cell electrochemical tests, the materials were assembled in Ref. [50]. Throughout all half-cell measurements, an oversized electrode of 90% YP-80F + 10% PTFE was employed as counter electrode, where the mass of counter electrode was 2–4 times that of the working electrode. Electrode discs with a 12 mm diameter and ~600 μm thickness were cut out of the free-standing carbon films. Glass-fiber (GF/A, Whatman) was used as separator, and graphite foils were used as current collectors. A reference electrode (Ag/AgCl, 3 M NaCl) was placed at the side of the peek cell close to the sandwiched electrodes. An electrochemical workstation (potentiostat/galvanostat VSP300, Bio-Logic) was used to perform cyclic voltammetry (CV) and galvanostatic cycling with potential limitation (GCPL). 1 M NaCl aqueous solution was used as the electrolyte for all half-cell electrochemical characterizations. CV window-opening experiments were performed at both negative and positive potentials, with the negative potential ranging from 0 to −1.1 V and the positive potential ranging from 0 to 0.8 V, at a scan rate of 1 mV/s. The specific capacitance of the different electrodes is calculated by applying the equation **Eq. (1)**, where C is the specific capacitance of the material (F/g), I is the current (A), v is the scan rate (V/s), and m is the mass of the working electrode (g).

$$C = \frac{I}{v \bullet m} \tag{1}$$

During GCPL measurements, the specific current was increased in several steps from 0.1 A/g to 10 A/g with 10 s resting period between charging/discharging. For each electrode type, two replicates were prepared and tested individually and a mean value was calculated.

2.4. Electrochemical desalination

The free-standing carbon electrodes were cut into 30 mm diameter round discs with ~600 μm thickness and used as electrodes for CDI cells with symmetric electrode configuration. A flow-by cell architecture was used, where the middle feedwater channel separates a fixed 3 mm distance between the two electrodes, filled with eight glass fiber separators (Millipore). The feedwater comes from a 10 L electrolyte reservoir with constant nitrogen bubbling, pumped at a flow rate of 5 mL/min (via Masterflex peristaltic pump). NaCl (Sigma-Aldrich) was dissolved in MilliQ water to prepare 20 mM of NaCl solution for the electrolyte. The feedwater flowed out of the cell into a chamber containing the conductivity meter (Metrohm 856 conductivity), then flown into the pH meter (Metrohm 867 pH Module) chamber, and flowed back into the reservoir to complete the loop. The pH and conductivity data were then recorded in real-time using Tiamo software (Metrohm). All desalination experiments were conducted using GCPL, and the entire CDI setup was kept in a climate chamber constantly at 25 °C. Both charging and discharging steps were accomplished at a specific current of 0.1 A/g. In the charging half-cycle, 1.2 V cell voltage was applied and held for 1 h, while in the discharging half-cycle, 0.3 V cell voltage was applied and held for another 1 h. The desalination capacity (mg/g) was determined by **Eq. (2)**:

$$\textit{desalination capacity}\ (DC) = \left(v\frac{M_{NaCl}}{m_{total}}\right)\int C\,dt, \tag{2}$$

where v is the flow rate (mL/min), M_{NaCl} is the molar mass of NaCl (58.44 g/mol), m_{total} is the total mass of the electrodes (g), and $\int C\,dt$ is the concentration change of NaCl (mM) in the feedwater over the duration (min) of adsorption or desorption steps.

The charge efficiency (CE) was then calculated according to the following **Eq. (3)**:

$$\textit{charge efficiency}\ (CE) = \frac{F \times DC}{M_{NaCl} \times Q} \times 100\%, \tag{3}$$

where F is the Faraday constant (26 801 mAh/mol), DC is the desalination capacity obtained from **Eq. (2)**, and Q is the average of total charge stored/released in the two electrodes (normalized to the total electrode mass, mAh/g) during cycling. We chose a maximum number of 100 desalination cycles to overcome initial conditioning of the cell but to investigate the long-term stability, and the possible influence of additives, more extensive cycling will be needed.

3. Results and discussion

3.1. Materials characterization

As a first step to investigating the physicochemical properties of the carbon species employed in this study, SEM was carried out on as-received or as-synthesized powdery carbon samples. As observed in Fig. 1, the carbon samples vary morphologically in particle size and shapes. The most conspicuous sample in terms of particle size and shape is commercial activated carbon (Fig. 1A), which mostly consists of large coarse slate-like particles of tens of micrometers wide. After AC, OLC shows also aggregates of relatively larger sizes, where all other carbon types are finer and smaller in particle size. DLS measurements were performed (Fig. 2A) in an aqueous solution. The sonication treatment before and during the DLS measurement was not sufficient to disband the aggregates, therefore as a result all investigated samples are representing a certain level of polydispersity. Where, the DLS size values are to be seen as a convergence of primary particle sizes, particle clusters, and aggregates. Fig. 2A indicates that AC and OLC show the least population of sizes smaller than 1 μm compared to other carbon types. Apart from AC and OLC, which show a seemingly unimodal distribution centered at 10 μm, other carbon samples show multimodal size distributions. HSCB, in particular, exhibits a bimodal size distribution with two maxima at 0.1 μm and 1 μm. PC shows a distinct broad distribution with maxima at 0.1 μm, 0.8 μm, and 6 μm. The results of the sizes of samples also can be seen in the *Supporting Information*, Fig. S1, where d_{50} refers to the value of the particle diameters at 50% in the cumulative distribution, while d_{90} represents the said value at 90% in the cumulative distribution. PC shows the smallest particle size with an average particle size of 2.8 μm (d_{50}). The HSCB showed aggregates and particle clusters of 1–15 μm (d_{50} = 3.9 μm, d_{90} = 13.9 μm). AC, LSCB1, and LSCB2 have almost close average sizes of 5.5 μm, 5.7 μm, and 6.1 μm (d_{50}), respectively.

Raman spectra of the carbon samples in the range between 100 and 4000 cm^{-1} are shown in Fig. 2B and the fitting results can be found in **Table 2**. Well-defined first-order peaks of D-mode (related to carbon disorder) and G-mode (related to graphitic order) are observed at 1335-1355 cm^{-1} and 1585-1605 cm^{-1}, respectively. The highest degree of graphitic ordering is seen for OLC with an integral intensity ratio (I_D/I_G) of 1.2, followed by LSCB1 and LSCB2 with I_D/I_G ratio of 1.8 each. OLC also shows the narrowest first-order peaks with FWHM of 67 cm^{-1} and 63 cm^{-1} for D- and G-peaks, respectively. This is consistent with previous reports on the OLC synthesized by heat treatment of nanodiamonds under Argon, where OLCs with highly interconnected few-layer graphene nanoribbons will be produced. The G-mode position for all carbon samples is around 1598 ± 3 cm^{-1}, except for OLC, which has a G-mode at 1586 ± 3 cm^{-1}. The G-mode position in the latter sample is closest to ideal graphite [51], where the G-mode position is at 1581 cm^{-1}. The broad signal in between the D-mode and G-mode spanning from 1450 cm^{-1} to 1500 cm^{-1} indicates the presence of the amorphous carbon phase in all samples, though the least so in case of OLC. Broad and less distinct peaks in the second order range of carbon-related mods are evident in the range of 2500–3300 cm^{-1} for all samples. The exception to that is OLC, where we see a resonantly enhanced 2D mode [52].

We also performed XRD on carbon samples to entertain the

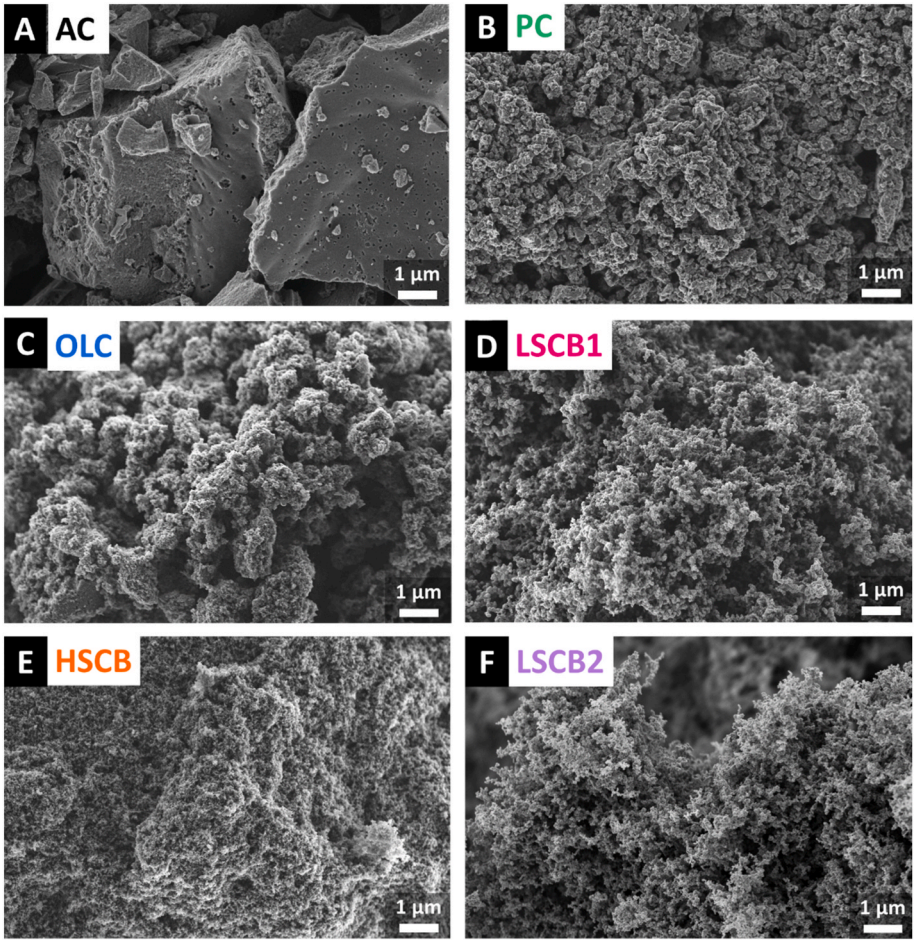

Fig. 1. Scanning electron micrographs of used carbon materials. (A) AC, (B) PC, (C) OLC, (D) LSCB1, (E) HSCB, and (F) LSCB2. (A colour version of this figure can be viewed online.)

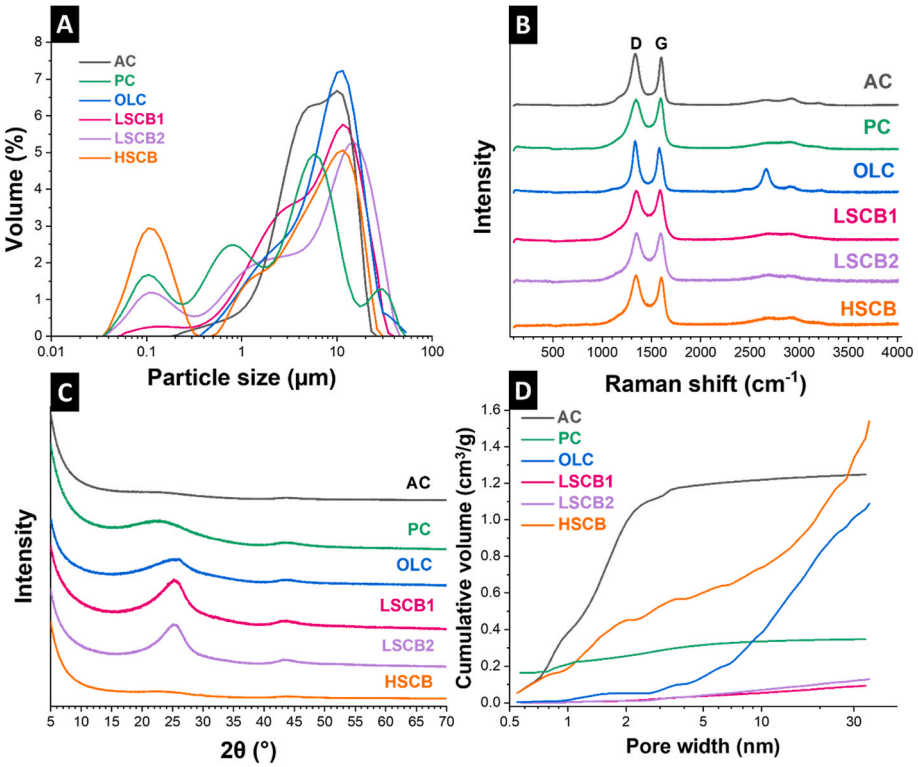

Fig. 2. Material characterization of the carbon materials: (A) particle size distribution, (B) Raman spectra, (C) X-ray diffractograms, and (D) pore volume distribution. (A colour version of this figure can be viewed online.)

Table 2
Spectral data of D and G bands obtained from peak fitting of Raman data.

Material	D-band (cm^{-1})		G-band (cm^{-1})		I_D/I_G
	Position	FWHM	Position	FWHM	
AC	1336 ± 1	98 ± 7	1600 ± 1	49 ± 2	2.2 ± 0.1
PC	1345 ± 1	147 ± 4	1597 ± 2	64 ± 1	2.5 ± 0.1
OLC	1340 ± 2	67 ± 2	1586 ± 3	63 ± 1	1.2 ± 0.0
LSCB1	1352 ± 2	119 ± 3	1600 ± 4	71 ± 3	1.8 ± 0.1
LSCB2	1347 ± 1	201 ± 2	1594 ± 2	109 ± 1	1.8 ± 0.0
HSCB	1344 ± 1	129 ± 11	1599 ± 5	66 ± 4	2.1 ± 0.1

possibility of any crystallographic ordering in carbon samples (Fig. 2C). As expected, no distinct peak is observed apart from the rather broad reflections around 25–26° 2θ for OLC, LSCB1, and LSCB2, signaling the presence of nanocrystalline domains in the material in addition to the amorphous carbon phase. Given that an Ideal graphite [53,54] shows a sharp (002) peak between 26.5 and 26.7° 2θ, we attribute the reflections in the latter samples to a weak but noticeable graphitic ordering, which is in agreement with Raman results outlined above.

Table 3 shows the elemental analysis for different carbon materials used in this study. LSCB2 is found to be the purest carbon sample among all, with no detectable oxygen or nitrogen contents. AC and PC have the highest oxygen content with around 3 mass%, as well as the highest hydrogen content at around 1 mass% each.

Table 3
Elemental analysis of the different carbon materials. "n.d." stands for "not detected", that is, values below the detection limit of the system.

Material	Carbon (mass %)	Hydrogen (mass %)	Nitrogen (mass %)	Oxygen (mass %)
AC	96.7 ± 0.4	1.1 ± 0.1	1.5 ± 0.1	2.8 ± 0.5
PC	96.0 ± 0.4	0.9 ± 0.1	1.3 ± 0.2	3.5 ± 0.1
OLC	98.9 ± 0.2	0.6 ± 0.1	1.8 ± 0.4	1.4 ± 0.2
LSCB1	100.6 ± 1.6	0.7 ± 0.1	n.d.	1.5 ± 0.4
LSCB2	100.2 ± 0.4	0.6 ± 0.1	n.d.	n.d.
HSCB	96.7 ± 0.4	0.5 ± 0.1	1.1 ± 0.2	2.0 ± 0.1

To study the pore size characteristics, nitrogen gas sorption analysis was performed on both the powder carbon samples and the fabricated electrodes thereof (*Supporting Information*, Fig. S2). Table 4 lists the specific surface area (SSA), average pore size, and pore volumes. AC possesses the highest SSA of close to 2000 m^2/g, followed by the HSCB with SSA close to 1200 m^2/g. The diversity of the studied carbon materials in this study can most clearly be observed in Fig. 2D, where it is shown how the pore populations are distributed across different pore size values and how they contribute to the total pore volume. As suggested by sample labels, the low surface carbon blacks (LSCB1 and

Table 4
Specific surface area of used powder materials and used electrodes, BET-SSA and QSDFT-SSA, average pore size, and pore volume.

Material and electrodes	QSDFT SSA (m^2/g)	Average pore size (nm)	Pore volume (cm^3/g)
AC	1981	1.42	1.25
PC	805	0.76	0.35
OLC	293	13.04	1.09
LSCB1	43	7.61	0.09
LSCB2	51	8.89	0.13
HSCB	1188	11.22	1.54
90% AC + 10% PTFE	1246	1.37	0.8
80% AC + 10% PC + 10% PTFE	1067	1.41	0.7
80% AC + 10% OLC + 10% PTFE	1351	1.48	0.92
80% AC + 10% LSCB1 + 10% PTFE	1263	1.42	0.84
80% AC + 10% LSCB2 + 10% PTFE	756	1.76	0.62
80% AC + 10% HSCB + 10% PTFE	1109	1.81	0.94
90% HSCB + 10% PTFE	1538	8.48	1.58

Table 5
The change in desalination rate, desalination capacity, charge efficiency, and energy consumption of the electrodes over long-term electrochemical desalination.

Electrode	Maximum desalination rate (μg/g/s)			Maximum desalination Capacity (mg/g)			Charge efficiency (%)			Energy consumption (10^3 × Wh/g)		
	10^{th} cycle	90^{th} cycle	Δ loss (%)	10^{th} cycle	90^{th} cycle	Δ loss (%)	10^{th} cycle	90^{th} cycle	Δ loss (%)	10^{th} cycle	90^{th} cycle	Δloss (%)
80% AC + 10% PC + 10% PTFE	8.3	5.3	36	8.8	5.6	36	86.6	70.3	19	5.3	5.2	2
80% AC + 10% OLC + 10% PTFE	11.1	8.5	23	8.3	6.2	25	79.3	66.6	16	5.5	5.1	8
80% AC + 10% LSCB1 + 10% PTFE	19.3	11.4	41	8.8	5.1	42	84.2	63.3	25	5.5	5.1	7
80% AC + 10% LSCB2 + 10% PTFE	12.9	10.0	23	8.2	7.2	12	90.6	62.6	31	6.4	5.7	11
80% AC + 10% HSCB + 10% PTFE	16.2	7.3	55	9.6	6.0	38	95.0	87.3	8	5.4	5.2	5
90% AC + 10% PTFE	10.6	4.0	62	10.4	7.2	31	93.0	88.9	4	5.8	5.6	4
90% HSCB + 10% PTFE	14.7	10.6	28	7.3	5.9	19	80.8	68.3	16	5.0	4.3	13

LSCB2) show the least SSA of around 40–50 m^2/g and pore volumes of ~0.1 cm^3/g each. AC exhibits a rather narrow pore size distribution profile with an average pore size at 1.4 nm. Conversely, HSCB and OLC show a broad pore size distribution profile with average pore size values of 11 nm and 13 nm, respectively.

In free-standing electrodes, the pore size distribution characteristics are distinctly different from the original properties of carbon additive precursors. **Table 4** shows how the pore size characteristics change upon electrode fabrication using the said carbon samples. Once an electrode is made out of AC, for instance 90% AC + 10% PTFE, the SSA drops from 2000 m^2/g down to 1200 m^2/g. This stems from the (I) replacement of the high surface area AC with a dead mass of the binder with little to no surface area, and (II) possible pore blockage of the AC material when mixed with binder [55,56]. As such, making an electrode out of AC, binder, and any type of carbon additive significantly decreases the SSA and pore volumes, though increasing the pore size values in case of electrodes with high pore size carbon additives (80% AC + 10% LSCB2 + 10% PTFE and 80% AC + 10% HSCB + 10% PTFE). The decrease in SSA upon electrode fabrication is illustrated by a parity plot (*Supporting Information*, Fig. S2C) that compares the measured and calculated SSA values for all electrodes. Assuming a linear relationship between the electrode constituent, one might consider the following relationship to calculate the resulting SSA, for instance for the electrode 80% AC + 10% PC + 10% PTFE: Final SSA = 0.8(AC-SSA) + 0.1(PTFE-SSA) + 0.1 (PC-SSA).

It is seen (*Supporting Information*, Fig. S2C) that only the electrode with HSCB additive (80% AC + 10% HSCB + 10% PTFE) falls on the parity line, implying the least pore blockage upon electrode fabrication out of powdery AC and HSCB precursors. The electrode with LSCB2 carbon additive (80% AC + 10% LSCB2 + 10% PTFE), however, suffers the most pore blockage, with a measured (experimental) SSA of around 900 m^2/g, deviating the most from its calculated SSA of around 1600 m^2/g.

3.2. Electrochemical behavior

Electrochemical characterizations including galvanostatic charge/discharge cycling with potential limitation (GCPL) and cyclic voltammetry (CV) of electrodes with and without additives were performed in 1 M NaCl. Such a high salt concentration was chosen to avoid possible issues related to ion starvation during the electrochemical measurements [57]. Window-opening CV measurements with 100 mV potential increments for positive and negative polarizations (*Supporting Information*, Fig. S3) indicate that all electrode materials, with slight variations, exhibit a stable and reversible working potentials within −0.8 V to +0.4 V window (vs. Ag/AgCl). The fact that the capacitance is similar during positive and negative polarizations indicates a similar ability of the electrodes for both sodium and chloride ions uptake [58,59]. The rectangular CV shapes hint a near-ideal capacitive behavior of all carbon electrodes and absence of any faradaic processes. The slight but significant increase in the width of cyclic voltammograms upon incremental potential increase observed both at positive and negative polarizations could be ascribed to the quantum capacitance effect due to the increase in the number of charge carriers in carbon over cycling [60]. As observed, exceeding the said potential window further to the negative or positive sides result in the emergence of hydrogen and oxygen evolution tails, respectively, in the shape of the measured cyclic voltammograms [61].

Based on the information obtained from CV, the rate handling capability behavior of the seven electrodes was then evaluated by GCPL technique within the stable potential window at rates ranging from 0.1 A/g to 10 A/g. The rate handling performances of electrodes at positive polarization (0 to +0.4 V vs. Ag/AgCl) and negative polarization (0 to −0.8 V vs. Ag/AgCl) are shown in Fig. 3. The data shows that the specific capacitance of AC electrode (without additives) exhibit clear enhancement at low specific current of 0.1 A/g upon cycling in negative polarizations. The latter result means that incorporation of any type of carbon additive compromises the specific capacitance (Fig. 3A). All electrodes show rather similar capacitances of 80 ± 5 F/g at slow rates, except for HSCB which considerably underperforms other electrodes at ~65 F/g.

Normalization of specific capacitance values with respect to the initial capacitance of each electrode at the slowest rate (0.1 A/g) is particularly instructive (Fig. 3B). The normalized rate handling data indicates that while HSCB shows the lowest capacitance at slow rates, it retains the highest among all samples when going to faster rates. Going from 0.1 A/g to 5 A/g, HSCB retains around 80% of its initial capacitance, while that value is below 50% for carbon electrodes with OLC, PC, LSCB1, HSCB additives, as well as for additive-free AC. At an extremely high specific rate of 10 A/g, HSCB and LSCB2 electrodes retain around 50% and 30% of their capacitances, respectively, while that drops to almost zero for all other samples.

The highest capacitance of additive-free AC at the slow rate stems from the fact that the gravimetric capacitance is always decreased at low rates by adding additives with lower surface areas [62]. However, the quick capacitance fading of the latter material at higher rates could be explained by the rather long time required to facilitate the rapid formation of the electric double layers on the surface of micrometer-sized AC particles pores, whereas it is much easier and faster accomplished in other nanometer-sized porous carbon like in HSCB electrode (i.e., with 90% HSCB content) [63].

Another set of rate handling examinations with newly made replicate cells was performed at positive polarizations, and the results are summarized in Fig. 3C and D. It is evident that the overall ability of all electrodes to retain the capacitance at higher rates is poorer in positive polarization compared to the negative polarization. Without any carbon additive, the capacitance of AC drops to almost zero when increasing the

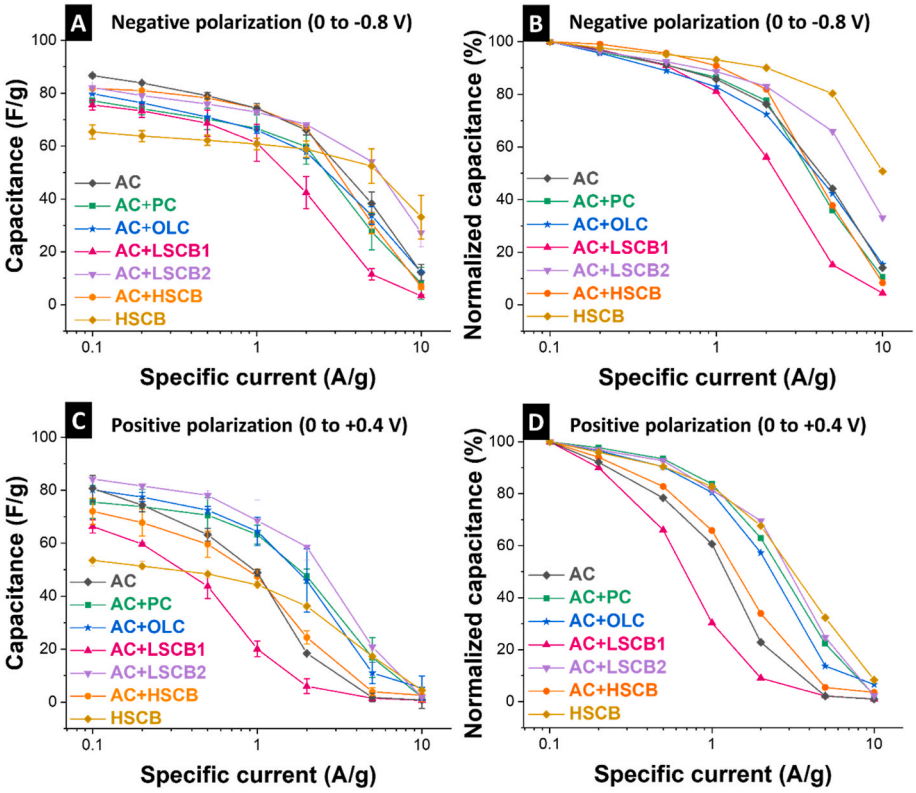

Fig. 3. Rate capability test in 1 M NaCl of electrodes with different carbon additives and without additives (A) at negative polarization (0 to −0.8 V) and (C) at positive polarization (0 to +0.4 V); The normalized capacitance vs. specific current curves of seven different electrodes (B) at negative polarization (0 to −0.8 V) and (D) at positive polarization (0 to +0.4 V). (A colour version of this figure can be viewed online.)

specific current from 0.1 A/g to 10 A/g, while electrodes with LSCB2, PC, and OLC additives, in addition to HSCB electrode, exhibit the highest capacitance retention. LSCB1 electrode, similar to its performance at negative polarization, performs also poorly at positive polarization both in terms of capacitance and rate handling capability.

3.3. *Electrochemical desalination performance*

Based on the electrochemical results obtained from the half-cell measurements, we adjusted the voltage window for the cell to cycle between 1.2 V and 0.3 V for charging and discharging, respectively. The rationale behind limiting the upper cut-off voltage to 1.2 V was to avoid water-splitting regimes. The choice of 0.3 V as the lower cut-off voltage was due to the fact that a non-zero discharge voltage helps to maximize the charge efficiency by avoiding crossing the potential of zero charge and the concomitant parasitic ion-exchange phenomenon [64,65]. All cells were initially run for 1 h before the desalination experiments to avoid possible first-cycle effects and ensure stable performance.

Extended (8+ days) electrochemical desalination experiments were then performed for each electrode for at least 100 cycles, in two replicate cells, using 20 mM NaCl as electrolyte. The DC and CE for each electrode vs. their cycle number up to 100 cycles can be found in *Supporting Information,* Fig. S4, and an average of DC and CE is included in *Supporting Information,* Fig. S5. The change in the desalination kinetics of the electrodes during the electrosorption process are illustrated by plots of DC vs. desalination rate, as shown in Fig. 4A and Fig. 4B. The latter kinetic plots, which differ from the Kim-Yoon plot (also known as CDI Ragone plot) [30], is a useful tool to study the desalination kinetics in the constant-voltage mode. The diagonal lines in Fig. 4A and B are used as a time reference, which helps to pinpoint the optimal operating points (characteristic times) for the desired electrosorption performance in terms of capacity or rate [66].

In early desalination cycles, represented by the 10th cycle (Fig. 4A), a more-or-less similar trend observed during half-cell electrochemical measurements of the electrodes (Fig. 3) is also mirrored here in terms of desalination performance (Fig. 4A). That is, at equilibrium times (diagonal line corresponding to 1 h), the additive-free AC electrode achieves the highest desalination performance with a DC of approximately 10 mg/g while the HSCB electrode shows the lowest DC of around 7 mg/g, with all other electrodes span between the latter two values. However, the said 10 mg/g DC for the additive-free AC electrode is obtained after over 30 min of charging, whereas the 7 mg/g DC of HSCB is accomplished within only 10 min of charging.

As observed from the half-cell electrochemical characterization results before (Fig. 3), incorporation of the low surface area carbon additive LSCB1 has led to a small decrease in capacitance enhancement of the AC + LSCB1 electrode. As a consequence, the contribution of the latter electrode to the desalination via ion electrosorption is also low (Fig. 4). Although the DC is not remarkable, the highest desalination rate of approximately 20 μg/g/s was obtained at an optimal operation time of only 10 min. Evidently, using a small, less porous carbon additive like LSCB1 can improve the rate handling, since it offers broader pore size distributions due to interparticle porosity and a large contribution from the surface layers. The latter electrode shows the highest rate handling due to its easily accessible pores and a relatively large specific surface area. Compared with HSCB electrode, the AC + HSCB electrode exhibits an enhanced DC. This can result from using a small, high-porosity carbon material like HSCB as the major electrode component, which increases the interparticle pathways and widens the ion diffusion corridors leading to a significantly lower DC of HSCB electrode. This situation is mitigated by improved size diversity for the AC + HSCB electrode.

After 90 cycles, the desalination capacity and rate of all electrodes decrease (Fig. 4B), due to extended cycling and aging of electrodes. Also, the point of optimum operation time has shifted to longer times,

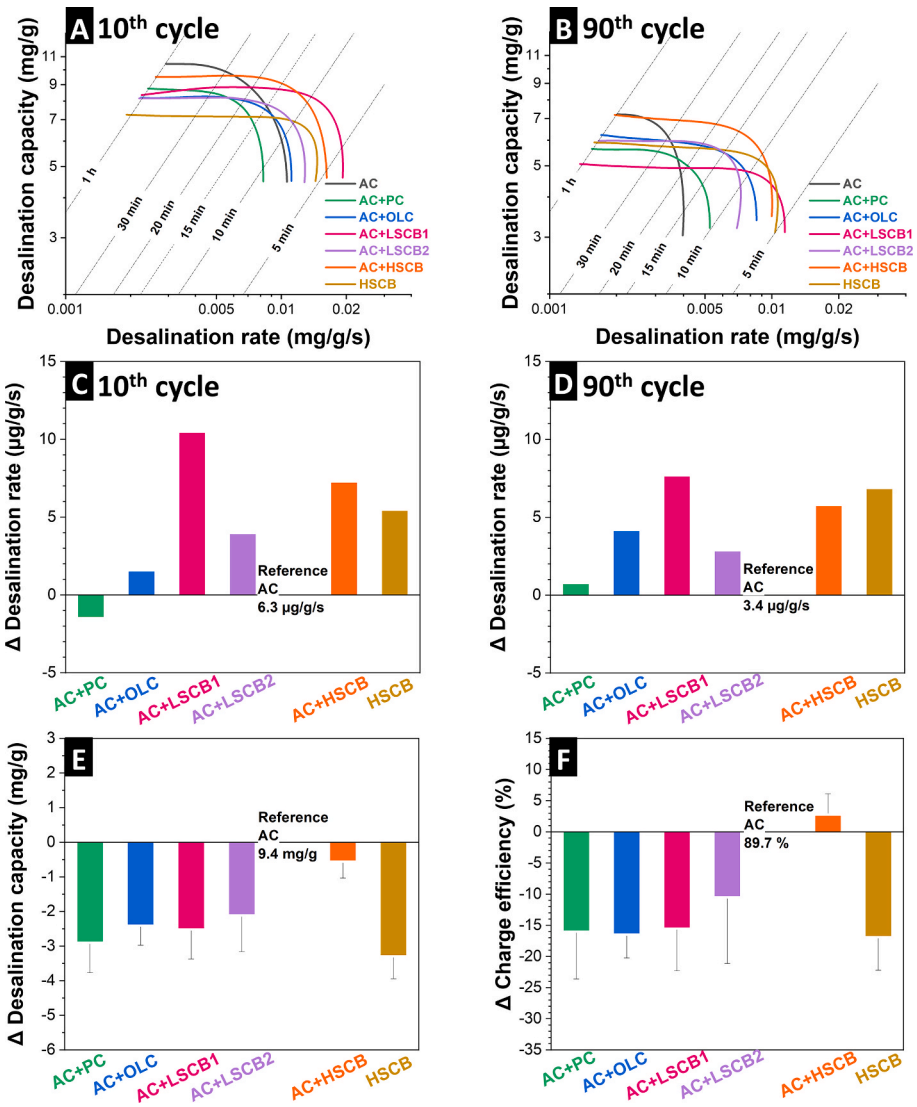

Fig. 4. Kinetic plot of seven different electrodes at 1.2 V in 20 mM NaCl at (A) the 10th cycle (B) and the 90th cycle. Gain (positive values) or loss (negative values) of desalination rate (C) in the 10th cycle and (D) in the 90th cycle for carbon additive composite electrodes in comparison to the performance of the AC electrodes (without additive). Gain (positive values) or loss (negative values) of (E) desalination capacity for carbon additive composite electrodes in comparison to the performance of the AC electrodes (without additive) and (F) charge efficiency for 100 cycles. The black line (and the value) marks the performance of the AC electrode. (A colour version of this figure can be viewed online.)

meaning that the curves approach the diagonal lines of more to the left-hand side. The most prominent is the most significant drop in the rate of AC electrodes, with a DC of 7.2 mg/g at a rate of 2 μg/g/s, the best operational time increases to almost 1 h. Moreover, the electrode mixed with LSCB1 also maintains a high desalination rate with an adsorption capacity of 4.6 mg/g and a desalination rate of 9 μg/g/s. In this case, the electrode of mixed HSCB is at an advantage both in terms of desalination capacity and rate, which indicates that it can endure prolonged cycling.

To better compare the influence of incorporating different carbon additives on DC, CE, and desalination rate, the electrodes performances were compared to that of additive-free AC electrode. Fig. 4C and D shows the gain (positive values) or loss (negative values) in the desalination rate of different electrodes compared to that of AC in early (cycle 10) and later (cycle 90) stages of desalination, which corresponds to the desalination rate of different electrodes at the optimal operating time. Compared to the AC electrode without additives (black split line), almost all the electrodes with additives except the one with PC exhibit excellent desalination rate performance in the early cycles. The most outstanding one belongs to the AC + LSCB1 electrode with 10.4 μg/g/s, which shows the capability to adsorb ions faster due to its favorable size dispersity and short ion diffusion pathway. For 100 cycles, all electrodes with additives showed improved desalination rates compared to the AC electrode. Even the rate performance of the electrode containing 90% HSCB additive is equivalent to that of the electrode containing only 10% LSCB1. Overall, adding small-sized, highly porous carbons has a positive effect on the long-term retention of desalination rate.

Fig. 4E and F shows the gain or loss in DC and CE values, respectively, while the baseline (horizontal line) in the graph represents the performance of the AC electrode. In agreement with the electrochemical behavior of electrodes in half-cell configurations (Fig. 3A and C), all electrodes, regardless of the additive type, are outperformed by the additive-free AC electrode in terms of DC. In terms of CE, almost the same detrimental effect is seen, except for AC + HSCB electrode, for which the CE slightly improves.

Fig. 5 schematically depicts the arrangement of carbon particles of different sizes next to each other in an electrode entangled by the polymeric binder. As seen, the desalination rate is highest when a combination of large, highly porous particles are mixed with particles of smaller sizes (though with less porosity). The latter size dispersity, best represented in the LSCB1 electrode (80% AC + 10% PTFE + 10% LSCB1), has thus yielded the highest desalination rate. As outlined before, incorporating particles with diverse sizes widens the ion diffusion corridors and eases the access of electrolyte ions to the electrode material, leading to a higher rate.

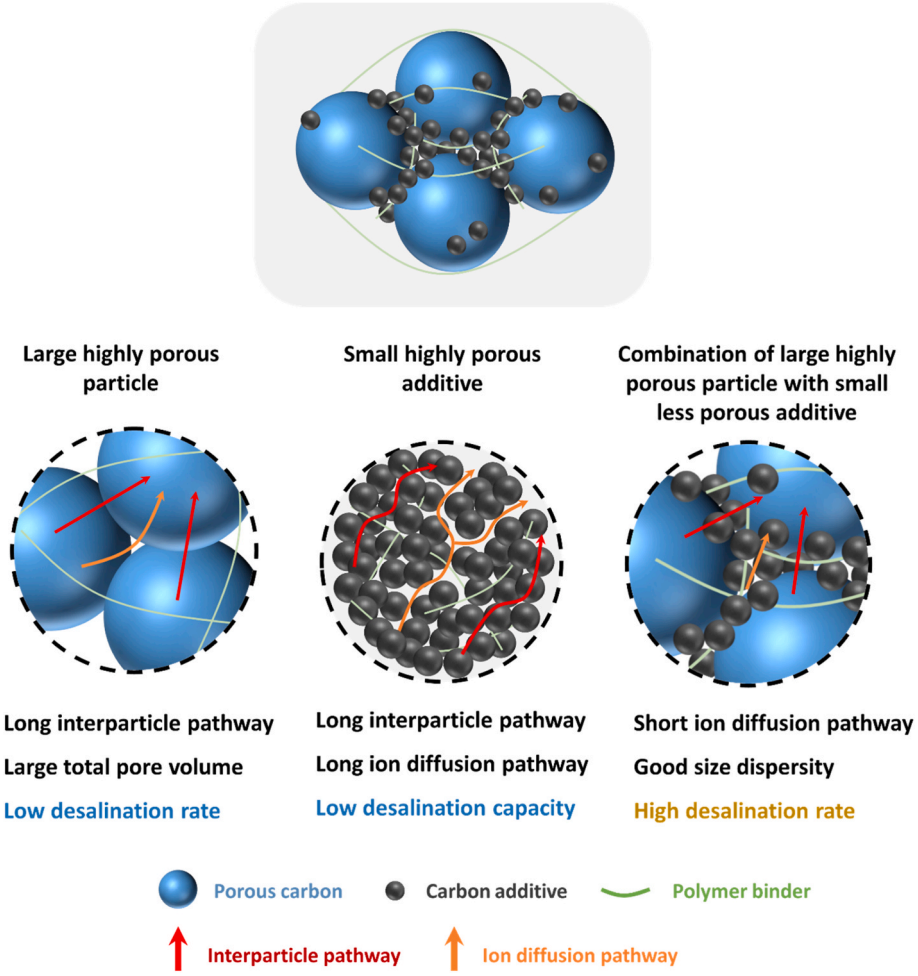

Fig. 5. Schematic illustration of particle influence on desalination rate. (A colour version of this figure can be viewed online.)

3.4. *Post mortem analysis of electrodes after electrochemical desalination cycling*

We carried out post mortem analysis and studied the chemical changes of the aged electrodes by SEM (Fig. 6) and CHNS–O to gain further insight into the origins of performance degradation over time. More scanning electron micrographs of the post mortem electrodes may be found in *Supporting Information,* Fig. S6. Scanning electron micrographs of the pristine electrodes containing additives (Fig. 6B–F) show additive particles at and around AC particles with ultrathin PTFE fibers as a binder in between. The electrode containing only 90% HSCB (Fig. 6G) exhibits a dense accumulation of small particles. After 100 desalination cycles, apart from some impurities on the surface of electrodes, there is no significant change in morphology compared to the pristine ones. As expected, electrochemical desalination does not change the particles' overall size or morphology.

Table 6 shows the elemental analysis of free-standing electrode films before the desalination experiment, with the carbon content of all electrodes above 80%, oxygen contents below 4%, and nitrogen and hydrogen contents below 2%. According to CHNS–O results after the desalination experiment (**Table 7**), there is a significant increase in the oxygen content of each electrode. Especially for the LSCB2 electrode (80% AC + 10% PTFE + 10% LSCB2), the oxygen content increased by 16%, and the carbon content decreased by 20%. The increase in the O content implies carbon oxidation, which could be due to the extended immersion of the electrode in the aqueous NaCl solution and exposure to water. Although constantly bubbled with nitrogen to remove oxygen, the aqueous electrolyte irreversibly takes part in parasitic electrochemical reactions with carbon, resulting in the loss of active material and decay in both DC and CE over time (*Supporting Information*, Fig. S3). Table 5 makes a comparison between the performances of each electrode during early (cycle 10) and later (cycle 90) stages of desalination. The least relative performance decay in desalination capacity and rate corresponds to LSCB2 electrode (80% AC + 10% PTFE + 10% LSCB2). However, the decay in terms of charge efficiency is the steepest, probably attributed to the highest oxidation degree of the latter electrode (**Table 7**). As listed in **Table 5**, energy consumption values between 0.005 and 0.006 Wh/g are obtained for all the electrodes, and it slightly decreases (favorable) up to 13% over long-term cycling in all cases.

This underscores that when selecting carbon additives, it is essential to consider the degree of electrochemical and desalination performance degradation of the corresponding fabricated electrodes, not just of each component individually. Seemingly simple parameters, such as electrode thickness or electrode electrical conductivity (Table 8), are not suitable to directly predict the resulting desalination rate, desalination capacity, or charge efficiency (**Table 5**). We see that all electrodes other than just activated carbon with binder show a larger charge efficiency drop when comparing the 10th with the 90th cycle. Conversely, the reduction in the maximum desalination rate and maximum desalination capacity of 90% AC + 10% PTFE is among the largest values. This demonstrates, at least at present, the need to benchmark composite electrodes versus key CDI performance parameters when exploring the performance and stability during extended cycling.

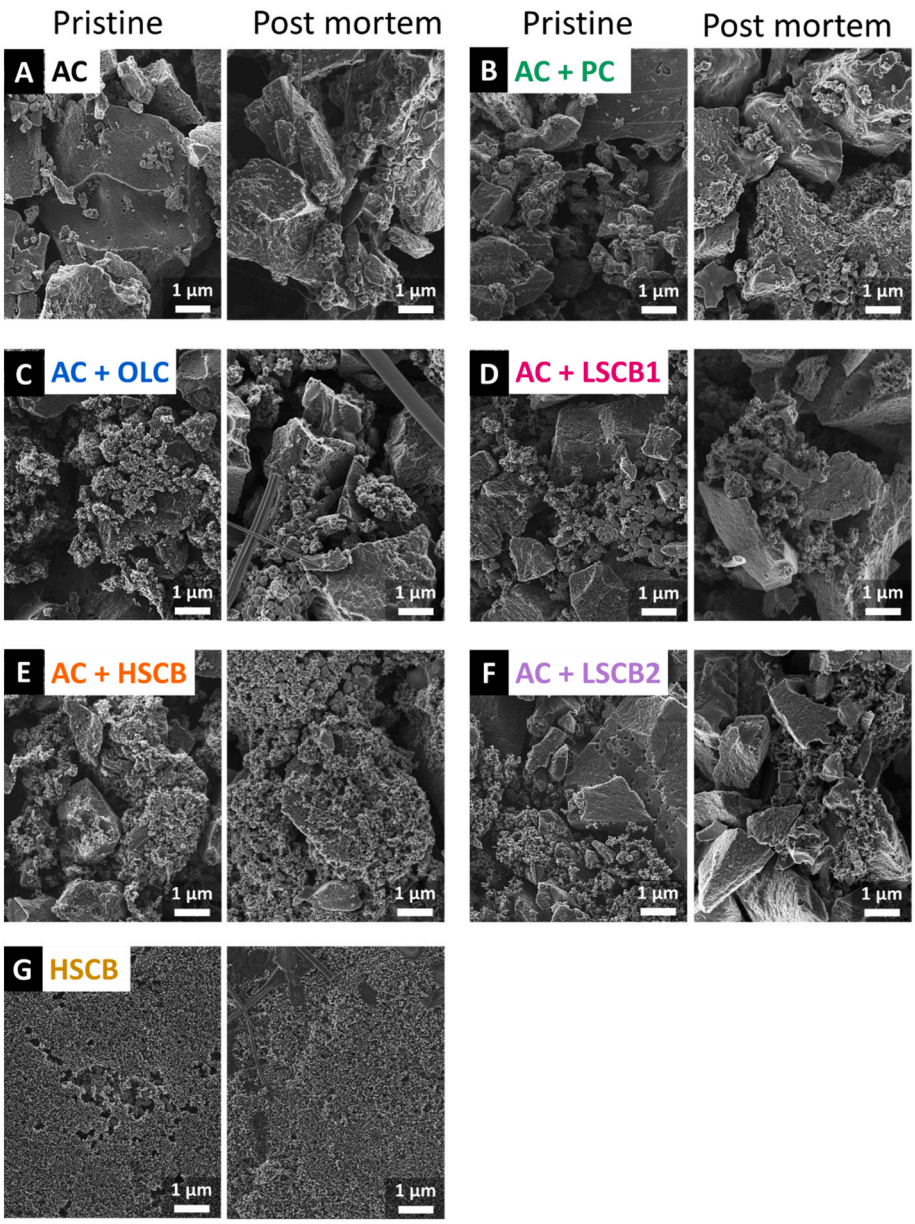

Fig. 6. SEM micrographs of free-standing electrode films with pristine and after 100 cycles of desalination, including (A) AC: 90% AC + 10% PTFE, (B) AC + PC: 80% AC + 10% PTFE + 10% PC, (C) AC + OLC: 80% AC + 10% PTFE + 10% OLC, (D) AC + LSCB1: 80% AC + 10% PTFE + 10% LSCB1, (E) AC + HSCB: 80% AC + 10% PTFE + 10% HSCB, (F) AC + LSCB2: 80% AC + 10% PTFE + 10% LSCB2, (G) HSCB: 90% HSCB + 10% PTFE. (A colour version of this figure can be viewed online.)

4. Conclusions

Highly conductive carbon additives like carbon blacks are commonly incorporated in capacitive deionization (CDI) electrodes to improve the desalination performance. In our study, we evaluated the use of five carbon additives, namely low surface area carbon black Super C45 (LSCB1) and Super C65 (LSCB2), medium surface area Porocarb (PC) and carbon onions (OLC), high surface area carbon black (HSCB) BP2000. These carbon additives were added to activated carbon (AC) to produce a free-standing electrode. We operated the cells in 20 mM sodium chloride aqueous solutions for up to 100 cycles of desalination. Without any carbon additive, the AC electrode achieved the best electrosorption capacity of approximately 10 mg/g, though having accomplished that with the low rate of 6 µg/g/s. While the highest desalination rate is enabled by mixing the AC electrode with minor and less porous additives like LSCB1, the ion diffusion path length will become shorter due to the increased size dispersion, improving the ion transport of the particles, which leads to higher desalination rates.

So, are conductive carbon additives the friend or a foe of capacitive deionization with activated carbon? The answer is not that simple. The effect of carbon additives strongly relies on the interplay of the entire pore structure and ion percolation pathways of the resulting electrode. Indeed, the overall design of CDI electrodes, combining the interparticle and intraparticle porosity and including electrode geometry (density, thickness) and overall electrode conductivity, is a defining parameter for the resulting desalination performance. Our data has also shown that some carbon black additions significantly lowered the performance stability during 100 cycles of electrochemical desalination. Thus, adding carbon additives should always be explored experimentally regarding the target application.

CRediT authorship contribution statement

Panyu Ren: Investigation, Data curation, Visualization, Supervision,

Table 6
Elemental analysis of free-standing electrode films before the desalination experiment.

Electrode	Carbon (mass%)	Hydrogen (mass%)	Nitrogen (mass%)	Oxygen (mass%)
80% AC + 10% PTFE + 10% PC	80.7 ± 0.1	0.9 ± 0.1	1.7 ± 0.4	4.1 ± 0.2
80% AC + 10% PTFE + 10% OLC	82.9 ± 0.9	0.8 ± 0.0	2.0 ± 0.3	3.1 ± 0.4
80% AC + 10% PTFE + 10% LSCB1	82.7 ± 2.4	0.6 ± 0.0	2.0 ± 0.7	2.9 ± 0.3
80% AC + 10% PTFE + 10% LSCB2	87.6 ± 2.9	0.6 ± 0.0	1.5 ± 0.3	2.6 ± 0.1
80% AC + 10% PTFE + 10% HSCB	80.3 ± 0.6	0.6 ± 0.0	1.5 ± 0.2	3.0 ± 0.1
90% AC + 10% PTFE	82.7 ± 2.4	0.9 ± 0.1	1.4 ± 0.4	3.5 ± 0.1
90% HSCB + 10% PTFE	82.1 ± 0.3	0.7 ± 0.1	1.1 ± 0.2	4.1 ± 0.2

Table 7
Elemental analysis of free-standing electrode films after the desalination experiment.

Electrode	Carbon (mass%)	Hydrogen (mass%)	Nitrogen (mass%)	Oxygen (mass%)
80% AC + 10% PTFE + 10% PC	78.9 ± 0.6	1.0 ± 0.1	1.7 ± 0.4	7.3 ± 0.3
80% AC + 10% PTFE + 10% OLC	87.2 ± 5.1	1.0 ± 0.0	1.9 ± 0.3	4.4 ± 0.2
80% AC + 10% PTFE + 10% LSCB1	77.5 ± 10.8	1.4 ± 0.1	1.5 ± 0.3	13.4 ± 0.7
80% AC + 10% PTFE + 10% LSCB2	67.2 ± 4.1	2.1 ± 0.4	1.4 ± 0.2	19.4 ± 1.1
80% AC + 10% PTFE + 10% HSCB	82.5 ± 0.6	0.8 ± 0.1	1.6 ± 0.4	4.3 ± 0.4
90% AC + 10% PTFE	81.3 ± 0.5	1.0 ± 0.1	1.7 ± 0.3	5.6 ± 0.2
90% HSCB + 10% PTFE	76.9 ± 0.6	1.4 ± 0.2	1.3 ± 0.3	8.7 ± 0.2

Table 8
Thickness, specific resistivity, and geometric density values for the free-standing electrodes.

Electrode	Thickness (μm)	Resistivity (Ω cm)	Electrode density (g/cm^3)
80% AC + 10% PTFE + 10% PC	709 ± 4	4.6	0.43
80% AC + 10% PTFE + 10% OLC	655 ± 15	2.1	0.39
80% AC + 10% PTFE + 10% LSCB1	713 ± 7	1.3	0.41
80% AC + 10% PTFE + 10% LSCB2	581 ± 6	4.2	0.30
80% AC + 10% PTFE + 10% HSCB	594 ± 9	0.4	0.41
90% AC + 10% PTFE	665 ± 9	4.5	0.40
90% HSCB + 10% PTFE	585 ± 7	1.5	0.36

Writing – original draft, Writing – review & editing. **Mohammad Torkamanzadeh:** Investigation, Data curation, Visualization, Supervision, Writing – original draft, Writing – review & editing. **Xiao Zhang:** Data curation. **Marek Twardoch:** Investigation, Data curation. **Choonsoo Kim:** Validation, Writing – review & editing. **Volker Presser:** Conceptualization, Supervision, Validation, Resources, Visualization, Writing – original draft, Writing – review & editing, Project administration, Funding acquisition.

Declaration of competing interest

The authors declare that they have no known competing financial interests or personal relationships that could have appeared to influence the work reported in this paper.

Acknowledgments

We acknowledge funding by the German Research Foundation (DFG, Deutsche Forschungsgemeinschaft) of the MXene-CDI project (PR-1173/11) and by a research grant from the Waste to Energy Recycling Human Resource Development Project of the Korean Ministry of Environment (ME). The authors thank Andrea Jung (INM) for the support with CHNS–O measurements, and Dr. Roberto Köferstein (Martin-Luther-Universität Halle-Wittenberg) and Dr. Wouter Maijenburg (Zentrum für Innovationskompetenz (ZIK) "SiLi-nano") for their support. We also thank Heraeus for providing sample material and the discussions (esp. Dr. Benjamin Krüner).

Appendix A. Supplementary data

Supplementary data to this article can be found online at https://doi.org/10.1016/j.carbon.2023.118191.

References

[1] M. Rodell, J.S. Famiglietti, D.N. Wiese, J.T. Reager, H.K. Beaudoing, F.W. Landerer, M.H. Lo, Emerging trends in global freshwater availability, Nature 557 (7707) (2018) 651–659.
[2] J. Bundschuh, M. Kaczmarczyk, N. Ghaffour, B. Tomaszewska, State-of-the-art of renewable energy sources used in water desalination: present and future prospects, Desalination 508 (2021), 115035.
[3] Z. Wang, T. Horseman, A.P. Straub, N.Y. Yip, D. Li, M. Elimelech, S. Lin, Pathways and challenges for efficient solar-thermal desalination, Sci. Adv. 5 (7) (2019), eaax0763.
[4] C. Dong, Y. Huang, H. Lin, L. Zhang, Performance intensification and anti-fouling of the two-phase flow enhanced direct contact membrane distillation for seawater desalination, Desalination 541 (2022), 116059.
[5] J.-M. Arana Juve, F.M.S. Christensen, Y. Wang, Z. Wei, Electrodialysis for metal removal and recovery: a review, Chem. Eng. J. 435 (2022), 134857.
[6] M.N.Z. Abidin, M.M. Nasef, J. Veerman, Towards the development of new generation of ion exchange membranes for reverse electrodialysis: a review, Desalination 537 (2022), 115854.
[7] H. Shimura, Development of an advanced reverse osmosis membrane based on detailed nanostructure analysis, Polym. J. 54 (6) (2022) 767–773.
[8] H. Saleem, S.J. Zaidi, Nanoparticles in reverse osmosis membranes for desalination: a state of the art review, Desalination 475 (2020), 114171.
[9] S. Porada, R. Zhao, A. van der Wal, V. Presser, P.M. Biesheuvel, Review on the science and technology of water desalination by capacitive deionization, Prog. Mater. Sci. 58 (8) (2013) 1388–1442.
[10] L. Wang, M. Torkamanzadeh, A. Majed, Y. Zhang, Q. Wang, B. Breitung, G. Feng, M. Naguib, V. Presser, Time-dependent cation selectivity of titanium carbide MXene in aqueous solution, Advanced Sustainable Systems 6 (3) (2022), 2100383.
[11] J.W. Blair, G.W. Murphy, Electrochemical demineralization of water with porous electrodes of large surface area, in: ACS (Ed.), Saline Water Conversion, American Chemical Society, Washington DC, 1960, pp. 206–223.
[12] J.G. Gamaethiralalage, K. Singh, S. Sahin, J. Yoon, M. Elimelech, M.E. Suss, P. Liang, P.M. Biesheuvel, R.L. Zornitta, L.C.P.M. de Smet, Recent advances in ion selectivity with capacitive deionization, Energy Environ. Sci. 14 (3) (2021) 1095–1120.
[13] L. Wang, Y. Zhang, K. Moh, V. Presser, From capacitive deionization to desalination batteries and desalination fuel cells, Current Opinion in Electrochemistry 29 (2021), 100758.
[14] P. Srimuk, X. Su, J. Yoon, D. Aurbach, V. Presser, Charge-transfer materials for electrochemical water desalination, ion separation and the recovery of elements, Nat. Rev. Mater. 5 (7) (2020) 517–538.
[15] X. Liu, H. Liu, M. Mi, W. Kong, Y. Ge, J. Hu, Nitrogen-doped hierarchical porous carbon aerogel for high-performance capacitive deionization, Separ. Purif. Technol. 224 (2019) 44–50.
[16] C. Zhang, X. Wang, H. Wang, X. Wu, J. Shen, A positive-negative alternate adsorption effect for capacitive deionization in nano-porous carbon aerogel electrodes to enhance desalination capacity, Desalination 458 (2019) 45–53.

[17] O. Sufiani, J. Elisadiki, R.L. Machunda, Y.A. Jande, Modification strategies to enhance electrosorption performance of activated carbon electrodes for capacitive deionization applications, J. Electroanal. Chem. 848 (2019), 113328.

[18] S. Ntakirutimana, W. Tan, M.A. Anderson, Y. Wang, Activated carbon electrode design: engineering tradeoff with respect to capacitive deionization performance, J. Electrochem. Soc. 167 (14) (2020), 143501.

[19] Y. Bian, P. Liang, X. Yang, Y. Jiang, C. Zhang, X. Huang, Using activated carbon fiber separators to enhance the desalination rate of membrane capacitive deionization, Desalination 381 (2016) 95–99.

[20] L. Men, C. Chen, A. Liu, S. Yu, J. Zhou, Y. Xie, D. Ju, N-doped porous carbon-based capacitive deionization electrode materials loaded with activated carbon fiber for water desalination applications, J. Environ. Chem. Eng. 10 (3) (2022), 107943.

[21] W. Kong, G. Wang, M. Zhang, X. Duan, J. Hu, X. Duan, Villiform carbon fiber paper as current collector for capacitive deionization devices with high areal electrosorption capacity, Desalination 459 (2019) 1–9.

[22] J. Xie, J. Ma, L. Wu, M. Xu, W. Ni, Y.-M. Yan, Carbon nanotubes in-situ cross-linking the activated carbon electrode for high-performance capacitive deionization, Separ. Purif. Technol. 239 (2020), 116593.

[23] S. Xiong, L. Ren, C. Zhang, J. Zhou, Y. Wang, Block copolymer coated carbon nanotube membrane anodes for enhanced and multipurpose hybrid capacitive deionization, Desalination 520 (2021), 115368.

[24] Y. Zhu, G. Zhang, C. Xu, L. Wang, Interconnected graphene hollow shells for high-performance capacitive deionization, ACS Appl. Mater. Interfaces 12 (26) (2020) 29706–29716.

[25] L. Chang, Y. Fei, Y.H. Hu, Structurally and chemically engineered graphene for capacitive deionization, J. Mater. Chem. 9 (3) (2021) 1429–1455.

[26] Y. Liu, X. Du, Z. Wang, L. Zhang, Q. Chen, L. Wang, Z. Liu, X. Dou, H. Zhu, X. Yuan, MoS_2 nanoflakes-coated electrospun carbon nanofibers for "rocking-chair" capacitive deionization, Desalination 520 (2021), 115376.

[27] Y. Li, Y. Liu, M. Wang, X. Xu, T. Lu, C.Q. Sun, L. Pan, Phosphorus-doped 3D carbon nanofiber aerogels derived from bacterial-cellulose for highly-efficient capacitive deionization, Carbon 130 (2018) 377–383.

[28] V. Presser, M. Heon, Y. Gogotsi, Carbide-derived carbons – from porous networks to nanotubes and graphene, Adv. Funct. Mater. 21 (5) (2011) 810–833.

[29] M. Oschatz, M. Zeiger, N. Jaeckel, P. Strubel, L. Borchardt, R. Reinhold, W. Nickel, J. Eckert, V. Presser, S. Kaskel, Emulsion soft templating of carbide-derived carbon nanospheres with controllable porosity for capacitive electrochemical energy storage, J. Mater. Chem. 3 (35) (2015) 17983–17990.

[30] T. Kim, J. Yoon, CDI ragone plot as a functional tool to evaluate desalination performance in capacitive deionization, RSC Adv. 5 (2) (2015) 1456–1461.

[31] J.-A. Lim, N.-S. Park, J.-S. Park, J.-H. Choi, Fabrication and characterization of a porous carbon electrode for desalination of brackish water, Desalination 238 (1) (2009) 37–42.

[32] S. Porada, L. Weinstein, R. Dash, A. Van Der Wal, M. Bryjak, Y. Gogotsi, P. Biesheuvel, Water desalination using capacitive deionization with microporous carbon electrodes, ACS Appl. Mater. Interfaces 4 (3) (2012) 1194–1199.

[33] S. Porada, L. Borchardt, M. Oschatz, M. Bryjak, J.S. Atchison, K.J. Keesman, S. Kaskel, P.M. Biesheuvel, V. Presser, Direct prediction of the desalination performance of porous carbon electrodes for capacitive deionization, Energy Environ. Sci. 6 (12) (2013) 3700–3712.

[34] Y. Zhang, P. Ren, Y. Liu, V. Presser, Particle size distribution influence on capacitive deionization: insights for electrode preparation, Desalination 525 (2022), 115503.

[35] K. Breitsprecher, M. Janssen, P. Srimuk, B.L. Mehdi, V. Presser, C. Holm, S. Kondrat, How to speed up ion transport in nanopores, Nat. Commun. 11 (1) (2020) 6085.

[36] B. Chen, A. Feng, K. Liu, J. Wu, Y. Yu, L. Song, Subsize $Ti_3C_2T_x$ derived from molten-salt synthesized Ti_3AlC_2 for enhanced capacitive deionization, Ceram. Int. 47 (3) (2021) 3665–3670.

[37] X. Shen, Y. Xiong, R. Hai, F. Yu, J. Ma, All-MXene-based integrated membrane electrode constructed using $Ti_3C_2T_x$ as an intercalating agent for high-performance desalination, Environ. Sci. Technol. 54 (7) (2020) 4554–4563.

[38] K. Pfeifer, S. Arnold, Ö. Budak, X. Luo, V. Presser, H. Ehrenberg, S. Dsoke, Choosing the right carbon additive is of vital importance for high-performance Sb-based Na-ion batteries, J. Mater. Chem. 8 (12) (2020) 6092–6104.

[39] M.-S. Balogun, Y. Luo, W. Qiu, P. Liu, Y. Tong, A review of carbon materials and their composites with alloy metals for sodium ion battery anodes, Carbon 98 (2016) 162–178.

[40] N. Jäckel, D. Weingarth, M. Zeiger, M. Aslan, I. Grobelsek, V. Presser, Comparison of carbon onions and carbon blacks as conductive additives for carbon supercapacitors in organic electrolytes, J. Power Sources 272 (1) (2014) 1122–1133.

[41] N. Jäckel, D. Weingarth, A. Schreiber, B. Krüner, M. Zeiger, A. Tolosa, M. Aslan, V. Presser, Performance evaluation of conductive additives for activated carbon supercapacitors in organic electrolyte, Electrochim. Acta 191 (1) (2016) 284–298.

[42] E.R. Reale, A. Shrivastava, K.C. Smith, Effect of conductive additives on the transport properties of porous flow-through electrodes with insulative particles and their optimization for Faradaic deionization, Water Res. 165 (2019), 114995.

[43] F. Yu, Z. Yang, Y. Cheng, S. Xing, Y. Wang, J. Ma, A comprehensive review on flow-electrode capacitive deionization: design, active material and environmental application, Separation and Purification Technology 281 (2022), 119870.

[44] M. Rohde, N. Büttner, A. Kuhn, E. Moerseburg, D. Weingarth, J. Becker, S. Pihan, J. Michaud-Bernlochner, D. Samuelis, T. Hucke, Improved Electrochemical Performance in Advanced Lithium-Ion Batteries with Porocarb® as Functional Additive, Electrochemical Society Meeting Abstracts, The Electrochemical Society, Inc., 2016, 505-505.

[45] S. Rümmler, M. Steimecke, S. Schimpf, M. Hartmann, S. Förster, M. Bron, Highly graphitic, mesoporous carbon materials as electrocatalysts for vanadium redox reactions in all-vanadium redox-flow batteries, J. Electrochem. Soc. 165 (11) (2018) A2510.

[46] C. Strietzel, K. Oka, M. Strømme, R. Emanuelsson, M. Sjödin, An alternative to carbon additives: the fabrication of conductive layers enabled by soluble conducting polymer precursors–a case study for organic batteries, ACS Appl. Mater. Interfaces 13 (4) (2021) 5349–5356.

[47] C.-C. Yang, Y.-W. Hung, S.J. Lue, The carbon additive effect on electrochemical performance of $LiFe_{0.5}Mn_{0.5}PO_4$/C composites by a simple solid-state method for lithium ion batteries, Batteries 2 (2) (2016) 18.

[48] S. Brunauer, P.H. Emmett, E. Teller, Adsorption of gases in multimolecular layers, J. Am. Chem. Soc. 60 (2) (1938) 309–319.

[49] G.Y. Gor, M. Thommes, K.A. Cychosz, A.V. Neimark, Quenched solid density functional theory method for characterization of mesoporous carbons by nitrogen adsorption, Carbon 50 (4) (2012) 1583–1590.

[50] D. Weingarth, M. Zeiger, N. Jäckel, M. Aslan, G. Feng, V. Presser, Graphitization as a universal tool to tailor the potential-dependent capacitance of carbon supercapacitors, Adv. Energy Mater. 4 (13) (2014), 1400316.

[51] N. Jäckel, D. Weingarth, A. Schreiber, B. Krüner, M. Zeiger, A. Tolosa, M. Aslan, V. Presser, Performance evaluation of conductive additives for activated carbon supercapacitors in organic electrolyte, Electrochim. Acta 191 (2016) 284–298.

[52] M. Zeiger, N. Jäckel, M. Aslan, D. Weingarth, V. Presser, Understanding structure and porosity of nanodiamond-derived carbon onions, Carbon 84 (1) (2015) 584–598.

[53] G.B. Barin, I. de Fátima Gimenez, L.P. da Costa, A.G.S. Filho, L.S. Barreto, Influence of hydrothermal carbonization on formation of curved graphite structures obtained from a lignocellulosic precursor, Carbon 78 (2014) 609–612.

[54] H. Chi-Sun, C. Nam-Sook, Y. Hyun-Sang, Conversion of graphite into mellitic acid, Carbon 19 (3) (1981) 225–229.

[55] M. Aslan, D. Weingarth, P. Herbeck-Engel, I. Grobelsek, V. Presser, Polyvinylpyrrolidone/polyvinyl butyral composite as a stable binder for castable supercapacitor electrodes in aqueous electrolytes, J. Power Sources 279 (1) (2015) 323–333.

[56] M. Aslan, D. Weingarth, N. Jäckel, J.S. Atchison, I. Grobelsek, V. Presser, Polyvinylpyrrolidone as binder for castable supercapacitor electrodes with high electrochemical performance in organic electrolytes, J. Power Sources 266 (1) (2014) 374–383.

[57] M. Aslan, M. Zeiger, N. Jäckel, I. Grobelsek, D. Weingarth, V. Presser, Improved capacitive deionization performance of mixed hydrophobic/hydrophilic activated carbon electrodes, J. Phys. Condens. Matter 28 (11) (2016), 114003.

[58] Y. Zhang, P. Ren, L. Wang, E.P. Yambou, S. Husmann, V. Presser, Selectivity toward heavier monovalent cations of carbon ultramicropores used for capacitive deionization, Desalination 542 (2022), 116053.

[59] Y. Zhang, J. Peng, G. Feng, V. Presser, Hydration shell energy barrier differences of sub-nanometer carbon pores enable ion sieving and selective ion removal, Chem. Eng. J. 419 (2021), 129438.

[60] M. Torkamanzadeh, L. Wang, Y. Zhang, O. Budak, P. Srimuk, V. Presser, MXene/activated-carbon hybrid capacitive deionization for permselective ion removal at low and high salinity, ACS Appl. Mater. Interfaces 12 (23) (2020) 26013–26025.

[61] Y. Zhang, P. Srimuk, S. Husmann, M. Chen, G. Feng, V. Presser, Effect of pore size on the ion electrosorption and hydrogen/deuterium electrosorption using sodium chloride in H_2O and D_2O, J. Electrochem. Soc. 166 (16) (2019) A4158.

[62] N. Jäckel, D. Weingarth, M. Zeiger, M. Aslan, I. Grobelsek, V. Presser, Comparison of carbon onions and carbon blacks as conductive additives for carbon supercapacitors in organic electrolytes, J. Power Sources 272 (2014) 1122–1133.

[63] C.R. Pérez, S.-H. Yeon, J. Ségalini, V. Presser, P.-L. Taberna, P. Simon, Y. Gogotsi, Structure and electrochemical performance of carbide-derived carbon nanopowders, Adv. Funct. Mater. 23 (8) (2013) 1081–1089.

[64] E. Avraham, M. Noked, Y. Bouhadana, A. Soffer, D. Aurbach, Limitations of charge efficiency in capacitive deionization: II. on the behavior of CDI cells comprising two activated carbon electrodes, J. Electrochem. Soc. 156 (10) (2009) P157–P162.

[65] E. Avraham, Y. Bouhadana, A. Soffer, D. Aurbach, Limitation of charge efficiency in capacitive deionization: I. on the behavior of single activated carbon, J. Electrochem. Soc. 156 (6) (2009) P95–P99.

[66] R.L. Zornitta, P. Srimuk, J. Lee, B. Krüner, M. Aslan, L.A.M. Ruotolo, V. Presser, Charge and potential balancing for optimized capacitive deionization using lignin-derived, low-cost activated carbon electrodes, ChemSusChem 11 (13) (2018) 2101–2113.

Supporting Information

Conductive carbon additives:

Friend or foe of capacitive deionization with activated carbon?

Panyu Ren,[1,2] Mohammad Torkamanzadeh,[1,2] Xiao Zhang,[1,2]

*Marek Twardoch,[1] Choonsoo Kim,[4] Volker Presser[1,2,3]**

[1] INM – Leibniz Institute for New Materials, Campus D2 2, 66123, Saarbrücken, Germany

[2] Department of Materials Science & Engineering, Saarland University, Campus D2 2, 66123, Saarbrücken, Germany

[3] Saarene – Saarland Center for Energy Materials and Sustainability, Campus C4 2, 66123 Saarbrücken, Germany

[4] Department of Environmental Engineering with Institute of Energy/Environment Convergence Technologies and Department of Future Convergence Engineering, Kongju National University, 1223-24, Cheonan-daero, Cheonan-si 31080, Republic of Korea

* Corresponding authors: volker.presser@leibniz-inm.de (VP)

Figures

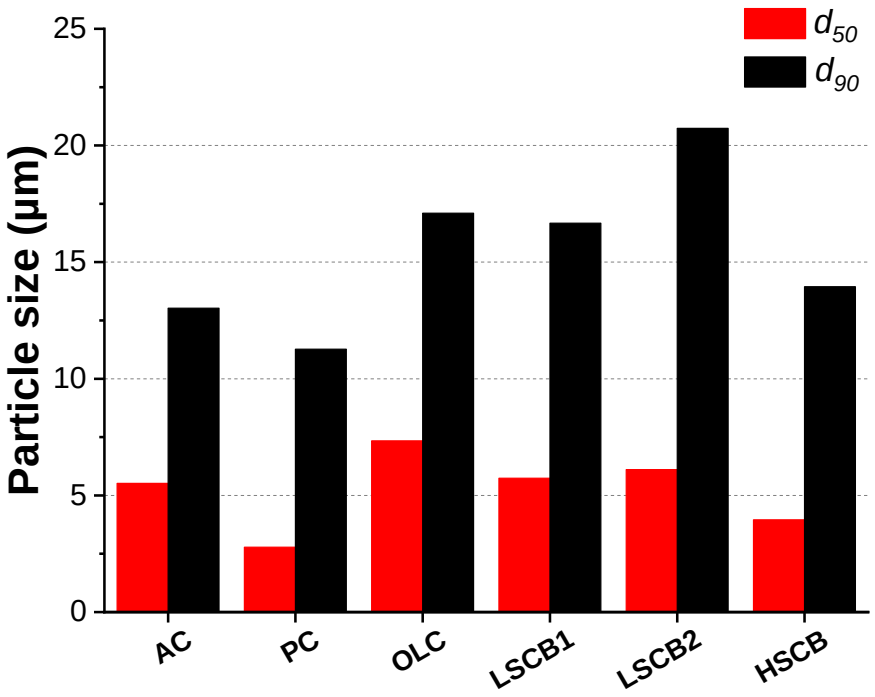

Fig. S1: Particle size distributions of the carbon materials used in this study, derived by dynamic light scattering (DLS) analysis.

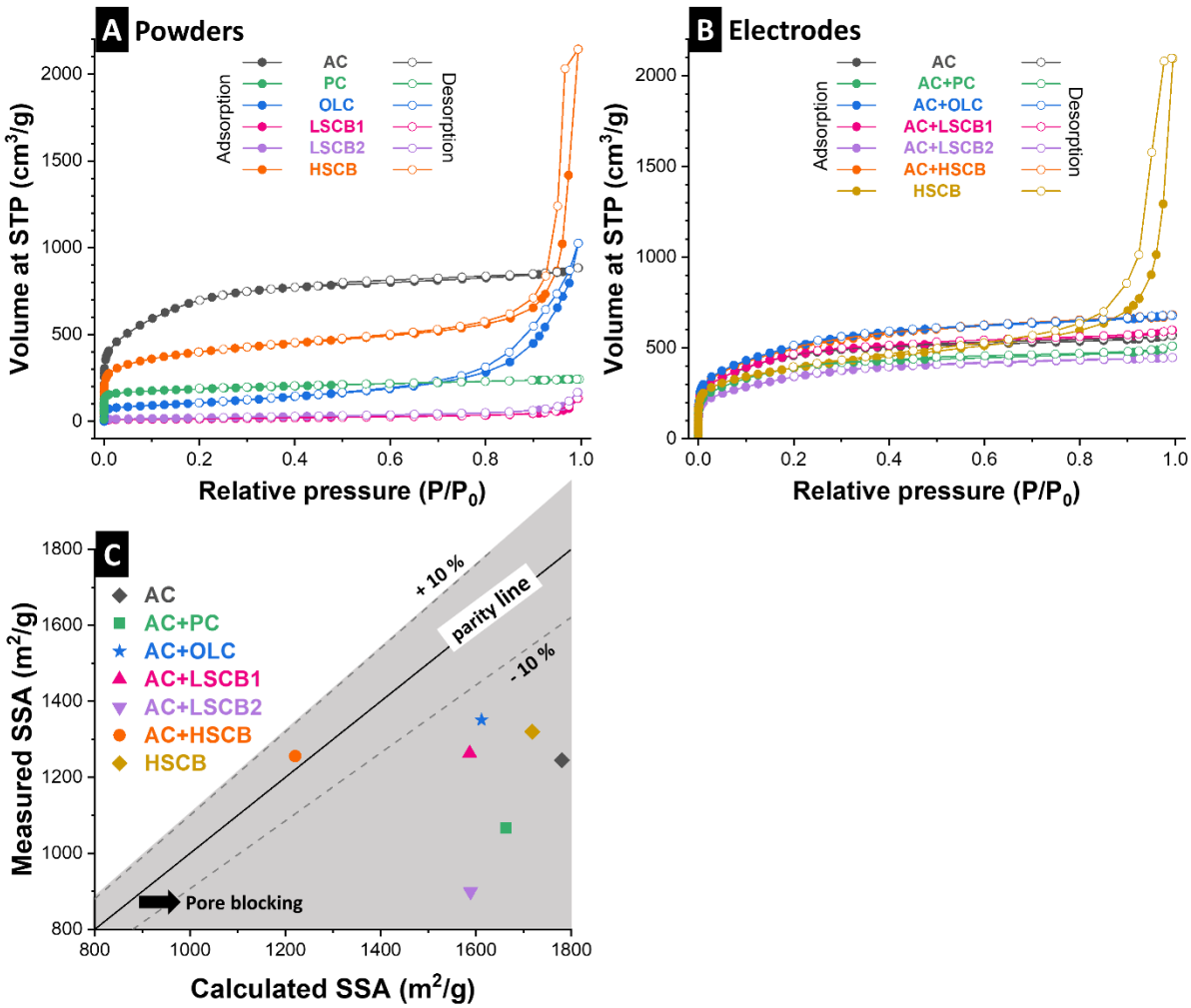

Fig. S2: Nitrogen sorption isotherms of (A) used carbon materials and (B) used electrodes. (C) Parity plot of measured versus calculated specific surface area (SSA).

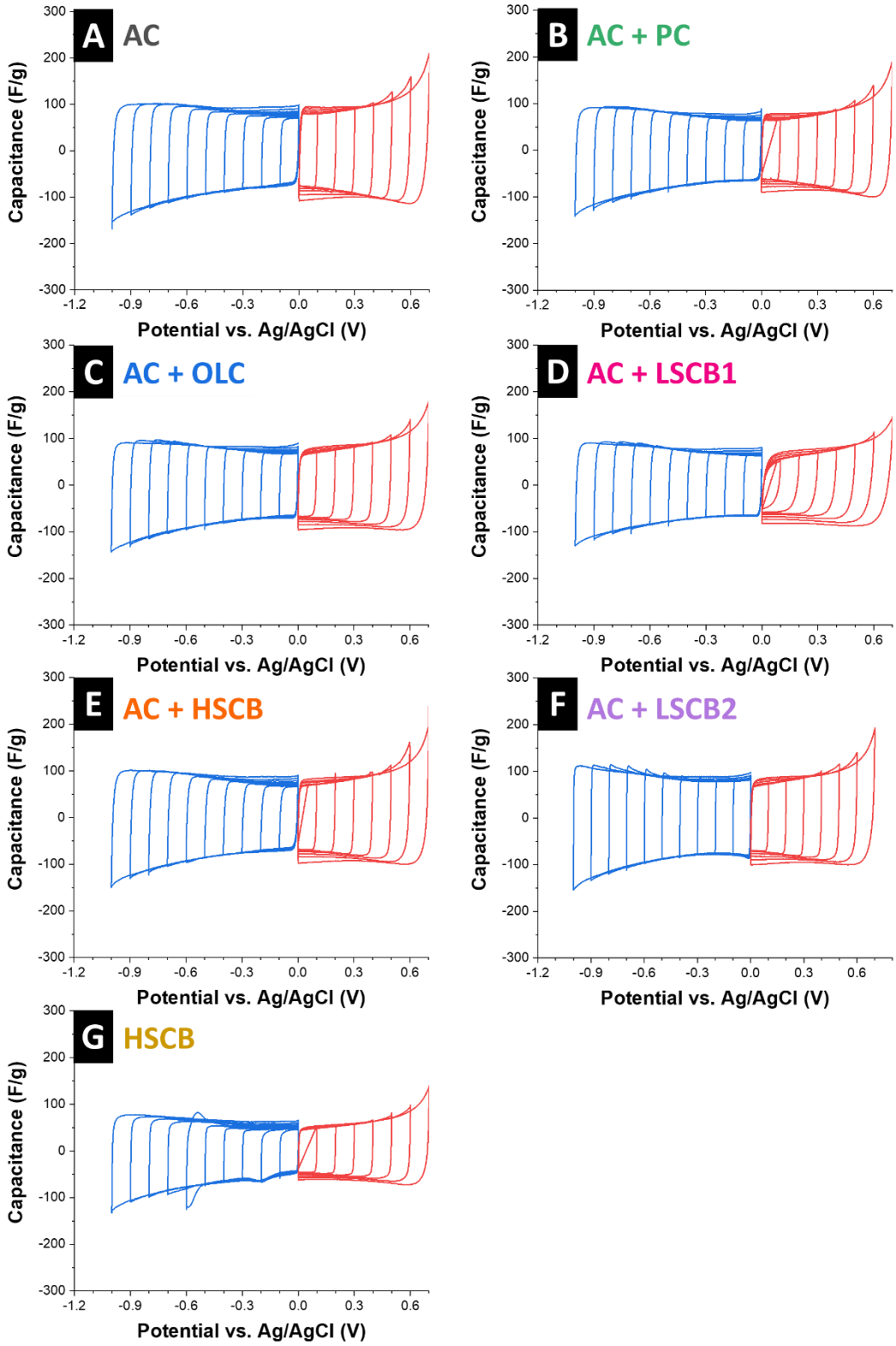

Fig. S3: Half-cell electrochemical characterizations: window-opening cyclic voltammograms for (A) AC: 90% AC + 10% PTFE, (B) AC + PC: 80% AC + 10% PTFE + 10% PC, (C) AC + OLC: 80% AC + 10% PTFE + 10% OLC, (D) AC + LSCB1: 80% AC + 10% PTFE + 10% LSCB1, (E) AC + HSCB: 80% AC + 10% PTFE + 10% HSCB, (F) AC + LSCB2: 80% AC + 10% PTFE + 10% LSCB2, (G) HSCB: 90% HSCB + 10% PTFE. All measurements were carried out in 1 M NaCl from positive range (−1 to 0 V vs Ag/AgCl) to negative range (0 to +0.7 V vs Ag/AgCl).

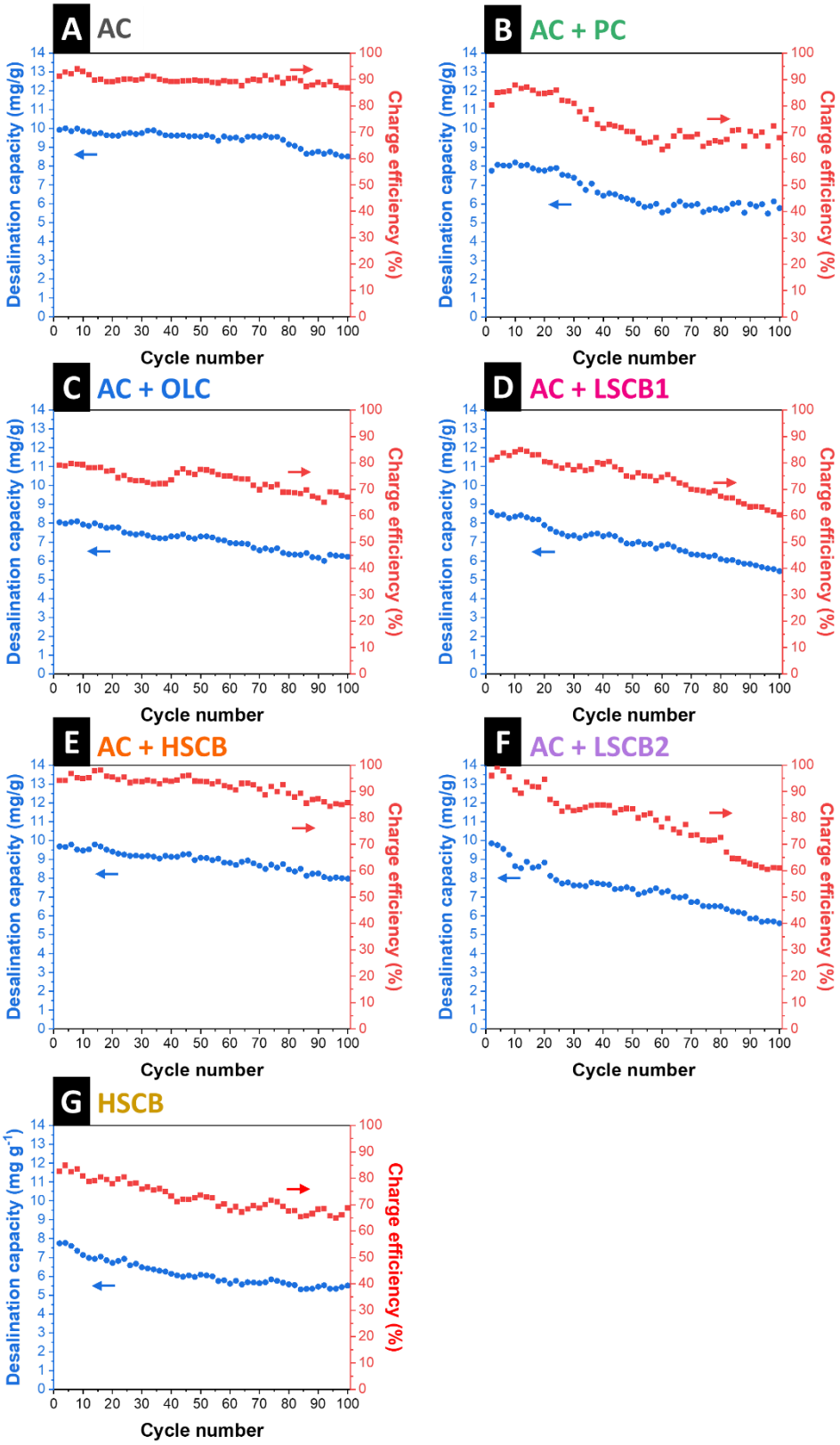

Fig. S4: Salt removal capacity stability and charge efficiency for (A) AC: 90% AC + 10% PTFE, (B) AC + PC: 80% AC + 10% PTFE + 10% PC, (C) AC + OLC: 80% AC + 10% PTFE + 10% OLC, (D) AC + LSCB1: 80% AC + 10% PTFE + 10% LSCB1, (E) AC + HSCB: 80% AC + 10% PTFE + 10% HSCB, (F) AC + LSCB2: 80% AC + 10% PTFE + 10% LSCB2, (G) HSCB: 90% HSCB + 10% PTFE. All measurements were carried out in 20 mM NaCl (100 cycles) for cells without membrane.

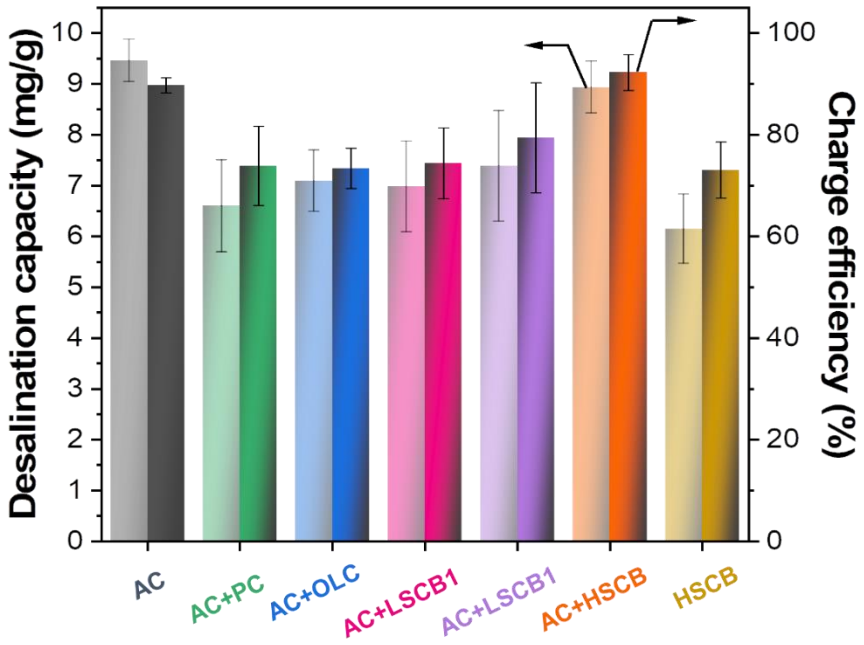

Fig. S5: Average desalination capacity and charge efficiency of used electrodes in 20 mM NaCl after 100 cycles.

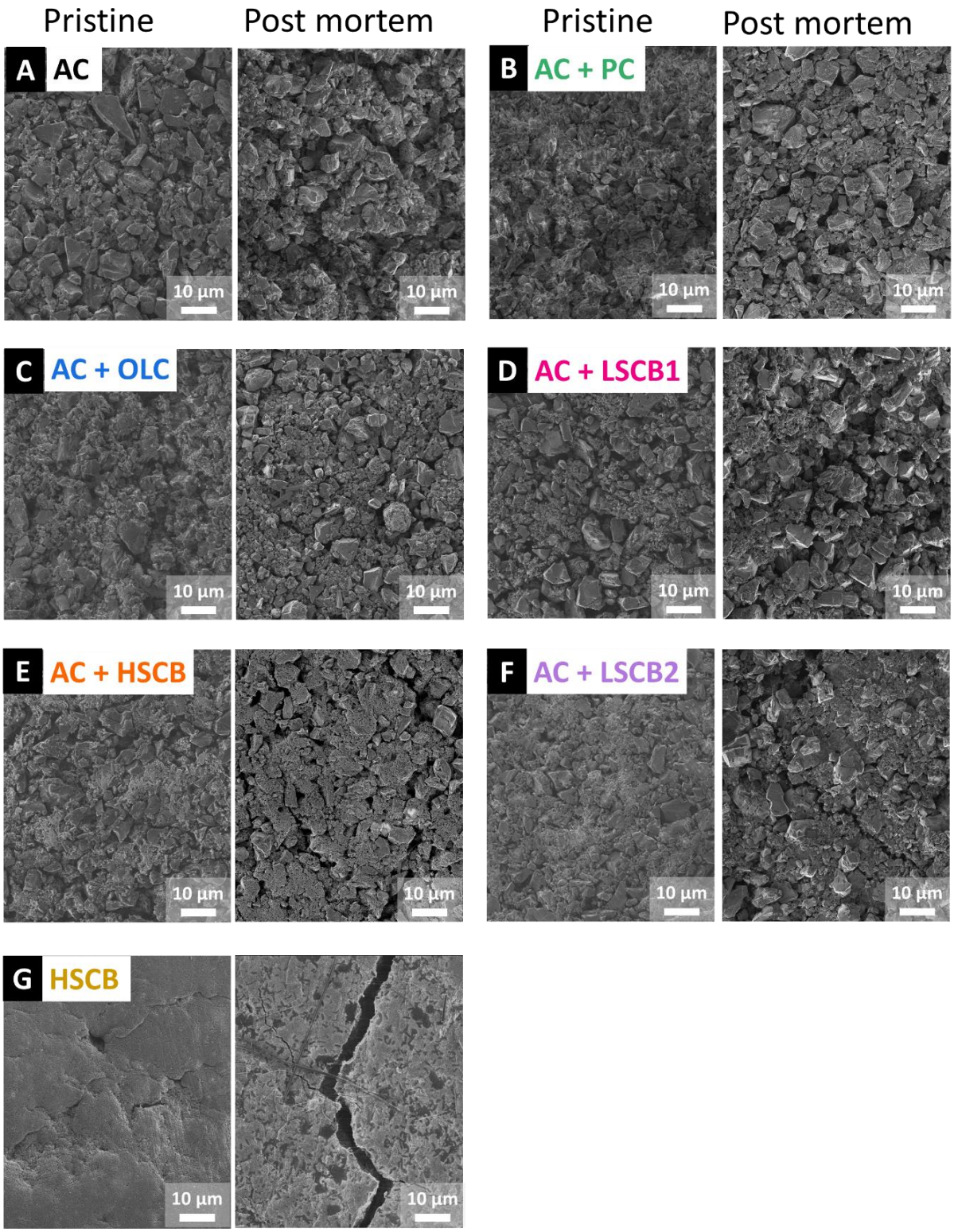

Fig. S6: Scanning electron micrographs of free-standing electrode films with pristine and after 100 cycles of desalination, including (A) AC: 90% AC + 10% PTFE, (B) AC + PC: 80% AC + 10% PTFE + 10% PC, (C) AC + OLC: 80% AC + 10% PTFE + 10% OLC, (D) AC + LSCB1: 80% AC + 10% PTFE + 10% LSCB1, (E) AC + HSCB: 80% AC + 10% PTFE + 10% HSCB, (F) AC + LSCB2: 80% AC + 10% PTFE + 10% LSCB2, (G) HSCB: 90% HSCB + 10% PTFE.

4.4. Selectivity toward heavier monovalent cations of carbon ultramicropores used for capacitive deionization

Yuan Zhang,[1,2] Panyu Ren,[1,2] Lei Wang,[1,2]

Emmanuel Pameté,[1] Samantha Husmann,[1] and Volker Presser[1,2,3]

[1] *INM - Leibniz Institute for New Materials, Campus D2 2, 66123, Saarbrücken, Germany*

[2] *Department of Materials Science & Engineering, Saarland University, Campus D2 2, 66123, Saarbrücken, Germany*

[3] *saarene - Saarland Center for Energy Materials and Sustainability, Campus C4 2, 66123 Saarbrücken, Germany*

Citation:

Y. Zhang, P. Ren, L. Wang, E. Pameté, S. Husmann, and V. Presser, Selectivity toward heavier monovalent cations of carbon ultramicropores used for capacitive deionization, Desalination 542 (2022) 116053.

Own contribution:

Validation, Review & Editing, Investigation.

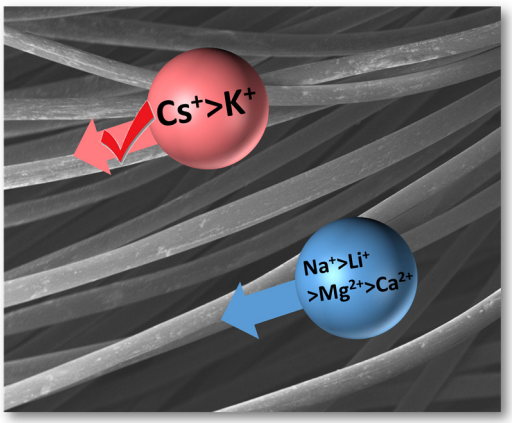

Desalination 542 (2022) 116053

Contents lists available at ScienceDirect

Desalination

journal homepage: www.elsevier.com/locate/desal

Selectivity toward heavier monovalent cations of carbon ultramicropores used for capacitive deionization

Yuan Zhang [a,b], Panyu Ren [a,b], Lei Wang [a,b], Emmanuel Pameté [a], Samantha Husmann [a], Volker Presser [a,b,c,*]

[a] INM - Leibniz Institute for New Materials, Campus D2 2, 66123 Saarbrücken, Germany
[b] Saarland University, Campus D2 2, 66123 Saarbrücken, Germany
[c] Saarene - Saarland Center for Energy Materials and Sustainability, Campus C4 2, 66123 Saarbrücken, Germany

HIGHLIGHTS

- Selective monovalent heavy metal removal
- Chemical online monitoring of ion uptake
- Ion transport in subnanometer confinement

ARTICLE INFO

Keywords:
Monovalent cations
Selective ion removal
Dehydration
Ion insertion

ABSTRACT

Electrolyte confinement inside carbon nanopores strongly affects ion electrosorption in capacitive deionization. A thorough understanding of the intricate pore size influence enables enhanced charge storage performance and desalination in addition to ion separation. In subnanometer pores, where the pore size is smaller than hydrated ion size, a dehydration energy barrier must be overcome before the ions can be electrosorbed into the pores. Ion sieving is observed when the dehydration energy is larger than the applied energy. However, when a high electrochemical potential is used, the ions can desolvate and enter the pores. Capitalizing on the difference in size and dehydration energy barriers, this work applies the subnanometer porous carbon material, and a high electrochemical ion selectivity for Cs^+ and K^+ over Na^+, Li^+, Mg^{2+}, and Ca^{2+} is observed. This establishes a possible way for selective heavy metal removal by varying pore and solvated ion sizes. Our work also shows the transition from double-layer capacitance to diffusion-limited electrochemical features in narrow ultramicropores.

1. Introduction

Because of the rapid pace of economic and population growth, the scarcity of fresh water is becoming one of the most significant issues in the world [1–3]. This concerns the need to derive fresh water from seawater and remove pollutants. In particular, some heavy metal ions have become a concerning pollutant to freshwater, and they are considered eminent toxicants of the environment. [4,5] Current water deionization technologies include distillation, [6,7] reverse osmosis, [8,9] electrodialysis, [7,10–13] and capacitive deionization (CDI) [14]. However, saline water often contains multiple ions in addition to NaCl, to which more attention should be paid. One challenge for water treatment is that some ions like heavy metals or toxic ions that constitute significant health and environmental concerns should be selectively removed. [15] The selectivity is essential to ensure efficient wastewater decontamination as heavy metals are typically at lower concentrations than competing ions. Among the extensive portfolio of water treatment technologies, CDI provides simple operation by use of electricity (ideally generated by renewable sources), facile electrode regeneration (including energy recovery), and the use of abundantly available electrode materials (like activated carbon from natural precursors). [16–18] Particularly, selective ion removal has emerged as an important research area within the CDI community.

Due to their large specific surface area and their potential-independent capacitive electrochemical behavior, porous carbons are the most commonly used CDI electrode materials. [17,19–22] In

* Corresponding author at: INM - Leibniz Institute for New Materials, Campus D2 2, 66123 Saarbrücken, Germany.
E-mail address: volker.presser@leibniz-inm.de (V. Presser).

https://doi.org/10.1016/j.desal.2022.116053
Received 11 June 2022; Received in revised form 28 July 2022; Accepted 12 August 2022
Available online 1 September 2022

particular, microporous carbons provide pores smaller than 2 nm and have been studied for their ion selectivity in mixed-ion electrolytes. [23–25] In larger pores, divalent cations preferentially screen the surface charge due to their high valence, and small monovalent cations approach closer to the charged surface. [26] To achieve higher ion selectivity, one can capitalize on the ion sieving effect by applying carbons with sub-nanometer pores smaller than the hydrated ion size of the species targeted for selective exclusion. [27,28] For ions with the same valence number, the larger the bare ion radius, the weaker the ion-dipole interaction, and the lower the hydration energies. [29] The required dehydration energy is an energy barrier toward ion uptake during electrosorption which could lead to an affinity to some ions. For instance, Zhan et al. investigated the transport of monovalent cations into 0.6 nm and 0.8 nm slit pores by combining density functional theory (DFT) and a continuum solvation model. The DFT simulated results showed a superior separation in 0.6 nm slit pores compared to 0.8 nm for K^+/Na^+, Cs^+/Na^+, K^+/Li^+, and Cs^+/Li^+. [30] In our previous work, we reported a relatively low selectivity factor of 1.5 (K^+/Na^+) and 3.6 (K^+/Ni^{2+}) on a carbon cloth with an average pore size of 0.59 nm in a mixture electrolyte containing K^+, Na^+, Ca^{2+}, Mg^{2+}, and Ni^{2+}. [27] The current challenge to enhance ion selectivity in mixed-ion solutions is either by applying carbon materials with subnanometer pores and narrow distribution of pore sizes or through carbon chemical modifications. Guyes et al. applied oxidized carbon cloth and discovered an enhanced ion selectivity of K^+ over Li^+ from ~1.0 to 1.8. [31] Other approaches, such as applying aminated carbon, [32,33] ethylenediamine triacetic acid-treated carbon, [34] and sulfonated carbon [35], can also enhance the ion selectivity in aqueous mixed-ion electrolytes.

This work uses carbons with subnanometer pores and extremely narrow pore size distribution. [27] Our work investigates ion electroadsorption of different monovalent cations, and we observed the effect of ion sieving and forced shedding of the solvation shell. We obtained a relatively high selectivity factor among monovalent ions compared with normal microporous carbon by applying this effect. In the meantime, this material switched the preference between monovalent and divalent cations of common micropore carbon. When Li^+, Na^+, K^+, Cs^+, Ca^{2+}, and Mg^{2+} are present in the electrolyte, heavy metal Cs^+ and alkali metal K^+ are preferentially removed, while Li^+, Na^+, and divalent cations remain in the feed solution. The use of carbon cloth allows facile binder-free electrode design and scaled device development.

2. Material and methods

2.1. Materials

Commercially available novoloid fiber cloth (named Novo) from Kynol was applied as the precursor of the activated carbon cloth. They are made from three-dimensional cross-linked phenolic resin. The novoloid fiber cloth was heated from room temperature to 700 °C in Ar at a heating rate of 15 °C/min, and then the temperature was held for 2 h in the Ar atmosphere. After cooling down, a microporous carbon cloth (labeled as ACC-P) is obtained. We also benchmarked ACC-5092-10 (labeled as ACC-0.6), derived from the novoloid fiber from Kynol with a similar pore structure and an average pore size of 0.59 nm to test the monovalent cation selectivity. [27,36,37]

To analyze the pore size distribution of the materials, nitrogen gas sorption analysis was conducted by the Quadrasorb IQ system (Anton Paar, formerly Quantachrome) at -196 °C with liquid nitrogen applied to control the temperature. During the outgassing process, the sample was annealed at 200 °C for 1 h and then heated up to 300 °C for 20 h. The pore size distribution of the materials was obtained by applying quenched solid density functional theory and assuming a slit-shaped pore configuration. The average pore size d_{50} corresponds with the pore size at half the total pore volume.

The chemical composition of C, H, and N of the carbon materials was obtained by a MICRO Cube (Elementar Analysensysteme GmbH) at 1150 °C at the combustion tube and 850 °C at the reduction tube. The O content was analyzed with an OXY cube elemental analyzer (Elementar Analysensysteme GmbH) with a pyrolysis temperature of 1450 °C.

Fourier-transform infrared spectroscopy (FTIR) was performed to characterize functionalities using a Tensor 27 FT-IR Spectrometer from Bruker Optics with a Golden Gate Diamond ATR Unit from Specac. Before the measurement, the electrode fibers were dried at 120 °C in the vacuum oven for 12 h. Air-background calibration was done before measuring the samples placed on the sample holder as they are free-standing fabrics.

We used scanning electron microscopy to characterize the electrode morphology. This was done using a Zeiss Gemini 500 SEM with an accelerating voltage of 1 kV and a working distance of 5.3 mm. The electrode materials are attached to an adhesive Cu foil on the sample holder, and no additional sputter coating was employed.

2.2. Electrochemical characterizations

For the electrochemical characterizations, an oversized ACC-5092-20 electrodes (Kynol; specific capacitance of around 100 F/g for Cl^- uptake) was applied as counter electrodes, [27] and the mass of counter electrodes was 2–4 times compared to the working electrode. We used ACC-P and Novo disks with a diameter of 12 mm and a thickness of 600 μm as working electrodes in our custom-built polyether ether ketone cells. [38] The mass and density values of the electrodes are listed in Table 1. We used Ag/AgCl reference electrodes (kept in 3 M NaCl solution). We used glass fiber mat discs (GF/A) with a diameter of 13 mm as the separator. The schematic of the cells used in our work is found elsewhere. [38]

We used a mixed-ion aqueous solution containing 1 M LiCl, NaCl, KCl, and CsCl as the electrolyte for the basic electrochemical characterization to avoid ion starvation. A BioLogic VSP-300 potentiostat was applied to conduct the electrochemical characterization. During the cyclic voltammetry measurement, a potential range from −0.5 V to +0.5 V vs. Ag/AgCl and a scan rate of 1 mV/s were set. The specific capacitance of the materials under different electrolytes is calculated by applying the following equation Eq. (1), where C is the specific capacitance of the material, I is current, v is the scan rate, and m is the mass of the electrode.

$$C = \frac{I}{v \cdot m}. \quad (1)$$

For the electrochemical impedance spectroscopy (EIS) at the frequency range between 10 kHz and 10 mHz with a potential holding for 30 min before each measurement, we used two conditions: (1) open circuit potential and (2) an electrode potential of -0.5 V vs. Ag/AgCl.

2.3. Chemical online monitoring via inductively coupled plasma-optical emission spectroscopy (ICP-OES)

To study the ion selectivity of the materials in a mixed ion system, we carried out chemical online monitoring via inductively coupled plasma-optical emission spectroscopy (online ICP-OES). [27,39] Proper mass balancing has been applied to ensure the studied ACC-P material uptake cations and counter electrode uptake anions. Using the desalination cell described elsewhere, [40] the cell consists of an ACC-P electrode (0.66 g) as the counter electrode and activated cloth ACC-5092-20 (0.84 g) from Kynol as a working electrode (Fig. S1, *Supporting Information*).

Table 1
Electrode mass and density of Novo, ACC-P, and ACC-0.6.

	Novo	ACC-P	ACC-0.6
Mass (mg)	36 ± 2.1	33 ± 0.9	27 ± 1.3
Thickness (μm)	547 ± 6	633 ± 11	500 ± 7
Density (g/cm^3)	0.59	0.45	0.48

Before the experiments, the electrodes were soaked in the electrolyte overnight. Between the electrodes, glass fiber separators (glass fiber prefilter, Millipore, 380 μm) were applied, and we employed an aqueous electrolyte of 10 mM LiCl, NaCl, KCl, CsCl, $CaCl_2$, and $MgCl_2$. We also used an Ag/AgCl (3 M NaCL) reference electrode. The electrolyte flow was at a rate of 1 mL/min while a cell voltage of 0.7 V was applied between the working and counter electrodes with a potential holding time of 30 min at the limiting potentials. The current density is set at 0.01 A/g_{CE} for galvanostatic charging and discharging. After reaching the cut-off potential, the potential was held for 15 min. The electrolyte from the cell was continuously pumped to the spray chamber of the ICP-OES system (ARCO FHX22, SPECTRO Analytical Instruments) at a flow rate of 1 mL/min. The generated aerosol was sent to the argon plasma, and the detected intensity at different wavelengths was translated into the ion concentration of the effluent stream from the cell. The ion uptake capacity of the electrode material can be calculated by applying Eq. (2), where V is the electrolyte flow rate, $m_{electrode}$ is the mass of the electrode, and c is the measured ion concentration.

$$\text{Ion uptake capacity} = \frac{V}{m_{electrode}} \int c \cdot dt \quad (2)$$

For comparison, a symmetric CDI cell with ACC-0.6 activated carbon cloth electrodes was benchmarked in the mixed electrolyte of 10 mM LiCl, 10 mM NaCl, and 10 mM KCl via galvanostatic charging and discharging at the cell voltage of 0–1 V with a potential holding time of 15 min at the limiting potentials, the specific current is 0.01 A/g.

3. Results and discussion

3.1. Pore structure analysis and chemical composition

Fig. 1 shows the material characterizations of the materials. The scanning electron micrograph in Fig. 1A–C displays the fiber morphology of Novo, ACC-P, and ACC-0.6 with an average fiber diameter of 20–30 μm. The insets in Fig. 1A–C also show photographs of the three materials (discs with 12 mm diameter). Fig. 1D–E and Table 2 show the pore structure of the original novoloid cloth (Novo), the pyrolyzed ACC-P, and for comparison, activated carbon cloth ACC-0.6. [27] Using quenched-solid density functional theory and assuming slit-pores, we calculated the surface area and pore volume from nitrogen gas sorption analysis (Fig. 1D–E). [41,42] Novo shows a specific surface area (SSA) of 9 m^2/g with a pore volume of 0.01 cm^3/g, while ACC-P and ACC-0.6 show the SSA of 641 m^2/g and 1032 m^2/g with a pore volume of 0.21 cm^3/g and 0.34 cm^3/g, respectively. Compared with Novo, which has a very low pore volume without micropores, ACC-P shows a much higher pore volume due to the pyrolysis process (Fig. 1B). Specifically, ACC-P shows a microporous pore structure with 89 % of the total pore volume contribution at the pore size below 0.7 nm. For comparison, 78 % of the total pore volume of ACC-0.6 relates to pores no larger than 0.7 nm. Although ACC-P has a lower cumulative pore volume and specific surface area, the micropore size distribution of ACC-P is narrower than that of ACC-0.6.

Table 2
Porosity analysis obtained from nitrogen gas sorption applying quenched solid density functional theory (QSDFT; assuming slit-shaped pores) and the Brunauer-Emmett-Teller theory (BET). SSA: specific surface area. The average pore size refers to the volume-normalized value of d_{50}.

	SSA BET (m^2/g)	SSA QSDFT (m^2/g)	DFT total pore volume (cm^3/g)	Average pore size d_{50} (nm)
Novo	9	9	0.01	2.4
ACC-P	545	641	0.21	0.59
ACC-0.6	916	1032	0.34	0.59

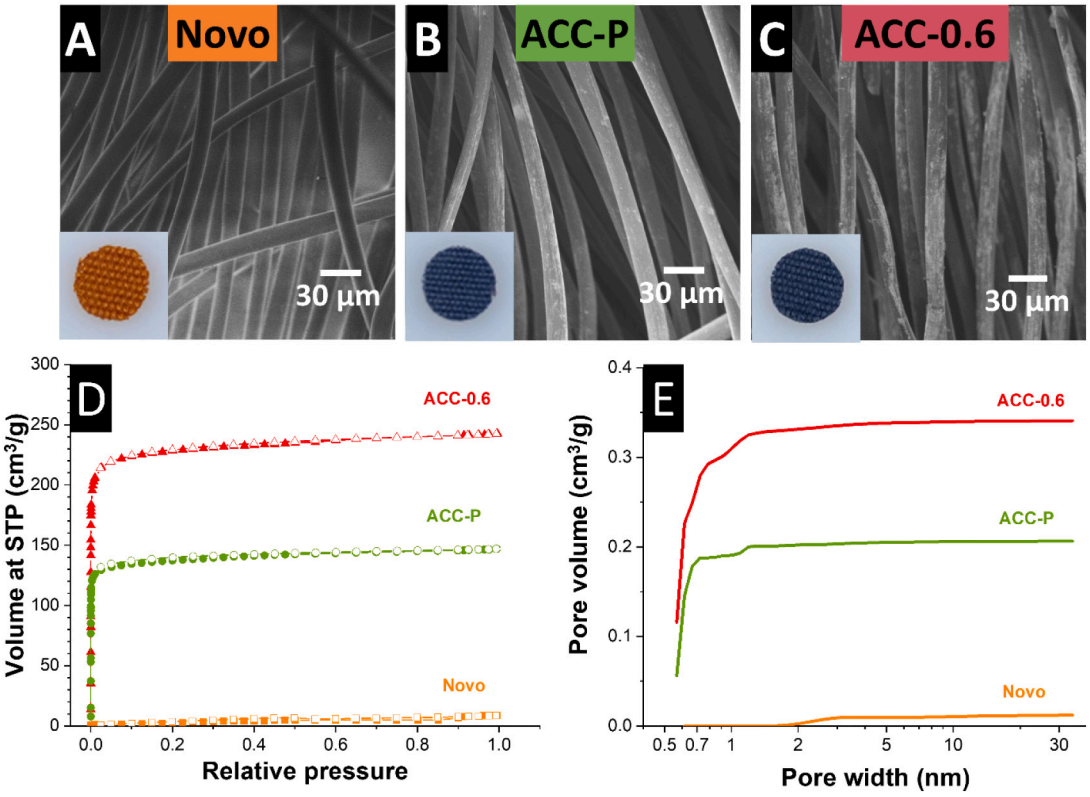

Fig. 1. Material characterization of Novo, ACC-P, and ACC-0.6. A–C) Scanning electron micrograph and pictures of the electrode Novo, ACC-P, and ACC-0.6. D) Gas sorption isotherm curve of Novo, ACC-P, and ACC-0.6; STP = standard temperature and pressure. E) Cumulative pore size distribution of Novo, ACC-P, and ACC-0.6 obtained from nitrogen gas sorption (assuming slit-shaped pores and applying the quenched solid density functional theory).

Table 3
Chemical analysis of the electrode materials. "n.d." means the values are below the detection limit of the system.

	Carbon (mass%)	Hydrogen (mass%)	Nitrogen (mass%)	Oxygen (mass%)
Novo	72.6 ± 0.4	5.5 ± 0.1	0.5 ± 0.1	20.0 ± 0.9
ACC-P	92.6 ± 0.2	1.6 ± 0.0	0.4 ± 0.1	4.6 ± 0.2
ACC-0.6	94.2 ± 0.5	1 ± 0.0	n.d.	5.1 ± 1

Table 3 shows the elemental CHNS-O analysis of the materials. The original Novo cloth has a high oxygen content of up to 20.0 mass% and a hydrogen mass of up to 5.5 %. After pyrolysis, the oxygen and hydrogen content decreased to 1.5 mass% and 4.6 mass%, respectively. After CO_2 activation, ACC-0.6 shows a similar oxygen, nitrogen, and hydrogen content, which indicates that most elemental impurities have been removed during the pyrolysis process. The changes in composition are also confirmed by FTIR analysis (Fig. S2, *Supporting Information*). The Novo cloth shows characteristic bands of oxygenated functional groups, with a broad hydroxylic band above 3200 cm^{-1} and a group of bands between 1700 cm^{-1} and 1200 cm^{-1} corresponding to C═O, C-O, O-H, and C-O-H bonds arising from both carboxyl and carbonyl groups. After activation and heat treatment, all bands are suppressed, and only aromatic overtones are observed in both ACC-P and ACC-0.6 samples. The removal of C-H modes between 2800 cm^{-1} and 3050 cm^{-1} also indicates a higher degree of graphitization.

3.2. Electrochemical characterization

Fig. 2A shows the cyclic voltammetry measurement of the ACC-P and the precursor before the pyrolysis. Before pyrolysis, the novoloid fibers have low specific capacitance due to the low pore volume and the low specific surface area. After the pyrolysis treatment, the materials had an open micropore structure, which enables ion adsorption. However, the average pore size is smaller than hydrated Na^+, and ion sieving and desolvation occur. [27,43,44] In Fig. 2B, different monovalent cations (Li, Na, K, Cs) at the concentration of 1 M are tested. For all different cations, a narrowing in the profile between −0.2 V and −0.1 V vs. Ag/AgCl was observed. The cathodic specific current that represents cation adsorption decreases as the sweeping potential decreases to −0.2 V, this is related to ion sieving due to the larger hydrated ion sizes compared to the carbon pore size. As the potential further decreases to −0.5 V (vs. Ag/AgCl), there is a significant specific capacitance increase for KCl and CsCl electrolytes, and the capacitance-turning overpotential for the aqueous solution of CsCl is lower than that for KCl. For NaCl and LiCl, the increase of the capacitance is less pronounced. Although NaCl shows a small capacitance increase at −0.5 V vs. Ag/AgCl, the overpotential for the capacitance increase is higher than CsCl and KCl. In aqueous LiCl, we observe ion sieving at the negative potential region, which indicates Li^+ cannot enter the pores of ACC-P. The dehydration energy enthalpy for Li^+, Na^+, K^+, and Cs^+ is listed in Table 4. [27,29,45,46] The different overpotential for capacitance increase in different monovalent cation systems is in the same order as the hydration energy barrier, which indicates the increase of the specific capacitance at the low potential region is caused by the ion dehydration and insertion into the pores.

We employed electrochemical impedance spectroscopy to evaluate further the properties of the different material and electrolyte systems. The results obtained at open circuit potential and −0.5 V vs. Ag/AgCl are shown in Fig. 3. At the high-frequency region, all the four types of cells qualitatively show the same dependence on voltage with no semicircle observed. They are characterized by a diffusion tail in the Nyquist plot, which is inclined at ca. 45° to the real axis. A significant difference between the different electrolyte systems is observed in the low-frequency range, where the capacitive properties are determined by the overvoltage of the kinetically inhibited charge transfer and mass transport processes. At open circuit potential (Fig. 3A), the cells are at the uncharged state and operate as capacitors (dominated by double-layer capacitance), as confirmed by nearly similar imaginary impedance for all four types of cations. At −0.5 V vs. Ag/AgCl (Fig. 3B), the curves start bending as the frequency decreases, and the Imaginary impedance has an order of $Li^+ > Na^+ > K^+ > Cs^+$. This is linked to the difference in the hydrated ion size and hydration enthalpy between the four cations, leading to a difference in the ion transportation inside the porous structure of the electrode. The diffusion of ions inside the pores

Table 4
Hydrated size of different cations and the hydration energy.

Ion	Hydrated ion size (nm)	Hydration energy (kg m^2 s^{-2} mol^{-1})
Li^+	0.76; Ref. [45]	$0.51{\cdot}10^6$; Ref. [46]
Na^+	0.72; Ref. [45]	$0.41{\cdot}10^6$; Ref. [46]
K^+	0.66; Ref. [45]	$0.3{\cdot}10^6$; Ref. [46]
Cs^+	0.65; Ref. [45]	$0.28{\cdot}10^6$; Ref. [46]
Ni^{2+}	0.81; Ref. [27,45]	$1.98{\cdot}10^6$ Ref. [27,29]
Ca^{2+}	0.82; Ref. [27,45]	$1.50{\cdot}10^6$; Ref. [27,29]
Mg^{2+}	0.85; Ref. [27,45]	$1.83{\cdot}10^6$; Ref. [27,29]

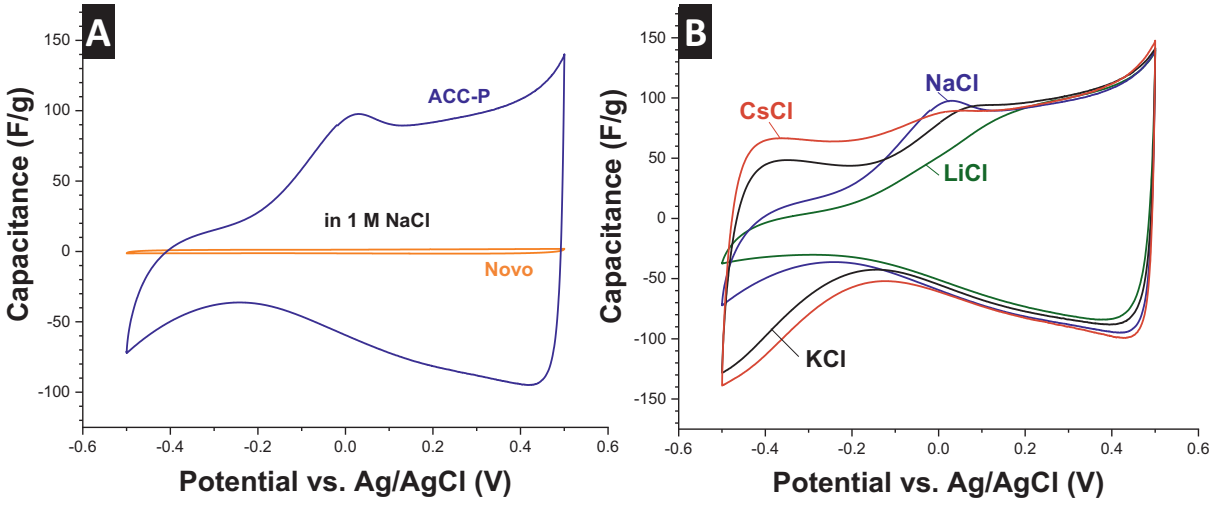

Fig. 2. Cyclic voltammograms ACC-P at the scan rate of 1 mV/s and potential range of −0.5 V to +0.5 V vs. Ag/AgCl A) capacitance comparison between original Novo cloth and pyrolyzed carbon cloth ACC-P in 1 M NaCl; B) Comparison of the cathodic capacitance of ACC-P in 1 M LiCl, NaCl, KCl, and CsCl aqueous electrolytes.

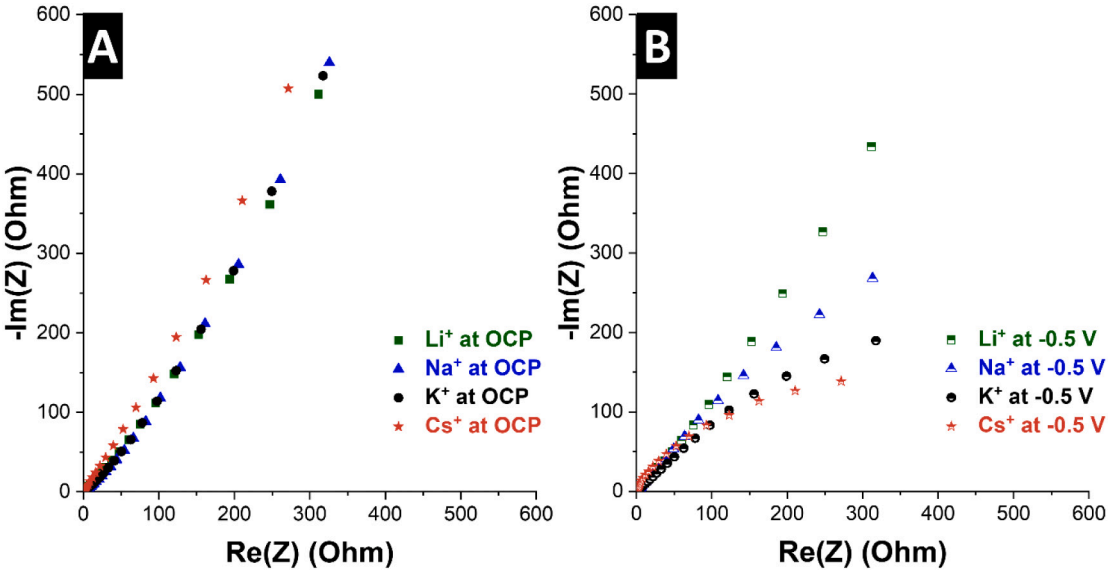

Fig. 3. Electrochemical impedance spectroscopy measurements of electrochemical cells with ACC-P as the working electrode in 1 M LiCl, 1 M NaCl, 1 M KCl, 1 M CsCl aqueous electrolyte, separately. Data recorded A) at open circuit potential (OCP) and B) at −0.5 V vs. Ag/AgCl.

of the electrode material and the charging response are influenced by different dehydration enthalpies of the cationic species. The gradual bending of the Nyquist curves with decreasing hydrated monovalent cations size ($Li^+ > Na^+ > K^+ > Cs^+$) indicates a decrease in diffusion-limitation of the ion electrosorption process. [47]

3.3. Ion selectivity of different monovalent cations

We quantified the ion selectivity in a mixed ion system based on the ion size and potential-dependent properties. As shown in Fig. 4A, we employed chemical online ICP-OES monitoring in an aqueous mixture of LiCl, NaCl, KCl, CsCl, $MgCl_2$, and $CaCl_2$; each salt has a concentration of 10 mM. During galvanostatic charging and discharging between 0 V and 0.7 V cell voltage, Cs^+ shows the highest concentration change, which is in alignment with its lowest desolvation energy barrier. K^+ shows slightly lower ion uptake ability, with the hydrated ion size being larger than Cs^+, K^+ has a higher dehydration energy barrier which leads to its higher dehydration overpotential and lower ion adsorption ability. The concentration change for Na^+ is much lower for both adsorption and desorption processes. This shows the ion diffusion into the carbon pore is much more difficult, and the applied potential is not high enough to overcome the energy barrier. For Li^+, Mg^{2+}, and Ca^{2+}, there are no pronounced concentration changes due to the highest dehydration energy and larger hydrated ion size. For better comparison, ACC-0.6 with a wider pore size distribution is applied and shows a less pronounced monovalent cation selectivity for K^+ over Li^+ and Na^+ (Fig. S3, *Supporting Information*). This illustrates that the dehydration process can enhance the selectivity of smaller hydrated cations.

In Fig. 4B, we calculated the ion uptake capacity during the online ICP-OES measurement. Over 10 cycles, Cs^+ and K^+ have the highest ion uptake capacity, up to around 20 μmol/g. For Na^+, this value is as low as around 5 μmol/g, and all the other cations have an ion uptake capacity of below 5 μmol/g. These values align with order of the hydrated ion size and their desolvation enthalpies, $Cs^+ < K^+ < Na^+ < Li^+ < Ca^{2+} < Mg^{2+}$, seen in Table 4. The selectivity factors of all cations compared to Na^+ are calculated in Table 5, a high Cs^+ and K^+ selectivity factors of 3.75 and 3.50 compared to Na^+ are obtained, which is higher than the reported results with micropores carbon (general selectivity factor of 1–2) as shown in Table 5, and the theoretical calculation for the micropore electric double layers. [25] Compared with Li^+, Mg^{2+}, and Ca^{2+}, ACC-0.6 prefers Na^+ with the selectivity factors of 0.26, 0.32, and 0.16, respectively, due to the dehydration energy barriers and confined pores.

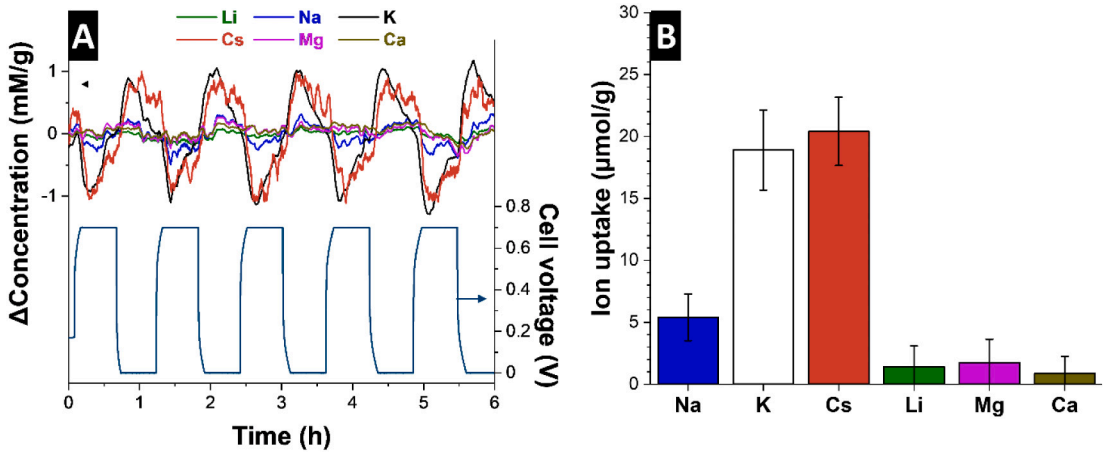

Fig. 4. Chemical online ICP-OES monitoring during charging and discharging of the asymmetric CDI cell with ACC-P as the working electrode. A) Concentration profiles of different ions during galvanostatic charging and discharging from 0 to 0.7 V cell voltage. B) Calculated ion uptake capacity (averaged over 10 cycles).

Table 5
Comparison of selectivity performance with literature, where carbons or intercalation pseudocapacitive material are used as the electrodes.

Electrode material	Pore size range (nm)	Electrolyte (mM)	Selectivity factor (K)	Reference
Activated carbon	1–10	K^+, 2 Na^+, 2 Ca^{2+}, 2	$K_{K/Na}$ 1.1 $K_{Ca/Na}$ 1.2	[50]
Activated carbon	1–10	VO^{2+}, 4.5 Fe^{2+}, 5.4 Al^{3+}, 11.1	$K_{Fe/V}$ 0.92 $K_{Al/V}$ 1.01	[49]
Activated carbon cloth oxidized by nitric acid	0.4–1.5	K^+, 2 Li^+, 2	$K_{K/Li}$ 1.84	[31]
MoS_2@CNT@carbon sphere	~0.67 (interlayer spacing)	Na^+, 10 K^+, 10 Mg^{2+}, 10 Ca^{2+}, 10	$K_{K/Na}$ 0.24 $K_{Mg/Na}$ 0.90 $K_{Ca/Na}$ 1.35	[48]
$Ti_3C_2T_z$-CNT	1.04 (d-spacing)	Li^+, 10 Na^+, 10 K^+, 10 Mg^{2+}, 10 Ca^{2+}, 10	$K_{Li/Na}$ 1.42 $K_{K/Na}$ 1.13 $K_{Mg/Na}$ 3.03 $K_{Ca/Na}$ 2.68	[39]
Ultramicroporous activated carbon cloth	0.6–1.0	Li^+, 10 Na^+, 10 K^+, 10 Cs^+, 10 Mg^{2+}, 10 Ca^{2+}, 10	$K_{Li/Na}$ 0.26 $K_{K/Na}$ 3.50 $K_{Cs/Na}$ 3.78 $K_{Mg/Na}$ 0.32 $K_{Ca/Na}$ 0.16	This work

This phenomenon differs from the most reported work about carbon and some two-dimensional intercalation pseudocapacitive material which prefers divalent (e.g., Ca^{2+} and Mg^{2+}) ions toward Na^+, with the selectivity factor of 1–4 (Table 5). Compared with current literature results, our result shows that ACC-P material, as an ultramicroporous material, can block the entrance of larger divalent cations, and also has the highest selectivity factor among different sizes of monovalent cations, such as K^+, Na^+, and Cs^+ vs. Li^+, and K^+, and Cs^+ vs Na^+. [31,48–50] This phenomenon has so far not been observed with other types of porous carbon materials. Due to the narrow pore size distribution and small average pore size of ACC-P, the hydrated Li^+, Na^+, Mg^{2+}, and Ca^{2+} must partially dehydrate to enter the pores of ACC-P. As a consequence, the ACC-P prefers to uptake Cs^+, K^+, and Na^+ for lower dehydration energy compared with that of Li^+, Mg^{2+}, and Ca^{2+}. In contrast, in case there is a larger space for ion transportation, the cations do not need to dehydrate to enter the bigger pores; in that case, the divalent ions are more completive for their higher charge. [27,39]

The selective uptake of ions is an exciting and promising perspective to conventional seawater and wastewater treatment. For example, much effort has been done toward the selective removal of radioactive Cs^+. However, the efficient extraction is limited by the relatively low concentration compared to Na^+. [51] Through selective electrosorption, specific ions like Cs^+ could be continuously removed from the stream. Our work contributes toward a comprehensive technological platform to tune electrosorption selectivity based on pore size and (de)hydration energy. A design of flow cells based on these phenomena could sequentially uptake ions by tuning the applied potential and consecutively increasing the pore size in an array of electrodes.

4. Conclusions

We investigated carbon cloth with an average pore size smaller than hydrated monovalent cations and a narrow pore size distribution to achieve selective monovalent ions removal. Due to the difference in hydrated ion size and dehydration energy, a transition from ion sieving to dehydration and ion insertion is observed. The nanoconfinement of the pores limits the ion diffusion within the pores. Combined with the dehydration of the ions, a diffusion-controlled process is observed in both cyclic voltammetry and impedance spectroscopy measurements. While Li^+ and Na^+ show the ion sieving, K^+ and Cs^+ can be stored within the pores. In mixed cation systems, larger cations such as divalent cations and Li^+ cannot enter the pores during charging/discharging, and the heavier monovalent cations such as Cs^+ and K^+ are selectively removed from the feedwater and are stored in the nanoconfinement of the electrode material. Our work has shown that by applying sub-nanometer pores, we observed a pronounced selectivity of Cs^+ and K^+ removal compared to Li^+ and Na^+, which shows it is possible to achieve selective monovalent cation removal in a multi-monovalent-ion aqueous solution by applying the pore size effect.

CRediT authorship contribution statement

Y.Z.: Data Curation, Writing - Original Draft, Visualization, Investigation.
P.R.: Validation, Review & Editing, Investigation.
L.W.: Data Curation, Review & Editing, Investigation.
E.P.: Data Curation, Review & Editing, Investigation.
S·H: Data Curation, Review & Editing, Investigation.
V.P.: Conceptualization, Data Curation, Writing - Review & Editing, Visualization, Funding acquisition, Project administration, Supervision.

Declaration of competing interest

The authors declare the following financial interests/personal relationships which may be considered as potential competing interests:
Volker Presser reports financial support was provided by RAG-Stiftung. Lei Wang reports financial support was provided by China Scholarship Council.

Data availability

Data will be made available on request.

Acknowledgments

The authors thank Eduard Arzt (INM) for his continuing support. The authors thank Andrea Jung and Christina Muth from INM for the support with CHNS-O and FT-IR measurements. Y.Z. and V.P. acknowledge support for the MERLIN project from the RAG-Stiftung; the RAG-Stiftung generates long-term momentum for the transformation of the regions along the Ruhr and Saar Rivers and in Ibbenbüren. L.W. acknowledges funding from the China Scholarship Council (CSC) via the award number 201906260277.

Appendix A. Supplementary data

Supplementary data to this article can be found online at https://doi.org/10.1016/j.desal.2022.116053.

References

[1] R.F. Service, Desalination freshens up, Science 313 (2006) 1088–1090.
[2] M. Elimelech, W.A. Phillip, The future of seawater desalination: energy, technology, and the environment, Science 333 (2011) 712–717.
[3] D. Hlushkou, K.N. Knust, R.M. Crooks, U. Tallarek, Numerical simulation of electrochemical desalination, J. Phys. Condens. Matter 28 (2016), 194001.
[4] M.A. Shannon, P.W. Bohn, M. Elimelech, J.G. Georgiadis, B.J. Mariñas, A. M. Mayes, Science and technology for water purification in the coming decades, Nature 452 (2008) 301–310.
[5] D. Kapoor, M.P. Singh, 10 - Heavy metal contamination in water and its possible sources, in: V. Kumar, A. Sharma, A. Cerdà (Eds.), Heavy Metals in the Environment, Elsevier, 2021, pp. 179–189.
[6] D. Curto, V. Franzitta, A. Guercio, A review of the water desalination technologies, Appl. Sci.Basel 11 (2021) 670. Basel.

[7] A. Al-Karaghouli, L.L. Kazmerski, Energy consumption and water production cost of conventional and renewable-energy-powered desalination processes, Renew. Sustain. Energy Rev. 24 (2013) 343–356.
[8] L.F. Greenlee, D.F. Lawler, B.D. Freeman, B. Marrot, P. Moulin, Reverse osmosis desalination: water sources, technology, and today's challenges, Water Res. 43 (2009) 2317–2348.
[9] K.C. Ng, M. Burhan, Q. Chen, D. Ybyraiymkul, F.H. Akhtar, M. Kumja, R.W. Field, M.W. Shahzad, A thermodynamic platform for evaluating the energy efficiency of combined power generation and desalination plants, npj CleanWater 4 (2021) 25.
[10] E. Vera, J. Ruales, M. Dornier, J. Sandeaux, R. Sandeaux, G. Pourcelly, Deacidification of clarified passion fruit juice using different configurations of electrodialysis, J. Chem. Technol. Biotechnol. 78 (2003) 918–925.
[11] M. Fidaleo, M. Moresi, Electrodialysis applications in the food industry, in: Advances in Food And Nutrition Research, Academic Press, 2006, pp. 265–360.
[12] F. Gonçalves, C. Fernandes, P. Cameira dos Santos, M.N. de Pinho, Wine tartaric stabilization by electrodialysis and its assessment by the saturation temperature, J. Food Eng. 59 (2003) 229–235.
[13] S. Al-Amshawee, M.Y.B.M. Yunus, A.A.M. Azoddein, D.G. Hassell, I.H. Dakhil, H. A. Hasan, Electrodialysis desalination for water and wastewater: a review, Chem. Eng. J. 380 (2020), 122231.
[14] M.A. Anderson, A.L. Cudero, J. Palma, Capacitive deionization as an electrochemical means of saving energy and delivering clean water. Comparison to present desalination practices: will it compete? Electrochim. Acta 55 (2010) 3845–3856.
[15] X. Su, A. Kushima, C. Halliday, J. Zhou, J. Li, T.A. Hatton, Electrochemically-mediated selective capture of heavy metal chromium and arsenic oxyanions from water, Nat. Commun. 9 (2018) 4701.
[16] S. Porada, R. Zhao, A. van der Wal, V. Presser, P.M. Biesheuvel, Review on the science and technology of water desalination by capacitive deionization, Prog. Mater. Sci. 58 (2013) 1388–1442.
[17] M.E. Suss, S. Porada, X. Sun, P.M. Biesheuvel, J. Yoon, V. Presser, Water desalination via capacitive deionization: what is it and what can we expect from it? Energy Environ. Sci. 8 (2015) 2296–2319.
[18] E. Garcia-Quismondo, C. Santos, J. Soria, J. Palma, M.A. Anderson, New operational modes to increase energy efficiency in capacitive deionization systems, Environ.Sci.Technol. 50 (2016) 6053–6060.
[19] S. Porada, L. Weinstein, R. Dash, A. van der Wal, M. Bryjak, Y. Gogotsi, P. M. Biesheuvel, Water desalination using capacitive deionization with microporous carbon electrodes, ACS Appl. Mater. Interfaces 4 (2012) 1194–1199.
[20] P.M. Biesheuvel, S. Porada, M. Levi, M.Z. Bazant, Attractive forces in microporous carbon electrodes for capacitive deionization, J. Solid State Electrochem. 18 (2014) 1365–1376.
[21] P. Liu, T. Yan, L. Shi, H.S. Park, X. Chen, Z. Zhao, D. Zhang, Graphene-based materials for capacitive deionization, J. Mater. Chem. A 5 (2017) 13907–13943.
[22] M.E. Suss, V. Presser, Water desalination with energy storage electrode materials, Joule 2 (2018) 10–15.
[23] R. Zhao, M. van Soestbergen, H.H.M. Rijnaarts, A. van der Wal, M.Z. Bazant, P. M. Biesheuvel, Time-dependent ion selectivity in capacitive charging of porous electrodes, J. Colloid Interface Sci. 384 (2012) 38–44.
[24] J.E. Dykstra, J. Dijkstra, A. van der Wal, H.V.M. Hamelers, S. Porada, On-line method to study dynamics of ion adsorption from mixtures of salts in capacitive deionization, Desalination 390 (2016) 47–52.
[25] M.E. Suss, Size-based ion selectivity of micropore electric double layers in capacitive deionization electrodes, J. Electrochem. Soc. 164 (2017) E270–E275.
[26] C.H. Hou, P. Taboada-Serrano, S. Yiacoumi, C. Tsouris, Electrosorption selectivity of ions from mixtures of electrolytes inside nanopores, J. Chem. Phys. 129 (2008), 224703.
[27] Y. Zhang, J. Peng, G. Feng, V. Presser, Hydration shell energy barrier differences of sub-nanometer carbon pores enable ion sieving and selective ion removal, Chem. Eng. J. 419 (2021), 129438.
[28] S.A. Hawks, M.R. Ceron, D.I. Oyarzun, T.A. Pham, C. Zhan, C.K. Loeb, D. Mew, A. Deinhart, B.C. Wood, J.G. Santiago, M. Stadermann, P.G. Campbell, Using ultramicroporous carbon for the selective removal of nitrate with capacitive deionization, Environ.Sci.Technol. 53 (2019) 10863–10870.
[29] Y. Marcus, Thermodynamics of solvation of ions. Part 5. —Gibbs free energy of hydration at 298.15 K, J. Chem. Soc. Faraday Trans. 87 (1991) 2995–2999.
[30] C. Zhan, F. Aydin, E. Schwegler, A. Noy, T.A. Pham, Understanding cation selectivity in carbon nanopores with hybrid first-principles/continuum simulations: implications for water desalination and separation technologies, ACS Appl.Nano Mater. 3 (2020) 9740–9748.
[31] E.N. Guyes, T. Malka, M.E. Suss, Enhancing the ion-size-based selectivity of capacitive deionization electrodes, Environ.Sci.Technol. 53 (2019) 8447–8454.
[32] Z.Y. Leong, H.Y. Yang, Capacitive deionization of divalent cations for water softening using functionalized carbon electrodes, ACS Omega 5 (2020) 2097–2106.
[33] D.I. Oyarzun, A. Hemmatifar, J.W. Palko, M. Stadermann, J.G. Santiago, Ion selectivity in capacitive deionization with functionalized electrode: theory and experimental validation, Water Res.X 1 (2018), 100008.
[34] P. Liu, T. Yan, J. Zhang, L. Shi, D. Zhang, Separation and recovery of heavy metal ions and salt ions from wastewater by 3D graphene-based asymmetric electrodes via capacitive deionization, J. Mater. Chem. A 5 (2017) 14748–14757.
[35] R. Uwayid, E.N. Guyes, A.N. Shocron, J. Gilron, M. Elimelech, M.E. Suss, Perfect divalent cation selectivity with capacitive deionization, Water Res. 210 (2022), 117959.
[36] Y. Zhang, C. Prehal, H. Jiang, Y. Liu, G. Feng, V. Presser, Ionophobicity of carbon sub-nanometer pores enables efficient desalination at high salinity, <sb:contribution><sb:title>Cell Rep. Phys.</sb:title></sb:contribution><sb:host><sb:issue><sb:series><sb:title>Sci.</sb:title></sb:series></sb:issue></sb:host> (2021), 100689.
[37] S. Bi, Y. Zhang, L. Cervini, T. Mo, J.M. Griffin, V. Presser, G. Feng, Permselective ion electrosorption of subnanometer pores at high molar strength enables capacitive deionization of saline water, Sustain.Energy Fuel 4 (2020) 1285–1295.
[38] D. Weingarth, M. Zeiger, N. Jäckel, M. Aslan, G. Feng, V. Presser, Graphitization as a universal tool to tailor the potential-dependent capacitance of carbon supercapacitors, Adv. Energy Mater. 4 (2014) 1400316.
[39] L. Wang, M. Torkamanzadeh, A. Majed, Y. Zhang, Q. Wang, B. Breitung, G. Feng, M. Naguib, V. Presser, Time-dependent cation selectivity of titanium carbide MXene in aqueous solution, Adv.Sustain.Syst. 6 (2022), 2100383.
[40] M. Aslan, M. Zeiger, N. Jäckel, I. Grobelsek, D. Weingarth, V. Presser, Improved capacitive deionization performance of mixed hydrophobic/hydrophilic activated carbon electrodes, J. Phys. Condens. Matter 28 (2016), 114003.
[41] G.Y. Gor, M. Thommes, K.A. Cychosz, A.V. Neimark, Quenched solid density functional theory method for characterization of mesoporous carbons by nitrogen adsorption, Carbon 50 (2012) 1583–1590.
[42] A.V. Neimark, Y. Lin, P.I. Ravikovitch, M. Thommes, Quenched solid density functional theory and pore size analysis of micro-mesoporous carbons, Carbon 47 (2009) 1617–1628.
[43] J.G. Gamaethiralalage, K. Singh, S. Sahin, J. Yoon, M. Elimelech, M.E. Suss, P. Liang, P.M. Biesheuvel, R.L. Zornitta, L.C.P.M. de Smet, Recent advances in ion selectivity with capacitive deionization, Energy Environ. Sci. 14 (2021) 1095–1120.
[44] R.K. Kalluri, M.M. Biener, M.E. Suss, M.D. Merrill, M. Stadermann, J.G. Santiago, T. F. Baumann, J. Biener, A. Striolo, Unraveling the potential and pore-size dependent capacitance of slit-shaped graphitic carbon pores in aqueous electrolytes, Phys. Chem. Chem. Phys. 15 (2013) 2309–2320.
[45] E.R. Nightingale, Phenomenological theory of ion solvation.Effective radii of hydrated ions, J. Phys. Chem. 63 (1959) 1381–1387.
[46] K. Kuma, A. Usui, W. Paplawsky, B. Gedulin, G. Arrhenius, Crystal structures of synthetic 7 angstrom and 10 angstrom manganates substituted by mono- and divalent cations, Mineral. Mag. 58 (1994) 425–447.
[47] S. Fleischmann, Y. Zhang, X. Wang, P.T. Cummings, J. Wu, P. Simon, Y. Gogotsi, V. Presser, V. Augustyn, Continuous transition from double-layer to Faradaic charge storage in confined electrolytes, Nat.Energy 7 (2022) 222–228.
[48] Y. Cai, W. Zhang, R. Fang, D. Zhao, Y. Wang, J. Wang, Well-dispersed few-layered MoS2 connected with robust 3D conductive architecture for rapid capacitive deionization process and its specific ion selectivity, Desalination 520 (2021), 115325.
[49] J. Duan, S. Bao, Y. Zhang, The characteristics of resin/carbon composite electrode and application in selective adsorption of vanadium(IV) by capacitive deionization, Chem. Eng. Res. Des. 132 (2018) 178–186.
[50] C.-H. Hou, C.-Y. Huang, A comparative study of electrosorption selectivity of ions by activated carbon electrodes in capacitive deionization, Desalination 314 (2013) 124–129.
[51] M.R. Awual, T. Yaita, T. Kobayashi, H. Shiwaku, S. Suzuki, Improving cesium removal to clean-up the contaminated water using modified conjugate material, J. Environ.Chem.Eng. 8 (2020), 103684.

Supporting Information

Selectivity towards heavier monovalent cations of carbon ultramicropores used for capacitive deionization

Yuan Zhang,[1,2] Panyu Ren,[1,2] Lei Wang,[1,2] Emmanuel Pameté,[1]
Samantha Husmann[1] and Volker Presser[1,2,3*]

[1] INM - Leibniz Institute for New Materials, Campus D2 2, 66123 Saarbrücken, Germany

[2] Saarland University, Campus D2 2, 66123 Saarbrücken, Germany

[3] Saarene - Saarland Center for Energy Materials and Sustainability, Campus C4 2, 66123 Saarbrücken, Germany

* Corresponding author's eMail: volker.presser@leibniz-inm.de

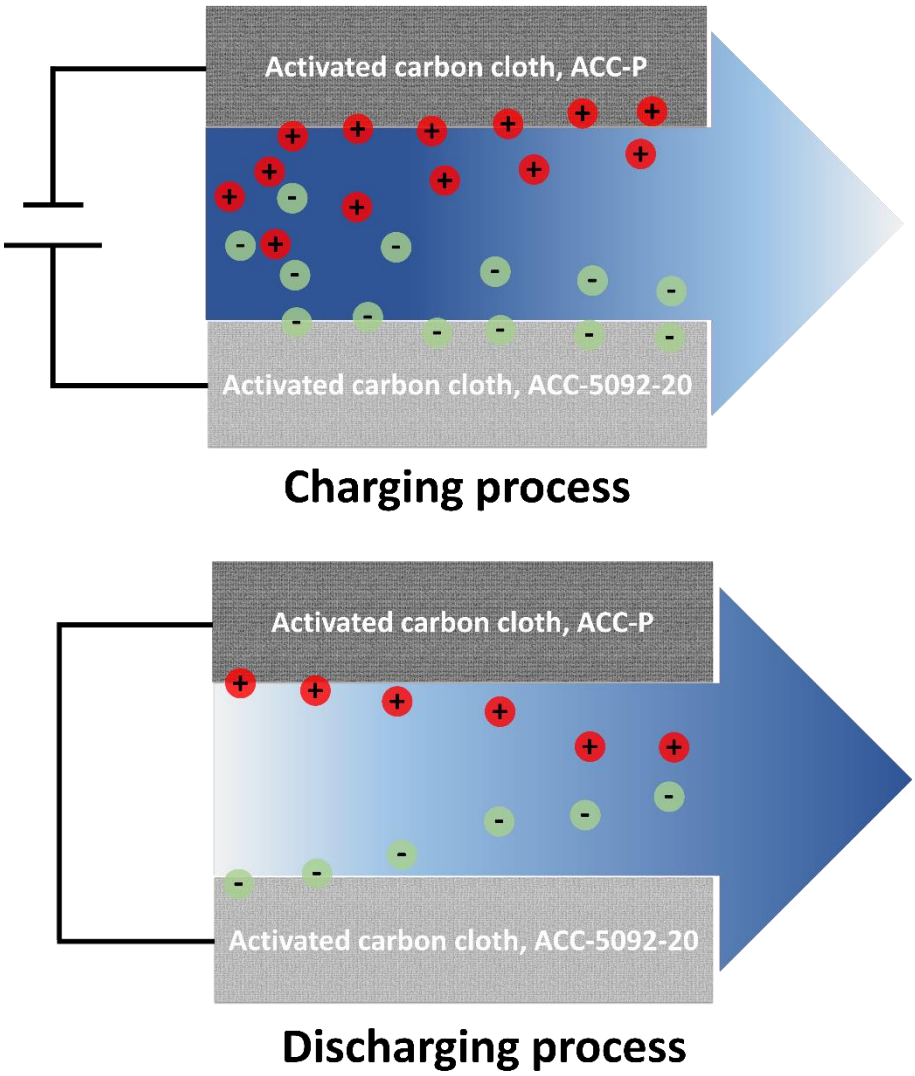

Figure S1: Schematic diagram of CDI devices during charging and discharging process, exemplified for the pairing of ACC-5092-20 and ACC-P.

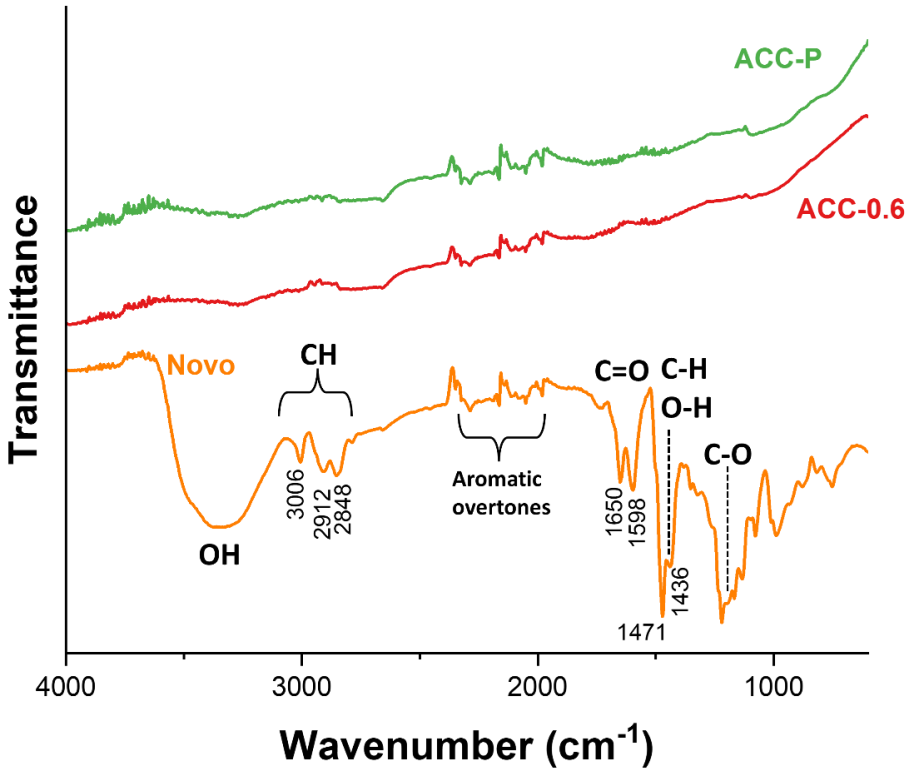

Figure S2: FTIR spectra of Novo, ACC-P, and ACC-0.6 carbon cloth.

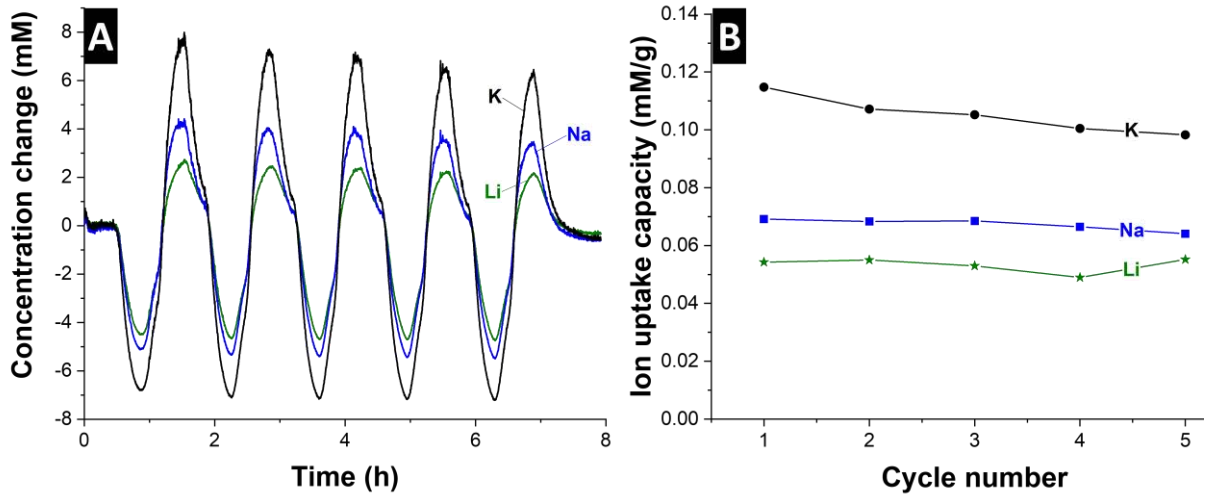

Figure S3: Online ICP-OES measurement of the symmetric CDI cell with ACC-0.6 activated carbon cloth in a mixed electrolyte of 10 mM LiCl, 10 mM NaCl, and 10 mM KCl. A) online concentration change of different ions during galvanostatic charging and discharging and B) calculated ion uptake capacity.

4.5. Cation selectivity during flow electrode capacitive deionization

Panyu Ren,[1,2] Bin Wang,[1] Jean Gustavo de Andrade Ruthes,[1,2]

Mohammad Torkamanzadeh,[1] and Volker Presser[1,2,3]

[1] *INM - Leibniz Institute for New Materials, Campus D2 2, 66123, Saarbrücken, Germany*

[2] *Department of Materials Science & Engineering, Saarland University, Campus D2 2, 66123, Saarbrücken, Germany*

[3] *saarene - Saarland Center for Energy Materials and Sustainability, Campus C4 2, 66123 Saarbrücken, Germany*

Citation:

P. Ren, B. Wang, J. G. de Andrade Ruthes, M. Torkamanzadeh, and V. Presser, Cation selectivity during flow electrode capacitive deionization, Desalination 592 (2024) 118161.

Own contribution:

Investigation. Investigation, Data curation, Visualization, Writing - original draft, Writing - review & editing.

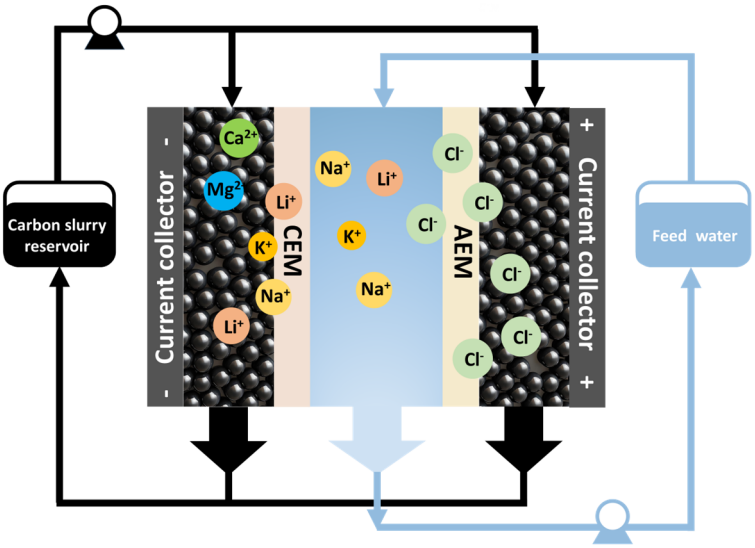

Desalination 592 (2024) 118161

Contents lists available at ScienceDirect

Desalination

journal homepage: www.elsevier.com/locate/desal

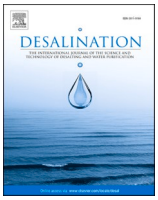

Cation selectivity during flow electrode capacitive deionization

Panyu Ren [a,b], Bin Wang [a], Jean Gustavo de Andrade Ruthes [a,b], Mohammad Torkamanzadeh [a], Volker Presser [a,b,c,*]

[a] INM - Leibniz Institute for New Materials, Campus D2 2, 66123 Saarbrücken, Germany
[b] Department of Materials Science & Engineering, Saarland University, Campus D2 2, 66123 Saarbrücken, Germany
[c] saarene - Saarland Center for Energy Materials and Sustainability, Campus C4 2, 66123 Saarbrücken, Germany

HIGHLIGHTS

- FCDI enables ion removal via continuous operation.
- Higher charge-to-size ratio favors bivalent cations in ion removal.
- Activated carbon content at 10 % mass optimizes FCDI performance.
- Conductive carbon black enhances ion uptake and separation efficiency.

GRAPHICAL ABSTRACT

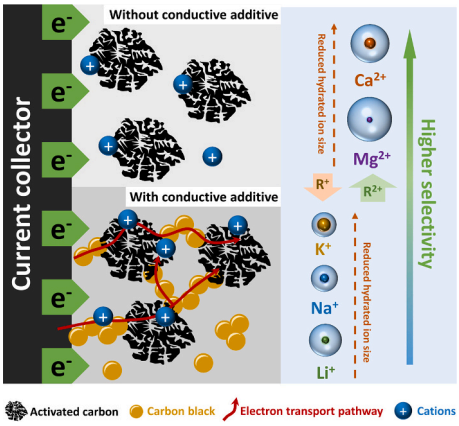

ARTICLE INFO

Keywords:
Activated carbon
Cation separation
Flowable electrode capacitive deionization

ABSTRACT

Efficient separation of specific ions from aqueous media is crucial for advanced water treatment and resource recovery. Flow electrode capacitive deionization (FCDI) offers potential for selective ion removal through continuous operation. This study evaluates the performance of selective cation separation using a commercial activated carbon slurry in a multi-ion solution of monovalent (Li^+, Na^+, K^+) and bivalent (Ca^{2+}, Mg^{2+}) cations. We assess ion removal and cation selectivity under different operational parameters, such as applied potential, slurry flow rate, and feed water flow rate. Our data show that bivalent cations, namely Ca^{2+} and Mg^{2+}, are preferentially removal due to their higher charge-to-size ratio, aligning with hydrated ion sizes. The highest separation rate was observed for Ca^{2+} (5.7 μg cm^{-2} min^{-1}), and the lowest for Li^+ (0.2 μg cm^{-2} min^{-1}). At the highest applied voltage (1.2 V), charge efficiencies reached 70 %, with an energy consumption of 41 Wh mol^{-1} for nearly complete cation removal. Optimal conditions were identified with a slurry flow rate of 6 mL min^{-1}, feed water flow rate of 2 mL min^{-1}, activated carbon content of 10 mass%, 1 mass% carbon black, and a cell voltage of 1.2 V. These findings highlight the importance of optimizing operational parameters to enhance ion removal.

* Corresponding author at: INM - Leibniz Institute for New Materials, Campus D2 2, 66123 Saarbrücken, Germany.
E-mail address: volker.presser@leibniz-inm.de (V. Presser).

https://doi.org/10.1016/j.desal.2024.118161
Received 13 August 2024; Received in revised form 25 September 2024; Accepted 26 September 2024
Available online 28 September 2024

1. Introduction

The accessibility of freshwater is increasingly challenged by the intersecting pressures of climate variability, burgeoning populations, expanding industrialization, and escalating contamination of water sources. [1] Commonly, water contains multi-salts like Li^+, Na^+, K^+, [2,3] hardness ions like Ca^{2+}, Mg^{2+}, [2,4] and toxic metal ions like Pb^{2+} and Cd^{2+} [5,6]. Toxic metal ions removal is important owing to their negative health and environmental impact, [7] while extracting precious elements, especially lithium, is strongly motivated by commercial interests in the wake of global electrification and rapid growth of battery production. [8] Hardness ions are also important for selective extraction due to scale formation in various applications employing hardness-ion-containing aqueous media, including, depending on the regional composition of the water, household devices like washing machines or dishwashers. [4]

Present-day water treatment methods mainly include technologies such as reverse osmosis (RO) [9] and thermal desalination methods such as multi-stage flash (MSF) [10] and multiple effect distillation (MED). [11] However, with a transition toward carbon neutrality and reduction of energy consumption, alternative water remediation and ion separation technologies with higher overall efficiency, lower energy consumption, and added functionality toward ion selectivity are intensively explored. [12,13] As one of these technologies, capacitive deionization (CDI) [14] is an electrochemical ion adsorption method used for the separation of salts, [15,16] toxic metal ions, [17,18] hardness ions, [19,20] and various anions [21] from water.

CDI typically uses static film electrodes, comprising either a layer of electrode material cast onto the current collector by a binder or a free-standing electrode placed in contact with the current collector. The performance (per cycle) is mainly determined by the salt adsorption capacity of the electrodes, which are charged and discharged cyclically. [22] The change from static film electrodes to suspended carbon particles in the flow electrode transitions CDI from cyclic charge/discharge (ion removal/ion release) operation toward continuous desalination. [23,24] The continuous operation also aligns more closely with the scalability requirements of electrochemical desalination in industrial settings, as it enables a steady process flow, ensuring consistent effluent water quality. [25] Another significant advantage of flow electrode CDI (FCDI) over CDI is the separate control over the system's capacity for ion removal and its rate of ion removal, analogous to the decoupled energy-power advantage of flow batteries. [26] That is, the desalination capacity in FCDI is determined by the volume of the flowable electrode (slurry tank), whereas the ion separation rate depends on the cell size (area of the membranes).

Over time, various FCDI cell and system configurations have emerged, including one-cell and two-cell setups, modifications of the current collectors, and an array of flow channel designs. [27–33] With its different technological variants, CDI offers unique benefits, including the capacity for precise or preferential removal of specific ions. [22,34] Selective ion removal is crucial because it can potentially recover specific valuable ions from water as a resource and target the specific removal of harmful species. [35] Various optimized materials and strategies have been developed for CDI to achieve selective ion separation. [36,37] Activated carbon (AC) enables selective ion separation by sieving specific ions based on the pore size. [38] For instance, Uwayid et al. demonstrated perfect selectivity for bivalent cations (Ca^{2+}) while excluding the competing monovalent Na^+ ions through an electrode made of sulfonated AC. [39] Subnanometer porous carbon developed by Zhang et al. achieved Cs^+ and K^+ selectivity factors of 3–4 compared to Na^+. [16]

Beyond nanoporous carbons, other electrode materials have been explored. [40] For example, copper hexacyanoferrate (Prussian blue analog) can selectively extract calcium ions. Xu et al. showed that charging the cell from 0.4 V to 1.2 V removes 127 μmol g^{-1} of bivalent Ca^{2+} while slightly expelling monovalent Na^+ in feed water containing 15 mM NaCl and 3 mM $CaCl_2$. [41] Demonstrated experimentally and by modeling, vanadium hexacyanoferrate prefers bivalent Ca^{2+} ions over monovalent Na^+ with a separation factor of $\beta_{Ca/Na} \approx 3.5$. [42] Additionally, multiple factors, such as ionic properties and operational parameters, affect the electrochemical ion-selective separation. Gao et al. observed preferential adsorption of multivalent cations from aqueous solutions with the order $Fe^{3+} > Cu^{2+} > Zn^{2+} > Na^+$, attributed to larger charge cations being more readily adsorbed onto electrode surfaces due to the electric field. [43] Among cations with the same valency, those with smaller hydrated radii were more effectively captured, as evidenced by $Cu^{2+} > Zn^{2+}$. [43]

While the research on ion selectivity has mainly focused on static electrodes, works have also started to explore ion selectivity for FCDI. For example, Zhang et al. employed FCDI to selectively separate Cu^{2+} in the coexistence of competing Na^+ from a saline solution with the assistance of electrodeposition in the short-circuited closed-cycle (SCC) mode. [44] Another study investigated the selective phosphorous recovery through the adjustment of charging and discharging procedures of the FCDI system, [45] which achieved a satisfactory phosphorus recovery performance (164 mg L^{-1} at each cycle) and selectivity factors above 2 (versus Cl^-) under optimized conditions (i.e., a carbon content of 5 mass%, charge and discharge current densities of +10 A m^{-2} and -15 A m^{-2}, respectively). Other strategies to induce selectivity in FCDI systems include functionalizing the ion-exchange membranes, where a favorable sodium extraction from Na^+/Ca^{2+} mixtures has been reported. [46]

Unlike the abundant research on mono−/multivalent cation-selective separation via CDI, selective ion separation via FCDI remains underexplored in the scientific community. This work systematically investigates the selective cation removal performance of AC and other carbon materials in multi-salt (Li^+, Na^+, K^+, Ca^{2+}, Mg^{2+}) mixed solutions under different operational parameters. We investigated the selectivity of AC toward cations (Na^+, K^+, Ca^{2+}, Mg^{2+}) compared to Li^+ as a function of the AC content, cell voltage, flow rate, and the mass loading of carbon black introduced as a conductive additive.

2. Materials and methods

2.1. Materials

Commercially available activated carbons (ACs) of YP-80F (AC1, Kuraray Chemicals Co.), YP-50F (AC2, Kuraray Chemicals Co.), and MSP-20 (AC3, Kansai Coke and Chemicals) were used. To serve as a conductive additive, we used VULCAN XC72R Specialty carbon black (CB, CAS No. 1333-86-4) from Cabot. Lithium chloride (LiCl, CAS: 7447-41-8, 99 %), sodium chloride (NaCl, CAS: 7647-14-5, 99 %), potassium chloride (KCl, CAS: 7447-40-7, 99 %), magnesium chloride ($MgCl_2$, CAS: 7786-30-3, 99 %), and calcium chloride ($CaCl_2$, CAS 10043-52-4, 99 %) were purchased from Sigma Aldrich. Cation and anion exchange membranes (Fumasep FKS-PET-130/ED-100 and Fumasep FAS-PET-130/ED-100, Fumatech) were employed in the FCDI cells. Deionized water (resistivity: 18 MΩ cm^{-2}) obtained from a Mili-Q purification system was utilized throughout this research.

2.2. Material characterization

Scanning electron microscopy (SEM) was performed using a ZEISS GEMINI 500 with an accelerating voltage of 1 kV for imaging. The electrode materials were attached to an adhesive Cu foil on the Al sample holder without additional sputter-coating. Nitrogen gas sorption analysis (GSA) was conducted by an iQ system (Quantachrome; formerly Anton-Paar) at −196 °C. The samples were first degassed at +300 °C for 24 h to remove humidity. The specific surface area (SSA) was calculated using the ASiQwin software following the Brunauer-Emmett-Teller (BET) equation.

The viscosity of slurries was examined through rheological studies

using an Anton Paar MCR 302e rheometer equipped with a stainless-steel concentric cylinder cup geometry to minimize particle settling. Measurements were conducted at shear rates ranging from 0.001 s^{-1} to 200 s^{-1}, maintaining a constant temperature of 25 °C throughout all experiments. The experimental data was evaluated with the Ostwald-de Waele power-law model presented in Eq. (1):

$$\eta = k \bullet \gamma^{n-1} \quad (1)$$

where η is the viscosity, k is the consistency index, and n is the shear thinning index. The data analysis is reported in Table 1.

2.3. FCDI cell operation and performance calculations

10 mass% AC and 1 mass% CB were soaked in the solution, which contained the same composition as the feed water. The mixture was sonicated for 1 h and stirred for another 3 h before pumping into the cell. The slurry was continuously stirred on a magnetic stirrer during the experiment to maintain homogeneity and avoid precipitation. The schematic diagram in Fig. 1 displays the experimental setup of our FCDI system utilizing single cycle (SC) mode. [47] A single cell operates with the feed water channel between the cation and anion exchange membranes and flowable electrode channels on either side of the ion exchange membranes. The FCDI cell is powered using an electrochemical potentiostat (VSP300, Bio-Logic). The feed electrodes (FE, carbon slurry) stored in the reservoir are pumped through the flow electrode channels. As they flow out of the flow channels, they are returned to the reservoir and constantly recirculated, forming the SC mode in which the anions and cations can neutralize in the reservoir. The bottom panel of Fig. 1 shows the flow channel cut according to the cell structure using the rubber sheet with ~4 mm width.

Previous studies have investigated the effect of initial feedwater salt concentration on FCDI performance, demonstrating its significant impact on desalination efficiency and energy consumption. [48,49] Our multi-component salt solution contained 10 mM Li^+, 10 mM Na^+, 10 mM K^+, 10 mM Ca^{2+}, and 10 mM Mg^{2+}, used as both the feed water channel and the supporting electrolyte of the slurry to maintain the same concentration across those channels, to minimize ionic migration due to unequal osmotic pressure. The latter solution was also used to soak all ion exchange membranes overnight. To investigate the effect of the flow rates on the cation separation performance, the flow rates of feed water were set as 1 mL min^{-1}, 2 mL min^{-1}, and 4 mL min^{-1}, while the flow rate of electrodes slurry was set at 6 mL min^{-1}, 12 mL min^{-1}, and 24 mL min^{-1}.

Inductively coupled plasma optical emission spectroscopy (ICP-OES) was used to quantify the cation separation in a mixed cation system. Samples were extracted from the feed water reservoir of the FCDI system at time intervals of 0 h, 4 h, 8 h, 12 h, 24 h, and 32 h, diluted with Mili-Q water and tested by ICP-OES offline mode. This ICP-OES mode can be flexible in sample collection and processing and can analyze samples in batch mode rather than quasi-real-time. ICP-OES tests were repeated three times for each sample, with the mean value used for analysis. Before the offline test, we constructed the relationship between each ion concentration and the correspondent ICP signal intensity following the procedure outlined in our previous work. [50] Briefly, mixed ion solutions with known concentrations of 0.2 mM, 0.5 mM, 1 mM, 2 mM, 5 mM, and 10 mM LiCl, NaCl, KCl, $CaCl_2$, and $MgCl_2$ were used for the calibration.

Table 1
Rheological parameters of the activated carbon suspension electrodes.

Carbon content	Carbon black content	Consistency index (k)	Shear thinning index (n)
10 mass% AC1	1 mass%	0.41	0.59
10 mass% AC2	1 mass%	0.25	0.41
10 mass% AC3	1 mass%	0.24	0.35
10 mass% AC1	0 mass%	0.38	0.40
10 mass% AC1	2 mass%	0.592	0.56
5 mass% AC1	1 mass%	0.22	0.46
15 mass% AC1	1 mass%	0.78	0.68

The performance metrics of FCDI cells were analyzed regarding ion separation ratio (ISR), average ion separation rate (AISR, μg cm^{-2} min^{-1}), ion selectivity factor (ISF), charge efficiency (CE, %), and average energy consumption (AEC, Wh mol^{-1}). ISR is defined as the concentration ratio of a specific cation in the treated water to initial feed water by following Eq. (2):

$$ISR = \frac{C_t}{C_0} \quad (2)$$

where C_t is the ion concentration (mM) at time t, and C_0 is the initial ion concentration (mM). As such, an ISR value of unity for a specific ion indicates the system's indifference toward that ion, whereas an ISR value close to zero means a complete removal of that ion from the feed by the system.

AISR is measured to assess the salt removal rate per unit geometric contact area between target water and electrode slurry, which is calculated following Eq. (3):

$$AISR = \frac{(C_0 - C_t) \times V}{S_A \times t} \quad (3)$$

where V is the volume of feed water (mL), S_A represents the effective contact area (cm^2), and t is the operation time of the FCDI system.

ISF_i is defined as the ion selectivity of the FCDI system toward a specific ion compared to Li^+, which is obtained using Eq. (4):

$$ISF_i = \frac{\Delta C_i}{\Delta C_{Li^+}} \quad (4)$$

where ΔC_i represents the concentration change of a specific cation in the outflow reservoir (mol L^{-1}), and ΔC_{Li+} is the molecular concentration change of lithium in the outflow reservoir (mol L^{-1}).

CE is defined as the ratio of ionic charge (salt) removed to the invested electric charge (electrons) calculated using Eq. (5):

$$CE = \frac{\sum \Delta C_f \times z \times V \times F}{(\int I\, dt)} \times 100\% \quad (5)$$

where F represents the Faraday constant (96,485 C mol^{-1}), z is the valency (e.g., z = 1 for Na^+ and z = 2 for Mg^{2+}), $\sum \Delta C_f$ is the sum of concentration changes (mM) of all ionic species in the process, I is the real-time current monitored by the electrochemical workstation, and dt is the duration during which the latter current and concentration changes were measured.

AEC (Wh mol^{-1}) is defined as the invested energy to remove one mole of salt. The latter could be expressed as the product of applied cell voltage E (V) and the measured charge divided by the number of moles of salt removed by the FCDI system, *V* is the volume of the feed water (L). following Eq. (6):

$$AEC = \frac{(\int I\, dt) \times E}{(C - C_0) \times V} \quad (6)$$

3. Results and discussion

3.1. Cation separation performance of different carbon materials

Three commercial carbon materials with different pore characteristics and surface features, AC1, AC2, and AC3, were used as flowable carbon electrodes for our FCDI system (Fig. 2). Nitrogen sorption isotherms provided the total pore volume of AC1, AC2, and AC3 as 1.4 cm^3 g^{-1}, 0.84 cm^3 g^{-1} and 0.94 cm^3 g^{-1}, with the mean pore size of 1.6 nm, 0.76 nm, and 0.81 nm, respectively (*Supporting Information,* Table S1). The size and shape of the AC particles differed for the different

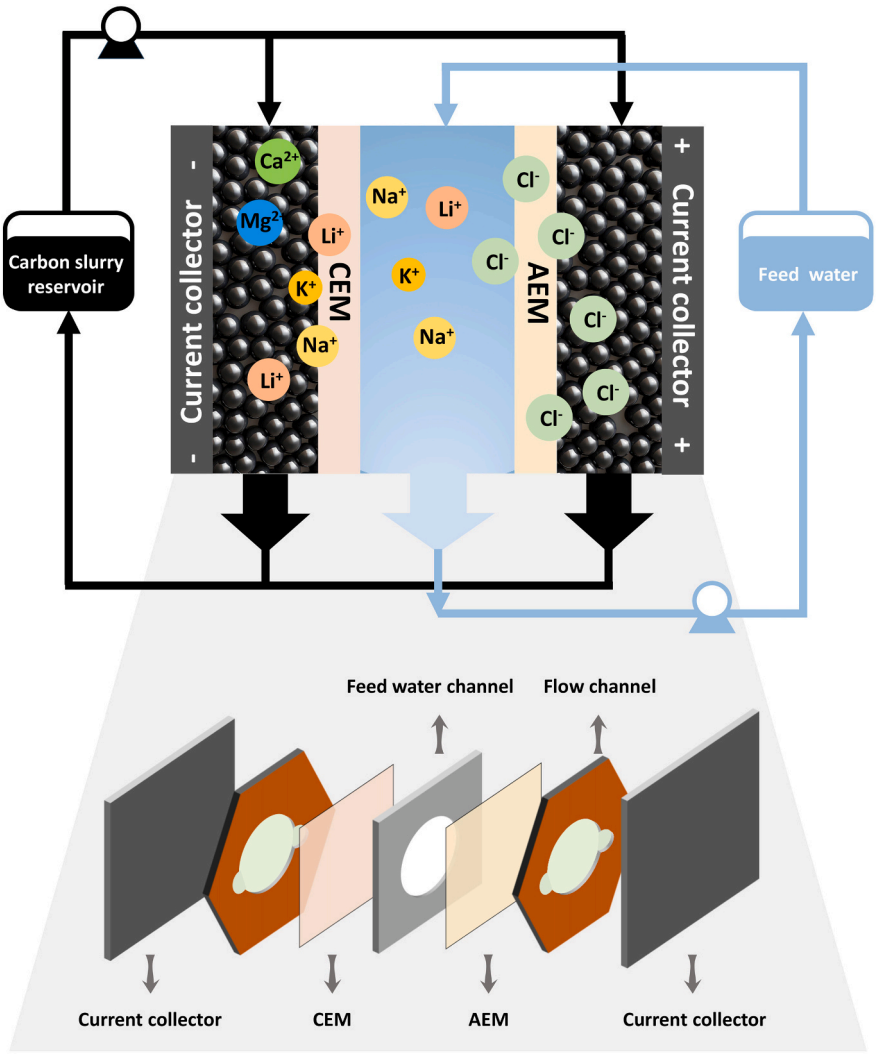

Fig. 1. Schematic illustration of the cell structure of flowable electrode capacitive deionization system, the experimental setup, and the operating principle.

materials. AC1 and AC2 are very similar (*Supporting Information*, Fig. S1A–D), consisting mainly of large, coarse particles tens of micrometers wide and numerous smaller particles. In contrast, AC3 has a relatively large particle compared to those surrounded by debris (*Supporting Information*, Fig. S1F). Scanning electron micrographs of the conductive carbon black additives sample show a finer and smaller particle size (*Supporting Information*, Fig. S1G–H).

A decreasing concentration trend was observed for the three carbons, gradually separating most of the monovalent and multivalent cations from the bulk solution throughout 32 h (Fig. 2A–C). The FCDI system followed the ion removal order of $Ca^{2+} > Mg^{2+} > K^{+} > Na^{+} > Li^{+}$. This order relates to the varied valence and hydration radius of these ions. [16] That is, the ions with higher valency are more effectively removed via ion electrosorption in equilibrium, which is in agreement with the order of the adsorption rate consistently observed in our FCDI system: Ca^{2+} and Mg^{2+} removal exceeded that of K^{+}, Na^{+}, and Li^{+}. [51,52] Three carbon materials also showed different cation separation rates and efficiency due to varied porous features. AC1 showed the fastest cation separation and highest ion removal efficiency, almost completely removing all ionic species after 32 h. Also, AC1 removed nearly 60 % of Li^{+} and 100 % of Ca^{2+} from the solution within 24 h, whereas the Li^{+} removal was 24 % for AC2 (Ca^{2+}: 88 %) and 39 % for AC3 (Ca^{2+}: 86 %) after the same time. Accordingly, the calculated average cation separation rates for AC1 were noticeably higher than the other two carbons, as illustrated in Fig. 2D–F.

When operating the systems for 12 h, the average separation rate of Ca^{2+} (5.7 μg cm^{-2} min^{-1}), Mg^{2+} (2.8 μg cm^{-2} min^{-1}), K^{+} (3.3 μg cm^{-2} min^{-1}), Na^{+} (0.9 μg cm^{-2} min^{-1}) and Li^{+} (0.2 μg cm^{-2} min^{-1}) was shown by AC1 flowable electrode. Within the same duration, AC2 and AC3 showed lower average separation rates. The superior performance of AC1 could be ascribed to its higher pore volume and broader pore size distribution compared to AC2 and AC3 (*Supporting Information*, Fig. S2B). Initially, the removal rate of bivalent cations (Ca^{2+} and Mg^{2+}) for all three carbon electrodes was generally much higher than that of monovalent cations (K^{+}, Na^{+}, and Li^{+}). Then, it decreased with prolonged operation time while more monovalent cations began to be captured. The separation sequence of ions was determined by their valance and hydration radius. The higher charge/hydration size ratio of Ca^{2+} and Mg^{2+} ensured a more sensitive response to the electrical field, facilitating the uptake of these bivalent cations by flow electrode. Among the monovalent cations, K^{+} showed the highest separation rates, attributed to the highest ion mobility for K^{+} compared to Li^{+} and Na^{+}. [53] According to the results above, AC1 was selected for the subsequent optimizations of FCDI system performance.

The effect of the carbon additive was further evaluated with different AC carbons, as displayed in *Supporting Information,* Fig. S3. Although with slight deviations in the viscosity, attributed to the different particle size and arrangement of the aggregated structures, the impact of the different morphologies of each AC over the viscosity indicates a synergistic behavior between AC1 and CB, enabling a more packed flow

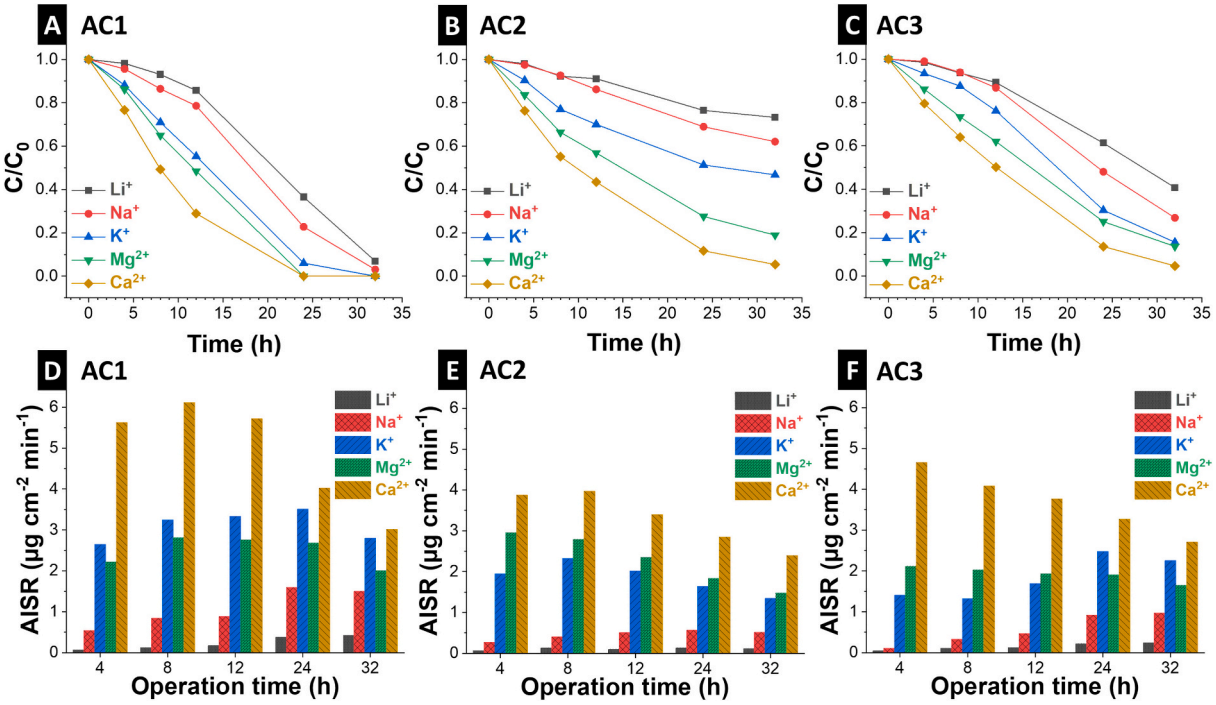

Fig. 2. Ion separation and average ion separation rate of different carbon materials: (A and D) AC1, (B and E) AC2, (C and F) AC3 at a flow rate of 6 mL min^{-1} for flowable electrode and 2 mL min^{-1} for feed water, with 10 mass% of carbon and 1 mass% CB at 1.2 V.

network with higher conductivity, consequently increasing the selectivity factor.

3.2. *Effect of conductive additives and AC mass content*

The FCDI setup, with its flow electrode particles dispersed in the electrolyte solution, inherently limits effective charge transfer between different electrode particles and the solid-liquid interface. Conductive additives such as carbon black are commonly used to increase electrical conductivity, as the added particles act as a conductive bridge between suspended AC particles and the current collector or between different suspended AC particles. [15,54] The carbon black additive is utilized in this study to enhance the performance of poorly conductive suspension electrodes in our FCDI systems. We studied how introducing carbon

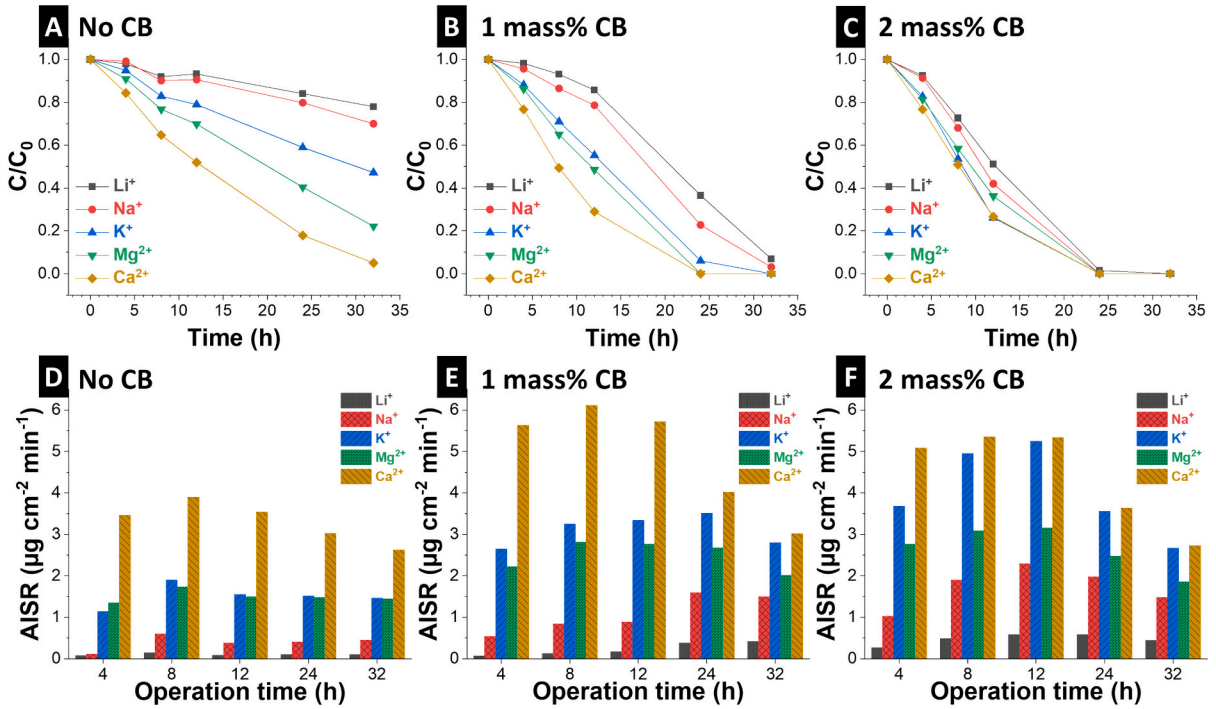

Fig. 3. Ion separation curve and average ion separation rate at different CB content: no carbon black (A, D), 1 mass% CB (B, E), and 2 mass% CB (C, F). For all data, the flow rate was 6 mL min^{-1} for the flowable electrode and 2 mL min^{-1} for the feed water, with a mass loading of 10 mass% AC1.

black as an additive affects the cation selectivity and/or removal rates. To this end, different amounts of carbon black (no addition, 1 mass%, and 2 mass%) were added to the carbon slurry to evaluate the effect of conductive additives on FCDI performance (Fig. 3).

The addition of CB notably facilitated the separation of ions, especially the monovalent cations (Li^+, Na^+, and K^+). This trend was further observed at a high CB content of 2 mass%. With the CB content increasing from 0 mass% to 2 mass%, the average Ca^{2+} separation rate increased from 3.5 μg cm^{-2} min^{-1} to 5.3 μg cm^{-2} min^{-1}, and there was a significant increase from 0.1 μg cm^{-2} min^{-1} to 0.6 μg cm^{-2} min^{-1} (~ 6 times higher than the blank) for Li^+. A similar trend was also observed for the separation profile of Na^+ and K^+, increasing the separation rate from 0.4 μg cm^{-2} min^{-1} and 1.6 μg cm^{-2} min^{-1} to 2.3 μg cm^{-2} min^{-1} and 5.2 μg cm^{-2} min^{-1}, respectively. Additionally, to study whether the CB alone as a conductive agent in the flow electrode can adsorb cations, we tested 1 mass% CB without any AC. As shown in the *Supporting Information*, Fig. S4, having other parameters constant, no significant reduction in ion concentration occurs when the AC is absent in the slurry solution.

Viscosity analysis of the AC1 sample with different CB content (Fig. 4A) demonstrated a shear-thinning, or pseudoplastic, behavior for all the electrodes, indicating a fluid structure with a finite yield stress with a viscosity of 64 mPa•s at a shear rate of 20 s^{-1}. [55,56] Upon adding carbon additive (carbon black), the viscosity increased at the same shear rate, achieving values of 180 mPa•s with 1 % CB and 268 mPa•s with 2 % CB. Simultaneously, the rheological behavior of the samples with the CB additive displayed a rise in the viscosity at 20 s^{-1}, which can be attributed to the agglomeration of carbon particles. [57]

The impact of CB addition is also noted in the selectivity of lithium ions, as presented in Fig. 4B–D. This can be attributed to the packing effect promoted by the different particle sizes of AC1 and CB (*Supporting Information*, Fig. S1A,H), which increased the connectivity and electric conductivity of the flow network while allowing the flow of aqueous media. [58–60] Furthermore, the additive particles increase interactions with the feed water and more friction between the carbon particles, promoting repulsion forces that lead to higher viscosity at low shear rates and facilitate the formation of agglomerates, as observed in 20 s^{-1}. [60–62] As the shear rate increases, the interactions between particles are less effective, hence the drop in viscosity values. [61–63] Besides CB additive effects, AC serves as the active mass content in the slurry that predominantly determines the cation separation performance of our FCDI system. The active electrode material allows charged ions to be captured and stored in its nanostructure by ion electrosorption. In addition, the AC content also dictates the viscosity of electrode slurry, particle density, and, thereby, the slurry channel's conductivity, which could significantly affect operation stability and efficiency. [64] As such, the effect of AC content in the slurry was studied at mass loadings of 5 %, 10 %, and 15 % (Fig. 5).

As observed in Fig. 5A–C, an enhanced ion removal was achieved at higher AC1 mass contents. While only 14 % of Li^+ and 67 % of Ca^{2+} were captured after 36 h operation at a mass loading of 5 %, nearly all the ions were removed at a mass loading of 10 %. Previous reports [4] linked this trend to the decreased charge and ion transfer owing to fewer available electrode sites and particle collision due to reduced viscosity and particle density of the electrode slurry. Although faster ion removals were obtained from 10 mass% to 15 mass% AC1, the latter composition resulted in a very dense slurry and the consequent particle aggregation and clogging issues (*Supporting Information*, Fig. S5) both in the flow

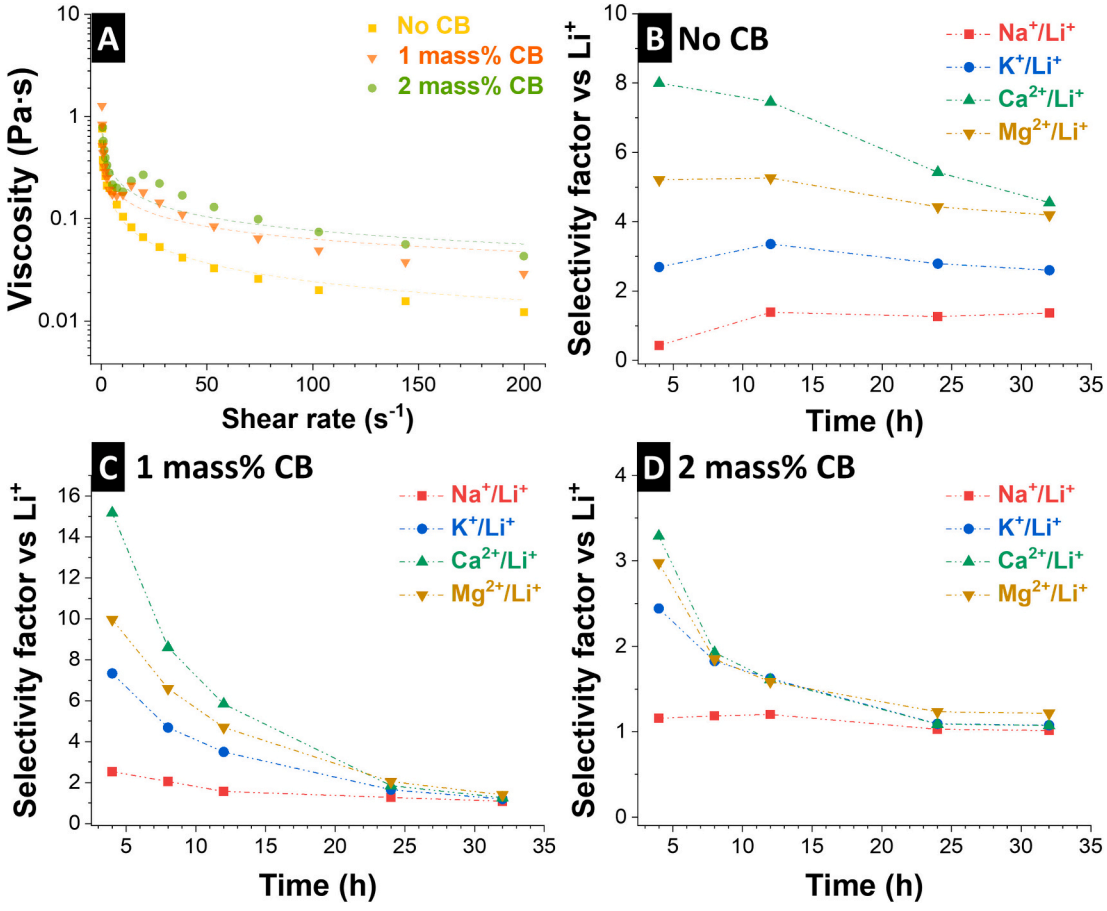

Fig. 4. (A) Rheological behavior of the flowable electrode at three CB contents; Ion selectivity factors at different CB contents of (B) 0 mass% CB, (C) 1 mass% CB, and (D) 2 mass% CB at a flow rate of 6 mL min^{-1} for flowable electrode and 2 mL min^{-1} for feed water, with 10 mass% of AC1 and different CB content at 1.2 V.

channel and tubes. As such, 10 % of the carbon mass was chosen as the highest content feasible for the efficient and stable operation of our FCDI system. So far, various approaches have been reported to address the limitation of flowability with high mass loading, e.g., by oxidizing the active material (increased repulsion between particles) to achieve less aggregation or by mixing two different particle sizes of activated carbon (broadening the particle size distribution) to improve the flowability of the slurry. [59] Additionally, surface-modified AC particles can be used as a dispersant for hydrophobic AC particles in aqueous solutions. [65,66] One can also modify the surface chemical properties of electrode particles to suppress the flow electrode clogging in an FCDI cell.

To better understand the role of the AC1 mass loading, viscosity analysis was performed on electrodes with different mass amounts and the absence of carbon additives (carbon black). The viscosity curves are presented in Fig. 5D, where the pseudoplastic behavior of the carbon electrodes is maintained, although with a broader range of agglomeration at small shear rate values due to the bigger particle sizes of AC1. [59,63] The consistency of slurries is also affected, as shown in Table 1, where the increase in the mass of AC1 with the rise in k (consistency) values indicates a more viscous material. [63,67]

We further investigated the merits of our FCDI system in terms of cation selectivity vs. Li^+ ions. Selectivity profiles (vs. Li^+) of the ions with different carbon black contents were calculated from the data presented in Fig. 3 and plotted in Fig. 4. Gradually reducing selectivity factors of Ca^{2+}, Mg^{2+}, K^+, and Na^+ with respect to Li^+ are observed within the investigated time intervals. Compared to Li^+, other cations were preferentially removed from the bulk solution within the first few hours, with the selectivity order related to the hydrated radius and valency of these cations (Fig. 6). When an electrostatic field is applied, cations (Ca^{2+} and Mg^{2+}) with higher valence charges undergo stronger electrostatic driving force compared to monovalent cation, which causes their faster electrokinetic behavior and migration from bulk solution to slurry channel. [68] Regarding cations with the same valance, ion selectivity will be mainly regulated by the hydrated radius of different cations, which is related to the resistance and mobility of these ions in solution. [69] According to the Stokes-Einstein relation, the self-diffusion coefficient of an ion in water is inversely proportional to its effective radius; [70] an ion with a smaller radius has higher mobility in aqueous solution. The higher mobility and transport kinetic also facilitate ion diffusion into the inner pore structure of carbon particles, causing preferable capture and storage within the pore volume. Bivalent cations Ca^{2+} have a smaller hydrated radius than bivalent Mg^{2+} (4.12 Å vs. 4.28 Å). As a result, Ca^{2+} shows higher transport ability and preferable selectivity compared to Mg^{2+}. Overall, monovalent cations exhibit lower removal rates and selectivity than divalent cations due to valence difference and follow the removal order of $K^+ > Na^+ > Li^+$, which agrees with their hydrated radius difference (*Supporting Information,* Table S2).

During continuous ion removal by flowing electrode, cations are generally adsorbed onto the flowable carbon particles with a negative

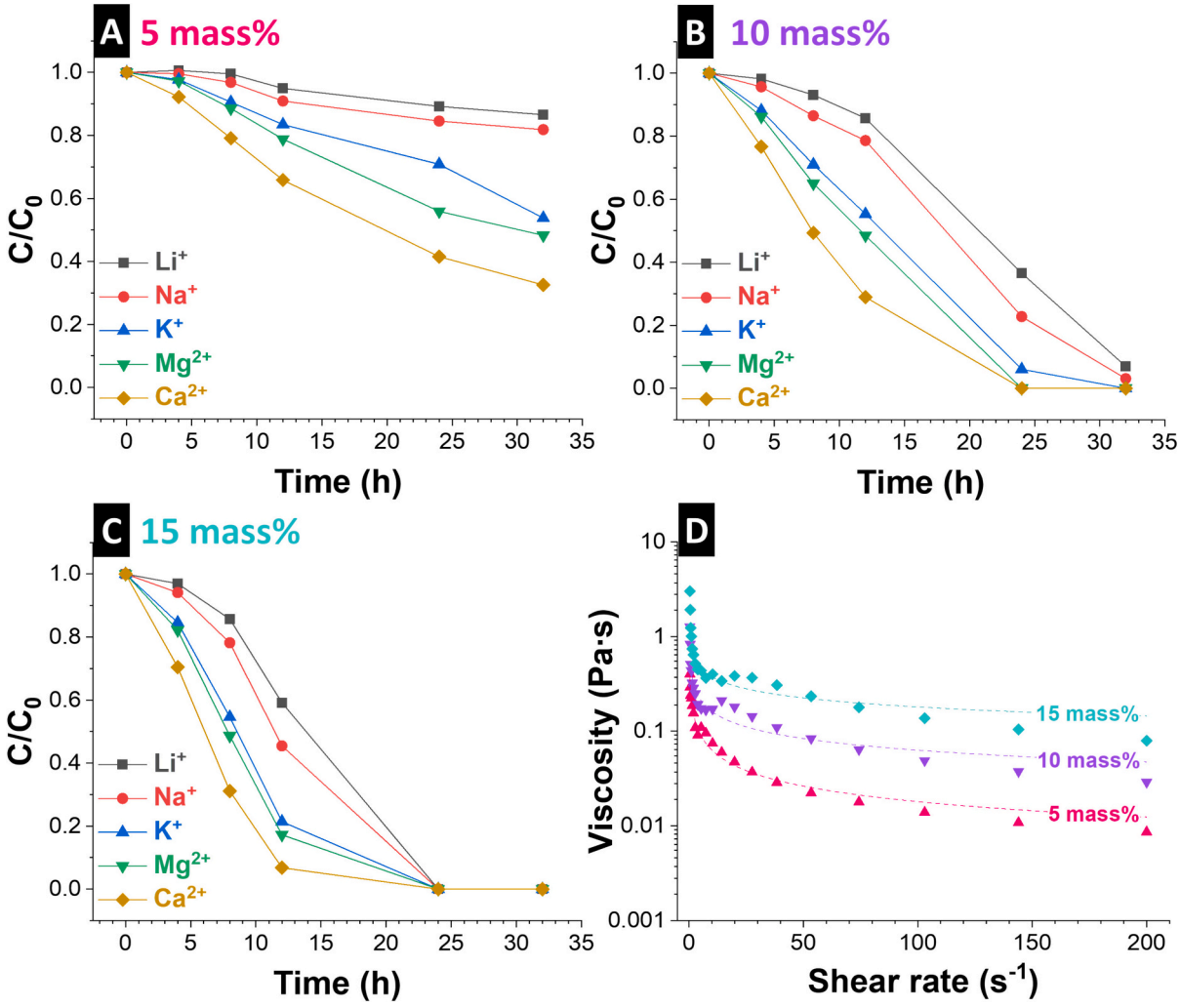

Fig. 5. Ion separation over time of different carbon content: (A) 5 mass%, (B) 10 mass%, and (C) 15 mass%, at a flow rate of 6 mL min^{-1} for flowable electrode and 2 mL min^{-1} for feed water, with 1 mass% CB at 1.2 V. (D) Rheological behavior of the flowable electrode at three AC1 contents (5 mass%, 10 mass%, 15 mass%).

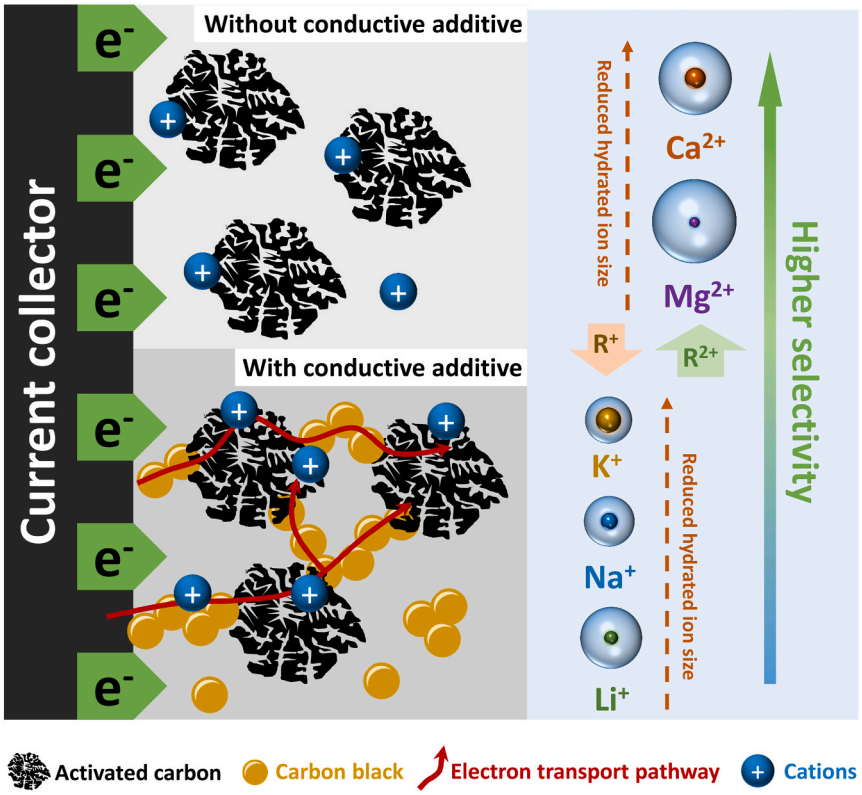

Fig. 6. Schematic illustration of ion separation and selectivity in the FCDI system with and without the addition of carbon black.

charge under the force of an electric field and then carried along with the carbon material into the slurry reservoir by pumping. Since our FCDI system uses the SC mode, these cations will eventually be neutralized by anions (Cl^-) in the slurry reservoir. Hence, bivalent cations are more readily adsorbed on the flowable electrode surface than monovalent cations, resulting in higher electrosorption selectivity as well Regulated by intrinsic hydrated radius and valency, the mobility and transport of investigated cations in aqueous solution vary under the driving force of the electrostatic field, rendering ion removal by flowable electrodes following the consequence of $Ca^{2+} > Mg^{2+} > K^+ > Na^+ > Li^+$. The specific selectivity also comes from the preferable capture and storage of divalent cation on electrode carbon nanopores to screen the negatively charged AC surface. Compared to Li^+, other cations will preferably be removed from the feed at the initial stage. Li^+ remains in the solution, while other cations can be taken up more quickly from the feed. Benefiting from higher residual concentration, Li^+ becomes more competitive, and the dynamic interaction between Li + and electrode surface increases, causing a gradual decrease in ion selectivity with time.

FCDI without carbon black additive, which had the slowest cation separation kinetics (Fig. 3A), exhibited modest selectivity factors of 1.0–5.0 for Ca^{2+}, Mg^{2+}, K^+, and Na^+ vs. Li^+ at the end of experiments. Although adding 1 % or 2 % mass carbon black could largely enhance ion removal kinetics, the cation selectivity factors decrease to below 2. Overall, adding CB could accelerate the migration and uptake of cations, especially monovalent cations Na^+ and Li^+, resulting in low selectivity factors of Ca^{2+}, Mg^{2+}, K^+, and Na^+ versus Li^+. As Li^+ ions possess significantly larger hydration sizes than hydrated Na^+ and K^+ ions, [71] the system exhibits a reduced selectivity toward the uptake of Li^+ ions and, hence, an overall preference for bivalent cations. In this case, conductive carbon black could act as a conductive bridge (Fig. 6) between electrode particles and charged ions and between different electrode particles, [47,72,73] enhancing charge transfer in the solid-electrolyte interface and facilitating electrochemical migration and storage of charged species on electrode materials (Fig. 6). Similarly, Reale et al. reported that the size and mass fraction of conductive additives could affect the effective electronic conductivity, ionic conductivity, and hydraulic permeability of porous electrodes, and increasing any one of these properties could increases salt removal rate at fixed specific energy consumption [74].

Considering ions separation performance, selectivity behavior, and mass loading amount, 1 mass% of carbon black was used in this study as a conductive additive content.

As illustrated by Fig. 2A–C, different types of AC show similar selectivity trends for monovalent and bivalent cations ($Ca^{2+} > Mg^{2+} > K^+ > Na^+ > Li^+$). However, AC1 has a relatively higher affinity toward monovalent cations than AC2, which prefers bivalent cations. The latter is attributed to a broader pore size distribution of AC1 (*Supporting Information*, Fig. S2B). With the same cation concentrations, cations with smaller hydrated radius, for example, K^+ (3.31 Å, *Supporting Information,* Table S2), show a higher selectivity than Li^+ (3.82 Å, *Supporting Information,* Table S2), exhibiting their size-affinity to access the pores in the flowable carbon particles. A similar observation is found for bivalent cations. For example, Ca^{2+} with a smaller hydrated ion size (4.12 Å, *Supporting Information,* Table S2) shows a higher cation selectivity than Mg^{2+} (4.28 Å).

3.3. *Effect of applied voltage*

During FCDI operation, the applied potential bias serves as the driving force that induces the migration of ions from the bulk solution toward the electrode surface. [75] This migration process significantly influences both desalination efficiency and adsorption capacity. In theory, higher voltages result in stronger electrostatic forces. However, the applied voltage in CDI is typically limited to below 1.2 V to prevent faradaic side reactions like water electrolysis when the voltage exceeds 1.23 V. [76] Furthermore, excessive electrostatic forces may cause high mobility of all ions, thereby reducing selectivity toward target ions. As such, the applied voltage is an influential operational parameter that

plays a crucial role in ion migration rates, influencing the overall cation separation performance.

The cation separation behavior of the FCDI system was studied with the applied voltages of 0.4 V, 0.8 V, and 1.2 V, as demonstrated by Fig. 7. Additionally, the applied cell voltage and the current response profiles of the latter 3 tested voltages can be found in *Supporting Information,* Fig. S6. As seen, the overall ion removal performance was very low at 0.4 V, with only 13–68 % of initial ions removed after 32 h operation. In contrast, cation separation (especially monovalent cations) was more effectively accomplished at 0.8 V and 1.2 V. Going from 0.4 V to 0.8 V, the Li^+, Na^+, and K^+ separation performance experienced a notable increase from 14 %, 21 %, and 40 % to 80 %, 84 %, and 98 %, respectively. The Ca^{2+} and Mg^{2+} ions could be entirely removed by the FCDI system already at 0.8 V. The cation separation was further enhanced at 1.2 V, with the removal efficiency of all ions over 93 %. The CE profile at different applied voltages was also enhanced from 63 % to 70 % when the cell voltage increased from 0.4 V to 1.2 V. The energy consumption increased slightly from 0.4 V to 1.2 V, with 40.6 Wh mol^{-1} required to remove all cations from the feed water at 1.2 V (Fig. 7D).

Energy consumption data and the average cation separation rate of the FCDI cell at different conditions were summarized in *Supporting Information,* Table S3. Compared to AC2 and AC3, AC1 could maintain the highest cation separation rate at the end of the experiment with the lowest energy consumption. Adding 1 mass% conductive CB could decrease systematic energy consumption from 49.2 Wh mol^{-1} to 40.6 Wh mol^{-1}, whereas more energy-intensive operation of FCDI was observed when CB content increased to 2 mass%. A similar trend was also observed in the mass loading range of 5–15 mass%, showing that the adjustment of operation parameters is of great significance in improving the energy efficiency of the FCDI system.

3.4. Initial techno-economic analysis

Understanding the economic viability of the FCDI system is crucial for real-world applications in water treatment and resource recovery. [77,78] The primary capital cost of the FCDI cell and infrastructure, including the modules, pumps, power supplies, and control systems, constitutes the major expense for a one-time setup of a pilot-scale system. [79,80] Once the latter is installed, the operational costs encompass material replenishment and energy consumption. The expenses for activated carbon vary greatly based on its quality, which in turn depends on the source of raw material used for its production and its pyrolysis and activation routes. As such, prices as low as ~1 € per kg have been reported for commercial-scale activated carbon production in Africa. [81] For supercapacitor-grade activated carbons, higher costs of 10–15 € per kg can be assumed. Taking a conservative estimate of 15 € per kg for the price of high-performance AC1, the cost for the 4 g used in the slurry solution would be 0.06 €. Since carbon black constituted only a minor part of the slurry solution, it has been neglected in our calculations.

The energy consumption includes the electrical energy invested to charge the system and the pumping energy. As outlined above, the charging energy required to remove cations from the feed solution within 32 h of operation at a cell voltage of 1.2 V is approximately 41 Wh mol^{-1}. Given the volume of feed solution at 80 mL and each salt concentration of 10 mM, this translates to total salt moles of 4 mmol. An energy consumption of 41 Wh mol^{-1} means 0.164 Wh of energy consumed per cycle to remove all the cations from the feed solution.

Given the 32 h of operation of the peristaltic pump with a maximum power of 15 W, the pumping energy is estimated at a maximum of 0.48 kWh. As the charging energy is negligible compared to the latter pumping energy, the overall electricity consumption depends on the pumping at 0.48 kWh per cycle. Assuming an average electricity price in Germany in the second half of 2023 (0.402 € per kWh, Eurostat 04/2024) for household consumers, the pumping energy consumption

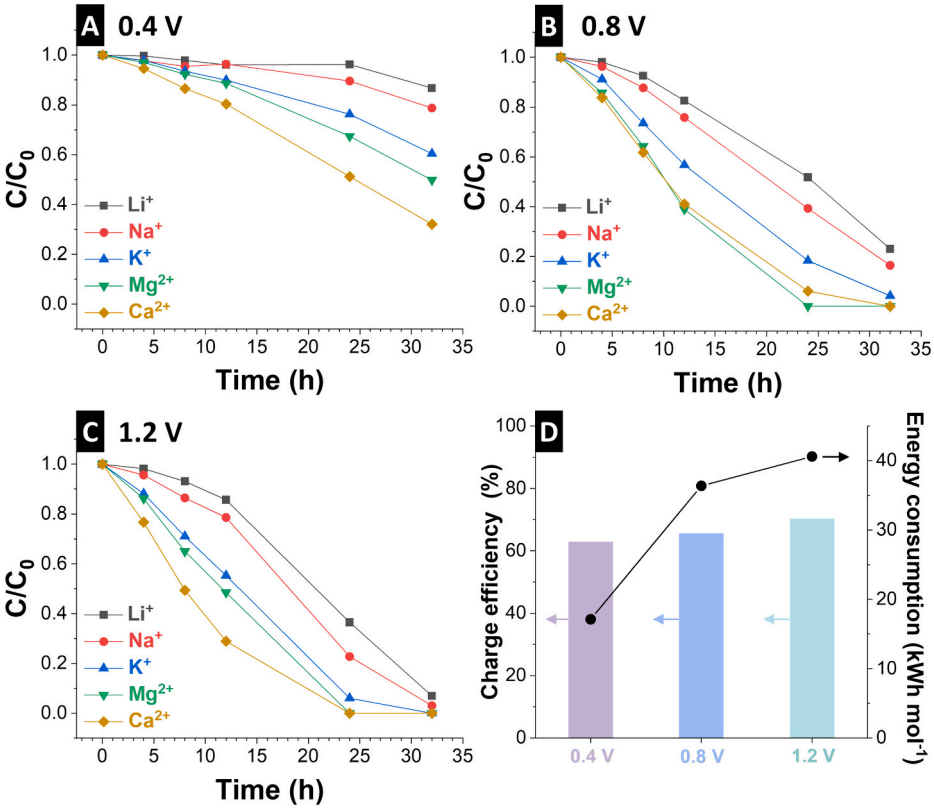

Fig. 7. Ion separation at (A) 0.4 V, (B) 0.8 V, and (C) 1.2 V applied potential at a flow rate of 6 mL min^{-1} for flow electrode and 2 mL min^{-1} for feed water, with 10 mass% of AC1 and 1 mass% CB. (D) Charge efficiency and energy consumption at different cell voltages.

would translate to around 0.19 € and almost half of that for non-household (such as industrial) consumers. In total, the material cost of 0.06 € and energy consumption of 0.19 € sum up to 0.25 € per cycle. The latter value is estimated for our laboratory-scale setup, assuming no energy recovery during discharging in a parallel system and that each carbon slurry is discarded after one charge. As the FCDI technology scales and matures, these costs could significantly decrease, making FCDI a more competitive and sustainable option for large-scale water treatment and resource recovery applications.

3.5. Effect of slurry and feed flow rate

In the last step to optimizing the FCDI system operation, we turned to the flow rate of electrode slurry and feed water to examine their potential impacts on the ion removal performance. Generally, a higher feed water flow rate promotes more ion accessibility toward the electrode surface in CDI, causing ions to be captured by electrode material to reach saturation more rapidly. [82] However, an excessively high flow rate could impede effective contact and interaction between ions and electrode surface, reducing adsorption capacity and desalination efficiency. [75] Hence, it is crucial to balance the cation separation efficiency and energy consumption (for pumping) when aiming for optimal ion removal through solution flow rate adjustments. As such, we investigated the flow rate as another influential parameter for our FCDI system by varying the slurry and feed flow rates and measuring the cation separation performance.

By keeping a constant feed flow rate of 2 mL min^{-1} and varying the slurry flow rate from 6 mL min^{-1} to 12 mL min^{-1} (Fig. 8A–B), no noticeable change was observed for the cation separation profiles of different ions. Further boosting the slurry flow rate to 24 mL min^{-1} also barely resulted in performance enhancements. As such, a slurry flow rate of 6 mL min^{-1} is chosen as an optimum value for further tests. The lower flow rate is also associated with lower pumping energy, minimizing the operational cost and energy consumption for potential scaling-up applications. The negligible effect of increased slurry flow rate on the cation separation could indicate that the ion migration and mobility on the slurry side are not rate-determining stages. Upon applying an electric field, the critical process and rate-controlling step will be the migration of charged ions from the feed's bulk solution side to the electrode channel through the cation exchange membrane. This is seen from the significant changes in ion separation profiles induced by varying feed flow rates (Fig. 8D–F).

By keeping the slurry flow rate constant at 6 mL min^{-1} and reducing the flow rate of feed water from 2 mL min^{-1} to 1 mL min^{-1}, the overall removal performance of ions, especially bivalent cations Ca^{2+} and Mg^{2+} decreased notably, which could be leveraged to adjust the ion selectivity performance of the FCDI system. For instance, at the operation time of 12 h, calculated selectivity factors of bivalent Ca^{2+} and Mg^{2+} ions versus Li^{+} were 1.4 and 1.9, respectively, for a feed rate of 1 mL min^{-1}. In contrast, the selectivity factors of Ca^{2+} and Mg^{2+} vs. Li^{+} were 5.8 and 4.7, respectively, at a feed rate of 2 mL min^{-1}. Increasing the feed water flow rate from 2 mL min^{-1} to 4 mL min^{-1} decreased the overall ion removal performance kinetics, corresponding to fewer ions transported from the feed channel to the slurry side due to the shorter retention time of feed water in the cell.

4. Conclusions

This study highlights FCDI for continuous cation separation from water. Our work evaluated a set of different activated carbon materials together with various contents of carbon additives as flowable electrodes. In addition, various operational parameters, including cell voltage and feed water flow rate and slurry, were investigated to optimize the FCDI ion sorption performance toward a multi-ion salt solution (Li^{+}, Na^{+}, K^{+}, Ca^{2+}, Mg^{2+}). The bivalent Ca^{2+} and Mg^{2+} ions were preferentially removed with faster kinetics due to their higher charge-to-size ratio, followed by K^{+}, Na^{+}, and Li^{+} in the order of their hydrated ion sizes. The optimum operational parameters for our FCDI system were identified: flow rate of electrode slurry at 6 mL min^{-1} and feed water at 2 mL min^{-1}, with 10 mass% activated carbon and 1 mass% carbon black at a cell voltage of 1.2 V. The system achieved average ion separation rates ranging from 5.7 μg cm^{-2} min^{-1} for Ca^{2+} to 0.2 μg cm^{-2} min^{-1} for

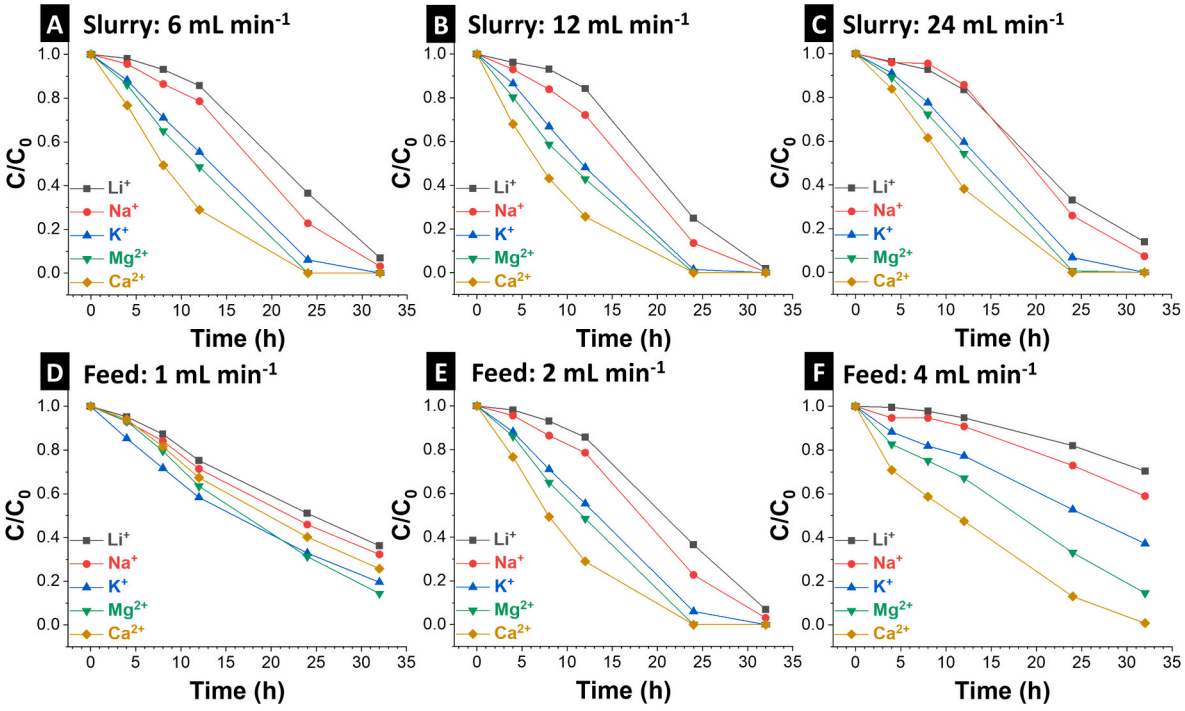

Fig. 8. Ion separation curves at varied slurry flow rates: (A) 6 mL min^{-1}, (B) 12 mL min^{-1}, and (C) 24 mL min^{-1}, with feed flow rate fixed at 2 mL min^{-1}; Ion separation curves at different flow rates of feed water: (D) 1 mL min^{-1}, (E) 2 mL min^{-1} and (F) 4 mL min^{-1}, with the flow rate of slurry fixed at 6 mL min^{-1}.

Li^+. An average energy consumption of ~41 Wh mol^{-1} was shown to be required to remove almost all the cations in the feed solution within 32 h of operation, which occurred at a cell voltage of 1.2 V with the highest charge efficiency of 70 %. We further showed how the adjustment of each operational parameter (except for slurry flow rate) could be leveraged to induce selectivity toward specific ions. In our experiments, we have seen the lowest uptake for lithium ions in competition with other monovalent cations or bivalent cations. This can be used to pre-treat, for example, hydrothermal water or hydrometallurgical battery recycling leaching solutions so that ions other than lithium ions are stripped to obtain an effluent stream with higher lithium ion contents. Overall, the findings contribute to the understanding and insights into FCDI technology and its potential application in sustainable water treatment and resource recovery efforts.

CRediT authorship contribution statement

Panyu Ren: Investigation, Data curation, Visualization, Writing – original draft, Writing – review & editing. **Bin Wang:** Investigation, Data curation, Visualization, Writing – original draft, Writing – review & editing. **Jean Gustavo de Andrade Ruthes:** Investigation, Data curation, Visualization, Writing – original draft, Writing – review & editing. **Mohammad Torkamanzadeh:** Investigation, Data curation, Visualization, Writing – original draft, Writing – review & editing. **Volker Presser:** Conceptualization, Supervision, Validation, Resources, Visualization, Writing – original draft, Writing – review & editing, Project administration, Funding acquisition.

Declaration of competing interest

The authors declare the following financial interests/personal relationships which may be considered as potential competing interests: Volker Presser reports financial support was provided by German Research Foundation. If there are other authors, they declare that they have no known competing financial interests or personal relationships that could have appeared to influence the work reported in this paper.

Data availability

Raw data are available upon request from the corresponding author.

Acknowledgments

We acknowledge funding of the SELECT project (PR 1173/33) by the German Research Foundation (DFG, Deutsche Forschungsgemeinschaft). B.W. acknowledges funding from the China Scholarship Council (CSC) via award number 202206270142.

Appendix A. Supplementary data

Supplementary data to this article can be found online at https://doi.org/10.1016/j.desal.2024.118161.

References

[1] M.A. Shannon, P.W. Bohn, M. Elimelech, J.G. Georgiadis, B.J. Mariñas, A. M. Mayes, Science and technology for water purification in the coming decades, Nature 452 (7185) (2008) 301–310.
[2] A.N. Shocron, R.S. Roth, E.N. Guyes, R. Epsztein, M.E. Suss, Comparison of ion selectivity in electrodialysis and capacitive deionization, Environ. Sci. Technol. Lett. 9 (11) (2022) 889–899.
[3] Z. Sahray, A.N. Shocron, R. Uwayid, C.E. Diesendruck, M.E. Suss, Extreme monovalent ion selectivity via capacitive ion exchange, Water Res. 246 (2023) 120684.
[4] S.-J. Seo, H. Jeon, J.K. Lee, G.-Y. Kim, D. Park, H. Nojima, J. Lee, S.-H. Moon, Investigation on removal of hardness ions by capacitive deionization (CDI) for water softening applications, Water Res. 44 (7) (2010) 2267–2275.
[5] H.H. Kyaw, M.T.Z. Myint, S. Al-Harthi, M. Al-Abri, Removal of heavy metal ions by capacitive deionization: effect of surface modification on ions adsorption, J. Hazard. Mater. 385 (2020) 121565.
[6] L. Xu, C. Yu, Y. Mao, Y. Zong, B. Zhang, H. Chu, D. Wu, Can flow-electrode capacitive deionization become a new in-situ soil remediation technology for heavy metal removal? J. Hazard. Mater. 402 (2021) 123568.
[7] R. Chen, T. Sheehan, J.L. Ng, M. Brucks, X. Su, Capacitive deionization and electrosorption for heavy metal removal, Environmental Science: Water Research & Technology 6 (2) (2020) 258–282.
[8] L. Wang, S. Arnold, P. Ren, Q. Wang, J. Jin, Z. Wen, V. Presser, Redox flow battery for continuous and energy-effective lithium recovery from aqueous solution, ACS Energy Lett. 7 (10) (2022) 3539–3544.
[9] A.A.M. Abusultan, J.A. Wood, T. Sainio, A.J.B. Kemperman, W.G.J. van der Meer, Ion exchange resin - bipolar membrane electrodialysis hybrid process for reverse osmosis permeate remineralization: preparative ion exchange chromatography for $C^{a2}{}_+$ and Mg^{2+} recovery, Sep. Purif. Technol. 317 (2023) 123799.
[10] M. Hafiz, R. Alfahel, A. Altaee, A.H. Hawari, Techno-economic assessment of forward osmosis as a pretreatment process for mitigation of scaling in multi-stage flash seawater desalination process, Sep. Purif. Technol. 309 (2023) 123007.
[11] S.B. Rauer, S. Wang, N. Köller, D.J. Bell, Y. Zhang, X. Wang, C.J. Linnartz, M. Wessling, J. Linkhorst, PEDOT:PSS-CNT composite particles overcome contact resistances in slurry electrodes for flow-electrode capacitive deionization, Adv. Funct. Mater. 33 (38) (2023) 2303606.
[12] L. Wang, Y. Zhang, K. Moh, V. Presser, From capacitive deionization to desalination batteries and desalination fuel cells, Curr. Opin. Electrochem. 29 (1) (2021) 100758.
[13] J.G. Gamaethiralalage, K. Singh, S. Sahin, J. Yoon, M. Elimelech, M.E. Suss, P. Liang, P.M. Biesheuvel, R.L. Zornitta, L.C.P.M. de Smet, Recent advances in ion selectivity with capacitive deionization, Energ. Environ. Sci. 14 (3) (2021) 1095–1120.
[14] J.W. Blair, G.W. Murphy, Electrochemical Demineralization of Water with Porous Electrodes of Large Surface Area, Saline Water Conversion, American Chemical Society1960, pp. 206–223.
[15] P. Ren, M. Torkamanzadeh, X. Zhang, M. Twardoch, C. Kim, V. Presser, Conductive carbon additives: friend or foe of capacitive deionization with activated carbon? Carbon 213 (2023) 118191.
[16] Y. Zhang, P. Ren, L. Wang, E. Pameté, S. Husmann, V. Presser, Selectivity toward heavier monovalent cations of carbon ultramicropores used for capacitive deionization, Desalination 542 (2022) 116053.
[17] Q. Dong, X. Guo, X. Huang, L. Liu, R. Tallon, B. Taylor, J. Chen, Selective removal of lead ions through capacitive deionization: role of ion-exchange membrane, Chem. Eng. J. 361 (2019) 1535–1542.
[18] Y. Sun, Y. Su, Z. Zhao, J. Zhao, M. Ye, X. Wen, Capacitive heavy metal ion removal of 3D self-supported nitrogen-doped carbon-encapsulated titanium nitride nanorods via the synergy of faradic-reaction and electro-adsorption, Chem. Eng. J. 443 (2022) 136542.
[19] T.K.A. Nguyen, N.T.N. Anh, M.D. Nguyen, V.T. Nguyen, R.-a. Doong, Boosting capacitive deionization of monovalent and hardness ions using Ti3C2Tx MXene as an intercalation-type pseudocapacitive electrode, Sep. Purif. Technol. 327 (2023) 124934.
[20] Y. Xu, S. Xiang, H. Zhou, G. Wang, H. Zhang, H. Zhao, Intrinsic pseudocapacitive affinity in manganese spinel ferrite nanospheres for high-performance selective capacitive removal of Ca^{2+} and Mg^{2+}, ACS Appl. Mater. Interfaces 13 (32) (2021) 38886–38896.
[21] W. Deng, Y. Chen, Z. Wang, X. Chen, M. Gao, F. Chen, W. Chen, T. Ao, Regulation, quantification and application of the effect of functional groups on anion selectivity in capacitive deionization, Water Res. 222 (2022) 118927.
[22] M.E. Suss, S. Porada, X. Sun, P.M. Biesheuvel, J. Yoon, V. Presser, Water desalination via capacitive deionization: what is it and what can we expect from it? Energ. Environ. Sci. 8 (8) (2015) 2296–2319.
[23] Y. Gendel, A.K.E. Rommerskirchen, O. David, M. Wessling, Batch mode and continuous desalination of water using flowing carbon deionization (FCDI) technology, Electrochem. Commun. 46(0) (2014) 152–156.
[24] S.I. Jeon, H.R. Park, J.G. Yeo, S. Yang, C.H. Cho, M.H. Han, D.K. Kim, Desalination via a new membrane capacitive deionization process utilizing flow-electrodes, Energ. Environ. Sci. 6 (5) (2013) 1471–1475.
[25] C. Kim, P. Srimuk, J. Lee, M. Aslan, V. Presser, Semi-continuous capacitive deionization using multi-channel flow stream and ion exchange membranes, Desalination 425 (2018) 104–110.
[26] L. Zhang, R. Feng, W. Wang, G. Yu, Emerging chemistries and molecular designs for flow batteries, Nat. Rev. Chem. 6 (8) (2022) 524–543.
[27] A. Rommerskirchen, Y. Gendel, M. Wessling, Single module flow-electrode capacitive deionization for continuous water desalination, Electrochem. Commun. 60 (2015) 34–37.
[28] A. Rommerskirchen, C.J. Linnartz, F. Egidi, S. Kendir, M. Wessling, Flow-electrode capacitive deionization enables continuous and energy-efficient brine concentration, Desalination 490 (2020) 114453.
[29] J. Ma, L. Chen, F. Yu, Environmental applications and perspectives of flow electrode capacitive deionization (FCDI), Sep. Purif. Technol. 335 (2024) 126095.
[30] J. Ma, C.X. Zhai, F. Yu, Review of flow electrode capacitive deionization technology: research progress and future challenges, Desalination 564 (2023) 116701.
[31] B. Xie, Q. Liu, C. Hu, H. Li, G. Tan, D. Xiao, Enhanced desalination performance in flow electrode capacitive deionization with nitrogen doped porous carbon, New J. Chem. 47 (18) (2023) 8625–8637.

[32] C. He, J. Ma, C. Zhang, J. Song, T.D. Waite, Short-circuited closed-cycle operation of flow-electrode CDI for brackish water softening, Environ. Sci. Technol. 52 (16) (2018) 9350–9360.
[33] N. Köller, M. Perrey, L.K. Brückner, P. Schäfer, S. Werner, C.J. Linnartz, M. Wessling, Comparison of current collector architectures for flow-electrode capacitive deionization, Desalination 582 (2024) 117595.
[34] J. Oladunni, J.H. Zain, A. Hai, F. Banat, G. Bharath, E. Alhseinat, A comprehensive review on recently developed carbon based nanocomposites for capacitive deionization: from theory to practice, Sep. Purif. Technol. 207 (2018) 291–320.
[35] P. Sivasubramanian, M. Kumar, V.S. Kirankumar, M.S. Samuel, C.D. Dong, J. H. Chang, Capacitive deionization and electrosorption techniques with different electrodes for wastewater treatment applications, Desalination 559 (2023) 116652.
[36] X. Zhang, K. Zuo, X. Zhang, C. Zhang, P. Liang, Selective ion separation by capacitive deionization (CDI) based technologies: a state-of-the-art review, Environmental Science: Water Research & Technology 6 (2) (2020) 243–257.
[37] E.N. Guyes, A.N. Shocron, Y. Chen, C.E. Diesendruck, M.E. Suss, Long-lasting, monovalent-selective capacitive deionization electrodes, npj clean, Water 4 (1) (2021) 22.
[38] M.E. Suss, Size-based ion selectivity of micropore electric double layers in capacitive deionization electrodes, J. Electrochem. Soc. 164 (9) (2017) E270.
[39] R. Uwayid, E.N. Guyes, A.N. Shocron, J. Gilron, M. Elimelech, M.E. Suss, Perfect divalent cation selectivity with capacitive deionization, Water Res. 210 (2022) 117959.
[40] P. Srimuk, X. Su, J. Yoon, D. Aurbach, V. Presser, Charge-transfer materials for electrochemical water desalination, ion separation and the recovery of elements, Nat. Rev. Mater. 5 (7) (2020) 517–538.
[41] Y. Xu, H. Zhou, G. Wang, Y. Zhang, H. Zhang, H. Zhao, Selective pseudocapacitive deionization of calcium ions in copper hexacyanoferrate, ACS Appl. Mater. Interfaces 12 (37) (2020) 41437–41445.
[42] K. Singh, G. Li, J. Lee, H. Zuilhof, B.L. Mehdi, R.L. Zornitta, L.C.P.M. de Smet, Divalent ion selectivity in capacitive deionization with vanadium hexacyanoferrate: experiments and quantum-chemical computations, Adv. Funct. Mater. 31 (41) (2021) 2105203.
[43] Y. Gao, L. Pan, H. Li, Y. Zhang, Z. Zhang, Y. Chen, Z. Sun, Electrosorption behavior of cations with carbon nanotubes and carbon nanofibres composite film electrodes, Thin Solid Films 517 (5) (2009) 1616–1619.
[44] X. Zhang, F. Yang, J. Ma, P. Liang, Effective removal and selective capture of copper from salty solution in flow electrode capacitive deionization, Environ. Sci.: Water Res. Technol. 6 (2) (2020) 341–350.
[45] L. Xu, C. Yu, S. Tian, Y. Mao, Y. Zong, X. Zhang, B. Zhang, C. Zhang, D. Wu, Selective recovery of phosphorus from synthetic urine using flow-electrode capacitive deionization (FCDI)-based technology, ACS ES&T Water 1 (1) (2021) 175–184.
[46] T.M. Khoi, N.A.T. Tran, H.B. Jung, V.P. Huynh, Y. Kim, J. Hong, C.-Y. Yoo, H. S. Kang, Y. Cho, Selective and continuous ion recovery using flow electrode capacitive deionization with polymer multilayers functionalized ion exchange membrane, Desalination 558 (2023) 116626.
[47] C. Zhang, J. Ma, L. Wu, J. Sun, L. Wang, T. Li, T.D. Waite, Flow electrode capacitive deionization (FCDI): recent developments, environmental applications, and future perspectives, Environ. Sci. Technol. 55 (8) (2021) 4243–4267.
[48] D. Moreno, M.C. Hatzell, Influence of feed-electrode concentration differences in flow-electrode Systems for Capacitive Deionization, Ind. Eng. Chem. Res. 57 (26) (2018) 8802–8809.
[49] S. Yang, J. Choi, J.-g. Yeo, S.-i. Jeon, H.-r. Park, D.K. Kim, Flow-electrode capacitive deionization using an aqueous electrolyte with a high salt concentration, Environ. Sci. Technol. 50(11) (2016) 5892–5899.
[50] M. Torkamanzadeh, C. Kök, P.R. Burger, P. Ren, Y. Zhang, J. Lee, C. Kim, V. Presser, Best practice for electrochemical water desalination data generation and analysis, Cell Reports Physical Science 4 (11) (2023) 101661.
[51] Z. Chen, H. Zhang, C. Wu, Y. Wang, W. Li, A study of electrosorption selectivity of anions by activated carbon electrodes in capacitive deionization, Desalination 369 (2015) 46–50.
[52] H. Li, L. Zou, L. Pan, Z. Sun, Using graphene nano-flakes as electrodes to remove ferric ions by capacitive deionization, Sep. Purif. Technol. 75 (1) (2010) 8–14.
[53] S.H. Lee, J.C. Rasaiah, Molecular dynamics simulation of ion mobility. 2. Alkali metal and halide ions using the SPC/E model for water at 25 °C, J. Phys. Chem. 100 (4) (1996) 1420–1425.
[54] S. Nadakatti, M. Tendulkar, M. Kadam, Use of mesoporous conductive carbon black to enhance performance of activated carbon electrodes in capacitive deionization technology, Desalination 268 (1) (2011) 182–188.
[55] A. Carmona-Orbezo, R.A.W. Dryfe, Understanding the performance of flow-electrodes for capacitive deionization through hydrodynamic voltammetry, Chem. Eng. J. 406 (2021) 126826.
[56] B. Akuzum, P. Singh, D.A. Eichfeld, L. Agartan, S. Uzun, Y. Gogotsi, E.C. Kumbur, Percolation characteristics of conductive additives for capacitive flowable (semi-solid) electrodes, ACS Appl. Mater. Interfaces 12 (5) (2020) 5866–5875.
[57] C.L. Barrie, P.C. Griffiths, R.J. Abbott, I. Grillo, E. Kudryashov, C. Smyth, Rheology of aqueous carbon black dispersions, J. Colloid Interface Sci. 272 (1) (2004) 210–217.
[58] Y. Wang, R.H. Ewoldt, New insights on carbon black suspension rheology - anisotropic thixotropy and antithixotropy, Journal of Rheology 66 (5) (2022) 937–953.
[59] M. Tauk, M. Bechelany, S. Lagerge, P. Sistat, R. Habchi, M. Cretin, F. Zaviska, Influence of particle size distribution on carbon-based flowable electrode viscosity and desalination efficiency in flow electrode capacitive deionization, Sep. Purif. Technol. 306 (2023) 122666.
[60] A. Narayanan, F. Mugele, M.H.G. Duits, Mechanical history dependence in carbon black suspensions for flow batteries: a rheo-impedance study, Langmuir 33 (7) (2017) 1629–1638.
[61] H. Hou, C.C. Sun, Quantifying effects of particulate properties on powder flow properties using a ring shear tester, J. Pharm. Sci. 97 (9) (2008) 4030–4039.
[62] G. Barthelmes, S.E. Pratsinis, H. Buggisch, Particle size distributions and viscosity of suspensions undergoing shear-induced coagulation and fragmentation, Chem. Eng. Sci. 58 (13) (2003) 2893–2902.
[63] J.B. Hipp, J.J. Richards, N.J. Wagner, Structure-property relationships of sheared carbon black suspensions determined by simultaneous rheological and neutron scattering measurements, J. Rheol. 63 (3) (2019) 423–436.
[64] G. Folaranmi, M. Tauk, M. Bechelany, P. Sistat, M. Cretin, F. Zaviska, Investigation of fine activated carbon as a viable flow electrode in capacitive deionization, Desalination 525 (2022) 115500.
[65] H.-r. Park, J. Choi, S. Yang, S.J. Kwak, S.-i. Jeon, M.H. Han, D.K. Kim, Surface-modified spherical activated carbon for high carbon loading and its desalting performance in flow-electrode capacitive deionization, RSC Adv. 6(74) (2016) 69720–69727.
[66] J. Lee, D. Weingarth, I. Grobelsek, V. Presser, Use of surfactants for continuous operation of aqueous electrochemical flow capacitors, Energ. Technol. 4 (1) (2016) 75–84.
[67] K.B. Hatzell, M.C. Hatzell, K.M. Cook, M. Boota, G.M. Housel, A. McBride, E. C. Kumbur, Y. Gogotsi, Effect of oxidation of carbon material on suspension electrodes for flow electrode capacitive deionization, Environ. Sci. Technol. 49 (5) (2015) 3040–3047.
[68] L. Firdaous, J.P. Malériat, J.P. Schlumpf, F. Quéméneur, Transfer of monovalent and divalent cations in salt solutions by Electrodialysis, Sep. Sci. Technol. 42 (5) (2007) 931–948.
[69] Y. Marcus, Ionic radii in aqueous solutions, Chem. Rev. 88 (8) (1988) 1475–1498.
[70] R.W. Impey, P.A. Madden, I.R. McDonald, Hydration and mobility of ions in solution, J. Phys. Chem. 87 (25) (1983) 5071–5083.
[71] J. Luo, S. Ye, T. Li, E. Sarnello, H. Li, T. Liu, Distinctive trend of metal binding affinity via hydration shell breakage in nanoconfined cavity, J. Phys. Chem. C 123 (23) (2019) 14825–14833.
[72] K. Tang, S. Yiacoumi, Y. Li, C. Tsouris, Enhanced water desalination by increasing the electroconductivity of carbon powders for high-performance flow-electrode capacitive deionization, ACS Sustainable Chemistry & Engineering 7 (1) (2019) 1085–1094.
[73] I. Hwang, D. Lee, Y. Jung, K. Park, Y.-G. Jung, D. Kim, G.-H. Cho, S.-i. Jeon, Y.-k. Byeun, U. Paik, S. Yang, T. Song, Cross effect of surface area and electrical conductivity for carbonaceous materials in flow-electrode capacitive mixing (F-CapMix) and flow-electrode capacitive deionization (FCDI): solid-like behavior of flow-electrode, ACS Sustain. Chem. Eng. 9(40) (2021) 13514–13525.
[74] E.R. Reale, A. Shrivastava, K.C. Smith, Effect of conductive additives on the transport properties of porous flow-through electrodes with insulative particles and their optimization for faradaic deionization, Water Res. 165 (2019) 114995.
[75] S. Chai, J. Xi, L. Chen, W. He, J. Shen, H. Gong, Selective ion removal by capacitive deionization (CDI)-based technologies, Processes 10 (6) (2022) 1075.
[76] M. Torkamanzadeh, L. Wang, Y. Zhang, Ö. Budak, P. Srimuk, V. Presser, MXene/activated-carbon hybrid capacitive deionization for permselective ion removal at low and high salinity, ACS Appl. Mater. Interfaces 12 (23) (2020) 26013–26025.
[77] S. Porada, D. Weingarth, H.V.M. Hamelers, M. Bryjak, V. Presser, P.M. Biesheuvel, Carbon flow electrodes for continuous operation of capacitive deionization and capacitive mixing energy generation, J. Mater. Chem. A 2 (24) (2014) 9313–9321.
[78] Y.-U. Shin, J. Lim, C. Boo, S. Hong, Improving the feasibility and applicability of flow-electrode capacitive deionization (FCDI): review of process optimization and energy efficiency, Desalination 502 (2021) 114930.
[79] E. Guillén-Burrieza, D.-C. Alarcón-Padilla, P. Palenzuela, G. Zaragoza, Techno-economic assessment of a pilot-scale plant for solar desalination based on existing plate and frame MD technology, Desalination 374 (2015) 70–80.
[80] N. Köller, L. Mankertz, S. Finger, C.J. Linnartz, M. Wessling, Towards pilot scale flow-electrode capacitive deionization, Desalination 572 (2024) 117096.
[81] R. Kayiwa, H. Kasedde, M. Lubwama, J.B. Kirabira, The potential for commercial scale production and application of activated carbon from cassava peels in Africa: a review, Bioresource Technology Reports 15 (2021) 100772.
[82] Y. Zhang, P. Ren, Y. Liu, V. Presser, Particle size distribution influence on capacitive deionization: insights for electrode preparation, Desalination 525 (2022) 115503.

Supporting Information

Cation selectivity during flow electrode capacitive deionization

Panyu Ren,[1,2] Bin Wang,[1,2] Jean Gustavo de Andrade Ruthes,[1,2]

*Mohammad Torkamanzadeh,[1] Volker Presser[1,2,3]**

[1] INM - Leibniz Institute for New Materials, Campus D2 2, 66123, Saarbrücken, Germany

[2] Department of Materials Science & Engineering, Saarland University, Campus D2 2, 66123, Saarbrücken, Germany

[3] saarene - Saarland Center for Energy Materials and Sustainability, Campus C4 2, 66123 Saarbrücken, Germany

* Corresponding authors: volker.presser@leibniz-inm.de (VP)

Supporting Tables

Table S1: Specific surface area of used powder materials, quenched solid density functional theory specific surface area (QSDFT SSA), average pore size, and total pore volume.

Material	QSDFT SSA ($m^2 g^{-1}$)	Average pore size (nm)	Pore volume ($cm^3 g^{-1}$)
YP-80F	2253	1.6	1.4
YP-50F	1807	0.76	0.84
MSP-20	2140	0.81	0.94
CB	235	2.14	0.28

Table S2. Hydrated radius and ion radius of different cations used in this work.

Cation	Hydrated radius (Å)	Ion radius (Å)	Hydration ratio	Reference
Li^+	3.82	0.6	6.37	[1]
Na^+	3.58	0.95	3.77	[1]
K^+	3.31	1.33	2.49	[1]
Ca^{2+}	4.12	0.99	4.16	[1]
Mg^{2+}	4.28	0.65	6.58	[1]

Table S3. Energy consumption in FCDI for ion (Li^+, Na^+, K^+, Ca^{2+}, and Mg^{2+}) separation at a flow rate of 6 mL min^{-1} for flow electrode and 2 mL min^{-1} for feed water

Carbon content	Carbon black content	Cell voltage	Average ion separation rate for 32 h (μmol cm^{-2} min^{-1})	Energy consumption (Wh mol^{-1})
10 mass% AC1	1 mass%	1.2 V	3.6	40.6
10 mass% AC2	1 mass%	1.2 V	1.9	53.9
10 mass% AC3	1 mass%	1.2 V	2.7	51.1
10 mass% AC1	0 mass%	1.2 V	3.4	49.2
10 mass% AC1	2 mass%	1.2 V	2.0	49.6
5 mass% AC1	1 mass%	1.2 V	0.6	49.9
15 mass% AC1	1 mass%	1.2 V	3.6	48.2
10 mass% AC1	1 mass%	0.8 V	3.3	36.4
10 mass% AC1	1 mass%	0.4 V	1.4	17.1

Supporting Figures

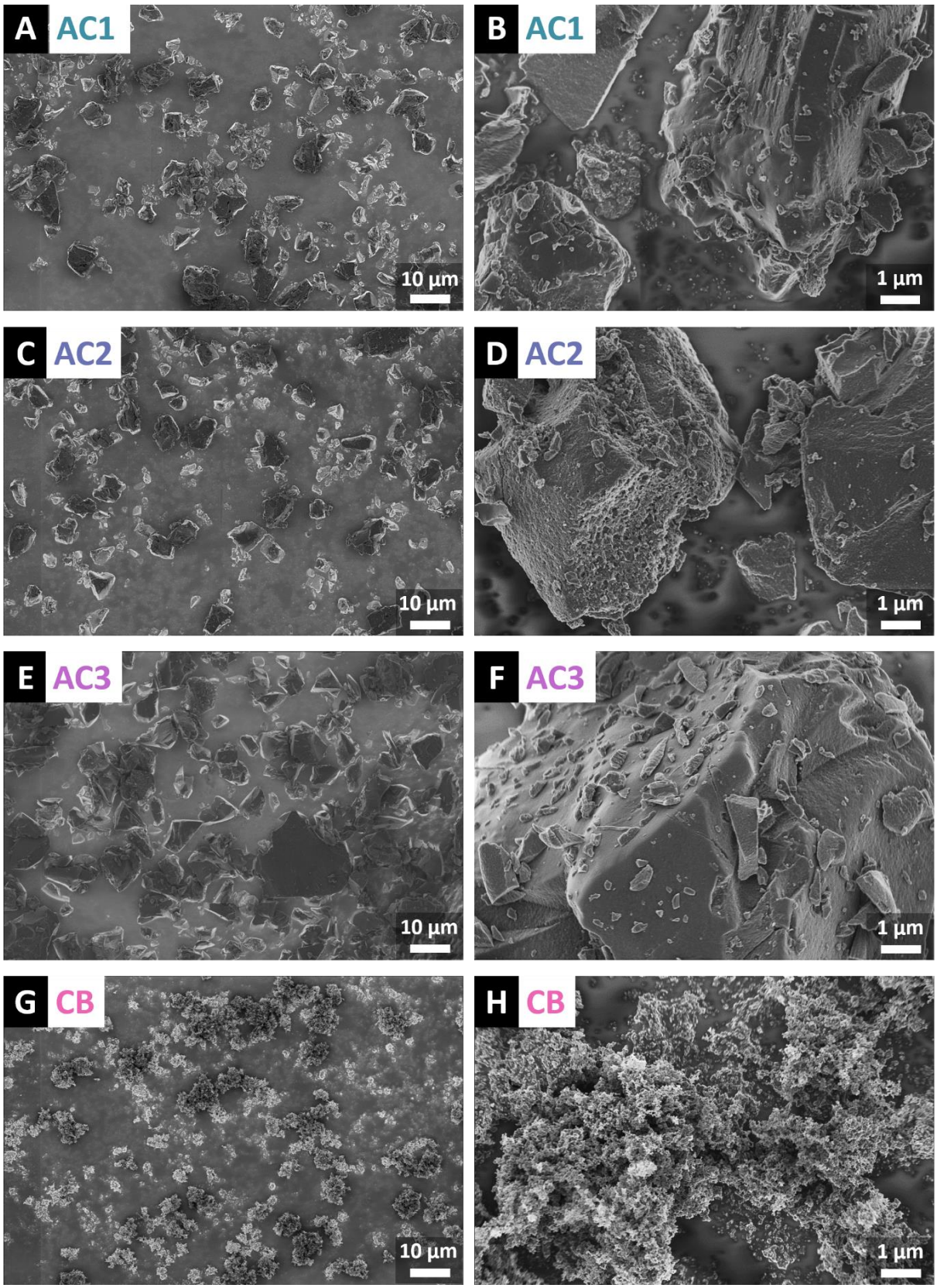

Fig. S1: Scanning electron micrographs of used carbon materials. (A-B) AC1, (C-D) AC2, (E-F) AC3, (G-H) CB.

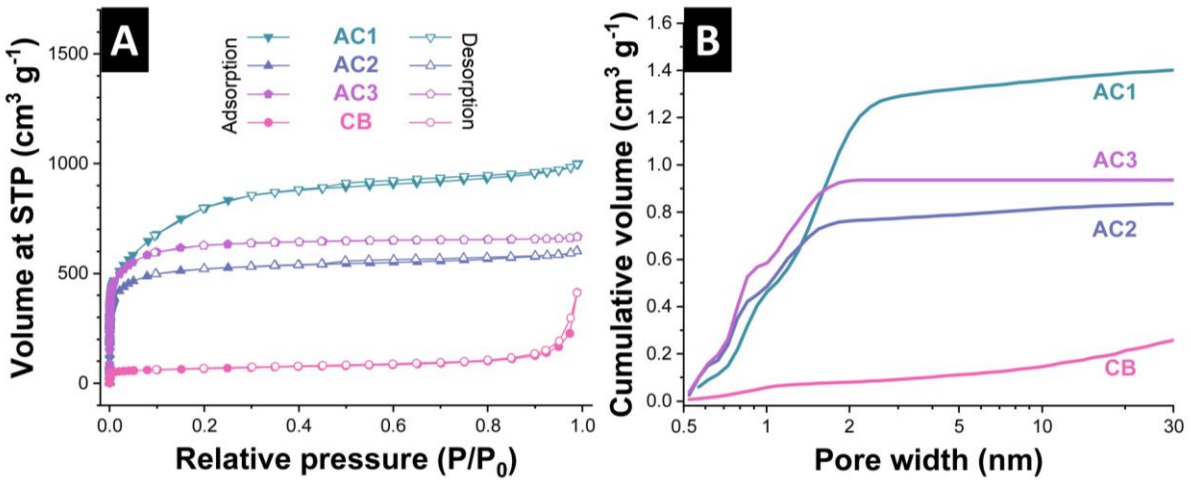

Fig. S2: Nitrogen sorption isotherms (A) of the carbon materials and the corresponding quenched-solid density functional (QSDFT) derived cumulative pore volume distributions assuming slit-shaped pores (B).

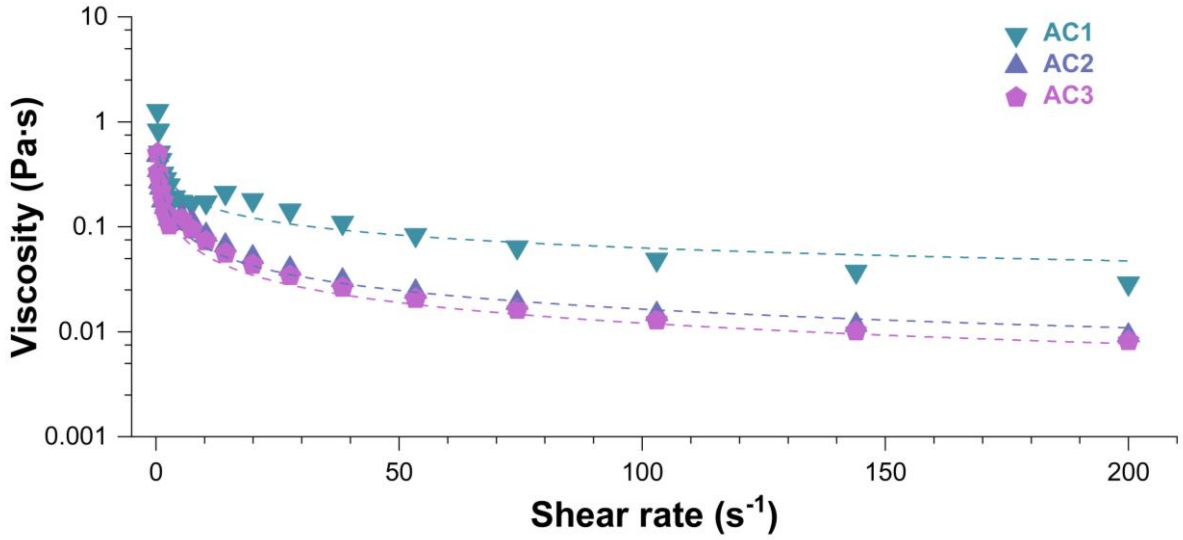

Fig. S3: Rheological behavior of capacitive flowable electrode of 10 mass% of AC1, AC2, and AC3 with 1 mass% CB.

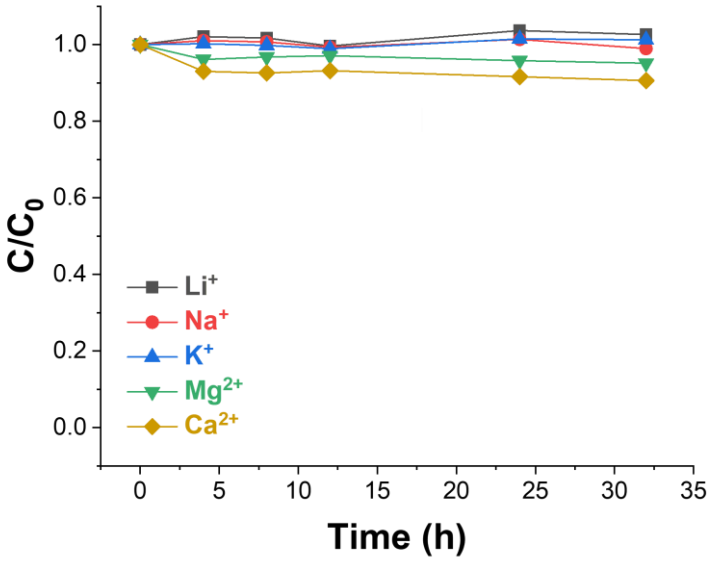

Fig. S4: Ion separation curve of 1 mass% CB at a flow rate of 6 mL min^{-1} for flowable electrode and 2 mL min^{-1} for feed water at 1.2 V.

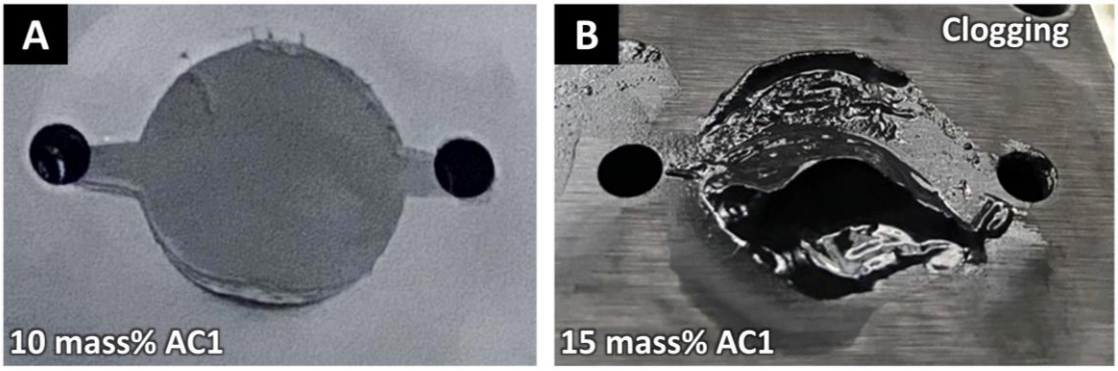

Fig. S5: Photographs of the flow channel after 36 h operation with (A) 10 mass% AC1 and (B) 15 mass% AC1 (clogging).

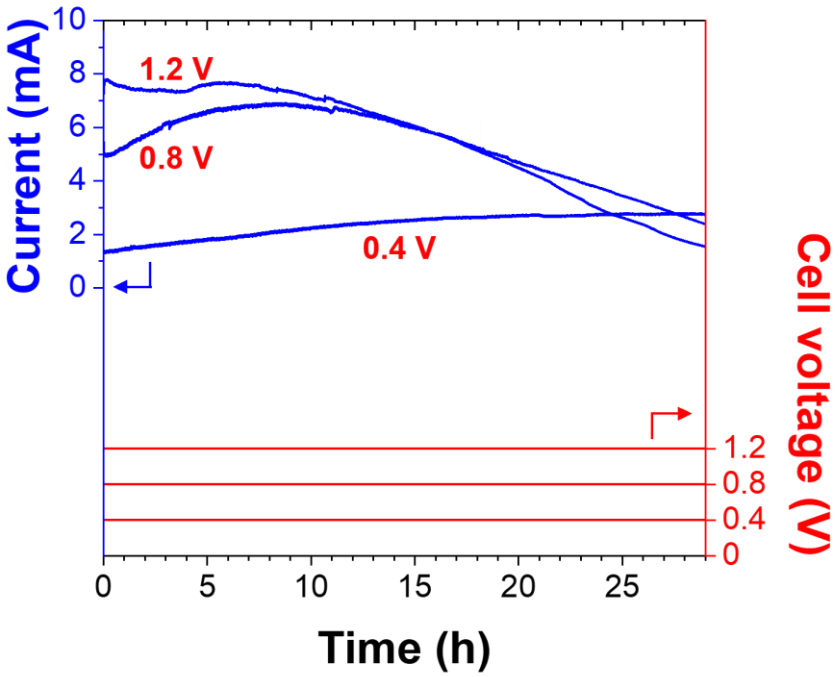

Fig. S6: Applied cell voltage and the current response profiles of the 3 tested cell voltages at 0.4 V, 0.8 V, and 1.2 V.

Supporting Reference

[1] E.R. Nightingale, Jr., Phenomenological Theory of Ion Solvation. Effective Radii of Hydrated Ions, The Journal of Physical Chemistry 63(9) (1959) 1381-1387.

4.6. Redox flow battery for continuous and energy-effective lithium recovery from aqueous solution

Lei Wang,[1,2] Stefanie Arnold,[1,2] Panyu Ren,[1,2] Qingsong Wang,[1]

Jun Jin,[3] Zhaoyin Wen,[3,4] and Volker Presser[1,2,5]

[1] *INM - Leibniz Institute for New Materials, 66123 Saarbrücken, Germany*

[2] *Department of Materials Science and Engineering, Saarland University, 66123 Saarbrücken, Germany*

[3] *CAS Key Laboratory of Materials for Energy Conversion Shanghai Institute of Ceramics, Chinese Academy of Sciences, Shanghai, 200050 P. R. China*

[4] *State Key Lab of High Performance Ceramics and Superfine Microstructure, Shanghai Institute of Ceramics, Chinese Academy of Sciences, Shanghai, 200050 P. R. China*

[5] *saarene, Saarland Center for Energy Materials and Sustainability, Campus C4 2, 66123 Saarbrücken, Germany*

Citation:

L. Wang, S. Arnold, P. Ren, Q. Wang, J. Jin, Z. Wen, and V. Presser, Redox Flow Battery for Continuous and Energy-Effective Lithium Recovery from Aqueous Solution, ACS Energy Letters 7 (2022) 3539-3544.

Own contribution:

Investigation, and writing-review & editing.

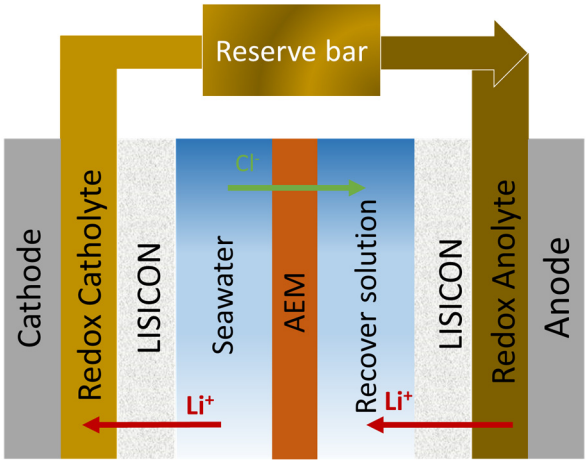

ACS Energy LETTERS

http://pubs.acs.org/journal/aelccp

Redox Flow Battery for Continuous and Energy-Effective Lithium Recovery from Aqueous Solution

Lei Wang, Stefanie Arnold, Panyu Ren, Qingsong Wang, Jun Jin, Zhaoyin Wen,* and Volker Presser*

Cite This: *ACS Energy Lett.* 2022, 7, 3539–3544

Read Online

ACCESS | Metrics & More | Article Recommendations | Supporting Information

ABSTRACT: **Lithium-ion batteries are the primary power source for electric vehicles and portable electronic devices, creating a massive demand to mine and extract lithium. So far, lithium extraction has focused on brine and geological deposits. Yet, access to the enormous amount of lithium (at low concentration) in the earth's oceans and other aqueous media remains challenging. Electrodialysis with Li-selective ceramic membranes could effectively separate lithium from seawater but at a high energy cost. Reversible electrochemical processes, like redox flow batteries, can overcome the limitation of electrodialysis-based systems. Herein we propose a system combining Li-selective ceramic membranes and a simple redox flow electrolyte to accomplish continuous lithium recovery from seawater. The lithium-extraction redox flow battery (LE-RFB) extracts dissolved lithium with a purity of 93.5% from simulated seawater, corresponding to a high Li/Mg selectivity factor of about 500.000:1. Benefiting from a low operating voltage, 1 g of lithium is extracted with only 2.5 Wh of energy consumption.**

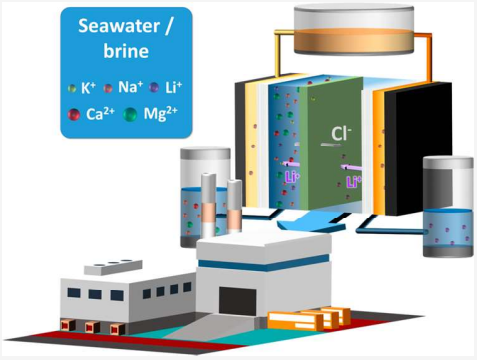

With the universal usage of portable electronic equipment and electric vehicles, the demand for lithium-ion batteries has increased tremendously.[1] This sharply increasing consumption would result in a complete depletion of terrestrial lithium before this century is over.[2] Thereby, it is crucial to find alternative lithium reservoirs and environmentally friendly ways for lithium extraction. Apart from recycling lithium from abandoned lithium-ion batteries, seawater is another available lithium reserve containing 230 billion tons of lithium.[3] However, the low lithium concentration (around 0.17 mg_{Li}/L on average) and high concentration of other competing cations, like Na^+ and Mg^{2+}, bring tremendous challenges to extracting lithium from seawater.[3,4] So far, several approaches, such as coprecipitation,[5] sorption,[6] liquid–liquid extraction,[7] membrane processes,[8] and electrochemical methods,[9,10] have been adapted to recover lithium from seawater.[11] However, coprecipitation, liquid–liquid extraction, and sorbent regeneration require many chemicals and are energy-costly and time-consuming.[12] In addition, while membrane-based processes can continuously extract lithium, this technology suffers from the low selectivity factor of the commercial membranes.[13]

Electrochemical methods are an energy-efficient approach with relatively high selectivity toward Li^+, as recent studies show. For example, Joo et al. used an electrode pair of λ-MnO_2 and AgCl to treat the actual desalination of concentrated seawater on a pilot scale.[14] After the enrichment, the purity of Li^+ increased from 0.0048 to 88%.[14] In another example, an electrolysis-based technique was proposed to extract lithium from seawater utilizing a solid-state lithium superionic conductor membrane (LISICON membrane).[2] On the cathode side, elemental lithium metal was formed, while the Cl_2 or O_2 was produced in the anode area. However, the electrochemical methods have not yet been able to perform continuous lithium recovery with the typical cell configuration (i.e., a lithium-capture electrode + a chloride-capture electrode or a cation-release electrode).[15,16] Kim et al. proposed a hybrid system with a redox flow battery system and lithium-selective adsorbent.[17] In this system, the water can be continuously desalinated, while the lithium recovery process is not continuous. Meanwhile, the regeneration of adsorbents consumes acid. Recently, Li et al.[18] put forward a continuous electrical pump membrane process, where a $Li_{0.33}La_{0.56}TiO_3$

Received: August 2, 2022
Accepted: September 14, 2022
Published: September 23, 2022

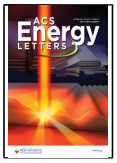

https://doi.org/10.1021/acsenergylett.2c01746
ACS Energy Lett. 2022, 7, 3539–3544

membrane accomplished the selective extraction of lithium; the catalytic reactions occurred on the cathode and anode sides formed the driven force for lithium migration. After the treatment, the lithium concentration increased from 0.2 mg/L to 9 g/L. However, due to the high voltage, the energy consumption to enrich 1 kg of lithium is about 76 kWh. With humankind striving for more sustainable technologies, there is a high demand for an economical approach with continuous operation, a high selectivity factor, and low energy consumption for the large-scale lithium extraction from the seawater.

This work reports an innovative electrochemical cell configuration for continuously recovering lithium from seawater. Our system strives toward low-cost materials and environmental friendliness. The lithium-extraction redox flow battery (LE-RFB) uses a redox pair electrolyte ($Fe[CN]_6^{4-}$/$Fe[CN]_6^{3-}$) and operates at a low applied voltage of just 600 mV for continuous lithium extraction. The LE-RFB shows an excellent selectivity toward Li^+ with a low energy consumption of 2.5 $Wh/g_{Li\text{-}extraction}$. We also demonstrate the universal usage of this system with various lithium concentrations from seawater (ca. 0.17 mg/L) to lithium-rich brines (>1000 mg/L).

The LE-RFB cell contains four channels: one recovery-solution channel, one feedwater channel, and two redox-electrolyte channels (Figure 1A; Experimental Methods, Table S1, and Figure S1 in Supporting Information). The recovery-solution channel and the feedwater channel are each separated from the redox-electrolyte channels by a LISICON membrane. A polymer anion exchange membrane localized between the recovery-solution and feedwater channels serves to separate different compartments. During operation, the charging process results in the enrichment of lithium in the recovery-solution channel and the uptake of lithium from the feedwater channel. The ferricyanide is reduced to the ferrocyanide in the cathode area, drawing one cation (i.e., Li^+, on the basis of the selectivity of LISICON membrane) from the feedwater channel into the redox-electrolyte reservoir. At the other end, the ferrocyanide in the anode area is oxidized into ferricyanide, releasing lithium into the recovery solution through the LISICON membrane. Simultaneously, the Cl^- will migrate through the anion exchange membrane to keep the charge balanced. The reactions in the anolyte and catholyte are shown as follows. These reactions are continuously ongoing because the initial redox electrolyte contains equimolar ferricyanide and ferrocyanide, and with this continuous circulation, the uptaken Li^+ is continuously brought from the catholyte through the redox-electrolyte reservoir to the anolyte.

$$K_3[Fe(CN)_6] + Li^+ + e^- \rightarrow K_3Li[Fe(CN)_6] \quad \text{catholyte reaction}$$

$$K_3Li[Fe(CN)_6] \rightarrow K_3[Fe(CN)_6] + Li^+ + e^- \quad \text{anolyte reaction}$$

As the core component of the LE-RFB system, the LISICON membrane plays the role of selectively uptaking and releasing Li^+. The LISICON membrane used in this work consists of $Li_{1+x}Al_xGe_{2-x}(PO_4)_3$ (x = 0.5, LAGP), prepared by a solid-state-reaction method as reported previously[19,20] and as described in the Experimental Methods in the Supporting Information. Cross-sectional scanning electron micrographs confirm the presence of a dense membrane, having a thickness of about 500 μm without cracks (Figure 1B). The grain size of the particles ranges from 100 nanometers to several micrometers (Figure 1C), similar to that in the reported work.[21] The energy-dispersive X-ray mapping results (Supporting Information, Figure S2) also suggest that the distribution of elements is uniform, indicating the membrane is very homogeneous. LAGP is a superionic conductor with lower energy barriers for the migration of Li^+ compared to other cations[21] and superior stability in aqueous media[22,23] (Figure 1D). The crystal structure of the membrane was verified using the XRD pattern of the LISICON membrane, which is consistent with the standard pattern of $LiGe_2(PO_4)_3$ (Figure 1D). There is a small reflection at 20.7° 2θ, which aligns with trace amounts of $AlPO_4$, the common impurity of the LAGP ceramic membrane.[24] The Li^+ conductivity of the LAGP membrane is around 1.2 × 10^{-4} S cm^{-1}, calculated according to the impedance results in the Supporting Information, Figure S3.

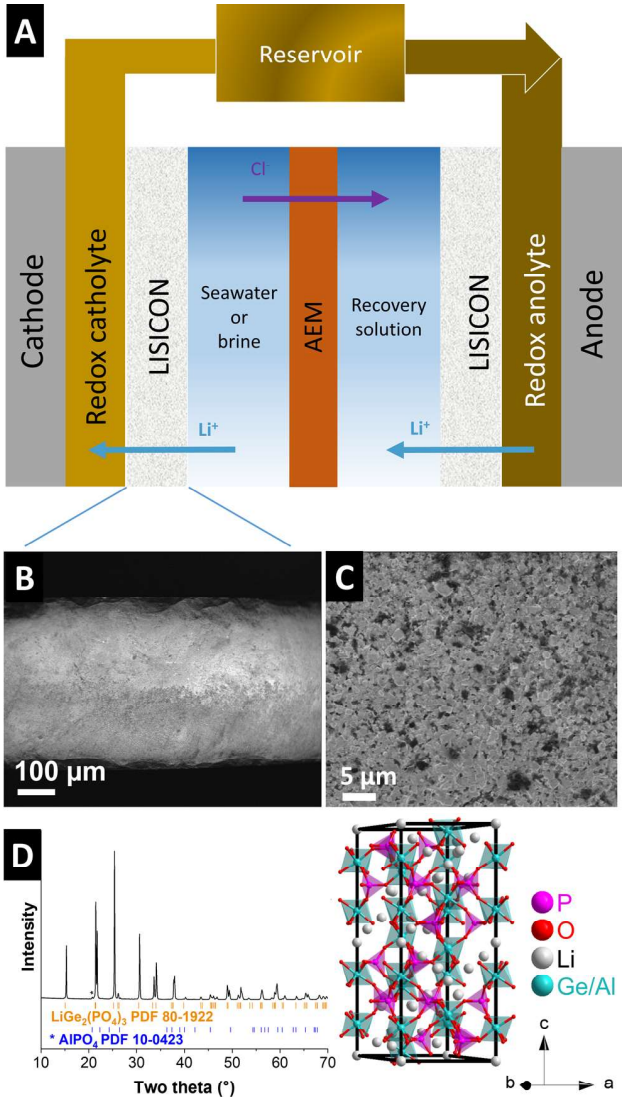

Figure 1. (A) The schematic images of a lithium-extraction redox flow battery. Cross-sectional scanning electron micrograph of the LISICON membrane at (B) low and (C) high magnification. (D) X-ray diffraction patterns of the LISICON membrane and the structure of $Li_{1+x}Al_xGe_{2-x}(PO_4)_3$; the crystal structure is based on ref 40.

To demonstrate the feasibility and investigate the performance of the LE-RFB system, we first explored LE-RFB for Li^+

https://doi.org/10.1021/acsenergylett.2c01746
ACS Energy Lett. 2022, 7, 3539−3544

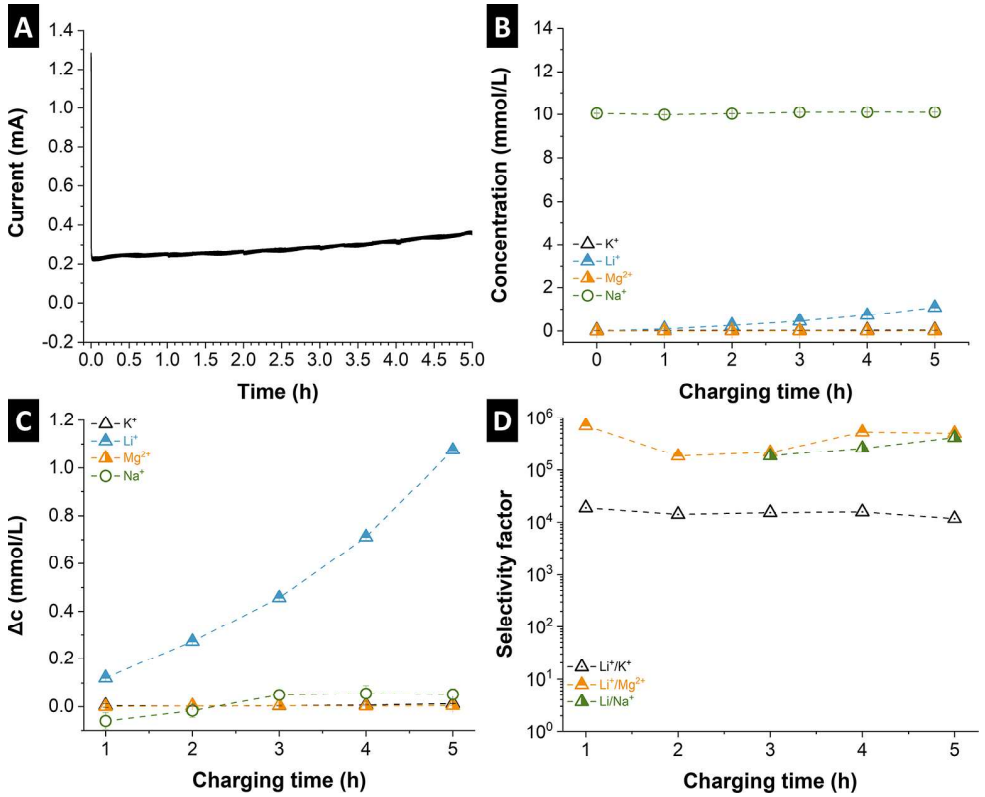

Figure 2. Lithium extraction from seawater by a lithium-extraction redox flow battery: (A) current curve, (B) concentration, (C) concentration change of cations in the recovery solution, and (D) selectivity factors between Li^+ and other cations at different times.

extraction in simulated seawater (24 μM Li^+; see Tables S1 and S2 in the Supporting Information). Figure 2A shows the trend of current change with increasing charging time. When the cell is charged at 0.6 V, the current increases from 0.22 to 0.36 mA. This is linked to the rise of the lithium-ion concentration in the recovery solution (Figure 2B), which also lowers the system resistance. In contrast to the Li^+ concentration, the other cations only change slightly. The concentration of Ca^{2+} is below the detection limit and is, therefore, not displayed. For better visualization of the cation concentration changes, we calculated the differences between the concentration at different charging times and the initial concentration of the recovery solution, as shown in Figure 2C. As it can be seen, the concentration of Li^+ increases by 1.07 ± 0.06 mM after a 5 h enrichment, while the concentrations of K^+, Na^+, and Mg^{2+} are $1.3 \times 10^{-2} \pm 1.1 \times 10^{-3}$ mM, $5.1 \times 10^{-2} \pm 2.4 \times 10^{-2}$ mM, and $5.0 \times 10^{-3} \pm 6.2 \times 10^{-5}$ mM, respectively.

To confirm that the enriched Li^+ originated from the feedwater and not from the Li^+ in the redox electrolyte, we measured the concentration of all the cations in the redox electrolyte (Supporting Information, Table S1). The Li^+ concentration in the redox electrolyte remains stable at a concentration of 9.35−9.37 mM, concluding that Li^+ in the recovery solution comes, indeed, just from the feedwater. Additionally, pH values of the redox electrolyte were continuously controlled to stay between 6 and 7 before and after the lithium recovery experiment. This is a crucial benefit for redox couples that can achieve better functioning with outstanding electrochemical stability.[25]

The LE-RFB system shows excellent selectivity of Li^+ toward other cations. The selectivity factors of $K_{Li/K}$, $K_{Li/Na}$, and $K_{Li/Mg}$ after the 5 h enrichment are 1.2×10^4, 4.1×10^5, and 5.0×10^5, respectively (Figure 2D). These extremely high selectivities yield a Li^+ purity of 93.5% in the extract. Mg^{2+}, which strongly influences the chemical precipitation of Li^+, is present at a ratio of 0.43% (Supporting Information, Figure S4). The absence of $K_{Li/Na}$ at 1 and 2 h is due to the concentration change at these two data points being less than the standard error.

Much higher Li^+ concentrations than in seawater can be found, for example, in brines. Subsequently, we used brine with a Li^+ concentration of 210 mM (see Table S2 in Supporting Information) to demonstrate that the LE-RFB system is suitable for lithium extraction from a low to a high concentration. When brine is used as the feedwater, the amount of Mg^{2+} (0.21%) in the extracts is similar. In contrast, more K^+ and Na^+ (accounting for 4.48 and 30.7%, respectively) migrate into the recovery solution (Supporting Information, Figure S5). This may indicate a gradual reduction in membrane selectivity over time due to the changes in structure, composition, and inhomogeneous mechanical stress.[26,27]

The lithium-extraction rate and energy consumption are other important parameters to evaluate the system's performance. The average lithium-extraction rate of LE-RFB is 0.04 mg/cm^2/h, which is comparable to other technologies for Li^+ extraction from seawater (Figure 3).[18,28−30] However, only 2.5 Wh is consumed for extracting 1 g of Li^+, which is at least 7 times lower than the electrodialysis-based technologies, which show a similar lithium purification effect (Figure 3). Considering the global average cost of the electricity fee (0.13 US$ per kWh), the energy cost of this system would at least save 2.2 US$ to extract 1 kg of lithium ions from seawater.

https://doi.org/10.1021/acsenergylett.2c01746
ACS Energy Lett. 2022, 7, 3539−3544

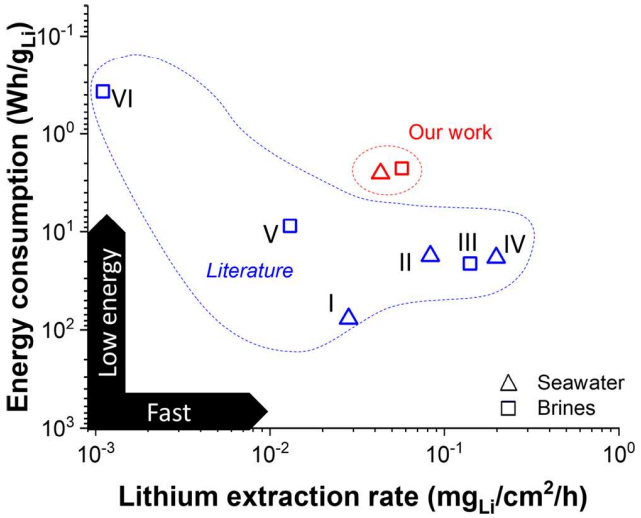

Figure 3. Comparison of lithium-extraction energy consumption and lithium-extraction rate for different extraction technologies. Data I, II, III, IV, V, and VI from refs 18, 29, 30, 28, 41, and 15, respectively.

This phenomenon is due to the low voltage of the system. Concerning lithium extraction from brines, our LE-RFB system is also energy efficient with the consumption of 2.3 Wh/g_{Li}, compared with nanofiltration (30−50 Wh/g_{Li})[13] or an electrodialysis system (2−50 Wh/g_{Li}).[31−33] The electrochemical ion pumping system is another popular electrochemical lithium-extraction system, generally utilizing $LiFePO_4$ or $LiMn_2O_4$ as the lithium-selective electrodes.[34] The energy consumption of this technology (0.1−3.0 Wh/g_{Li})[35] is lower than the LE-RFB system due to the energy recovery process. However, the ion pumping system could not accomplish continuous lithium extraction and suffers from switching between feedwater and recovery solution, which is time-consuming.

Herein, we present a brief technoeconomic analysis exploring the feasibility of LE-RFB for the industrial application (key economic price assumption shown in the Supporting Information, Table S3). Assuming an LE-RFB system with an effective area of 1 m^2, 18.4 kg of Li_2CO_3 could be produced per year (with a lithium-extraction rate of 0.04 mg/cm^2/h), valued at 1256 US$. That means the system requires about 6 years to compensate for the initial investment cost and energy consumption (excluding the cost of the pump and electricity consumed by the pump). The key costs relate to pumping energy (1130 US$), which could be addressed by enhancing the lithium recovery rate by using thinner membranes/membranes with more rapid Li^+ transport.

Further improvements to the LE-RFB system will leverage synergetic advances in ceramic solid electrolyte technology. For example, very thin ceramic membranes of just 55 μm have been reported (meaning a higher lithium-ion extraction rate), although such thin membranes bring further requirements for an improved cell design to avoid mechanical failure.[18] Flexible hybrid organic−inorganic LAGP membranes have been synthesized, which could address the mechanical drawback of ceramic membranes, though the ion selectivity of hybrid membranes should be investigated.[36] The possible approaches for the improvement of our system could be but are not limited to optimizing the operation parameters,[37] using a LISICON membrane with higher Li^+ permeance and ionic conductivity, optimized electrodes with high specific surface area and fluid permeability, and improved flow fields for uniform distribution of redox chemicals across the electrode surface.

In summary, we have demonstrated a continuous electrochemical lithium-extraction battery that utilizes flow redox electrolytes and LISICON membranes to mine lithium from aqueous solutions. Among the extracted ions from seawater, Li^+ predominates with a content of 93.5%. Using the redox pairs of $Fe[CN]_6^{3-}/Fe[CN]_6^{4-}$, the battery runs greenly, with no toxic byproducts, no safety concerns, and low energy consumption of 2.5 Wh/g_{Li}, which means less emission of CO_2. Furthermore, a LE-RFB system can utilize feedwater with varying chemical compositions. We see the potential of the LE-RFB system for lithium extraction from acidic leaching solution of spent lithium-ion batteries via hydrometallurgical processing.[38,39]

■ ASSOCIATED CONTENT

Supporting Information

The Supporting Information is available free of charge at https://pubs.acs.org/doi/10.1021/acsenergylett.2c01746.

Full description of the experimental methods, calculation methods, photographs, results from energy-dispersive X-ray spectroscopy, and supplemental lithium-extraction performance (PDF)

■ AUTHOR INFORMATION

Corresponding Authors

Zhaoyin Wen − *CAS Key Laboratory of Materials for Energy Conversion, Shanghai Institute of Ceramics, Chinese Academy of Sciences, Shanghai 200050, P. R. China; State Key Lab of High Performance Ceramics and Superfine Microstructure, Shanghai Institute of Ceramics, Chinese Academy of Sciences, Shanghai 200050, P. R. China;* orcid.org/0000-0003-1698-7420; Email: zywen@mail.sic.ac.cn

Volker Presser − *INM - Leibniz Institute for New Materials, 66123 Saarbrücken, Germany; Department of Materials Science & Engineering, Saarland University, 66123 Saarbrücken, Germany; Saarene, Saarland Center for Energy Materials and Sustainability, 66123 Saarbrücken, Germany;* orcid.org/0000-0003-2181-0590; Email: volker.presser@leibniz-inm.de

Authors

Lei Wang − *INM - Leibniz Institute for New Materials, 66123 Saarbrücken, Germany; Department of Materials Science & Engineering, Saarland University, 66123 Saarbrücken, Germany*

Stefanie Arnold − *INM - Leibniz Institute for New Materials, 66123 Saarbrücken, Germany; Department of Materials Science & Engineering, Saarland University, 66123 Saarbrücken, Germany*

Panyu Ren − *INM - Leibniz Institute for New Materials, 66123 Saarbrücken, Germany; Department of Materials Science & Engineering, Saarland University, 66123 Saarbrücken, Germany*

Qingsong Wang − *INM - Leibniz Institute for New Materials, 66123 Saarbrücken, Germany;* Present Address: Bavarian Center for Battery Technology (BayBatt), University of Bayreuth, Universitätsstrasse 30, 95447 Bayreuth, Germany and Department of Chemistry, University of

https://doi.org/10.1021/acsenergylett.2c01746
ACS Energy Lett. 2022, 7, 3539−3544

Bayreuth, Universitätsstrasse 30, 95447 Bayreuth, Germany; orcid.org/0000-0001-5879-8009

Jun Jin − *CAS Key Laboratory of Materials for Energy Conversion, Shanghai Institute of Ceramics, Chinese Academy of Sciences, Shanghai 200050, P. R. China*

Complete contact information is available at: https://pubs.acs.org/10.1021/acsenergylett.2c01746

Notes

The authors declare no competing financial interest.

■ ACKNOWLEDGMENTS

The authors thank Eduard Arzt (INM) for his continuing support. L.W. acknowledges funding from the China Scholarship Council (CSC) via award number 201906260277. We acknowledge support for the eLiRec project and eWeWa project by the European Union from the European Regional Development Fund (EFRE) and the State of Saarland, Germany.

■ REFERENCES

(1) Greim, P.; Solomon, A. A.; Breyer, C. Assessment of lithium criticality in the global energy transition and addressing policy gaps in transportation. *Nat. Commun.* **2020**, *11* (1), 4570.

(2) Yang, S.; Zhang, F.; Ding, H.; He, P.; Zhou, H. Lithium metal extraction from seawater. *Joule* **2018**, *2* (9), 1648−1651.

(3) Diallo, M. S.; Kotte, M. R.; Cho, M. Mining critical metals and elements from seawater: Opportunities and challenges. *Environ. Sci. Technol.* **2015**, *49* (16), 9390−9399.

(4) Zhao, X.; Yang, H.; Wang, Y.; Sha, Z. Review on the electrochemical extraction of lithium from seawater/brine. *J. Electroanal. Chem.* **2019**, *850*, 113389.

(5) Um, N.; Hirato, T. Precipitation behavior of $Ca(OH)_2$, $Mg(OH)_2$, and $Mn(OH)_2$ from $CaCl_2$, $MgCl_2$, and $MnCl_2$ in NaOH-H_2O solutions and study of lithium recovery from seawater via two-stage precipitation process. *Hydrometallurgy* **2014**, *146*, 142−148.

(6) Liu, C.; Tao, B.; Wang, Z.; Wang, D.; Guo, R.; Chen, L. Preparation and characterization of lithium ion sieves embedded in a hydroxyethyl cellulose cryogel for the continuous recovery of lithium from brine and seawater. *Chem. Eng. Sci.* **2021**, *229*, 115984.

(7) Harvianto, G. R.; Kim, S.-H.; Ju, C.-S. Solvent extraction and stripping of lithium ion from aqueous solution and its application to seawater. *Rare Metals* **2016**, *35* (12), 948−953.

(8) Yu, C.; Lu, J.; Dai, J.; Dong, Z.; Lin, X.; Xing, W.; Wu, Y.; Ma, Z. Bio-inspired fabrication of Ester-functionalized imprinted composite membrane for rapid and high-efficient recovery of lithium ion from seawater. *J. Colloid Interface Sci.* **2020**, *572*, 340−353.

(9) Liu, C.; Li, Y.; Lin, D.; Hsu, P.-C.; Liu, B.; Yan, G.; Wu, T.; Cui, Y.; Chu, S. Lithium extraction from seawater through pulsed electrochemical intercalation. *Joule* **2020**, *4* (7), 1459−1469.

(10) Joo, H.; Lee, J.; Yoon, J. Short review: Timeline of the electrochemical lithium recovery system using the spinel $LiMn_2O_4$ as a positive electrode. *Energies* **2020**, *13* (23), 6235.

(11) Santos, C.; La Mantia, F. Recent advances in reactor design and control for lithium recovery by means of electrochemical ion pumping. *Current Opinion in Electrochemistry* **2022**, *35*, 101089.

(12) Swain, B. Recovery and recycling of lithium: A review. *Sep. Purif. Technol.* **2017**, *172*, 388−403.

(13) Li, X.; Mo, Y.; Qing, W.; Shao, S.; Tang, C. Y.; Li, J. Membrane-based technologies for lithium recovery from water lithium resources: A review. *J. Membr. Sci.* **2019**, *591*, 117317.

(14) Joo, H.; Kim, S.; Kim, S.; Choi, M.; Kim, S.-H.; Yoon, J. Pilot-scale demonstration of an electrochemical system for lithium recovery from the desalination concentrate. *Environ. Sci.: Water Res. Technol.* **2020**, *6* (2), 290−295.

(15) Wang, L.; Frisella, K.; Srimuk, P.; Janka, O.; Kickelbick, G.; Presser, V. Electrochemical lithium recovery with lithium iron phosphate: what causes performance degradation and how can we improve the stability? *Sustainable Energy & Fuels* **2021**, *5* (12), 3124−3133.

(16) Zhang, H.; Ren, Y.; Wu, X.; Wang, N. An interface-modified solid-state electrochemical device for lithium extraction from seawater. *J. Power Sources* **2021**, *482*, 228938.

(17) Kim, N.; Su, X.; Kim, C. Electrochemical lithium recovery system through the simultaneous lithium enrichment via sustainable redox reaction. *Chemical Engineering Journal* **2021**, *420*, 127715.

(18) Li, Z.; Li, C.; Liu, X.; Cao, L.; Li, P.; Wei, R.; Li, X.; Guo, D.; Huang, K.-W.; Lai, Z. Continuous electrical pumping membrane process for seawater lithium mining. *Energy Environ. Sci.* **2021**, *14* (5), 3152−3159.

(19) Wang, Q.; Jin, J.; Wu, X.; Ma, G.; Yang, J.; Wen, Z. A shuttle effect free lithium sulfur battery based on a hybrid electrolyte. *Phys. Chem. Chem. Phys.* **2014**, *16* (39), 21225−21229.

(20) Xu, X.; Wen, Z.; Wu, X.; Yang, X.; Gu, Z. Lithium ion-conducting glass-ceramics of $Li_{1.5}Al_{0.5}Ge_{1.5}(PO_4)_3$-x$Li_2O$ (x = 0.0−0.20) with good electrical and electrochemical properties. *J. Am. Ceram. Soc.* **2007**, *90* (9), 2802−2806.

(21) Fu, L.; Teng, Y.; Liu, P.; Xin, W.; Qian, Y.; Yang, L.; Lin, X.; Hu, Y.; Kong, X.-Y.; Jiang, L.; et al. Electrochemical ion-pumping-assisted transfer system featuring a heterogeneous membrane for lithium recovery. *Chemical Engineering Journal* **2022**, *435*, 134955.

(22) Zhang, M.; Takahashi, K.; Uechi, I.; Takeda, Y.; Yamamoto, O.; Im, D.; Lee, D.-J.; Chi, B.; Pu, J.; Li, J.; et al. Water-stable lithium anode with $Li_{1.4}Al_{0.4}Ge_{1.6}(PO_4)_3$-$TiO_2$ sheet prepared by tape casting method for lithium-air batteries. *J. Power Sources* **2013**, *235*, 117−121.

(23) Zhang, P.; Wang, H.; Lee, Y.-G.; Matsui, M.; Takeda, Y.; Yamamoto, O.; Imanishi, N. Tape-cast water-stable NASICON-Type high lithium ion conducting solid electrolyte films for aqueous lithium-air batteries. *J. Electrochem. Soc.* **2015**, *162* (7), A1265−A1271.

(24) Nikodimos, Y.; Abrha, L. H.; Weldeyohannes, H. H.; Shitaw, K. N.; Temesgen, N. T.; Olbasa, B. W.; Huang, C.-J.; Jiang, S.-K.; Wang, C.-H.; Sheu, H.-S.; et al. A new high-Li^+-conductivity Mg-doped $Li_{1.5}Al_{0.5}Ge_{1.5}(PO_4)_3$ solid electrolyte with enhanced electrochemical performance for solid-state lithium metal batteries. *Journal of Materials Chemistry A* **2020**, *8* (48), 26055−26065.

(25) Luo, J.; Sam, A.; Hu, B.; DeBruler, C.; Wei, X.; Wang, W.; Liu, T. L. Unraveling pH dependent cycling stability of ferricyanide/ferrocyanide in redox flow batteries. *Nano Energy* **2017**, *42*, 215−221.

(26) Sun, Q.; He, L.; Zheng, F.; Wang, Z.; An Oh, S. J.; Sun, J.; Zhu, K.; Lu, L.; Zeng, K. Decomposition failure of $Li_{1.5}Al_{0.5}Ge_{1.5}(PO_4)_3$ solid electrolytes induced by electric field: A multi-scenario study using Scanning Probe Microscopy-based techniques. *J. Power Sources* **2020**, *471*, 228468.

(27) Paolella, A.; Zhu, W.; Xu, G.-L.; La Monaca, A.; Savoie, S.; Girard, G.; Vijh, A.; Demers, H.; Perea, A.; Delaporte, N.; et al. Understanding the reactivity of a thin $Li_{1.5}Al_{0.5}Ge_{1.5}(PO4)_3$ solid-state electrolyte toward metallic lithium anode. *Adv. Energy Mater.* **2020**, *10* (32), 2001497.

(28) Liu, G.; Zhao, Z.; He, L. Highly selective lithium recovery from high Mg/Li ratio brines. *Desalination* **2020**, *474*, 114185.

(29) Zhao, X.; Zhang, H.; Yuan, Y.; Ren, Y.; Wang, N. Ultra-fast and stable extraction of Li metal from seawater. *Chem. Commun.* **2020**, *56* (10), 1577−1580.

(30) Zhang, F.; Yang, S.; Du, Y.; Li, C.; Bao, J.; He, P.; Zhou, H. A low-cost anodic catalyst of transition metal oxides for lithium extraction from seawater. *Chem. Commun.* **2020**, *56* (47), 6396−6399.

(31) Guo, Z.-Y.; Ji, Z.-Y.; Chen, Q.-B.; Liu, J.; Zhao, Y.-Y.; Li, F.; Liu, Z.-Y.; Yuan, J.-S. Prefractionation of LiCl from concentrated seawater/salt lake brines by electrodialysis with monovalent selective ion exchange membranes. *Journal of Cleaner Production* **2018**, *193*, 338−350.

(32) Ji, P.-Y.; Ji, Z.-Y.; Chen, Q.-B.; Liu, J.; Zhao, Y.-Y.; Wang, S.-Z.; Li, F.; Yuan, J.-S. Effect of coexisting ions on recovering lithium from

high Mg^{2+}/Li^{+} ratio brines by selective-electrodialysis. *Sep. Purif. Technol.* **2018**, *207*, 1−11.
(33) Gmar, S.; Chagnes, A. Recent advances on electrodialysis for the recovery of lithium from primary and secondary resources. *Hydrometallurgy* **2019**, *189*, 105124.
(34) Calvo, E. J. Direct lithium recovery from aqueous electrolytes with electrochemical ion pumping and lithium intercalation. *ACS Omega* **2021**, *6* (51), 35213−35220.
(35) Battistel, A.; Palagonia, M. S.; Brogioli, D.; La Mantia, F.; Trócoli, R. Electrochemical methods for lithium recovery: A comprehensive and critical review. *Adv. Mater.* **2020**, *32* (23), 1905440.
(36) Safanama, D.; Adams, S. Flexible light-weight lithium-ion-conducting inorganic-organic composite electrolyte membrane. *ACS Energy Letters* **2017**, *2* (5), 1130−1136.
(37) Smith, K. C.; Dmello, R. Na-ion desalination (NID) enabled by Na-blocking membranes and symmetric na-intercalation: Porous-electrode modeling. *J. Electrochem. Soc.* **2016**, *163* (3), A530−A539.
(38) Kim, K.; Candeago, R.; Rim, G.; Raymond, D.; Park, A.-H. A.; Su, X. Electrochemical approaches for selective recovery of critical elements in hydrometallurgical processes of complex feedstocks. *iScience* **2021**, *24* (5), 102374.
(39) Vieceli, N.; Nogueira, C. A.; Guimarães, C.; Pereira, M. F. C.; Durão, F. O.; Margarido, F. Hydrometallurgical recycling of lithium-ion batteries by reductive leaching with sodium metabisulphite. *Waste Management* **2018**, *71*, 350−361.
(40) Weiss, M.; Weber, D. A.; Senyshyn, A.; Janek, J.; Zeier, W. G. Correlating transport and structural properties in $Li_{1+x}Al_xGe_{2-x}(PO_4)_3$ (LAGP) prepared from aqueous solution. *ACS Appl. Mater. Interfaces* **2018**, *10* (13), 10935−10944.
(41) Kim, S.; Kim, J.; Kim, S.; Lee, J.; Yoon, J. Electrochemical lithium recovery and organic pollutant removal from industrial wastewater of a battery recycling plant. *Environ. Sci.: Water Res. Technol.* **2018**, *4* (2), 175−182.

https://doi.org/10.1021/acsenergylett.2c01746
ACS Energy Lett. 2022, 7, 3539−3544

Supporting Information

Redox Flow Battery for Continuous and Energy-Effective Lithium Recovery from Aqueous Solution

Lei Wang,[1,2] Stefanie Arnold,[1,2] Panyu Ren,[1,2]
Qingsong Wang[1,‖], Jun Jin[3], Zhaoyin Wen[3,4,*], Volker Presser,[1,2,5,*]

[1] *INM - Leibniz Institute for New Materials, D2 2, 66123, Saarbrücken, Germany*

[2] *Department of Materials Science & Engineering, Saarland University, Campus D2 2, 66123, Saarbrücken, Germany*

[3] *CAS Key Laboratory of Materials for Energy Conversion, Shanghai Institute of Ceramics, Chinese Academy of Sciences, Shanghai, 200050 P. R. China*

[4] *State Key Lab of High Performance Ceramics and Superfine Microstructure, Shanghai Institute of Ceramics, Chinese Academy of Sciences, Shanghai, 200050 P. R. China*

[5] *Saarene, Saarland Center for Energy Materials and Sustainability, Campus C4 2, 66123 Saarbrücken, Germany*

* Corresponding author's email: zywen@mail.sic.ac.cn volker.presser@leibniz-inm.de

‖ *Current address: Bavarian Center for Battery Technology (BayBatt), University of Bayreuth, Universitätsstrasse 30, 95447 Bayreuth, Germany and Department of Chemistry, University of Bayreuth, Universitätsstrasse 30, 95447 Bayreuth, Germany*

Experimental Methods

Synthesis and manufacturing of the LISICON membranes

Briefly, a mixture of precursors containing lithium carbonate Li_2CO_3, alumina Al_2O_3, germanium oxide GeO_2 (99.99%), and ammonium dihydrogen phosphate $(NH_4)H_2PO_4$ was dispersed in isopropanol and thoroughly mixed by planetary ball-milling with ZrO_2 balls for 6 h at 400 rpm. The well-mixed precursor was dried and calcinated at 800 °C for 6 h. Afterward, the synthesized powder was pressed into pellets (thickness of 0.8 mm) and sintered in a Pt crucible at 900 °C for 12 h. The obtained ceramic pellets were further polished before use.

Component and operation of the LE-RFB system

Two commercial symmetric carbon felt electrodes (discs with a diameter of 14 mm, SGL Carbon) were employed as the cathode and anode, contacting with the redox electrolyte channels. The redox electrolyte with the volume of 50 mL contained 280 mM $K_3[Fe(CN)_6]$, 280 mM $K_4[Fe(CN)_6]$, and 10 mM LiCl (to increase the lithium extraction rate), which is maintained in a brown bottle to avoid the deterioration of $K_3[Fe(CN)_6]$ when exposed to light. A 10 L tank of simulated seawater prepared according to the concentration of primary cations from the norm D1141-98 (Ref. [1]) of the American Society for Testing and Materials (**Table S2**) was applied as the feed water. The anions were chloride ions. The recovery solution consisted of 65 mL of 10 mM NaCl solution. The feed water and recovery solution were separated by an anion exchange membrane (diameter 50 mm, FAS-PET-130, Fumatech). These two solutions were separated from the redox electrolyte by the LISICON membrane (effective area 1.5 cm^2, thickness ~500 μm, geometric density 3.26 g/cm^3). All these three solutions were circulated from and back to the reservoirs through the peristaltic pump (Masterflex L/S) with a flow rate of 5 mL/min. The recovery solution and redox electrolyte reservoirs were constantly stirred at 400 rpm by magnetic stirring (Variomag, MULTIPOINT magnetic HP6). The setup of the LE-RFB system was operated in a climate chamber (Binder) at a constant temperature of 25±1 °C, shown in **Figure S1**. The LE-RFB was first charged at a constant current density of 1 mA/cm^2 limited to 0.6 V by VSP300 potentiostat/galvanostat (Bio-Logic). Subsequently, the battery was held at 0.6 V for 5 h. The concentration of all the cations in the recovery solution at various charging times was tested by an inductively coupled plasma optical emission spectrometer (ICP-OES, ARCOS FHX22, SPECTRO Analytical Instruments). The experiment of recovering lithium from brines water was complemented with the same LISICON membranes, and the other experimental conditions were the same except for the composition of the feed water (100 mL, prepared according to Ref. [2]) and the volume of recovery solution (75 mL). The chemical composition of the redox electrolyte and of the seawater and brine is provided in **Table S1** and **Table S2**, respectively.

Characterization

X-ray diffraction (XRD) analysis was carried out via a D8 Advanced diffractometer (Bruker AXS) with a copper X-ray source (Cu-K_α, λ = 1.5406 Å; 40 kV, 40 mA). The samples were examined in the range of 10° to 70° 2θ and with 1 s per step: Scanning electron microscopy (SEM) was conducted using a ZEISS Gemini 500 system at acceleration voltages of 1-3 kV. A small piece of the LISICON membrane was vertically mounted on an aluminum sample holder and analyzed without the aid of an additional, conductive sputter coating. Energy-dispersive X-ray spectroscopy (EDX) spectra were obtained with an in-lens secondary electron (SE) detector at 15 kV employing an X-Max Silicon Detector from Oxford Instruments attached to the electron microscope.

Ionic conductivity measurement

To measure the ionic conductivity of ceramic pellets, we applied a thin layer via gold sputtering as ion conducting blocking electrode. The electrochemical impedance spectroscopy was measured in the frequency range of 100 kHz to 0.1 Hz with a perturbation voltage of 10 mV.

Calculations

The extraction ratio of all the cations is calculated according to **Equation S1**.

$$Extraction\ ratio\ (\%) = \frac{\Delta c_x}{\Delta c_{all}} \times 100 \quad \textbf{(Eq. S1)}$$

where, Δc_x and Δc_{all} are the concentration change of x (x = Li^+, K^+, Mg^{2+} or Na^+) and all the cations in the recovery solution.

We also calculated the selectivity factors ($K_{Li/M}$) between Li^+ and other cations M (M = Na^+, K^+, Mg^{2+}), which involves the initial concentration of cations, according to the **Equation S2**

$$K_{Li/M} = \frac{\Delta c_{Li}}{\Delta c_M} \times \frac{c_{m-initial}}{c_{Li-initial}} \quad \textbf{(Eq. S2)}$$

where, Δc_{Li} and Δc_M are the concentration change of Li^+ and M in the recovery solution, respectively. $c_{m\text{-}initial}$ and $c_{Li\text{-}initial}$ are the concentration of M and Li^+ in the initial feed water, respectively.

The lithium retraction rate and energy consumption are also important indexes to evaluate the system's performance, calculated by **Equation S3** and **Equation S4**, respectively.

$$Lithium\ extraction\ rate = \frac{\Delta c_{Li} \times V}{t \times A \times M_{Li}} \quad \textbf{(Eq. S3)}$$

where Δc_{Li} is the concentration change of Li^+ in the recovery solution, V is the volume, t is the time, A the effective area of LISICON membrane, M_{Li} is the molar mass of Li.

$$Energy\ consumption = \frac{E}{V \times \Delta c_{Li} \times M_{Li}} \quad \textbf{(Eq. S4)}$$

where E is the consumed electrical energy during the charging operation, Δc_{Li} is the concentration change of Li^+ in the recovery solution, V is the volume, M_{Li} is the molar mass of Li

Supporting Figures

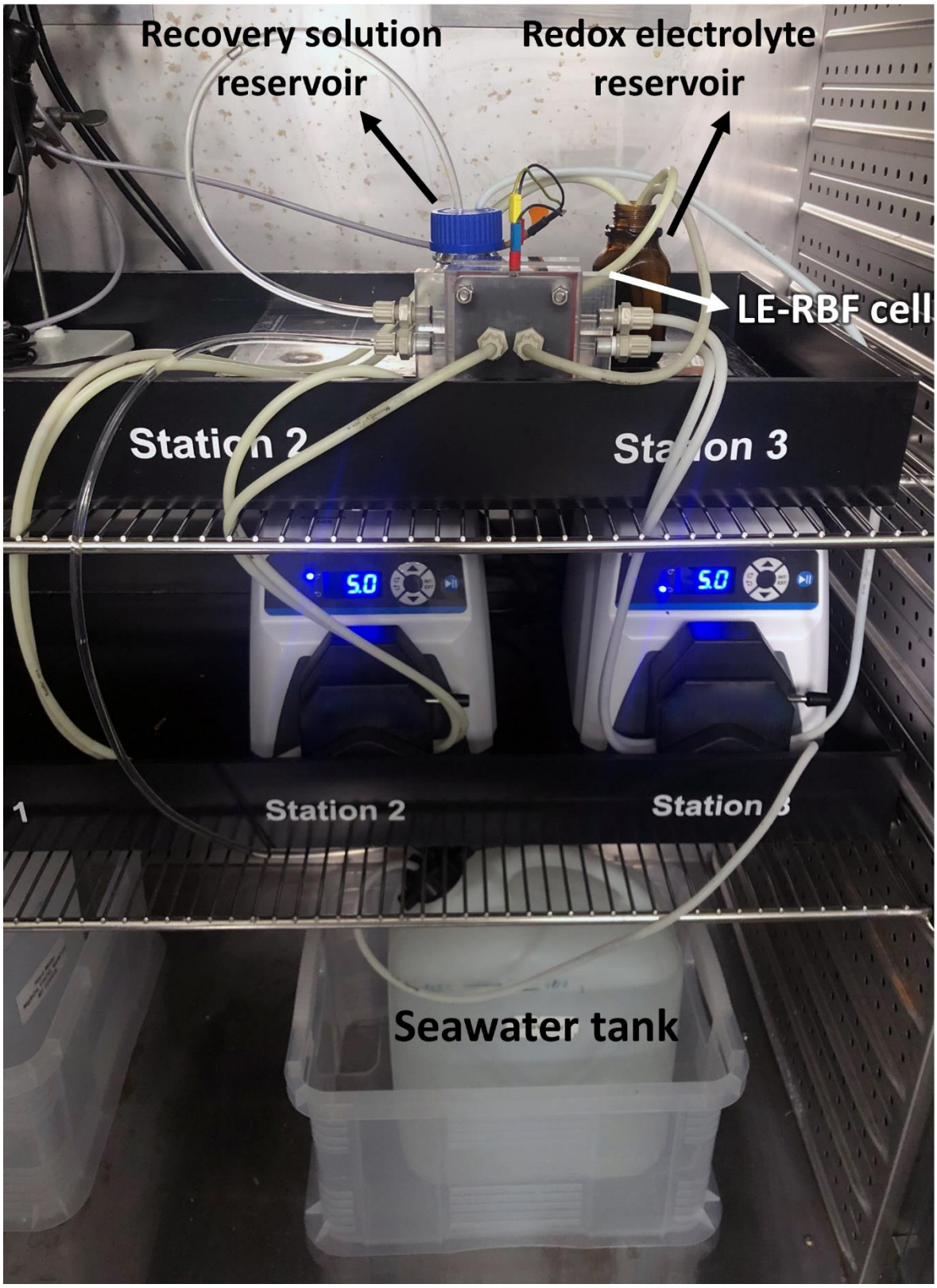

Figure S1: Photograph of the setup of lithium-extraction redox flow battery system.

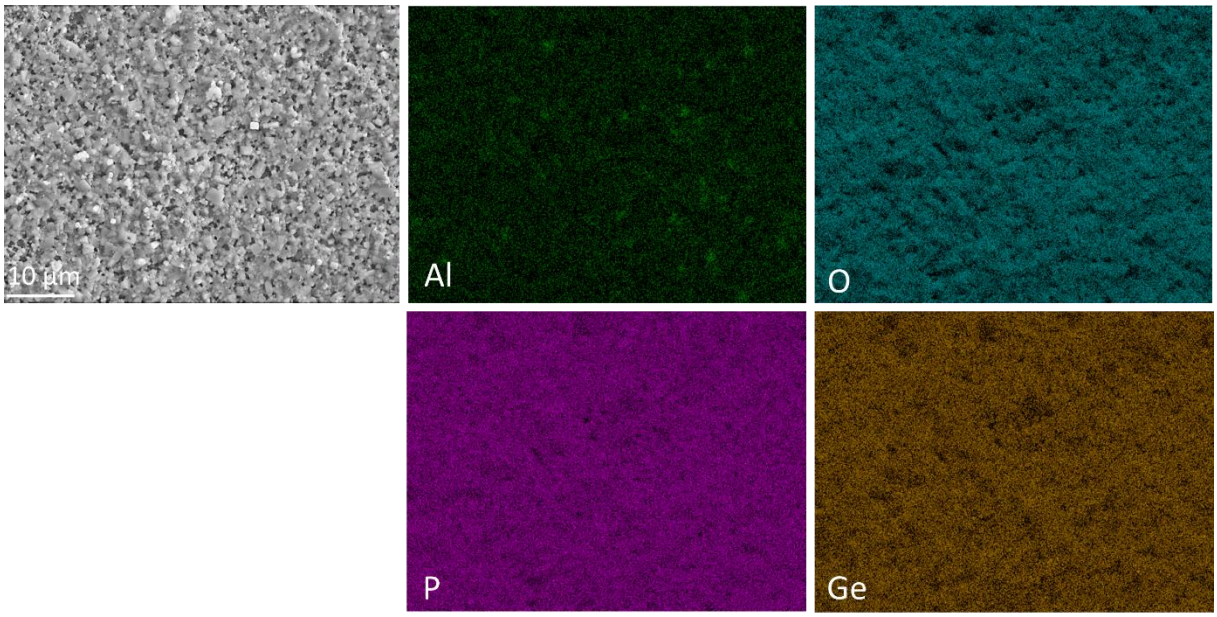

Figure S2: A cross-sectional scanning electron micrograph of the LISICON membrane and corresponding EDX mapping of Al, Ge, P, and O. All elemental maps show the same area (with same resolution) as the electron micrograph.

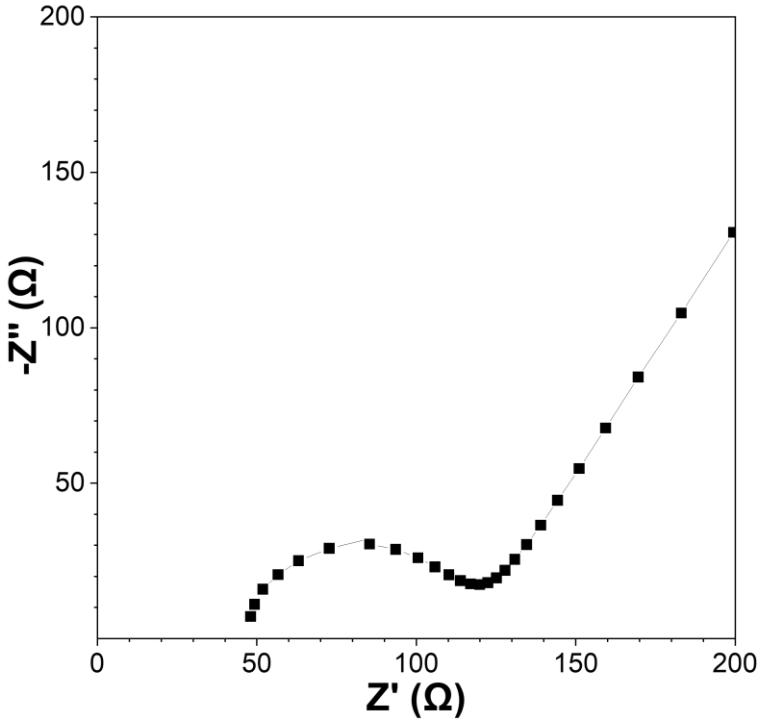

Figure S3: The electrochemical impedance spectrum of the LAGP membrane with an area of 323.5 mm^2.

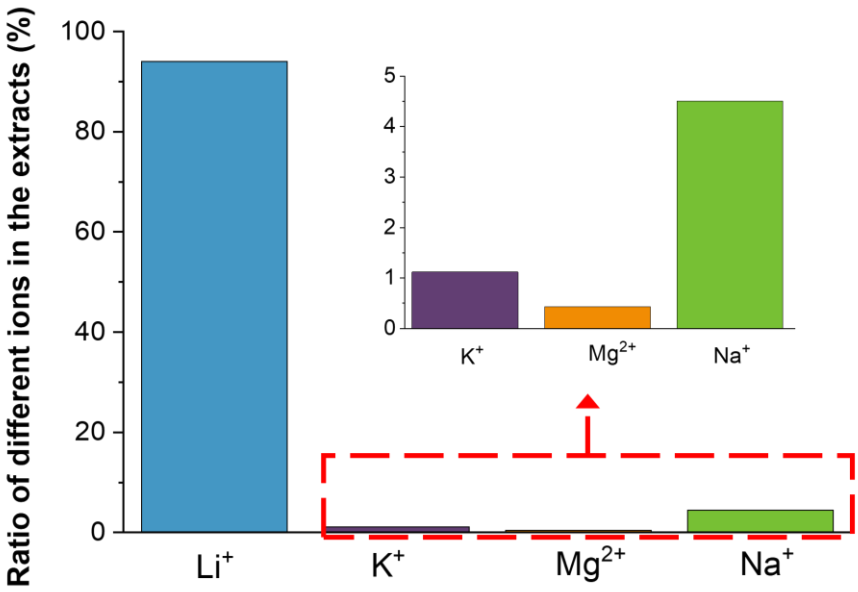

Figure S4: The percentage of all cations in the cations extracted from seawater. Insert: magnification of column graph for the K^+, Mg^{2+}, and Na^+.

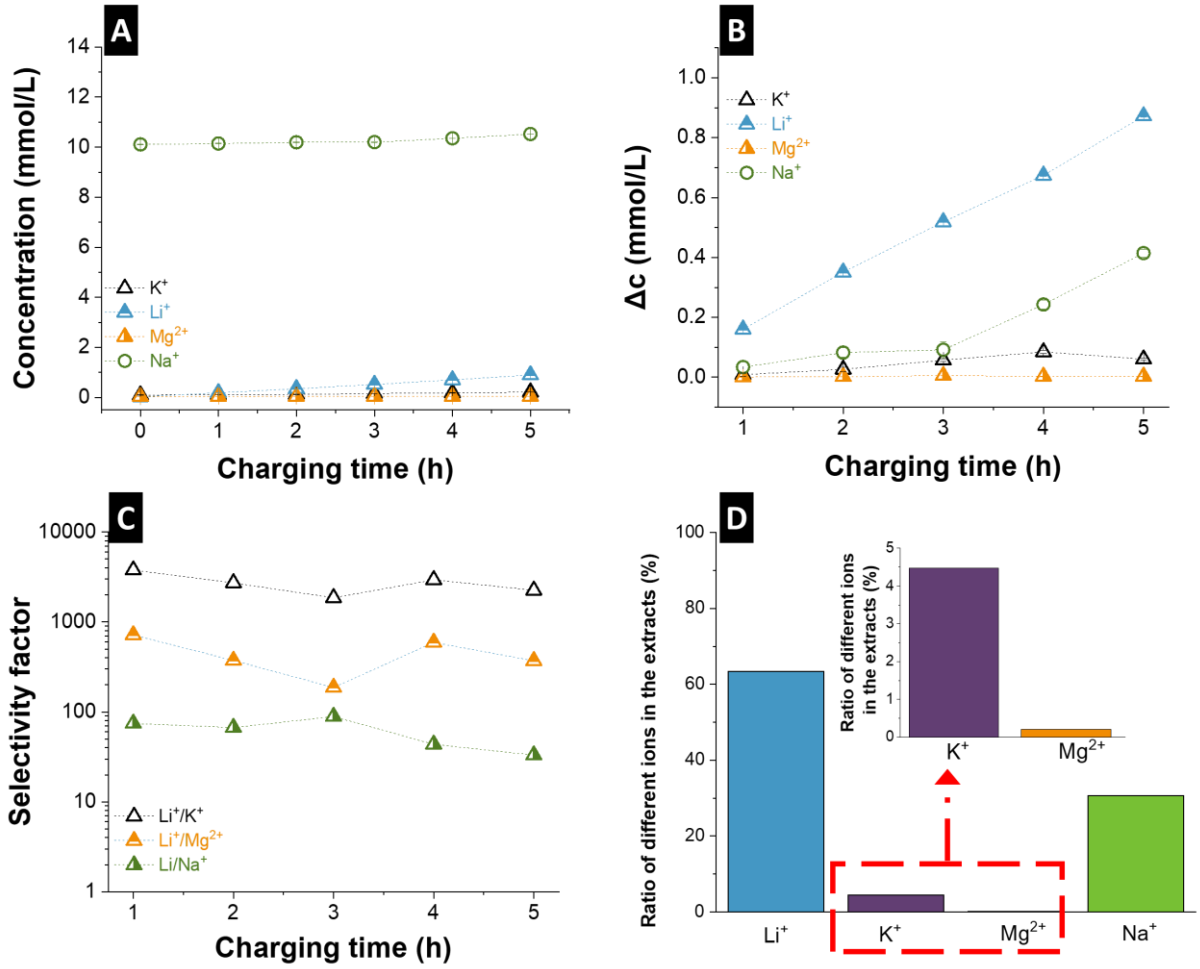

Figure S5: Lithium extraction from seawater by lithium-extraction redox flow battery: (A) the concentration and (B) concentration change of cations in the recovery solution at different times; (C) the selectivity factors between Li^+ and other cations; (D) The percentage of all cations in the cations extracted from brine. Inset: magnification of column graph for the K^+ and Mg^{2+}.

Supporting Tables

Table S1: The concentration of main cations and Li^+ in the redox electrolyte in the experiment for lithium extraction from seawater. No calcium was detected.

Concentration (mM)	Initial	After
Li^+	9.35±0.01	9.37±0.01
Na^+	0.95±0.01	1.13±0.01
K^+	2095.2±3.8	2119.4±2.1
Ca^{2+}	-	-
Mg^{2+}	$3.6\cdot10^{-3}\pm3.3\cdot10^{-5}$	$1.0\cdot10^{-2}\pm4.8\cdot10^{-5}$
Fe^{3+}	571.7±0.6	579.8±0.9
pH	6.75	6.25

Table S2: The concentration of main cations and Li^+ in the simulated seawater (Ref. [1]) and brine water (Ref. [2]).

Concentration (mM)	Seawater	Brine water
Li^+	0.024	210
Na^+	477.5	3300
K^+	9.3	460
Ca^{2+}	10.5	7.75
Mg^{2+}	54.6	400

Table S3: Key economic and technical price assumption for a simplified techno-economic analysis of LE-RFB system with an effective area of 1 m^2.

Price assumption		Economic assumptions		Technical assumptions
LISICON membrane ($/$m^2$) Ref. [3]	461	Depreciation (% yr^{-1} of fixed capital)	10	1.1 times as the effective area
Anion exchange membrane ($/$m^2$)	780	Depreciation (% yr^{-1} of fixed capital)	5	1.5 times as the effective area
Graphite block ($/kg)	3	Processing fee (%)	20	
PMMA ($/kg)	4	Processing fee (%)	20	
Carbon felt ($/$m^2$)	30			
Other components of the LE-RFB system ($)	200			Including gasket, O-rings, screws
Tax (%)	19			
Na_2CO_3 ($/kg) Ref. [3]	0.3			
Li_2CO_3 ($/kg)*	68			
Electricity ($/kWh)**	0.13			The power of the pump is 1 kW

* https://www.chemanalyst.com/Pricing-data/lithium-carbonate-1269

** https://www.globalpetrolprices.com/electricity_prices

Supporting References

(1) ASTM. *D1141-98 Standard Practice for the Preparation of Substitute Ocean Water*; 2013. Access date: 14.09.2022
(2) Liu, G.; Zhao, Z.; He, L. Highly selective lithium recovery from high Mg/Li ratio brines. *Desalination* **2020**, *474*, 114185. DOI: 10.1016/j.desal.2019.114185.
(3) Hu, J.; Jiang, Y.; Li, L.; Yu, Z.; Wang, C.; Gill, G.; Xiao, J.; Cavagnaro, R. J.; Kuo, L.-J.; Asmussen, R. M.; et al. A Lithium Feedstock Pathway: Coupled Electrochemical Extraction and Direct Battery Materials Manufacturing. *ACS Energy Letters* **2022**, *7* (8), 2420-2427. DOI: 10.1021/acsenergylett.2c01216.

4.7. Redox flow desalination for tetramethylammonium hydroxide removal and recovery from semiconductor wastewater

Dayoung Ahn[1,†], Seonghwan Kim[1,2,†], Panyu Ren,[3,4] Volker Presser,[3,4,5] and Choonsoo Kim[1]

[1] *Department of Environmental Engineering and Institute of Energy/Environment Convergence Technologies, Kongju National University, 1223-24, Cheonan-daero, Cheonan-si 31080, Republic of Korea*

[2] *Samsung Research, Samsung Electronics Co., Ltd.*

[3] *INM - Leibniz Institute for New Materials, Campus D2.2, 66123 Saarbrücken, Germany*

[4] *Department of Materials Science and Engineering, Saarland University, Campus D2.2, 66123 Saarbrücken, Germany*

[5] *Saarene - Saarland Center for Energy Materials and Sustainability, Campus C4.2, 66123 Saarbrücken, Germany*

†The authors contributed equally to this work.

Citation:

D. Ahn, S. Kim, P. Ren, V. Presser, and C. Kim, Redox flow desalination for tetramethylammonium hydroxide removal and recovery from semiconductor wastewater, Journal of Industrial and Engineering Chemistry 118 (2023) 147-154.

Own contribution:

Investigation, and writing-review & editing.

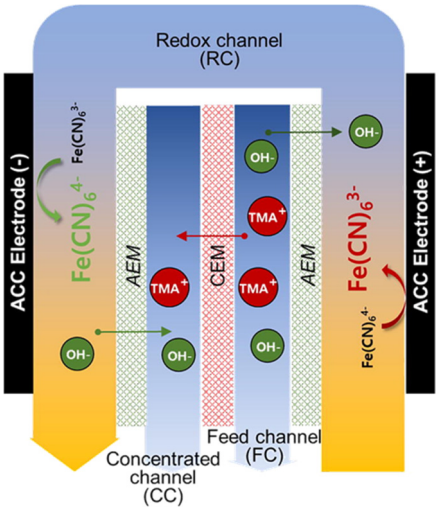

Journal of Industrial and Engineering Chemistry 118 (2023) 147–154

Contents lists available at ScienceDirect

Journal of Industrial and Engineering Chemistry

journal homepage: www.elsevier.com/locate/jiec

Redox flow desalination for tetramethylammonium hydroxide removal and recovery from semiconductor wastewater

Dayoung Ahn [a,1], Seonghwan Kim [a,b,1], Panyu Ren [c,d], Volker Presser [c,d,e,*], Choonsoo Kim [a,*]

[a] Department of Environmental Engineering with Institute of Energy/Environment Convergence Technologies and Department of Future Convergence Engineering, Kongju National University, 1223-24, Cheonan-daero, Cheonan-si 31080, Republic of Korea
[b] Samsung Research, Samsung Electronics Co., Ltd
[c] INM – Leibniz Institute for New Materials, Campus D2.2, 66123 Saarbrücken, Germany
[d] Department of Materials Science and Engineering, Saarland University, Campus D2.2, 66123 Saarbrücken, Germany
[e] Saarene – Saarland Center for Energy Materials and Sustainability, Campus C4.2, 66123 Saarbrücken, Germany

ARTICLE INFO

Article history:
Received 29 July 2022
Revised 10 October 2022
Accepted 30 October 2022
Available online 4 November 2022

Keywords:
Water desalination
Redox flow desalination
Redox chemistry
tetramethylammonium hydroxide (TMAH)
Valorization

ABSTRACT

As part of humankind's path towards more sustainable water technologies, redox flow desalination (RFD) has emerged as a promising technology due to its high energy efficiency and easy operation. So far, RFD research has focused on removing and recovering inorganic salts such as lithium-ions, heavy metal ions, or phosphate and nitrate ions. Thus, the potential of RFD in water desalination and resource recovery processes has not been fully demonstrated. Therefore, this study aimed to assess RFD for the valorization of tetramethylammonium hydroxide (TMAH) as value-added organic compounds from wastewater beyond inorganic elements, which is widely being used as an etching solvent, photoresist developer, and surfactant in semiconductor and display industries. By applying a low cell voltage (<1.2 V), a reversible redox reaction allowed a continuous removal of TMAH from the wastewater stream and a simultaneous recovery for reuse as a form of tetramethylammonium cation. The TMAH removal rate was approximately 4.3 mM/g/h with a 40% recovery ratio. With various operational conditions (i.e., TMAH concentration, cell voltage, and flow rate), our system exhibited a high potential for the valorization of TMAH with 60% reduction in capital cost compared to conventional desalination processes.

Introduction

The management of water resources has drawn widespread attention as a global issue in the 21st century to avoid/alleviate the immanent global (and regional) water crises and to enable sustainable development [1,2]. Seawater desalination is currently playing an important role in achieving sustainable water management [3–5]. In particular, wastewater desalination also gains a huge interest to secure water resource that removes drastically discharged hazardous ionic pollutants into an environment such as various cation (i.e., minerals, heavy metal ions, lithium-ions) and anion (i.e., fluoride, sulfate, phosphate and nitrate ions) [6–8]. Besides, simultaneously by recovering the ionic pollutants from wastewater, it can be a provisional supplier for valuable natural resources mitigating economic and environmental pressure for a rapid decline of natural resources [9–11]. This creates a powerful win–win situation where next-generation sustainable technologies along the value-chain of the emerging circular economy help to address both environmental and economic challenges. Several studies have reported water desalination including membrane [12,13], distillation [14,15], and electrochemical processes [16–18]. Among them, electrochemical methods have emerged as a promising water desalination technology due to their high energy efficiency and eco-friendliness [16,19,20]. Depending on the way

Abbreviations: TMAH, tetramethylammonium hydroxide; RDF, redox flow desalination; ACC, activated carbon cloth; ED, electrodialysis; CDI, capacitive deionization.

* Corresponding authors at: INM – Leibniz Institute for New Materials, Campus D2.2, 66123 Saarbrücken, Germany (V. Presser); Department of Environmental Engineering with Institute of Energy/Environment Convergence Technologies and Department of Future Convergence Engineering, Kongju National University, 1223-24, Cheonan-daero, Cheonan-si 31080, Republic of Korea (C. Kim).

E-mail addresses: volker.presser@leibniz-inm.de (V. Presser), choonsoo@kongju.ac.kr (C. Kim).

[1] The authors contributed equally to this work.

https://doi.org/10.1016/j.jiec.2022.10.053
1226-086X/

by which ion removal is accomplished [21], we can differentiate between ion electrosorption technologies (via capacitive deionization, CDI) [22–25], desalination batteries [21,26], desalination fuel cells [27], and electrodialysis (ED) [28,29].

Within the diversification and continued exploration of electrochemical desalination technologies, it has become attractive to implement methods for continuous operation. That is, not operate in cycles of charging/discharging cycles that correspond with desalination/regeneration [18,30]. A very promising approach is redox-mediated electrodialysis (also known as redox flow desalination, RFD) [31–37]. RFD improves traditional ED technologies with a redox reaction analogous to batteries (Faradaic characteristic), but instead of the water-splitting reaction at the end-electrodes [33,37]. In this way, it is possible to combine a low operational cell voltage resulting from redox couple reactions, and the possibility for energy recovery with different redox couples, as opposed to the large voltages required in a traditional ED. RFD also offer a large variety of electrode materials (including activated carbons) because of the lack of need for extreme reaction condition (it is not required expensive metal oxide electrodes such as dimensionally stable anodes) [31]. Moreover, this system could be easily scaled-up with only stacking of carbon electrodes that have a large surface area. Also importantly, since this system does not electrolyze water resulting in less production of byproducts or large pH swings. Consequently, this system can adjust the pH value electrochemically to help downstream processes [32].

The quickly rising number of RFD research has, so far, studied water management regarding inorganic ionic substances such as minerals, lithium-ion, heavy metal ions, or phosphate and nitrate ions. Thus, its potential as a deionization process has not been fully demonstrated with the various applications. Herein, beyond inorganic elements in water desalination, we assess the potential of RFD with the valorization of tetramethylammonium hydroxide (TMAH, a quaternary ammonium salt with a chemical formula of $N^+(CH_3)_4OH^-$) as value-added organic compounds from wastewater, which is widely being used as etching and photo-developing solvent in the semiconductor and display industries [38–40]. As an exponential growth of semiconductor and display industries, a large amount of wastewater containing TMAH is currently discharged [40], that must be treated due to its high bio-toxicity and -corrosiveness, causing severe damage to human health and the ecosystem and inhibiting the biological wastewater treatment process [41–43].

Experimental description

RFD cell

The cell configuration of RFD consists of multichannels, as depicted in Fig. 1, which is similar to the conventional ED cell design. As shown in Fig. 1A, in the outer channels (denoted as redox channel, $4 \times 4 \times 0.2$ cm^3), a pair of activated carbon electrodes (ACC 5092-20, Kynol) with an area of 3×3 cm^2 with an average mass of 1300 mg were placed on titanium current collectors (Fig. 1B). The redox couple (100 mM ferricyanide ($Fe(CN)_6^{3-}$)/-ferrocyanide ($Fe(CN)_6^{4-}$)) stream containing 100 mM NaOH circulates onto the electrode surface for sustainable oxidation and reduction reactions. In the feed and concentrated channels ($4 \times 4 \times 0.2$ cm^3), the TMAH-containing feed stream flows while the tetramethylammonium cation (TMA^+) and hydroxide ion (OH^-) are selectively accumulated for TMAH enrichment. The channels were fully separated by the alternative introduction of cationic (CMX, Neosepta) and anionic (AMV, Selemion) exchange membranes (5×5 cm^2), offering selective ion migration and no mixing among the streams.

Characterization of ACC electrode

The activated carbon cloth (ACC) electrode is a fabric of porous activated carbon fibers (Kynol 15, Kuraray) with a high carbon content (>95%) and a large surface area of around 1500 m^2/g (see also Ref. [44]). The electrochemical properties of ACC were examined by cyclic voltammetry (CV) with a three-electrode system in a custom-built electrode analysis cell (*Supplementary Information*, Fig. S1): ACC was employed as a working electrode with an average mass of 80 mg, and counter electrodes with an excess mass, respectively. We used an Ag/AgCl (in saturated KCl) reference electrode. The scan rates varied from 2 mV/s to 100 mV/s within a potential range from 0.0 V to 0.6 V.

Evaluation of valorization of TMAH in RFD

TMAH valorization (i.e., removal and recovery) in RDF was examined in a semi-batch mode: redox stream of a 100 mM NaOH solution containing a 100 mM $Na_3Fe(CN)_6$/$Na_4Fe(CN)_6$ (100 mL) at redox channel, a feed stream of 0.5 mM-10 mM TMAH solution (100 mL) at feed channel, and recovery stream of 10 mM NaOH solution (100 mL) at the concentrated channel. For the pretreatment of the RFD system, the electrode was activated with an applied cell voltage of 1.2 V for 30 min. TMAH valorization was tested with an applying cell voltage of 1.2 V for 4 h using a battery cycler (WBCS3000, WonATech Co.). All experiments were conducted in a climate chamber under constant conditions (25 °C temperature, 60% relative humidity; *Supplementary Information*, Fig. S2).

To quantify the RFD performance for TMAH valorization, the effluent was analyzed by conductivity (F-54BW, HORIBA), and pH (9615S-10D, HORIBA) meters to measure the TMAH concentration (via monitoring the effluent conductivity), and the effluent pH value. These data were used to calculate the key performance indices, such as salt removal rate, charge efficiency, recovery ratio, and energy consumption. Also, to investigate the concentration differences of TMAH and other cations, the solution in the feed and concentrate channels were sampled 0 h, 1 h, 2 h, 3 h, and 4 h, and quantified using ion chromatography (Aquion, Thermo Fisher Scientific). In addition, a parametric investigation of the applied voltages from 0.6 V to 1.2 V, the flow rate from 1 mL/min to 10 mL/min, and the stack of ACC electrodes from a single pair electrode to three pairs of electrodes were conducted to understand the performance of RFD for TMAH valorization. The conditions for the parametric investigation were employed to effectively analyze our RFD system in consideration of system ohmic drop, pump capacity, and system volume. The performance was also evaluated in synthetic TMAH wastewater containing 2.5 mM KCl, 1.5 mM NaCl, and 0.25 mM $CaCl_2$ based on a real-wastewater matrix discharged from semiconductor manufacturing [45,46].

Analysis of TMAH valorization performance parameters

The removal capacity, removal rate, recovery ratio, and charge efficiency were calculated by using Eqs. (1)–(3):

$$Removal\ \ capacity = \sum_{n=0}^{k}(C_{n,F} - C_{0,F}) \cdot \nu \cdot M_{TMAH} \cdot (t_n - t_{n-1})/m \quad (1)$$

$$Removal\ \ rate = Removal\ \ capacity/t_{total} \quad (2)$$

$$Recovery\ \ ratio = C_{n,C}/C_{0,F} \quad (3)$$

where $C_{n,F}$ and $C_{0,F}$ are the initial and effluent concentration (mM) calculated from the conductivity in the feed channel, respectively, while $C_{n,C}$ is the effluent concentration (mM) in the concentrated

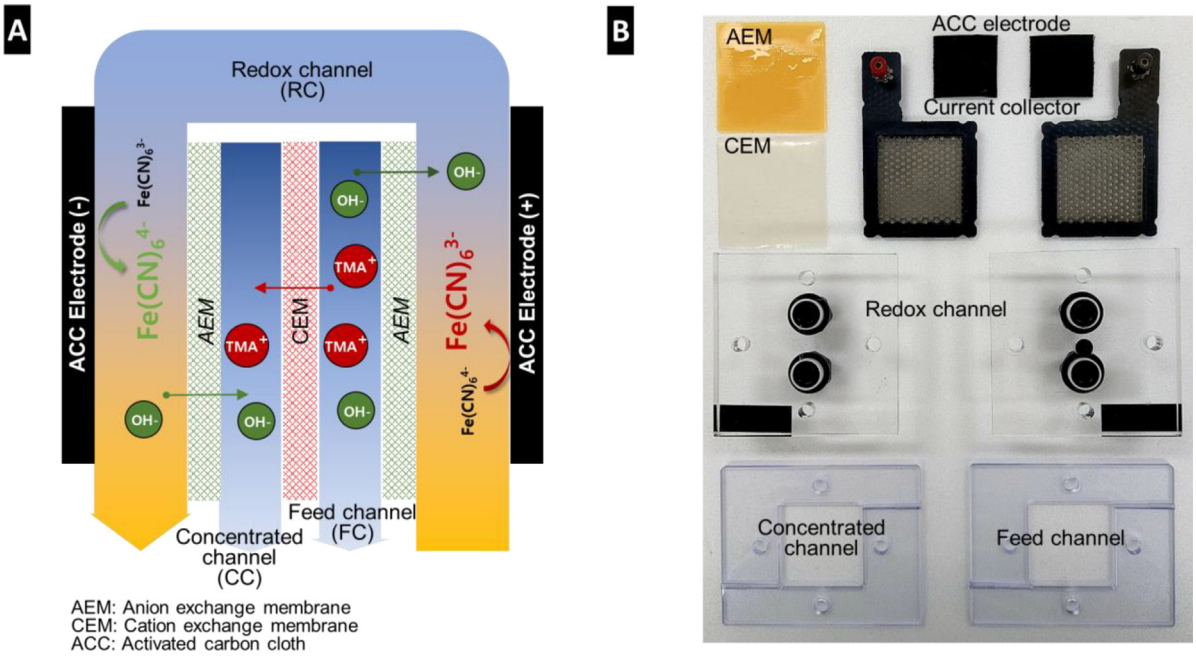

Fig. 1. Cell configuration of the RFD: (A) schematic illustration of the RDF system and (B) its cell components. The TMA^+ and OH^- indicate tetramethylammonium cation and hydroxide ion, respectively.

channels. ν is the flow rate (L/min). M_{TMAH} is the molecular weight of TMAH (91.95 g/mol), and t_n-t_{n-1} is the time intervals (min) to measure conductivity. t_{total} is total operational time (h), and m is the total mass of the electrode (g).

The energy consumption was expressed by using Eqs. (4) and (5):

$$Charge\ \ efficiency = \frac{Removal\ \ capacity}{M_{TMAH}} \Big/ \left(\frac{\int Idt}{F}\right) \tag{4}$$

$$E = \frac{V}{m_{overall}} \int_{t_1}^{t_2} Idt \tag{5}$$

where V, I, and $m_{overall}$ are the applied cell voltage (V), current (A), and the total amount of removed TMAH (mol) during the operating time (t_2-t_1) (min), respectively. F is the Faradaic constant (96485 C/mol). We triplicated all experiments to reliably confirm the result's reproducibility.

Results and discussion

Removal performance of TMAH in RFD

Fig. 2 shows the conductivity and pH profiles of effluent in the feed channel of RFD containing 0.5–10 mM TMAH solution with a cell voltage of 1.2 V. As shown in Fig. 2, the effluent conductivity and the effluent pH steadily declined as the operational time increased, that indicates a continuous ion removal from the feed solution. This is quite different from typical sinusoidal conductivity and pH profile patterns originating from charging and discharging in the conventional CDI [47], but this is significantly similar to those of ED [33]. When considering a low cell voltage of 1.2 V (no water-splitting reaction), we see that a sustainable redox reaction in the redox channel governs a continuous ion migration, which has a low reduction and oxidation peaks potential of 0.23 V and 0.42 V, respectively, seen by cyclic voltammetry (*Supplementary Information*, inset Fig. S3). The redox reaction is a diffusion-controlled process verified by the high linearity (Faradaic mechanism) between peak current and the square root of scan rate (*Supplementary Information*, Fig. S3).

Our setup employs carbon cloth electrodes. While ED cells mandate precious metal oxide electrodes to maintain harsh water-splitting reactions, the ACC electrode proved to be an excellent and cost-attractive choice to transfer charge into (and out from) the redox electrolyte. Furthermore, by applying cell voltage, the current was reached to quasi-steady state in varying TMAH concentrations (inset Fig. 2A), implying a consecutive ion migration of ionic TMAH species (i.e., TMA^+ and OH^-) with appropriate ion permeation in ion-exchange membranes. This is supported by the continuous decrease of the effluent's channel conductivity and pH values (Fig. 2A and B). TMAH ions are identified as the major component in consecutive ion migration because the permeation of the redox couple through the ion exchange membranes is negligible. Fig. 2 confirms the ability of our RFD system to remove dissolved TMAH, although being a much larger organic compound than inorganic salt ions [48]. Nevertheless, the high pH in feed resulting from TMAH solution (Fig. 2**B**) could affect the degradation of ion exchange membranes, and the redox couples can harm the environment and maintenance costs. To ensure the high feasibility in practical applications, this system could be equipped with highly pH-stable permselective membranes and cheaper/less harmful redox materials.

The key RFD TMAH removal performance (removal rate, charge efficiency, and energy consumption) are presented in Fig. 3. The TMAH removal performance strongly depended on the TMAH concentration in the feedwater stream. As the TMAH concentration in the feed increased, RFD exhibited better performance with a removal rate of 4.3 mM/g/h and 87.9% charge efficiency at a highly saline feed solution (10 mM TMAH) than that (removal rate of 0.31 mM/g/h and 20.6% charge efficiency) at a low saline feed solution (0.5 mM TMAH). Accordingly, a significant decrease in energy consumption was found from 59.3 kJ/mol to 14.9 kJ/mol, which is a ~4-fold-enhancement in energy-wise at a high feed solution. In low saline TMAH feed, the reason for low performance is probably due to poor ionic strength in the feed channel leading to the ohmic drop and deficiency of ion transportation. As a result, it can cause

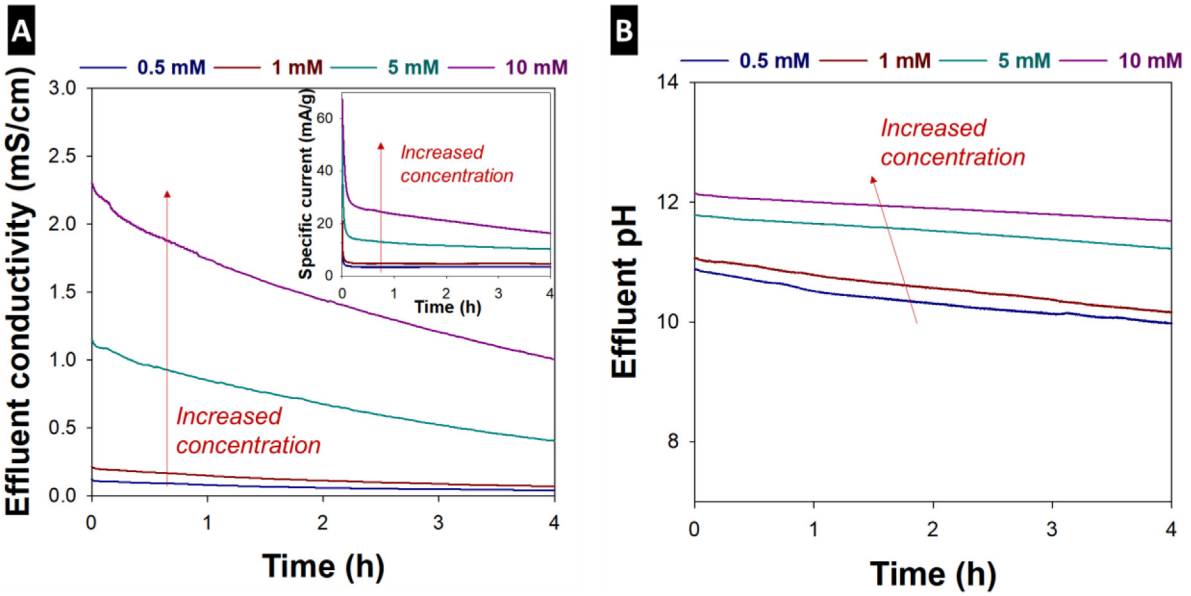

Fig. 2. The conductivity (A) and pH profiles (B) of effluent in the feed channel of RFD. The TMAH removal test was performed with a 0.5–10 mM TMAH solution in the feed channel, a redox couple stream containing a 100 mM $Na_4Fe(CN)_6$/100 mM NaOH solution, and 10 mM NaOH solution in the concentrated channel for TMAH recovery. The RFD was operated with a cell voltage of 1.2 V and a flow rate of 5 mL/min.

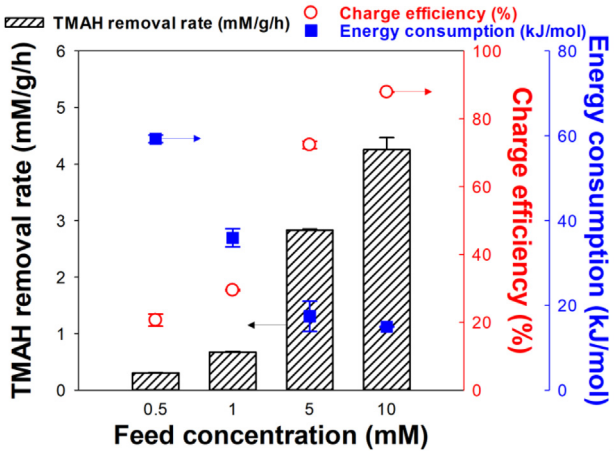

Fig. 3. TMAH removal performance examined by standard metrics including removal rate, charge efficiency, and energy consumption of RFD. The standard metric was calculated from the conversion of effluent conductivity in Fig. 2A.

high systematic resistance and unexpected side reactions such as carbon oxidation and oxygen reduction reactions [49]. Nonetheless, TMAH removal performance is comparable with the NaCl removal (i.e., conventional desalination of inorganic salt) reportedly in previous RFD research (Table 1), indicating a high potential of RFD in the treatment of charged organic compounds.

Recovery performance of TMAH in RFD

Fig. 4 presents the recovery of TMAH in RFD examined by the rate of removal and recovery of TMAH in the feed and concentrated channels, respectively (Fig. 4A), and the overall TMAH accumulation and its recovery ratio in the concentrated channel (Fig. 4B). The difference between the initial concentration and the effluent concentration in the elapsed time is denoted as ΔTMAH. For 10 mM TMAH, our system removes 4.3 mM TMAH from the feed channel over a duration of 4 h, while there is a concurrent increase of 4.1 mM in the concentrated channel. In Fig. 4A, the removal and recovery of TMAH linearly increased with the elapsed time, and their rates were proportionally related to the feed concentration of TMAH. In addition, there was no significant difference in the slope of removal and recovery (i.e., TMAH removal rate ≅ TMAH recovery rate).

The results in Fig. 4A demonstrate two major aspects. First, the high concentration dependency of TMAH in the removal rate (feed channel) demonstrates that the RFD performance is governed by a diffusion-controlled process; namely, the surface redox reaction is very fast and reversible. This means that TMAH does have a sufficient permeation rate through the ion-exchange membranes. Additionally, the optimized operational conditions can improve RFD for the TMAH removal and recovery, such as a faster flow rate or the addition of high saline supporting electrolytes. This includes the design of systems with different geometry and thinner membranes. Second, the rate balance between removal and recovery addresses that TMAH is well migrated from feed channel to concentrated channel without unexpected adsorption or loss. Moreover, for the 10 mM TMAH system, we confirmed an overall TMAH accumulation of 4.1 mM in the concentrated channel with a recovery of around 40% (Fig. 4B). This result highlights that the RDF system successfully enables a continuous TMAH removal from the wastewater stream and a simultaneous recovery for reuse. In particular, with the high linearity of the rate of removal and recovery (Fig. 4A), it is anticipated that the long operational time would enhance the recovery ratio. Additionally, the volume reduction in the concentrated channel is probably able to remarkably enrich TMAH with a higher recovery ratio instead of the symmetrically identical volume of feed and concentrated channels (∼100 mL) in this study.

Effect of Operational parameters on TMAH valorization in RFD

In the next step, the effect of operational parameters on the valorization performance of TAMH in RFD was investigated (Figs. 5–7), such as cell voltage, flow rate, several ACC electrode stacks, and real-wastewater matrix. As presented in Fig. 5A, with an increase of operational cell voltage from 0.6 V to 1.2 V, the removal rate was enhanced from 3.1 mM/g/h to 4.3 mM/g/h with a charge

Table 1
Comparison of the desalination performance of RFD for NaCl (inorganic salt) and TMAH (organic salt) solution under various experimental conditions.

Redox material	Electrode material	Cell voltage (V)	Initial concentration (mM)	Removal rate (mM/g/h)/energy consumption (kJ/mol)	Ref.
1,1′-Bis[3-(trimethylammonio)-propyl]ferrocene dichloride	Carbon fiber	0.5	600 (NaCl)	32.68/52.56	[50]
$Na_3Fe(CN)_6/Na_4Fe(CN)_6$	ACC	1.2	10 (NaCl)	1.18/122.0	[33]
$Na_3Fe(CN)_6/Na_4Fe(CN)_6$	ACC	1.2	10 (NaCl)	1.53/94.88	[31]
$Na_3Fe(CN)_6/Na_4Fe(CN)_6$	ACC	1.2	0.5 (TMAH) 10 (TMAH)	0.31/59.3 4.26/14.9	This study

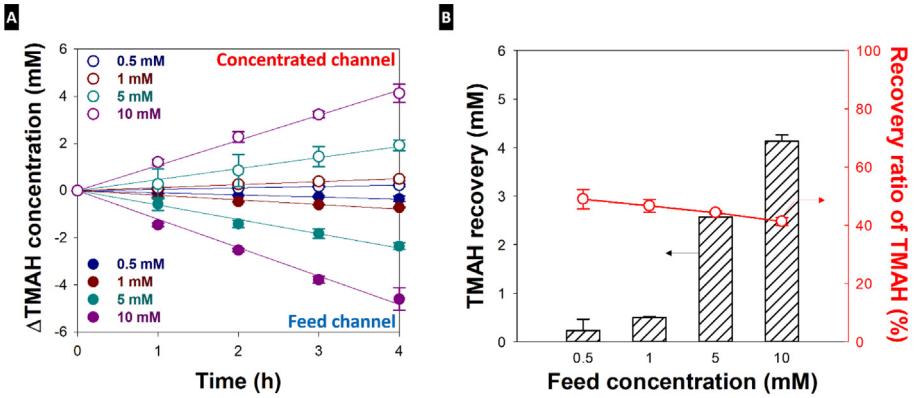

Fig. 4. Recovery performance of TMAH in RFD: (A) TMAH removal and recovery in the feed and concentrated channels, respectively as a function of operational time, and (B) overall TMAH accumulation and its recovery ratio in the concentrated channel. TMAH was collected for 1 h from the effluent in the feed and concentrated channels during RFD operation (refer to the experimental condition in Fig. 2) and quantitatified by ion chromatography.

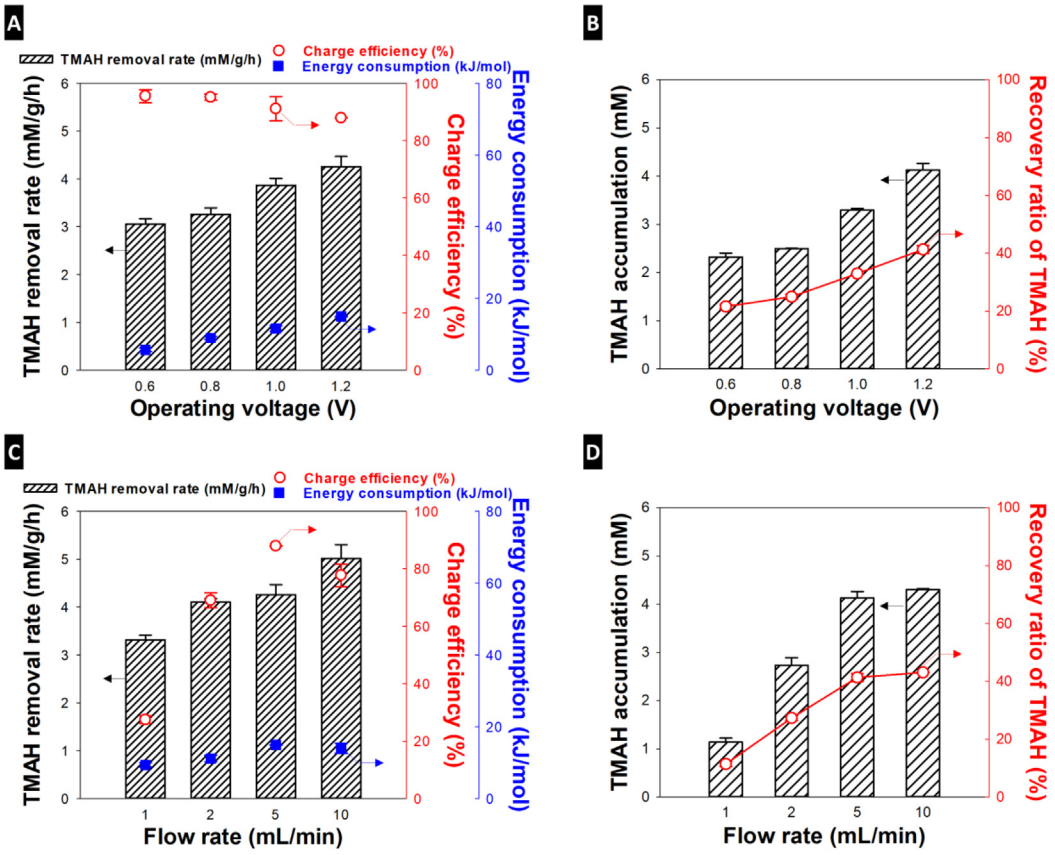

Fig. 5. Effect of operating parameters including cell voltage and flow rate on removal and recovery of TMAH in RFD. Performances were analyzed by standard metrics including removal rate, charge efficiency and energy consumption, and overall recovery and its ratio in varying cell voltages (A and B) and flow rates (C and D). The removal and recovery of TMAH were performed with a 10 mM TMAH solution in the feed channel, a redox couple stream containing a 100 mM $Na_4Fe(CN)_6$/100 mM NaOH solution, and 10 mM NaOH solution in the concentrated channel for TMAH accumulation. The RFD was operated with a varying cell voltage of 0.6–1.2 V and the flow rate of 1–10 mL/min.

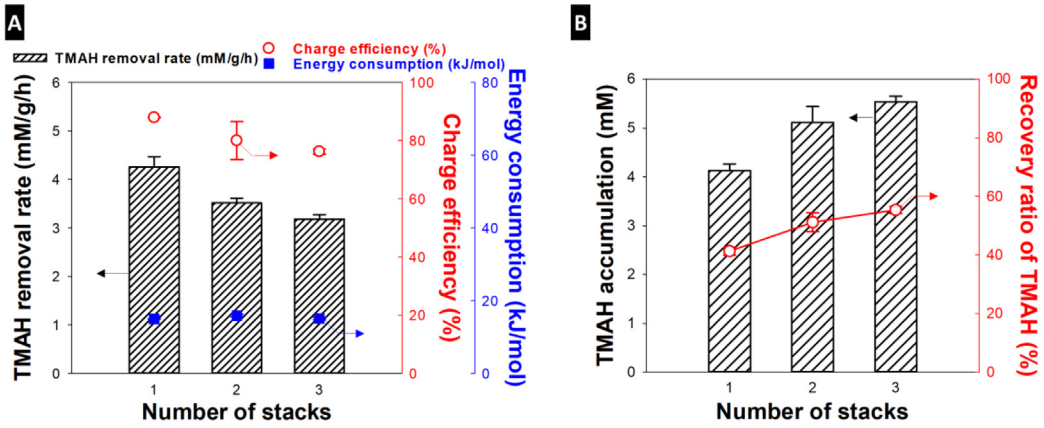

Fig. 6. Effect of ACC electrode stacks on the removal and recovery of TMAH in RFD. Performance was analyzed by standard metrics, including removal rate, charge efficiency and energy consumption (A), and overall recovery and its ratio (B) in different numbers of ACC electrode stacks. The removal and recovery of TMAH were performed with a 10 mM TMAH solution in the feed channel, a redox couple stream containing a 100 mM $Na_4Fe(CN)_6$/100 mM NaOH solution, and 10 mM NaOH solution in the concentrated channel for TMAH accumulation. The RFD was operated with a cell voltage of 1.2 V and a flow rate of 5 mL/min.

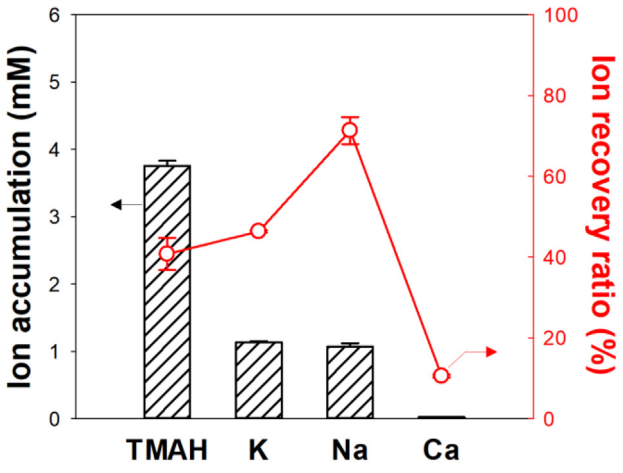

Fig. 7. Overall recovery ratio and recovery ratio in TMAH valorization of RFD from the synthetic semiconductor wastewater: The TMAH valorization test was performed with synthetic wastewater containing 10 mM TMAH, 2.5 mM KCl, 1.5 mM NaCl, and 0.25 mM $CaCl_2$ in the feed channel, a redox couple stream containing a 100 mM $Na_4Fe(CN)_6$/100 mM NaOH solution, and 10 mM NaOH solution in the concentrated channel for TMAH accumulation. The RFD was operated with a cell voltage of 1.2 V and a flow rate of 5 mL/min.

efficiency of ~90% and an energy consumption of ~15 kJ/mol. As the cell voltage increased, RFD allowed a large accumulation of TMAH with a higher recovery ratio (~40%) at a high cell voltage of 1.2 V than that (~21%) at a low cell voltage of 0.6 V (Fig. 5B). The effect of flow rate on TMAH valorization is exemplified in Fig. 5C and D. At a high flow rate (10 mL/min), RFD shows a good removal rate of 5.0 mM/g/h with a charge efficiency of ~80% and energy consumption of ~14 kJ/mol. This is about 1.5-fold-improvement in removal rate of 3.3 mM/g/h at a low flow rate (1 mL/min) with a charge efficiency of 27.4% and energy consumption of 9.3 kJ/mol. The fast flow rate led to a high TMAH recovery ratio of around 40%. It is plausible that the high cell voltage and fast flow rate can offer an optimized environment for redox reaction implying that sufficient cell voltage and flow rate are needed to drive effective redox reaction in RFD.

The influence of ACC electrode stacks on the removal and recovery of TMAH was further investigated in Fig. 6. As the number of ACC electrode stacks increased from one to three pairs (Fig. 6A), the removal rate slightly decreased from 4.3 mM/g/h to 3.2 mM/g/h. The charge efficiency was 80–90%, and the energy consumption remained at around 15 kJ/mol. The increased number of ACC electrode stacks can lead to a performance decrease in removal rate due to the systematic imperfections in a stack assembly, such as biased redox couple stream and asymmetric voltage distribution among ACC electrode stacks [51]. The accumulation of TMAH improved by 28% with three pairs of ACC electrode stacks (from 4.1 mM to 5.5 mM) with a high recovery ratio of around 55% (Fig. 6B). Thereby, the stack of ACC electrodes would be an effective approach for improving TMAH valorization since the stack of ACC electrodes is much simpler and cheaper to obtain high performance than the stacking of multiple unit cells, requiring many ion-exchange membranes and complicated cell assembly (which contributes to increased costs).

To better understand the practical aspect of removal and recovery of TMAH in RFD, the performance was examined in the synthetic semiconductor wastewater (Fig. 7). As a proof-of-concept, real semiconductor wastewater matrix containing 10 mM TMAH was prepared with K^+ (2.5 mM), Na^+ (1.5 mM), and Ca^{2+} (0.25 mM) as the major competitive inorganic cations reported in previous literature [45]. To quantitatively analyze TMAH valorization, the concentration of TMAH and the competing cations were measured by ion chromatography. Despite the competitive cations in the synthetic semiconductor wastewater, RFD accumulated TMAH to 3.8 mM in the concentrated channel during 4 h. In contrast, the recovery of K^+ and Na^+ was approximately 1 mM with a negligible recovery of Ca^{2+}. The recovery ratio of TMAH (~43%) was smaller than that of K^+ (~50%) and Na^+ (~80%). This is probably attributed to the larger size of TMAH than others leading to retardation of the ion transportation. The results mean that the charge and size of ions in the feed stream significantly affect the recovery performance in RFD. Consequently, to enhance the recovery performance of TMAH, the end-product should be further purified for the effective valorization of TMAH. For the purification, it is required to provide subsequent post-treatment steps for selective recovery of TMAH with electrodes, adsorbents, or membranes.

Techno-economic Analysis of RFD for TMAH valorization

The economic feasibility of our RFD system was evaluated by calculating its capital cost and recovery profit compared to the conventional ED system (Fig. 8). We analyzed the required costs and expected recovery profit to treat the TMAH wastewater

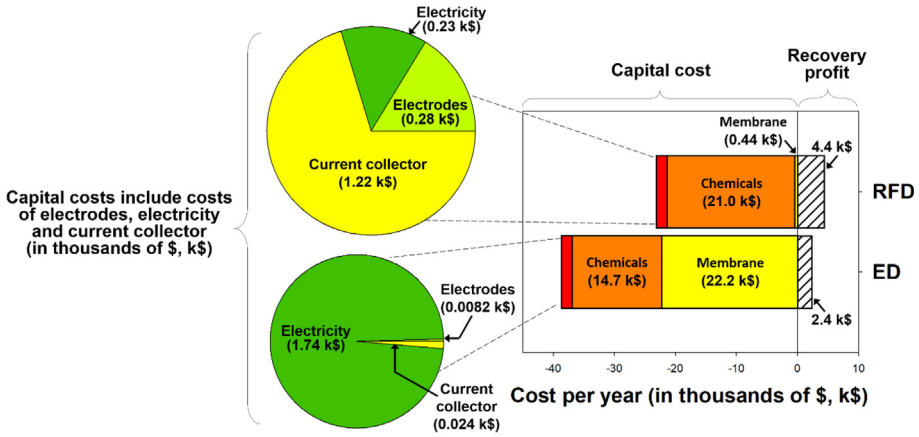

Fig. 8. Economic analysis of TMAH removal and recovery in RFD compared to the conventional ED. The capital cost regarding electrodes and electricity was much smaller than the other expenses (larger circle diagram).

(1,000 L per day) for a year with a scale-up system considered previous literature (see *Supplementary Information*)[45,46,51]. In particular, to clarify the insight into the benefits of RFD in cell assembly, the RFD cell assembly was built up with electrode stacks instead of multiple unit cells in the ED process. The capital cost for each system was simplified with the electrode, current collector, ion exchange membranes and chemicals for a cell assembly, and the consumed electricity for TMAH removal and recovery (*Supplementary Information*, Table S1 and Fig. S2). The consumed electricity assumed a charge efficiency of less than 50% in RFD with a single ACC electrode stack based on the results in Figs. 4–6. In addition, we assumed for the RFD system a recovery of 20% (assuming 50% efficiency of the results of 50% recovery from a one electrode pair unit cell in Fig. 4B to compensate for the additional post-treatment steps for the useful end-product valorization and performance degradation originating from the increase of stack numbers of the electrode in the scale-up). In comparison, the recovery of ED was calculated with 11% as reported in the previous literature. As presented in Fig. 8, a significant reduction in the capital cost was found in RFD ($23,112), which was approximately 60% in conventional ED ($38,660) (*Supplementary Information*, Table S1). The ion exchange membranes were a decisive factor in decreasing the RFD capital cost originating from multi-electrode stacks for scale-up contrary to increased unit cells in ED. The electrical cost in RFD (~$232) was much smaller than that in ED ($1,738) due to the low operational cell voltage for the reversible redox reaction. In addition, our system could make a net cost of ~$18,700 while the overall required cost of conventional ED was ~$36,300 considered the recovery profit. This reveals the high TMAH recovery effectiveness of the RFD system, implying that the recovery could be a good strategy to compensate for the capital cost of TMAH treatment. Overall, the RFD system is a promising, sustainable, and cost-effective for the valorization of TMAH in wastewater treatment.

Conclusions

We introduce RFD as an effective TMAH removal and recovery system, as exemplified by experimental data that include actual semiconductor industry wastewater. We chose TMAH as an important material, but the RFD technology clearly extends to other organic compounds. For example, with a low cell voltage of 1.2 V, the RFD system continuously removed TMAH from the wastewater stream in feed water with removal rate of ~4.3 mM/g/h, charge efficiency of ~90%, and energy consumption of ~15 kJ/mol while TMAH was simultaneously recovered with a recovery of ~40%. The system capitalizes on the reversible redox reaction in the redox channel instead of the water-splitting reaction. In addition, its performance in TMAH treatment was comprehensively examined in various experimental conditions, including TMAH concentration, cell voltage, flow rate, electrode stacking, and real-wastewater matrix. This confirmed the high effectiveness of RFD in TMAH with low operational cost and energy consumption compared to conventional ED processes. The results suggest RFD could be a useful approach for TMAH valorization, and thus we envision new opportunities for RFD in wastewater treatment via the removal and recovery of charged organic pollutants in water.

Declaration of Competing Interest

The authors declare that they have no known competing financial interests or personal relationships that could have appeared to influence the work reported in this paper.

Acknowledgments

This research was supported by the research grant of Kongju National University in 2022 and by the research grant of the Waste to Energy Recycling Human Resource Development Project of Korea Ministry of Environment (ME). The INM authors thank Eduard Arzt (INM) for his continued support. We acknowledge support for the eLiRec project by the European Union from the European Regional Development Fund (EFRE) and the State of Saarland, Germany.

Appendix A. Supplementary data

Supplementary data to this article can be found online at https://doi.org/10.1016/j.jiec.2022.10.053.

References

[1] A. Maddocks, R.S. Young, P. Reig, (2015).
[2] K.D. Orner, J.R. Mihelcic, Environ. Sci.: Water Res. Technol. 4 (2018) 16–32.
[3] A.D. Khawaji, I.K. Kutubkhanah, J.-M. Wie, Desalination 221 (2008) 47–69.
[4] I.C. Karagiannis, P.G. Soldatos, Desalination 223 (2008) 448–456.
[5] H. Lim, Y. Ha, H.B. Jung, P.S. Jo, H. Yoon, D. Quyen, N. Cho, C.-Y. Yoo, Y. Cho, J. Ind. Eng. Chem. 81 (2020) 317–322.
[6] A. Subramani, J.G. Jacangelo, Water Res. 75 (2015) 164–187.
[7] S. Lattemann, M.D. Kennedy, J.C. Schippers, G. Amy, Sustainab. Sci. Eng. 2 (2010) 7–39.
[8] J. Eke, A. Yusuf, A. Giwa, A. Sodiq, Desalination 495 (2020) 114633.

[9] Z.-L. Ye, K. Ghyselbrecht, A. Monballiu, L. Pinoy, B. Meesschaert, Water Res. 160 (2019) 424–434.
[10] L. Gurreri, A. Tamburini, A. Cipollina, G. Micale, Membranes 10 (2020) 146.
[11] S. Hube, M. Eskafi, K.F. Hrafnkelsdóttir, B. Bjarnadóttir, M.Á. Bjarnadóttir, S. Axelsdóttir, B. Wu, Sci. Total Environ. 710 (2020) 136375.
[12] G. Amy, N. Ghaffour, Z. Li, L. Francis, R.V. Linares, T. Missimer, S. Lattemann, Desalination 401 (2017) 16–21.
[13] T. Matsuura, Desalination 134 (2001) 47–54.
[14] I. Khoshrou, M.J. Nasr, K. Bakhtari, Sol. Energy 153 (2017) 115–125.
[15] N.M. Wade, Desalination 136 (2001) 3–12.
[16] P. Srimuk, X. Su, J. Yoon, D. Aurbach, V. Presser, Nat. Rev. Mater. 5 (2020) 517–538.
[17] V. Pothanamkandathil, J. Fortunato, C.A. Gorski, Environ. Sci. Technol. 54 (2020) 3653–3662.
[18] D. Desai, E.S. Beh, S. Sahu, V. Vedharathinam, Q. van Overmeere, C.F. de Lannoy, A.P. Jose, A.R. Voïkel, J.B. Rivest, ACS Energy Lett. 3 (2018) 375–379.
[19] H. Yoon, J. Lee, S. Kim, J. Yoon, Sep. Purif. Technol. 215 (2019) 190–207.
[20] M.A. Alkhadra, X. Su, M.E. Suss, H. Tian, E.N. Guyes, A.N. Shocron, K.M. Conforti, J.P. De Souza, N. Kim, M. Tedesco, Chem. Rev. 122 (2022) 13547–13635.
[21] L. Wang, Y. Zhang, K. Moh, V. Presser, Curr. Opin. Electrochem. 29 (2021).
[22] M. Suss, S. Porada, X. Sun, P. Biesheuvel, J. Yoon, V. Presser, Energy Environ. Sci. 8 (2015) 2296–2319.
[23] N. Kim, J. Lee, S. Kim, S.P. Hong, C. Lee, J. Yoon, C. Kim, Appl. Sci. 10 (2020) 683.
[24] J.-W. Son, H.-C. Roh, J.-H. Choi, Environ. Eng. Res. 27 (1) (2022) 200650.
[25] F. Zhang, F. Yang, Environ. Eng. Res. 28 (1) (2023) 210430.
[26] M. Pasta, C.D. Wessells, Y. Cui, F. La Mantia, Nano Lett. 12 (2012) 839–843.
[27] M.E. Suss, Y. Zhang, I. Atlas, Y. Gendel, E. Ruck, V. Presser, Electrochem. Commun. 136 (2022) 107211.
[28] T. Xu, C. Huang, AIChE J. 54 (2008) 3147–3159.
[29] S. Al-Amshawee, M.Y.B.M. Yunus, A.A.M. Azoddein, D.G. Hassell, I.H. Dakhil, H. A. Hasan, Chem. Eng. J. 380 (2020) 122231.
[30] S.-I. Jeon, H.-R. Park, J.-G. Yeo, S. Yang, C.H. Cho, M.H. Han, D.K. Kim, Energy Environ. Sci. 6 (2013) 1471–1475.
[31] N. Kim, J. Jeon, J. Elbert, C. Kim, X. Su, Chem. Eng. J. 428 (2022) 131082.
[32] N. Kim, X. Su, C. Kim, Chem. Eng. J. 420 (2021) 127715.
[33] D. Ahn, D. Kim, J.H. Park, N. Kim, E. Lim, C. Kim, Desalination 520 (2021) 115333.
[34] F. Chen, J. Wang, C. Feng, J. Ma, T.D. Waite, Chem. Eng. J. 401 (2020) 126111.
[35] K. Ramalingam, Y. Zhu, J. Wang, M. Liang, Q. Wei, X. Chen, F. Sun, D. Chen, Z. Zhang, S.H. Aung, ACS Sustain. Chem. Eng. 9 (2021) 12779–12787.
[36] M. Liang, K. Feng, R. Karthick, L. Zhang, Y. Shi, K. San Hui, K.N. Hui, F. Jiang, F. Chen, Green Chem. 22 (2020) 4133–4139.
[37] G. Mohandass, T. Kim, S. Krishnan, ACS ES&T Eng. 1 (2021) 1678–1687.
[38] R.H. French, H.V. Tran, Annu. Rev. Mater. Res. 39 (2009) 93–126.
[39] J. Lv, Y. Wang, M. Fu, C. Ou, F. Xiao, J. Cleaner Prod. 279 (2021) 123502.
[40] H.-M. Chang, S.-S. Chen, S.-S. Hsiao, W.-S. Chang, I.-C. Chien, C.C. Duong, T.X.Q. Nguyen, J. Hazard. Mater. 427 (2022) 128200.
[41] Y.-C. Liu, Y.-C. Hu, I.-M. Chu, Y.-H. Wei, S.-L. Tsai, J. Environ. Chem. Eng. 10 (2022) 106931.
[42] T.-K. Kim, T. Kim, I. Lee, K. Choi, K.-D. Zoh, J. Hazard. Mater. 409 (2021) 123759.
[43] C.-C. Lin, C.-C. Yang, J. Ger, J.-F. Deng, D.-Z. Hung, Clin. Toxicol. 48 (2010) 213–217.
[44] C. Kim, P. Srimuk, J. Lee, S. Fleischmann, M. Aslan, V. Presser, Carbon 122 (2017) 329–335.
[45] Y. Wang, Z. Zhang, C. Jiang, T. Xu, Ind. Eng. Chem. Res. 52 (2013) 18356–18361.
[46] J. Coenen, A. Martin, O. Dahl, M. Åslin, J. Membr. Sci. 579 (2019) 283–293.
[47] N. Kim, S.P. Hong, J. Lee, C. Kim, J. Yoon, ACS Sustain. Chem. Eng. 7 (2019) 16182–16189.
[48] S. Porada, G. Feng, M. Suss, V. Presser, RSC Adv. 6 (2016) 5865–5870.
[49] C. Kim, P. Srimuk, J. Lee, V. Presser, Desalination 443 (2018) 56–61.
[50] E.S. Beh, M.A. Benedict, D. Desai, J.B. Rivest, ACS Sustain. Chem. Eng. 7 (2019) 13411–13417.
[51] N. Kim, J. Lee, S.P. Hong, C. Lee, C. Kim, J. Yoon, Desalination 479 (2020) 114315.

Supplementary Information

Redox flow desalination for tetramethylammonium hydroxide removal and recovery from semiconductor wastewater

Dayoung Ahn[1,†], Seonghwan Kim[1,2,†], Panyu Ren,[3,4] Volker Presser,[3,4,5] and Choonsoo Kim[1,*]*

[1] *Department of Environmental Engineering with Institute of Energy/Environment Convergence Technologies and Department of Future Convergence Engineering, Kongju National University, 1223-24, Cheonan-daero, Cheonan-si 31080, Republic of Korea*

[2] *Samsung Research, Samsung Electronics Co., Ltd.*

[3] *INM – Leibniz Institute for New Materials, Campus D2.2, 66123 Saarbrücken, Germany*

[4] *Department of Materials Science and Engineering, Saarland University, Campus D2.2, 66123 Saarbrücken, Germany*

[5] *Saarene – Saarland Center for Energy Materials and Sustainability, Campus C4.2, 66123 Saarbrücken, Germany*

*Corresponding author's eMail: choonsoo@kongju.ac.kr (CK) and volker.presser@leibniz-inm.de (VP)

[†]The authors contributed equally to this work.

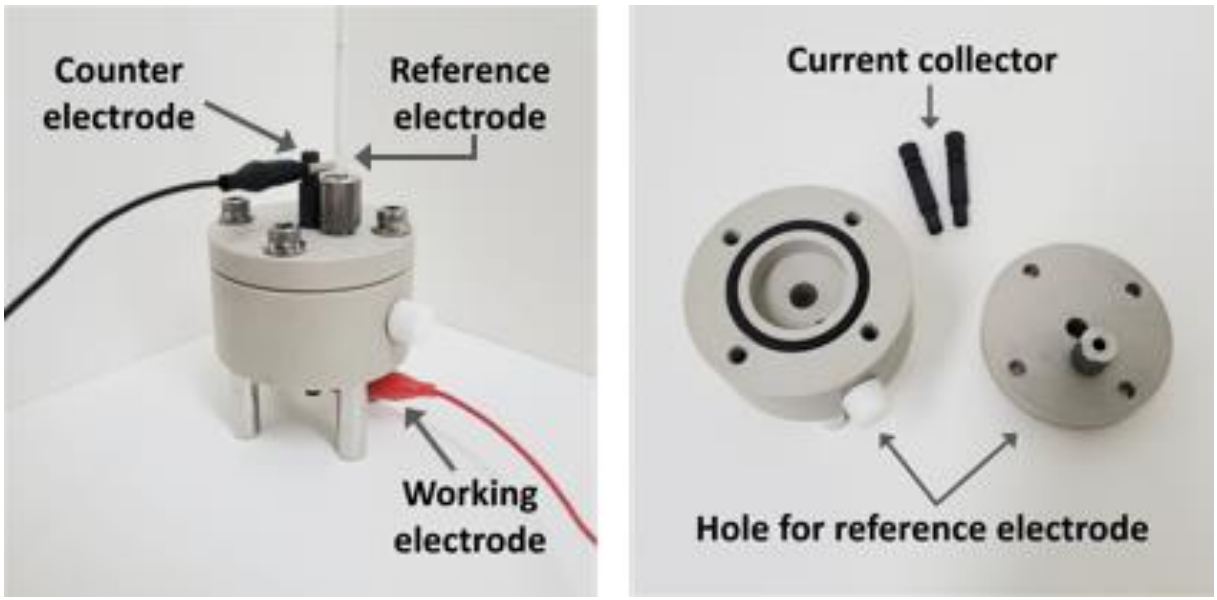

Fig. S1: Custom-built electrode system with Ag/AgCl reference electrode for electrochemical analysis

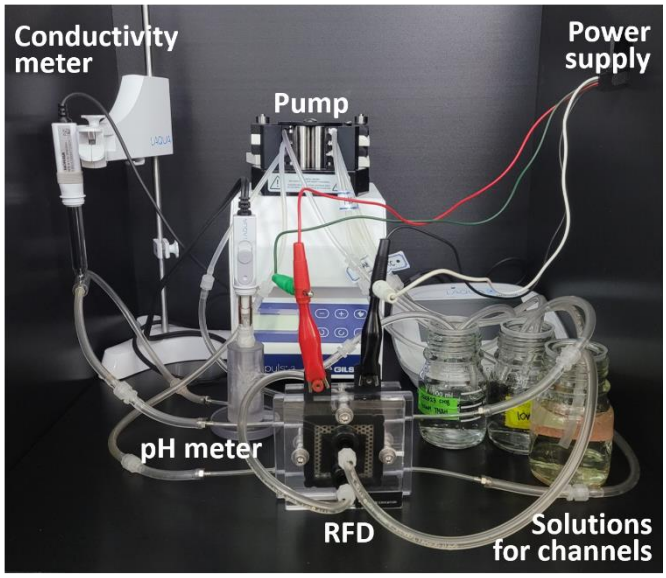

Fig. S2: Constant temperature and humidity chamber for evaluation of TMAH valorization.

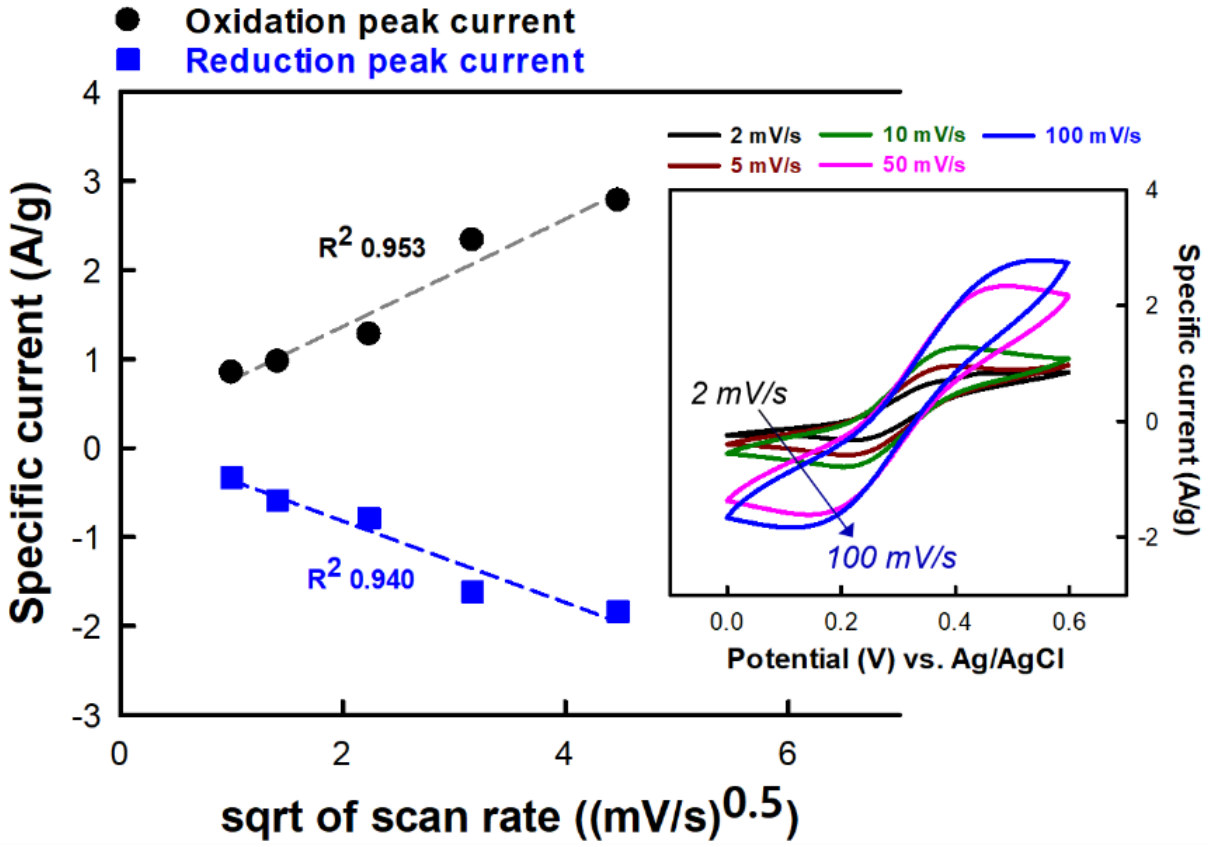

Fig. S3: Linearization of the peak current examined with cyclic voltammograms (the inset) of ACC electrode (diameter of 1 cm). Cyclic voltammetry was conducted with different scan rates ranging from 2 mV/s to 100 mV/s in 100 mM $Na_4Fe(CN)_6$/100 mM NaOH.

Table S1: Capital and operating cost of TMAH removal in RFD

	$/yr	Unit prices
Electrode[1]	282	5.86 $/m^2 (DSA®)
Ion exchange membrane[2]	444	200 $/m^2 AEM 170 $/m^2 CEM
Current collector (Carbon steel) [3]	1,216	19 $/m^2
Chemicals [4-6]	20,938	11.34 $/L Ferricyanide 3.7 $/L Ferrocyanide 3.5 $/L Sodium hydroxide
Electricity	232	0.09 $/kWh
Total	23,112	

Table S2: Capital and operating cost of TMAH removal in ED.

	$/yr	Unit prices
Electrode [1]	8.25	5.86 $/m^2 (DSA®)
Ion exchange membrane [2]	22,200	200 $/m^2 AEM 170 $/m^2 CEM
Current collector (Carbon Steel) [3]	24	19 $/m^2
Chemicals [7-8]	14,690	50.7136 $/L 3.2% TMAH (CC) 6.336 $/L 0.3 M Na_2SO_4 (rinse electrolyte) 0.0127 $/g Activated carbon (rinse wastewater)
Electricity	1,738	0.09 $/kWh
Total	38,660	

Table S3: Recovery profit of TMAH removal and recovery in RFD compared to ED.

	RFD		ED	
	Recovery profit	Unit prices	Recovery profit	Unit prices
TMAH recovery	43,848 $/yr (20% recovery)	0.84 $/L TMAH	23,678 $/yr (10.8% recovery)	0.84 $/L TMAH

To analyze the capital costs and recovery profit for RFD and ED (**Table S1** and **S2**), the following assumptions were made:
First, 500 L of TMAH wastewater was treated in each round, and all processes were operated twice a day for 5 days in 52 weeks. The techno-economic analysis (TEA) was calculated in $/yr and only the major components used in the system were considered for simplification. The unit price indicates the normalized cost for each component in a single-cell assembly. Additional conditions considered for the scale-up system were:

1) System (**Fig. S4**):
   · All systems could be scaled up to 100 cm × 100 cm module size and 80 cm × 80 cm for electrodes and current collectors [9]. Approximately 10% of carbon electrodes are replaced in a year, and several studies have shown that the membrane replacement should be done approximately every five years [10-11]. The fully inclusive cost included component replacement.
   ·The ED system consisted of 50 pairs of ion-exchange membranes and one pair of electrodes

(TiO_2/RuO_2).

·The RFD system comprised 50 pairs of ACC electrodes and one pair of ion exchange membranes, where the carbon electrodes are of the same size and the large surface area of the stacks can enable expansion of the RFD system.

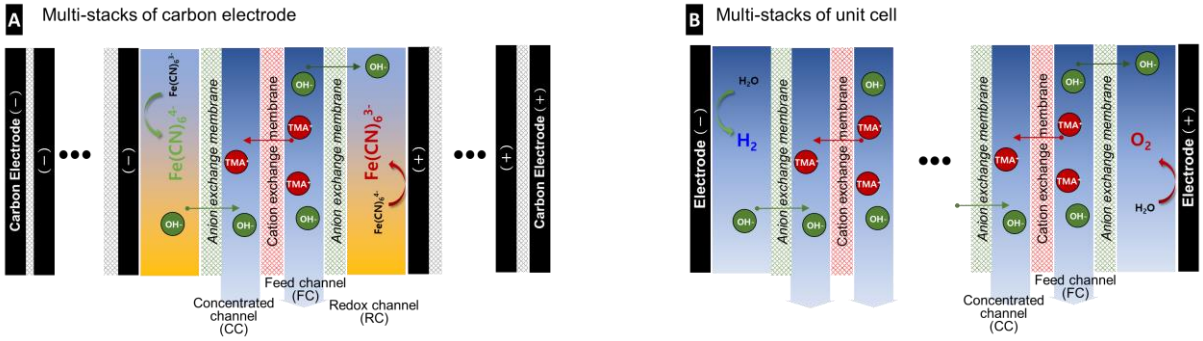

Fig. S4: Configuration of Scale-up module of RFD and ED: (A) RFD system with multi-stacks of a carbon electrode and (B) ED system with multi-stacks of a unit cell.

2) Chemicals:

· The ED system uses chemicals such as 3.2% TMAH solution for TMAH recovery in the concentrated channel, 0.3 M Na_2SO_4 for the water-splitting reaction, and activated carbon for rinsing wastewater.

· The RFD system uses 10 mM NaOH for TMAH recovery in the concentrated channel and 100 mM ferri-/ferrocyanide for the redox reaction.

3) Electricity:

· In the ED system, the current density was ~30 mA/cm^2 during the operation time of 78 min as the optimized condition with an electrical charge of 0.09 $/kWh. The electricity cost was calculated to be $6.67 for a single cell.

· In the RFD system, cell operation was performed with a constant voltage of 1.2 V during the operation time of 4 h. The electricity cost was calculated to be $0.89 for a single cell with an electrical charge of 0.09 $/kWh.

4) Recovery profit:

· In the ED system, the recovery profit was calculated from the reported recovery ratio of 10.8% in a single-cell assembly.

· In the RFD system, the recovery ratio was assumed to have 50% efficiency of the recovery ratio (~40%) obtained with a unit cell (**Fig. 4B**).

· After considering post-treatment reusage of TMAH, the overall recovery profit was estimated by a factor of 0.1.

References:

[1] Activated carbon clothes, https://korean.alibaba.com/p-detail/100-60667369198.html?spm=a2700.galleryofferlist.topad_classic.d_title.25a749b30e2h4Y
[2] Ion-exchange membrane, http://www.changjotechno.co.kr/page/0206_2_1.php
[3] Flat, Stl. https://www.grainger.com/product/DIRECT-METALS-Expanded-Sheet-5PAX6.
[4] Tetramethylammonium hydroxide, https://www.sigmaaldrich.com/KR/ko/search/tmah?focus=products&page=1&perpage=30&sort=relevance&term=tmah&type=product
[5] Ferri-/ferro-cyanide, https://www.alibaba.com/trade/search?fsb=y&IndexArea=product_en&CatId=&tab=all&SearchText=ferrocyanide
[6] Sodium hydroxide, https://www.dslab.co.kr/?act=shop.goods_view&CM=7967&GC=GD0L02
[7] Y. Wang, Z. Zhang, C. Jiang, T. Xu, Ind. Eng. Chem. Res., 52 (2013) 18356-18361.
[8] Sodium sulfate solution, https://www.flinnsci.com/search-results/?type=All&defaultType=Products&query=sodium+sulfate
[9] N. Kim, J. Lee, S.P. Hong, C. Lee, C. Kim, J. Yoon, Desalination, 479 (2020) 114315.
[10] H. Strathmann, Desalination 264(3) (2010) 268-288.
[11] J. Shen, J. Huang, H. Ruan, J. Wang, B. Van der Bruggen, Desalination 342 (2014) 118-125.

4.8. Life after death: Re-purposing end-of-life supercapacitors for electrochemical water desalination

Panyu Ren,[1,2] Mohammad Torkamanzadeh,[1] Stefanie Arnold,[1]

Emmanuel Pameté,[1] and Volker Presser,[1,2,3]

[1] *INM - Leibniz Institute for New Materials, Campus D2 2, 66123, Saarbrücken, Germany*

[2] *Department of Materials Science & Engineering, Saarland University, Campus D2 2, 66123, Saarbrücken, Germany*

[3] *saarene - Saarland Center for Energy Materials and Sustainability, Campus C4 2, 66123 Saarbrücken, Germany*

Citation:

P. Ren, M. Torkamanzadeh, S. Arnold, E. Pameté, and V. Presser, Life after death: Re-purposing end-of-life supercapacitors for electrochemical water desalination, Batteries & Supercaps (2024): e202400506

Own contribution:

Investigation, Data curation, Visualization, Writing - Original Draft, Writing - Review &Editing.

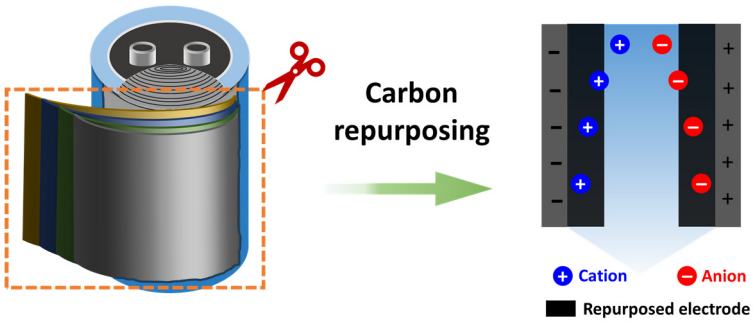

Batteries & Supercaps

Research Article
doi.org/10.1002/batt.202400506

Chemistry Europe
European Chemical Societies Publishing

www.batteries-supercaps.org

Life After Death: Re-Purposing End-of-Life Supercapacitors for Electrochemical Water Desalination

Panyu Ren,[a, b] Mohammad Torkamanzadeh,[a] Stefanie Arnold,[a] Emmanuel Pameté,[a] and Volker Presser*[a, b, c]

This study explores the potential of re-purposing end-of-life commercial supercapacitors as electrochemical desalination cells, aligning with circular economy principles. A commercial 500-Farad supercapacitor was disassembled, and its carbon electrodes underwent various degrees of modification. The most straightforward modification involved NaOH-etching of the aluminum current collector to produce free-standing carbon films. More advanced modifications included CO_2 activation and binder-added wet processing of the electrodes. When evaluated as electrodes for electrochemical desalination via capacitive deionization of low-salinity (20 mM) NaCl solutions, the minimally modified NaOH-etched carbon electrodes achieved an average desalination capacity of 5.8 mg g^{-1} and a charge efficiency of 80%. In contrast, the CO_2-activated, wet-processed electrodes demonstrated an improved desalination capacity of 7.9 mg g^{-1} and a charge efficiency above 90% with stable performance over 20 cycles. These findings highlight the feasibility and effectiveness of recycling supercapacitors for sustainable water desalination applications, offering a promising avenue for resource recovery and re-purposing in pursuing environmental sustainability.

Introduction

We have seen a significant shift towards a circular economy emphasizing sustainability and waste reduction in recent years.[1] This transition aims to minimize waste and maximize the lifecycle of products, fostering a more sustainable approach to resource management. As a result, innovative strategies for the intelligent re-purposing of spent resources have garnered significant academic and industrial interest. Numerous studies now explore these strategies, seeking to develop efficient methods to transform waste into valuable inputs for new products and processes, contributing to a more sustainable future. Examples include carbon materials derived from a host of bio-wastes[2,3] or manufactured wastes such as cigarette filters[4–6] and face masks during the pandemic,[7] utilized as electrodes for energy storage devices or electrochemical desalination systems. Non-carbon waste has also been the subject of many other studies, such as re-using rusted iron wire waste collected from construction sites as supercapacitor electrodes made of carbon/Fe_3O_4 nanocomposites.[8]

In addition to the derivatization of wastes, direct re-use of end-of-life devices is another promising approach toward a circular economy. Examples include disassembling old electrical motors and directly re-using the permanent magnets in their core, containing rare earth elements, in a new motor.[9] The direct re-use strategy is widely applied for the recovery of magnets.[10,11] For batteries, it depends on the state of health and target application conditions. For example, batteries from retired electric vehicles can often be re-purposed for a second-life application without dismantling the devices for stationary applications. Also, recent research explores the regeneration of spent battery electrodes rather than the elaborate process of elemental recovery through hydrometallurgical or pyrometallurgical processing.[12,13] Recently, we also reported a facile recycling process for end-of-life MXene ($Ti_3C_2T_x$) electrodes for re-use in Li-ion and Na-ion battery anodes.[14] Most commonly, emerging on a large scale due to evolving governmental regulations,[15,16] most batteries at present and in the near future will undergo a complete recycling process, much like recycling glass or paper toward closing the loop for precious element recovery toward new cell production.

As a technology different from batteries, supercapacitors enable rapid and effective energy storage for high-power applications ranging from consumer electronics to renewable energies.[17,18] Due to their high-power capabilities, supercapacitors are coupled with batteries in almost any battery-powered system to either render burst-mode delivery of electric energy, such as in a camera flash, or to store a suddenly generated high amount of electric energy, such as in regenerative braking.[19] Depending on the operational conditions, commonly, after hundreds of thousands of cycles,[20,21] the supercapacitors reach their end of life, which is characterized by a decrease in their

[a] P. Ren, M. Torkamanzadeh, S. Arnold, E. Pameté, V. Presser
INM – Leibniz Institute for New Materials, D2 2, 66123 Saarbrücken, Germany
E-mail: volker.presser@leibniz-inm.de

[b] P. Ren, V. Presser
Department of Materials Science & Engineering, Saarland University, Campus D2 2, 66123 Saarbrücken, Germany

[c] V. Presser
saarene, Saarland Center for Energy Materials and Sustainability, Campus C4 2, 66123 Saarbrücken, Germany

Supporting information for this article is available on the WWW under https://doi.org/10.1002/batt.202400506

capacitance (−20%) and/or increase in their equivalent series resistance (+100%).[22,23] Without containing precious elements, such as lithium, cobalt, or nickel, supercapacitor recycling, while eco-relevant, faces particular economic challenges.[24] Although various re-use or recycling strategies[25,26] such as shredding,[27] thermal treatments,[28,29] and hydrometallurgical processes[30] have been so far developed for lithium-ion battery recycling, supercapacitor recycling[31] has not seen significant attention to date. End-of-life supercapacitor devices are, as a result, not effectively recycled. Conventional supercapacitors may not contain precious materials like batteries, but there may be potentially hazardous electrolytes (e.g., acetonitrile and $TEABF_4$) dispersed in the activated carbon electrodes.[32] Hence, re-using activated carbon can partially compensate for the cost of recycling. It was reported that a method of supercapacitor recycling based on shredding and mild thermal treatment can recycle activated carbon, aluminum, and acetonitrile while leaving the electrolyte salt and the polymer binder behind in the activated carbon, making the recycled activated carbon has a high surface area up to 1200 $m^2 g^{-1}$ and 40 mass% of acetonitrile with high purity.[31] Chodankar et al. regenerated activated carbon materials from end-of-life supercapacitors through a straightforward thermal activation process and successfully reintegrated them into high-voltage, ultra-stable supercapacitors.[33] Additionally, Wu et al. successfully recycled activated carbon (surface area up to 1403 $m^2 g^{-1}$) from a used HYPSC-002R7–3000 supercapacitor and re-purposed it as a cost-effective adsorbent for the efficient removal of toxic Ag(I) and Cr(VI) ions from aqueous solutions.[34] This approach is not just recycling the used supercapacitor material for the same purpose but adapting it for the treatment of contaminated wastewater. Among various water treatment techniques, capacitive deionization is regarded as the most effective process for ion separation due to its low cost, high efficiency, and ease of operation.[35] Various electrochemical desalination strategies have been developed in different water media,[35] which included desalination,[36,37] water softening,[38,39] and heavy metal removal.[40–43] Developing a simple, cost-effective method for recycling supercapacitors demands significant research attention, particularly regarding the potential hazards posed by conventional electrolytes, solvents, and polymer binders at the end of the device's life. Additionally, the re-use of recycled materials should be considered.[32]

As the first study of this type, the present work examines the feasibility of turning a commercial supercapacitor with a capacitance of 500 F into an electrochemical desalination cell for capacitive deionization. To transform its application, we investigate several routes, ranging from the least to the highest modification degrees made to the device. The least-invasive modification degree pertains to making holes in the supercapacitor device and passing a saline aqueous electrolyte (NaCl) through it. The highest modification degree pertains to a whole disassembly of the supercapacitor, removal of its carbon electrodes (separating the aluminum substrate and activated carbon electrodes by NaOH etching), reprocessing them into new electrodes, and testing them as electrodes for electrochemical desalination. The electrode fabrication in the latter route also branches out into CO_2 activation and binder-added wet processing of the electrodes (Figure 1). The CO_2 activation is conducted with the goal of potential enhancement in the porosity and wettability of the electrodes. We then assess the merit of each of the said routes in terms of desalination capacity, charge efficiency, and cycle stability, together with the efforts associated with each trajectory.

Results and Discussion

Physicochemical Characterizations

Figure 1 schematically shows the procedure through which the commercial supercapacitor electrodes were reprocessed and re-purposed for use as electrochemical desalination electrodes. Photographs and videos from the disassembly process are in *Supporting Information*, Figure S1 and Video S1–2. The obtained electrode coating from the commercial supercapacitor has been subjected to detailed physicochemical characterizations. To remove the aluminum current collector from the carbon electrodes, the electrode bundle was immersed into a 10 mass% aqueous NaOH solution. The scanning electron

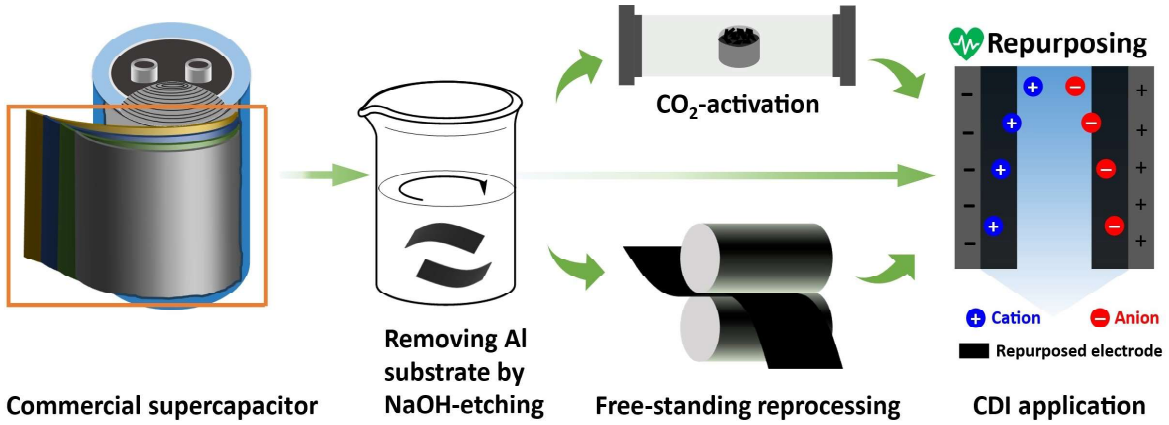

Figure 1. Schematic representation of the step-by-step processes involved in disassembling the commercial supercapacitor in this study and their re-purposing for electrochemical desalination electrodes.

micrographs in Figure 2A–B show the electrode films after being detached from the aluminum current collector and thoroughly dried under vacuum. The etching process could cause the cracked features on the electrode. However, the electrode delivers a homogenous and dense packing of carbon particles with an average size of around 2 μm. Scanning electron micrographs of the supercapacitor separator and additional images of the supercapacitor electrodes are provided in *Supporting Information*, Figure S2–S3. The relatively large particles (Figure 2A–B and *Supporting Information*, Figure S3) are attributed to activated carbon used in the electrode surrounded by small debris (assumed to be carbon black particles used as a conductive additive).

The X-ray diffraction (XRD) data in Figure 2C shows broad reflections at around 23° and 43° 2θ in alignment with incompletely graphitic carbon (PDF# 41-1487). The sharp reflection at 18° 2θ indicates the presence of a polymer binder, such as polytetrafluoroethylene (PTFE), to hold the active

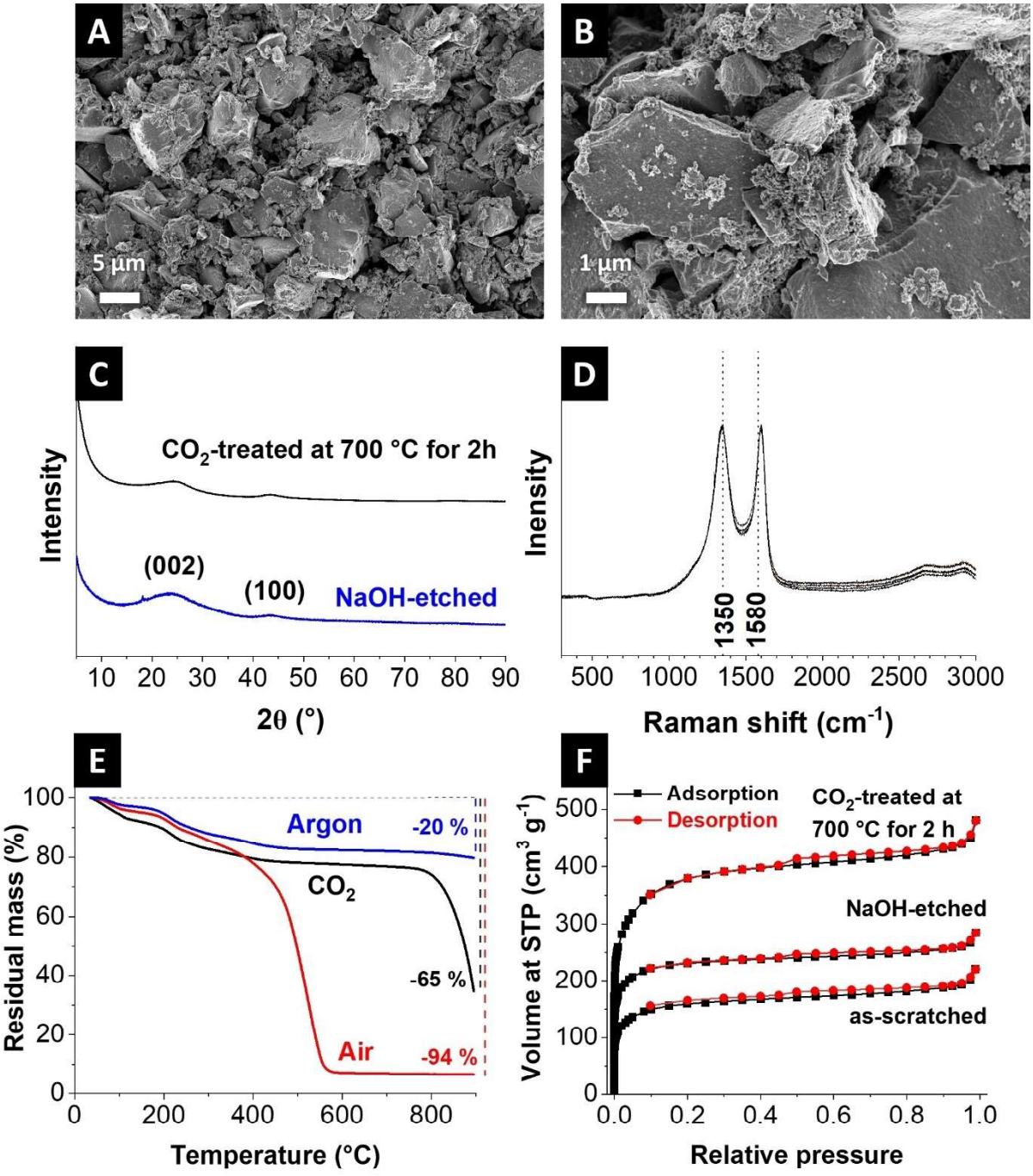

Figure 2. (A, B) Scanning electron micrographs of NaOH-etched carbon electrode peeled off from the aluminum current collector, its (C) X-ray diffraction pattern (including pattern after CO_2 activation at 700 °C for 2 h), (D) Raman spectra, (E) thermogravimetric analysis in argon, air, and CO_2 atmospheres, and (F) nitrogen gas sorption measurement at −196 °C. (STP: standard temperature and pressure).

materials together and enhance their adhesion to the current collector (aluminum foil). The X-ray diffractogram of the CO_2-activated sample (700 °C for 2 h) shows no significant difference from the etched sample, and the prevalence of broad peaks aligns with the presence of incompletely crystalline/amorphous lattices. The thermal CO_2 treatment did not produce a crystalline structure, and the reflection of the binder material is no longer present due to decomposition during the heat treatment.

Elemental analysis (Table 1) of the supercapacitor electrodes (labeled NaOH-etched) reveals a 68 mass% carbon content and a relatively large oxygen content of 23 ± 3 mass%, possibly arising from the partial oxidation during NaOH etching. The fluorine content of around 1 mass% documents the presence of standard polymeric binders such as polytetrafluoroethylene or polyvinylidene fluoride.

Raman spectra (Figure 2D) show the characteristic D-mode, G-mode, and D'-mode at 1350 cm^{-1}, 1580 cm^{-1}, and 2680 cm^{-1}, respectively. The G-mode corresponds to graphitic carbon in-plane vibrations with E_{2g} symmetry, and the D-mode is generally associated with breathing vibrations of sp^2 rings, characterizing A_{1g} symmetry disallowed in graphite, further confirming that the commercial supercapacitor consisted of carbon as the active material.[44,45]

Thermogravimetric analysis (TGA) revealed that the supercapacitor electrode experiences complete mass loss in air at temperatures above 500 °C, while under an argon atmosphere, only 20% of the initial mass is lost when heated up to 800 °C (Figure 2E). The significant mass loss in the air indicates that the electrode material undergoes combustion (oxidation) processes at high temperatures. The lower decomposition temperature than other carbonaceous materials suggests a larger surface area and/or smaller particle sizes.[46,47] The remaining 6% of the sample's mass is likely due to residues from the aluminum current collector (as confirmed by EDX analysis in Table 1), potentially in Al_2O_3, which might form during NaOH etching of the black mass. Under an inert argon atmosphere, the 22% mass loss indicates a lower reactivity, representing the extent of degradation and/or oxidation processes in the absence of oxygen at temperatures up to 800 °C. To better understand the behavior of the electrode under CO_2 activation, samples were also tested in a CO_2 atmosphere. Besides the initial footprint of the binder decomposition, 76 mass% of the sample remains up to the temperature of 750 °C. At around 900 °C, the residual mass amounts to 65%, indicating only a partial combustion/oxidation under a CO_2 environment.

To study the pore size characteristics of the pristine supercapacitor electrode, we gently scratched the surface of the carbon-coated aluminum current collector to collect the carbon powder. Nitrogen gas sorption measurements were performed on the latter material (as-scratched) and the NaOH-etched supercapacitor electrode (Figure 2F). The nitrogen adsorption-desorption results show isotherm shapes typical for microporous carbons.[48] The analysis shows specific surface areas of 520 $m^2 g^{-1}$ (average pore size of 0.57 nm) and 810 $m^2 g^{-1}$ (average pore size of 0.61 nm) for the as-scratched and NaOH-etched materials, respectively, showing increases in pore volume after the NaOH etching (Table 2). To study potential enhancement in the electrochemical desalination performance, we also performed CO_2 treatment on the supercapacitor electrodes to modify pore size characteristics (*Supporting Information*, Figure S4). Conducted at 700 °C for 2 h, the CO_2 treatment of the supercapacitor electrodes significantly increased the specific surface area to 1216 $m^2 g^{-1}$ and the average pore size to 0.79 nm, even though the morphology showed no visible change (*Supporting Information*, Figure S3). Our further experimentations for physical activation by adjusting the maximum holding temperature and duration did not result in substantially higher surface areas (*Supporting Information*, Table S1, and Figure S5).

Table 1. Elemental analysis of the NaOH-etched carbon electrode, removed from the aluminum substrate.

Element	EDX (mass%)	CHNS–O (mass%)
C	84 ± 18	67.9 ± 0.5
H	–	3.4 ± 0.1
N	–	2.5 ± 2.5
S	–	–
O	12 ± 14	23 ± 3
F	2 ± 1	–
Al	2 ± 4	–
Na, Si, Br	< 1	–

Electrochemical Characterization of the Recycled Electrodes

The analysis of the as-extracted carbon electrode from the commercial supercapacitor (NaOH-etched) in a 1 M aqueous NaCl solution by cyclic voltammetry towards hydrogen evolution is shown in Figure 3A. Initially, as the negative vertex

Table 2. Summary of gas sorption analysis performed on the as-scratched supercapacitor electrode, after NaOH etching, and after the subsequent CO_2 treatment (QSDFT: quenched solid density functional theory, BET: Brunauer-Emmett-Teller theory).

Sample	Surface area QSDFT ($m^2 g^{-1}$)	Surface area BET ($m^2 g^{-1}$)	Average pore width d_{50} (nm)	Pore volume ($cm^3 g^{-1}$)
As-scratched	520	517	0.57	0.28
NaOH-etched	810	889	0.61	0.37
CO_2-treated at 700 °C for 2 h	1216	975	0.79	0.64

Research Article
doi.org/10.1002/batt.202400506
Chemistry Europe
European Chemical Societies Publishing

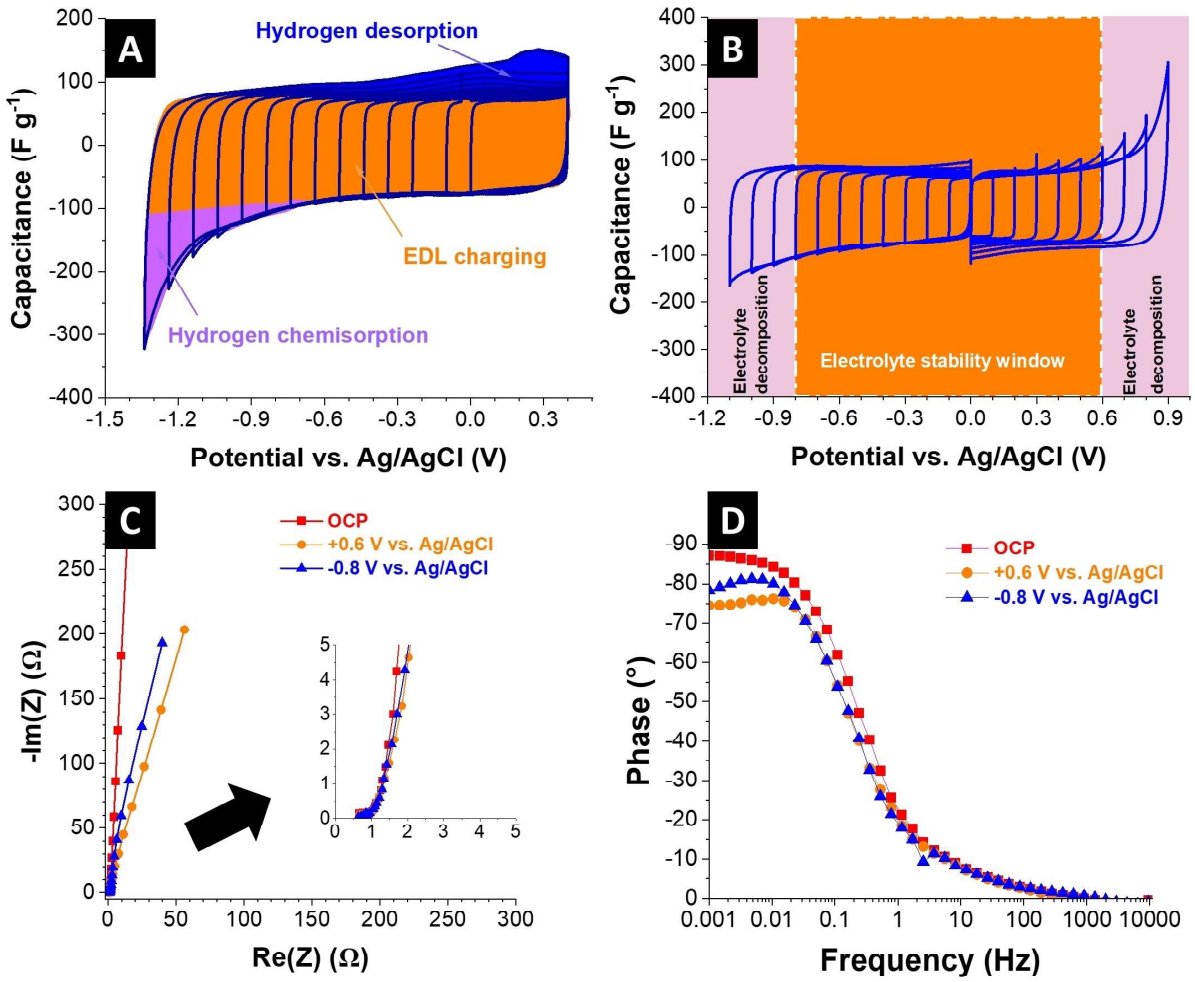

Figure 3. Half-cell electrochemical characterizations of NaOH-etched supercapacitor electrodes in 1 M aqueous NaCl solutions, including (A) the analysis of the voltammograms at negative polarization and (B) cycling voltammetry at negative and positive polarizations; (C) Nyquist plots of the impedance spectra and (D) Bode diagrams at various potentials (OCP: open circuit potential).

potential is reduced, the cyclic voltammograms demonstrate a characteristic pattern associated with electrical double-layer (EDL) charging. This phenomenon persists until the electrode reaches a potential of −0.7 V vs. Ag/AgCl. However, electrochemical water reduction occurs with a further decrease in the vertex potential, leading to the generation of nascent hydrogen. This hydrogen is produced and chemisorbed onto the carbon electrode.[49] As the vertex potential dips below −0.7 V vs. Ag/AgCl, a redox peak appears at around +0.15 V vs. Ag/AgCl during the anodic scan, suggesting the desorption of the previously chemisorbed hydrogen. When pushing the vertex potential further down to −1.3 V vs. Ag/AgCl, the negative current leap due to hydrogen chemisorption and the desorption counterpart during the anodic scan are more intense. This observation aligns with previous work demonstrating that applying a low potential to a porous carbon electrode in an aqueous environment triggered the creation and adsorption of nascent hydrogen on the carbon surface accompanied by hydroxyl OH^- ions.[50] This chemical environment led to localized changes in pH within the porosity and a negative shift in the Nernst potential.[49,50]

Accordingly, to assess the electrochemical stability region of the electrolyte, cyclic voltammograms were recorded separately on freshly extracted (NaOH-etched) electrodes, with both negative and positive polarizations (Figure 3B). During the negative sweeps, the negative vertex potential was gradually decreased from 0.0 V vs. Ag/AgCl in increments of 0.1 V. In contrast, during the positive sweeps, the positive vertex potential was gradually increased from 0.0 V vs. Ag/AgCl by the same increments.[51] This process continued until the electrolyte decomposition was observed in both cells. The region of electrolyte stability, characterized by purely box-like shapes of the cyclic voltammograms representing the EDL charging, was found between −0.8 V vs. Ag/AgCl and +0.6 V vs. Ag/AgCl by calculating the S-values for the negative and negative polarizations (*Supporting Information*, Figure S6).

The negatively polarized electrode's potential limit is −0.8 V vs. Ag/AgCl, which is lower than the thermodynamic reduction potential of water at the measured electrolyte pH of 5.6 (E_H = −0.527 V vs. Ag/AgCl). This indicates that when our NaOH-etched supercapacitor electrode is polarized below the hydrogen evolution potential in a 1 M aqueous NaCl solution, the

OH^- anions produced by water electrolysis are trapped in the carbon's pores.[49] This results in a local pH increase and a negative shift in the Nernst hydrogen evolution potential by 0.27 V. Conversely, below −0.8 V vs. Ag/AgCl cyclic voltammograms displaying nascent parasitic shapes indicated electrolyte decomposition.[50] Cyclic voltammograms of the CO_2-activated electrodes show similar stability regions (*Supporting Information*, Figure S7).

In addition to the cyclic voltammetry results, we also examined electrochemical impedance spectroscopy (EIS) data from the same experimental conditions to comprehensively understand the electrochemical performance. The EIS measurements in Figure 3C–D were conducted at three distinct electrode potentials: open circuit potential (OCP), −0.8 V vs. Ag/AgCl, and +0.6 V vs. Ag/AgCl. At OCP (Figure 3C), the equivalent series resistance (ESR) was determined to be 0.50 Ωcm^2, closely mirrored by the ESR values of 0.49 Ωcm^2 at −0.8 V vs. Ag/AgCl and 0.51 Ωcm^2 at +0.6 V vs. Ag/AgCl.

The phase angle versus frequency plots (Figure 3D) provide insights into the system's impedance behavior. At OCP, a phase angle of 87° was observed, indicative of a highly capacitive response. At −0.8 V vs. Ag/AgCl, the phase angle slightly decreased to 78°, suggesting a subtle shift towards a more resistive behavior. Finally, at 0.6 V vs. Ag/AgCl, the phase angle further decreased to 75°, signifying a shift towards even greater resistive behavior.

A fresh commercial supercapacitor with the same type as the one disassembled above underwent long-term electrochemical characterization. The specifications of the commercial supercapacitor provided by the manufacturer are listed in *Supporting Information*, Table S2. After soldering cables to the supercapacitor terminals (*Supporting Information*, Figure S8), the cylindrical cell was subjected to charging and discharging cycles by applying an external current of 1 A for over 11,000 cycles. The obtained cell voltage versus time plots and cycle stability tests are shown in *Supporting Information*, Figure S9. Despite operating at a relatively low current intensity of 1 A, given that the present supercapacitor can nominally be charged at a maximum of 230 A, the cell only achieves a capacitance of approximately 0.5 F (compared to 500 F as per manufacturer specifications).

Electrochemical Desalination with the Recycled Electrodes

As a first step to re-purposing and re-using the supercapacitor electrodes, holes were drilled in the two ends of the cylindrical supercapacitor, which allows direct flow of the aqueous solution (20 mM NaCl) through the cell (*Supporting Information*, Figure S10). No significant effluent water conductivity (concentration) reduction was observed upon charging the cell. The latter could be due to the electro-oxidation of aluminum current collectors upon their contact with aqueous NaCl electrolyte. As such, separate electrochemical water desalination cells were made with the electrodes extracted from another fresh supercapacitor cell.

We conducted a series of tests on the newly assembled cells to further investigate and validate the feasibility of using repurposed supercapacitor electrodes for desalination. Figure 4A shows the concentration change profiles of the effluent stream of a symmetric electrochemical desalination cell with NaOH-etched supercapacitor electrodes cycled in 20 mM NaCl electrolyte. Distinct decrease and rise concentration patterns were observed upon cycling the cell by charging at 1.2 V and discharging at 0.3 V, respectively. The mechanical properties of the electrodes were insufficient because we directly repurposed the thin electrode sheets after NaOH etching as electrodes for the desalination application. The analysis of the electrochemical desalination performance during 20 cycles (Figure 4B) yields an average desalination capacity (DC) of 5.8 mg g^{-1} and charge efficiency (CE) above 80%. We have previously shown that predictive tools based on the modified Donnan model could link the pore structure of porous carbon electrodes to their desalination performance.[52,53] Feeding the latter model with the pore size distributions of the NaOH-etched electrode (*Supporting Information*, Figure S4A) results in a DC of 6.4 mg g^{-1}, assuming a CE of 100%.

To enhance the DC as well as the flexibility of the electrodes, we have reprocessed the latter electrodes through the wet processing approach by admixing 5 mass% PTFE binder to them and calendaring it to form uniform, free-standing electrodes with a thickness of 600 μm. As presented in Figure 4C–D, the reprocessed electrode, however, showed lower DC values (3.8 mg g^{-1}). The latter could be due to the pore blockage in the carbon electrodes caused by adding the polymeric binder and increased electrode thickness. We then performed a series of heat treatments on the NaOH-etched supercapacitor electrodes in a CO_2 environment to activate the carbon electrodes (*Supporting Information*, Table S1), followed by admixing 5 mass% binder and calendaring. The CO_2 activation at 700 °C for 2 h has improved electrochemical desalination performance metrics (Figure 4E–F) compared to NaOH-etched electrodes (Figure 4A–B) and the CO_2-activated electrode at 800 °C for 1 h (*Supporting Information*, Figure S11). Namely, a DC of 7.9 mg g^{-1} and a CE of above 90% was achieved for the CO_2-treated electrodes and a more stable performance throughout 20 cycles. Given the pore size distribution of the CO_2-activated carbon material (*Supporting Information*, Figure S4B), an estimated DC of 8.7 mg g^{-1} is obtained, assuming a CE of unity using the predictive model outlined above.[52,53] The latter enhancement in NaCl removal capacity and stability of carbon electrodes upon CO_2 activation agrees with previous reports.[54,55] It is attributed to a better wettability of the CO_2-activated electrodes,[55] their higher surface area, larger pore volume (Table 2), and a possible de-blocking of the supercapacitor carbon pores, which were previously immersed in an organic electrolyte.[56]

The Kim-Yoon plot,[57] analogous to the Ragone plot in the energy storage field, is a tool for assessing performance metrics in electrochemical desalination by mapping desalination capacity against rate. As illustrated in Figure 5, while reprocessing (admixing 5 mass% binder) of the recovered supercapacitor electrode negatively impacts the DC, it slightly improves its

Research Article
doi.org/10.1002/batt.202400506
Chemistry Europe
European Chemical Societies Publishing

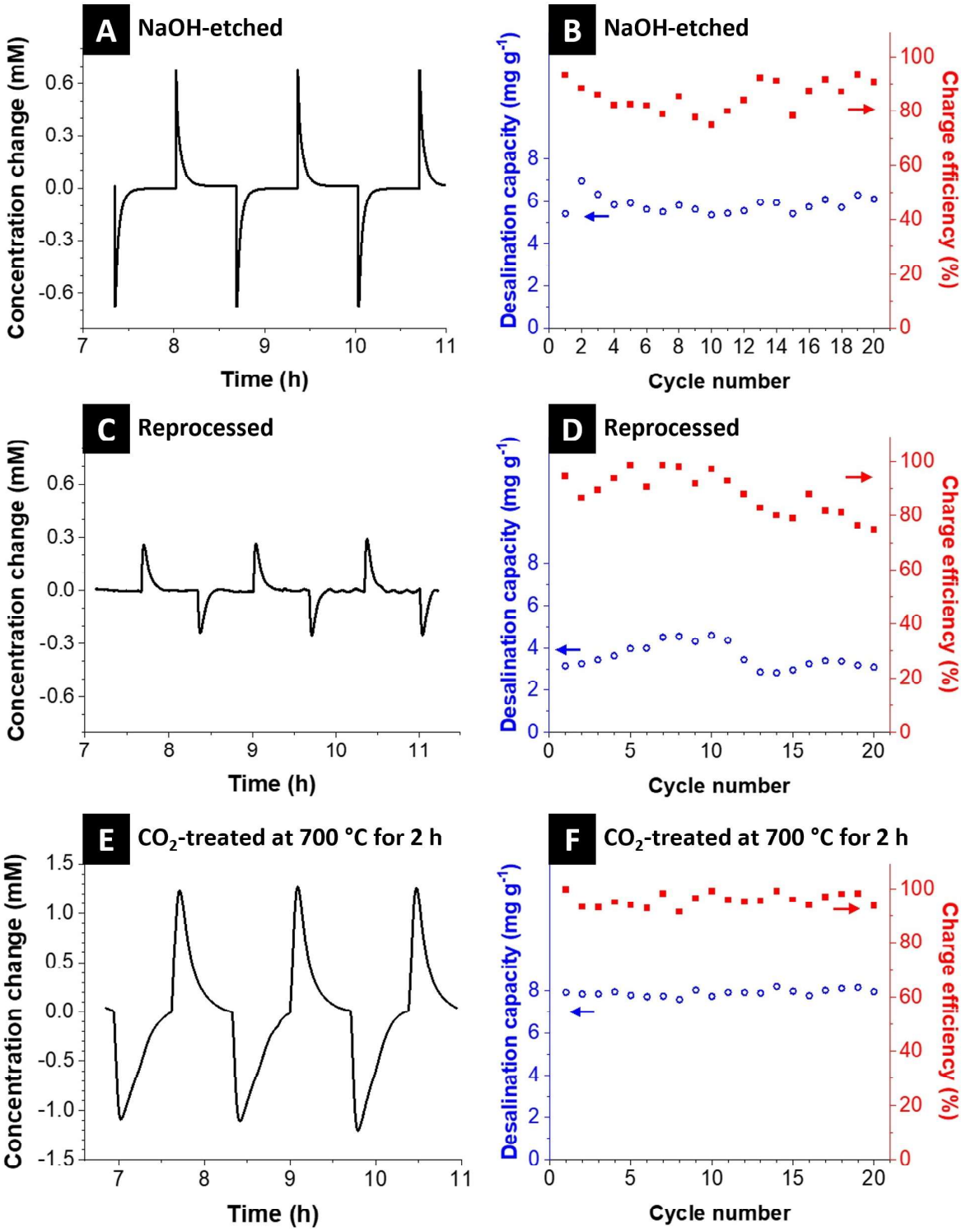

Figure 4. NaCl concentration-time profiles of the effluent water of the electrochemical cells made from the (A) NaOH-etched supercapacitor electrodes, (C) reprocessed electrodes, and (E) CO_2-treated electrodes at 700 °C for 2 h; Desalination capacity and charge efficiencies of the (B) NaOH-etched supercapacitor electrodes, (D) reprocessed electrodes, and (F) CO_2-treated and reprocessed electrodes at 700 °C for 2 h.

maximum salt removal rate from 0.007 mg g^{-1} s^{-1} (for NaOH etched electrode) to 0.008 mg g^{-1} s^{-1} (reprocessed electrode). The latter desalination rates are generally lower than commercial activated carbon (YP-80 F, Kuraray) film electrodes (~0.011 mg g^{-1} s^{-1}) when tested under conditions like electrodes for electrochemical desalination of aqueous 20 mM NaCl.[58] The relatively lower desalination rates in the present work could be explained by the sub-nanometer pore regimes of the supercapacitor carbon electrodes, which are in the range of 0.6–0.8 nm (Table 2), compared to the larger pore sizes (~1.4 nm) of

Research Article
doi.org/10.1002/batt.202400506
Chemistry Europe
European Chemical Societies Publishing

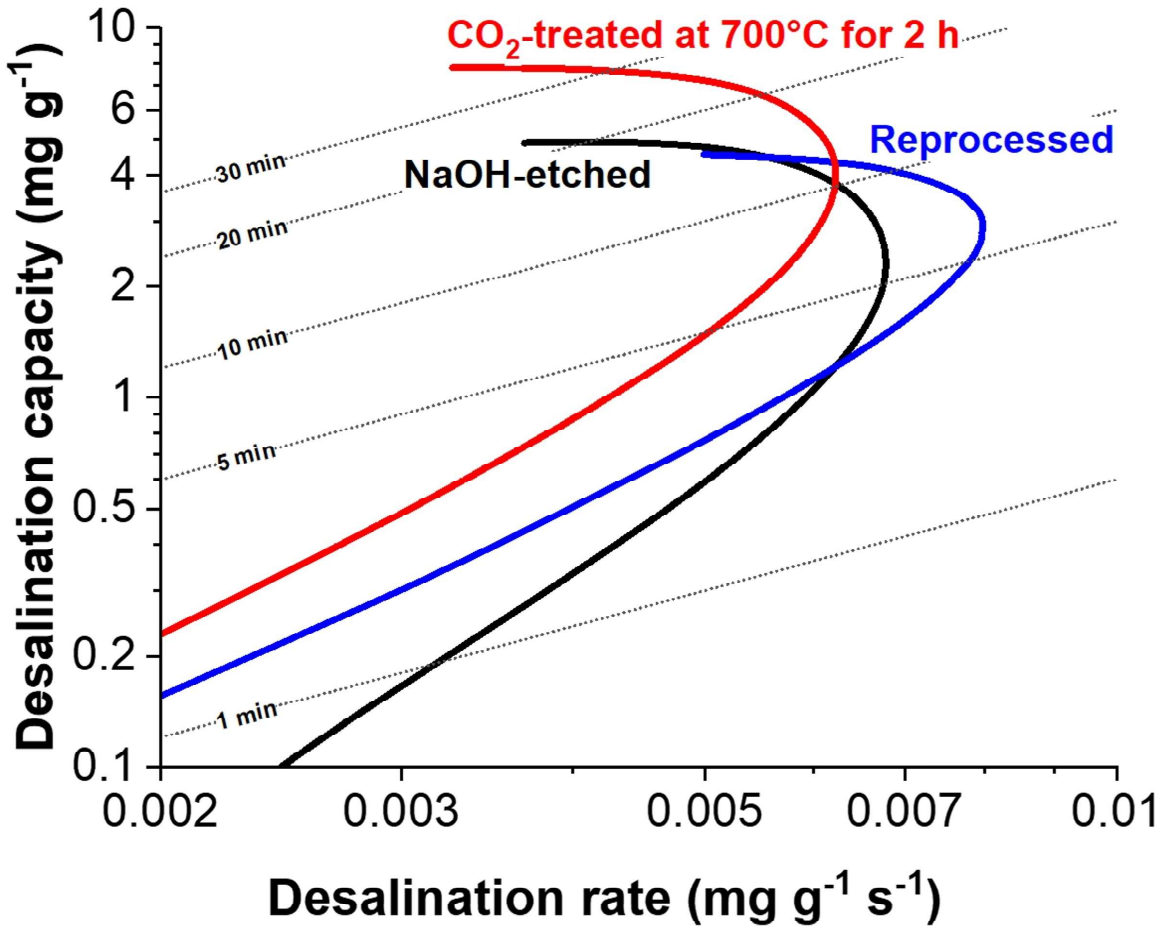

Figure 5. Electrochemical performance of NaOH-etched supercapacitor electrodes, reprocessed electrodes, and CO_2-treated at 700 °C for 2 h electrodes regarding desalination capacity and rates (Kim-Yoon plot).

carbon films in our previous work.[58] However, the CO_2 activation and reprocessing significantly improve the DC while having minimal influence on the desalination rate. Additionally, we evaluated the energy consumption of the electrodes used, as shown in Table 3. The CO_2-treated electrodes provide the best desalination performance and overall lower energy consumption (41.5 Wh mol^{-1}).

Although there is a rich literature on electrochemical desalination with carbon electrodes derived from the pyrolysis of a host of biomass sources,[59–62] there are no reports to the best of our knowledge on recycling or re-purposing an already-existing electrode material for electrochemical desalination. Nevertheless, a comparison is made to adjacent works to provide a broader context for the present study (as listed in *Supporting Information*, Table S3). While carbon from commercial sources typically yields desalination capacities of 10–16 mg g^{-1}, the derived carbons from waste sources vary mainly depending on their source, pyrolysis, and activation routes. This comparison underscores our approach's novelty and potential impact, paving the way for future research to explore and refine the re-purposing of supercapacitor materials for sustainable desalination technologies. CO_2 activation enhances the electrochemical desalination performance, which indicates that the current performance metrics can be significantly improved with further fine-tuning of the activation parameters. Further optimizing the CO_2 activation process could yield more developed carbons with enhanced properties.[63]

Table 3. Energy consumption of supercapacitor electrode after NaOH etching, reprocessed, and after the subsequent CO_2 treatment.

Sample	Energy consumption (Wh mol^{-1})
NaOH-etched	60.7
Reprocessed	42.6
CO_2-treated at 700 °C for 2 h	41.5

A Look at the Market and Volume of Activated Carbon Supercapacitors

The global supercapacitor market, valued at approximately 4.5 billion USD in 2023, is poised for substantial growth projected to exceed 12 billion USD by 2032.[64] The latter expansion in market size reflects annual growth rates estimated

between 12–16%,[64–67] driven primarily by rising demand in the automotive, energy, and consumer electronics industries, with the fastest growth rates in Asia-Pacific regions.[68,69] As these sectors continue to embrace supercapacitors for their rapid charge-discharge capabilities and reliability, the volume of end-of-life supercapacitors is expected to increase significantly along with market adoption. Effective recycling and re-purposing strategies will play a pivotal role in mitigating environmental impact and optimizing resource utilization.

The activated carbon market for supercapacitors is segmented by type into four categories based on surface area: under 1500 $m^2 g^{-1}$, 1500–1900 $m^2 g^{-1}$, 2000–2200 $m^2 g^{-1}$, and above 2200 $m^2 g^{-1}$. The segment under 1500 $m^2 g^{-1}$ leads the market,[65] which is also the type investigated in the current study (Table 2). This segmentation reflects the diverse applications and performance requirements across industries. However, precise industry-specific data on exact annual tonnages used remains undisclosed due to competitive reasons and proprietary formulations. As a general estimate, based on our specific device, we assume that activated carbon material constitutes approximately 10% of the device's total mass, equating to about 10 g in a typical 100 g device (*Supporting Information*, Table S2). This figure supports our hypothesis that activated carbon, even in relatively small amounts, has significant potential for recycling and re-purposing. For example, with minimal modification, such as NaOH etching, these 10 g of activated carbon could be re-purposed as electrodes for electrochemical desalination cells. Assuming a desalination cell with a lifetime of 200 cycles and a salt removal capacity of 6 mg g^{-1} per cycle (Figure 4B), this would translate to 12 g of NaCl removal in the supercapacitor's second life as a desalination cell, which would otherwise be disposed of.

Further advancements, as demonstrated by CO_2 treatment in this study (Figure 4E), can enhance both desalination capacity and stability, potentially increasing the salt removal capacity even further. Based on the specifications of a typical tube furnace, a maximum power of 1.5 kW is required for the heat treatment. Given the heating rate of 5 °C min^{-1} to reach 700 °C from room temperature, followed by 2 h holding time at 700 °C, a duration of 255 min furnace operation could be assumed, resulting in 4.25 kWh electrical energy consumption. The latter consumed electrical energy, which translates to a price of 1.70 € for each heat treatment trial, taking an average electricity price of 0.402 € per kWh in Germany in the second half of 2023 for household consumers (eurostat 04/2024). Going from laboratory-scale to industrial-scale practices, the latter price could further plummet when the mass of treated carbon in each heat treatment trial reaches kilogram levels. As such, we speculate that the benefits gained in terms of desalination capacity and stability by the CO_2 heat treatment of supercapacitor electrodes would outweigh the costs incurred because of heat treatment.

The re-purposing strategy not only extends the lifecycle of the materials but also contributes to reducing waste and promoting sustainability. The supercapacitors, known for their high specific power of approximately 10 kW kg^{-1},[70] generally have low specific energy contents. For instance, the energy content of the commercial supercapacitor used in this study is calculated to be only 0.625 Wh for a device weighing around 100 g (*Supporting Information*, Table S2). As such, future studies could explore re-purposing battery-type electrodes to achieve substantially higher desalination capacities. However, the latter approach presents specific challenges, particularly concerning electrode stability in aqueous media.

While traditional desalination technologies such as reverse osmosis (RO) are well-established, they require significant energy inputs, complex infrastructure, and often high operational costs.[71] A direct comparison between the performance metrics of RO and electrochemical desalination systems is often complicated by the non-equal salt rejection of the two. That is, RO systems have salt rejection rates of above 99%,[72] while it is much lower in electrochemical desalination systems (depending on the water recovery ratio; Ref.[73,74]). As such, a bypass stream from the feed to the product water is commonly considered in an RO setup to reduce its salt rejection rate close to that of an electrochemical desalination system.[75,76] Electrochemical desalination, mainly capacitive deionization, system becomes more energy efficient than RO for desalination of lower salinity regimes (brackish water), where NaCl concentration in the feedwater is lower than 2 g L^{-1} (or 34 mM).[75–78] The present study, which studies the capacitive deionization to desalinate NaCl solutions with 20 mM concentration, falls within the latter energy-efficient regime. Additionally, the re-purposing of end-of-life supercapacitors for electrochemical desalination presents a cost-effective solution by leveraging existing materials that would otherwise contribute to electronic waste.

Conclusions

The present work demonstrates the feasibility of re-purposing end-of-life commercial supercapacitors as electrochemical desalination systems, aligning with circular economy principles. By dissecting a commercial 500-Farad supercapacitor and extracting its electrodes, we investigated various modification methods, including NaOH-etching, CO_2 activation, and binder-added wet processing. We studied their performance for electrochemical water desalination applications. While the NaOH-etched electrodes showed an average desalination capacity of 5.8 mg g^{-1}, the CO_2-activated electrodes significantly improved desalination capacity (7.9 mg g^{-1}) and charge efficiency (above 90%) with stable performance over 20 cycles. These findings highlight a novel and practical approach to recycling supercapacitors, potentially reducing electronic waste and contributing to sustainable water desalination technologies. As such, this work opens new avenues for resource recovery and re-purposing, emphasizing the importance of resource management in achieving environmental sustainability.

Experimental Section

Supercapacitor Disassembly Process and Recovery of Material

Several HY-CAP 500 F 3 V supercapacitors were purchased from Reichelt Elektronik GmbH. The technical specifications of the latter commercial supercapacitor are listed in *Supporting Information*, Table S1. Figure S1 and Videos S1–2 in the *Supporting Information* demonstrate the step-by-step process of opening the commercial supercapacitor and recovering the electrodes. Typically, the electrode bundle is removed and unrolled after force-opening the aluminum casing of the commercial supercapacitor and discarding the small amount of electrolyte inside. The unrolled electrode consists of a white, non-woven separator paper covering a meter-long carbon-coated aluminum current collector. Scanning electron micrographs of the separator paper can be found in *Supporting Information*, Figure S2. After removing the separator, the carbon-coated aluminum current collector is dipped in 10 mass% NaOH solution using a tweezer. The carbon coating then easily peels off from the aluminum substrate after around 1 min, which is then washed with ample water and dried in a vacuum oven overnight at room temperature. The latter carbon electrode obtained is labeled herein as a NaOH-etched electrode. In the next step, the latter electrode is placed in a tube furnace (Carbolite Gero) at the rate of 5 °C min^{-1} under Ar atmosphere to reach 700 °C. Ar gas is then replaced by CO_2 at 700 °C for 2 h. At the end of 2 h, the CO_2 flow is again replaced with Ar while the furnace cools to the ambient temperature at 5 °C min^{-1}.

Electrode Preparation

To prepare counter electrodes for half-cell electrochemical testing, we followed the procedure described in our previous works to prepare free-standing carbon films.[55,79] Typically, the free-standing electrodes were fabricated by mixing activated carbon (type YP-80 F, Kuraray) with ethanol in an Agate mortar until the mixture was thoroughly wetted, using a pestle for manual stirring. Once a homogenous consistency was achieved, polytetrafluoroethylene binder (PTFE, 60 mass% dispersion in water from Sigma Aldrich) was added to serve as a polymeric binder, maintaining a carbon-to-binder mass ratio of 9 : 1. The stirring continued under a fume hood until the ethanol partially evaporated, resulting in a carbon paste. The latter paste was then cold rolled using a rolling machine (MTI HR01, MTI Corp.), resulting in free-standing carbon films with a thickness of ~600 μm. The films were gently placed on an aluminum foil and dried in a vacuum oven (Memmert) at +50 °C overnight. The latter resulted in carbon film electrodes with ~22 mg cm^{-2} mass loadings.

The NaOH-etched electrode material was blended with 5 mass% of PTFE binder and calendared with a rolling machine to reprocess supercapacitor electrodes. The resulting free-standing carbon films with a wet thickness of 600 μm were then dried in a vacuum oven at +50 °C overnight. Electrodes of 12 mm were punched for electrochemical characterization.

Electrochemical Half-Cell Measurements

We employed custom-built cells constructed from polyether ether ketone (PEEK) equipped with spring-loaded titanium pistons for electrochemical benchmarking in aqueous electrolytes.[80] These cells were configured in a three-electrode setup for electrochemical assessments. The electrode discs, each having a diameter of 12 mm (1.13 cm^2), were obtained by punching them out from electrode films. An Ag/AgCl electrode with 3 M KCl (E_0 Ag/AgCl = 0.210 V vs. normal hydrogen electrode) served as the reference electrode. A graphite current collector (0.25 mm thin foils, Sigraflex F02510TH, SGL Carbon) served as the current collector. Initially, a round piece of the latter graphite foil with a 12 mm diameter was punched and placed in the bottom of the cell. Then, a round-shaped working electrode with 12 mm diameter was placed onto the graphite current collector, followed by placing two vacuum-dried, 13 mm diameter, compressed glass-fiber separator disks (GF/A, 210 μm thickness, Whatman) to prevent short-circuiting. The counter electrode was punched into round-shaped films with a 12 mm diameter and positioned on top of the separator. Finally, another piece of graphite current collector was placed on top of the latter. Two titanium pistons are loaded with springs to sandwich the cell components together. The electrolyte was an aqueous 600 mM NaCl filled into the cell by vacuum backfilling. The Ag/AgCl reference electrode was positioned on top of a glass fiber separator in a cavity designed in the cell to be close to the sandwiched stack of working and counter electrodes.

The electrochemical performance testing included cyclic voltammetry (CV) and electrochemical impedance spectroscopy (EIS), utilizing a VMP3 multi-channel potentiostat/galvanostat from Bio-Logic with the EC-Lab software. CV was conducted to ascertain the electrochemical behavior and stability window of the system, employing a scan rate of 1 mV s^{-1}, commencing at 0 V vs. Ag/AgCl to a potential of +1.0 V/−1.0 V vs. Ag/AgCl in steps of 0.1 V. EIS measurements was carried out at open circuit potential (OCP), +0.6 V vs. Ag/AgCl and −0.8 V vs. Ag/AgCl with a sinusoidal signal of 5 mV in the frequency range from 100 kHz to 1 mHz. The commercial supercapacitor underwent galvanostatic charge and discharge with a cell voltage of 2.8 V at 1 A current with a Bio-Logic battery cycler. All electrochemical measurements were performed in a climate chamber (Binder) where the temperature was constant at +25 ± 1 °C.

To determine the electrochemical stability region of the electrolyte, the S-values for the positive and negative polarizations were calculated following Equation (1) and Equation (2), respectively:[51]

$$S_{pos} = \frac{Q_+}{Q_-} - 1 \quad (1)$$

$$S_{neg} = \frac{Q_-}{Q_+} - 1 \quad (2)$$

where Q_+ and Q_- are the integrated charges during the anodic and cathodic scans, respectively.

Electrochemical Desalination

The electrochemical desalination tests were performed following the best practice methods we recently reported.[81] A symmetric cell with a pair of electrodes (extracted from the supercapacitor) was fabricated. An electrochemical workstation (Bio-Logic VSP300) was programmed to charge and discharge the cell repeatedly at 0.1 A g^{-1} based on the combined average mass of both carbon electrodes. A 10 L tank containing 20 mM aqueous NaCl electrolyte was constantly flushed with nitrogen gas to remove dissolved oxygen. The 20 mM NaCl concentration was chosen to mimic the brackish water salinity levels[40,81] and as a concentration regime where electrochemical desalination is more energy-efficient than conventional desalination technologies such as reverse osmosis.[75–78]

A peristaltic pump (Masterflex) continuously circulated the latter electrolyte to the cell at 2 mL min^{-1}, which was subsequently passed through a chamber housing a conductivity meter (Met-

rohm). The conductivity was then related to the concentration using the calibration equation that measured several NaCl stock solutions in the 1 mM to 50 mM aqueous NaCl concentration range. The desalination capacity (DC) is then calculated following Equation (3).

$$DC = \frac{\nu\, M}{60\, m_{total}} \int C\, dt \tag{3}$$

where ν is the flow rate (mL min^{-1}), M is the molar mass of the NaCl (58.44 g mol^{-1}), m_{total} is the total mass of both electrodes combined (mg), t is the time (s) during which a concentration change (mM) occurs, and DC (mg g^{-1}) is the amount of salt (mg) taken up per gram of the electrodes. The charge efficiency (CE) of the system is calculated according to Equation (4).

$$CE = \frac{DC\, F\, m_{total}}{1000\, q\, M} \times 100\% \tag{4}$$

where F is the Faraday constant (96485 C mol^{-1}), and q is the electronic charge (mA s) stored in the electrodes.

The energy consumption of the system is calculated according to Equation (5).

$$\text{Energy consumption} = \frac{\frac{U_{charge}}{m_{total}}}{\frac{DC}{M_{NaCl}}} \tag{5}$$

Where the (U_{charge}) is the energy consumed during the charging, m_{total} is the total mass of both electrodes, DC is obtained from Equation (3) and 58.44 g mol^{-1} for the molar mass of NaCl (M_{NaCl}).

Material Characterizations

X-ray diffraction (XRD) analysis was conducted using a D8 Advance diffractometer (Bruker AXS) equipped with a copper X-ray source (Cu–Kα, λ = 1.5406 Å, 40 kV, 40 mA). The samples were analyzed over the 3.5° to 80° 2θ range at 0.033 s per step. Before analysis, the dry powder was pressed onto an optical glass sample holder featuring a 0.5 mm deep notch for sample preparation. Scanning electron microscopy (SEM) images were captured using a ZEISS GEMINI 500 field-emission scanning electron microscope with 0.5–1 kV acceleration voltage. Energy-dispersive X-ray (EDX) spectroscopy was conducted at 15 kV utilizing an X–Max Silicon Detector from Oxford Instruments with the AZtec software. Sample preparation involved mounting them on an aluminum stub using double-sided copper tape without an additional sputtering step. At least 20 random points were selected on each sample for point elemental analysis, with subsequent calculation of the average quantities of the detected elements.

Nitrogen adsorption at −196 °C was carried out using an Autosorb iQ system (Quantachrome, now Anton Paar). Before analysis, samples underwent degassing at 200 °C for 12 h. Specific surface area (SSA) calculations were conducted using Brunauer-Emmett-Teller (BET) theory alongside quenched-solid density functional theory (QSDFT), assuming a slit-shaped pore model. Raman spectroscopic analysis was conducted using a Renishaw inVia Raman microscope featuring a Nd:YAG laser (532 nm). Laser power at the sample's focal point was rigorously maintained at 0.05 mW, with a numerical aperture of 0.75. Spectra were recorded at five distinct points for each sample, with an exposure time of 30 s per point and measurements accumulated five times to bolster reliability. The to-be-analyzed powder samples were firmly pressed onto glass slides to ensure stability. Spectra underwent meticulous processing for cosmic ray removal and subsequent normalization to ensure consistency (0–1). System calibration with a silicon standard was rigorously performed before and after the measurements to uphold accuracy. Thermogravimetric analysis (TGA) was performed using a Netzsch TG-209–1 Libra. Mass changes up to 900 °C were recorded at a heating rate of 5 °C min^{-1} in an oxidative atmosphere (synthetic air) with argon as a protective gas. Further runs were conducted using pure argon and CO_2 atmosphere.

Supporting Information Summary

Supporting information is available online, which includes: Two videos showing the disassembly process of the commercial supercapacitor and unrolling of the electrode bundle, a summary of gas sorption results (Table S1), specifications of the commercial supercapacitor (Table S2), a comparison with other electrochemical desalination works (Table S3), pictures of the step-by-step disassembly process of the supercapacitor (Figure S1), SEM images of supercapacitor separator (Figure S2) and active materials (Figure S3), nitrogen gas sorption analysis of the electrodes (Figure S4), nitrogen gas sorption isotherms of the CO_2-activated electrodes (Figure S5), plots of potential stability limits (Figure S6), cyclic voltammetry measurement of CO_2-activated electrodes (Figure S7), picture of the soldered commercial supercapacitor (Figure S8), electrochemical characterization of the commercial supercapacitor (Figure S9), pictures of the supercapacitor with holes for direct re-purposing as electrochemical desalination cell (Figure S10), and electrochemical desalination performance of an additional CO_2-activated electrode (Figure S11).

Author Contributions

Panyu Ren: Investigation, Data curation, Visualization, Writing – Original Draft, Writing – Review & Editing. **Mohammad Torkamanzadeh**: Investigation, Data curation, Visualization, Supervision, Writing – Original Draft, Writing – Review & Editing. **Stefanie Arnold**: Investigation, Data curation, Visualization, Supervision, Writing – Original Draft, Writing – Review & Editing. **Emmanuel Pameté**: Methodology, Investigation, Data curation, Writing – Original Draft, Writing – Review & Editing. **Volker Presser**: Conceptualization, Supervision, Validation, Resources, Visualization, Writing – Original Draft, Writing – Review & Editing, Project administration, Funding acquisition.

Acknowledgements

The authors acknowledge Dr. Gracita Raquel Tomboc, Dr. Behnoosh Bornamehr, and Dr. Tamara Winter (all at INM, present or past) for their kind support in conducting various tests for us. E.P. acknowledges funding from the Alexander von Humboldt Foundation. V.P. and E.P. acknowledge funding of the joint Polish-German project SUPILMIX (PR-1173/27) by the

German Research Foundation (DFG, Deutsche Forschungsgemeinschaft) and the Polish National Science Centre (NCN, National Science Centre). Open Access funding enabled and organized by Projekt DEAL.

Conflict of Interests

The authors declare no conflict of interest.

Data Availability Statement

The data that support the findings of this study are available from the corresponding author upon request.

Keywords: Carbon · Electrochemistry · Recycling · Supercapacitor · Water desalination

[1] A. K. Awasthi, V. R. S. Cheela, I. D'Adamo, E. Iacovidou, M. R. Islam, M. Johnson, T. R. Miller, K. Parajuly, A. Parchomenko, L. Radhakrishan, M. Zhao, C. Zhang, J. Li, *Resources, Environment and Sustainability* **2021**, *3*, 100014.
[2] S. Sundriyal, V. Shrivastav, H. D. Pham, S. Mishra, A. Deep, D. P. Dubal, *Resour., Conserv. Recycl.* **2021**, *169*, 105548.
[3] Y. Wang, Y. Zhang, L. Pei, D. Ying, X. Xu, L. Zhao, J. Jia, X. Cao, *Sci. Rep.* **2017**, *7*, 41523.
[4] Y. Yang, S. Mao, Z. Li, Z. Sun, R. Zhao, *Water Sci. Technol.* **2021**, *84*, 1011–1022.
[5] L. Minzae, K. Gil-Pyo, S. Hyeon Don, P. Soomin, Y. Jongheop, *Nanotechnol.* **2014**, *25*, 345601.
[6] Y. Wang, M. Jiang, Y. Yang, F. Ran, *Electrochim. Acta* **2016**, *222*, 1914–1921.
[7] J. Sreńscek-Nazzal, J. Serafin, A. Kamińska, A. Dymerska, E. Mijowska, B. Michalkiewicz, *J. Colloid Interface Sci.* **2022**, *627*, 978–991.
[8] M. M. Vadiyar, X. Liu, Z. Ye, *ChemSusChem* **2018**, *11*, 2410–2420.
[9] J. H. Rademaker, R. Kleijn, Y. Yang, *Environ. Sci. Technol.* **2013**, *47*, 10129–10136.
[10] K. Baba, Y. Hiroshige, T. Nemoto, *Hitachi Rev.* **2013**, *62*, 452–455.
[11] S. Högberg, T. S. Pedersen, F. B. Bendixen, N. Mijatovic, B. B. Jensen, J. Holboll, *Direct reuse of rare earth permanent magnets – Wind turbine generator case study, 2016 XXII International Conference on Electrical Machines (ICEM)*, IEEE, **2016**, 1625–1629, https://ieeexplore.ieee.org/abstract/document/7732741.
[12] J. Zhu, I. Mathews, D. Ren, W. Li, D. Cogswell, B. Xing, T. Sedlatschek, S. N. R. Kantareddy, M. Yi, T. Gao, Y. Xia, Q. Zhou, T. Wierzbicki, M. Z. Bazant, *Cell Rep. Phys. Sci.* **2021**, *2*, 100537.
[13] J. Thakur, C. Martins Leite de Almeida, A. G. Baskar, *J. Cleaner Prod.* **2022**, *375*, 134066.
[14] Y. Li, S. Arnold, S. Husmann, V. Presser, *J. Energy Storage* **2023**, *60*, 106625.
[15] J. Wu, M. Zheng, T. Liu, Y. Wang, Y. Liu, J. Nai, L. Zhang, S. Zhang, X. Tao, *Energy Storage Mater.* **2023**, *54*, 120–134.
[16] L. Zhang, Z. Xu, Z. He, *ACS Sustain. Chem. Eng.* **2020**, *8*, 11596–11605.
[17] J. Zhang, M. Gu, X. Chen, *Micro and Nano Eng.* **2023**, *21*, 100229.
[18] F. Béguin, V. Presser, A. Balducci, E. Frackowiak, *Adv. Mater.* **2014**, *26*, 2219–2251.
[19] J. Zhao, A. F. Burke, *J. Energy Chem.* **2021**, *59*, 276–291.
[20] P. Saha, S. Dey, M. Khanra, *J. Power Sources* **2021**, *496*, 229824.
[21] S. Zhang, N. Pan, *Adv. Energy Mater.* **2015**, *5*, 1401401.
[22] R. Chaari, O. Briat, J. Y. Delétage, E. Woirgard, J. M. Vinassa, *Microelectron. Reliab.* **2011**, *51*, 1976–1979.
[23] E. Pameté, L. Köps, F. A. Kreth, S. Pohlmann, A. Varzi, T. Brousse, A. Balducci, V. Presser, *Adv. Energy Mater.* **2023**, *13*, 2301008.
[24] H. Trivedi, K.D. Verma, K.K. Kar, *Recycling of Supercapacitor Materials, Handbook of Nanocomposite Supercapacitor Materials IV: Next-Generation Supercapacitors*, Springer **2023**, 331, 393-411, https://link.springer.com/chapter/10.1007/978-3-031-23701-0_16.
[25] J. Mao, C. Ye, S. Zhang, F. Xie, R. Zeng, K. Davey, Z. Guo, S. Qiao, *Energy Environ. Sci.* **2022**, *15*, 2732–2752.
[26] Z. J. Baum, R. E. Bird, X. Yu, J. Ma, *ACS Energy Lett.* **2022**, *7*, 712–719.
[27] X. Wang, G. Gaustad, C. W. Babbitt, *Waste Manage.* **2016**, *51*, 204–213.
[28] X. Qu, B. Zhang, J. Zhao, B. Qiu, X. Chen, F. Zhou, X. Li, S. Gao, D. Wang, H. Yin, *Green Chem.* **2023**, *25*, 2992–3015.
[29] X. Qu, M. Cai, B. Zhang, H. Xie, L. Guo, D. Wang, H. Yin, *Green Chem.* **2021**, *23*, 8673–8684.
[30] E. Gratz, Q. Sa, D. Apelian, Y. Wang, *J. Power Sources* **2014**, *262*, 255–262.
[31] G. Jiang, S. J. Pickering, *Waste Manage.* **2016**, *48*, 465–470.
[32] A. Dutta, J. Mahanta, T. Banerjee, *Adv. Sustainable Syst.* **2020**, *4*, 2000182.
[33] N. R. Chodankar, S. J. Patil, S.-K. Hwang, P. A. Shinde, S. V. Karekar, G. S. R. Raju, K. S. Ranjith, A. G. Olabi, D. P. Dubal, Y. S. Huh, Y.-K. Han, *Energy Storage Materials.* **2022**, *49*, 564–574.
[34] F. Wu, T. Zhao, Y. Yao, T. Jiang, B. Wang, M. Wang, *Chemosphere* **2020**, *238*, 124638.
[35] J. Choi, P. Dorji, H. K. Shon, S. Hong, *Desalination* **2019**, *449*, 118–130.
[36] S. Lei, T. Yang, C. Tian, T. Yan, X. Li, W. Song, W. Liu, L. Yan, Y. Zhao, *Desalination* **2024**, *574*, 117248.
[37] S. Porada, R. Zhao, A. van der Wal, V. Presser, P. M. Biesheuvel, *Prog. Mater. Sci.* **2013**, *58*, 1388–1442.
[38] S.-J. Seo, H. Jeon, J. K. Lee, G.-Y. Kim, D. Park, H. Nojima, J. Lee, S.-H. Moon, *Water Res.* **2010**, *44*, 2267–2275.
[39] L. Wang, S. Lin, *Environ. Sci. Technol.* **2019**, *53*, 5797–5804.
[40] L. Huang, T. Yan, A. E. D. Mahmoud, S. Li, J. Zhang, L. Shi, D. Zhang, *Environ. Sci.: Nano* **2021**, *8*, 950–959.
[41] G. Wang, T. Yan, J. Shen, J. Zhang, L. Shi, D. Zhang, *Environ. Sci.: Nano.* **2021**, *8*, 122–130.
[42] M. Mao, T. Yan, J. Shen, J. Zhang, D. Zhang, *Environ. Sci. Technol.* **2021**, *55*, 3333–3340.
[43] L. Wang, L. Deligniere, S. Husmann, R. Leiner, C. Bahr, S. Zhang, C. Dun, M. M. Montemore, M. Gallei, J. J. Urban, C. Kim, V. Presser, *Nano Res.* **2023**, *16*, 9352–9363.
[44] A. Jänes, H. Kurig, E. Lust, *Carbon* **2007**, *45*, 1226–1233.
[45] R. P. Vidano, D. B. Fischbach, L. J. Willis, T. M. Loehr, *Solid State Commun.* **1981**, *39*, 341–344.
[46] Y. Zheng, R. Zhang, P. Vanaphuti, J. Fu, Z. Yang, Y. Wang, *ACS Sustainable Chem. Eng.* **2021**, *9*, 6087–6096.
[47] L. A. Gomez-Moreno, A. Klemettinen, R. Serna-Guerrero, *iScience* **2023**, *26*, 107782.
[48] K. S. W. Sing, D. H. Everett, R. A. W. Haul, L. Moscou, R. A. Pierotti, J. Rouquerol, T. Siemieniewska, *Pure Appl Chem.* **1985**, *57*, 603–619.
[49] Q. Gao, L. Demarconnay, E. Raymundo-Pinero, F. Beguin, *Energy Environ. Sci.* **2012**, *5*, 9611–9617.
[50] E. Pameté, F. Beguin, *Electrochim. Acta* **2021**, *389*, 138687.
[51] D. Weingarth, H. Noh, A. Foelske-Schmitz, A. Wokaun, R. Kotz, *Electrochim. Acta* **2013**, *103*, 119–124.
[52] S. Porada, L. Borchardt, M. Oschatz, M. Bryjak, J. S. Atchison, K. J. Keesman, S. Kaskel, P. M. Biesheuvel, V. Presser, *Energy Environ. Sci.* **2013**, *6*, 3700–3712.
[53] C. Kim, P. Srimuk, J. Lee, S. Fleischmann, M. Aslan, V. Presser, *Carbon* **2017**, *122*, 329–335.
[54] B. Krüner, P. Srimuk, S. Fleischmann, M. Zeiger, A. Schreiber, M. Asian, A. Quade, V. Presser, *Carbon* **2017**, *117*, 46–54.
[55] M. Aslan, M. Zeiger, N. Jäckel, I. Grobelsek, D. Weingarth, V. Presser, *J. Phys.: Condens. Matter* **2016**, *28*, 114003.
[56] N. Jäckel, M. Rodner, A. Schreiber, J. Jeongwook, M. Zeiger, M. Aslan, D. Weingarth, V. Presser, *J. Power Sources* **2016**, *326*, 660–671.
[57] T. Kim, J. Yoon, *RSC Adv.* **2015**, *5*, 1456–1461.
[58] P. Ren, M. Torkamanzadeh, X. Zhang, M. Twardoch, C. Kim, V. Presser, *Carbon* **2023**, *213*, 118191.
[59] A. P. Silva, A. Argondizo, P. T. Juchen, L. A. M. Ruotolo, *Sep. Purif. Technol.* **2021**, *271*, 118872.
[60] J. Kim, Y. Yi, D.-H. Peck, S.-H. Yoon, D.-H. Jung, H. S. Park, *Environ. Sci.: Nano* **2019**, *6*, 916–924.
[61] Z. Xie, X. Shang, J. Yan, T. Hussain, P. Nie, J. Liu, *Electrochim. Acta* **2018**, *290*, 666–675.
[62] M. Kim, H. Lim, X. Xu, M. S. A. Hossain, J. Na, N. N. Awaludin, J. Shah, L. K. Shrestha, K. Ariga, A. K. Nanjundan, D. J. Martin, J. G. Shapter, Y. Yamauchi, *Microporous and Mesoporous Mater.* **2021**, *312*, 110757.
[63] M. E. Suss, S. Porada, X. Sun, P. M. Biesheuvel, J. Yoon, V. Presser, *Energy Environ. Sci.* **2015**, *8*, 2296–2319.

[64] Precedence Research, Supercapacitors market size, share, and trends 2024 to 2034, **2024**, https://www.precedenceresearch.com/supercapacitors-market.
[65] Precedence Research, Supercapacitor activated carbon market report overview, **2024**, https://www.businessresearchinsights.com/market-reports/supercapacitor-activated-carbon-market-104798.
[66] MarketsandMarkets Research, Supercapacitor market by type (double layer capacitors, pseudocapacitors, hybrid capacitors), electrode material (carbon, metal oxide, conducting polymers, composites)application (automotive, energy, consumer electronics- Global Forecast to 2027, 2024, https://www.marketsandmarkets.com/Market-Reports/supercapacitor-market-37140453.html.
[67] https://www.transparencymarketresearch.com/supercapacitor-market.htmlMarketsandMarkets Research, Supercapacitor Market, 2024, https://www.transparencymarketresearch.com/supercapacitor-market.htmlhttps://www.marketsandmarkets.com/Market-Reports/supercapacitor-market-37140453.html.
[68] S. Ghosh, S. Yadav, A. Devi, T. Thomas, *Renewable Sustainable Energy Rev.* **2022**, *161*, 112412.
[69] Y. Yang, Y. Han, W. Jiang, Y. Zhang, Y. Xu, A.M. Ahmed, *Applied Sciences* **2021**, *12*, 354.
[70] S. M. Benoy, M. Pandey, D. Bhattacharjya, B. K. Saikia, *J. Energy Storage* **2022**, *52*, 104938.
[71] M. Qasim, M. Badrelzaman, N. N. Darwish, N. A. Darwish, N. Hilal, *Desalination* **2019**, *459*, 59–104.
[72] C. Bartels, R. Franks, S. Rybar, M. Schierach, M. Wilf, *Desalination* **2005**, *184*, 185–195.
[73] S. Porada, L. Zhang, J. E. Dykstra, *Desalination* **2020**, *488*, 114383.
[74] H. K. Mutha, H. J. Cho, M. Hashempour, B. L. Wardle, C. V. Thompson, E. N. Wang, *Desalination* **2018**, *437*, 154–163.
[75] M. Qin, A. Deshmukh, R. Epsztein, S. K. Patel, O. M. Owoseni, W. S. Walker, M. Elimelech, *Desalination* **2019**, *455*, 100–114.
[76] P. Sharan, T. J. Yoon, S. M. Jaffe, T. Ju, R. P. Currier, A. T. Findikoglu, *Cleaner Eng. Technol.* **2021**, *3*, 100102.
[77] X. Liu, S. Shanbhag, T. V. Bartholomew, J. F. Whitacre, M. S. Mauter, *ACS ES&T Eng.* **2021**, *1*, 261–273.
[78] S.-Y. Pan, A. Z. Haddad, A. Kumar, S.-W. Wang, *Water Res.* **2020**, *183*, 116064.
[79] M. Torkamanzadeh, L. Wang, Y. Zhang, O. Budak, P. Srimuk, V. Presser, *ACS App. Mater. Interfaces* **2020**, *12*, 26013–26025.
[80] D. Weingarth, M. Zeiger, N. Jäckel, M. Aslan, G. Feng, V. Presser, *Adv. Energy Mater.* **2014**, *4*, 1400316.
[81] M. Torkamanzadeh, C. Kök, P. R. Burger, P. Ren, Y. Zhang, J. Lee, C. Kim, V. Presser, *Cell Rep. Phys. Sci.* **2023**, *4*, 101661.

Manuscript received: July 28, 2024
Revised manuscript received: August 26, 2024
Accepted manuscript online: August 27, 2024
Version of record online: October 23, 2024

Batteries & Supercaps

Supporting Information

Life After Death: Re-Purposing End-of-Life Supercapacitors for Electrochemical Water Desalination

Panyu Ren, Mohammad Torkamanzadeh, Stefanie Arnold, Emmanuel Pameté, and Volker Presser*

Supplemental Information

Life after death: Re-purposing end-of-life supercapacitors for electrochemical water desalination

Panyu Ren,[1,2] Mohammad Torkamanzadeh,[1] Stefanie Arnold,[1]

Emmanuel Pameté,[1] and Volker Presser,[1,2,3,]*

[1] *INM - Leibniz Institute for New Materials, D2 2, 66123, Saarbrücken, Germany*

[2] *Department of Materials Science & Engineering, Saarland University, Campus D2 2, 66123, Saarbrücken, Germany*

[3] *saarene, Saarland Center for Energy Materials and Sustainability, Campus C4 2, 66123 Saarbrücken, Germany*

* Corresponding author's email: volker.presser@leibniz-inm.de

Supporting Tables

Table S1. Summary of gas sorption analysis performed on the CO_2-activated supercapacitor carbon material at various target temperatures and holding times (QSDFT: quenched solid density functional theory, BET: Brunauer-Emmett-Teller theory).

Sample	Surface area QSDFT ($m^2\ g^{-1}$)	Surface area BET ($m^2\ g^{-1}$)	Average pore width d_{50} (nm)	Pore volume ($cm^3\ g^{-1}$)
CO_2-treated at 700 °C for 2 h	1216	975	0.79	0.64
CO_2-treated at 800 °C for 1 h	1187	1297	0.79	0.58

Table S2. Specifications of the HY-CAP 500F 3V commercial supercapacitor provided by Reichelt Elektronik GmbH.

Parameter	Value
Rated voltage (V)	3.0
Capacitance (F)	500
Max. current (A)	230.0
Leakage current (mA, 72 h)	1.500
Mass (g)	96.0
Volume (mL)	78.9
Equivalent series resistance (mΩ):	
AC (1 kHz)	3.0
DC	4.5
Cycle	Over 500,000
ΔC	$\leq$ 30 % of initial value

Table S3. Comparison of electrochemical desalination works with electrodes derived from various waste sources.

Electrode material	Material source	Electrolyte concentration (NaC mM)	Cell voltage (V)	Flow rate (mL min^{-1})	Desalination capacity range (mg g^{-1})	Ref.
Activated carbon	Jackfruit peels (*Artocarpus heterophyllus*)	0.5-9	1.2-2.0	2.5	1-6	[1]
Mesoporous carbon	Calcium citrate salts	-	2.0	-	1.4	[2]
Activated carbon	Date palm leaves	2	1.0-1.8	3	5.4	[3]
Activated carbon	Rice husk	2	1.5	20	6-18	[4]
Activated carbon	Rice husk	10	1.2	25	16	[5]
Activated carbon film	Commercial	20	1.2	2	12	[6]
Activated carbon cloth	Commercial	5	1.2	22	10-16	[7]
Porous carbon	**Commercial supercapacitor**	**20**	**1.2**	**2**	**3-8**	**This work**

Supporting Figures

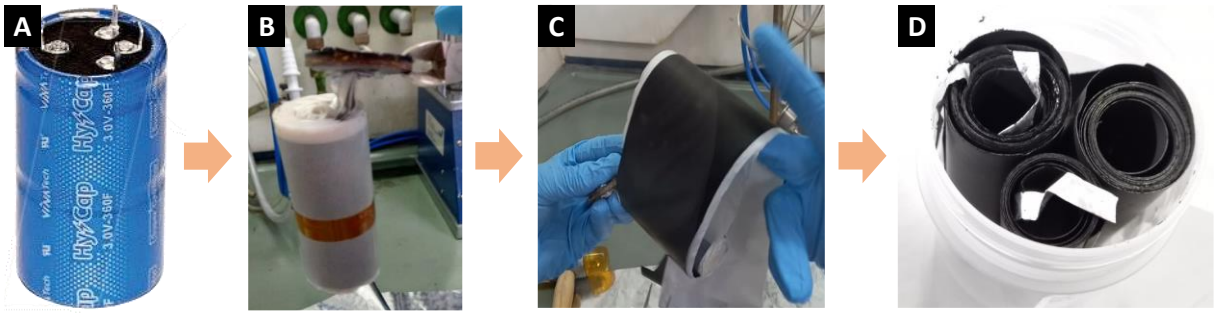

Figure S1. Step-by-step disassembly process of the commercial supercapacitor (A) HY-CAP 500 F 3 V supercapacitor with 35.0 mm diameter and 82.0 mm height. (B) aluminium casing removed: rolls of carbon electrode are seen together with separator, (C) un-rolling, resulting in around 2 m-long rectangular electrodes, and (D) separators removed, leaving carbon electrodes on the aluminium current collector.

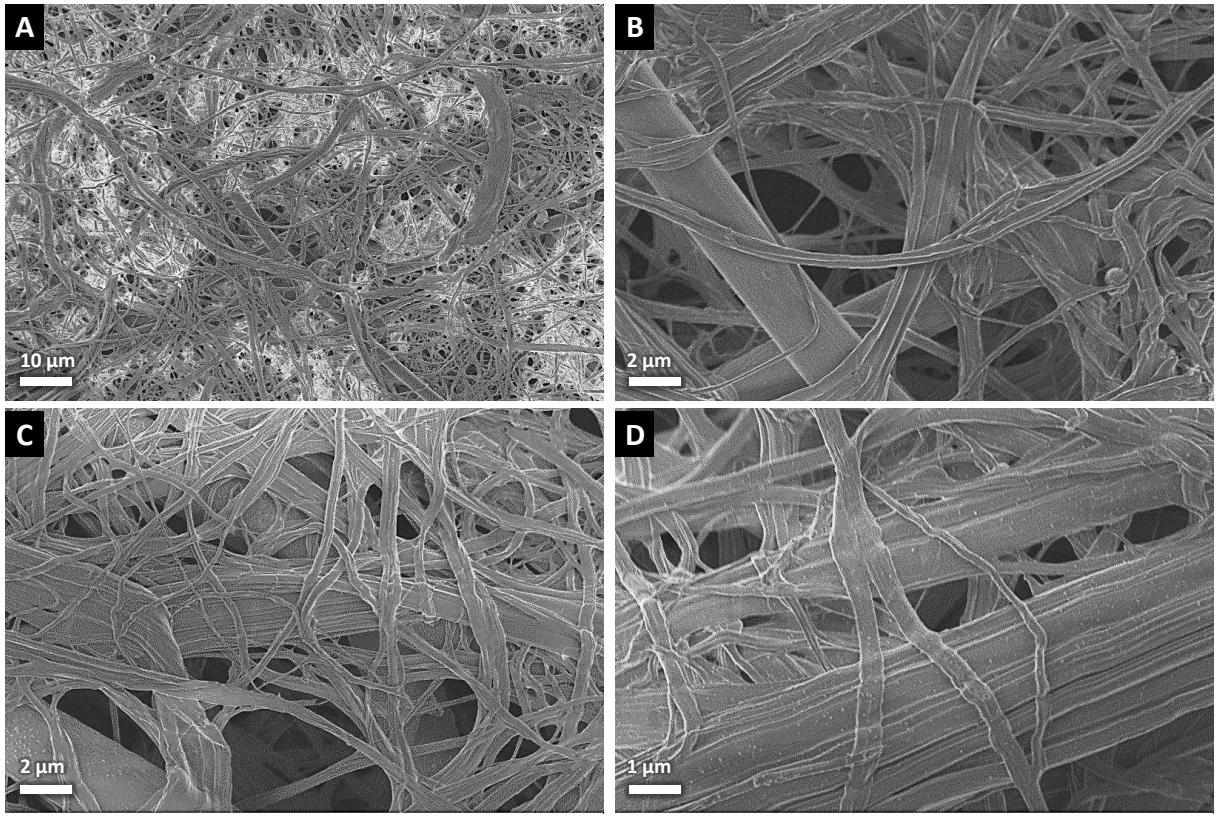

Figure S2. Scanning electron micrographs of the separator disassembled from the commercial supercapacitor.

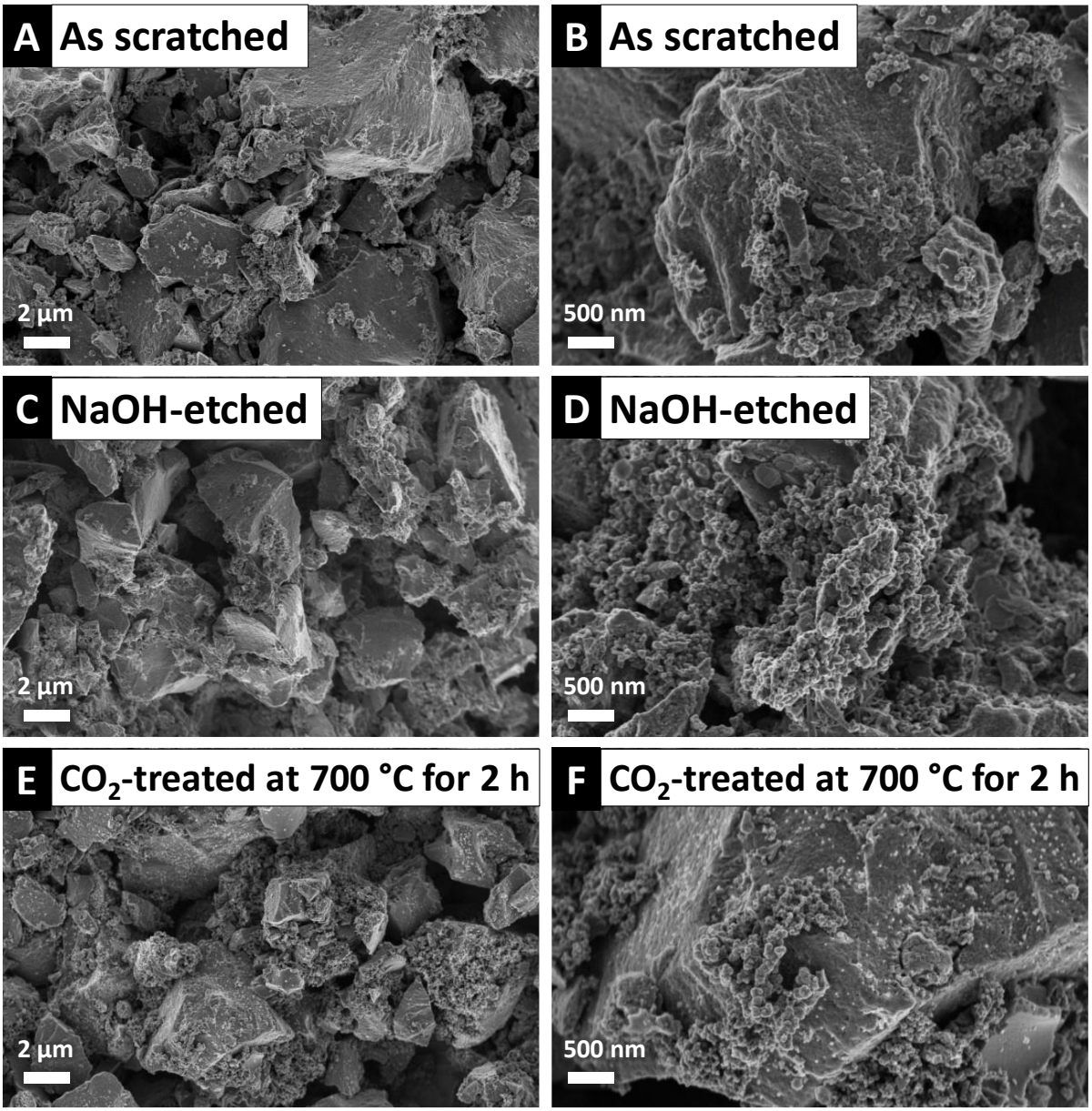

Figure S3. Scanning electron micrographs of the carbon from the commercial supercapacitor (A-B) pristine powder after scratching from the current collector (no NaOH etching), (C-D) after NaOH etching, and (E-F) after CO_2 treatment at 700 °C for 2 h.

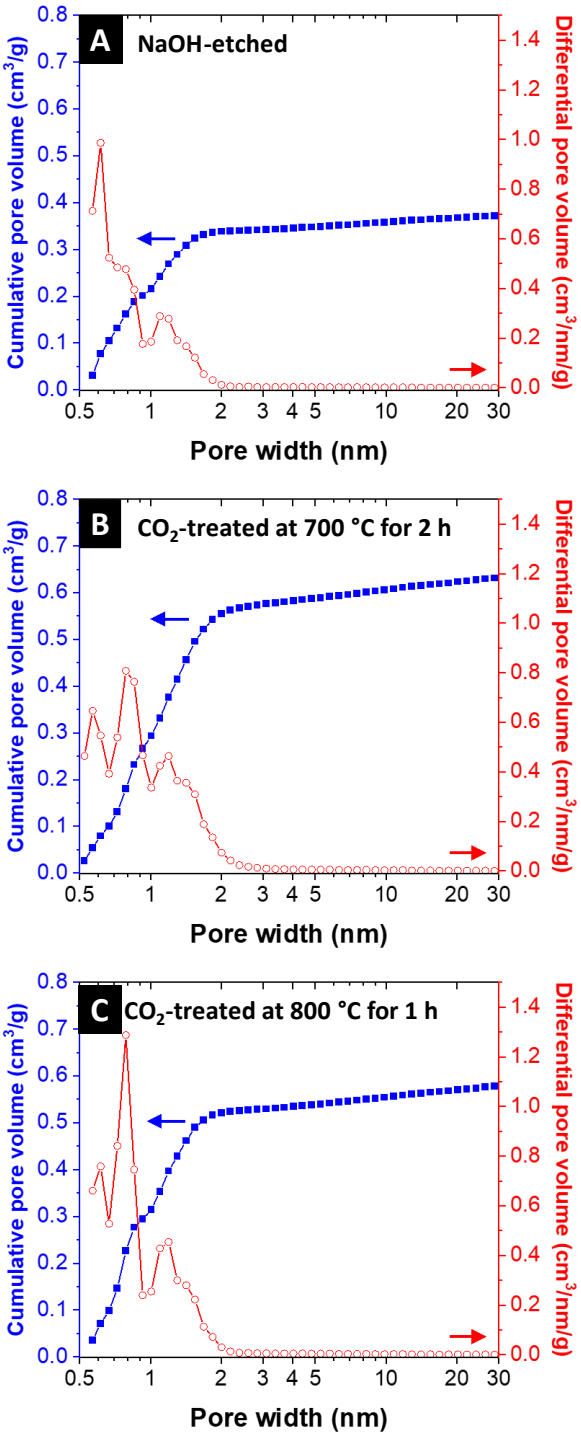

Figure S4. Nitrogen gas sorption analysis showing cumulative and differential pore volume profiles versus pore width in supercapacitor carbon material after (A) NaOH etching, (B) CO_2 treatment at 700 °C for 2 h, (C) CO_2 treatment at 800 °C for 1 h.

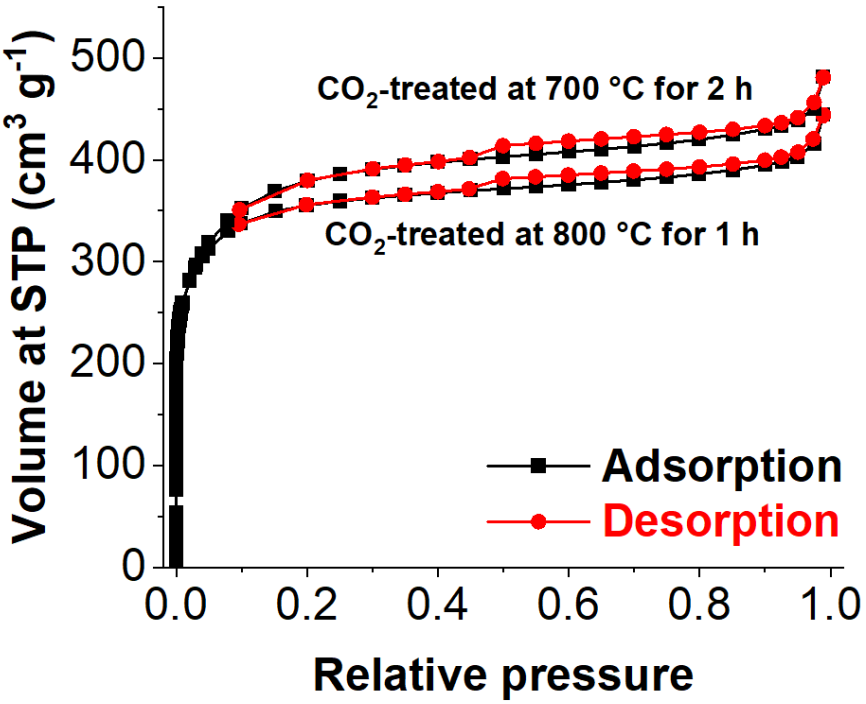

Figure S5. Nitrogen gas sorption measurement at -196 °C performed on the supercapacitor carbon electrode after CO_2 activation at various target temperatures and holding times. (STP: standard temperature and pressure).

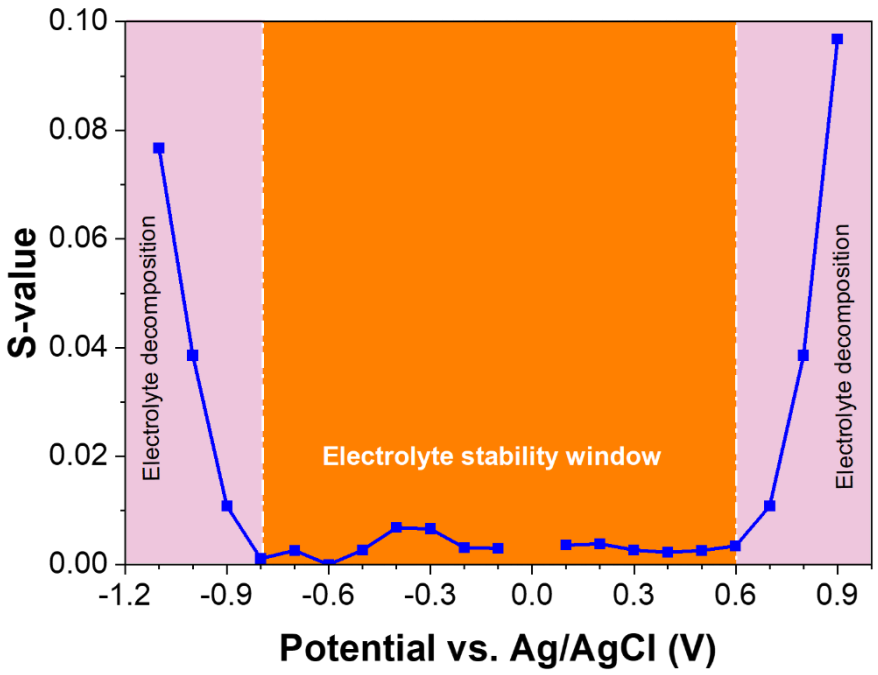

Figure S6. The plot of S-values vs. vertex potential calculated from the cyclic voltammograms with potential window opening. The plot shows the limit for the electrolyte stability and decomposition regions.

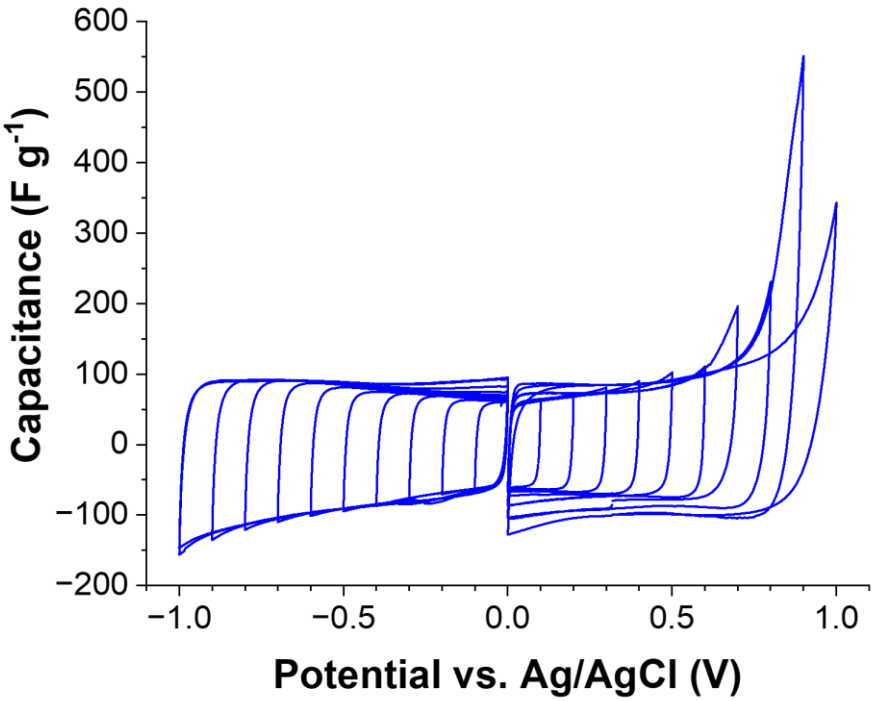

Figure S7. Half-cell cyclic voltammograms with a potential window opening of CO_2-activated electrode (at 700 °C for 2 h) with a scanning rate of 1 mV s^{-1} in aqueous 600 mM NaCl electrolyte.

Figure S8. A photograph of the commercial supercapacitor under long-term charge and discharge tests. The positive and negative terminals of the supercapacitor are soldered to adapt to the cables of the electrochemical workstation.

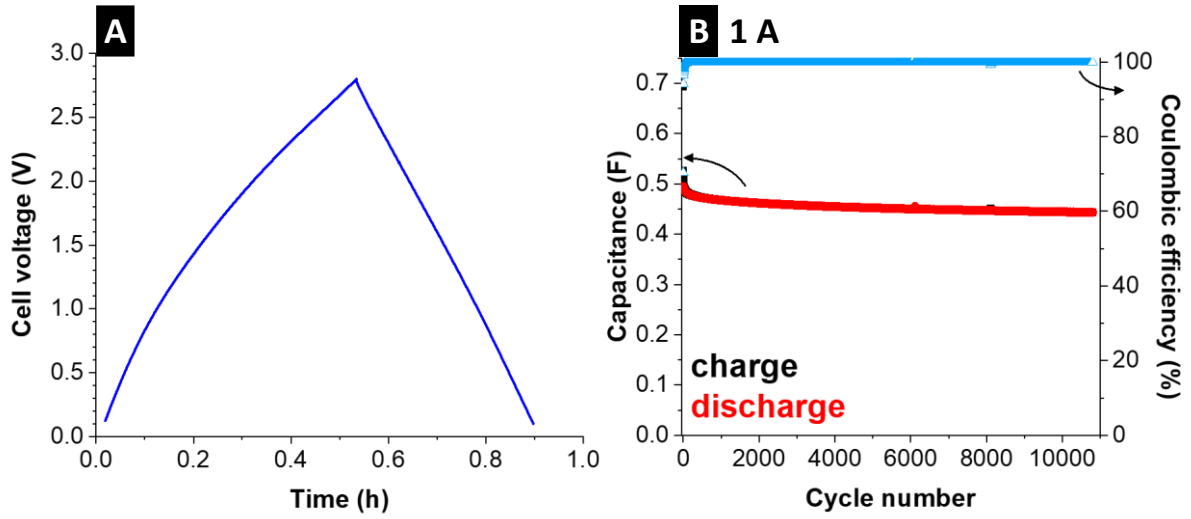

Figure S9. Electrochemical characterization of the commercial supercapacitor. (A) Cell voltage vs. time plots obtained from GCPL measurements at 1 A, (B) cycling stability via capacitance vs. cycle number in charge and discharge cycles combined with corresponding Coulombic efficiency.

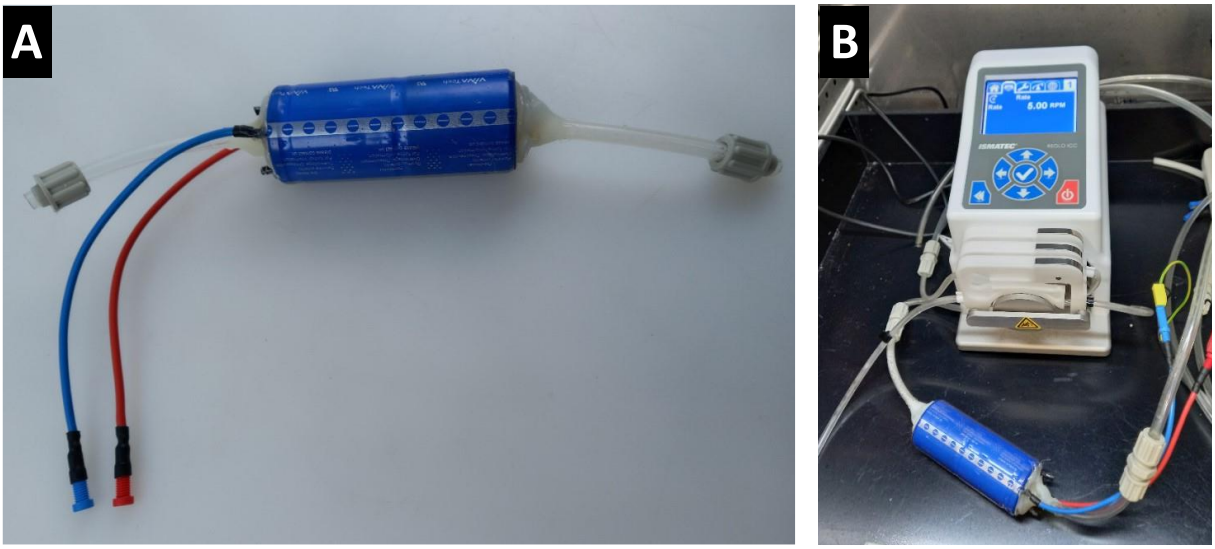

Figure S10. Photographs of (A) the commercial supercapacitor with holes at two ends of the cylindrical cell where tubes are attached, and (B) the latter cell used as an electrochemical water desalination cell with 20 mM aqueous NaCl solution being pumped through it.

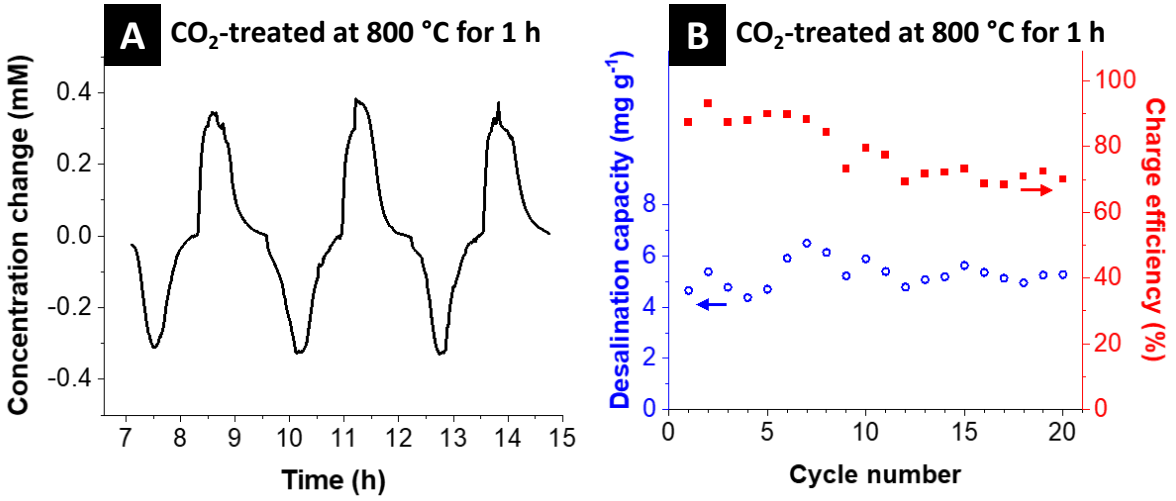

Figure S11. (A) NaCl concentration-time profiles of the effluent water of the electrochemical cells made from CO_2-treated electrodes at 800 °C for 1 h and (B) its corresponding desalination capacity and charge efficiency.

Supporting References

[1] J. Elisadiki, Y. A. C. Jande, R. L. Machunda, T. E. Kibona *Carbon*. **2019**, *147*, 582-593.
[2] J. Yang, L. Zou *Microporous and Mesoporous Materials*. **2014**, *183*, 91-98.
[3] H. H. Kyaw, S. M. Al-Mashaikhi, M. T. Z. Myint, S. Al-Harthi, E.-S. I. El-Shafey, M. Al-Abri *Chemical Engineering and Processing - Process Intensification*. **2021**, *161*, 108311.
[4] J. Kim, Y. Yi, D.-H. Peck, S.-H. Yoon, D.-H. Jung, H. S. Park *Environmental Science: Nano*. **2019**, *6*, 916-924.
[5] A. P. Silva, A. Argondizo, P. T. Juchen, L. A. M. Ruotolo *Separation and Purification Technology*. **2021**, *271*, 118872.
[6] M. Torkamanzadeh, L. Wang, Y. Zhang, Ö. Budak, P. Srimuk, V. Presser *ACS Applied Materials & Interfaces*. **2020**, *12*, 26013-26025.
[7] C. Kim, P. Srimuk, J. Lee, S. Fleischmann, M. Aslan, V. Presser *Carbon*. **2017**, *122*, 329-335.

5. Conclusions and Outlook

Electrochemical desalination is a promising technology that aims to be environmentally friendly and energy-efficient. The range of electrochemical desalination technologies includes CDI with carbon materials and desalination batteries capable of recovering lithium ions or extracting heavy metal ions. Carbon materials, known for their large pore volumes and high specific surface area, are commonly utilized in CDI to enhance desalination capacity.

My doctoral work has explored the performance of carbon materials for ion separation and ion-selective extraction. By systematically addressing the research objectives outlined in the introduction, the work has advanced the understanding of CDI and highlighted areas requiring further investigation. The findings emphasize the importance of ion and electrode properties for electrochemical ion separation.

The particle size distribution of carbon materials is a critical factor influencing the desalination performance. Larger particles result in longer diffusion pathways within the particles, while smaller particles hinder ion transport between particles. As a result, the size distribution affects intraparticle and interparticle ion diffusion. Achieving higher desalination performance requires a balance, for instance, by combining large and small particles and optimizing the electrode density.

Conductive additives are commonly added during the fabrication of electrodes for energy storage, catalysis, and other applications. The selection of suitable additives should be tailored to the specific application conditions. In this thesis, we found that the activated carbon electrode achieved an electrosorption capacity of approximately 10 mg g^{-1} without any conductive additives, although at a relatively low rate of 6 µg g^{-1} s^{-1}. In contrast, mixing the activated carbon electrode with small, less porous additives significantly enhanced the desalination rate. This improvement is attributed to the shorter ion diffusion path length resulting from increased size dispersion, facilitating better ion transport within the particles and higher desalination rates. The relationships between the physicochemical properties of different carbon types and their resulting electrochemical desalination performance were explored. The knowledge of which characteristics can improve ion transfer kinetics and which can result in pore blockage and adversely affect performance will inspire future research.

Selective ion removal has been of great importance in water purification and resource recovery. For CDI, when the pore size is smaller than the hydrated divalent cations (0.6 nm), the divalent cations cannot be absorbed into the pores due to the high dehydration energy barrier. However, due to their smaller hydrated ion sizes, monovalent cations can enter the carbon material's pores. The heavy monovalent cation can be selectively removed from a multi-cation-contained aqueous media by applying carbon material with a small average pore size and narrow pore size distribution.

Replacing the static electrodes with flowable electrodes enables continuous ion separation. Studies have focused on ion-selective removal using CDI, whereas knowledge of FCDI operation for selective ion separation in multi-cation systems has remained limited. The relationship between pore features and ion selectivity was also studied. Key parameters for the FCDI system, including mass loading, conductive additives, applied voltage, feedwater flow rate, and slurry, were investigated and optimized for selective ion separation. Results showed efficient separation of all ions (nearly 100 % removed) within 32 h at optimized operation parameters, with charge efficiency over 70%. Moreover, the universal ion separation sequence (Ca^{2+} > Mg^{2+} > K^{+} > Na^{+} > Li^{+}) was found for FCDI configurations, which was related to the valence and hydration size of these cations. Further, ion selectivity could be well tuned by adjusting key systematical parameters, paving the way to realize controlled separation of specific ions from multi-ion surroundings. Overall, the presented findings provide new insights into the ion separation process and valuable reference for the practical application of the electrochemical process.

Lithium-ion recovery is increasingly critical due to the rising demand for lithium in energy storage technologies, requiring efficient and sustainable methods to extract lithium from resources like seawater and brines. A novel electrochemical cell configuration was designed to recover lithium continuously from seawater. The redox couple of ($[Fe(CN)_6]^{3-}$/$[Fe(CN)_6]^{4-}$ provides the driving force for the migration of cations, and the LISICON membrane plays the role of selectively extracting lithium. After 5 h treatment for the seawater, the selectivity factors of $K_{Li/K}$, $K_{Li/Na,}$ and $K_{Li/Mg}$ after the 5 h enrichment are 12,000, 410,000, and 500,000, respectively, corresponding to the purity of Li^{+} of 93.5 % in the extracts and an extracted Mg^{2+} ratio of 0.43 %, which strongly impacts the chemical precipitation of Li^{+}.

RFD is effective for the removal and recovery of TMAH from semiconductor industry wastewater, achieving a removal rate of approximately 4.3 mM g^{-1} h^{-1} with a charge efficiency of around 90 % and energy consumption of about 15 kJ mol^{-1} while recovering about 40 % of TMAH at a low cell voltage of 1.2 V. The system utilizes a reversible redox reaction in the redox channel rather than a water-splitting reaction, demonstrating high effectiveness in various experimental conditions and offering low operational costs and energy consumption compared to ED. The results open new opportunities for wastewater treatment by removing and recovering charged organic pollutants.

Our research explores the use of supercapacitor electrodes for electrochemical water desalination. Specifically, we repurpose carbon electrodes from commercial 500-Farad supercapacitor devices for CDI, supporting circular economy principles. The modified electrodes can be utilized for the electrochemical desalination of low-salinity NaCl solutions. While various strategies are being developed for recycling lithium-ion batteries, supercapacitors have received comparatively little attention. Our study introduces an innovative approach that repurposes supercapacitor electrodes for electrochemical desalination, emphasizing a novel and valuable pathway for reuse in this field. This work addresses waste management issues and enhances the utility of supercapacitor materials in sustainable applications.

Although electrochemical ion separation holds promise for effective ion separation and selective ion removal, significant challenges remain. (1) Enhancing removal performance while maintaining high selectivity is difficult, as greater selectivity often reduces efficiency. Issues such as carbon oxidation and membrane fouling require long-term stability studies and protective strategies. (2) FCDI's complex electrochemical processes demand deeper theoretical insights into flow electrode morphology and charge dynamics, along with the development of selective, high-performance flow electrodes. (3) CDI/FCDI industrialization faces early-stage hurdles, including cost-effective materials, system integration, and electrode durability. Pilot-scale studies are essential to validate large-scale applications and accelerate commercialization.

6. Abbreviations

CDI	Capacitive deionization
MSF	Multi-stage flash evaporation
MED	Multi-effect distillation
RO	Reverse osmosis
ED	Electrodialysis
FCDI	Flow electrode capacitive deionization
IEMs	Ion exchange membranes
EDL	Electrical double-layer
GCS	Gouy-Chapman-Stern
TMDs	Transition metal dichalcogenides
3D	Three-dimensional
CNTs	Carbon nanotubes
CV	Cyclic voltammograms
CEM	Cation exchange membrane
MCDI	Membrane capacitive deionization
HCDI	Hybrid capacitive deionization
ASAR	Average salt adsorption rate
i.e.,	In other words
EDLc	Double-layer capacitance
AEM	Anion exchange membrane
SAC	Salt adsorption capacity
CAs	Conductive additives
ZLD	Zero-liquid discharge
rGO	Reduced graphene oxide
TNT	Titanium dioxide nanotubes
NSCCE	Nitrate-selective composite carbon electrode
MSMCDI	Monovalent selective membrane capacitive deionization
LMO	Lithium manganese oxide
e.g.,	For example
EFC	Electrochemical flow capacitor

mass %	Solid mass percentage
CB	Carbon black
H_2Q	Hydroquinone
PPD	P-phenylenediamine
MPD	M-phenylenediamine
Q	Benzoquinone
MEA	Membrane-electrode assembly
BP	Bipolar plate
OC	Open cycle
ICC	Isolated closed-cycle
SCC	Short-circuited closed cycle
SC	Single cycle
RFD	Redox flow desalination
ETDA	Ethylenediamine triacetic acid
PBAs	Prussian blue analogs

7. References

[1] M. Elimelech, W.A. Phillip, The future of seawater desalination: Energy, technology, and the environment, Science, 333 (2011) 712-717.
[2] F.a.A. Organization, Water scarcity, Published in 2006, https://www.fao.org/land-water/water/water-scarcity/en/.
[3] P. Kumar, A. Date, N. Mahmood, R. Kumar Das, B. Shabani, Freshwater supply for hydrogen production: An underestimated challenge, International Journal of Hydrogen Energy, 78 (2024) 202-217.
[4] U.E. Programme, As shortages mount, countries hunt for novel sources of water, Published in 2024, https://www.unep.org/news-and-stories/story/shortages-mount-countries-hunt-novel-sources-water.
[5] S. Lin, H. Zhao, L. Zhu, T. He, S. Chen, C. Gao, L. Zhang, Seawater desalination technology and engineering in China: A review, Desalination, 498 (2021) 114728.
[6] W. Suwaileh, D. Johnson, N. Hilal, Membrane desalination and water re-use for agriculture: State of the art and future outlook, Desalination, 491 (2020) 114559.
[7] A. Subramani, J.G. Jacangelo, Emerging desalination technologies for water treatment: A critical review, Water Research, 75 (2015) 164-187.
[8] H.T. El-Dessouky, H.M. Ettouney, Y. Al-Roumi, Multi-stage flash desalination: Present and future outlook, Chemical Engineering Journal, 73 (1999) 173-190.
[9] A. Dashputre, A. Kaushik, A. Pal, D. Jariwala, K. Yadav, M. Shah, Geothermal energy integrated multi-effect evaporator (MEE) and multi-effect distillation (MED)-based desalination systems: An ecofriendly and sustainable solutions, Environmental Science and Pollution Research, 30 (2023) 67941-67952.
[10] L.F. Greenlee, D.F. Lawler, B.D. Freeman, B. Marrot, P. Moulin, Reverse osmosis desalination: Water sources, technology, and today's challenges, Water Research, 43 (2009) 2317-2348.
[11] B. Peñate, L. García-Rodríguez, Current trends and future prospects in the design of seawater reverse osmosis desalination technology, Desalination, 284 (2012) 1-8.
[12] S. Al-Amshawee, M.Y.B.M. Yunus, A.A.M. Azoddein, D.G. Hassell, I.H. Dakhil, H.A. Hasan, Electrodialysis desalination for water and wastewater: A review, Chemical Engineering Journal, 380 (2020) 122231.
[13] A. Campione, L. Gurreri, M. Ciofalo, G. Micale, A. Tamburini, A. Cipollina, Electrodialysis for water desalination: A critical assessment of recent developments on process fundamentals, models and applications, Desalination, 434 (2018) 121-160.
[14] M.E. Suss, T.F. Baumann, W.L. Bourcier, C.M. Spadaccini, K.A. Rose, J.G. Santiago, M. Stadermann, Capacitive desalination with flow-through electrodes, Energy & Environmental Science, 5 (2012) 9511-9519.
[15] J. Lee, S. Kim, C. Kim, J. Yoon, Hybrid capacitive deionization to enhance the desalination performance of capacitive techniques, Energy & Environmental Science, 7 (2014) 3683-3689.
[16] J. Ma, C. Zhai, F. Yu, Review of flow electrode capacitive deionization technology: Research progress and future challenges, Desalination, 564 (2023) 116701.
[17] J. Ma, L. Chen, F. Yu, Environmental applications and perspectives of flow electrode capacitive deionization (FCDI), Separation and Purification Technology, 335 (2024) 126095.
[18] V.K. Chauhan, S.K. Shukla, J.V. Tirkey, P.K. Singh Rathore, A comprehensive review of direct solar desalination techniques and its advancements, Journal of Cleaner Production, 284 (2021) 124719.
[19] P. Fiorini, E. Sciubba, C. Sommariva, A new formulation for the non-equilibrium allowance in MSF processes, Desalination, 136 (2001) 177-188.

[20] S.M. Alsadaie, I.M. Mujtaba, Dynamic modelling of heat exchanger fouling in multistage flash (MSF) desalination, Desalination, 409 (2017) 47-65.
[21] J. Zhao, M. Wang, H.M.S. Lababidi, H. Al-Adwani, K.K. Gleason, A review of heterogeneous nucleation of calcium carbonate and control strategies for scale formation in multi-stage flash (MSF) desalination plants, Desalination, 442 (2018) 75-88.
[22] A. Yaroshchuk, "Breakthrough" osmosis and unusually high power densities in pressure-retarded osmosis in non-ideally semi-permeable supported membranes, Scientific Reports, 7 (2017) 45168.
[23] S. Lin, M. Elimelech, Staged reverse osmosis operation: Configurations, energy efficiency, and application potential, Desalination, 366 (2015) 9-14.
[24] J. Kim, K. Park, D.R. Yang, S. Hong, A comprehensive review of energy consumption of seawater reverse osmosis desalination plants, Applied Energy, 254 (2019) 113652.
[25] C. Fritzmann, J. Löwenberg, T. Wintgens, T. Melin, State-of-the-art of reverse osmosis desalination, Desalination, 216 (2007) 1-76.
[26] M.E. Suss, S. Porada, X. Sun, P.M. Biesheuvel, J. Yoon, V. Presser, Water desalination via capacitive deionization: what is it and what can we expect from it?, Energy & Environmental Science, 8 (2015) 2296-2319.
[27] S.K. Patel, M. Qin, W.S. Walker, M. Elimelech, Energy efficiency of electro-driven brackish water desalination: electrodialysis significantly outperforms membrane capacitive deionization, Environmental Science & Technology, 54 (2020) 3663-3677.
[28] S.S. Shenvi, A.M. Isloor, A.F. Ismail, A review on RO membrane technology: Developments and challenges, Desalination, 368 (2015) 10-26.
[29] Y.D. Ahdab, D. Rehman, J.H. Lienhard, Brackish water desalination for greenhouses: Improving groundwater quality for irrigation using monovalent selective electrodialysis reversal, Journal of Membrane Science, 610 (2020) 118072.
[30] H. Wang, Y. Liu, Y. Li, X. Xu, X. Liu, Y. Yao, T. Lu, L. Pan, Tactics for boosting the desalination stability of capacitive deionization, Chemical Engineering Journal, 496 (2024) 153808.
[31] F.A. AlMarzooqi, A.A. Al Ghaferi, I. Saadat, N. Hilal, Application of capacitive deionisation in water desalination: a review, Desalination, 342 (2014) 3-15.
[32] S. Porada, R. Zhao, A. van der Wal, V. Presser, P.M. Biesheuvel, Review on the science and technology of water desalination by capacitive deionization, Progress in Materials Science, 58 (2013) 1388-1442.
[33] P. Srimuk, X. Su, J. Yoon, D. Aurbach, V. Presser, Charge-transfer materials for electrochemical water desalination, ion separation and the recovery of elements, Nature Reviews Materials, 5 (2020) 517-538.
[34] L. Wang, Z. Liu, Z. Wang, Q. Ma, Z. Guo, G. Shen, K. Wang, X. Xu, Y. Liu, X. Yuan, Up-shifting the desalination rate limit of capacitive deionization via integrating chloride-capturing Bi nanocluster with flow-through cell architecture, Chemical Engineering Journal, 460 (2023) 141726.
[35] J.E. Dykstra, K.J. Keesman, P.M. Biesheuvel, A. van der Wal, Theory of pH changes in water desalination by capacitive deionization, Water Research, 119 (2017) 178-186.
[36] Z. Hao, X. Sun, J. Chen, X. Zhou, Y. Zhang, Recent progress and challenges in Faradic capacitive desalination: from mechanism to performance, Small, 19 (2023) 2300253.
[37] J.G. Gamaethiralalage, K. Singh, S. Sahin, J. Yoon, M. Elimelech, M.E. Suss, P. Liang, P.M. Biesheuvel, R.L. Zornitta, L.C.P.M. de Smet, Recent advances in ion selectivity with capacitive deionization, Energy & Environmental Science, 14 (2021) 1095-1120.
[38] W. Shi, X. Liu, T. Deng, S. Huang, M. Ding, X. Miao, C. Zhu, Y. Zhu, W. Liu, F. Wu, C. Gao, S.-W. Yang, H.Y. Yang, J. Shen, X. Cao, Enabling superior sodium capture for efficient water

desalination by a tubular polyaniline decorated with prussian blue nanocrystals, Advanced Materials, 32 (2020) 1907404.
[39] S. Porada, L. Borchardt, M. Oschatz, M. Bryjak, J.S. Atchison, K.J. Keesman, S. Kaskel, P.M. Biesheuvel, V. Presser, Direct prediction of the desalination performance of porous carbon electrodes for capacitive deionization, Energy & Environmental Science, 6 (2013) 3700-3712.
[40] W. Tang, J. Liang, D. He, J. Gong, L. Tang, Z. Liu, D. Wang, G. Zeng, Various cell architectures of capacitive deionization: Recent advances and future trends, Water Research, 150 (2019) 225-251.
[41] O. Stern, The theory of the electrolytic double-layer, Zeitschrift für Elektrochemie, 30 (1924) 1014-1020.
[42] M. Gouy, Sur la constitution de la charge électrique à la surface d'un électrolyte, Journal of Physics: Theories and Applications, 9 (1910) 457-468.
[43] D.L. Chapman, LI. A contribution to the theory of electrocapillarity, The London, Edinburgh, and Dublin Philosophical Magazine and Journal of Science, 25 (1913) 475-481.
[44] L. Wang, P.M. Biesheuvel, S. Lin, Reversible thermodynamic cycle analysis for capacitive deionization with modified Donnan model, Journal of Colloid and Interface Science, 512 (2018) 522-528.
[45] R. Zhao, P. Biesheuvel, H. Miedema, H. Bruning, A. Van der Wal, Charge efficiency: a functional tool to probe the double-layer structure inside of porous electrodes and application in the modeling of capacitive deionization, The Journal of Physical Chemistry Letters, 1 (2010) 205-210.
[46] P. Biesheuvel, S. Porada, M. Levi, M.Z. Bazant, Attractive forces in microporous carbon electrodes for capacitive deionization, Journal of Solid State Electrochemistry, 18 (2014) 1365-1376.
[47] M.E. Suss, Size-based ion selectivity of micropore electric double layers in capacitive deionization electrodes, Journal of The Electrochemical Society, 164 (2017) E270.
[48] P. Ratajczak, M.E. Suss, F. Kaasik, F. Béguin, Carbon electrodes for capacitive technologies, Energy Storage Materials, 16 (2019) 126-145.
[49] H. Ji, X. Zhao, Z. Qiao, J. Jung, Y. Zhu, Y. Lu, L.L. Zhang, A.H. MacDonald, R.S. Ruoff, Capacitance of carbon-based electrical double-layer capacitors, Nature Communications, 5 (2014) 3317.
[50] L. Chen, B. Tu, X. Lu, F. Li, L. Jiang, M. Antonietti, K. Xiao, Unidirectional ion transport in nanoporous carbon membranes with a hierarchical pore architecture, Nature Communications, 12 (2021) 4650.
[51] P. Srimuk, J. Lee, S. Fleischmann, S. Choudhury, N. Jäckel, M. Zeiger, C. Kim, M. Aslan, V. Presser, Faradaic deionization of brackish and sea water via pseudocapacitive cation and anion intercalation into few-layered molybdenum disulfide, Journal of Materials Chemistry A, 5 (2017) 15640-15649.
[52] C. Prehal, D. Weingarth, E. Perre, R.T. Lechner, H. Amenitsch, O. Paris, V. Presser, Tracking the structural arrangement of ions in carbon supercapacitor nanopores using in situ small-angle X-ray scattering, Energy & Environmental Science, 8 (2015) 1725-1735.
[53] T. Kim, J. Dykstra, S. Porada, A. Van Der Wal, J. Yoon, P. Biesheuvel, Enhanced charge efficiency and reduced energy use in capacitive deionization by increasing the discharge voltage, Journal of Colloid and Interface Science, 446 (2015) 317-326.
[54] K. Sun, M. Tebyetekerwa, C. Wang, X. Wang, X. Zhang, X.S. Zhao, Electrocapacitive deionization: mechanisms, electrodes, and cell designs, Advanced Functional Materials, 33 (2023) 2213578.

[55] F. Sauvage, L. Laffont, J.-M. Tarascon, E. Baudrin, Study of the insertion/deinsertion mechanism of sodium into $Na_{0.44}MnO_2$, Inorganic Chemistry, 46 (2007) 3289-3294.
[56] C. Tan, X. Cao, X.-J. Wu, Q. He, J. Yang, X. Zhang, J. Chen, W. Zhao, S. Han, G.-H. Nam, Recent advances in ultrathin two-dimensional nanomaterials, Chemical Reviews, 117 (2017) 6225-6331.
[57] L. Wang, K. Frisella, P. Srimuk, O. Janka, G. Kickelbick, V. Presser, Electrochemical lithium recovery with lithium iron phosphate: what causes performance degradation and how can we improve the stability?, Sustainable Energy & Fuels, 5 (2021) 3124-3133.
[58] M. Gao, W. Xiao, L. Miao, Z. Yang, W. Liang, T. Ao, Q. Yang, W. Chen, Prussian blue and its analogs: A robust platform for efficient capacitive deionization, Desalination, 574 (2024) 117278.
[59] B. Wang, Y. Han, X. Wang, N. Bahlawane, H. Pan, M. Yan, Y. Jiang, Prussian blue analogs for rechargeable batteries, Iscience, 3 (2018) 110-133.
[60] B. Chen, Y. Wang, Z. Chang, X. Wang, M. Li, X. Liu, L. Zhang, Y. Wu, Enhanced capacitive desalination of MnO_2 by forming composite with multi-walled carbon nanotubes, RSC Advances, 6 (2016) 6730-6736.
[61] J. Zheng, P. Cygan, T. Jow, Hydrous ruthenium oxide as an electrode material for electrochemical capacitors, Journal of the Electrochemical Society, 142 (1995) 2699.
[62] J.B. Flanagan, S. Margel, A.J. Bard, F.C. Anson, Electron transfer to and from molecules containing multiple, noninteracting redox centers. Electrochemical oxidation of poly (vinylferrocene), Journal of the American Chemical Society, 100 (1978) 4248-4253.
[63] I. Cohen, B. Shapira, E. Avraham, A. Soffer, D. Aurbach, Bromide ions specific removal and recovery by electrochemical desalination, Environmental Science & Technology, 52 (2018) 6275-6281.
[64] N. Kim, S.P. Hong, J. Lee, C. Kim, J. Yoon, High-desalination performance via redox couple reaction in the multichannel capacitive deionization system, ACS Sustainable Chemistry & Engineering, 7 (2019) 16182-16189.
[65] J. Lee, P. Srimuk, S. Carpier, J. Choi, R.L. Zornitta, C. Kim, M. Aslan, V. Presser, Confined redox reactions of iodide in carbon nanopores for fast and energy-efficient desalination of brackish water and seawater, ChemSusChem, 11 (2018) 3460-3472.
[66] S. Wang, G. Wang, T. Wu, C. Li, Y. Wang, X. Pan, F. Zhan, Y. Zhang, S. Wang, J. Qiu, Membrane-free hybrid capacitive deionization system based on redox reaction for high-efficiency NaCl removal, Environmental Science & Technology, 53 (2019) 6292-6301.
[67] S. Wang, G. Wang, X. Che, S. Wang, C. Li, D. Li, Y. Zhang, Q. Dong, J. Qiu, Enhancing the capacitive deionization performance of $NaMnO_2$ by interface engineering and redox-reaction, Environmental Science: Nano, 6 (2019) 2379-2388.
[68] W. Tang, P. Kovalsky, D. He, T.D. Waite, Fluoride and nitrate removal from brackish groundwaters by batch-mode capacitive deionization, Water Research, 84 (2015) 342-349.
[69] E.M. Remillard, A.N. Shocron, J. Rahill, M.E. Suss, C.D. Vecitis, A direct comparison of flow-by and flow-through capacitive deionization, Desalination, 444 (2018) 169-177.
[70] Y. Algurainy, D.F. Call, Asymmetrical removal of sodium and chloride in flow-through capacitive deionization, Water Research, 183 (2020) 116044.
[71] J.-B. Lee, K.-K. Park, H.-M. Eum, C.-W. Lee, Desalination of a thermal power plant wastewater by membrane capacitive deionization, Desalination, 196 (2006) 125-134.
[72] L. Wang, S. Lin, Theoretical framework for designing a desalination plant based on membrane capacitive deionization, Water Research, 158 (2019) 359-369.

[73] K. Tang, Y.-h. Kim, J. Chang, R.T. Mayes, J. Gabitto, S. Yiacoumi, C. Tsouris, Seawater desalination by over-potential membrane capacitive deionization: Opportunities and hurdles, Chemical Engineering Journal, 357 (2019) 103-111.
[74] P. Długołecki, A. van der Wal, Energy recovery in membrane capacitive deionization, Environmental Science & Technology, 47 (2013) 4904-4910.
[75] W. Tang, D. He, C. Zhang, P. Kovalsky, T.D. Waite, Comparison of Faradaic reactions in capacitive deionization (CDI) and membrane capacitive deionization (MCDI) water treatment processes, Water Research, 120 (2017) 229-237.
[76] M. Pasta, C.D. Wessells, Y. Cui, F. La Mantia, A desalination battery, Nano letters, 12 (2012) 839-843.
[77] A. Siekierka, B. Tomaszewska, M. Bryjak, Lithium capturing from geothermal water by hybrid capacitive deionization, Desalination, 436 (2018) 8-14.
[78] B.W. Byles, D.A. Cullen, K.L. More, E. Pomerantseva, Tunnel structured manganese oxide nanowires as redox active electrodes for hybrid capacitive deionization, Nano Energy, 44 (2018) 476-488.
[79] M. Torkamanzadeh, L. Wang, Y. Zhang, O. Budak, P. Srimuk, V. Presser, MXene/activated-carbon hybrid capacitive deionization for permselective ion removal at low and high salinity, ACS Applied Materials & Interfaces, 12 (2020) 26013-26025.
[80] J.W. Blair, G.W. Murphy, Electrochemical demineralization of water with porous electrodes of large surface area, Saline Water Conversion, 27 (1960) 206-223.
[81] A.M. Johnson, The electrosorb process for desalting water, U.S. Department of the Interior, Published in 1970.
[82] J.-B. Lee, K.-K. Park, H.-M. Eum, C.-W. Lee, Desalination of a thermal power plant wastewater by membrane capacitive deionization, Desalination, 196 (2006) 125-134.
[83] S.-i. Jeon, H.-r. Park, J.-g. Yeo, S. Yang, C.H. Cho, M.H. Han, D.K. Kim, Desalination via a new membrane capacitive deionization process utilizing flow-electrodes, Energy & Environmental Science, 6 (2013) 1471-1475.
[84] Z.-H. Huang, Z. Yang, F. Kang, M. Inagaki, Carbon electrodes for capacitive deionization, Journal of Materials Chemistry A, 5 (2017) 470-496.
[85] C. Kim, P. Srimuk, J. Lee, M. Aslan, V. Presser, Semi-continuous capacitive deionization using multi-channel flow stream and ion exchange membranes, Desalination, 425 (2018) 104-110.
[86] R. Chen, X. Liu, M. Wang, Y. Shu, M. Zhang, B. Liu, Z. Wang, A novel two-stage continuous capacitive deionization system with connected flow electrode and freestanding electrode, Chemical Engineering Journal, 491 (2024) 152133.
[87] J. Ma, D. He, W. Tang, P. Kovalsky, C. He, C. Zhang, T.D. Waite, Development of redox-active flow electrodes for high-performance capacitive deionization, Environmental Science & Technology, 50 (2016) 13495-13501.
[88] S.B. Rauer, S. Wang, N. Köller, D.J. Bell, Y. Zhang, X. Wang, C.J. Linnartz, M. Wessling, J. Linkhorst, PEDOT: PSS-CNT composite particles overcome contact resistances in slurry electrodes for flow-electrode capacitive deionization, Advanced Functional Materials, 33 (2023) 2303606.
[89] S. Ahualli, G.R. Iglesias, Á.V. Delgado, Principles and theoretical models of CDI: Experimental approaches, Interface Science and Technology, 24 (2018) 169-192.
[90] N.-L. Liu, S.-H. Sun, C.-H. Hou, Studying the electrosorption performance of activated carbon electrodes in batch-mode and single-pass capacitive deionization, Separation and Purification Technology, 215 (2019) 403-409.

[91] L. Zou, L. Li, H. Song, G. Morris, Using mesoporous carbon electrodes for brackish water desalination, Water Research, 42 (2008) 2340-2348.
[92] V.H. Le, L.T.N. Huynh, T.N. Tran, T.T.N. Ho, M.N. Hoang, T.H. Nguyen, Comparative desalination performance of activated carbon from coconut shell waste/carbon nanotubes composite in batch mode and single-pass mode, Journal of Applied Electrochemistry, 51 (2021) 1313-1322.
[93] Y. Jande, W.-S. Kim, Modeling the capacitive deionization batch mode operation for desalination, Journal of Industrial and Engineering Chemistry, 20 (2014) 3356-3360.
[94] S. Huo, X. Song, Y. Zhao, W. Ni, H. Wang, K. Li, Insight into the significant contribution of intrinsic carbon defects for the high-performance capacitive desalination of brackish water, Journal of Materials Chemistry A, 8 (2020) 19927-19937.
[95] X. He, W. Chen, Z. Jiang, Q. Wang, B. Li, X.-y. Li, L. Lin, Importance of the conductivity and specific surface area of electrode particles to the desalination performance and energy efficiency of flow-electrode capacitive deionization, Separation and Purification Technology, 304 (2023) 122308.
[96] S. Liu, P. Zhang, Y. Wang, M. He, W. Zhang, Z. Xu, K. Li, Uniformly dispersed Fe-N active centers on hierarchical carbon electrode for high-performance capacitive deionization: plentiful adsorption sites and conductive electron transfer, ACS Sustainable Chemistry & Engineering, 11 (2023) 8847-8857.
[97] Z. Li, B. Song, Z. Wu, Z. Lin, Y. Yao, K.-S. Moon, C.P. Wong, 3D porous graphene with ultrahigh surface area for microscale capacitive deionization, Nano Energy, 11 (2015) 711-718.
[98] X. Gong, S. Zhang, W. Luo, N. Guo, L. Wang, D. Jia, Z. Zhao, S. Feng, L. Jia, Enabling a large accessible surface area of a pore-designed hydrophilic carbon nanofiber fabric for ultrahigh capacitive deionization, ACS Applied Materials & Interfaces, 12 (2020) 49586-49595.
[99] M. Son, N. Yoon, K. Jeong, A. Abass, B.E. Logan, K.H. Cho, Deep learning for pH prediction in water desalination using membrane capacitive deionization, Desalination, 516 (2021) 115233.
[100] M.A. Luciano, H. Ribeiro, G.E. Bruch, G.G. Silva, Efficiency of capacitive deionization using carbon materials based electrodes for water desalination, Journal of Electroanalytical Chemistry, 859 (2020) 113840.
[101] C. Kim, P. Srimuk, J. Lee, S. Fleischmann, M. Aslan, V. Presser, Influence of pore structure and cell voltage of activated carbon cloth as a versatile electrode material for capacitive deionization, Carbon, 122 (2017) 329-335.
[102] S. Porada, F. Schipper, M. Aslan, M. Antonietti, V. Presser, T.P. Fellinger, Capacitive deionization using biomass‐based microporous salt‐templated heteroatom‐doped carbons, ChemSusChem, 8 (2015) 1867-1874.
[103] D.W. Wang, F. Li, M. Liu, G.Q. Lu, H.M. Cheng, 3D aperiodic hierarchical porous graphitic carbon material for high‐rate electrochemical capacitive energy storage, Angewandte Chemie International Edition, 47 (2008) 373-376.
[104] C.-L. Yeh, H.-C. Hsi, K.-C. Li, C.-H. Hou, Improved performance in capacitive deionization of activated carbon electrodes with a tunable mesopore and micropore ratio, Desalination, 367 (2015) 60-68.
[105] S. Ntakirutimana, W. Tan, M.A. Anderson, Y. Wang, Editors' Choice-Review-Activated carbon electrode design: Engineering tradeoff with respect to capacitive deionization performance, Journal of The Electrochemical Society, 167 (2020) 143501.
[106] B. Jia, W. Zhang, Preparation and application of electrodes in capacitive deionization (CDI): a state-of-art review, Nanoscale Research Letters, 11 (2016) 64.

[107] Y. Lian, H. Chen, Z. Cao, J. Sun, J. Zhao, H. Zhang, Interface functional groups protected by confinement effect for flexible supercapacitor and capacitive deionization, Desalination, 532 (2022) 115758.
[108] Z. Wang, M. Gao, J. Peng, L. Miao, W. Chen, T. Ao, Nanoarchitectonics of heteroatom-doped hierarchical porous carbon derived from carboxymethyl cellulose carbon aerogel and metal-organic framework for capacitive deionization, International Journal of Biological Macromolecules, 241 (2023) 124596.
[109] L. Zou, G. Morris, D. Qi, Using activated carbon electrode in electrosorptive deionisation of brackish water, Desalination, 225 (2008) 329-340.
[110] M. Seredych, E. Rodríguez-Castellón, M.J. Biggs, W. Skinner, T.J. Bandosz, Effect of visible light and electrode wetting on the capacitive performance of S- and N-doped nanoporous carbons: Importance of surface chemistry, Carbon, 78 (2014) 540-558.
[111] X. Xu, A.E. Allah, C. Wang, H. Tan, A.A. Farghali, M.H. Khedr, V. Malgras, T. Yang, Y. Yamauchi, Capacitive deionization using nitrogen-doped mesostructured carbons for highly efficient brackish water desalination, Chemical Engineering Journal, 362 (2019) 887-896.
[112] M. Aslan, M. Zeiger, N. Jäckel, I. Grobelsek, D. Weingarth, V. Presser, Improved capacitive deionization performance of mixed hydrophobic/hydrophilic activated carbon electrodes, Journal of Physics: Condensed Matter, 28 (2016) 114003.
[113] I. Villar, D.J. Suarez-De la Calle, Z. González, M. Granda, C. Blanco, R. Menéndez, R. Santamaría, Carbon materials as electrodes for electrosorption of NaCl in aqueous solutions, Adsorption, 17 (2011) 467-471.
[114] J. Chmiola, G. Yushin, Y. Gogotsi, C. Portet, P. Simon, P.-L. Taberna, Anomalous increase in carbon capacitance at pore sizes less than 1 nanometer, Science, 313 (2006) 1760-1763.
[115] S. Kondrat, C.R. Pérez, V. Presser, Y. Gogotsi, A.A. Kornyshev, Effect of pore size and its dispersity on the energy storage in nanoporous supercapacitors, Energy & Environmental Science, 5 (2012) 6474-6479.
[116] S. Porada, L. Weinstein, R. Dash, A. Van Der Wal, M. Bryjak, Y. Gogotsi, P. Biesheuvel, Water desalination using capacitive deionization with microporous carbon electrodes, ACS Applied Materials & Interfaces, 4 (2012) 1194-1199.
[117] Z. Peng, D. Zhang, L. Shi, T. Yan, High performance ordered mesoporous carbon/carbon nanotube composite electrodes for capacitive deionization, Journal of Materials Chemistry, 22 (2012) 6603-6612.
[118] X. Wen, D. Zhang, L. Shi, T. Yan, H. Wang, J. Zhang, Three-dimensional hierarchical porous carbon with a bimodal pore arrangement for capacitive deionization, Journal of Materials Chemistry, 22 (2012) 23835-23844.
[119] M. Shi, X. Hong, C. Liu, H. Qiang, F. Wang, M. Xia, Green double organic salt activation strategy for one-step synthesis of N-doped 3D hierarchical porous carbon for capacitive deionization, Chemical Engineering Journal, 453 (2023) 139764.
[120] Z. Miao, N. Che, W. Chai, M. Zhang, F. Wang, Hierarchical porous carbons derived from porous biomass for high-performance capacitive deionization, The Journal of Physical Chemistry C, 128 (2024) 4038-4047.
[121] H. Wang, D. Wei, H. Gang, Y. He, H. Deng, L. Hou, Y. Shi, S. Wang, W. Yang, L. Zhang, Hierarchical porous carbon from the synergistic “pore-on-pore” strategy for efficient capacitive deionization, ACS Sustainable Chemistry & Engineering, 8 (2019) 1129-1136.
[122] H. Gang, H. Deng, L. Yan, B. Wu, S.I. Alhassan, Y. Cao, D. Wei, H. Wang, Surface redox pseudocapacitance boosting Fe/Fe_3C nanoparticles-encapsulated N-doped graphene-like carbon for high-performance capacitive deionization, Journal of Colloid and Interface Science, 638 (2023) 252-262.

[123] Z. Zhao, F. Wang, B. Li, Z. Chen, H. Zhou, X. Wen, M. Ye, Rational fabrication strategies of freestanding/binder-free electrodes for efficient capacitive deionization, Materials Advances, 4 (2023) 2247-2268.
[124] M.-H. Ryou, J. Kim, I. Lee, S. Kim, Y.K. Jeong, S. Hong, J.H. Ryu, T.-S. Kim, J.-K. Park, H. Lee, Mussel-inspired adhesive binders for high-performance silicon nanoparticle anodes in lithium-ion batteries, Advanced Materials (Deerfield Beach, Fla.), 25 (2012) 1571-1576.
[125] O. Gerard, A. Numan, S. Krishnan, M. Khalid, R. Subramaniam, R. Kasi, A review on the recent advances in binder-free electrodes for electrochemical energy storage application, Journal of Energy Storage, 50 (2022) 104283.
[126] A. Tolosa, S. Fleischmann, I. Grobelsek, A. Quade, E. Lim, V. Presser, Binder‐free hybrid titanium-niobium oxide/carbon nanofiber mats for lithium-ion battery electrodes, ChemSusChem, 11 (2018) 159-170.
[127] J.C. Farmer, D.V. Fix, G.V. Mack, R.W. Pekala, J.F. Poco, Capacitive deionization of NaCl and $NaNO_3$ solutions with carbon aerogel electrodes, Journal of the Electrochemical Society, 143 (1996) 159.
[128] S. Dahiya, B.K. Mishra, Enhancing understandability and performance of flow electrode capacitive deionisation by optimizing configurational and operational parameters: A review on recent progress, Separation and Purification Technology, 240 (2020) 116660.
[129] K. Tang, S. Yiacoumi, Y. Li, J. Gabitto, C. Tsouris, Optimal conditions for efficient flow-electrode capacitive deionization, Separation and Purification Technology, 240 (2020) 116626.
[130] N. Jäckel, D. Weingarth, A. Schreiber, B. Krüner, M. Zeiger, A. Tolosa, M. Aslan, V. Presser, Performance evaluation of conductive additives for activated carbon supercapacitors in organic electrolyte, Electrochimica Acta, 191 (2016) 284-298.
[131] R. Zhao, O. Satpradit, H.H.M. Rijnaarts, P.M. Biesheuvel, A. van der Wal, Optimization of salt adsorption rate in membrane capacitive deionization, Water Research, 47 (2013) 1941-1952.
[132] T. Kim, J. Yoon, CDI ragone plot as a functional tool to evaluate desalination performance in capacitive deionization, RSC Advances, 5 (2015) 1456-1461.
[133] T. Christen, M.W. Carlen, Theory of Ragone plots, Journal of Power Sources, 91 (2000) 210-216.
[134] L. Wang, J. Dykstra, S. Lin, Energy efficiency of capacitive deionization, Environmental Science & Technology, 53 (2019) 3366-3378.
[135] S.F. Evans, M.R. Ivancevic, D.J. Wilson, Z.D. Hood, S.P. Adhikari, A.K. Naskar, C. Tsouris, M.P. Paranthaman, Carbon polyaniline capacitive deionization electrodes with stable cycle life, Desalination, 464 (2019) 25-32.
[136] I. Cohen, E. Avraham, Y. Bouhadana, A. Soffer, D. Aurbach, Long term stability of capacitive de-ionization processes for water desalination: The challenge of positive electrodes corrosion, Electrochimica Acta, 106 (2013) 91-100.
[137] F. Chen, Y. Huang, L. Guo, L. Sun, Y. Wang, H.Y. Yang, Dual-ions electrochemical deionization: a desalination generator, Energy & Environmental Science, 10 (2017) 2081-2089.
[138] T. Kim, J. Yu, C. Kim, J. Yoon, Hydrogen peroxide generation in flow-mode capacitive deionization, Journal of Electroanalytical Chemistry, 776 (2016) 101-104.
[139] P. Biesheuvel, A. Van der Wal, Membrane capacitive deionization, Journal of Membrane Science, 346 (2010) 256-262.
[140] J. Lee, P. Srimuk, K. Aristizabal, C. Kim, S. Choudhury, Y.C. Nah, F. Mücklich, V. Presser, Pseudocapacitive desalination of brackish water and seawater with vanadium‐pentoxide‐decorated multiwalled carbon nanotubes, ChemSusChem, 10 (2017) 3611-3623.

[141] L. Wang, Y. Zhang, K. Moh, V. Presser, From capacitive deionization to desalination batteries and desalination fuel cells, Current Opinion in Electrochemistry, 29 (2021) 100758.
[142] S.-J. Seo, H. Jeon, J.K. Lee, G.-Y. Kim, D. Park, H. Nojima, J. Lee, S.-H. Moon, Investigation on removal of hardness ions by capacitive deionization (CDI) for water softening applications, Water Research, 44 (2010) 2267-2275.
[143] C. He, J. Ma, C. Zhang, J. Song, T.D. Waite, Short-circuited closed-cycle operation of flow-electrode CDI for brackish water softening, Environmental Science & Technology, 52 (2018) 9350-9360.
[144] L. Wang, S. Lin, Mechanism of selective ion removal in membrane capacitive deionization for water softening, Environmental Science & Technology, 53 (2019) 5797-5804.
[145] R. Chen, T. Sheehan, J.L. Ng, M. Brucks, X. Su, Capacitive deionization and electrosorption for heavy metal removal, Environmental Science: Water Research & Technology, 6 (2020) 258-282.
[146] Z. Huang, L. Lu, Z. Cai, Z.J. Ren, Individual and competitive removal of heavy metals using capacitive deionization, Journal of Hazardous Materials, 302 (2016) 323-331.
[147] Q. Dong, X. Guo, X. Huang, L. Liu, R. Tallon, B. Taylor, J. Chen, Selective removal of lead ions through capacitive deionization: Role of ion-exchange membrane, Chemical Engineering Journal, 361 (2019) 1535-1542.
[148] Y. He, A. Gong, A. Osabutey, T. Gao, N. Haleem, X. Yang, P. Liang, Emerging electro-driven technologies for phosphorus enrichment and recovery from wastewater: A review, Water Research, 246 (2023) 120699.
[149] Y. Bian, X. Chen, L. Lu, P. Liang, Z.J. Ren, Concurrent nitrogen and phosphorus recovery using flow-electrode capacitive deionization, ACS Sustainable Chemistry & Engineering, 7 (2019) 7844-7850.
[150] O. Pastushok, F. Zhao, D.L. Ramasamy, M. Sillanpää, Nitrate removal and recovery by capacitive deionization (CDI), Chemical Engineering Journal, 375 (2019) 121943.
[151] M. Askari, S. Rajabzadeh, L. Tijing, H.K. Shon, Advances in capacitive deionization (CDI) systems for nutrient recovery from wastewater: Paving the path towards a circular economy, Desalination, 583 (2024) 117695.
[152] J. Si, C. Xue, S. Li, L. Yang, W. Li, J. Yang, J. Lan, N. Sun, Selective membrane capacitive deionization for superior lithium recovery, Desalination, 572 (2024) 117154.
[153] J. Choi, P. Dorji, H.K. Shon, S. Hong, Applications of capacitive deionization: Desalination, softening, selective removal, and energy efficiency, Desalination, 449 (2019) 118-130.
[154] M.M. AL-Rajabi, F.A. Abumadi, T. Laoui, M.A. Atieh, K.A. Khalil, Capacitive deionization for water desalination: Cost analysis, recent advances, and process optimization, Journal of Water Process Engineering, 58 (2024) 104816.
[155] E. Liu, L.Y. Lee, S.L. Ong, H.Y. Ng, Treatment of industrial brine using capacitive deionization (CDI) towards zero liquid discharge - challenges and optimization, Water Research, 183 (2020) 116059.
[156] Y. Xu, H. Zhou, G. Wang, Y. Zhang, H. Zhang, H. Zhao, Selective pseudocapacitive deionization of calcium ions in copper hexacyanoferrate, ACS Applied Materials & Interfaces, 12 (2020) 41437-41445.
[157] H. Yoon, J. Lee, S.-R. Kim, J. Kang, S. Kim, C. Kim, J. Yoon, Capacitive deionization with Ca-alginate coated-carbon electrode for hardness control, Desalination, 392 (2016) 46-53.
[158] J.J. Lado, R.E. Pérez-Roa, J.J. Wouters, M.I. Tejedor-Tejedor, M.A. Anderson, Evaluation of operational parameters for a capacitive deionization reactor employing asymmetric electrodes, Separation and Purification Technology, 133 (2014) 236-245.

[159] J.J. Wouters, M.I. Tejedor-Tejedor, J.J. Lado, R. Perez-Roa, M.A. Anderson, Influence of metal oxide coatings, carbon materials and potentials on ion removal in capacitive deionization, Journal of The Electrochemical Society, 165 (2018) E148.
[160] J.H. Duffus, " Heavy metals" a meaningless term?, Pure and Applied Chemistry, 74 (2002) 793-807.
[161] F. Fu, Q. Wang, Removal of heavy metal ions from wastewaters: a review, Journal of Environmental Management, 92 (2011) 407-418.
[162] Y. Oren, Capacitive deionization (CDI) for desalination and water treatment - past, present and future (a review), Desalination, 228 (2008) 10-29.
[163] P. Rana, N. Mohan, C. Rajagopal, Electrochemical removal of chromium from wastewater by using carbon aerogel electrodes, Water Research, 38 (2004) 2811-2820.
[164] S.D. Datar, R.S. Mane, N. Kumar, V. Sawant, S. Malpure, N. Jha, Effective removal of heavy metal-lead and inorganic salts by microporous carbon derived from Zeolitic Imidazolate Framework-67 electrode using capacitive deionization, Desalination, 558 (2023) 116619.
[165] L. Yang, Z. Shi, W. Yang, Enhanced capacitive deionization of lead ions using air-plasma treated carbon nanotube electrode, Surface and Coatings Technology, 251 (2014) 122-127.
[166] C.-C. Huang, Y.-J. Su, Removal of copper ions from wastewater by adsorption/electrosorption on modified activated carbon cloths, Journal of Hazardous Materials, 175 (2010) 477-483.
[167] S.-Y. Huang, C.-S. Fan, C.-H. Hou, Electro-enhanced removal of copper ions from aqueous solutions by capacitive deionization, Journal of Hazardous Materials, 278 (2014) 8-15.
[168] Z. Song, L. Li, Y. Chen, X. Duan, N. Ren, Efficient removal and recovery of Cd^{2+} from aqueous solutions by capacitive deionization (CDI) method using biochars, Journal of Materials Science & Technology, 148 (2023) 10-18.
[169] H. Li, L. Zou, L. Pan, Z. Sun, Using graphene nano-flakes as electrodes to remove ferric ions by capacitive deionization, Separation and Purification Technology, 75 (2010) 8-14.
[170] C.-S. Fan, S.-C. Tseng, K.-C. Li, C.-H. Hou, Electro-removal of arsenic (III) and arsenic (V) from aqueous solutions by capacitive deionization, Journal of Hazardous Materials, 312 (2016) 208-215.
[171] T.N. Tan, S. Babel, T. Bora, P. Sreearunothai, K. Laohhasurayotin, Preparation of heterogeneous cation exchange membrane and its contributions in enhancing the removal of Ni^{2+} by capacitive deionization system, Chemosphere, 350 (2024) 141115.
[172] D. Marmanis, K. Dermentzis, A. Christoforidis, K. Ouzounis, Cadmium removal from aqueous solution by capacitive deionization with nano-porous carbon electrodes, Journal of Engineering Science and Technology Review, 6 (2013) 165-166.
[173] J. Li, X. Wang, H. Wang, S. Wang, T. Hayat, A. Alsaedi, X. Wang, Functionalization of biomass carbonaceous aerogels and their application as electrode materials for electro-enhanced recovery of metal ions, Environmental Science: Nano, 4 (2017) 1114-1123.
[174] M. Mao, T. Yan, G. Chen, J. Zhang, L. Shi, D. Zhang, Selective capacitive removal of Pb^{2+} from wastewater over redox-active electrodes, Environmental Science & Technology, 55 (2020) 730-737.
[175] L. Bautista-Patacsil, J.P.L. Lazarte, R. Dipasupil, G. Pasco, R. Eusebio, A. Orbecido, R. Doong, Deionization utilizing reduced graphene oxide-titanium dioxide nanotubes composite for the removal of Pb^{2+} and Cu^{2+}, Journal of Environmental Chemical Engineering, 8 (2020) 103063.
[176] D.J. Conley, H.W. Paerl, R.W. Howarth, D.F. Boesch, S.P. Seitzinger, K.E. Havens, C. Lancelot, G.E. Likens, Controlling eutrophication: nitrogen and phosphorus, Science, 323 (2009) 1014-1015.

[177] Y.-J. Kim, J.-H. Choi, Selective removal of nitrate ion using a novel composite carbon electrode in capacitive deionization, Water Research, 46 (2012) 6033-6039.
[178] Q. Lu, P. Liu, T. Zhou, R. Huang, K. Zhang, L. Hu, R. Liu, Z. Ren, J. Wang, X. Wang, Recent progress on electro-sorption technology for lithium recovery from aqueous sources, Nano Research, 17 (2024) 2563-2573.
[179] C. Liu, J. Lin, H. Cao, Y. Zhang, Z. Sun, Recycling of spent lithium-ion batteries in view of lithium recovery: A critical review, Journal of Cleaner Production, 228 (2019) 801-813.
[180] V. Flexer, C.F. Baspineiro, C.I. Galli, Lithium recovery from brines: A vital raw material for green energies with a potential environmental impact in its mining and processing, Science of the Total Environment, 639 (2018) 1188-1204.
[181] W. Shi, X. Liu, C. Ye, X. Cao, C. Gao, J. Shen, Efficient lithium extraction by membrane capacitive deionization incorporated with monovalent selective cation exchange membrane, Separation and Purification Technology, 210 (2019) 885-890.
[182] D.-H. Lee, T. Ryu, J. Shin, J.C. Ryu, K.-S. Chung, Y.H. Kim, Selective lithium recovery from aqueous solution using a modified membrane capacitive deionization system, Hydrometallurgy, 173 (2017) 283-288.
[183] Y. Ha, H.B. Jung, H. Lim, P.S. Jo, H. Yoon, C.-Y. Yoo, T.K. Pham, W. Ahn, Y. Cho, Continuous lithium extraction from aqueous solution using flow-electrode capacitive deionization, Energies, 12 (2019) 2913.
[184] K.B. Hatzell, M. Boota, Y. Gogotsi, Materials for suspension (semi-solid) electrodes for energy and water technologies, Chemical Society Reviews, 44 (2015) 8664-8687.
[185] J.W. Campos, M. Beidaghi, K.B. Hatzell, C.R. Dennison, B. Musci, V. Presser, E.C. Kumbur, Y. Gogotsi, Investigation of carbon materials for use as a flowable electrode in electrochemical flow capacitors, Electrochimica Acta, 98 (2013) 123-130.
[186] M. Boota, K. Hatzell, M. Alhabeb, E. Kumbur, Y. Gogotsi, Graphene-containing flowable electrodes for capacitive energy storage, Carbon, 92 (2015) 142-149.
[187] Y. Li, T. Yong, J. Qi, J. Wu, R. Lin, Z. Chen, J. Li, Enhancing the electronic and ionic transport of flow-electrode capacitive deionization by hollow mesoporous carbon nanospheres, Desalination, 550 (2023) 116381.
[188] P. Ren, B. Wang, J.G. de Andrade Ruthes, M. Torkamanzadeh, V. Presser, Cation selectivity during flow electrode capacitive deionization, Desalination, 592 (2024) 118161.
[189] A. Rommerskirchen, M. Alders, F. Wiesner, C.J. Linnartz, A. Kalde, M. Wessling, Process model for high salinity flow-electrode capacitive deionization processes with ion-exchange membranes, Journal of Membrane Science, 616 (2020) 118614.
[190] K.B. Hatzell, E. Iwama, A. Ferris, B. Daffos, K. Urita, T. Tzedakis, F. Chauvet, P.-L. Taberna, Y. Gogotsi, P. Simon, Capacitive deionization concept based on suspension electrodes without ion exchange membranes, Electrochemistry Communications, 43 (2014) 18-21.
[191] F. Yu, Z. Yang, Y. Cheng, S. Xing, Y. Wang, J. Ma, A comprehensive review on flow-electrode capacitive deionization: Design, active material and environmental application, Separation and Purification Technology, 281 (2022) 119870.
[192] N. Minh Phuoc, N. Anh Thu Tran, T. Minh Khoi, H. Bin Jung, W. Ahn, E. Jung, C.-Y. Yoo, H.S. Kang, Y. Cho, ZIF-67 metal-organic frameworks and CNTs-derived nanoporous carbon structures as novel electrodes for flow-electrode capacitive deionization, Separation and Purification Technology, 277 (2021) 119466.
[193] Y. Sun, Y. Cheng, F. Yu, J. Ma, Enhanced salt removal performance using graphene-modified sodium vanadium fluorophosphate in flow electrode capacitive deionization, ACS Applied Materials & Interfaces, 13 (2021) 53850-53858.

[194] J. Cao, Y. Wang, L. Wang, F. Yu, J. Ma, $Na_3V_2(PO_4)_3$@C as Faradaic electrodes in capacitive deionization for high-performance desalination, Nano Letters, 19 (2019) 823-828.
[195] H. Chand, Z. Liu, Q. Wei, M.S. Gaballah, W. Li, O. Osmolovskaya, A. Podurets, M. Voznesenskiy, N. Pismenskaya, L.P. Padhye, C. Zhang, Performance and mechanism of chromium removal using flow electrode capacitive deionization (FCDI): Validation and optimization, Separation and Purification Technology, 340 (2024) 126696.
[196] F. Yang, Y. He, L. Rosentsvit, M.E. Suss, X. Zhang, T. Gao, P. Liang, Flow-electrode capacitive deionization: A review and new perspectives, Water Research, 200 (2021) 117222.
[197] B. Kastening, Properties of slurry electrodes from activated carbon powder, Berichte der Bunsengesellschaft für Physikalische Chemie, 92 (1988) 1399-1402.
[198] V. Presser, C.R. Dennison, J. Campos, K.W. Knehr, E.C. Kumbur, Y. Gogotsi, The electrochemical flow capacitor: a new concept for rapid energy storage and recovery, Advanced Energy Materials, 2 (2012) 895-902.
[199] T.K. Dongguk Kim, Chulhee Cho, Jongsoo Park, Goyeon Choo, and Jeonggu Yeo, Water Treatment Device using Flow-electrode device, 2013.
[200] Y.Y. Yongwoo Kim, and Jaean Lee, Flowable Electrode and the Electrode Structure, 2015.
[201] Y. Xu, F. Duan, Y. Li, H. Cao, J. Chang, H. Pang, J. Chen, Enhanced desalination performance in asymmetric flow electrode capacitive deionization with nickel hexacyanoferrate and activated carbon electrodes, Desalination, 514 (2021) 115172.
[202] Z. Tan, W. Song, X. Mao, L. Wang, J. Xu, H. Zou, G. Liu, Efficient capacitive deionization with hierarchical porous carbon flow electrodes, Desalination, 591 (2024) 118051.
[203] M. Shi, G. Ji, X. Cui, C. Liu, X. Hong, Z. Ding, H. Qiang, F. Wang, M. Xia, Simple control of carbon mass loading in capacitive deionization for efficient deionized water production, Separation and Purification Technology, 301 (2022) 121962.
[204] T.T.A. Lwin, X. Chen, M. Zaw, S.K.K. Aung, N.W. Lwin, T.Z. Oo, A.Q. Zarifzoda, K.S. Hui, F. Chen, Enhanced desalination performance of flow capacitive deionization with the addition of conductive polymer in redox couples and activated carbon, Carbon, 231 (2025) 119703.
[205] H.-r. Park, J. Choi, S. Yang, S.J. Kwak, S.-i. Jeon, M.H. Han, D.K. Kim, Surface-modified spherical activated carbon for high carbon loading and its desalting performance in flow-electrode capacitive deionization, RSC Advances, 6 (2016) 69720-69727.
[206] K.B. Hatzell, M.C. Hatzell, K.M. Cook, M. Boota, G.M. Housel, A. McBride, E.C. Kumbur, Y. Gogotsi, Effect of Oxidation of Carbon Material on Suspension Electrodes for Flow Electrode Capacitive Deionization, Environmental Science & Technology, 49 (2015) 3040-3047.
[207] A. Carmona-Orbezo, R.A.W. Dryfe, Understanding the performance of flow-electrodes for capacitive deionization through hydrodynamic voltammetry, Chemical Engineering Journal, 406 (2021) 126826.
[208] S.-i. Jeon, J.-g. Yeo, S. Yang, J. Choi, D.K. Kim, Ion storage and energy recovery of a flow-electrode capacitive deionization process, Journal of Materials Chemistry A, 2 (2014) 6378-6383.
[209] H. Lim, Y. Ha, H.B. Jung, P.S. Jo, H. Yoon, D. Quyen, N. Cho, C.-Y. Yoo, Y. Cho, Energy storage and generation through desalination using flow-electrodes capacitive deionization, Journal of Industrial and Engineering Chemistry, 81 (2020) 317-322.
[210] G. Folaranmi, M. Tauk, M. Bechelany, P. Sistat, M. Cretin, F. Zaviska, Investigation of fine activated carbon as a viable flow electrode in capacitive deionization, Desalination, 525 (2022) 115500.
[211] Q. Wei, L. Tang, K. Ramalingam, M. Liang, J. Ma, Y. Shi, K.N. Hui, K. San Hui, F. Chen, Redox-catalysis flow electrode desalination in an organic solvent, Journal of Materials Chemistry A, 9 (2021) 22254-22261.

[212] C. Zhang, J. Ma, L. Wu, J. Sun, L. Wang, T. Li, T.D. Waite, Flow electrode capacitive deionization (FCDI): recent developments, environmental applications, and future perspectives, Environmental Science & Technology, 55 (2021) 4243-4267.
[213] X. Zhang, J. Zhou, H. Zhou, H. Zhang, H. Zhao, Enhanced desalination performance by a novel archimedes spiral flow channel for flow-electrode capacitive deionization, ACS ES&T Engineering, 2 (2022) 1250-1259.
[214] H. Saif, T. Gebregeorgis, J. Crespo, S. Pawlowski, The influence of flow electrode channel design on flow capacitive deionization performance: Experimental and CFD modelling insights, Desalination, 578 (2024) 117452.
[215] K. Singh, S. Porada, H. De Gier, P. Biesheuvel, L. De Smet, Timeline on the application of intercalation materials in capacitive deionization, Desalination, 455 (2019) 115-134.
[216] M. Seredych, D. Hulicova-Jurcakova, G.Q. Lu, T.J. Bandosz, Surface functional groups of carbons and the effects of their chemical character, density and accessibility to ions on electrochemical performance, Carbon, 46 (2008) 1475-1488.
[217] C. Dennison, M. Beidaghi, K. Hatzell, J. Campos, Y. Gogotsi, E. Kumbur, Effects of flow cell design on charge percolation and storage in the carbon slurry electrodes of electrochemical flow capacitors, Journal of Power Sources, 247 (2014) 489-496.
[218] Y. Cai, X. Zhao, Y. Wang, D. Ma, S. Xu, Enhanced desalination performance utilizing sulfonated carbon nanotube in the flow-electrode capacitive deionization process, Separation and Purification Technology, 237 (2020) 116381.
[219] D. Li, X.-A. Ning, C. Yang, X. Chen, Y. Wang, Rich heteroatom doping magnetic carbon electrode for flow-capacitive deionization with enhanced salt removal ability, Desalination, 482 (2020) 114374.
[220] X. Xu, M. Wang, Y. Liu, T. Lu, L. Pan, Ultrahigh desalinization performance of asymmetric flow-electrode capacitive deionization device with an improved operation voltage of 1.8 V, ACS Sustainable Chemistry & Engineering, 5 (2017) 189-195.
[221] J. Chang, F. Duan, H. Cao, K. Tang, C. Su, Y. Li, Superiority of a novel flow-electrode capacitive deionization (FCDI) based on a battery material at high applied voltage, Desalination, 468 (2019) 114080.
[222] T. Kim, C.A. Gorski, B.E. Logan, Low energy desalination using battery electrode deionization, Environmental Science & Technology Letters, 4 (2017) 444-449.
[223] Y. Dong, W. Xing, K. Luo, J. Zhang, J. Yu, W. Jin, J. Wang, W. Tang, Effective and continuous removal of Cr (VI) from brackish wastewater by flow-electrode capacitive deionization (FCDI), Journal of Cleaner Production, 326 (2021) 129417.
[224] Y.-U. Shin, J. Lim, C. Boo, S. Hong, Improving the feasibility and applicability of flow-electrode capacitive deionization (FCDI): Review of process optimization and energy efficiency, Desalination, 502 (2021) 114930.
[225] B. Akuzum, P. Singh, D.A. Eichfeld, L. Agartan, S. Uzun, Y. Gogotsi, E.C. Kumbur, Percolation characteristics of conductive additives for capacitive flowable (semi-solid) electrodes, ACS Applied Materials & Interfaces, 12 (2020) 5866-5875.
[226] P. Ren, M. Torkamanzadeh, X. Zhang, M. Twardoch, C. Kim, V. Presser, Conductive carbon additives: Friend or foe of capacitive deionization with activated carbon?, Carbon, 213 (2023) 118191.
[227] P. Liang, X. Sun, Y. Bian, H. Zhang, X. Yang, Y. Jiang, P. Liu, X. Huang, Optimized desalination performance of high voltage flow-electrode capacitive deionization by adding carbon black in flow-electrode, Desalination, 420 (2017) 63-69.

[228] Y. Cho, C.-Y. Yoo, S.W. Lee, H. Yoon, K.S. Lee, S. Yang, D.K. Kim, Flow-electrode capacitive deionization with highly enhanced salt removal performance utilizing high-aspect ratio functionalized carbon nanotubes, Water Research, 151 (2019) 252-259.
[229] G. Hwang, A. Gomez-Flores, S.A. Bradford, S. Choi, E. Jo, S.B. Kim, M. Tong, H. Kim, Analysis of stability behavior of carbon black nanoparticles in ecotoxicological media: Hydrophobic and steric effects, Colloids and Surfaces A: Physicochemical and Engineering Aspects, 554 (2018) 306-316.
[230] N. Song, C.J. Gagliardi, R.A. Binstead, M.-T. Zhang, H. Thorp, T.J. Meyer, Role of proton-coupled electron transfer in the redox interconversion between benzoquinone and hydroquinone, Journal of the American Chemical Society, 134 (2012) 18538-18541.
[231] S.-K. Park, J. Shim, J.H. Yang, C.-S. Jin, B.S. Lee, Y.-S. Lee, K.-H. Shin, J.-D. Jeon, The influence of compressed carbon felt electrodes on the performance of a vanadium redox flow battery, Electrochimica Acta, 116 (2014) 447-452.
[232] S. Yang, J. Choi, J.-g. Yeo, S.-i. Jeon, H.-r. Park, D.K. Kim, Flow-electrode capacitive deionization using an aqueous electrolyte with a high salt concentration, Environmental Science & Technology, 50 (2016) 5892-5899.
[233] Q. Liu, B. Xie, D. Xiao, High efficient and continuous recovery of iodine in saline wastewater by flow-electrode capacitive deionization, Separation and Purification Technology, 296 (2022) 121419.
[234] S.-T. Myung, Y. Hitoshi, Y.-K. Sun, Electrochemical behavior and passivation of current collectors in lithium-ion batteries, Journal of Materials Chemistry, 21 (2011) 9891-9911.
[235] A. Heidarian, S.C. Cheung, G. Rosengarten, The effect of flow rate and concentration on the electrical conductivity of slurry electrodes using a coupled computational fluid dynamic and discrete element method (CFD-DEM) model, Electrochemistry Communications, 126 (2021) 107017.
[236] N. Köller, M. Perrey, L.K. Brückner, P. Schäfer, S. Werner, C.J. Linnartz, M. Wessling, Comparison of current collector architectures for flow-electrode capacitive deionization, Desalination, 582 (2024) 117595.
[237] S. Porstmann, T. Wannemacher, W.-G. Drossel, A comprehensive comparison of state-of-the-art manufacturing methods for fuel cell bipolar plates including anticipated future industry trends, Journal of Manufacturing Processes, 60 (2020) 366-383.
[238] L. Xu, Y. Mao, Y. Zong, S. Peng, X. Zhang, D. Wu, Membrane-current collector-based flow-electrode capacitive deionization system: A novel stack configuration for scale-up desalination, Environmental Science & Technology, 55 (2021) 13286-13296.
[239] X. Zhang, M. Pang, Y. Wei, F. Liu, H. Zhang, H. Zhou, Three-dimensional titanium mesh-based flow electrode capacitive deionization for salt separation and enrichment in high salinity water, Water Research, 251 (2024) 121147.
[240] R. Chen, X. Deng, C. Wang, J. Du, Z. Zhao, W. Shi, J. Liu, F. Cui, A newly designed graphite-polyaniline composite current collector to enhance the performance of flow electrode capacitive deionization, Chemical Engineering Journal, 435 (2022) 134845.
[241] Y. Li, J. Ma, M. Yu, J. Niu, J. Gu, M. Chen, P. Zhang, J. Zhang, C. Liu, Carbon felt (CF) acted as an “ionic capacitor” to enhance flow electrode capacitive deionization (FCDI) desalination performance, Desalination, 575 (2024) 117341.
[242] C.J. Linnartz, A. Rommerskirchen, J. Walker, J. Plankermann-Hajduk, N. Köller, M. Wessling, Membrane-electrode assemblies for flow-electrode capacitive deionization, Journal of Membrane Science, 605 (2020) 118095.

[243] H. Zhang, Y. Li, J. Han, Y. Sun, M. He, Z. Hao, T. Jiang, B. Wang, W. Wang, M. Liu, Influence of ion exchange membrane arrangement on dual-channel flow electrode capacitive deionization: Theoretical analysis and experimentations, Desalination, 548 (2023) 116288.
[244] J. Ma, J. Ma, C. Zhang, J. Song, R.N. Collins, T.D. Waite, Water recovery rate in short-circuited closed-cycle operation of flow-electrode capacitive deionization (FCDI), Environmental Science & Technology, 53 (2019) 13859-13867.
[245] T. Luo, S. Abdu, M. Wessling, Selectivity of ion exchange membranes: A review, Journal of Membrane Science, 555 (2018) 429-454.
[246] A. Hassanvand, K. Wei, S. Talebi, G.Q. Chen, S.E. Kentish, The role of ion exchange membranes in membrane capacitive deionisation, Membranes, 7 (2017) 54.
[247] K. Fang, F. Peng, E. San, K. Wang, The impact of concentration in electrolyte on ammonia removal in flow-electrode capacitive deionization system, Separation and Purification Technology, 255 (2021) 117337.
[248] S.J. Kim, S.H. Ko, K.H. Kang, J. Han, Direct seawater desalination by ion concentration polarization, Nature Nanotechnology, 5 (2010) 297-301.
[249] G.M. Geise, B.D. Freeman, D.R. Paul, Sodium chloride diffusion in sulfonated polymers for membrane applications, Journal of Membrane Science, 427 (2013) 186-196.
[250] C. Zhang, L. Wu, J. Ma, A.N. Pham, M. Wang, T.D. Waite, Integrated flow-electrode capacitive deionization and microfiltration system for continuous and energy-efficient brackish water desalination, Environmental Science & Technology, 53 (2019) 13364-13373.
[251] Y. Gendel, A.K.E. Rommerskirchen, O. David, M. Wessling, Batch mode and continuous desalination of water using flowing carbon deionization (FCDI) technology, Electrochemistry Communications, 46 (2014) 152-156.
[252] M. Liu, Z. Xue, H. Zhang, Y. Li, Dual-channel membrane capacitive deionization based on asymmetric ion adsorption for continuous water desalination, Electrochemistry Communications, 125 (2021) 106974.
[253] N.A.T. Tran, T.M. Khoi, N.M. Phuoc, H.B. Jung, Y. Cho, A review of recent advances in electrode materials and applications for flow-electrode desalination systems, Desalination, 541 (2022) 116037.
[254] J. Ma, L. Chen, F. Yu, Environmental applications and perspectives of flow electrode capacitive deionization (FCDI), Separation and Purification Technology, 335 (2023) 126095.
[255] S. Yang, H. Kim, S.-i. Jeon, J. Choi, J.-g. Yeo, H.-r. Park, J. Jin, D.K. Kim, Analysis of the desalting performance of flow-electrode capacitive deionization under short-circuited closed cycle operation, Desalination, 424 (2017) 110-121.
[256] K. Luo, T. Hu, W. Xing, G. Zeng, W. Tang, Polyaniline/activated carbon composite based flowing electrodes for highly efficient water desalination with single-cycle operational mode, Chemical Engineering Journal, 481 (2024) 148454.
[257] J. Ma, C. Zhang, F. Yang, X. Zhang, M.E. Suss, X. Huang, P. Liang, Carbon black flow electrode enhanced electrochemical desalination using single-cycle operation, Environmental Science & Technology, 54 (2019) 1177-1185.
[258] S.A. Hawks, A. Ramachandran, S. Porada, P.G. Campbell, M.E. Suss, P. Biesheuvel, J.G. Santiago, M. Stadermann, Performance metrics for the objective assessment of capacitive deionization systems, Water Research, 152 (2019) 126-137.
[259] A. Rommerskirchen, Y. Gendel, M. Wessling, Single module flow-electrode capacitive deionization for continuous water desalination, Electrochemistry Communications, 60 (2015) 34-37.

[260] H.J. Chung, J. Kim, D.I. Kim, G. Gwak, S. Hong, Feasibility study of reverse osmosis-flow capacitive deionization (RO-FCDI) for energy-efficient desalination using seawater as the flow-electrode aqueous electrolyte, Desalination, 479 (2020) 114326.
[261] C. Zhang, M. Wang, W. Xiao, J. Ma, J. Sun, H. Mo, T.D. Waite, Phosphate selective recovery by magnetic iron oxide impregnated carbon flow-electrode capacitive deionization (FCDI), Water Research, 189 (2021) 116653.
[262] S. Yang, S.-i. Jeon, H. Kim, J. Choi, J.-g. Yeo, H.-r. Park, D.K. Kim, Stack design and operation for scaling up the capacity of flow-electrode capacitive deionization technology, ACS Sustainable Chemistry & Engineering, 4 (2016) 4174-4180.
[263] Y. Cho, K.S. Lee, S. Yang, J. Choi, H.-r. Park, D.K. Kim, A novel three-dimensional desalination system utilizing honeycomb-shaped lattice structures for flow-electrode capacitive deionization, Energy & Environmental Science, 10 (2017) 1746-1750.
[264] J. Ma, J. Ma, C. Zhang, J. Song, W. Dong, T.D. Waite, Flow-electrode capacitive deionization (FCDI) scale-up using a membrane stack configuration, Water Research, 168 (2020) 115186.
[265] N. Köller, L. Mankertz, S. Finger, C.J. Linnartz, M. Wessling, Towards pilot scale flow-electrode capacitive deionization, Desalination, 572 (2024) 117096.
[266] D.L. Correll, The role of phosphorus in the eutrophication of receiving waters: a review, Journal of Environmental Quality, 27 (1998) 261-266.
[267] C. Zhang, X. Cheng, M. Wang, J. Ma, R. Collins, A. Kinsela, Y. Zhang, T.D. Waite, Phosphate recovery as vivianite using a flow-electrode capacitive desalination (FCDI) and fluidized bed crystallization (FBC) coupled system, Water Research, 194 (2021) 116939.
[268] J. Song, J. Ma, C. Zhang, C. He, T.D. Waite, Implication of non-electrostatic contribution to deionization in flow-electrode CDI: Case study of nitrate removal from contaminated source waters, Frontiers in Chemistry, 7 (2019) 146.
[269] F. Yu, X. Zhang, Z. Yang, P. Yang, L. Li, J. Wang, M. Shi, J. Ma, Carbon aerogel electrode for excellent dephosphorization via flow capacitive deionization, Desalination, 528 (2022) 115614.
[270] L. Lin, J. Hu, J. Liu, X. He, B. Li, X.-y. Li, Selective ammonium removal from synthetic wastewater by flow-electrode capacitive deionization using a novel $K_2Ti_2O_5$-activated carbon mixture electrode, Environmental Science & Technology, 54 (2020) 12723-12731.
[271] H. Geng, Y. Xu, L. Zheng, H. Gong, L. Dai, X. Dai, An overview of removing heavy metals from sewage sludge: Achievements and perspectives, Environmental Pollution, 266 (2020) 115375.
[272] W. Gong, Y. Yang, H. Chang, T. Wang, H. Liang, Evaluating the performance of flow-electrode capacitive deionization for cadmium removal from aqueous solution, Journal of Water Process Engineering, 46 (2022) 102595.
[273] J. Lim, Y.-U. Shin, S. Hong, Enhanced capacitive deionization using a biochar-integrated novel flow-electrode, Desalination, 528 (2022) 115636.
[274] J. Ma, Y. Zhang, R.N. Collins, S. Tsarev, N. Aoyagi, A.S. Kinsela, A.M. Jones, T.D. Waite, Flow-electrode CDI removes the uncharged Ca-UO_2-CO_3 ternary complex from brackish potable groundwater: Complex dissociation, transport, and sorption, Environmental Science & Technology, 53 (2019) 2739-2747.
[275] J.H. Luong, C. Tran, D. Ton-That, A paradox over electric vehicles, mining of lithium for car batteries, Energies, 15 (2022) 7997.
[276] A. Khalil, S. Mohammed, R. Hashaikeh, N. Hilal, Lithium recovery from brine: Recent developments and challenges, Desalination, 528 (2022) 115611.

[277] H. Saif, J. Crespo, S. Pawlowski, Lithium recovery from brines by lithium membrane flow capacitive deionization (Li-MFCDI) - A proof of concept, Journal of Membrane Science Letters, 3 (2023) 100059.
[278] N. Kim, J. Jeon, J. Elbert, C. Kim, X. Su, Redox-mediated electrochemical desalination for waste valorization in dairy production, Chemical Engineering Journal, 428 (2022) 131082.
[279] X. Hou, Q. Liang, X. Hu, Y. Zhou, Q. Ru, F. Chen, S. Hu, Coupling desalination and energy storage with redox flow electrodes, Nanoscale, 10 (2018) 12308-12314.
[280] J. Wang, J. Dai, Z. Jiang, B. Chu, F. Chen, Recent progress and prospect of flow-electrode electrochemical desalination system, Desalination, 504 (2021) 114964.
[281] D. Desai, E.S. Beh, S. Sahu, V. Vedharathinam, Q. van Overmeere, C.F. de Lannoy, A.P. Jose, A.R. Völkel, J.B. Rivest, Electrochemical desalination of seawater and hypersaline brines with coupled electricity storage, ACS Energy Letters, 3 (2018) 375-379.
[282] R. Wang, X. Duan, S. Wang, N.-q. Ren, S.-H. Ho, Production, properties, and catalytic applications of sludge derived biochar for environmental remediation, Water Research, 187 (2020) 116390.
[283] H. Kim, S. Kim, D. Ahn, C. Kim, Improved desalination via cell voltage extension and simultaneous energy recovery of redox flow desalination using organic supporting electrolyte, Separation and Purification Technology, 324 (2023) 124490.
[284] D. Lu, Z. Yao, L. Jiao, M. Waheed, Z. Sun, L. Zhang, Separation mechanism, selectivity enhancement strategies and advanced materials for mono-/multivalent ion-selective nanofiltration membrane, Advanced Membranes, 2 (2022) 100032.
[285] Q. Xiao, J. Ma, L. Xu, K. Zuo, H. Guo, C.Y. Tang, Membrane capacitive deionization (MCDI) for selective ion separation and recovery: Fundamentals, challenges, and opportunities, Journal of Membrane Science, 699 (2024) 122650.
[286] X. Sun, Z. Hao, X. Zhou, J. Chen, Y. Zhang, Advanced capacitive deionization for ion selective separation: Insights into mechanism over a functional classification, Chemosphere, 346 (2024) 140601.
[287] N. Han, R. Gao, H. Peng, Q. He, Z. Miao, K. Wan, Selective recovery of lithium ions from acidic medium based on capacitive deionization-enhanced imprinted polymers, Journal of Cleaner Production, 373 (2022) 133773.
[288] J. Gamaethiralalage, K. Singh, S. Sahin, J. Yoon, M. Elimelech, M. Suss, P. Liang, P. Biesheuvel, R.L. Zornitta, L. De Smet, Recent advances in ion selectivity with capacitive deionization, Energy & Environmental Science, 14 (2021) 1095-1120.
[289] X. Zhang, K. Zuo, X. Zhang, C. Zhang, P. Liang, Selective ion separation by capacitive deionization (CDI) based technologies: a state-of-the-art review, Environmental Science: Water Research & Technology, 6 (2020) 243-257.
[290] K. Zuo, L. Yuan, J. Wei, P. Liang, X. Huang, Competitive migration behaviors of multiple ions and their impacts on ion-exchange resin packed microbial desalination cell, Bioresource Technology, 146 (2013) 637-642.
[291] Y. Bian, X. Yang, P. Liang, Y. Jiang, C. Zhang, X. Huang, Enhanced desalination performance of membrane capacitive deionization cells by packing the flow chamber with granular activated carbon, Water Research, 85 (2015) 371-376.
[292] J. Choi, H. Lee, S. Hong, Capacitive deionization (CDI) integrated with monovalent cation selective membrane for producing divalent cation-rich solution, Desalination, 400 (2016) 38-46.
[293] J. Kim, A. Jain, K. Zuo, R. Verduzco, S. Walker, M. Elimelech, Z. Zhang, X. Zhang, Q. Li, Removal of calcium ions from water by selective electrosorption using target-ion specific nanocomposite electrode, Water Research, 160 (2019) 445-453.

[294] S.A. Hawks, M.R. Cerón, D.I. Oyarzun, T.A. Pham, C. Zhan, C.K. Loeb, D. Mew, A. Deinhart, B.C. Wood, J.G. Santiago, Using ultramicroporous carbon for the selective removal of nitrate with capacitive deionization, Environmental Science & Technology, 53 (2019) 10863-10870.
[295] S. Kim, H. Yoon, D. Shin, J. Lee, J. Yoon, Electrochemical selective ion separation in capacitive deionization with sodium manganese oxide, Journal of Colloid and Interface Science, 506 (2017) 644-648.
[296] Y. Zhang, J. Peng, G. Feng, V. Presser, Hydration shell energy barrier differences of sub-nanometer carbon pores enable ion sieving and selective ion removal, Chemical Engineering Journal, 419 (2021) 129438.
[297] Y. Zhang, P. Ren, L. Wang, E. Pameté, S. Husmann, V. Presser, Selectivity toward heavier monovalent cations of carbon ultramicropores used for capacitive deionization, Desalination, 542 (2022) 116053.
[298] L. Eliad, G. Salitra, A. Soffer, D. Aurbach, Ion sieving effects in the electrical double layer of porous carbon electrodes: estimating effective ion size in electrolytic solutions, The Journal of Physical Chemistry B, 105 (2001) 6880-6887.
[299] Y. Li, C. Zhang, Y. Jiang, T.-J. Wang, H. Wang, Effects of the hydration ratio on the electrosorption selectivity of ions during capacitive deionization, Desalination, 399 (2016) 171-177.
[300] O. ul Haq, D.-S. Choi, J.-H. Choi, Y.-S. Lee, Carbon electrodes with ionic functional groups for enhanced capacitive deionization performance, Journal of Industrial and Engineering Chemistry, 83 (2020) 136-144.
[301] P. Liu, T. Yan, J. Zhang, L. Shi, D. Zhang, Separation and recovery of heavy metal ions and salt ions from wastewater by 3D graphene-based asymmetric electrodes via capacitive deionization, Journal of Materials Chemistry A, 5 (2017) 14748-14757.
[302] E.N. Guyes, T. Malka, M.E. Suss, Enhancing the ion-size-based selectivity of capacitive deionization electrodes, Environmental Science & Technology, 53 (2019) 8447-8454.
[303] Q. Li, Y. Zheng, D. Xiao, T. Or, R. Gao, Z. Li, M. Feng, L. Shui, G. Zhou, X. Wang, Faradaic electrodes open a new era for capacitive deionization, Advanced Science, 7 (2020) 2002213.
[304] K. Singh, Z. Qian, P. Biesheuvel, H. Zuilhof, S. Porada, L.C. de Smet, Nickel hexacyanoferrate electrodes for high mono/divalent ion-selectivity in capacitive deionization, Desalination, 481 (2020) 114346.
[305] D.I. Oyarzun, A. Hemmatifar, J.W. Palko, M. Stadermann, J.G. Santiago, Ion selectivity in capacitive deionization with functionalized electrode: Theory and experimental validation, Water Research X, 1 (2018) 100008.
[306] L. Wang, L. Deligniere, S. Husmann, R. Leiner, C. Bahr, S. Zhang, C. Dun, M.M. Montemore, M. Gallei, J.J. Urban, Selective Pb^{2+} removal and electrochemical regeneration of fresh and recycled FeOOH, Nano Research, 16 (2023) 9352-9363.
[307] J. Zhou, S. Xiang, X. Wang, D.-M. Shin, H. Zhou, Highly selective lithium extraction from salt lake via carbon-coated lithium vanadium phosphate capacitive electrode, Chemical Engineering Journal, 482 (2024) 148985.
[308] S. Sahin, J.E. Dykstra, H. Zuilhof, R.L. Zornitta, L.C. de Smet, Modification of cation-exchange membranes with polyelectrolyte multilayers to tune ion selectivity in capacitive deionization, ACS Applied Materials & Interfaces, 12 (2020) 34746-34754.
[309] P. Nativ, O. Lahav, Y. Gendel, Separation of divalent and monovalent ions using flow-electrode capacitive deionization with nanofiltration membranes, Desalination, 425 (2018) 123-129.

[310] L. Wang, S. Arnold, P. Ren, Q. Wang, J. Jin, Z. Wen, V. Presser, Redox flow battery for continuous and energy-effective lithium recovery from aqueous solution, ACS Energy Letters, 7 (2022) 3539-3544.
[311] J. Jiang, D.I. Kim, P. Dorji, S. Phuntsho, S. Hong, H.K. Shon, Phosphorus removal mechanisms from domestic wastewater by membrane capacitive deionization and system optimization for enhanced phosphate removal, Process Safety and Environmental Protection, 126 (2019) 44-52.
[312] R. Zhao, M. Van Soestbergen, H. Rijnaarts, A. Van der Wal, M. Bazant, P. Biesheuvel, Time-dependent ion selectivity in capacitive charging of porous electrodes, Journal of Colloid and Interface Science, 384 (2012) 38-44.
[313] R. Wang, Y. Zhang, K. Sun, C. Qian, W. Bao, Emerging green technologies for recovery and reuse of spent lithium-ion batteries - a review, Journal of Materials Chemistry A, 10 (2022) 17053-17076.
[314] M.-M. Titirici, R.J. White, N. Brun, V.L. Budarin, D.S. Su, F. Del Monte, J.H. Clark, M.J. MacLachlan, Sustainable carbon materials, Chemical Society Reviews, 44 (2015) 250-290.
[315] F.-W. Wellmer, J. Becker-Platen, Sustainable development and the exploitation of mineral and energy resources: a review, International Journal of Earth Sciences, 91 (2002) 723-745.
[316] M. Gao, C.-C. Shih, S.-Y. Pan, C.-C. Chueh, W.-C. Chen, Advances and challenges of green materials for electronics and energy storage applications: from design to end-of-life recovery, Journal of Materials Chemistry A, 6 (2018) 20546-20563.
[317] M. Joulié, R. Laucournet, E. Billy, Hydrometallurgical process for the recovery of high value metals from spent lithium nickel cobalt aluminum oxide based lithium-ion batteries, Journal of Power Sources, 247 (2014) 551-555.
[318] L. Sun, K. Qiu, Vacuum pyrolysis and hydrometallurgical process for the recovery of valuable metals from spent lithium-ion batteries, Journal of Hazardous Materials, 194 (2011) 378-384.
[319] C.C.B.M. De Souza, J.A.S. Tenório, Simultaneous recovery of zinc and manganese dioxide from household alkaline batteries through hydrometallurgical processing, Journal of Power Sources, 136 (2004) 191-196.
[320] Y. Yao, M. Zhu, Z. Zhao, B. Tong, Y. Fan, Z. Hua, Hydrometallurgical processes for recycling spent lithium-ion batteries: A critical review, ACS Sustainable Chemistry & Engineering, 6 (2018) 13611-13627.
[321] G.A.M. Ali, M.M. Yusoff, E.R. Shaaban, K.F. Chong, High performance MnO_2 nanoflower supercapacitor electrode by electrochemical recycling of spent batteries, Ceramics International, 43 (2017) 8440-8448.
[322] E.C. Vermisoglou, M. Giannouri, N. Todorova, T. Giannakopoulou, C. Lekakou, C. Trapalis, Recycling of typical supercapacitor materials, Waste Management & Research, 34 (2016) 337-344.
[323] G. Jiang, S.J. Pickering, Recycling supercapacitors based on shredding and mild thermal treatment, Waste Management, 48 (2016) 465-470.
[324] S. Dong, Z. Li, Z. Yi, H. Li, Y. Tian, S. Liu, Recycling of activated carbons from spent supercapacitors to refabricate improved supercapacitors, Journal of Energy Storage, 102 (2024) 114182.
[325] F. Wu, T. Zhao, Y. Yao, T. Jiang, B. Wang, M. Wang, Recycling supercapacitor activated carbons for adsorption of silver (I) and chromium (VI) ions from aqueous solutions, Chemosphere, 238 (2020) 124638.

[326] R. Seif, F.Z. Salem, N.K. Allam, E-waste recycled materials as efficient catalysts for renewable energy technologies and better environmental sustainability, Environment, Development and Sustainability, 26 (2024) 5473-5508.